

# Bioclimatic Design of Sustainable Campuses using Advanced Optimisation Methods

THÈSE N° 7756 (2017)

PRÉSENTÉE LE 29 SEPTEMBRE 2017

À LA FACULTÉ DE L'ENVIRONNEMENT NATUREL, ARCHITECTURAL ET CONSTRUIT  
LABORATOIRE D'ÉNERGIE SOLAIRE ET PHYSIQUE DU BÂTIMENT  
PROGRAMME DOCTORAL EN ENERGIE

ÉCOLE POLYTECHNIQUE FÉDÉRALE DE LAUSANNE

POUR L'OBTENTION DU GRADE DE DOCTEUR ÈS SCIENCES

PAR

**Silvia COCCOLO**

acceptée sur proposition du jury:

Prof. C. Ludwig, président du jury  
Prof. J.-L. Scartezzini, Prof. J. H. Kämpf, directeurs de thèse  
Prof. D. Pearlmutter, rapporteur  
Prof. E. Ng, rapporteur  
Dr F. Vigliotti, rapporteur



ÉCOLE POLYTECHNIQUE  
FÉDÉRALE DE LAUSANNE

Suisse  
2017





*L'essenza del costruire è il "far abitare».*  
*Il tratto essenziale del costruire è l'edificare luoghi, mediante il disporre i loro spazi.*  
*Solo se abbiamo la capacità di abitare, possiamo costruire.*  
Heidegger



A Carlo Nereo



# Acknowledgements

I would like to thank Prof. Scartezzini and Prof. Kaempf, for guiding this thesis, and providing the scientific rigor to my ideas.

I am thankful to the jury members Prof. Ludwig, Prof. Ng, Prof. Pearlmutter and Dr Vigliotti, for their attention in reading this thesis, as well as for their questions, comments and suggestions.

I am grateful to the EPFL Middle East and to Mr Danial, for their financial and human support, for providing all the instruments to realize this thesis and for creating a learning bridge between the two countries.

I would like to thank Dr Kriesi, for collaborating in the development of the Minergie standard for Tropical climate. I am grateful to Prof. Erell, for sharing the monitoring data, realized in the Sede Boqer campus, with us. A special thanks to Prof. Pearlmutter, for introducing me in the world of the “outdoor human comfort”, and for the fruitful discussions during these years. I am particularly thankful to Prof. Jennifer Vanos, for supporting the development of the COMFA\* budget, within CitySim.

I am thankful to Laurent, Pierre and Christian for their help, ideas and support during the set-up of the weather stations in Dubai. A special thanks to the IT team, being always kind in solving all my “informatics problems”. A special thanks to Barbara and Davide, for attentively reading and correcting this thesis, as well as to Suzanne and Marlene, for their help and support during this years.

It is my pleasure to thank all my colleagues at LESO-PB, making my working place pleasant and inspiring during these years.

Finally, un ringraziamento speciale alla mia famiglia, in particolare a mio papà, per avermi insegnato l’architettura, a mia mamma per incoraggiarmi ogni giorno, e mia sorella, per essermi sempre vicina. Al piccolo Carlo Nereo, per i suoi sorrisi, e a Marco, semplicemente.

*Lausanne, 10<sup>th</sup> July 2017*



# Abstract

Cities occupy 0.5% of the earth surface, but they consume 75% of worldwide energy, and they are responsible of 50% to 80% of CO<sub>2</sub> emissions. Cities are directly responsible for the climate change. However, they are the key for providing solutions to this problem. More specifically, a city comprises a very large number of microclimates, according to their urban and environmental design. A sustainable and liveable urban planning could well improve the urban environmental conditions by mitigating the energy fluxes of the city.

The objective of this thesis is to address the energy fluxes within the urban environment, in time and space. The study focuses on the improvement of the energy demand of buildings as well as the outdoor human comfort. To do so, we try to establish a new bridge between the biometeorology and the architecture and to find a simplified approach to bring this research into practice. More specifically, the human comfort is well addressed in the research domain but, due to its complexity, it is quite difficult to use it in the real practice. In order to overcome this problem, we introduce three new modules in the software CitySim Pro. CitySim is an urban energy modelling tool which is able to quantify, dynamically, the energy demand from a building scale to the city scale. A first module, developed in this doctoral thesis, focuses on the quantification of the outdoor human comfort by the Index of Thermal Stress (ITS) and the COMFA\* budget. The second module aims to understand the radiative environment by the calculation of the Mean Radiant Temperature (MRT). The third module focuses on the cooling potential of the vegetation and evaluates the shadings and the evapotranspiration provided by greenings. Based on the modules, Comfort Maps are designed, representing an important instrument to bring the research into practice: these maps are proposed as an effective way to share information between architects and municipalities, providing indications on the urban microclimatic conditions. Finally, the developed modules are used to optimize, using the hybrid CMA-ES/HDE evolutionary algorithm, the energy demand and the outdoor human comfort of two campuses: EPFL campus in Lausanne (Switzerland), and the Swiss International School (SISD) campus in Dubai (United Arab Emirates). On site monitoring, realized in the SISD campus, underlined the impact of the built environment, as well as the shadowing strategies, by punctual monitoring in five locations of the campus.

The results show that i) we should not limit an architectural design to a single building, but it is important to think and design at the district/ city scale. There is ii) a strong relationship between the energy demand of buildings and the outdoor human comfort, consequently both of them should be jointly addressed by architects and urban planners, focusing on the building and the “space between buildings” design. Finally, iii) a sound urban design should derive from the bioclimatology, transforming the climatic adversities into design opportunities. Finally, a list of practical recommendations is defined, providing a support for a sound architectural design in time, and space.

**Keywords:** outdoor human comfort, urban energy simulation, urban greenings.





# Résumé

Les villes occupent 0.5% de la surface de la Terre, mais elles consomment 75% de l'énergie mondiale et sont responsables de 50% à 80% des émissions de CO<sub>2</sub>. Les villes sont directement responsables du changement climatique. Néanmoins, elles sont aussi la clé pour fournir des solutions à ce problème. Plus précisément, une ville contient un grand nombre de microclimats, générés par leurs caractéristiques urbaines et environnementales. Une planification urbaine durable et vivable pourrait réellement améliorer les conditions environnementales urbaines en réduisant les flux d'énergie de la ville.

L'objectif de cette thèse est de traiter des flux d'énergie dans l'environnement urbain. L'étude se concentre sur l'amélioration de la demande énergétique des bâtiments et sur le confort humain à l'extérieur. Pour ce faire, nous cherchons à établir un pont entre la biométéorologie et l'architecture, et à trouver une manière simple d'appliquer cette recherche à la pratique. Plus précisément, le confort humain est largement couvert dans son domaine de recherche mais, de par sa complexité, il est difficile d'appliquer les résultats de la recherche. Pour résoudre ce problème, nous introduisons trois nouveaux modules dans le logiciel CitySim Pro. CitySim est un outil de modélisation urbaine qui permet de quantifier dynamiquement la demande énergétique des bâtiments à l'échelle urbaine. Un premier module, développé dans cette thèse, se concentre sur la quantification du confort humain à l'extérieur à l'aide de l'Indice de Stress Thermal (ITS) et du budget COMFA\*. Le second module vise à comprendre l'environnement radiatif par le calcul de la Température Radiante Moyenne (MRT). Le troisième module se concentre sur le potentiel de refroidissement de la végétation et évalue l'ombrage et l'évapotranspiration fournis par la verdure. Sur la base de ces modules, des Cartes de Confort sont générées, qui représentent un instrument important pour transmettre les résultats de la recherche à la pratique : la carte est la manière habituelle de partager des informations entre architectes et communes, en fournissant des indications sur les conditions microclimatiques. Finalement, les modules développés sont utilisés pour optimiser, en utilisant l'algorithme hybride évolutionnaire CMA-ES/HDE, la demande énergétique et le confort humain de deux campus : le campus de l'EPFL à Lausanne (Suisse) et le campus de l'École Suisse Internationale (SISD) à Dubaï (Émirats Arabes Unis). Des mesures ponctuelles réalisées à cinq emplacements du campus SISD soulignent l'impact de l'environnement bâti, ainsi que des stratégies de refroidissement microclimatique.

Les résultats montrent que i) la conception architecturale ne devrait pas se limiter à un seul bâtiment, mais que l'on doit penser et concevoir à l'échelle du quartier ou de la ville ; ii) il y a une corrélation forte entre la demande énergétique des bâtiments et le confort humain à l'extérieur, par conséquent ces deux sujets devraient être considérés par les architectes et urbanistes, en se concentrant sur la conception des bâtiments et de l'espace inter-bâtiments ; iii) finalement, la pratique urbaine devrait se baser sur la bioclimatologie et transformer les difficultés climatiques en opportunités de conception. Finalement, on propose une liste de recommandations pratiques aidant à l'élaboration d'un design architectural adapté aux principes bioclimatiques, dans le temps et dans l'espace.

**Mots-clés :** confort humain à l'extérieur, simulation énergétique à l'échelle urbaine, écologie urbaine.



# Nomenclature

$A$	(m)	Altitude of the site
$A_{du}$	(m <sup>2</sup> )	Dubois surface area
$A_{eff}$	(-)	Reduction factor based on the radiative area of a man
$A_{pe}$	(m <sup>2</sup> )	Outer surface area of pedestrian
$C$	(W), (W·m <sup>-2</sup> )	Environmental exchanges due to convection
$C_b$	(-)	Constant for height correction, as function of the barometric altitude
$c_c$	(-)	Clothing coefficient
$c_p$	(kJ·kg <sup>-1</sup> ·K <sup>-1</sup> )	Specific heat of the air
$D$	(kPa)	Vapour deficit of air
$d$	(m)	Diameter of the cylinder
$E$	(W)	Cooling rate produced by sweat
$e_{\theta_a}$	(kPa)	Vapour pressure of the air
$e_{s,\theta_a}$	(kPa)	Saturation vapour pressure of the air
$E_i$	(W·m <sup>-2</sup> )	Evaporative heat loss through skin diffusion
$E_m$	(W·m <sup>-2</sup> )	Maximal evaporative heat loss through skin diffusion
$E_{max}$	(W)	Evaporative capacity of the air
$E_s$	(W·m <sup>-2</sup> )	Evaporative heat loss through perspiration
$E_{s+i}$	(W·m <sup>-2</sup> )	Evaporative heat loss
$f$	(-)	Cooling efficiency of sweating
$G$	(W)	Soil heat flux
$g$	(m·s <sup>-2</sup> )	Earth-surface gravitational acceleration
$g_1$	(W·m <sup>-2</sup> ·K <sup>-1</sup> )	Conductance to the first considered ground layer at temperature $\theta_1$
$g_{Ha}$	(mol·m <sup>-2</sup> ·s <sup>-1</sup> )	Heat conductance
$g_{Hr}$	(mol·m <sup>-2</sup> ·s <sup>-1</sup> )	Sum of boundary layer radiative conductance
$g_r$	(mol·m <sup>-2</sup> ·s <sup>-1</sup> )	Radiative conductance
$g_v$	(mol·m <sup>-2</sup> ·s <sup>-1</sup> )	Conductance of vapour
$g_{va}$	(mol·m <sup>-2</sup> ·s <sup>-1</sup> )	Boundary layer conductance for vapour
$g_{vs}^{ab}$	(mol·m <sup>-2</sup> ·s <sup>-1</sup> )	Stomatal conductance
$H$	(m)	Height of the person
$h$	(°)	Sun height
$h_b$	(-)	Correction for the heat loss consumed through breathing
$h_c$	(W·m <sup>-2</sup> ·K <sup>-1</sup> )	Heat transfer coefficient
$I$	(W·m <sup>-2</sup> )	Solar irradiation
$I_{cl}$	(clo)	Intrinsic clothing insulation
$ITS$	(W)	Index of Thermal Stress
$j$	(-)	Constant for seasonal correction
$k$	(m <sup>2</sup> ·s <sup>-1</sup> )	Thermal diffusivity of the air
$K_{b(abs)}$	(W)	Sum of direct beam radiation absorbed per each surface of pedestrian
$K_{d(abs)}$	(W)	Sum of diffuse solar radiation absorbed per each surface of pedestrian
$K_{dir}$	(W·m <sup>-2</sup> )	Direct short wave radiation impinging the human body
$K_{dif}$	(W·m <sup>-2</sup> )	Diffuse short wave radiation impinging the human body
$K_h$	(W·m <sup>-2</sup> )	Indirect radiation incident on the body, reflected from the horizontal surfaces

$K_v$	$(W \cdot m^{-2})$	Indirect radiation incident on the body, reflected from the vertical surfaces
$L_{a(abs)}$	$(W)$	Sum of atmospherical longwave radiation absorbed per each surface of pedestrian
$L_d$	$(W \cdot m^{-2})$	Longwave radiation incident on the human body emitted downward by the sky
$L_{g(abs)}$	$(W)$	Sum of ground surface longwave radiation absorbed per each surface of pedestrian
$L_h$	$(W \cdot m^{-2})$	Longwave radiation incident on the human body emitted by the horizontal surfaces
$L_{hv}$	$(J \cdot kg^{-1})$	Latent heat of vaporization
$L_i$	$(W \cdot m^{-2})$	Longwave radiation received by the environment
$L_s$	$(W \cdot m^{-2})$	Longwave radiation emitted by the body to the environment
$L_v$	$(W \cdot m^{-2})$	Longwave radiation incident on the human body emitted by the vertical surfaces
$LW_{em}$	$(W \cdot m^{-2})$	Longwave radiation emitted by the surface
$LW_{net}$	$(W \cdot m^{-2})$	Balance between the longwave radiation received from the environment and the emitted one
$LW_{rec}$	$(W \cdot m^{-2})$	Longwave radiation received from the environment
$M$	$(W), (W \cdot m^{-2})$	Body's metabolic rate
$M_a$	$(kg \cdot mol^{-1})$	Molar mass of dry air
$M_h$	$(W \cdot m^{-2})$	Metabolic heat
$MRT$	$(^{\circ}C)$	Mean Radiant Temperature
$n$	$(-)$	Number of days
$Nu$	$(-)$	Nusselt number
$P_a$	$(kPa)$	Air pressure
$Pr$	$(-)$	Prandtl number
$p_o$	$(kPa)$	Sea level standard atmospheric pressure
$Pv_a$	$(mm \text{ Hg})$	Vapour pressure of the air
$Pv_s$	$(kPa)$	Saturation vapour pressure
$Q_{et}$	$(W)$	Energy required for evapotranspiration
$q_a$	$(kg \text{ of water vapour per } kg \text{ of moist air})$	Specific humidity of air
$q_s$	$(kg \text{ of water vapour per } kg \text{ of moist air})$	Specific humidity of skin
$R$	$(J \cdot kg^{-1} K^{-1})$	Specific gas constant
$r_a$	$(s \cdot m^{-1})$	Boundary air resistance
$R_{abs}$	$(W \cdot m^{-2})$	Absorbed short and long wave radiation
$r_{av}$	$(s \cdot m^{-1})$	Resistance of vapour transfer by air
$r_c$	$(s \cdot m^{-1})$	Clothing resistance
$r_{co}$	$(s \cdot m^{-1})$	Static clothing resistance
$r_{cv}$	$(s \cdot m^{-1})$	Resistance of vapour transfer by clothing
$r_{cv0}$	$(s \cdot m^{-1})$	Static clothing vapour resistance
$R_e$	$(-)$	Reynolds number
$R_{ecl}$	$(m^2 kPa \cdot W^{-1})$	Total evaporative resistance of clothing ensemble
$r_i$	$(s \cdot m^{-1})$	Bulk stomatal resistance
$R_n$	$(W)$	Environmental exchanges due to radiation
$R_{RT}$	$(W \cdot m^{-2})$	Radiation absorbed by the pedestrian
$r_t$	$(s \cdot m^{-1})$	Body tissue resistance
$R_s$	$(-)$	Reflectance of the surface
$r_{tv}$	$(s \cdot m^{-1})$	Resistance of vapour transfer by tissues
$RH$	$(\%)$	Relative humidity
$r_s$	$(s \cdot m^{-1})$	Bulk surface resistance
$s$	$(^{\circ}C^{-1})$	Slope of saturation mole fraction function
$S_{sun}$	$(min)$	Measured sunshine duration
$S_{str}$	$(W \cdot m^{-2})$	Mean radiant flux density
$Sc$	$(-)$	Schmidt number
$SW_{rec}$	$(W \cdot m^{-2})$	Shortwave radiation received from all directions

$T(\vec{\sigma})$	(K)	Absolute temperature of the surface in the direction of the infinitesimal solid angle $\vec{\sigma}$
$T_a$	(K)	Ambient air temperature
$T_{env}$	(K)	Equivalent temperature for the surrounding environment
$T_{grad}$	(K)	Ground temperature
$T_{kv}$	(K)	Virtual temperature
$T_s$	(K)	Surface temperature
$T_{sky}$	(K)	Sky temperature
$u$	( $m^2 \cdot s^{-1}$ )	Kinematic viscosity of the air
$v$	( $m \cdot s^{-1}$ )	Horizontal wind speed
$V$	( $m \cdot s^{-1}$ )	Wind speed
$v_a$	( $m \cdot s^{-1}$ )	Activity velocity
$v_r$	( $m \cdot s^{-1}$ )	Effective air velocity
$W$	(W)	Metabolic energy transformed in mechanical work
$W_p$	(kg)	Weight of the person
$WCT$	( $^{\circ}C$ )	Wind chill temperature

### Greek Letter

$\alpha_s$	(-)	Albedo of skin and clothing
$\alpha_{LW\_leaf}$	(-)	Long wave absorptivity of leaves
$\alpha_{SW\_leaf}$	(-)	Short wave absorptivity of the leaves
$\gamma$	( $kPa \cdot ^{\circ}C^{-1}$ )	Psychrometric constant
$\gamma^*$	( $^{\circ}C^{-1}$ )	Apparent psychrometric constant
$\delta$	( $^{\circ}$ )	Geocentric declination
$\epsilon$	(-)	Ratio molecular weight of water vapor and the dry air
$\epsilon_p$	(-)	Emissivity of the environmental surfaces
$\epsilon_s$	(-)	Emissivity of the body
$\epsilon_{sky}$	(-)	Sky emissivity
$\Delta\theta_a$	( $kPa \cdot ^{\circ}C^{-1}$ )	Saturation slope vapor pressure curve at the air temperature
$\theta_a$	( $^{\circ}C$ )	Air temperature
$\theta_c$	( $^{\circ}C$ )	Core's temperature
$\theta_d$	( $^{\circ}C$ )	Dew point temperature
$\theta_o$	( $^{\circ}C$ )	Leaf Temperature
$\theta_{sf}$	( $^{\circ}C$ )	Surface temperature of a person
$\theta_{sk}$	( $^{\circ}C$ )	Skin surface temperature
$\theta_w$	( $^{\circ}C$ )	Wet temperature
$\kappa$	( $W \cdot m^{-1}K^{-1}$ )	Thermal conductivity of the surface
$\Lambda$	(-)	Evapotranspiration source term
$\lambda$	( $W \cdot kg^{-1}$ )	Latent heat of vaporization
$\rho$	( $kg \cdot m^{-3}$ )	Density of the air
$\sigma$	( $W \cdot m^{-2}K^{-4}$ )	Stefan-Boltzmann constant
$\varphi$	( $^{\circ}$ )	Latitude of the site
$\Psi$	(W)	Evapotranspiration heat transfer coefficient
$\Omega_{p,grad}$	(sr)	Projected solid angle of the ground on the considered surface plane
$\Omega_{p,sky}$	(sr)	Projected solid angle of the unobstructed sky on the considered surface plane



# Contents

<b>Acknowledgements</b> .....	<b>v</b>
<b>Abstract</b> .....	<b>vii</b>
<b>Résumé</b> .....	<b>ix</b>
<b>Nomenclature</b> .....	<b>xi</b>
<b>Contents</b> .....	<b>xv</b>
<b>Chapter 1 Introduction</b> .....	<b>1</b>
1.0 Context .....	1
1.1 State of the art .....	2
1.1.1 Bioclimatic design .....	2
1.1.2 Sustainable campuses .....	4
1.1.3 Advanced optimisation methods .....	6
1.2 Problem statement .....	7
1.2.1 Thesis structure.....	8
<b>Chapter 2 Outdoor Human Comfort</b> .....	<b>11</b>
2.0 Introduction.....	11
2.1 Pedestrian design with CitySim Pro .....	14
2.2 Index of Thermal Stress .....	15
2.3 COMFA* budget .....	19
2.4 Sensitivity analysis of COMFA* and ITS models .....	24
2.4.1 COMFA* budget results.....	25
2.4.2 Index of Thermal Stress results.....	27
2.5 Mean Radiant Temperature.....	29
2.5.1 MRT model validation through on-site monitoring on the EPFL campus, Lausanne .....	31
2.5.2 MRT model validation through on-site monitoring in the SISD campus, Dubai .....	36
2.6 Conclusions and future outlook .....	42
<b>Chapter 3 Urban Greening</b> .....	<b>45</b>
3.0 Introduction.....	45
3.1 Modelling trees .....	46
3.1.1 Physical model of trees.....	47
3.1.2 Validation of the tree model by on-site monitoring .....	57

3.2	Modelling the evapotranspiration potential of greening .....	59
3.2.1	Physical model of evapotranspiration .....	60
3.2.2	Validation of the evapotranspiration model by on-site monitoring.....	62
3.3	Conclusions and future outlook .....	72
<b>Chapter 4</b>	<b>Energy performance and outdoor comfort of a campus in a temperate climate.....</b>	<b>73</b>
4.0	Introduction.....	73
4.1	Energy model of the EPFL Campus .....	74
4.1.1	Set-up of the model .....	76
4.1.2	Validation of the model .....	78
4.1.3	Site refurbishments in current and future climatic scenarios.....	79
4.1.4	Indoor human comfort .....	83
4.1.5	Energy demand in conjunction with the CIM model.....	86
4.2	Outdoor human comfort .....	92
4.2.1	Actual Sensation Vote and COMFA* .....	93
4.2.2	COMFA* with a Canopy Interface Model .....	99
4.2.3	Comfort Map of the EPFL campus .....	102
4.3	Conclusions and future outlook .....	108
<b>Chapter 5</b>	<b>Energy performance and outdoor comfort of a campus in a hot and arid climate .....</b>	<b>111</b>
5.1	Introduction.....	111
5.2	Energy model of the SISD campus .....	113
5.2.1	Climatic analysis of the site .....	113
5.2.2	Energy optimisation workflow.....	115
5.2.3	Sensitivity analysis .....	119
5.3	Outdoor Human Comfort .....	128
5.3.1	Outdoor human comfort and metabolic activity .....	128
5.3.2	Outdoor human comfort and urban landscape .....	132
5.3.3	Comfort Map of the SISD campus.....	140
5.4	Monitoring of the outdoor environment.....	149
5.4.1	Set-up of the weather stations .....	149
5.4.2	Monitoring the outdoor environment .....	155
5.5	Conclusions and future outlook .....	170
<b>Chapter 6</b>	<b>Hybrid Algorithm Optimization with Heuristics.....</b>	<b>173</b>
6.1	Introduction.....	173
6.2	The EPFL Campus .....	174
6.2.1	Zone-A_ Optimisation of the energy demand for heating and cooling and the outdoor human comfort.....	176



6.2.2	Zone-B_ Optimisation of the energy demand for heating and cooling .....	185
6.3	The Swiss International School Campus in Dubai .....	197
6.4	Conclusions and future outlook .....	209
<b>Chapter 7</b>	<b>Conclusions .....</b>	<b>211</b>
7.1	Bioclimatic and sustainable design for temperate climate .....	212
7.2	Bioclimatic and sustainable design for hot arid climate.....	215
7.3	Future outlook.....	220
<b>A.</b>	<b>Annex.....</b>	<b>223</b>
A.1	Mean Radiant Temperature .....	223
A.2	COMFA* Budget .....	223
A.3	Index of Thermal Stress .....	225
A.4	Tree model .....	226
<b>B.</b>	<b>Annex.....</b>	<b>229</b>
B.1	Buildings of the first stage of construction .....	229
B.2	Polydôme .....	230
B.3	LESO solar experimental building.....	231
B.4	Swiss International School of Dubai.....	233
B.5	Typical building in UAE .....	235
B.6	Green building regulation .....	235
B.7	Results from the optimization .....	235
B.8	Optimization_ Zone A .....	236
B.9	Optimization_ Zone B .....	237
B.10	Optimization SISD.....	237
<b>References .....</b>		<b>239</b>
<b>List of Figures .....</b>		<b>257</b>
<b>List of Tables.....</b>		<b>265</b>
<b>Curriculum Vitae.....</b>		<b>269</b>



# Chapter 1 Introduction

## 1.0 Context

Cities occupy 0.5% of the earth surface (Santamouris, 2015), but consume 75% of worldwide energy and are responsible for 50% to 80% of CO<sub>2</sub> emissions (UN HABITAT, 2012). In the present century, for the first time in history, urban population has exceeded rural population, and future trends suggest that in 2050 70% of the world population will live in cities. Asia and Africa will be most affected by urbanization in the next decades, as their urban population is expected to pass respectively from 40% to 56% and from 48% to 64%, by 2050 (ONU, 2014). It is evident that cities carry significant responsibility for climate change and hence are key for solving this problem. Consequently, we are obliged to rethink our way of living and to introduce new technologies and land policies to reduce our energy footprint. Following the Sustainable Innovation Forum COP 21 held in Paris in December 2015, our common objective is to harness climate change in order to guarantee a maximal increase in world temperature of 1.5°C, as defined by Article 2 (United Nations, 2015).

As mentioned above, urban planning has an essential role to play in the effort to reduce the impact of climate change; it can not only improve the energy performance of buildings, but can also positively impact outdoor human comfort and health. An interdisciplinary approach is essential, connecting all the aspects that characterize a city, from the urban climate to the energy performance of buildings, including cultural and social aspects. In this doctoral thesis, two main aspects are addressed: the energy performance of buildings and the outdoor human comfort. There is a clear relationship between the two: the energy demand of buildings is related to the climate, the urban microclimate and consequently the outdoor human comfort. The Mean Radiant Temperature and the outdoor human comfort are two ways to visualize urban microclimate. Both of them are investigated by biometeorology, an interdisciplinary science, which studies the interactions between atmospheric processes and living organisms (plants, animals and humans); the scope of this discipline is to understand how the weather and climate impact the well-being of all creatures (Gosling et al., 2014). Consequently, when addressing urban design, it is essential on one hand to quantify the microclimate (by biometeorology), and on the other, to correctly design the urban architectural environment.

If a precise definition exists for biometeorology, it is quite difficult to define architecture: in the Oxford dictionary it is defined as the art or practice of designing and constructing buildings (OUP, 2017). But more than a hundred different definitions exist (Quintal, 2016), considering this discipline not just as the capacity to build something, but a symbol of an epoch, as well as of human kind. As an example, Norman Foster describes architecture as “*an expression of values – the way we build is a reflection of the way we live*” (Tholl, 2014). Additionally, it is evident that architecture is interdisciplinary, linking history, design and science. Already Vitruvio, in his book *De Architectura*, described architecture with three words: *firmitas*, *utilitas* and *venustas* (Vitruvio, n.d.), linking solidity to utility and to beauty. Architecture is movement, something becoming and, as described by Richard Meier: “*Architecture is vital and enduring because it contains us; it describes space, space we move through, exist in and use*”. Finally, architecture is part of us, as we live in architecture, and as said by Philippe Daverio: “*Architecture is the only art that you can't help but feel. You can avoid paintings, you can avoid music, and you can even avoid history. But good luck getting away from architecture*” (Bates, 2014). The direct link between biometeorology and architecture is evident: each building is designed in a certain place, and interacts with the environment. The need of a design that is adapted to climatic conditions is addressed by bioclimatic design. One of the best examples of bioclimatic design is vernacular architecture. One of the biggest research projects in the bioclimatic field was conducted by Baruch Givoni, who proposes guidelines for bioclimatic design worldwide in his books, from building (Givoni, 1969) to urban scale (Givoni, 1998a) (Givoni, 1989). Another milestone in this topic was the work realized by Olgyay

(Olgyay, 1962), defining architecture as the point of convergence between climatology, biology and technology (Figure 1.1).

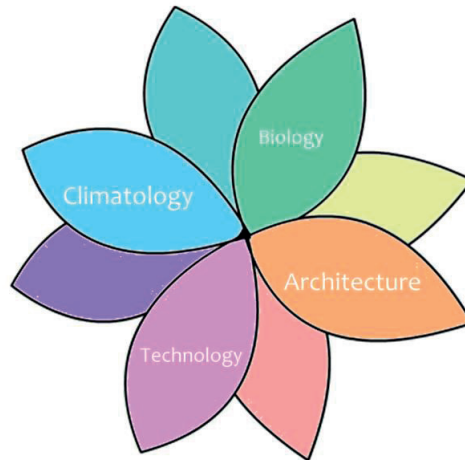


Figure 1.1 Biology, Architecture, Technology and Climatology. Adapted from (Olgyay, 1962).

The main problem in current practice is the difficulty to correlate the disciplines of architecture and bioclimatology: a lot of research is on-going concerning bioclimatology (Matzarakis and Fröhlich, 2015) (Vanos et al., 2012b) (Klemm et al., 2015) (Ng and Cheng, 2012) (Pearlmutter et al., 2014) (de Abreu-Harbich et al., 2015), but it is difficult, for an architect, to address it in a practical work, from architectural to urban scale.

## 1.1 State of the art

As stated in the previous section, the objective of this PhD thesis is to improve the sustainability of a city district by addressing the energy performance of buildings and the outdoor human comfort. These issues have already been condivided by the scientific community, but the novelty of this thesis is to propose a methodology to dynamically quantify the energy performance of buildings as well as the outdoor human comfort, using an urban energy modelling tool (i.e. CitySim Pro). A university campus in Lausanne, Switzerland, and a school campus in Dubai were studied as examples of urban architectural typology. In order to understand the issues addressed in this thesis, the following paragraphs present the state of the art of bioclimatic design, the studied campuses and advanced optimization methods. Additionally, a comprehensive state of the art is proposed at the beginning of each chapter of the thesis.

### 1.1.1 Bioclimatic design

Bioclimatic design considers the built environment as a function of climate; vernacular architecture is an excellent example of bioclimatic design, as it is built in accordance with the site, maximizing the use of on-site natural resources and minimizing energy needs (Shemirani, Seyed Majid Mofidi Nikghadam, 2013). Traditional architecture, especially in extreme climates, is usually more efficient than modern architecture. Several studies in hot arid climate show that the ancient city districts are more energy efficient as well as better designed for pedestrians compared to new ones (Johansson, 2006) (Coccolo et al., 2016c) (Taleb and Abu-Hijleh, 2013). Traditional architecture (Figure 1.2) is a historical evolution of bioclimatic principles, in accordance with the constructor's manual skills and technology. The field of bioclimatic design accordingly covers several disciplines: the development and planning of cities, urbanism (OUP, 2017), as well as the building design, architecture.

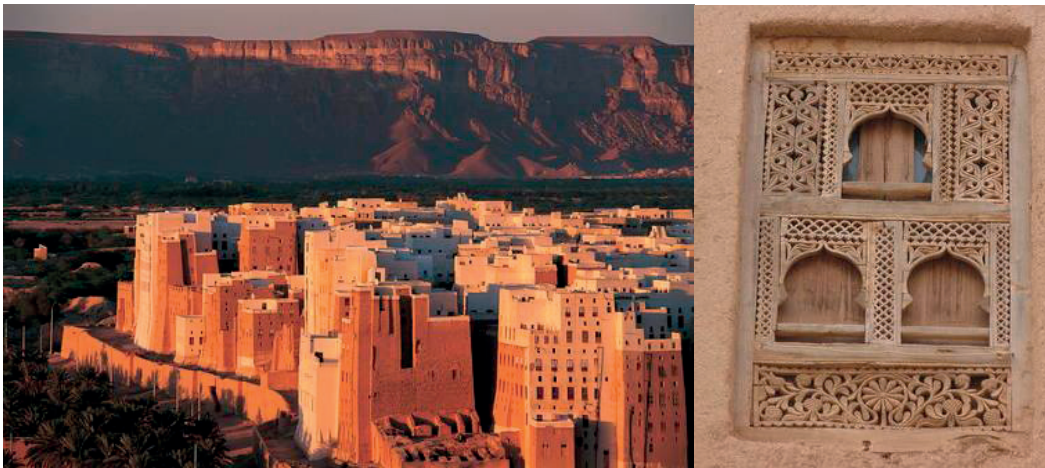


Figure 1.2 Old Walled City of Shibam (Yemen). Photos by Jean-Jacques Gelbart (left) and Aneta Ribarska (right) (UNESCO, 2017)

In order to apply bioclimatic design at all scales, it is essential to understand the city as well as its microclimate. A clear manifestation of urbanization is the Urban Heat Island effect (UHI), which nowadays represents a challenge for the sustainable urban development of cities. The UHI is defined as the air temperature difference between a city  $T_u$  and the rural area  $T_r$  ( $\Delta T_{u-r} = T_u - T_r$ ). This phenomenon varies in each urban environment, with time and space (Ng, 2010) and is a function of the meteorological and urban characteristics (Oke, 1987). A direct relationship was found between the UHI, the regional wind speed and the logarithm of the city size, as well as between the UHI and the urban density, expressed as a function of the height-width ratio (Oke, 1973). The urban heat island phenomenon is characterized, mainly, by the following elements: high absorption of shortwave solar radiation, high storage of sensible heat, anthropogenic heat, reduction in longwave radiation losses, low evapotranspiration and low sensible heat losses (Oke, 1987). It is directly related to the Urban Cool Island effect (UCI), which was first identified, within the UHI, in 1818 by Luke Howard (Howard, 1818), by monitoring the daytime reduction of the air temperature in the city of London. Several studies present the daily variation of the UCI phenomenon in Hong Kong (Ng, 2010), Putrajaya in Malaysia (Morris et al., 2016) and Singapore (Winston et al., 2006). The Urban Heat Island affects the energy performance of buildings, by increasing the energy required for cooling (Kolokotroni et al., 2006) and reducing the heating demand by 30% to 50% in the case study of Athens (Santamouris et al., 2001). It also affects the peak electricity demand during the summer time (Santamouris et al., 2015). Based on previous studies realized worldwide, the UHI impacts the energy performance of buildings by increasing their total energy demand (heating and cooling) by 11% and the global energy per unit of city surface by  $2.4 \text{ kWh}\cdot\text{m}^{-2}$ , which corresponds to  $0.74 \text{ kWh}\cdot\text{m}^{-2}$  per degree of UHI intensity, or 70 kWh pro capita per degree of UHI intensity (Santamouris, 2014). On the other side, the UHI considerably impacts people's wellbeing and health, because it enhances the intensity of heat wave phenomena. Previous studies showed that heat related mortality is higher in the city center compared to the rural environment (Tan et al., 2010) (Lowe, 2016). The relationship between heat related mortality and air temperature is a U-shaped curve, that rapidly exceeds the threshold temperature, which corresponds to  $29.4^\circ\text{C}$  in Mediterranean cities and  $23.3^\circ\text{C}$  in North-continental ones (Santamouris & Kolokotsa, 2016) (Baccini et al., 2008). Several strategies to reduce the urban heat island phenomenon exist, varying as a function of the climate and urban morphology: for instance the use of cool materials, characterized by high solar reflectance and high infrared emittance (Santamouris et al., 2011) or photovoltaic pavements, able to decrease surface temperature by 8K and the air temperature by 0.8K (Efthymiou et al., 2016). Good urban planning improves the natural ventilation in the built environment and the daylight availability in buildings (Ng, 2010), and maintains liveable outdoor conditions through smart landscape design, including parks, grass, trees, green roofs and vertical greening (Santamouris & Kolokotsa, 2016). Landscaping has a great potential in decreasing extreme climatic conditions, and improving the outdoor thermal comfort (Brown, 2011) by moderating the air temperature through shadowing and the evapotranspiration process (Shashua-Bar et al., 2011). The impact of vegetation varies as a function of its density: a case study in the

city of Athens shows that a park can reduce the air temperature inside its borders by 3.3 to 3.8K, and influence the neighborhood up to 300 m from its borders (Skoulika et al., 2014). This phenomenon is called the Park Cool Island effect (PCI), and is related to the shading from vegetation that reduces the surface temperature, the evapotranspiration process as well as the larger sky view factor (compared to the built environment) that allows heat dissipation during nighttime through radiative cooling (Erell et al., 2011a). The magnitude of the PCI is related to the type of vegetation, the size of the park, the topography of the city and the wind speed (Chow et al., 2011): a single tree impacts just its surroundings, while a cluster of trees or a park is able to extend its thermal impact to the neighborhoods (Streiling and Matzarakis, 2003) (Ng and Ren, 2015). Part of the PCI effect is related to the presence of grass, which has a great potential to decrease the UHI phenomena, as well as to improve outdoor human comfort through the evaporative cooling potential (by evapotranspiration) and its lower surface temperature, which means a reduction in the longwave radiation received by pedestrians (Erell et al., 2011a). Evapotranspiration contributes to the so called “oasis phenomenon”, described through the Bowen Ratio ( $\beta$ ) as the ratio of sensible heat flux to the latent heat flux (Santamouris & Asimakopoulos, 2001): the Bowen Ratio in a desert area figures larger than 10, 5 in the built environment and 0.5-2 in vegetative canopies (Taha, 1997). A low Bowen Ratio corresponds to a lower ambient temperature, and consequently an improvement of the urban microclimate (Ng, 2010). Finally, the positive impact of vegetation on the built environment is expressed by Figure 1.3, showing the relationship between plants, climate and buildings. Climate and buildings are in conflict with each other, and energy is required to mitigate them. In Figure 1.3 (left), plants positively interact with climate and buildings: the overlapped shaded area between them decreases, consequently less energy is required to mitigate the conflict between them. Figure 1.3 (right) shows the situation in which less plants are present in the system; consequently their influence is lower, and more energy is required to mitigate the conflict climate/buildings (Ng, 2010).

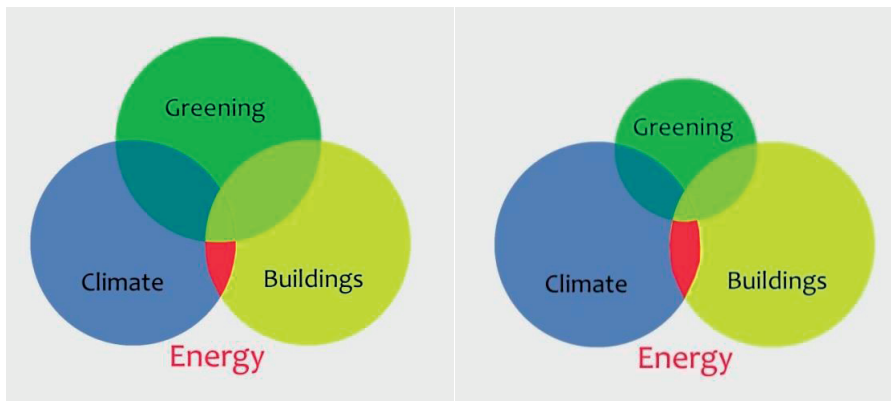


Figure 1.3 Energy relationship between plants, buildings and climate. Adapted from (Ng, 2010).

### 1.1.2 Sustainable campuses

The term sustainability was firstly introduced in the Brundtland Report (1987) as “*a development that meets the needs of the present, without compromising the future generations*”. Sustainability is commonly characterized by three interconnected aspects: society, economy and environment (Theis and Tomkin, 2013). Furthermore, a campus is an architectural typology, which is similar to a city district due to its dimension (number of buildings), autonomy (energy and functional) and heterogeneity (activities and population). Sustainable campuses are places where architecture and nature are integrative parts of the educational process of learning (Campos, 2008). In the last twenty years, there has been rising interest in campus typology (Figure 1.4), providing guidelines for the design of sustainable campuses, addressing economic, social and environmental aspects (Hasapis et al., 2017) (Cruz et al., 2017) (Jain et al., 2017) (Liu et al., 2017). In order to illustrate the rising interest in this urban typology, just during the first months of 2017 (retrieved the 6<sup>th</sup> March 2017), more than 20 papers addressed the topic of sustainable campuses.



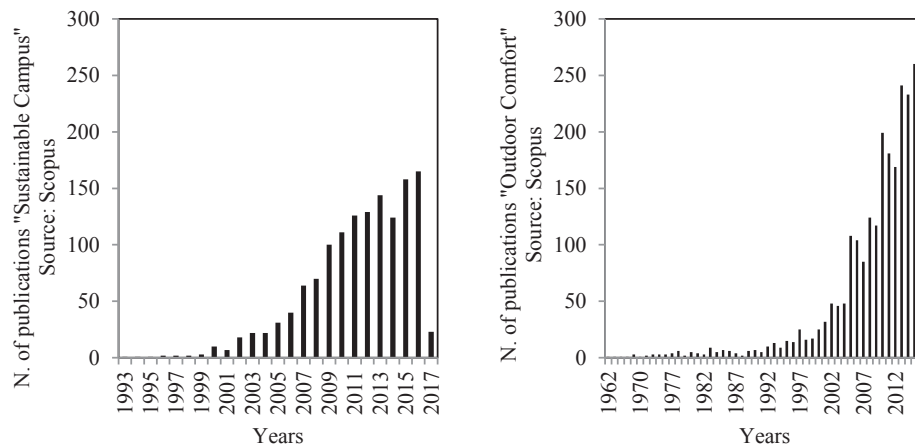


Figure 1.4 Number of publications available on Scopus, retrieved the 6<sup>th</sup> of March 2017. Keyword: “Sustainable campus” (left) and “Outdoor Comfort” (right).

As stated above in this doctoral thesis, the environmental aspect of sustainability is addressed, including energy performance and outdoor human comfort from building to campus scale. Considering that we are living in an urbanized world, it is obvious that the study of a single building should be directly related to urban city models. In order to do so, two approaches exist: top-down and bottom-up. Top-down models are based on the aggregation of empirical analyses (energy demand, CO<sub>2</sub> emissions, financial aspects etc.) in order to quantify the energy performance of single buildings (Kavgic et al., 2010). By contrast, bottom-up models estimate the energy consumption of an individual or a group of buildings; the results are then extrapolated in order to represent a city, a region or a nation (Swan and Ugursal, 2009). Bottom-up energy modelling has a key role in the estimation of the energy performance of buildings, from the district to the city scale. Urban Building Energy Modelling (UBEM) is a nascent field based on the application of physical models (heat and mass transfer) inside and outside a group of buildings, which is used to predict their energy performance as well as the indoor and outdoor environmental conditions (Reinhart and Davila, 2016). Naturally, when focusing on a large scale, it is essential to provide input data that are as precise as possible, but due to the complexity of the urban environment, not all data can be addressed completely. Based on a study performed in the city of Ludwigsburg (Germany), the inputs can be categorized into three typologies: i) *Must-have*, ii) *Relevant-to-have* and iii) *Nice-to-have*. Among the *Must-have*, we can find the year of construction, function, and refurbishment and residence type: these input data, if wrongly entered in models, can cause a major error of up to 30% (Nouvel et al., 2017). Several software programs exist to quantify the energy performance of edifices, from the building to the city scale: CitySim (Robinson et al., 2009), UMI (Urban Modelling Interface) (Reinhart et al., 2013) and SIMSTADT (Nouvel et al., 2015). Unlike in Building Energy Modelling (BEM), in Urban Building Energy Modelling, each urban simulation engine generally has its own tailor-made data-model, and there is nowadays no way of communication between these models. A first step to address this issue is the creation of an Urban Energy Information standard, such as the Application Domain Extension (ADE) of the CityGML urban information model. CityGML is a XML-based open data model for the storage and exchange of virtual 3D city models, issued by the Open Geospatial Consortium (OGC) (Gröger et al., 2012). CityGML is organized around a CityGML core model, extended by Application Domain Extensions (ADE) for different purposes such as: geometry, construction, occupancy and energy systems (Nouvel et al., 2013) (Nouvel et al., 2015) (Coccolo and Kämpf, 2015).

As stated above, we have also considered outdoor human comfort as being an integral part of environmental sustainability. The outdoor human comfort is a major factor in the evaluation of the liveability of a city. Sound outdoor planning and design can foster both thermal comfort and human health in an urban environment. As for the campus typology, the issue has received increasing attention during the last ten years (Figure 1.4). Human thermal comfort depends on physical factors, such as geographical location, local climate and the built

environment. A city comprises a very large number of microclimates, one for each urban building structure (Mayer and Höpfe, 1987). The direct connection between the indoor and the outdoor human comfort, as well as the energy demand of buildings is quite evident: due to the stressful outdoor climatic conditions, people's reliance on air-conditioned spaces (both heating and cooling) can be exacerbated in closed environments (e.g. buildings or vehicle). It is consequently important to focus on both parameters, in order to improve both indoor and outdoor environmental conditions, encouraging people to live the outdoor spaces. Different models exist to quantify outdoor human comfort (Coccolo et al., 2016a), mostly based on the energy balance between a person and his (her) surroundings, such as the Physiological Equivalent Temperature (Höppe, 1999), the COMFA\* model (Kenny et al., 2009a), the Standard Effective Temperature (Spagnolo and De Dear, 2003) and the Index of Thermal Stress (Pearlmutter et al., 2006). Among these standards, the Index of Thermal Stress (ITS) has already been validated for hot climates: a sound correlation with pedestrians' perceived thermal sensations was determined (Pearlmutter et al., 2014). The study of outdoor human comfort, especially in extreme climates, can help building and urban planners to promote a more conscious urban design, able to offer a comfortable outdoor environment for human activities. Several software programs exist to quantify the energy performance of buildings, from the edifice (NREL, 2017) (Klein, 2010) to the city scale (Reinhart et al., 2013) (Nouvel et al., 2015), as well as the microclimate and the outdoor human comfort (Huttner, 2012) (Lindberg et al., 2008) (Matzarakis et al., 2007); none of them can fully describe the energy fluxes of the urban metabolism, involving on one side, the energy performance of buildings and on the other side, the outdoor microclimate and human comfort. Naturally, sound examples of bioclimatic urban/ district design exist, and can be labelled under the name Eco-Cities (Joss, 2009); as an example the Masdar campus (Figure 1.5), designed by Foster & Partners, in Abu Dhabi (Nader, 2009) (Janajreh et al., 2013) (Reiche, 2010). But, when addressing sustainability, it is essential to work on built areas, as well as open ones: the open areas are the *spaces between buildings*, the liveable environments. A first step to bring biometeorology into practice was through the use of the Urban Climatic Maps (Ng and Ren, 2015) (Ren et al., 2014), where the urban microclimate is represented by colorful maps, giving insight into urban environmental conditions.

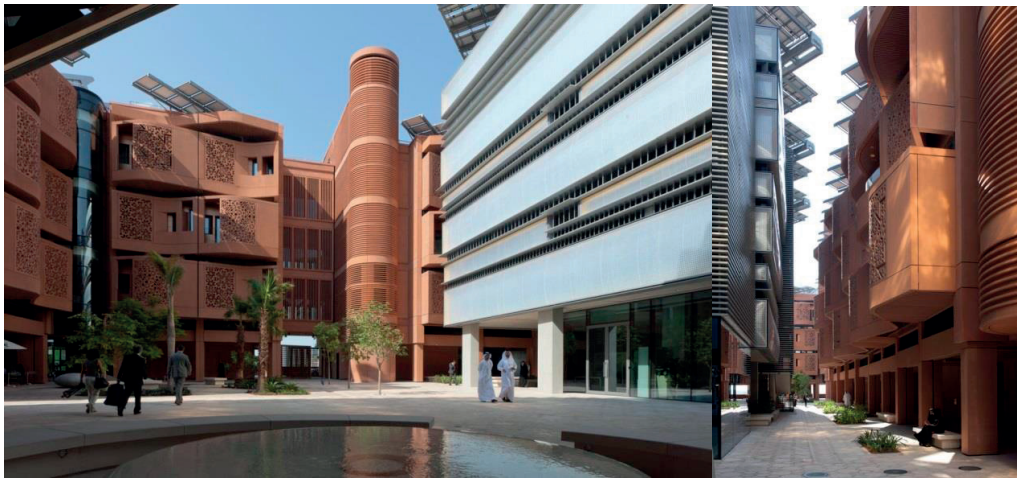


Figure 1.5 Masdar City (Foster, 2017).

### 1.1.3 Advanced optimisation methods

Optimization, also called mathematical programming, is defined as a collection of mathematical principles and methods that have the objective of solving quantitative problems. Optimization is dealing mainly by three elements: the objective function (to be maximized or minimized), the variables (numerical quantities to be defined by the optimizer) and constraints (restrictions imposed by environmental resources) (Coello et al., 2007) (Wright, 2013). Optimization problems are commonly subdivided into two main categories: single and multi-objective optimization. Single-objective optimization gives just a single optimal solution to maximise or minimize the objective function; on the other side a multi objective optimization, where two or more objective functions



coexist, yields a set of solutions, also called Pareto solution set, which passes the responsibility to choose the optimal solution between the proposed ranges of solutions to the decision maker (Ooka et al., 2008). When focusing on building design, due to conflicting objectives, the multi-objective optimization could help engineering in finding a range of suitable solutions (Evins, 2013). The formulation of a multi-objective optimization, according to some authors, is traced back to 1776, with the treatise “The Wealth of Nations” by Adam Smith (Coello et al., 2007). Multi-objective optimization derives, originally, from three areas: economic equilibrium and Welfare theories, game theory and pure mathematics (Marler and Arora, 2004). The relationship with the game theory (Borel, 1921) is evident: a game is a situation of conflict, or cooperation, between at least two players. All players have multiple strategies or moves, consequently they are intelligent and rational multi decision-makers that control the design variables (Marler and Arora, 2004).

As stated above, the objective of this thesis is to correlate the energy performance of buildings with the outdoor human comfort, providing recommendations for the bioclimatic design of sustainable campuses. This is clearly an optimization problem, which can be solved by the use of multi-objective optimization methods. Among the available optimization processes, the evolutionary algorithms permit to determine the optimal solution in accordance with the Darwinian principle of survival of the fittest: during each optimization step, a so-called generation, this selection is realised in accordance with mutations and crossovers with the poorest individual or set of variables being eliminated: the final selection defines the fittest individuals (Evins, 2013). For the purpose of this thesis, the hybrid algorithm CMA-ES/HDE (J. H. Kämpf, 2009), composed by the covariance matrix adaptation algorithm (CMA-ES) and the hybrid differential evolution (HDE), was chosen. The hybrid CMA-ES/HDE algorithm was originally developed to perform urban optimization, and consequently should be the most appropriate algorithm for the optimization of both outdoor human comfort and energy performance of buildings at the campus scale. The optimization of the indoor human comfort and the energy performance of buildings has been already considered by the scientific community (Figueiredo et al., 2016) (Yu et al., 2015) (Mofidi and Akbari, 2017) (Mostavi et al., 2017), but the optimization of the outdoor human comfort and the energy performance of buildings was, currently, not analysed in depth. During the last ten years, just a few papers were published on the optimization of the outdoor human comfort: a case study was realized in Tokyo, the design objective of identifying the optimal arrangement of trees and buildings being performed by decreasing the average Standard Effective Temperature (SET\*), reducing the cost of planting trees and increasing the pedestrian view measured by the sky view factor (Chen et al., 2008). Furthermore, there was a case study performed in Novi Sad (Serbia), where the outdoor human comfort, assessed by Universal Thermal Climate Index (UTCI), was optimized with Grasshopper for several street arrangements (Bajšanski et al., 2015). Another case study, in the city of Ancona (Italy) aimed to improve the outdoor human comfort quantified by the Predicted Mean Vote, and the energy performance at the urban scale (Grifoni et al., 2016).

## 1.2 Problem statement

As underlined above, the direct relationship between biometeorology and the disciplines of architecture and urban planning is obvious; but currently it is quite difficult to integrate outdoor human comfort and the energy performance of buildings in the architectural and urban design processes. In order to overcome this problem, this thesis presents the integration of comfort models as well as greening strategies in the urban energy modelling tool CitySim Pro. Firstly, the Index of Thermal Stress (ITS) and the COMFA\* budget were coded into CitySim Pro, as well as the Mean Radiant Temperature. The hourly results provided by the tool are then used to create Comfort Map, in order to grafically quantify the outdoor thermal comfort. The Comfort Maps are an important instrument to bring the research into practice: the map is the common way to share information between architects and municipalities, providing indications on the urban microclimatic conditions. The Comfort Map could be an integrative part of the Climatic Maps (Ng and Ren, 2015). Secondly, as stated in the previous paragraphs, greenings have an important impact on the energy demand of buildings and on the outdoor human comfort. Consequently, a new model in the software CitySim Pro is developed, in order to quantify the cooling effect of tree (by shadowing and evapotranspiration), as well of grass on the urban urban energy balance. Thirdly, the

previous models are applied to two school campuses, in temperate and hot arid climates, as well as used to optimize them by means of the hybrid CMA-ES/HDE evolutionary algorithm.

The problem statement of this thesis is summarized as follows:

- *How can we create a first preliminary link, in time and space, between the biometeorology and the architectural practice?*
- *How can we dynamically quantify the outdoor human comfort, bringing the latter directly part of the architectural practice, already at the master plan scale and stage?*
- *What is the cooling effect of greening, and how does it impact both the energy demand of buildings and the outdoor thermal comfort?*
- *How can we improve simultaneously the energy demand of buildings and the outdoor human comfort?*

The previous points are applied to two school campuses, the EPFL campus in Lausanne and the SISD campus in Dubai, improving their environmental conditions, as well as the urban microclimate.

### 1.2.1 Thesis structure

The content of each thesis chapter is summarized as follows.

#### *Chapter 2\_ Outdoor human comfort*

Several programs are available to quantify outdoor comfort conditions, such as ENVI-met, RayMan and SOLWEIG, but none of them is able to correlate the outdoor environmental conditions with the energy performance of buildings. For this reason, a new module in the software CitySim (Robinson, 2011) was developed during this thesis, in order to quantify outdoor environmental conditions in correlation with the energy performance of buildings, and thus to complete the information needed for the sustainable design of urban areas. Among the available comfort models, the Index of Thermal Stress (ITS) and the COMFA\* budget were selected in this work for their energy based approach and the related capacity to fully describe the human thermal behaviour (e.g. activity and clothing). The ITS was designed and well validated for hot arid conditions, by contrast the COMFA\* budget is well validated in temperate climate. The objective of this methodology is to consider the city as a whole system by linking the outdoor human comfort with the energy performance of buildings, integrating the human biometeorological factors in the urban planning process. Finally, the Mean Radiant Temperature (MRT) calculation was integrated into the tool in order to quantify the radiative environment and its variations within the urban factory.

#### *Chapter 3\_ Urban greening*

Greenings have a positive impact on outdoor thermal perception, as they improve the urban microclimate. The object of this chapter is to present a new methodology to dynamically model trees and to quantify the evapotranspiration process from the ground. Both models are analyzed in order to quantify their impact on the outdoor human comfort as well as on the energy performance of buildings.

#### *Chapter 4\_ Energy performance and outdoor comfort of a campus in a temperate climate*

This chapter presents the application of the above mentioned models in a real case study: the EPFL campus in Lausanne (Switzerland). The objective of these analyses is to create an energy model of the campus, and to quantify its behaviour in current and future climatic scenarios. Additionally, the outdoor human comfort is analysed by determining its sensibility to climate change, as well as the impact of wind profiles, by using the data provided by Meteororm, or using the detailed analysis with a Canopy Interface Model (CIM).

*Chapter 5\_ Energy performance and outdoor comfort of a campus in a hot and arid climate*

This chapter presents a study of the Swiss International School Campus in Dubai (United Arab Emirates). Energy simulations were performed, in order to provide recommendations for the architectural design and the development of a Minergie Standard for Topical Climate. The outdoor human comfort was analysed later on, and the on-site climate monitored on the campus site.

*Chapter 6\_ Hybrid Algorithm Optimization with Heuristics*

The objective of this optimization is to improve the energy performance of buildings as well as the outdoor environment; the optimization is applied to the EPFL Campus in Lausanne (temperate climate) and the Swiss International School Campus in Dubai (hot arid climate). The optimization of the outdoor human comfort is realized by increasing the number of hours characterized by a comfortable thermal sensation, as calculated by means of COMFA\* (COMfort FormulA) and ITS (Index of Thermal Stress). The results of the optimization were used to define the final recommendations for bioclimatic and sustainable campuses in hot arid and temperate climates.



## Chapter 2 Outdoor Human Comfort

*The work related to this chapter was published in the peer-reviewed journal Urban Climate (Coccolo et al., 2016a), presented at the conference Drylands, Desert and Desertification in Sede Boqer (Israel) in November 2014 (Coccolo et al., 2014), at the 9th International Conference on Urban Climate jointly with 12<sup>th</sup> Symposium on the Urban Environment, Toulouse (France) in July 2015 (Coccolo et al., 2015a) and at the Sustainable Built Environment Regional Conference, Zurich (Switzerland) in June 2016 (Coccolo, et al. 2016) (Mauree et al., 2016a). Finally, part of the work is submitted to the CISBAT International Conference, Lausanne (Switzerland) (Coccolo et al., 2017a) (Naboni et al., 2017b) and to the Passive Low Energy Architecture (PLEA), Edimburgh (UK) (Naboni et al., 2017a).*

### 2.0 Introduction

The outdoor human comfort is an essential factor to quantify the perceived quality of the urban microclimate; taking this dimension into account already into the design phase can lead to a more holistic view of sustainable urban development. Human thermal comfort is defined as the condition of mind which expresses satisfaction with the thermal environment (ASHRAE, 2010). The thermal assessment of human comfort is under consideration since the XX<sup>th</sup> century, when the first simplified models, based on the interaction of two simple meteorological variables (air temperature and relative humidity), were developed. During the Thirties, with the “two node model” developed by Gagge (Gagge, 1936) and for the first time, the principles of thermodynamics were applied to the energy exchanges between the human body and its thermal environment. These approaches were further developed by Givoni, who suggested in his doctoral thesis the Index of Thermal Stress (Givoni, 1963), as well as Fanger (Fanger, 1970) who developed during the Seventies the Predicted Mean Vote, a well-recognised standard (International Organization for Standardization, 2005) to quantify indoor human comfort. Finally, it is during the Eighties that a sufficient knowledge of the heat exchange processes and the use of PC allowed for an improvement in the research of the human thermal environment, and the development of indices based on the heat exchange (Fabbri, 2015).

Different models exist nowadays to quantify human comfort and thermal stress; they can be subdivided into indoor and outdoor human comfort. The indoor comfort was already studied in the last decades, and its quantification is well established; thanks to its stability, the indoor environment (air and surface temperature and relative humidity) is simple to be mechanically controlled in accordance with human activity. By contrast and up to now, it is a challenge to quantify the outdoor human comfort, because it is largely influenced by the rapid variability of the environment - the sun or shadows exposure (that vary from minutes to several hours) as well as the wind speed and direction. The variability in the exposures time influences the humans capacity to acclimatize and underlines the need of non-steady state models to quantify outdoor human comfort (Höppe, 2002). In the outdoor environment people carry out various activities, and each person has a different thermal history, memory and expectations (Nikolopoulou et al., 2001). The thermal history depicts the impact of a previous environment and activity on the thermal perception: a field study carried out on 24 subjects demonstrates that people’s thermal sensation is particularly sensitive (by 10 to 60% in relative terms) to variations of metabolic rate (Goto et al., 2006). For each modification of metabolic activity or environmental conditions the human body tends to adapt himself, basically in three different way (Nikolopoulou and Steemers, 2003):

- Physical adaptation: physical changes that a person undertakes, being active (as in changing clothes, drinking, or performing activities that affect metabolic heat production) or reactive (as opening an umbrella to protect from the sun),
- Physiological adaptation: change in the physiological responses to certain stimuli, related to the repeated exposure to a certain thermal environment (also called physiological acclimatisation),
- Psychological adaptation: naturalness of the climate, expectations, experience, time of exposure, perceived control (the reason of being in the space) and environmental stimuli.

All the actions realized by the pedestrians, as moving from the shadow to the sun (i.e. during the summer time), or changing clothes in order to feel comfortable with the outdoor environment, are part of the so called physical adaptation.

Psychological adaptation (naturalness to climate) is essential to quantify the thermal sensation: a European study, based on a survey of more than 10'000 people, shows how neutral sensation could vary by 10°C between Athens (23°C) and Freiburg (13°C); this difference is related to the recent experiences and expectation of the subjects, as an example, the thermal expectation in the transitional seasons (as spring and autumn) follows the thermal behaviour of the preceding one (Nikolopoulou and Lykoudis, 2006). Additionally culture and environmental attitude influence the thermal perception, underlining the need to connect the thermal comfort indices to the emotional perception of the environment (Knez and Thorsson, 2008). Another adaptation is the perceived control: people that can manage their thermal environment (as an example by moving from sun to shade) or that decide to stay outside (for doing a certain activity), can better tolerate the outdoor environmental conditions (Nikolopoulou and Steemers, 2003). An example of perceived control and the related thermal tolerance, a study presented in the Caribbean, showed that thermal preferences are 18°C higher for tourists at the beach, compared to people in urban parks (Rutty and Scott, 2015).

Regarding the Physiological approach (Fanger, 1970), people are comfortable if the body is in heat flow balance (body core temperature between 36.5 to 37.5°C), sweat rate is in comfort limits and skin temperature is 30°C in extremities and maximum 34-35°C in stem and head. These physical variables are interrelated with the following parameters (IUPS, 2001) (ASHRAE, 2010):

- Air temperature (°C): average temperature of the air surrounding a body,
- Wind speed (m·s<sup>-1</sup>): air velocity around the human body,
- Relative humidity (%): ratio between the partial pressure of the water vapour present in the air to the saturation pressure; from the relative humidity, the absolute humidity and the water vapour pressure can be estimated,
- Shortwave radiation (W·m<sup>-2</sup>): radiation received by the pedestrian from the sun, or reflected by the built environment,
- Longwave radiation (W·m<sup>-2</sup>): black body thermal radiation exchanged between the pedestrian and the environment,
- Human activity (met or W·m<sup>-2</sup>): rate of transformation of chemical energy into heat and mechanical work,
- Clothing level (clo): resistance to sensible heat transfer provided by clothing.

An artificial measure to express the degree of exposure to environmental radiation is the Mean Radiant Temperature (MRT), which is defined as the “the uniform surface temperature of an imaginary black enclosure in which an occupant would exchange the same amount of radiant heat as in the actual non uniform space” (ASHRAE, 2010). The Mean Radiant Temperature is affected by the solar shortwave radiation (direct, diffuse and reflected components) as well as by the terrestrial longwave radiation (atmospheric and environmental) (Kántor and Unger, 2011). MRT is more sensitive, than the air temperature, to the shadow generated by trees, the site topography and the buildings geometry (Matzarakis et al., 1999) (Mayer et al., 2008). The Mean Radiant Temperature has a major impact on thermal comfort of pedestrians: it is strongly affected by the urban configuration, such as the urban canyon's width, height and orientation, as well as their radiative properties, such as the albedo and the infrared emissivity (Herrmann and Matzarakis, 2010) (Ali-Toudert and Mayer, 2006)

(Taleghani et al., 2014) (Berkovic et al., 2012) (Lindberg et al., 2013). In addition MRT has a strong impact on different thermo-physiological indices, such as the Physiological Equivalent Temperature (Höppe, 1993) and the Predicted Mean Vote (Fanger, 1970).

Several software able to quantify the outdoor human comfort can be found on the market. Table 2.1 shows them as a function of the model that can be analysed. ENVI-met is a microclimatic software based on the interrelation between four systems: soil, vegetation, atmosphere and buildings. This software assesses the outdoor microclimate, using air temperature, Mean Radiant Temperature, wind speed and direction, short and longwave radiation from a single building to an entire city (Huttner et al., 2008). The post-processing tool called BioMet directly interacts with ENVI-met and determines the thermal comfort, in accordance with Predicted Mean Vote (PMV), Physiologically Equivalent Temperature (PET), Universal Thermal Climate Index (UTCI) (Bruse, 2014) and Mean Radiant Temperature (MRT). RayMan model calculates radiation fluxes and thermo-physiological indices, as PMV, PET, New Standard Effective Temperature (SET\*) (Matzarakis et al., 2007), UTCI, Perceived Temperature (PT) (Matzarakis, 2015) and the MRT. OTC model analyses Universal Thermal Climate Index (UTCI), Physiological Equivalent Temperature (PET) and Universal Effective Temperature (ETU) (Comfable, n.d.). SOLWEIG (SOlar and Long Wave Environmental Irradiance Geometry) is under development in the Goteborg Urban Climate Group; it quantifies PET, UTCI and MRT for complex urban settings (Lindberg, 2015). Finally UTCI calculator determines the pedestrian's thermal comfort, in accordance with the Universal Thermal Climate Index (Wojtach, n.d., www.utci.org). Some of these software calculate the mean radiant temperature, which as previously described is not considered as a variable to quantify the outdoor human comfort, but give insights concerning pedestrian's thermal perception, as well as the radiative environment.

Software	PMV	PET	UTCI	SET*	ETU	PT	MRT
ENVI-met and BioMet	✓	✓	✓				✓
RayMan	✓	✓	✓	✓		✓	✓
OTC model		✓	✓		✓		
SOLWEIG		✓	✓				✓
UTCI calculator			✓				

Table 2.1 List of available software able to quantify the outdoor human comfort, as a function of the calculated models (PMV, PET, UTCI, SET\*, ETU and PT) and MRT.

As mentioned above, several software are available to quantify outdoor comfort conditions, such as ENVI-met, RayMan and SOLWEIG, but none of them is able to correlate the outdoor environmental conditions with the energy demand of buildings. For this reason, a new module in the software CitySim (Robinson, 2011) was developed during this thesis, in order to quantify the outdoor environmental conditions with the energy demand of buildings, giving a complete outlook on the city sustainable design. Between the available comfort models, the Index of Thermal Stress (ITS) and the COMFA\* budget were selected in this work; the reason for that was i) their energy based approach and ii) the related capacity to fully describe the human thermal behaviour (activity and clothing). Additionally, iii) they were developed in order to describe human thermal conditions in two different climates, the hot one (ITS) and the temperate one (COMFA\*). The objective of this methodology is to consider the city as a whole system by linking the outdoor human comfort with the energy demand of buildings, integrating the human biometeorological factors in the urban planning process. Finally, the MRT calculation was integrated into the tool, in order to quantify its variations in accordance with the built environment, as well as the microclimatic conditions. We decided to integrate the MRT as it is an input parameter for other human comfort indices, used in the calculation of the Physiologically Equivalent Temperature (PET) and the Predicted Mean Vote (PMV). Indeed, the MRT calculated by CitySim can be used as input meteorological data for the tool RayMan (Coccolo et al., 2017a).

The next paragraphs present the comfort model implemented in CitySim, as well as the physical equations behind them.



## 2.1 Pedestrian design with CitySim Pro

Based on this methodology, virtual pedestrians located in the outdoor virtual environment and modelled with the software CitySim are shown using the Graphical User Interface (GUI) CitySim Pro (see Figure 2.1). The pedestrian are geometrically designed with Rhinoceros or Autocad, on the form of an octagonal prism inscribed in a circle of 0.17 m of diameter; the height of a pedestrian corresponds to 1.5 m (Erell et al., 2014). The design of the pedestrian, height and diameter, is based on the conceptual model developed by (Pearlmutter et al., 2006). For the MRT calculations, the pedestrian is designed as an octagonal prism inscribed in a circle of 0.17 m of diameter, with the upper face at 1.5 m height from the ground and the lowest face at 1.0 m height. This geometry is related to the methodology used to quantify the MRT: the Integral Radiation Measurement (Höppe, 1992). This method quantifies the MRT using the radiation received by a pedestrian from the six directions: the four cardinal directions, as well as below and above.

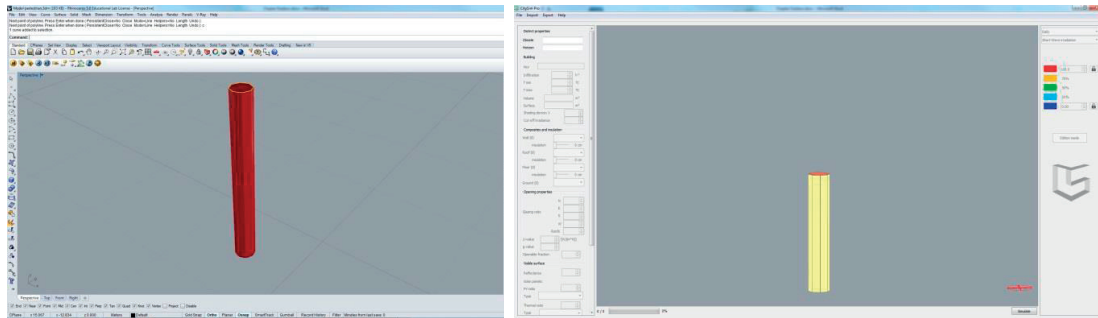


Figure 2.1 3D view of the pedestrian, as designed by Rhinoceros (left) and imported in CitySim Pro (right).

The pedestrians are then imported into the software CitySim Pro, where their physical properties are added as for normal buildings: the albedo of the person and clothing, corresponding to 0.37 (Erell et al., 2011b) and the longwave emissivity that corresponds to 0.95 (Erell et al., 2011b). Assuming an analogy between the pedestrian and a building, the internal temperature is maintained constant between 35°C and 37°C. Finally, the human body is considered as composed of four concentric layers: core, muscle, fat and skin (Parsons, 2014); the core is the internal part of the body and is composed of water. The properties of tissues employed in the modelling are described in Table 2.2 (Fiala et al., 2012).

Name	Density $\rho$ ( $\text{kg}\cdot\text{m}^{-3}$ )	Specific heat $c$ ( $\text{J}\cdot\text{kg}^{-1}\text{K}^{-1}$ )	Thermal conductivity $\kappa$ ( $\text{W}\cdot\text{m}^{-1}\text{K}^{-1}$ )
Skin	1,085	3,680	0.47
Fat	850	2,300	0.16
Muscle	1,085	3,768	0.42
Water	1,000	4,000	0.6

Table 2.2 Thermophysical parameters of the human body modelled with the software CitySim Pro, based on Fiala et al. (Fiala et al., 2012).

The pedestrian is located in the 3D environment, where the physical properties of the scene are described: envelope of buildings, shortwave reflectance and longwave emissivity of their envelope, as well as their energy demand (heating and cooling) and photovoltaic production. The ground covering is described by its physical properties (layers of materials), short and longwave reflectance, as well as its evaporative capacity. Finally, the impact of greening is described, as presented in Chapter 3.

With the proposed methodology, the outdoor human comfort can be quantified dynamically each hourly time step, creating Comfort Maps describing the outdoor environment, as a function of the metabolic activity of pedestrians, as well as the outdoor conditions (shadowing, materials, evapotranspiration and vegetation). In the following paragraph the basic equations of the Index of Thermal Stress and the COMFA\* budget are presented, as well as their adaptation to the software CitySim Pro.



## 2.2 Index of Thermal Stress

The first comfort model used in this thesis is the Index of Thermal Stress (ITS). The ITS was firstly defined by Givoni (Givoni, 1963) and described in his book (Givoni, 1969) as a biophysical model able to quantify the energy exchange between the body and the environment, and consequently the thermal stress (metabolic and environmental) of the human body. The ITS was firstly defined for indoor use, and later adapted to the outdoor environment (by including distinct direct and indirect radiation components) by (Pearlmutter et al., 2007). The basic concept under the ITS is the evaporative exchange between the body and the environment: the body maintains the thermal equilibrium in hot environments by decreasing its temperature by the way of evaporative cooling; its ability to evaporate depends on the efficiency of sweating, which is related to the environmental conditions (relative humidity and wind speed). This model was well applied in hot arid climate (Pearlmutter et al., 2014), (Pearlmutter et al., 2006), (Erell et al., 2013), (Erell et al., 2014), (Kalman et al., 2013), (Pearlmutter et al., 2007), (Saaroni et al., 2014), as well as in temperate climate (Pantavou et al., 2014). A case study performed at Ben-Gurion University of Israel showed a sound correlation coefficient ( $R^2=0.67$ ) between ITS and a survey realized by the means of questionnaires, and performed for 114 individuals during 13 summer days (Pearlmutter et al., 2014).

The first version of the ITS was expressed in  $\text{kcal}\cdot\text{h}^{-1}$ ; the model was later revised by Pearlmutter et al. (Pearlmutter et al., 2006) and expressed in watt, on a five point scale from -160 W (Cold) to +800 W (Very hot); the perception threshold appears every 320 W. The basic equation behind the model is the following (Erell et al., 2011a):

$$ITS = \frac{(M - W) + R_n + C}{f} \quad (2.1)$$

where  $M$  (W) is the body's metabolic rate,  $W$  (W) is the metabolic energy transformed in mechanical work,  $R_n$  (W) is the environmental exchanges due to radiation, this value is normally positive during daytime (the pedestrian receives the solar radiation) and can be negative during nighttime, due to the longwave radiation emitted by the pedestrian,  $C$  (W) is the environmental exchanges due to convection. As for the radiation, this value can be positive or negative as a function of the energy exchange between the pedestrian and the environment,  $f$  (-) is the cooling efficiency of sweating. All the above parameters are calculated in  $\text{W}\cdot\text{m}^{-2}$ , and then multiplied by the Dubois surface area  $A_{du}$  ( $\text{m}^2$ ) defined as follows:

$$A_{du} = 0.202 * W_p^{0.425} * H^{0.725} \quad (2.2)$$

where  $W_p$  (kg) is the weight of the person,  $H$  (m) is the height of the person; a person of 75 kg and 1.75m, has a surface area of  $1.89 \text{ m}^2$ . In the first analysis of the results obtained by the model, the DuBois surface area was used; then as a further improvement, a new area was defined: the sum of the external envelope of pedestrian, as designed in CitySim Pro, which corresponds to  $0.80111 \text{ m}^2$ .

The body's metabolic rate  $M$ , calculated in  $\text{W}\cdot\text{m}^{-2}$ , is based on the metabolic activity: as an example  $46 \text{ W}\cdot\text{m}^{-2}$  for reclining and  $200 \text{ W}\cdot\text{m}^{-2}$  for walking at  $5 \text{ km}\cdot\text{h}^{-1}$  (International Organization for Standardization, 2005). The metabolic energy transformed in mechanical work,  $W$  (W) is assumed to be equal to 20% of the difference between the performed metabolic activity and the rest level (Givoni, 1969).

$R_n$ , the environmental exchange due to radiation, is quantified as the balance between the short and long wave radiation absorbed by the pedestrian and the longwave radiation emitted, as follows:

$$R_n = (K_{dir} + K_{dif} + K_h + K_v) \cdot (1 - \alpha_s) + L_d + L_h + L_v - L_s \quad (2.3)$$

where  $K_{dir}$  and  $K_{dif}$  are the direct and diffuse short wave radiation impinging the human body;  $K_h$  and  $K_v$  are the indirect radiation incident on the body, reflected from the horizontal and vertical surfaces;  $\alpha_s$  (-) is the albedo of skin and clothing;  $L_d$ ,  $L_h$  and  $L_v$  are the longwave radiation absorbed by the human body emitted downward by the sky, as well as the horizontal and vertical surfaces; finally  $L_s$  is the longwave radiation emitted by the body to the environment. All energy fluxes are expressed in  $\text{W}\cdot\text{m}^{-2}$ .

The shortwave components are quantified by the software CitySim, as the impinging radiation received by the pedestrian (designed as described before, using a prism with octagonal base of 1.5 m height); the albedo of the pedestrian is already defined in the numerical model by assuming a shortwave reflectance of the prism that corresponds to 0.37 (Kenny et al., 2008). The longwave radiation absorbed by the environment  $L_i$ , corresponding to the sum of the longwave radiation absorbed by the human body emitted downward by the sky, the horizontal and vertical surfaces, is computed for each surface within CitySim using the Stefan- Boltzman equation:

$$L_i = \sigma \varepsilon_p T_{env}^4 \quad (2.4)$$

where  $\sigma$  ( $W \cdot m^{-2} K^{-4}$ ) is the Stefan-Boltzmann constant equal to  $5.67 \cdot 10^{-8}$ ,  $\varepsilon_p$  (-) is the emissivity of the considered receiving surface and  $T_{env}$  (K) is the equivalent temperature for the surrounding environment considered as a black body (emissivity equal to 1). The latter is evaluated as follows for a specific surface:

$$T_{env}^4 = \frac{1}{\pi} \int_{\Omega} \varepsilon(\vec{\sigma}) T^4(\vec{\sigma}) d\vec{\sigma} \cdot \vec{n} \quad (2.5)$$

where  $\Omega$  is the hemisphere seen from the centroid of the specific surface and  $\vec{n}$  the unitary normal vector of the surface. Furthermore,  $T(\vec{\sigma})$  (K) and  $\varepsilon(\vec{\sigma})$  are respectively the absolute temperature and the emissivity of the surface in the direction of the infinitesimal solid angle  $\vec{\sigma}$ . Considering the hemisphere is having three contributions: the homogeneous sky, the homogeneous ground and the others surfaces, Equation 2.5 can be reduced to the following sum:

$$T_{env}^4 = \frac{1}{\pi} [\varepsilon_{sky} T_{sky}^4 \cdot \Omega_{p,sky} + \varepsilon_{grd} T_{grd}^4 \cdot \Omega_{p,grd}] + \sum_{j=1}^{n_s} \varepsilon_j T_{s,j}^4 \cdot F_j \quad (2.6)$$

in which  $T_{sky}$  and  $T_{grd}$  (K) are respectively the sky and ground temperature,  $\Omega_{p,sky}$  and  $\Omega_{p,grd}$  are the projected solid angle of the unobstructed sky and the ground on the considered surface plane,  $T_{s,j}$  (K) is the surface temperature and  $F_j$  (-) is the view factor of surface  $j$  seen from the considered surface with  $j=1..n_s$  and  $n_s$  the total number of surfaces in the scene (please note that  $\frac{\Omega_{p,sky}}{\pi}$  is also known as the Sky View Factor for the considered surface). Finally for the sky, whose emissivity  $\varepsilon_{sky}$  is considered equal to 1, its contribution is determined as a function of the ambient air temperature  $T_a$  (K) as follows:

$$\varepsilon_{sky} T_{sky}^4 = \varepsilon_{sky}' \cdot T_a^4 \quad (2.7a)$$

where  $\varepsilon_{sky}'$  (-) is the sky emissivity as defined in Eicker and Dalibard (2011). In this thesis we used this approach to calculate the sky temperature, as in the software CitySim. Indeed, it would be interesting to analyze what is the impact, on the human's thermal sensation, of varying the sky temperature as follows (Duffie and Beckman, 2013):

$$T_{sky} = T_a - 6K \quad (2.7b)$$

The longwave radiation emitted by the pedestrian corresponds to:

$$L_s = \varepsilon_s \sigma T_s^4 \quad (2.8)$$

where  $\varepsilon_s$  (-) is the emissivity of the body and clothing, estimated to be equal to  $\sim 0.95$  (Kenny et al., 2008),  $\sigma$  ( $W \cdot m^{-2} K^{-4}$ ) is the Stefan- Boltzmann constant and  $T_s$  (K) is the surface temperature, equal to  $35^\circ C$  (Erell et al., 2011b).

The environmental exchanges due to convection  $C$  (W) are expressed as:

$$C = h_c \cdot \Delta T \quad (2.9)$$

where  $h_c$  ( $W \cdot m^{-2} K^{-1}$ ) is the heat transfer coefficient and  $\Delta T$  (K) is the difference between the surface temperature and the outdoor air temperature. The heat transfer coefficient is related to the wind speed as follows (Pearlmutter et al., 2006):

$$h_c = \rho c_p k Nu / d \quad (2.10)$$

where  $\rho c_p$  is the volumetric heat capacity of the air,  $C_p$  ( $\text{J}\cdot\text{kg}^{-1}\cdot\text{K}^{-1}$ ) corresponds to  $\approx 1,005$  for the considered temperature range and  $\rho$  ( $\text{kg}\cdot\text{m}^{-3}$ ) is calculated as a function of the air temperature.  $k$  ( $\text{m}^2 \text{ s}^{-1}$ ) is the thermal diffusivity of the air corresponding to  $\approx 2\cdot 10^{-5}$ ,  $d$  (m) is the diameter of the cylinder (or in this case the circle in which the octagonal prism is inscribed) and  $Nu$  (-) is the Nusselt number derived from the Reynolds number  $Re$  as follows:

$$Nu = A Re^B \quad (2.11)$$

where  $A$  and  $B$  are two coefficient, which for a typical pedestrian head height are equal to  $A=0.17$  and  $B=0.62$  if the Reynolds number is higher than  $4\cdot 10^3$ , and  $A=0.62$  and  $B=0.47$  if it is lower than  $4\cdot 10^3$  (Pearlmutter et al., 2006); the Reynolds number itself is calculated as follows:

$$Re = \frac{dV}{u} \quad (2.12)$$

where  $d$  (m) is the diameter of the cylinder (or the circle in which is inscribed the octagonal prism),  $V$  is the wind speed ( $\text{m s}^{-1}$ ) and  $u$  ( $\text{m}^2\text{s}^{-1}$ ) is the viscosity of the air assumed to be equal to  $1.6 \times 10^{-5}$ .

For a standing or walking pedestrian, represented as a vertical symmetric cylinder,  $h_c$  can be simplified using the following expression:

$$h_c = 8.3v^{0.6} \quad (2.13)$$

where  $v$  is the horizontal wind speed ( $\text{m s}^{-1}$ ) averaged over the height of the body.

The final term of the equation, the cooling efficiency of sweating ( $\frac{1}{f}$ ), is expressed as the ratio between the required cooling rate and the evaporative capacity of the air:

$$\left(\frac{1}{f}\right) = \exp\left[0.6 * \left(\frac{E}{E_{max}} - 0.12\right)\right] \quad (2.14)$$

where  $E_{max}$  (W) is an expression of the evaporative capacity of the air, in accordance with the wind speed, the relative humidity and the outdoor temperature, calculated as follows:

$$E_{max} = c_c V^{0.3} (42 - P v_a) \quad (2.15)$$

where  $c_c$  is the clothing coefficient, corresponding to 31.6 for semi-nude (bathing suit and hat), 20.5 for light summer clothing, and 12.0 for military overall over shorts (Givoni, 1976). In the proposed model we decided to maintain the clothing coefficient at 20.5 (personal communication with Prof. Pearlmutter).  $V$  ( $\text{m s}^{-1}$ ) is the wind speed, 42 (mm Hg) is the vapour pressure of the skin at  $35^\circ\text{C}$  (Givoni, 1976) and  $P v_a$  (mm Hg) is the vapour pressure of the air calculated as:

$$P v_a = 7.52 \left(\frac{RH}{100}\right) P v_s \quad (2.16)$$

where  $RH$  (%) is the relative humidity and  $P v_s$  (kPa) is the saturation vapour pressure:

$$P v_s = \exp\left[16.6536 - \left(\frac{4,030.183}{T + 235}\right)\right] \quad (2.17)$$

The sweating efficiency factor  $f$  corresponds to the capacity of the body to sweat, and it is directly related to the environmental characteristics: if the air is warm and humid, the factor  $f$  is less than 1. By contrast, if the air is cool and dry, the factor  $f$  corresponds to 1, which is its upper value (Pearlmutter, 2016).

The thermal sensation is defined in a five-point thermal sensation as described in Table 2.3 (Pearlmutter et al., 2014); a person is sensitive to a variation of 320 W (Pearlmutter et al., 2014) (see middle column of Table 2.3). In the previous thermal scale (D. Pearlmutter et al., 2007) (Shashua-Bar et al., 2011), based on climate chamber monitoring, the pedestrian was sensitive to a variation of 120W (see right column of Table 2.3).

Thermal Sensation	Index of Thermal Stress (W) (Pearlmutter et al., 2014)	Index of Thermal Stress (W) (D. Pearlmutter et al., 2007) (Shashua-Bar et al., 2011)
Cool	< -160	< -160
Comfortable	-160 to +160	-160 to +160
Warm	+160 to +480	+160 to +280
Hot	+480 to +800	+280 to +400
Very hot	>+800	>+400

Table 2.3 Thermal sensation as a function of the Index of Thermal Stress (W); this index is defined for hot climate, and the thermal sensation described varies from cool to very hot thermal sensation (Pearlmutter et al., 2014).

In order to validate the model implemented in CitySim Pro, the results obtained with the software were compared to the ones presented in Shashua-Bar (Shashua-Bar et al., 2011), in which the impact of trees as well as several urban configurations was defined as a function of the pedestrians thermal sensation. All data required for the model were obtained thanks to Prof. Erell and Prof. Pearlmutter, who shared their monitoring with us. For further details, please refer to Chapter 3, where all the data of the monitoring are defined. The simulations were performed with CitySim Pro in order to quantify the impact of the built environment, and doing so, the courtyard configuration 2 (Trees- Bare, Table 2.4) was selected and the normalized Index of Thermal Stress was defined, as follows:

$$ITS_{norm} = ITS \cdot \left( \frac{ITS_{ref}}{ITS_{ref}} \right) \quad (2.18)$$

where  $ITS$  is the Index of Thermal Stress, computed in the courtyard, and  $ITS_{ref}$  is the Index of Thermal Stress computed in the outdoor environment for the selected hours of measurement and the average of the selected hour in the set of selected days. All fluxes are expressed in watt.

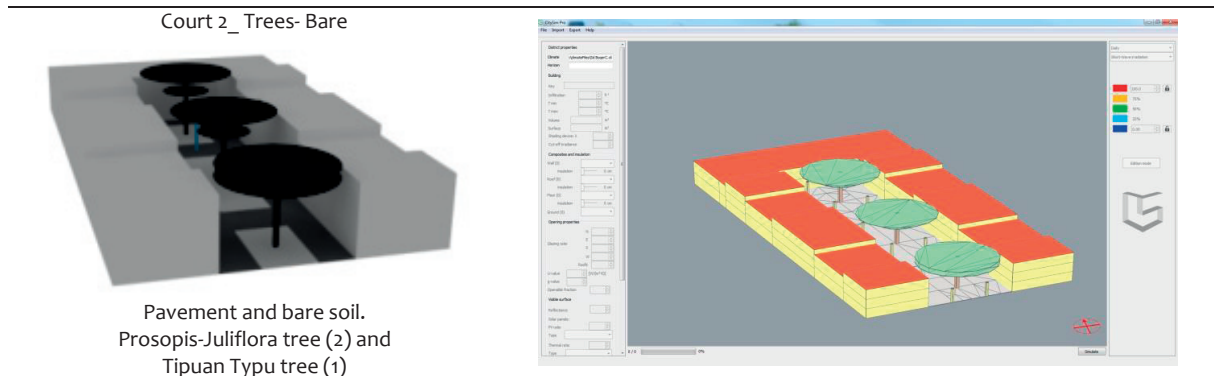


Table 2.4 Physical and geometrical properties of the court configuration (left) and 3D view from CitySim Pro (right).

The simulations were performed during all year, and the results obtained for the period of measurement (6<sup>th</sup> to 10<sup>th</sup> July 2007) were compared to the ones obtained by Shashua-Bar et al. (Shashua-Bar et al., 2011). Figure 2.2 shows the Index of Thermal Stress as computed by CitySim Pro and as calculated by the authors (Shashua-Bar et al., 2011): the CitySim Pro model slightly underestimates the Index of Thermal Stress during the daytime (maximal difference at 13:00 corresponding to 34 W). The difference between the above results is probably due to the tree model that ensures better shadowing than the reality (see Chapter 3). During the selected time frame of analysis, the correlation between the two models corresponds to 0.96, and the Root Mean Square Error is equal to 21 W. Knowing that a pedestrian is sensitive to a variation of 320 W in thermal sensation, a RMSE of 21 W can be considered to be within the tolerated error range. Finally, as presented in Figure 2.2, the difference between the results is inside the experimental error, assumed equal to  $\pm 10\%$ , by summing up the experimental error in calculating the energy exchanges, which corresponds to  $\pm 5\%$  (Pearlmutter et al., 2006) (Pearlmutter et al., 2005), and  $\pm 5\%$  related to the uncertainties of the model.

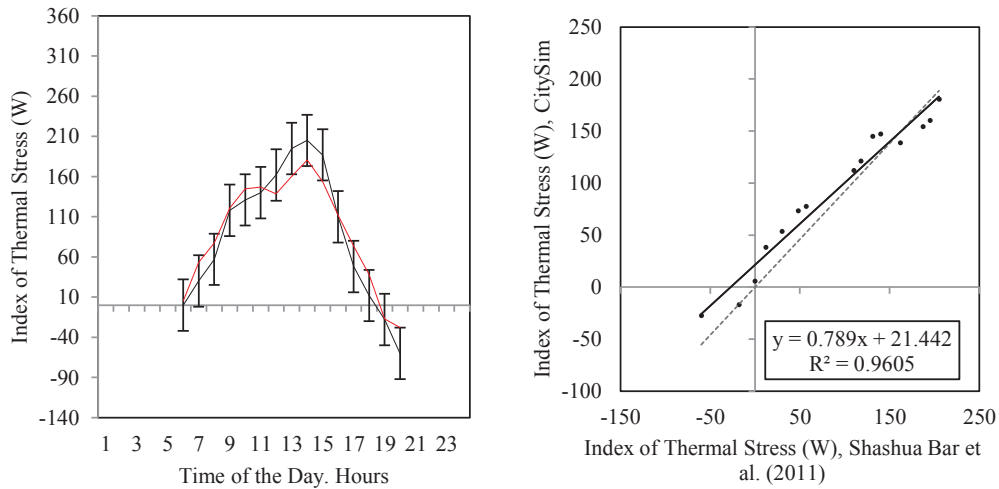


Figure 2.2 Index of Thermal Stress, comparison between monitoring performed in Sede-Boqer campus of Ben-Gurion University (black line), and the simulations performed with CitySim Pro (red line). Selected courtyard C2, tree and bare soil.

The outdoor human comfort in the SISD campus will be presented in Chapter 5 and dynamically quantified by the use of the ITS.

### 2.3 COMFA\* budget

The COMFA model was firstly developed by Brown and Gillespie (Brown and Gillespie, 1995) as a mathematical model to describe the human energy balance based on four elements: the perspiration rate, the energy budget, the core body and the skin temperature. The basic equation that describes this model is:

$$B = M_h + R_{RT} - C - E_{s+i} - L_s \quad (2.19)$$

where  $M_h$  is the metabolic heat generated by a person,  $R_{RT}$  is the radiation absorbed,  $C$  are the convective heat losses,  $E_{s+i}$  is the evaporation and  $L_s$  is the longwave radiation emitted by a person. All values are expressed in  $W m^{-2}$ .

The proposed methodology considers a further development of the COMFA model, called COMFA\*, where the model is improved by allowing a better calculation of thermal sensations for people performing high metabolic activity by redefining the following parameters: tissue resistance, relative air velocity, skin temperature, clothing and vapor resistance (Kenny et al., 2009a) (Kenny et al., 2009b) (Vanos et al., 2012b) (Vanos et al., 2012a). The revision is based on the concept that the COMFA model produces errors in estimating the heat and moisture exchanges between the body and the environment, if the pedestrians' activity is above  $> 400 W m^{-2}$ , if the outdoor environment is characterized by high wind speeds ( $> 4 ms^{-1}$ ) and in case of warm temperatures ( $> 28^\circ C$ ).

The first term of Equation 2.19, the metabolic heat  $M_h (W \cdot m^{-2})$ , is related to the metabolic activity performed by the person, and the heat losses by breathing. It is defined as:

$$M_h = (1 - h_b) M \quad (2.20)$$

where  $M (W \cdot m^{-2})$  is the metabolic intensity of the person in accordance with its activity and  $h_b (-)$  is the correction for the heat losses due to breathing.

$$h_b = 0.150 - (0.0173 e_{\theta_a}) - (0.0014 \theta_a) \quad (2.21)$$

where  $e_{\theta_a}$  (kPa) is the ambient vapour pressure and  $\theta_a (^\circ C)$  is the air temperature.

The ambient vapour pressure is derived from the saturation vapor pressure of the air:

$$e_{\theta_a} = e_{s,\theta_a} \cdot RH \quad (2.22)$$

where  $RH$  (%) is the relative humidity, and  $e_{s,\theta_a}$  is calculated as follows:

$$e_{s,\theta_a} = a \exp\left(\frac{b\theta_a}{\theta_a + c}\right) \quad (2.23)$$

where  $a, b, c$  are constant, equal to 0.611 (kPa), 17.502 (-) and 240.97 (°C) respectively (Gaylon S. Campbell and Norman, 1998); these constants are retrieved from the Tetens formula (Tetens, 1930) and later adapted by Buck (Buck, 1981) for temperature interval of -20 to +50°C.

The radiation absorbed by the pedestrian  $R_{RT}$  ( $W \cdot m^{-2}$ ) is calculated by the software CitySim Pro as follows (Kenny et al., 2008):

$$R_{RT} = \frac{(K_{b(abs)} + K_{d(abs)})(1 - \alpha) + L_{a(abs)} + L_{g(abs)}}{A_{pe}} \quad (2.24)$$

where  $K_{b(abs)}$  (W) is the sum of direct beam radiation absorbed by each surface element of the pedestrian,  $K_{d(abs)}$  (W) is the sum of the diffuse solar radiation absorbed by each surface of the pedestrian,  $\alpha$  (-) is the shortwave reflectance of the pedestrian (body and clothing), assumed equal to 0.37 as defined in (Kenny et al., 2008).  $L_{a(abs)}$  (W) is the sum of atmospheric longwave radiation absorbed by each surface element of the pedestrian,  $L_{g(abs)}$  (W) is the sum of ground surface longwave radiation absorbed by each surface element of the pedestrian. All fluxes are calculated by CitySim Pro, as presented in the ITS model (Equations 2.4 to 2.7).  $A_{pe}$  ( $m^2$ ) is the outer surface area of the pedestrian, which in the proposed model corresponds to 0.80111  $m^2$ . In the original formula (Vanos et al., 2012a), the radiation absorbed is then multiplied by a form factor  $FF$  that depends on the position of the pedestrian, and corresponds to 0.78 if standing, and 0.7 if sitting. In the proposed model it is not necessary to multiply it by the form factor, as the radiation received by the pedestrian is already normalized by its surface. This approach was validated by Prof. Vanos (Vanos, 2016)

The following term in the basic equation, representing the convective heat losses ( $W \cdot m^{-2}$ ), is defined as:

$$C = \rho C_p \left( \frac{\theta_{sk} - \theta_a}{r_c + r_a} \right) \quad (2.25)$$

where  $\rho C_p$  is the volumetric heat capacity of the air,  $C_p$  equals 1,000 ( $J \cdot kg^{-1} \cdot K^{-1}$ ) and  $\rho$  ( $kg \cdot m^{-3}$ ) is calculated as a function of the air temperature,  $\theta_{sk}$  (°C) is the skin surface temperature,  $r_c$  ( $s \cdot m^{-1}$ ) is the clothing resistance and  $r_a$  ( $s \cdot m^{-1}$ ) is boundary air resistance.

$\theta_{sk}$  (°C) is calculated as a function of the tissue, clothing and boundary air resistance (Kenny et al., 2009b):

$$\theta_{sk} = \left( \frac{\theta_c - \theta_a}{r_t + r_c + r_a} \right) (r_a + r_c) + \theta_a \quad (2.26)$$

where  $\theta_c$  is the core's temperature (°C), defined as a function of the metabolic activity (Kenny et al., 2009a):

$$\theta_c = 36.5 + 0.043M_h \quad (2.27)$$

The skin temperature varies as a function of the outdoor environmental conditions and is assumed to be equal to 30°C in a cool environment (e.g.  $\theta_a=8-10^\circ C$ ), 31-33°C in a neutral environment (e.g.  $\theta_a=20-24^\circ C$ ) and 33-37°C in a hot environment (e.g.  $\theta_a=30-40^\circ C$ ) (Kenny et al., 2009b). Results obtained by field experiments, show that the face skin temperature exposed to cold conditions, could vary between 30°C to 5°C after 20 minutes exposure in a cold environment (-10°C and wind speed up to 6  $ms^{-1}$ ) (Shabat and Shitzer, 2012). The following term in Equation 2.26, corresponding to the body tissue resistance  $r_t$  ( $s \cdot m^{-1}$ ), is defined as (Kenny et al., 2009b):

$$r_t = \frac{\rho C_p}{0.13E_s + 15} \quad (2.28)$$

where  $E_s$  ( $W \cdot m^{-2}$ ) is the evaporative heat loss through sweat or perspiration. Finally, the boundary layer resistance  $r_a$  ( $s \cdot m^{-1}$ ) is defined as (Kenny et al., 2009a):

$$r_a = \frac{0.17}{ARe^n Pr^{0.33} k} \quad (2.29)$$

where  $Re$  is the Reynolds number,  $Pr$  is the Prandtl number (equal to 0.71),  $k$  is the thermal diffusivity of the air ( $\approx 2.2 \cdot 10^{-5} m^2 \cdot s^{-1}$ ),  $A$  and  $n$  are empirical constants based on heat flow's experiments around cylinders:

- if  $Re < 4,000$ ,  $A = 0.683$  and  $n = 0.466$ ;
- if  $4,000 < Re < 40,000$ ,  $A = 0.193$  and  $n = 0.618$ ;
- if  $Re > 40,000$ ,  $A = 0.0266$  and  $n = 0.805$ .

The Reynolds number is calculated as follows, using the same equation as the one defined in the section relative to the ITS:

$$Re = \frac{0.17V}{u} \quad (2.30)$$

where  $u$  is the kinematic viscosity of the air (assumed as  $1.5 \cdot 10^{-5} m^2 \cdot s^{-1}$ ) and  $V$  is wind speed ( $m \cdot s^{-1}$ ).

The resistance of clothing  $r_c$  ( $s \cdot m^{-1}$ ) is defined as (Kenny et al., 2009b):

$$r_c = r_{co}(-0.37(1 - \exp(\frac{-v_a}{0.72})) + 1) \quad (2.31)$$

where  $r_{co}$  ( $s \cdot m^{-1}$ ) is the static clothing resistance and  $v_a$  ( $m \cdot s^{-1}$ ) is the activity velocity, that varies as a function of the activity as follows (International Organization for Standardization, 2004):

$$v_a = 0.0052 (M_h - 58) \quad (2.32)$$

The static clothing resistance is defined as follows:

$$r_{co} = I_{cl} \rho C_p \quad (2.33)$$

where  $I_{cl}$  (clo) is the intrinsic clothing insulation, based on the individual's ability to modify his/her clothing in accordance with the outdoor temperature;  $I_{cl}$  is defined as (Vanos et al., 2012a):

$$I_{cl} = 1.372 - 0.01866\theta_a - 0.0004849\theta_a^2 - 0.00000933\theta_a^3 \quad (2.34)$$

where  $\theta_a$  is the air temperature ( $^{\circ}C$ ).  $I_{cl}$  is calculated in clo units and converted in ( $m^2 K \cdot W^{-1}$ ) by the following relation:  $1 \text{ clo} = 0.1555 m^2 K \cdot W^{-1}$ . The limit of this formula is evident in Figure 2.3: when the air temperature corresponds to  $30^{\circ}C$ , the clothing insulations become negative. Because of this, based on (Vanos et al., 2012a), if the air temperature is higher than  $27^{\circ}C$ , a  $I_{cl}$  of 0.31 clo ( $0.048 m^2 K \cdot W^{-1}$  illustrated by the dashed red line in Figure 2.3) is used, as it corresponds to light summer clothes (panties, t-shirt, shirts, light socks and sandals)(International Organization for Standardization, 2007). The variation of the original clothing model, derived from the UTCI calculation (Havenith et al., 2012), is an outstanding improvement of the original COMFA model. Due to the new model, the user is not supposed to modify manually the clothing characteristics, as function of the climatic conditions, as it happens when working with other comfort indices, as an example with the Physiological Equivalent Temperature (PET).



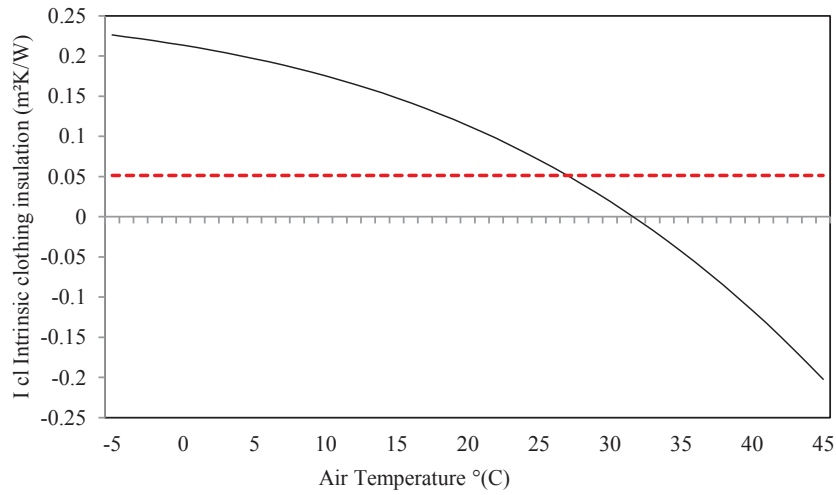


Figure 2.3 Intrinsic clothing insulation, analysis of the insulation as a function of the air temperature. The red dashed line corresponds to light summer clothes.

The evaporative heat loss ( $\text{W}\cdot\text{m}^{-2}$ ) is expressed as the sum of evaporative heat loss through perspiration  $E_s$  and evaporative heat loss through skin diffusion  $E_i$ . The evaporative heat loss through perspiration is defined as:

$$E_s = 0.42(M_h - 58) \quad (2.35)$$

and the evaporative heat loss through skin diffusion ( $\text{W}\cdot\text{m}^{-2}$ ) is defined as:

$$E_i = \rho\lambda \left( \frac{q_s - q_a}{(r_{cv} + r_{av} + r_{tv})} \right) \quad (2.36)$$

where  $\rho$  ( $\text{kg}\cdot\text{m}^{-3}$ ) is the air density,  $\lambda$  ( $\text{J}\cdot\text{kg}^{-1}$ ) is the latent heat of vaporization,  $q_s$  and  $q_a$  are the specific humidity of the skin and the air respectively ( $\text{kg}$  of water vapour per  $\text{kg}$  of moist air),  $r_{cv}$ ,  $r_{av}$  and  $r_{tv}$  ( $\text{s}\cdot\text{m}^{-1}$ ) are the resistance of vapour transfer by clothing, air and tissues respectively. A maximum possible evaporation is defined, in order to include high metabolic activities:

$$E_m = \rho\lambda \left( \frac{q_s - q_a}{(r_{cv} + r_{av})} \right) \quad (2.37)$$

The lowest value between  $E_i$  and  $E_m$  is the one included into the calculation;  $E_m$  represents the maximal evaporation of the human body, when ignoring the tissue resistance (Kenny et al., 2009a).

The air density ( $\text{kg}\cdot\text{m}^{-3}$ ) is defined as a function of the air temperature and the air pressure for a specific site:

$$\rho = \frac{P_a}{R \cdot T_a} \quad (2.38)$$

where  $P_a$  (Pa) is the air pressure,  $R$  is the specific gas constant assumed to be equal to  $287.04 \text{ J}\cdot\text{kg}^{-1}\cdot\text{K}^{-1}$  for dry air and  $T_a$  is the air temperature (K).

The latent heat of vaporization ( $\text{J}\cdot\text{kg}^{-1}$ ) is defined in accordance with (Bolton, 1980):

$$\lambda = (2501 - 2.37 \cdot \theta_a) \cdot 1000 \quad (2.39)$$

The specific humidity of skin  $q_s$  and the specific humidity of the air  $q_a$  are defined in accordance with the following formula (Kenny et al., 2009a):

$$q = 0.622 \left( \frac{e}{P_a - e} \right) \quad (2.40)$$

where  $e$  (see Equations 2.22 and 2.23) is the vapour pressure at the air temperature  $\theta_a$  and at skin temperature  $\theta_{sk}$ , respectively.



The resistance of vapour transfer by clothing  $r_{cv}$  ( $s \cdot m^{-1}$ ) is defined as (Kenny et al., 2009b):

$$r_{cv} = r_{cv0}(-0.8(1 - \exp(\frac{-v_r}{1.095})) + 1) \quad (2.41)$$

$v_r$  ( $m \cdot s^{-1}$ ) is the effective air velocity defined as (Holmér et al., 1999):

$$v_r = \sqrt{V^2 + v_a^2} \quad (2.42)$$

where  $V^2$  ( $m \cdot s^{-1}$ ) is the wind speed and  $v_a^2$  ( $m \cdot s^{-1}$ ) is the activity velocity.

The static clothing vapour resistance  $r_{cv0}$  ( $s \cdot m^{-1}$ ) is defined as follows:

$$r_{cv0} = \frac{0.622\lambda\rho R_{ecl}}{P_a - e_a} \quad (2.43)$$

where  $R_{ecl}$  ( $m^2kPa \cdot W^{-1}$ ) is the total evaporative resistance of clothing ensemble available in ISO 9920 (International Organization for Standardization, 2007); it is related to the clothing insulation by the following formula :

$$R_{ecl} = 0.18I_{cl} \quad (2.44)$$

The resistance of deep skin tissues  $r_{tv}$  is assumed to be equal to  $7.7 \cdot 10^3$  ( $s \cdot m^{-1}$ ) and the air resistance of vapour transfer  $r_{av}$  ( $s \cdot m^{-1}$ ) is defined as:

$$r_{av} = 0.92 r_a \quad (2.45)$$

where  $r_a$  is the boundary layer resistance ( $s \cdot m^{-1}$ ) (Brown and Gillespie, 1986).

The longwave radiation emitted by a person is defined as:

$$L_s = \varepsilon_s \sigma (\theta_{sf} + 273.15)^4 \quad (2.46)$$

where  $\varepsilon_s$  is the emissivity of the body and the clothing, assumed to be equal to  $\sim 0.95$  (Kenny et al., 2009a),  $\sigma$  is Stefan Boltzmann constant equal to  $5.67 \cdot 10^{-8}$  ( $W \cdot m^{-2} \cdot K^{-4}$ ) and  $\theta_{sf}$  ( $^{\circ}C$ ) is the surface temperature of a person. The original Equation 2.46 (Kenny et al., 2009a) was multiplied by the reduction factor  $A_{eff}$  based on the radiative area of the human body (equal to 0.78 is standing and 0.7 if cycling); as for the radiative balance in the proposed model, it is not necessary to multiply it by  $A_{eff}$ , as the radiation received is already normalized by the surface of the human body. This approach was validated by Prof. Vanos (Vanos, 2016).

The surface temperature of a person  $\theta_{sf}$  ( $^{\circ}C$ ) is defined as:

$$\theta_{sf} = \left( \frac{\theta_{sk} - \theta_a}{r_c + r_a} \right) r_a + \theta_a \quad (2.47)$$

A further study was conducted in the city of Kiruna ( $67^{\circ} 51' N$ ,  $20^{\circ} 13' E$ , 530 m asl, Cumulative Solar Irradiance:  $825 \text{ kWh} \cdot m^{-2}$ , Heating Degree Days: 7,176), in order to understand the impact of the ground covering in the human's thermal sensation. During the analyses was underlined an underestimation of the cold thermal sensation, by the COMFA\* model, because of the calculation of the surface temperature (Equation 2.47). Effectively, the surface temperature of a person and his/her skin temperature are directly related to the air temperature, as presented in Equations 2.26 and 2.47. Consequently, in extreme cold air temperatures,  $\theta_{sf}$  became too cold, and consequently the longwave radiation emitted by the body is too low, in respect to the reality. As an example, during a winter day, with an air temperature corresponding to  $-29^{\circ}C$  and with strong wind ( $9.4 \text{ ms}^{-1}$ ), the surface temperature of the body corresponds to  $-24.76^{\circ}C$ . This value is clearly too low, knowing, from previous studies, that the skin temperature, corresponds to  $30^{\circ}C$  in cool environment (if  $\theta_a=8-10^{\circ}C$ ),  $31-33^{\circ}C$  in neutral environment (if  $\theta_a=20-24^{\circ}C$ ) and  $33-37^{\circ}C$  in hot environment (if  $\theta_a=30-40^{\circ}C$ ) (Kenny et al., 2009b). Additionally, the face skin temperature exposed to cold conditions, could vary between  $30^{\circ}C$  to  $5^{\circ}C$  after 20 minutes exposure in cold environment ( $-10^{\circ}C$  and wind speed up to  $6 \text{ ms}^{-1}$ ) (Shabat and Shitzer, 2012). This phenomenon deals with the reduction of the heat emitted by the pedestrian, consequently reducing the heat losses by the human body. Further investigations, which unfortunately are beyond the scope of this thesis, are required in order to understand this behaviour.

Concluding, the thermal budget of a person is defined according to a seven-point scale, as expressed in Table 2.5 (Kenny et al., 2009a).

Thermal sensation	COMFA budget ( $W m^{-2}$ )
Cold	$\leq -201$
Cool	$-200$ to $-121$
Slightly cool	$-120$ to $-51$
Neutral	$-50$ to $+50$
Slightly warm	$+51$ to $+120$
Warm	$+121$ to $+200$
Hot	$\geq 201$

Table 2.5 Thermal sensation as a function of the COMFA\* budget.

Another thermal scale is proposed in order to quantify the thermal sensation of the pedestrian doing high metabolic activities; in this case the comfortable sensation is assumed between  $-20$  to  $+150$  ( $W m^{-2}$ ) (Kenny et al., 2009b). The outdoor human comfort, quantified by the use of the COMFA\* budget, in the EPFL campus will be presented in Chapters 4.

## 2.4 Sensitivity analysis of COMFA\* and ITS models

The following paragraph shows the results provided by both comfort models, when considering a pedestrian located in the outdoor environment, of six case studies (named A, B, C, D, E and F) presented in Table 2.6 and Figure 2.4. This includes an outdoor environment without any building and a street canyon oriented North-South and East-West, with height/width ratio equals to 2 (height equals to 5 meters and width equals to 2.5 meters). The COMFA\* budget is used to quantify the thermal sensation in the temperate climate of Lausanne (case study A, B and C); the Index of Thermal Stress is used to quantify the thermal sensation in the hot arid climate of Dubai (case study D, E and F), as summarized in Table 2.6. The objective of this analysis is to assess the sensibility of both approaches for different climates and during different periods of the year. In this case study we considers the canyon orientation, in the next chapter we will analyse the buildings orientation: the North-South canyons orientation corresponds to the East-West buildings orientation.

Climate	Thermal Model	Urban Canyon	Identity
Lausanne	COMFA*	North-South	Case study A
	COMFA*	East-West	Case study B
	COMFA*	No canyon	Case study C
Dubai	ITS	North-South	Case study D
	ITS	East-West	Case study E
	ITS	No canyon	Case study F

Table 2.6 Sensitivity analysis: case studies, as a function of the canyon orientation and the climate.

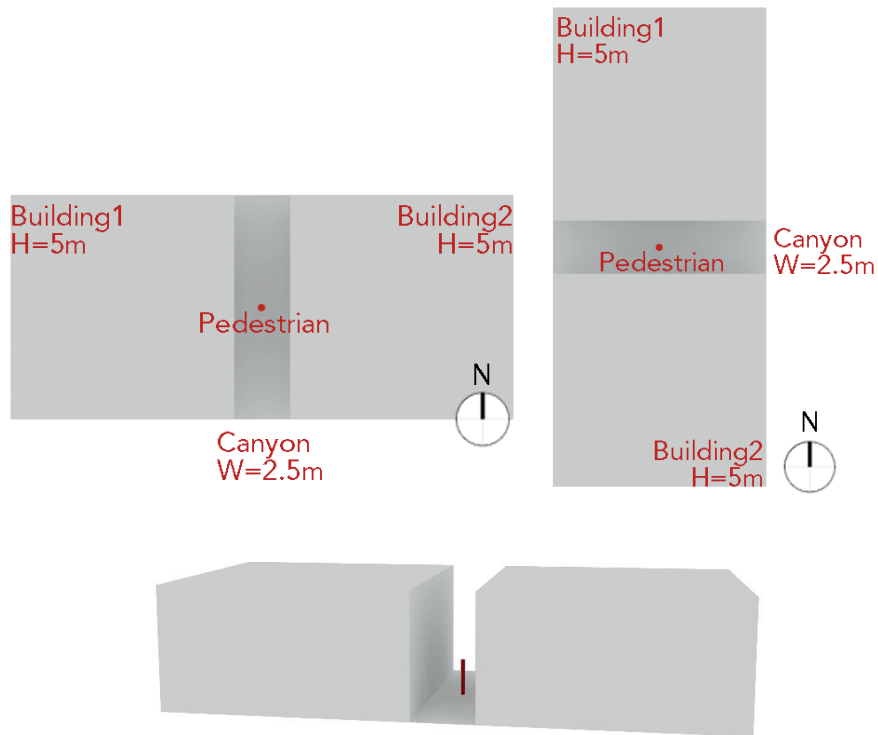


Figure 2.4 Urban canyon design. Top-left: North- South oriented. Top-right: East- West oriented. Bottom: 3D view of the urban canyon.

### 2.4.1 COMFA\* budget results

Table 2.7 summarizes the thermal sensation of a pedestrian, for the four cases studies: the annual comfortable hours (the ones with a COMFA\* budget between  $-50 \text{ W}\cdot\text{m}^{-2}$  and  $+50 \text{ W}\cdot\text{m}^{-2}$ ) in Lausanne are slightly lower for the North-South oriented canyon (567 hours) then for the East- West one (710 hours).

Case study	“ Cold ” hours	“Cool” hours	“Slightly cool” hours	“Comfortable” hours	“Slightly warm” hours	“Warm” hours	“ Hot” hours
Case study A (NS)	928	5,654	1,551	567	58	2	0
Case study B (EW)	938	5,590	1,405	710	113	4	0
Case study C	688	4,359	1,103	1,340	1,012	258	0

Table 2.7 COMFA\* budget. Analysis of the hours characterized by the same thermal sensation, as a function of the site (Lausanne) and the canyon orientation.

Figure 2.5 shows the COMFA\* budget for Lausanne ( $46^\circ 31' \text{ N}$ ,  $06^\circ 38' \text{ E}$ , 495 m asl, Cumulative Solar Irradiance:  $1,219 \text{ kWh}\cdot\text{m}^{-2}$ , Heating Degree Days: 3,273) during the winter (21<sup>st</sup> December) and summer solstice (21<sup>st</sup> June), as well as the spring equinox (21<sup>st</sup> March). The impact of the urban environment is obvious on the thermal sensation perceived by a pedestrian on the 21<sup>st</sup> of June in the climate of Lausanne. In a canyon oriented East-West, a person would feel “slightly warm” ( $\text{COMFA}^* > 51 \text{ W}\cdot\text{m}^{-2}$ ) in the afternoon (from 15:00 hours to 18:00 hours); by contrast for a canyon oriented North-South, a person would feel “slightly warm” just during the hottest hours of the day (from noon to 14:00 hours).

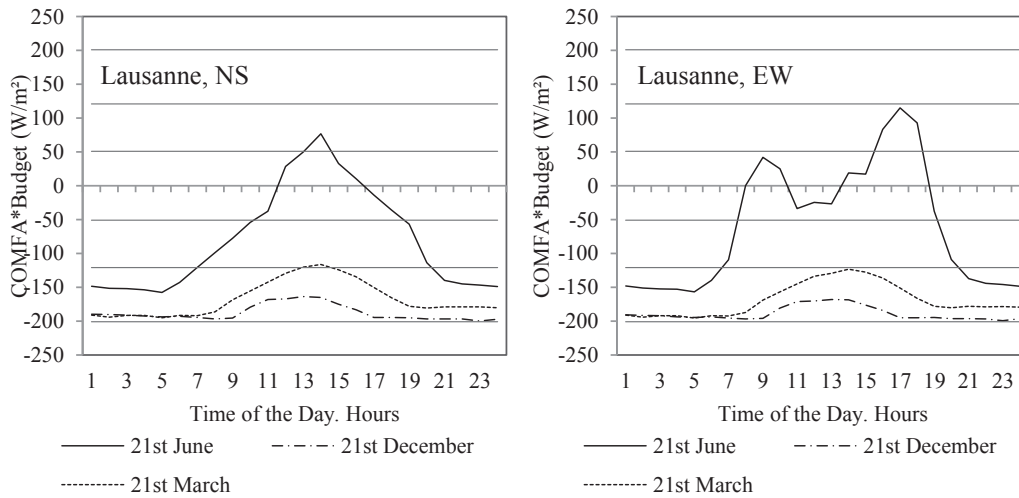


Figure 2.5 COMFA\* budget in the climate of Lausanne, for a canyon oriented North- South (left) and East- West (right). Time of analysis: 21<sup>st</sup> March, 21<sup>st</sup> June and 21<sup>st</sup> December.

In order to better understand the thermal behavior of a pedestrian located in the East-West oriented canyon, the energy fluxes are analyzed as shown in Figure 2.6 and 2.7. The objective of this analysis is to understand the way a pedestrian exchanges energy with the environment during a summer (21<sup>st</sup> of June) and winter day (21<sup>st</sup> December). By analyzing the total fluxes for each component of the budget (longwave radiation emitted by a person, evaporation, convective heat losses, radiation absorbed and metabolic heat), the main differences, expressed in daily average, are obvious on the radiation absorbed by the pedestrian ( $369.54 \text{ W}\cdot\text{m}^{-2}$  the 21<sup>st</sup> of June and just  $203.89 \text{ W}\cdot\text{m}^{-2}$  the 21<sup>st</sup> December) and on the convective heat losses ( $-41.74 \text{ W}\cdot\text{m}^{-2}$  the 21<sup>st</sup> of June and  $-95.88 \text{ W}\cdot\text{m}^{-2}$  the 21<sup>st</sup> December). The metabolic heat and the evaporation are similar. The radiation absorbed is related to the sun path and the environmental surface temperatures; the convective heat losses are related to the air temperature (on average  $22.7^\circ\text{C}$  and  $0.0^\circ\text{C}$  during the 21<sup>st</sup> of June and December, respectively) and wind speed ( $0.97 \text{ m}\cdot\text{s}^{-1}$  and  $1.01 \text{ m}\cdot\text{s}^{-1}$  during the 21<sup>st</sup> of June and December respectively). During the 21<sup>st</sup> of June the heat losses by convection are slightly higher during nighttime (up to  $-66.91 \text{ W}\cdot\text{m}^{-2}$ ) compared to daytime; by contrast the losses are larger on the 21<sup>st</sup> of December, up to  $-100.71 \text{ W}\cdot\text{m}^{-2}$ .

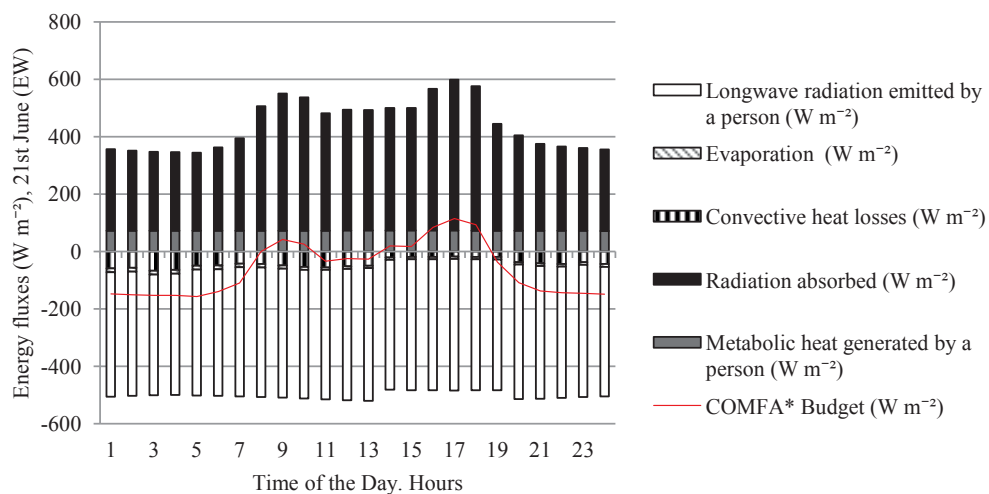


Figure 2.6 Energy fluxes in the COMFA\* budget in the climate of Lausanne, for a canyon oriented East- West. Time of analysis: 21<sup>st</sup> June.

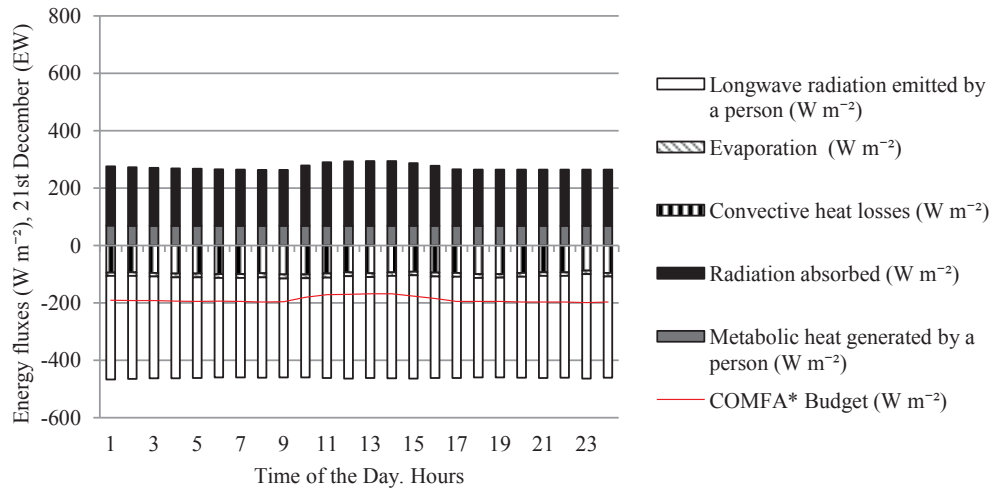


Figure 2.7 Energy fluxes in the COMFA\* budget in the climate of Lausanne, for a canyon oriented East- West. Time of analysis: 21<sup>st</sup> December.

### 2.4.2 Index of Thermal Stress results

As for the COMFA\* budget, the ITS was analyzed for the three case studies, in order to outline the sensibility of the method regarding the outdoor environmental conditions (Table 2.8). The comfortable hours in the case of Dubai (25°16'N, 55°20'E, 0 m asl, Cumulative Solar Irradiance: 1,997 kWh·m<sup>-2</sup>, Cooling Degree Days: 6,196) corresponds to 6,385 hours for the East- West oriented canyon (case study E), and 6,704 hours for the North-South oriented one (case study D). The built environment has a positive impact on the thermal sensation of a pedestrian: the case study F shows a reduction in the “comfortable” hours (5,292 hours), and an increase of the “warm” (1,661 hours), “hot” (1,073 hours) and “very hot” (212 hours) ones.

Case study	Index of Thermal Stress (W)				
	“Cool” hours (< -160)	“Comfortable” hours (-160 to +160)	“Warm” hours (160 to 480)	“Hot” hours (480 to 800)	“Very hot” hours (>800)
Case study D (NS)	915	6,704	1,131	10	0
Case study E (EW)	930	6,385	1,387	60	0
Case study F	522	5,292	1,661	1,073	212

Table 2.8 Index of Thermal Stress (W). Analysis of the hours characterized by the same thermal sensation, as a function of the site (Dubai) and the canyon orientation.

Figure 2.8 shows the Index of Thermal Stress for the site of Dubai in hourly values for the entire year; the ITS is characterized by a few “cool/ cold” thermal perceptions during winter time, which is normally comfortable. In the canyon oriented North- South, “warm” thermal sensations appear from mid-March; some “hot” events are happening during summer time (max value 561 Wm<sup>-2</sup>). On the contrary, a pedestrian located in an East- West canyon would face more hot events, with a peak at 596 Wm<sup>-2</sup>. These values are naturally related to a pedestrian exposed to the outdoor environment, with a metabolic activity of 80 Wm<sup>-2</sup>; it is clear that by increasing the metabolic activity, the number of stress events would increase. In any case in both locations, a pedestrian would feel warm, up to hot, during the day in summertime, during nighttime his/her thermal sensation would decrease to comfortable.

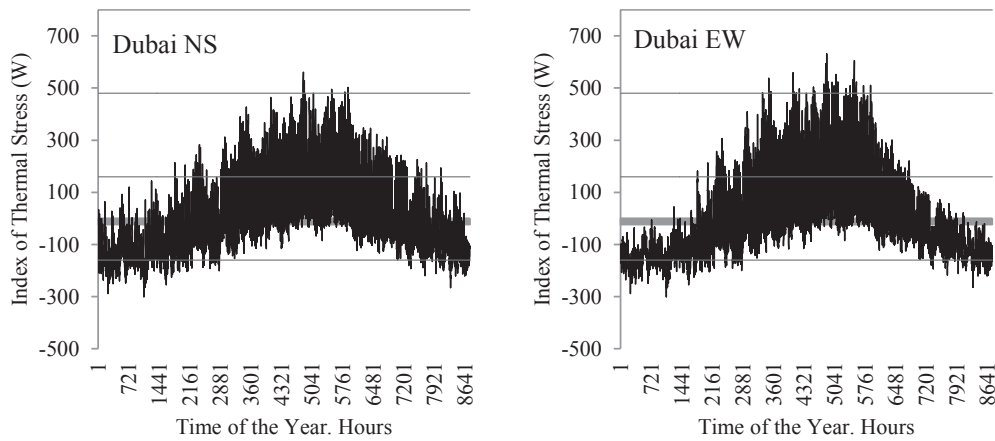


Figure 2.8 ITS in the climate of Dubai, for a canyon oriented North- South (left) and East- West (right). Time of analysis: hourly data during a typical meteorological year.

In order to understand and to quantify the impact of the built environment on the thermal sensation, the analyses were focused on a typical summer day (4<sup>th</sup> of July) depicted in Figure 2.9 showing the Index of Thermal Stress for the three case studies. In both case studies D and E, a pedestrian would face a “warm” thermal sensation during daytime, case study E being “hotter” in the morning and in the afternoon. But a pedestrian in case study F (no buildings) would face a “warm” thermal sensation already at 7:00 hours, “hot” from 9:00 hours, up to “very hot” from 10:00 hours to 18:00 hours.

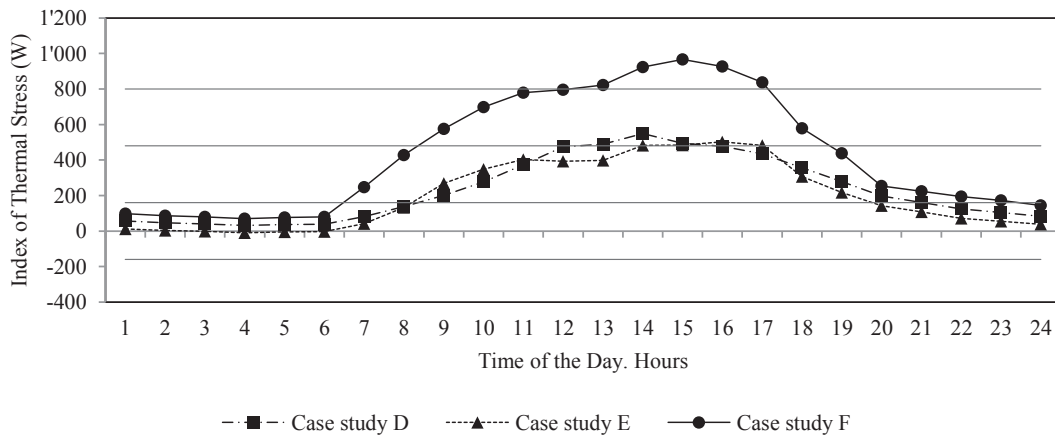


Figure 2.9 Index of Thermal Stress (W) for a typical summer day (4th July), for a pedestrian located in Case study D, E and F.

The Index of Thermal Stress is directly related to the metabolic activity of a pedestrian: as an example if the case study E (East-West oriented canyon) is considered by varying the metabolic activity from relaxed to walking at  $1.2 \text{ ms}^{-1}$  ( $150 \text{ Wm}^{-2}$ ), the hours characterized by a “cool” thermal sensation are significantly reduced passing from 930 to 498 hours and the hours characterized by a “hot” thermal sensation are increased from 60 to 237 hours (Figure 2.10).

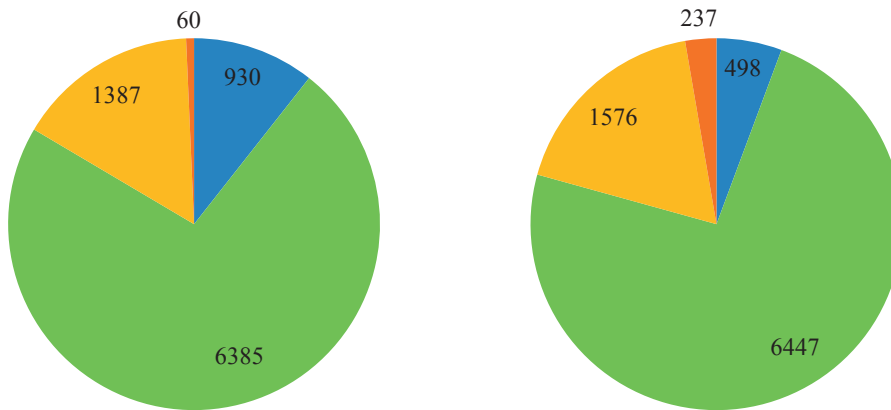


Figure 2.10 Index of Thermal Stress, for a pedestrian located in an East-West oriented canyon. Thermal sensation as a function of the total hours during the year, by varying the metabolic activity, from 80Wm<sup>-2</sup> (left) to 150Wm<sup>-2</sup> (right). Thermal sensation: “cool” (blue), “comfortable” (green), “warm” (yellow) and “hot” (orange).

## 2.5 Mean Radiant Temperature

The object of this study is to propose a new methodology to assess Mean Radiant Temperatures (MRT) in the built environment by the way of the urban simulation software CitySim Pro; this methodology is expected to simplify the urban design process and give access to the computation of outdoor human comfort for architects and urban planners. The input data are retrieved from a vectorial DXF 2000 format (Drawing eXchange Format), the typical file extension used by CAD software. The geometrical data read by the software are then coupled with the thermo-physical properties of the built environment (energy related data for buildings and microclimate information regarding the outdoor environment). The simulation results cover the energy demand of building (heating, cooling, electrical power demands and renewable energy generation) as well as the outdoor microclimate (short and longwave radiation, surfaces temperature and mean radiant temperatures). The following section presents the on-site monitoring of the EPFL campus located close to the city of Lausanne (Switzerland) and the Swiss International School (SISD) of Dubai (United Arab Emirates) used for the validation of the new methodology introduced in the software CitySim Pro.

The proposed Mean Radiant Temperature model is based on the integral radiation measurement (Höppe, 1992); the shortwave radiation (direct, diffuse and reflected by the built environment) and longwave radiation impinging on a pedestrian are computed using the software CitySim Pro (in W·m<sup>-2</sup>), and they are then multiplied by the area of each facade to obtain the total energy flux impinging on the pedestrian. The Mean Radiant Temperature (K) is defined accounting for the sum of the radiant fluxes issued from the surrounding built environment in the different directions as following:

$$T_{mrt} = \sqrt[4]{\left(\frac{S_{str}}{\varepsilon_p \sigma}\right)} \quad (2.48)$$

where  $S_{str}$  (Wm<sup>-2</sup>) is the mean radiant flux density,  $\varepsilon_p$  (-) is the emissivity of the human body and  $\sigma$  is the Stefan-Boltzmann constant (5.67·10<sup>-8</sup> W·m<sup>-2</sup>K<sup>4</sup>). We assumed the emissivity of the human body, knowing that, based on the Kirchhoff's laws,  $\varepsilon_p$  is equal to the absorption coefficient for longwave radiation (Thorsson et al., 2007). The mean radiant flux density  $S_{str}$  is equal to the sum of the short and long wave radiation impinging on each facade, multiplied by the corresponding angular weighting factor. Each distinct contribution is weighted by the corresponding absorption coefficient:

$$S_{str} = \alpha_k \sum_{i=1}^6 K_i F_i + \varepsilon_p \sum_{i=1}^6 L_i F_i \quad (2.49)$$

where  $\alpha_k$  (-) is the absorption coefficient of shortwave radiation (standard 0.7 value for a person),  $K_i$  ( $W \cdot m^{-2}$ ) is the shortwave irradiation flux on surface  $i$ ,  $F_i$  (-) is the angular weighted factor for surface  $i$  (Fanger, 1970), and  $L_i$  ( $Wm^{-2}$ ) is the longwave irradiation flux received by surface  $i$ .  $F_i$  are depending on the body posture and orientation: for a standing person it is equal to 0.22 for irradiation fluxes issued from the four cardinal orientations and 0.06 for fluxes impinging from above or below (Thorsson et al., 2007).

The input variables required by the integral radiation measurement procedure are determined by the software. The shortwave radiation impinging the surface  $K_i$  is calculated using the Simplified Radiosity Algorithm (SRA) (D Robinson and Stone, 2005) implemented within CitySim Pro; the solar radiation incident on a surface is a function of the site, the topography and the buildings geometry (Darren Robinson and Stone, 2005). The longwave radiation received by the surface  $L_i$  is calculated within CitySim Pro as defined for the ITS model, in Equations 2.4 to 2.7.

In this presented section, the Mean Radiant Temperature is generally expressed in K; to improve the readability of the results, it will be expressed in °C in the following sections. The CitySim Pro virtual environment is based on a CAD geometry: the human subjects considered for simulation are accordingly located in the 3D virtual model and represented as an octagonal prism inscribed in a circle of 0.17 m of diameter, with the upper face at 1.5 m height from the ground and the lowest face at 1.0 m height. Currently, the MRT calculation is performed for each prism (representing a human being) located in the virtual environment; to create a MRT mapping the prisms must be placed in accordance with a 1.5m grid, so that they will not interfere significantly with each other by impacting the short and long wave radiation they receive. In further developments of the CitySim Pro software, the virtual prisms will "not be visible" by each other; in this way they could be placed on a denser grid (with smaller distances) without interacting and impacting the calculations. The prismatic shape, representing a pedestrian, located on the point of MRT measurement was defined to account for the impinging solar radiation on different orientations: not only the cardinal directions, e.g. North, East, South and West directions are accounted for, but also the intermediate directions as it may occurs to the human body. An integral radiation calculation is implemented in the software: the user must import for that purpose the pedestrian virtual model and its location in the 3D virtual environment; the properties of the pedestrian are described using the following XML tag:

```
<Building Name="Pedestrian" id="o" key="p7" Simulate="true" mrt="true" mrtEpsilon="0.95">
```

where  $mrt="true"$  represent the MRT calculation for the selected object and  $mrtEpsilon$  represent the longwave emissivity of the object, equal to  $\sim 0.95$  (Thorsson et al., 2007).

Each object surface (wall, roof and floor) is characterized by the following XML tags:

```
<Wall id="15" type="7" ShortWaveReflectance="0.37" LongWaveEmissivity="0.95">
  <V0 x="4100.44" y="2587.68" z="9.01"/>
  <V1 x="4100.39" y="2587.71" z="9.01"/>
  <V2 x="4100.39" y="2587.71" z="8.51"/>
  <V3 x="4100.44" y="2587.68" z="8.51"/>
</Wall>
```

where  $ShortWaveReflectance="0.37"$  and  $LongWaveEmissivity="0.95"$  define the shortwave reflectance and the long wave emissivity of the object (comprised between 0 and 1);  $V_0$ ,  $V_1$ ,  $V_2$  and  $V_3$  are the vertex of the facade, followed by their x, y and z coordinates. Finally, the tag  $type="7"$  describes the physical properties of the envelope (density, conductivity and specific heat, as summarized in Table 2.2) for the pedestrian illustrated in what follows:

```
<Composite id="7" name="Pedestrian" color="-16711681" category="roof">
  <Layer Thickness="0.01" id="11" name="Skin" Density="1085.0" Cp="3680.0"
  Conductivity="0.47" abs="0.8" em="0.9" NRE="0.23" GWP="0.01" UBP="57.86" type="77"/>
  <Layer Thickness="0.01" id="11" name="Fat" Density="850.0" Cp="2300.0"
  Conductivity="0.16" abs="0.8" em="0.9" NRE="0.23" GWP="0.01" UBP="57.86" type="77"/>
```



```

<Layer Thickness="0.01" id="11" name="Muscle" Density="1085.0" Cp="3768.0"
Conductivity="0.42" abs="0.8" em="0.9" NRE="0.23" GWP="0.01" UBP="57.86" type="77"/>
<Layer Thickness="0.14" id="11" name="Water" Density="1000.0" Cp="4000.0"
Conductivity="0.6" abs="0.8" em="0.9" NRE="0.23" GWP="0.01" UBP="57.86" type="77"/>
</Composite>

```

In the next paragraphs the proposed model is validated, using on-site monitoring in the temperate and hot arid climates of EPFL and SISD campuses, respectively.

### 2.5.1 MRT model validation through on-site monitoring on the EPFL campus, Lausanne

The on-site monitoring was carried-out on the roof terrace of the LESO-building solar experimental building (46° 31' N, 06°38' E, 495 m asl) located on the EPFL campus using a grey (RAL 7001) plastic globe thermometer. The building (red rectangle illustrated on Figure 2.11) is located in the center of the campus; it is surrounded by other buildings and unobstructed on the South side facing a green court. Different methods are available to highlight the Mean Radiant Temperature in accordance with the type of globe (material, colour and dimensions) used for the measurements (Johansson et al., 2014). The considered globe has a diameter of 150 mm with an internal temperature sensor connected to a data logger (Tinytag); the temperature range of the device is equal to [-10°C, +40°C] and the accuracy of the instrument is equal to  $\pm 0.5^\circ\text{C}$ . The globe temperatures were recorded each 10 minutes and averaged hourly; the device was placed at 1.1 m height above the roof terrace, corresponding to the centre of gravity of an human body in accordance with ISO 7726 (International Organization for Standardisation, 1998). MRT measurements were performed during the months of August, September and October 2015; the monitoring period includes clear, partly cloudy and overcast sky conditions.

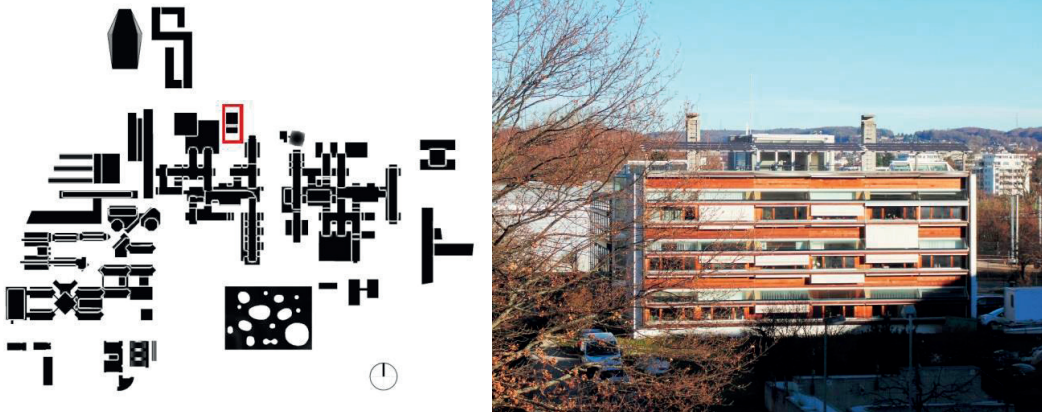


Figure 2.11 Map of the EPFL campus in Lausanne (Switzerland), the LESO building is enclosed by the red rectangle (left). View of the southern facade of the LE solar experimental building with its flat roof terrace, location of the monitoring (right).

The input meteorological data required for the calculations are available through an on-site weather station, located on the roof top of the building staircase at a + 2.5m height above the terrace floor; the weather station provides the air temperature (recorded each minute), wind velocity and direction (both recorded each 5 seconds), global horizontal irradiance and diffuse horizontal irradiance (both recorded each 30 seconds). The relative humidity (hourly average) and the Perraudeau relative nebulosity index (recorded each 10 minutes) are provided by two national weather stations located resp. in the cities of Pully (46° 30' N, 06°39' E, 426 m asl) and Payerne (46° 49' N, 06°56' E, 456 m asl). The monitoring period (see Table 2.9) was chosen in order to include the months of August, September and October 2015, and covers a total of 203 hours. These days represent typical summer and mid-season climatic conditions for Lausanne: summer days with maximum diurnal air temperature of 32°C and minimum temperature during nighttime of 12°C; mid seasons conditions with maximum temperature of 23°C during daytime and minimum temperature of 7°C during nighttime.

The monitored data ranges are:

- Ambient temperature: 7 to 32 °C
- Relative humidity: 37 to 96 %
- Wind speed: 0.01 to 12 m·s<sup>-1</sup>
- Nebulosity: 0 to 8 octas
- Global horizontal irradiance: 0 to 818 W·m<sup>-2</sup>
- Diffuse horizontal irradiance: 0 to 586 W·m<sup>-2</sup>

Day	Average ambient temperature (°C)	Maximum ambient temperature (°C)	Minimum ambient temperature (°C)	Average wind speed (m·s <sup>-1</sup> )	Average relative humidity (%)	Average global irradiance (W·m <sup>-2</sup> )	Average diffuse irradiance (W·m <sup>-2</sup> )
25.08.2015	18	22	13	0.2	58.3	474	69
26.08.2015	19	25	12	0.01	66.2	469	56
27.08.2015	23	28	16	0.1	60.3	426	125
28.08.2015	25	30	20	0.01	57.5	397	153
29.08.2015	25	30	18	0.01	65.7	425	67
30.08.2015	26	32	20	0.01	60.9	393	65
31.08.2015	26	32	20	0.01	55.6	415	66
01.09.2015	23	24	20	2.3	76.8	150	141
08.09.2015	15	21	10	1.4	62.2	417	83
09.09.2015	17	23	11	0.7	62.3	413	77
10.09.2015	16	22	11	1.2	70.8	319	127
14.09.2015	18	21	15	1.3	79.0	259	155
15.09.2015	16	18	13	0.7	66.0	160	152
16.09.2015	19	23	14	0.1	71.9	162	114
24.09.2015	13	19	10	1.2	66.5	365	50
25.09.2015	14	20	9	2.1	63.9	357	42
26.09.2015	14	18	10	2.1	71.6	230	158
27.09.2015	14	16	11	2.5	70.9	125	119
28.09.2015	12	17	8	8.0	61.8	299	85
29.09.2015	12	16	7	2.3	70.1	306	94
30.09.2015	11	15	7	4.2	68.4	308	315
01.10.2015	11	16	7	4.6	74.2	280	94
02.10.2015	12	17	8	0.01	82.5	260	107

Table 2.9 Meteorological conditions during the monitored period in Lausanne (August, September and October 2015).

Figure 2.12 shows the air temperature (°C) and the wind speed (m·s<sup>-1</sup>) during the selected days of measurements; all values are averaged per hour. The month of August is characterized by high diurnal temperatures, with a temperature difference between day and night corresponding to 10°C in average; during the month of September the air temperature is lower, with a maximum temperature of 23°C at noon. The wind speed is low during the month of August, and increases during the month of September, with a maximum wind speed of 14.6 m·s<sup>-1</sup> during the 28<sup>th</sup> of September.

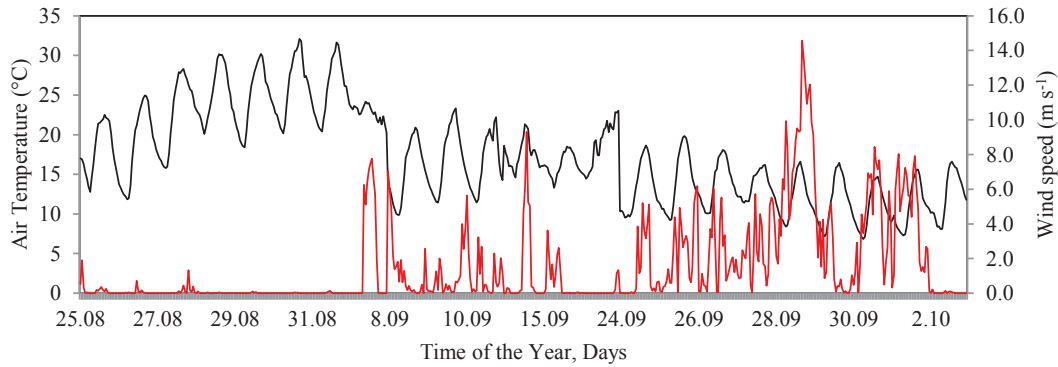


Figure 2.12 Air temperature (°C) and wind speed (m·s<sup>-1</sup>) during the monitoring performed in the EPFL campus in Lausanne (August, September and October 2015). Legend: air temperature (black line) and wind speed (red line).

Figure 2.13 shows the global and diffuse solar irradiance measured by the weather station on the LESO building rooftop, during the days of measurement. The global solar irradiance reaches 800 W·m<sup>-2</sup> at noon during the month of August, and decreases during the month of September, when the maximum global irradiance at noon reaches 600 W·m<sup>-2</sup> at the end of the month, and during the first week of October. As previously described, the measurements were carried out for several sky conditions, as shown in the graph: clear (as an example the 25<sup>th</sup> August, when the average global irradiation corresponds to 474 W·m<sup>-2</sup> and the diffuse radiation corresponds to 69 W·m<sup>-2</sup>), partly cloudy (as an example the 28<sup>th</sup> August, when the average global irradiation corresponds to 397 W·m<sup>-2</sup> and the diffuse radiation corresponds to 153 W·m<sup>-2</sup>) and overcast sky conditions (as an example the 27<sup>th</sup> September, when the average global irradiation corresponds to 125 W·m<sup>-2</sup> and the diffuse radiation corresponds to 119 W·m<sup>-2</sup>).

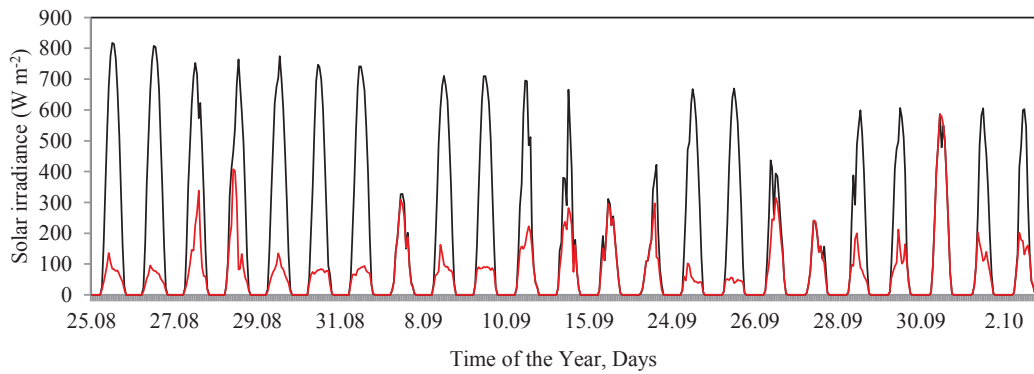


Figure 2.13 Solar irradiance (W·m<sup>-2</sup>) during the monitoring, performed in the EPFL campus in Lausanne (August, September and October 2015). Global irradiance (black line) and diffuse irradiance (red line).

The globe temperatures retrieved by monitoring are used to assess the Mean Radiant Temperature (MRT) following the international standard ISO 7726 (International Organization for Standardisation, 1998). The relation used to calculate the MRT from the globe temperature for a forced convection is expressed by Equation 2.50 (International Organization for Standardisation, 1998) :

$$T_{mrt} = \sqrt[4]{T_g^4 + \frac{1.1 \cdot 10^8 \cdot V_a^{0.6}}{\varepsilon_g \cdot D^{0.4}} * (T_g - T_a)} \quad (2.50)$$

where  $T_g$  (K) is the globe temperature,  $V_a$  (m·s<sup>-1</sup>) is the air velocity,  $\varepsilon_g$  (-) is the globe emissivity,  $D$  (m) is the globe diameters and  $T_a$  (K) is the air ambient temperature.

Based on the expression used to quantify the Mean Radiant Temperature, the experimental error was defined, by summing up the relative error of the instruments used during the calculation: the central weather station Siemens AP 257/22 and the globe thermometer; the experimental error of the analysis corresponds to 11%.

Figure 2.14 shows the 3D virtual environment created within CitySim Pro: the LESO building is unobstructed on its southern facade and the MRT monitoring is carried-out on its rooftop terrace (black circle). A staircase is located on the northern side of the terrace, on top of which a local weather station, providing the air temperature, the wind velocity and direction, the global and diffuse solar irradiance, was set-up. The thermo-physical properties of the building were defined (please refers to Chapter 4 for further details), including the envelope features, the occupancy profile, the indoor air temperature set-point and the properties of the terrace roof, made of concrete tiles with an 0.8 longwave infrared emissivity and an albedo of 0.2 (Erell et al., 2011a).

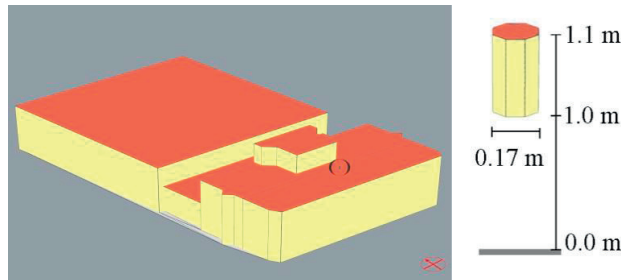


Figure 2.14 CitySim Pro 3D virtual model of the LE-building block on the EPFL campus. The black circle shows the location of the MRT monitoring station (left) and the prismatic shape as defined in the proposed methodology (right).

The results obtained with CitySim Pro show a Root Mean Square Error (RMSE) of 6.04°C (n=203) for the MRT and 4.76°C for the globe temperature (n=203) compared to the monitoring. The Willmott Index of agreement (Willmott et al., 2012) between the measured and simulated MRT values is equal to 0.97, showing a sound agreement between the simulation and the monitoring (Table 2.10). Figure 2.15 illustrates the correlation between the globe temperatures and the Mean Radiant Temperature, obtained by the way of monitoring and simulation; the black lines represent a 95% confidence interval. All points are located within the confidence interval, backing-up the model reliability.

Data	RMSE (°C)	Index of Agreement (-)	Mean Absolute Error (°C)
Globe Temperature	4.76	0.95	3.67
Mean Radiant Temperature	6.04	0.97	4.93

Table 2.10 Summarized results for the proposed methodology compared with on-site monitoring ; statistical analysis of the Root Mean Square Error (RMSE), Index of Agreement and Mean Absolute Error.

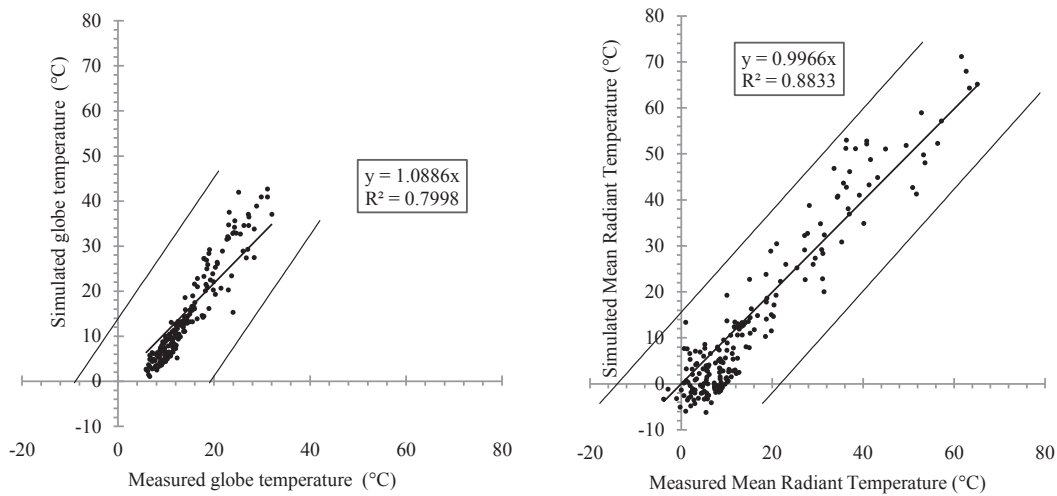


Figure 2.15 Statistical regression analysis between CitySim Pro calculations and on-site monitored data. Simulated and monitored globe temperatures (left). Simulated and monitored Mean Radiant Temperatures (right).

It is interesting to notice that the MRT has negative values, in particular environmental conditions: during the night between the 24<sup>th</sup> and the 25<sup>th</sup> of September, due to the low air temperature and the clear sky conditions (nebulosity equals to zero octas), the MRT simulated by CitySim goes slightly under 0°C.

The results provided by the software are text based: the Mean Radiant Temperature is calculated hourly and exported by CitySim Pro in a tab-separated text format. In this case study, the MRT is determined for a single point, corresponding to a pedestrian located on the roof terrace of the LESO building. Figure 2.16 shows the hourly monitored values of the Mean Radiant Temperature as well as the ones calculated with CitySim Pro (during the 30<sup>th</sup> of September, from 8:00 to 18:00): the largest difference can be observed in the afternoon and is equal to 7°C at 15:00.

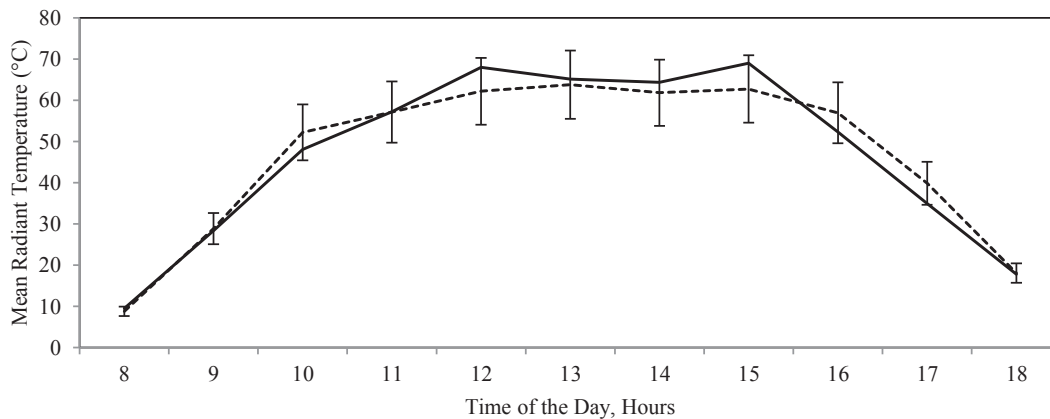


Figure 2.16 Hourly comparisons between the monitored Mean Radiant Temperature (dotted black line) and the one calculated by the software CitySim Pro (continuous black line); the experimental error of the measurements is defined by the error bars.

The differences between the monitored and the simulated MRT are related to three factors: i) the instruments accuracy (the globe, the air temperature and the wind speed), ii) the response time of the grey thermometer and iii) the shadowing pattern. Effectively, the temporal resolution in CitySim Pro corresponds to hourly values: if the building is shadowing the rooftop, and consequently reducing its temperature, this phenomenon is accounting for each 1 hours- step even if the same rooftop is in reality exposed to the sun for 10 minutes, then protected by shadows for 50 minutes. This phenomenon results in an over or underestimation of the shortwave radiation

fluxes, and consequently in the mean radiant temperature. Dynamic simulations, realized in hourly time-steps already describe sufficiently the outdoor environmental conditions, giving insight with a sound accuracy about the urban microclimate. By contrast, it is evident that the outdoor environment is affected by rapid changes on climatic conditions, which cannot always be perfectly described by the means of simulations methods.

### 2.5.2 MRT model validation through on-site monitoring in the SISD campus, Dubai

The on-site monitoring in the city of Dubai (25°16'N, 55°20'E, 0 m asl, Cumulative Solar Irradiance: 1,997 kWh·m<sup>-2</sup>, Cooling Degree Days: 6,196) was carried-out on a roof terrace of the main building of the Swiss International School of Dubai (please, refers to Chapter 5 for further details). In order to analyze the microclimate, three weather stations were located in the campus: one station, so called WS-1711, is located on the rooftop of the administrative building; the second station, so called WS-1712, is located on the first floor of the kindergarten (Figure 2.17), and the last one, so called WS-1713, is located on the ground floor.

Due to construction works on site, the last station was moved periodically in four different places: between the entrance of the school and the parking (from the end of November 2015 to the 15<sup>th</sup> of May), on the Southern entrance of the school, in a playground area (from the 17<sup>th</sup> of May to the 2<sup>nd</sup> of July), in the same location, but under a tree near the swimming pool (from the 13<sup>th</sup> of July 2016 to the 17<sup>th</sup> of September) and finally near a wall and upon the vegetation (from the 19<sup>th</sup> of September). In order to validate the MRT assessed by CitySim Pro, a 3D model of the campus was defined and the results provided by CitySim Pro were compared with the monitoring of WS-1712. The station 1712 is equipped with the following equipment: Campbell black globe thermometer, Decagon VP-3 (vapor pressure, temperature and relative humidity sensor) and Decagon DS-2 (sonic anemometer). The equipment is positioned between 1.1 and 1.5 m height, corresponding to the center of gravity of the human body. The MRT is measured by a Campbell black globe thermometer, a hollow copper sphere with a diameter of 15 cm, painted black and with a thermistor inside. The measurement range (all data are provided by the instrument's specification) between -5 to 95°C, the accuracy varies between ± 0.3°C (-3 to 90°C) and between ± 0.7 °C (-5 to 95°C); measurements were performed each minute. All the meteorological information were recorded by the WS-1712, except for the global and diffuse irradiance, measured by the main weather station (WS-1711) located on the rooftop of the main building. Measurements provided by each instrument, as well as their accuracy, are presented in Table 2.11.

Variable	Instrument	Accuracy
Vapor pressure (kPa)	Decagon VP-3	0.01 kPa
Air temperature (°C)	Decagon VP-3	±1°C to ±0.25°C
Wind speed (m·s <sup>-1</sup> )	Decagon DS-2	0.30 m·s <sup>-1</sup>
Wind direction (°)	Decagon DS-2	±3°
Mean Radiative Temperature	Campbell black globe thermometer	± 0.3°C (-3 to 90°C) and between ± 0.7 °C (-5 to 95°C)
Global solar irradiance (Wm <sup>-2</sup> )	Pyranometer (Delta-T)	SPN1 ± 5% or ±10 Wm <sup>-2</sup> in hourly values
Diffuse solar irradiance (Wm <sup>-2</sup> )	Pyranometer (Delta-T)	SPN1 ± 5% or ±10 Wm <sup>-2</sup> in hourly values

Table 2.11 On site monitoring in Dubai. Instruments type and their accuracy.



Figure 2.17 WS- 1712, located on the first floor, in the playground/ sport area.

The monitoring period (see Table 2.12) was chosen in a way to include all climatic conditions, from extreme cold to extreme hot events; doing so, the months of February, March, May and August 2016 were selected, covering in total 199 hours. These days represent typical summer, winter and mid-season climatic conditions for Dubai. Summer days with maximum diurnal air temperature of 46°C and minimum temperature during nighttime of 27°C (month of August). Mid seasons conditions with maximum temperature of 38°C during daytime and minimum temperature of 16°C during nighttime (month of March) and winter conditions, with maximum temperature of 34°C during daytime and minimum temperature of 12°C during nighttime (month of February).

The monitored data ranges are:

- Ambient temperature: 15.0 to 48.7 °C
- Relative humidity: 13 to 93 %
- Wind speed: 0.01 to 1 m·s<sup>-1</sup>
- Global solar irradiance: 0 to 872 W·m<sup>-2</sup>
- Diffuse solar irradiance: 0 to 421 W·m<sup>-2</sup>



Outdoor Human Comfort

Date	Average ambient temperature (°C)	Maximum ambient temperature (°C)	Minimum ambient temperature (°C)	Average wind speed (m·s <sup>-1</sup> )	Average relative humidity (%)	Average global irradiance (W·m <sup>-2</sup> )	Average diffuse irradiance (W·m <sup>-2</sup> )
19.02.2016	20.3	27.0	15.0	0.3	77.5	208.0	46.9
21.02.2016	21.4	30.5	15.0	0.2	63.0	211.8	40.8
02.03.2016	21.4	27.0	16.8	0.3	57.6	214.4	62.3
04.03.2016	24.8	33.1	20.2	0.2	62.5	204.1	92.6
10.03.2016	22.9	30.3	18.1	0.3	75.3	227.5	77.1
02.05.2016	28.1	35.4	22.0	0.4	55.9	279.8	79.4
03.05.2016	29.5	38.1	21.5	0.3	43.0	275.3	89.5
04.05.2016	32.1	41.7	23.9	0.2	33.5	269.0	125.1
05.05.2016	32.1	40.7	25.4	0.2	38.0	265.4	122.6
06.05.2016	35.3	44.1	27.5	0.2	27.5	259.2	144.7
22.05.2016	31.1	36.8	26.0	0.4	61.7	270.4	104.1
23.05.2016	30.5	37.6	24.8	0.4	63.5	261.4	111.5
27.05.2016	30.1	37.4	23.9	0.4	58.9	268.7	107.7
28.05.2016	31.6	41.6	24.1	0.3	61.9	350.4	150.5
22.08.2016	36.1	46.2	29.3	0.2	51.2	218.8	134.0
23.08.2016	37.0	45.9	29.3	0.2	39.8	216.0	135.2
25.08.2016	37.9	46.7	29.6	0.2	37.9	218.8	139.4
27.08.2016	36.4	46.9	29.4	0.2	48.3	214.6	128.6
28.08.2016	36.3	45.4	29.8	0.2	57.7	202.1	132.1
29.08.2016	37.3	48.7	30.1	0.2	33.9	209.6	132.7
30.08.2016	36.4	46.8	29.7	0.2	40.0	210.9	129.6
31.08.2016	35.6	44.9	29.4	0.2	58.2	202.9	130.2

Table 2.12 Meteorological conditions during the monitored period in Dubai, February, March, Mai and August 2016.

Figure 2.18 shows the air temperature (°C) and the wind speed (m·s<sup>-1</sup>) during the selected days of measurements; all values are averaged hourly. The month of August is characterized by higher temperatures, up to 48.7°C in the end of the month. The maximum difference in air temperature between day and night appears during the month of August, with an average temperature difference of 16.8°C (a maximum 18.6°C was experienced on the 29<sup>th</sup> of August). The wind speed is low during the month of August, and increases during the last week of May, with an average wind speed of 0.44 m·s<sup>-1</sup>.

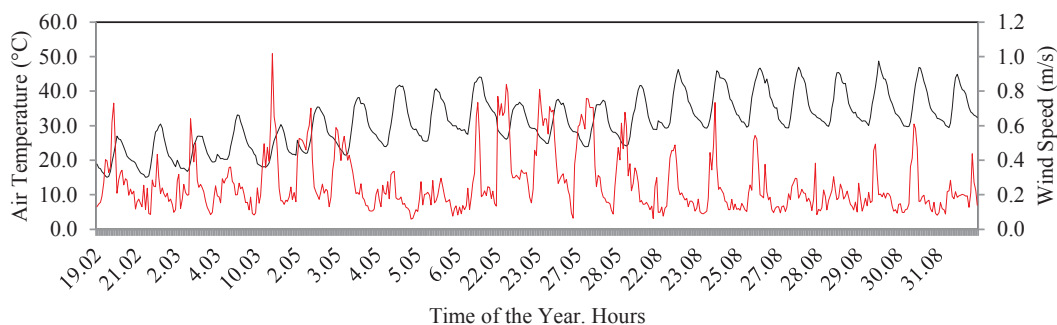


Figure 2.18 Air temperature (°C) and wind speed (m·s<sup>-1</sup>) during the monitoring performed in the SISD campus in Dubai (February, March, May and August 2016). Legend: air temperature (red line) and wind speed (black line).



Figure 2.19 shows the global and diffuse horizontal solar irradiance, monitored by the weather station for the days of measurement; generally, the main component of the radiation in this area is the direct one. Rain occurrence is exceptional in this region; all days of measurements were characterized by clear sky conditions, however the 4<sup>th</sup> of March was partially cloudy.

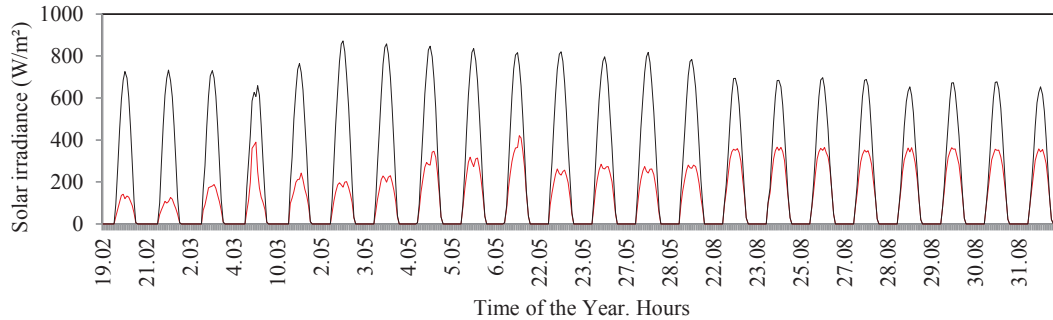


Figure 2.19 Solar irradiance ( $\text{W}\cdot\text{m}^{-2}$ ) during the monitoring, performed in the SISD campus in Dubai (February, March, May and August 2016). Global irradiance (black line) and diffuse irradiance (red line).

As for the case study in Lausanne, the globe temperatures retrieved by monitoring are used to assess the Mean Radiant Temperature following the international standards ISO 7726 “Ergonomics of the Thermal Environment. Instruments for Measuring Physical Quantities”. Based on the formula used to quantify the MRT, the experimental error was estimated by adding up the errors of the instruments used during the calculation: the Campbell black globe thermometer, the weather stations Decagon VP-3 and Decagon DS-2. The experimental error during the analyses is estimated to 9%, corresponding to the instruments errors, but neglecting the time lag of the globe thermometer response. It is important to underline that, due to the thermal inertia of the globe, the MRT calculation is quite sensitive to the air velocity, and this is why we placed the sonic anemometer immediately adjacent to the globe, measuring the rate of air flow over its surface.

Figure 2.20 shows the 3D model as designed in CitySim Pro; the pedestrian is located on the roof terrace of the kindergarten and he/she is protected by white shadowing devices. The results obtained with CitySim Pro show a Root Mean Square Error (RMSE) of  $4.11^{\circ}\text{C}$  ( $n=199$ ) for the MRT calculated during daytime (from 8:00 hours to 18:00 hours); the Willmott Index of agreement (Willmott et al., 2012) between the measured and simulated MRT values is equal to 0.99, showing an excellent agreement between the simulation and the monitoring. Figure 2.21 illustrates the correlation between the globe temperatures and the Mean Radiant Temperature, obtained by the way of monitoring and simulation ( $R^2=0.91$ ); all points are located within 95% confidence interval, backing-up the model reliability.

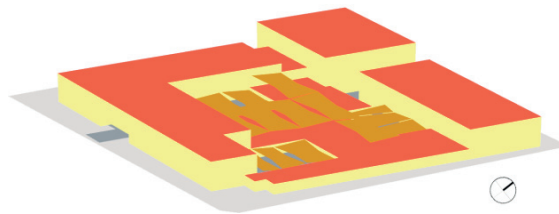


Figure 2.20 CitySim Pro 3D virtual model of the main building of the Swiss International School Campus.

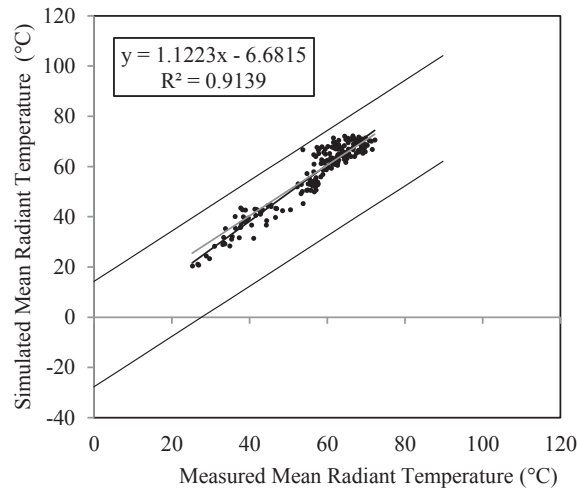


Figure 2.21 Statistical regression analysis between CitySim Pro calculations and on-site monitored data. Simulated and monitored Mean Radiant Temperatures (°C).

Figure 2.22 shows the daily MRT as calculated by the software CitySim Pro, and as monitored by the weather station: MRT calculated by CitySim Pro is underestimated during nighttime, with a difference between monitoring and modelling up to 11°C. This behavior was already identified by Lindberg et al (Lindberg et al., 2016) with on-site monitoring in Goteborg (Sweden) compared to SOLWEIG. The latter, just as CitySim, uses the Hoppe method to assess the MRT, which underestimates the Mean Radiant Temperature during nighttime up to 10°C. The difference can be related to the heat storage capacity of the built environment (due to the complexity of the model), or by an overestimation of the longwave radiation emitted by the sky, due to the physical properties of the textile meshes. In order to overcome this problem, further analyses are required in order to understand how to improve the model. Another difference between monitoring and modelled values is noticeable in cloudy conditions, as an example on the 4<sup>th</sup> of March, when at noon CitySim Pro underestimates the MRT by 6°C. Effectively, the weather stations installed in the campus do not record the nebulosity, consequently in these analyses the nebulosity of the site was always considered equal to zero. Due to this assumption, the MRT was underestimated during cloudy conditions. In order to overcome this problem, further investigations were defined, underling the variation of the MRT as function of the nebulosity, during the 4<sup>th</sup> of March. By modifying the weather file, and applying a nebulosity of 1, 3, 5 and 8 during all the day, the RMSE decreases from 6.9°C (original value), to 6.5°C, 5.8°C, 5.2°C and 4.3°C, respectively. It is consequently clear that the error during the 4<sup>th</sup> of March was related to the nebulosity and that probably the same error appears, but with a lower impact, in other days of analysis. Indeed, clouds cover impacts the sky temperature, increasing it, and consequently impacting the longwave exchanges between the pedestrian and the environment. Additionally, when clouds cover the sky, the globe is more susceptible to the variation in time, because it can be exposed to the sun and to the shade for several minutes, and this is not computed by CitySim, which provides the hourly values.

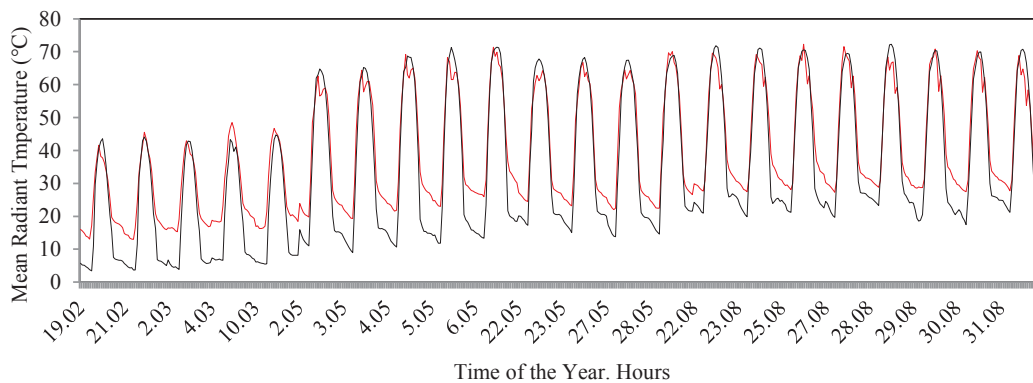


Figure 2.22 Mean Radiant Temperature as recorded by the weather station (black line) and modelled by CitySim (red line).

Finally, a difference between the monitored data and the model is related to the time step of the analysis: CitySim model uses hourly values; on the opposite the monitoring steps were each minute, with hourly averages. When varying the time step, as an example by calculating the MRT each minute then average it hourly, the difference between the two model increases, passing from a RMSE of 4.1°C to 4.9°C and increasing the mean absolute error from 3.2°C to 3.9°C. A further validation of the model will be presented in Chapter 5, when the Comfort Maps of the MRT will be designed for the SISD campus, showing that all the results are inside the experimental error.

As previously defined, the Mean Radiant Temperature is not used as a comfort variable alone, but it is used as an input for other comfort models, as an example the Physiological Equivalent Temperature. In order to understand the impact of the error produced by the proposed methodology, the Mean Radiant Temperature is used to calculate the Physiological Equivalent Temperature (PET), by the use of the software RayMan (Matzarakis et al., 2007). The PET is calculated for a standard pedestrian with a clothing insulation of 0.9 clo during winter time and 0.5 clo during summer time, a light metabolic activity of 80 W and a complete view of the sky vault (SVF=1). The air temperature varies from 0°C to 30°C and the Mean Radiant Temperature ranges by  $\pm 5^\circ\text{C}$  around the air temperature. The analysis considers a relative humidity of 35% and a wind speed of  $1.1 \text{ m}\cdot\text{s}^{-1}$ . The analyses are performed during the 21<sup>st</sup> of December and 21<sup>st</sup> of June at noon; the air temperature varies between 0°C to 10°C the 21<sup>st</sup> of December, and between 25°C to 35°C the 21<sup>st</sup> of June for the site of Lausanne. According to the results, a pedestrian is more sensitive to a variation of the Mean Radiant Temperature during summer time, compared to winter time: assuming a variation of 10°C in MRT, the PET varies of 2.6°C on the 21<sup>st</sup> of December, and 4°C on the 21<sup>st</sup> of June. Based on these results, an absolute error of 4.93°C has an impact lower than 2°C on the PET thermal sensation; it is not perceived by pedestrians because a person is sensitive to a variation of 5 to 6°C on the PET thermal scale (Matzarakis et al., 1999). Finally, the root mean square error appears to be elevated, but is in the same range for other software, for example SOLWEIG, with a RMSE equal to 6.79°C (Lindberg and Grimmond, 2011) and RayMan with a RMSE of 12.6 °C in accordance with the last study performed in 2016 (Lee et al., 2016). It is important to underline that the error could be related to two factors: measurements error as well as the simulations one. Effectively, a further improvement of this work would be to measure the MRT by a net radiometer, looking at the radiation balance by separating the radiation from all the cardinal directions, as well as from the top and the bottom.

### Future perspectives

The model of the MRT was in a sound way validated with on-site monitoring in Dubai and Lausanne. The following points however have to be addressed in the future:

- Assess the sensibility of CitySim Pro regarding the MRT by varying the ground covering, and the greening.
- Improve the MRT quantification during nighttime.

## 2.6 Conclusions and future outlook

A new approach to quantify the outdoor human comfort with the urban energy modelling CitySim Pro is proposed. The methodology makes use of the hourly output provided by the software (short-wave radiation, surface temperature and long-wave radiation) to calculate the Index of Thermal Stress, the COMFA\* budget and the Mean Radiant Temperature. The ITS is used to quantify the thermal sensation in a hot arid climate, and the COMFA\* in a temperate one. Between all the available thermal models, the above ones were selected due to their energy based approach; the ITS can perfectly describe the hot arid climate of Dubai, but neglects cold thermal sensations (slightly cool, cool and cold); on the opposite the COMFA\* budget, describes perfectly a temperate climate, but neglect extreme hot thermal sensations. Another important element that characterizes the ITS is the impact of the evaporation on the thermal sensation: it is obvious that in cold conditions a person exchanges heat mostly by radiation, and that in hot conditions, a person exchanges heat mostly by evaporation (as presented in Figure 2.23). Due to the last point, in the ITS the “cooling efficiency of sweating” has a strong impact on the thermal sensations, as it is directly multiplied by the other terms (radiation, metabolic heat and convection). By contrast, the evaporation is just part of the basic equation of COMFA\*, as the others, consequently has a low impact on the thermal sensation. Additionally, the ITS was created and validated in hot arid climates, so it indirectly considers the physiological acclimatisation and the naturalness of the climate.

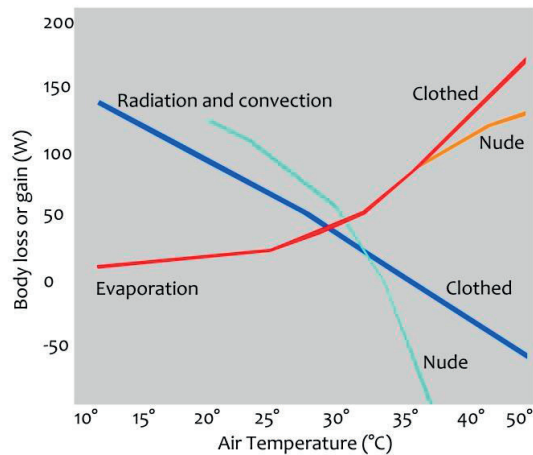


Figure 2.23 Thermal exchanges between the human body and the environment. Adapted from (Emery, 2014).

The proposed MRT model implemented in CitySim Pro was analyzed and validated with on-site monitoring in the climates of Lausanne and Dubai. The model is showing a nice correlation with the monitoring, leading to a RMSE of 4.11°C (n=199) in Dubai and 6.04°C (n=203) in Lausanne. The difference between the two cases is related to:

- **Accuracy of instruments:** the weather station in Dubai was installed in 2015 for the purpose of this thesis; the accuracy of the instruments was estimated to be 9%; on the opposite the weather station in Lausanne is an existing one (the last instruments were added since 2000) and due to its age the accuracy is estimated to 11%.
- **Accuracy of measurements:** in the case study of Dubai a new weather station was installed on-site, and the on-site monitoring (air temperature, wind speed and direction, relative humidity and MRT) was carried out at the pedestrian height (from 1.1 to 1.5 m). By contrast, in Lausanne the MRT measurements were carried out at 1.5m, the other data were taken from the meteorological station on the roof top of the building (+2.5m above the roof terrace). The weather station of Dubai is consequently well impacted by the surrounding buildings.
- **Monitoring:** all measurements carried out in Dubai were recorded simultaneously each minute; on the opposite the data acquisition unit in Lausanne was recording data each 1 to 5 minutes, in accordance with

the instrument, and finally, data from CitySim were provided hourly. Due to the great variability of the outdoor environmental conditions, the difference in time-steps lead to some differences in the results.

Based on the proposed models, Comfort Maps will be defined in the next chapters, showing the impact of the outdoor environment on the pedestrian thermal sensations, in the case studies of the EPFL campus (Lausanne) and the SISD campus (Dubai).

#### *Future outlook*

The outdoor human comfort is an ongoing discipline, showing a rising interest by researchers during the last years; the following points summarize a number of significant gaps in the field of outdoor human thermal comfort, addressing them could improve the quality of outdoor comfort analysis:

- Psychological adaptation: the impact of a person's "thermal history", as well as the expectations of a pedestrians in the outdoor environment, are not yet included in the simulation of the outdoor thermal comfort. Their inclusion in the models alongside the physical energy balance would improve the robustness and validity of the simulated results.
- A bridge between the energy models and the empirical models: if the former define a "universal" way to quantify human comfort, the latter are able to address thermal perception, including the thermal preferences of people, based on the climate, as well as their sensitivity to certain stimuli (Ng and Cheng, 2012) (Cheng et al., 2012) (Nikolopoulou and Lykoudis, 2006).
- Practice: urban climatic maps are under development and able to provide guidelines to urban planners and municipalities to improve the microclimate of cities (Ng and Ren, 2015) , but the analysis of the outdoor human comfort is not yet an integral part of the architectural practice. Further development is required to bring the research findings on human thermal comfort into the architectural and urban design practice.
- Sensation: the current energy models do not consider noise, odours or glare as sources of discomfort; the inclusion of these parameters in the quantification of global human comfort would improve the reliability of the evaluation by considering a whole interaction between the body and its environment.
- Radiation: radiation is often considered without differentiating the impact of solar (short-wave) and long-wave radiation, and thus without considering how the human body may react to radiation of different wave lengths (Hodder and Parsons, 2007) (Rox Anderson and M.D, 1981).
- Neuro-architecture: this new field of research combines neuroscience with architecture by analysing the space as perceived by our brain (Groh, 2014) (Eberhard, 2009a) (Eberhard, 2009b). The relationship between human comfort and neuro-architecture could enhance the sophistication of the design of the built environment, by adding knowledge to the human comfort.
- Psychophysics: the use of mental imagery could provide interesting information concerning the regions of the brains activated by certain environmental stimuli. The use of the psychophysics techniques would provide the visualization of the human's environmental perception, and consequently understanding the neuronal mechanisms behind the human's thermal perception (Tartaglia et al., 2017).



## Chapter 3 Urban Greening

*The work related to this chapter was presented at the 9th International Conference on Urban Climate jointly with 12th Symposium on the Urban Environment, Toulouse (France) in July 2015 (Coccolo et al., 2015a).*

### 3.0 Introduction

Outdoor human comfort is a major factor in the evaluation of the liveability of a city. Sound outdoor planning and design can foster both thermal comfort and human health in an urban environment. Human thermal comfort depends on physical factors, such as the geographical location, the local climate and the built environment. A city comprises a very large number of microclimates, one for each urban building structure (Mayer and Höpfe, 1987). The study of outdoor human comfort, especially in extreme climates, can help building and urban planners to promote a more conscious urban design, able to offer a comfortable outdoor environment for human activities. Among the available bioclimatic strategies, adding vegetation has one of the strongest positive impacts on outdoor human comfort, as it decreases the short and long wave radiation fluxes impinging on pedestrians and consequently reduces the outdoor air temperature by 2 to 6°C depending on the plant species and location (Shashua-Bar et al., 2011) (Lee et al., 2013) (Taleb and Taleb, 2014) (Santamouris and Kolokotsa, 2016). The impact of vegetation varies as a function of its density: a case study in the city of Athens showed that a park reduces the air temperature inside its borders by 3.3 to 3.8K, and influence the neighbors up to 300 m from its borders (Skoulika et al., 2014). The above phenomenon is called Park Cool Island effect (PCI), and is related to the shading provided by vegetation, which reduces the surface temperature, improves the evapotranspiration process and increases the sky view factor (compared to the built environment). It also allows the dissipation of heat during nighttime, through radiative cooling (Erell et al., 2011a). The magnitude of the PCI is related to the type of vegetation, the size of the park, the topography of the city and the wind speed (Chow et al., 2011). A single tree impacts just its surroundings; by contrast, a cluster of trees or a park extends its thermal impact to the neighborhoods (Streiling and Matzarakis, 2003) (Ng and Ren, 2015). Part of the PCI effect is related to the presence of grass, which has a great potential to decrease the UHI (Urban Heat Island) phenomenon as well as to improve the outdoor human comfort by its evaporative cooling potential (through evapotranspiration) and by its lower surface temperature, which means a reduction in the longwave radiation received by the pedestrians (Erell et al., 2011a). Consequently, trees have a positive impact on the outdoor human comfort, by improving the environmental conditions, providing shading effect, cooling the air through evapotranspiration and providing wind resistance (Kong et al., 2017). Currently several programs exist to quantify the energy demand of buildings, such as EnergyPlus (Crawley and Lawrie, 2000) or TRNSYS (Klein, 2010), and the urban microclimate (Bruse, 2014) (Lindberg et al., 2008), but none of them can quantify both phenomenon together, although the microclimate influences the energy demand of a building and conversely the energy demand can affect the urban environment and the urban climate. Because of the above limitations, the goal of this chapter is to present a new methodology to model trees and to quantify the evapotranspiration process from the ground. Both models are analyzed in order to quantify their impact on the outdoor human comfort, as well as on the energy demand of buildings. For the analysis of outdoor human comfort, the models are implemented in the software CitySim Pro, an urban energy modeling tool able to quantify the energy fluxes at the city scale. For the first model of trees, the methodology is validated by onsite monitoring on the Sede Boqer Campus of the Ben-Gurion University (Israel). The second model of ground evapotranspiration, is an improvement of an existing model (Upadhyay et al., 2015). In order to improve

the accuracy of results, the evapotranspiration's heat transfer coefficient was modified by adding the ground heat flux from the grass to the soil, as well as by modifying the bulk surface resistance as a function of the environmental conditions. Finally, the old model slightly overestimates the evapotranspiration; the error was corrected in the new model. The new model is validated with on-site monitoring provided by the weather station of MeteoSuisse, located in the city of Pully (Switzerland). The model proposed in this chapter will be applied in case studies of the EPFL and SISD campus, showing their vegetation's impact on the energy demand, as well as on the outdoor human comfort.

### 3.1 Modelling trees

The following paragraphs present the methodology behind the tree model, the equations as well as the validation of the proposed methodology. The physical phenomenon behind the cooling effect of trees is their ability to absorb the heat irradiated from the urban environment and dissipate it through evapotranspiration to the atmosphere and conduction to the soil (Oke et al., 1989). The impact of evapotranspiration on the ambient air temperature is lower for trees compared to grass: their cooling effect is mainly due to the shadowing effect (80%), a small part being due to evapotranspiration occurring on the top layer of trees (Shashua-Bar and Hoffman, 2000) (Oke et al., 1989). Leaves constitute the exchange surface between a plant and the outdoor environment for heat, vapour and CO<sub>2</sub> fluxes; this exchange occurs through small cells called stomata. Each stoma works as a regulatory valve between the leaf and the atmosphere, allowing the transport of water vapour from the leaf as well as CO<sub>2</sub> to the leaf (Oke, 1987). Based on their photosynthetic activity, plants are classified into the following groups (Figure 3.1): C<sub>3</sub> carbon fixation, C<sub>4</sub> carbon fixation and CAM (Crassulacean acid metabolism). The first group, C<sub>3</sub>, represents 85% of all plant species; they are typically found in temperate climates. C<sub>4</sub> plants are present mostly in tropical and arid climates and CAM, as example succulent plants, are mostly located in arid climates. A characteristic of CAM plants is the inverted day- night cycle for the stomatal cycle: stomata are open during nighttime and closed during daytime (Jones, 2014) (Lee, 2010). This chapter presents a dynamic simulation model used to quantify the impact of trees on the outdoor thermal comfort in the built environment.





Figure 3.1 Example of plants. Top, left: Orange Tree (C<sub>3</sub>). Source: britannica.com. Top, right: corn (C<sub>4</sub>), and bottom: cactus (CAM). Source: Wikipedia

### 3.1.1 Physical model of trees

Trees are modelled with CitySim Pro, an urban energy modelling software (J. Kämpf, 2009), considering their geometrical properties (height, diameter of foliage and leaf width) and their physical properties (Leaf Area Index, longwave emissivity, shortwave absorptivity and reflectance). Two variables are commonly used to describe the shape of trees and their canopy (Fahmy et al., 2010) (Hosoi, 2009):

- Leaf Area Index (LAI), representing the ratio between the total upper leaves area and the ground tree area, varying according to seasons and years.
- Leaf Area Density (LAD), representing the total leaves area per unit of layer volume, similar to horizontal leaves slices.

Based on previous research, the cooling effect of trees is directly related to i) the leaf color on the top, ii) the foliage density, iii) the leaf thickness and texture, showing that light green leaves are more efficient than dark green ones (Lin and Lin, 2010). The foliage density of the canopy is quantified by the LAI: a larger LAI improves the evaporation and transpiration of the canopy, consequently its cooling effect (Lin and Lin, 2010). Based on the three cooling characteristics of trees, as defined above, we tried to address both of them in the proposed model. Firstly, assuming that the plant impacts the thermal sensation by radiative cooling, as well as by shading effect, we decided to design the plant based on their Leaf Area Index (LAI) and Leaf Area Density (LAD), assuming that higher is the LAI, higher is the shading effect as well as the reduction of longwave radiation. The proposed computational model is defined by superposing the leave surfaces, as shown in Figures 3.2 and 3.3. Effectively, by designing the leaves as surfaces, superposed, we can directly perceive the variation of the longwave radiation (related to the surface temperature) as well as the shortwave radiation. The LAI, in the proposed model, could vary, manually, throughout the seasons, as well as the years.

### Urban Greening

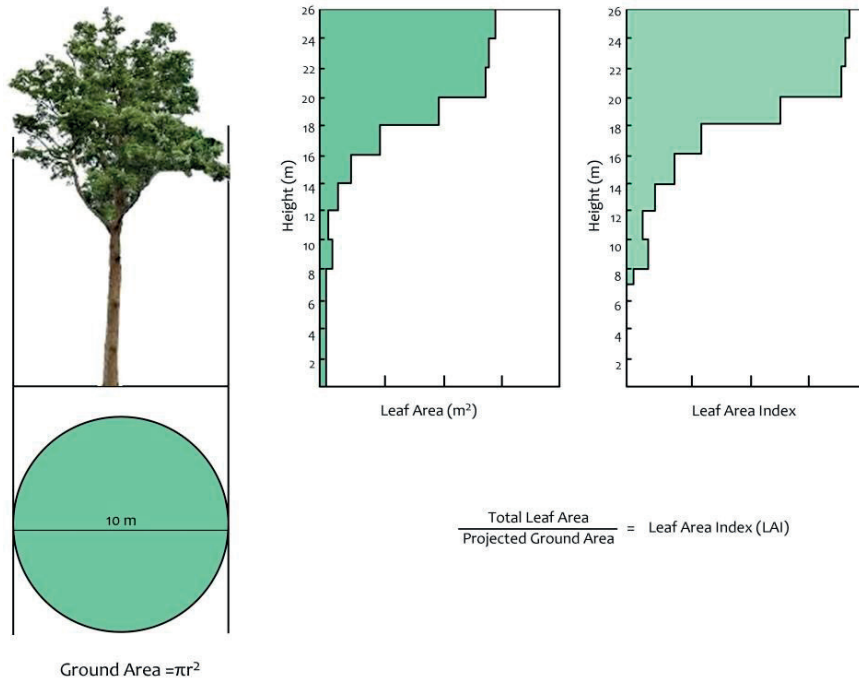


Figure 3.2 Leaf Area Index as function of the Leaf Area and the Ground Area. Adapted from: 2006, Pearson Education.

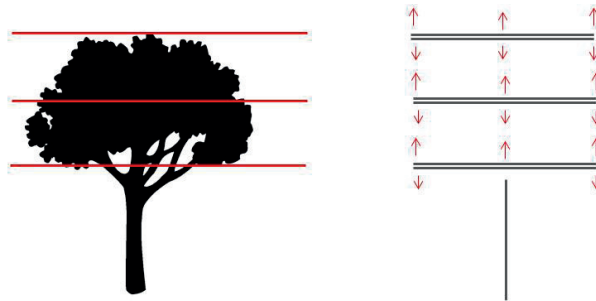


Figure 3.3 Schematic description of the tree model: view of the plant (left) and schematic model in CitySim Pro (right) with three surfaces representing the LAI index; where each LAI is oriented normally to the ground and to the sky (red arrows).

Knowing that 80% of the cooling effect of trees is due to shadowing and only a small fraction due to evapotranspiration occurring in the top layer of plants (Shashua-Bar and Hoffman, 2000) (Oke et al., 1989), the model determines the shadowing effect of the plant and calculates the evapotranspiration as well as the leaf temperature at the top of the canopy. In accordance with (Gaylon S. Campbell and Norman, 1998), the leaf temperature,  $\theta_o$ , °C, is given by:

$$\theta_o = \theta_a + \frac{\gamma^*}{s + \gamma^*} \left[ \frac{R_{abs} - \epsilon_s \sigma T_a^4}{g_{Hr} c_p} - \frac{D}{p_a \gamma^*} \right] \quad (3.1)$$

where  $\theta_a$  (°C) is the ambient air temperature,  $\gamma^*$  (°C<sup>-1</sup>) the apparent psychrometric constant,  $s$  (°C<sup>-1</sup>) the slope of saturation mole fraction function,  $R_{abs}$  (W·m<sup>-2</sup>) the absorbed short and long wave radiation,  $\epsilon_s \sigma T_a^4$  (W·m<sup>-2</sup>) the emitted longwave radiation as a function of the air absolute temperature  $T_a$  (K),  $g_{Hr}$  (mol·m<sup>-2</sup>·s<sup>-1</sup>) the sum of

boundary layer radiative conductance,  $C_p$  ( $\text{J}\cdot\text{mol}^{-1}\cdot\text{°C}^{-1}$ ) the specific heat of air assumed to be equal to 29.3,  $D$  (kPa) the vapour deficit of air and  $P_a$  (kPa) the atmospheric pressure.

The radiation absorbed by the leaf is defined as follows:

$$R_{abs} = \alpha_{SW\_leaf} (SW_{rec}) + \alpha_{LW\_leaf} (LW_{rec}) \quad (3.2)$$

where the shortwave radiation absorbed by the leaf is equal to the sum of the shortwave radiation received from all directions  $SW_{rec}$ , multiplied by  $\alpha_{SW\_leaf}$ , which is the shortwave absorptivity of the leaves, assumed to be equal to 0.5 in accordance with (Gaylon S. Campbell and Norman, 1998) (Oke, 1987). The longwave radiation absorbed is equal to the longwave radiation received from the environment  $LW_{rec}$  multiplied per  $\alpha_{LW\_leaf}$  (-), which is the infrared absorptivity of leaves equal to 0.95 (Oke, 1987). The term  $LW_{rec}$  is determined using the longwave net balance  $LW_{net}$  (difference between the longwave received from the environment and the longwave emitted by the surface in accordance with its temperature), which is computed within CitySim Pro:

$$LW_{net} = (LW_{rec} - LW_{em}) \quad (3.3)$$

The longwave radiation emitted by the leaf surface  $LW_{em}$  is calculated, as follows:

$$LW_{em} = T_a^4 \cdot \varepsilon_s \cdot \sigma \quad (3.4)$$

where  $T_a$ (K) is the air temperature,  $\varepsilon_s$  (-) the emissivity of leaves (assumed as 0.95) and  $\sigma$  ( $\text{W}\cdot\text{m}^{-2}\cdot\text{K}^{-4}$ ) the Stefan-Boltzmann constant equal to  $5.670373 \cdot 10^{-8} \text{ W}\cdot\text{m}^{-2}\cdot\text{K}^{-4}$ . Table 3.1 and Figure 3.4 summarize the radiative properties of the leaf, according to the wavelength (Gaylon S Campbell and Norman, 1998):

- Absorptivity ( $\alpha$ ): the fraction of incident radiant flux, according to a certain wavelength range, which is absorbed by the leaf,
- Reflectivity ( $\rho$ ): the fraction of incident radiant flux reflected by the surface,
- Transmissivity ( $\tau$ ): the fraction of incident radiant flux transmitted by the leaf.

	Shortwave radiation (0.35- 0.80 $\mu\text{m}$ )	Longwave radiation (3.0- 100 $\mu\text{m}$ )
Reflection	<b>0.3</b>	0.05
Transmission	0.2	0.0
Absorption	<b>0.5</b>	<b>0.95</b>

Table 3.1 Short and long wave reflection, transmission and absorption for leaves. Adapted from (Oke, 1987)

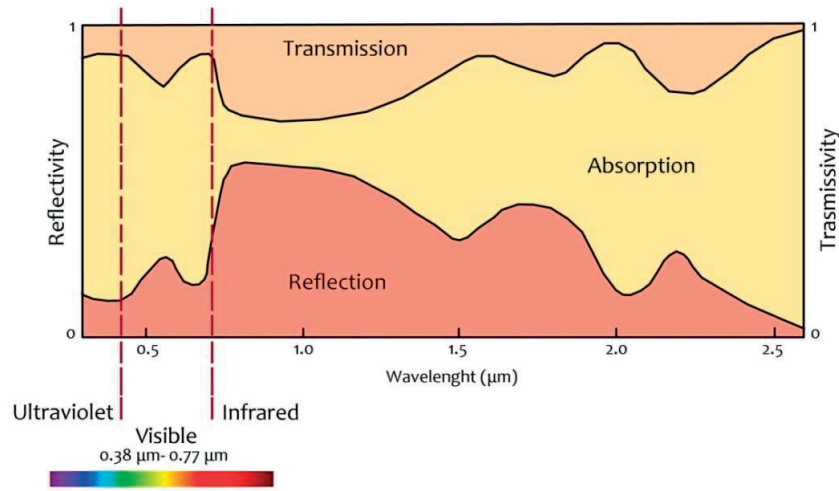


Figure 3.4 Schematic relationship between the wavelength and the reflection, transmission and absorption of the leaf. Adapted from (Oke, 1987) (Santamouris, 2001).

The waveband between  $0.4 \mu\text{m}$  to  $0.7 \mu\text{m}$  is designed as the photosynthetically active radiation (PAR); within this range there is a small peak of reflection between  $0.5 \mu\text{m}$  and  $0.55 \mu\text{m}$  (green portion of the visible spectrum), this explains why the vegetation is perceived green by our eyes. The absorption is maximal in the longwave spectrum, and the primary absorption agent is the water. In this region leaves are mostly full radiators, consequently, according to Kirkoff Law, also perfect emitters of longwave radiation. Consequently, the leaf absorbs the radiation useful for the photosynthetic activity and emits the longwave radiation, ceding heat to the environment (Oke, 1987). Each leaf exchanges vapour and heat with its surroundings; these exchanges are represented by the apparent psychrometric constant  $\gamma^*$  ( $^{\circ}\text{C}^{-1}$ ), calculated as:

$$\gamma^* = 6.67 \cdot 10^{-4} \left( \frac{g_{Hr}}{g_v} \right) \quad (3.5)$$

where  $6.67 \cdot 10^{-4}$  ( $^{\circ}\text{C}^{-1}$ ) is the thermodynamic psychrometric constant expressed as the ratio between the specific heat capacity of the air  $C_p$  ( $\text{J} \cdot \text{mol}^{-1} \cdot ^{\circ}\text{C}^{-1}$ ) and the latent heat of water evaporation ( $\text{J} \cdot \text{mol}^{-1}$ );  $g_{Hr}$  ( $\text{mol} \cdot \text{m}^{-2} \cdot \text{s}^{-1}$ ) is the convective-radiative conductance and  $g_v$  ( $\text{mol} \cdot \text{m}^{-2} \cdot \text{s}^{-1}$ ) the conductance of vapour.

The convective-radiative conductance ( $\text{mol} \cdot \text{m}^{-2} \cdot \text{s}^{-1}$ ) is the sum of two terms: the heat conductance  $g_{Ha}$ , depending on the wind speed and leaf geometry, and the radiative conductance  $g_r$  representing the longwave radiation emitted by the surface. The heat conductance  $g_{Ha}$  ( $\text{mol} \cdot \text{m}^{-2} \cdot \text{s}^{-1}$ ) is defined as:

$$g_{Ha} = 1.4 \cdot 0.135 \sqrt{\frac{V}{d_L}} \quad (3.6)$$

where 1.4 (-) is a constant applied in the outdoor environment,  $V$  ( $\text{m} \cdot \text{s}^{-1}$ ) the wind speed,  $d_L$  the characteristic dimension of the leaf, which is equal to 0.72 multiplied by the leaf width (m), if one considers the leaf shape as an intersecting parabola. The term  $g_{Ha}$  is derived from the boundary layer heat conductance for the face of a rectangular plate (by assuming the air properties), as follows:

$$g_H = \frac{0.664 \rho D_H R_e^{1/2} Pr^{1/3}}{d_x} \quad (3.7)$$

where  $\rho$  ( $\text{mol} \cdot \text{m}^{-3}$ ) is the molar density of the air,  $D_H$  ( $\text{m}^2 \cdot \text{s}^{-1}$ ) is the thermal diffusivity,  $R_e$  (-) is the Reynolds number,  $Pr$  (-) is the Prandtl number and  $d_x$  (m) is the characteristic dimension of the surface.

By adding the equation of the Reynolds and Prandtl number, Equation 3.7 becomes:

$$g_H = \frac{0.664 \rho D_H \left(\frac{d_x V}{u}\right)^{1/2} \left(\frac{u}{D_H}\right)^{1/3}}{d_x} \quad (3.8)$$

where  $u$  ( $\text{m}^2 \cdot \text{s}^{-1}$ ) is the kinematic viscosity of the air.

$$g_H = \frac{0.664 \rho D_H^{2/3} V^{1/2}}{d_x^{1/2} u^{1/6}} \quad (3.9)$$

$$g_H = \frac{0.664 \rho D_H^{2/3}}{u^{1/6}} \cdot \sqrt{\frac{V}{d_x}} \quad (3.10)$$

By assuming the properties of the air at 20°C (Gaylon S. Campbell and Norman, 1998):  $\rho$  corresponds to  $41.6 \text{ mol} \cdot \text{m}^{-3}$ ,  $D_H$  corresponds to  $0.0000214 \text{ m}^2 \cdot \text{s}^{-1}$  and  $u$  corresponds to  $0.0000151 \text{ m}^2 \cdot \text{s}^{-1}$ . By solving the first part of the equation we obtain Equation 3.6. The term 1.4 (-), defined as a constant used for the calculation in the outdoor environment, derives from Mitchell relation (Mitchell, 1976). Effectively, the previous equations can be used for conductance in a controlled environment; knowing that the outdoor environment is naturally turbulent, the conductance calculated by the previous formulas could underestimate the energy exchanges by conductance. In order to overcome this problem, the coefficient of 1.4 is applied; this coefficient derives from the measurements of Mitchell, which correlated the measured convective heat transfer of spheres and the ratio between the sphere diameter and the distance from the ground (knowing that the eddy size increase with height in the atmosphere) (Gaylon S. Campbell and Norman, 1998).

The radiative conductance  $g_r$  ( $\text{mol} \cdot \text{m}^{-2} \cdot \text{s}^{-1}$ ) is defined as:

$$g_r = \frac{4\varepsilon_s \sigma T_a^3}{C_p} \quad (3.11)$$

where  $\varepsilon_s$  is the emissivity of the surface, assumed to be equal to 1 in accordance with (Gaylon S. Campbell and Norman, 1998),  $T_a$  the ambient air temperature (K) and  $C_p$  ( $\text{J} \cdot \text{mol}^{-1} \cdot \text{C}^{-1}$ ) the specific heat of air, assumed to be equal to  $29.3 \text{ J} \cdot \text{mol}^{-1} \cdot \text{C}^{-1}$ .

The second term of Equation 3.1 defines the apparent psychrometric constant  $\gamma^*$  ( $^{\circ}\text{C}^{-1}$ ), which represents the exchange of vapour between a leaf and its surroundings; this phenomenon is expressed by the conductance of vapour  $g_v$  ( $\text{mol} \cdot \text{m}^{-2} \cdot \text{s}^{-1}$ ) depending on the stomatal conductance  $g_{vs}^{ab}$  ( $\text{mol} \cdot \text{m}^{-2} \cdot \text{s}^{-1}$ ) and the boundary layer conductance for vapour  $g_{va}$  ( $\text{mol} \cdot \text{m}^{-2} \cdot \text{s}^{-1}$ ):

$$g_v = \frac{0.5 g_{vs}^{ab} g_{va}}{g_{vs}^{ab} + g_{va}} + \frac{0.5 g_{vs}^{ad} g_{va}}{g_{vs}^{ad} + g_{va}} \quad (3.12)$$

where *ab* and *ad* refer to abaxial and adaxial surface conductance. The abaxial surface is the lower surface of a leaf and the adaxial surface is the upper surface of a leaf (OUP, 2017).

As previously explained, the surface of exchange between plants and the environment is the leaf, and the process stomatal self-regulation. Stomatal opening is related to light availability (stomata are closed during the night in C3 and C4 plants), ambient temperature, humidity and CO<sub>2</sub> concentration; as an example, stomata are closed if the plant is facing water stress, blocking the vapour exchange (Oke, 1987). Figure 3.5, adapted from (Oke, 1987), schematically represents the vapour, CO<sub>2</sub> and heat exchanges between a leaf and its environment.

### Urban Greening

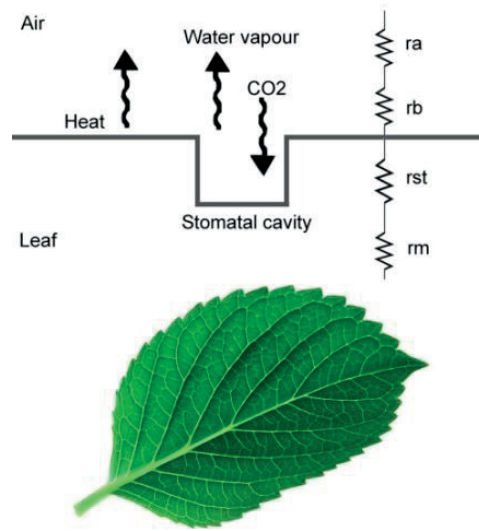


Figure 3.5 Schematic description of the water vapour, heat and carbon dioxide exchange on the stomata of the leaf. Adapted from (Oke, 1987).

In the suggested model, the stomatal conductance is set to  $0.3 \text{ (mol}\cdot\text{m}^{-2}\cdot\text{s}^{-1}\text{)}$ , if solar radiation is present, and is equal to  $0.01$  in absence of solar irradiance where stomata are closed (Gaylon S. Campbell and Norman, 1998). The proposed strategy is a simplification of the complex system that regulates the stomata apparatus, which is also related to the water status of the plant, the difference of vapour pressure between the air and the leaf, the CO<sub>2</sub> concentration and the temperature (Hopkins and Huener, 2008). In this model abaxial and adaxial surface conductance are assumed to be equal. Boundary layer conductance for vapour  $g_{va} \text{ (mol}\cdot\text{m}^{-2}\cdot\text{s}^{-1}\text{)}$  is assumed to be given for forced convection by:

$$g_{va} = 1.4 \cdot 0.147 \sqrt{\frac{V}{d_L}} \quad (3.13)$$

where  $1.4$  (-) is a constant,  $V \text{ (m}\cdot\text{s}^{-1}\text{)}$  the wind speed and  $d_L \text{ (m)}$  the characteristic dimension of the leaf, equal to  $0.72$  multiplied by the leaf width (m) if assuming the leaf shape as an intersecting parabola. The term  $0.147$ , similarly as for the calculation of the heat conductance  $g_{Ha}$ , derives by the following equation (Gaylon S. Campbell and Norman, 1998):

$$g_j = \frac{0.664 \rho D_j Re^{1/2} Sc^{1/3}}{d_x} \quad (3.14)$$

where  $D_j \text{ (m}^2 \text{ s}^{-1}\text{)}$  is the thermal diffusivity of the substance  $j$  and  $Sc$  (-) is the Schmidt number, defined as the ratio between the kinematic viscosity of the air,  $u \text{ (m}^2\cdot\text{s}^{-1}\text{)}$  and the thermal diffusivity of the substance  $D_j \text{ (m}^2 \text{ s}^{-1}\text{)}$ . Consequently, as done above, the equation is rewritten as follows:

$$g_j = \frac{0.664 \rho D_j \left(\frac{d_x V}{u}\right)^{1/2} \left(\frac{u}{D_j}\right)^{1/3}}{d_x} \quad (3.15)$$

$$g_j = \frac{0.664 \rho D_j^{2/3} V^{1/2}}{d_x^{1/2} u^{1/6}} \quad (3.16)$$

$$g_j = \frac{0.664 \rho D_j^{2/3}}{u^{1/6}} \cdot \sqrt{\frac{V}{d_x}} \quad (3.17)$$



by assuming the properties of the air at 20°C (Gaylon S. Campbell and Norman, 1998):  $\rho$  corresponds to 41.6 mol·m<sup>-3</sup>, and  $u$  corresponds to 0.000151 m<sup>2</sup>·s<sup>-1</sup>, then  $D_j$  is the thermal diffusivity of vapour, equals to 2.4·10<sup>-5</sup>. By solving the first part of the equation we obtain Equation 3.13.

Considering the formula giving the leaf temperature, the denominator of the apparent psychrometric constant is the slope of saturation mole fraction function  $s$  (°C<sup>-1</sup>) defined as the ratio between the slope of vapour pressure  $\Delta_{\theta_a}$  (kPa·°C<sup>-1</sup>) evaluated at the ambient temperature ( $\theta_a$ ) and the atmospheric pressure  $P_a$  (kPa):

$$s = \frac{\Delta_{\theta_a}}{P_a} \quad (3.18)$$

where the atmospheric pressure  $P_a$  (kPa) is a function of the altitude  $A$  of the site expressed in meters above the sea level. The vapour pressure gradient  $\Delta_{\theta_a}$  (kPa·°C<sup>-1</sup>) is the derivative with respect to the ambient air temperature of the saturation vapour pressure of air  $e_s$  (kPa):

$$\Delta_{\theta_a} = \frac{d}{d\theta_a} e_{s,\theta_a} = \frac{bc}{(c + \theta_a)^2} e_{s,\theta_a} \quad (3.19)$$

with:

$$e_{s,\theta_a} = a \exp\left(\frac{b\theta_a}{\theta_a + c}\right) \quad (3.20)$$

where  $a, b, c$  are constant, equal to 0.611 kPa, 17.502 (-) and 240.97 (°C) respectively (Gaylon S. Campbell and Norman, 1998); these constants are retrieved from the Tetens formula (Tetens, 1930) and were later adapted by (Buck, 1981) for temperature intervals ranging from -20 to +50°C.

Finally the vapour deficit of the ambient air  $D$  (kPa) is derived from the partial pressure of water vapour in air  $e_{\theta_a}$  (kPa):

$$D = e_{s,\theta_a} - e_{\theta_a} \quad (3.21)$$

The leaf temperature varies with the leaf dimension: increasing the leaf size reduces the surface temperature, as the leaf has a larger exchange area (vapour and heat) with the environment (air and wind).

Based on the above methodology, the user imports the 3D model (in DXF format) of a tree in the software CitySim Pro. Each single tree needs to be positioned on a different layer called "TREE" (Figure 3.6). Once imported, the user can modify the property of the plant by changing the Leaf Area Index, the distance between leaves and the leaf width.

## Urban Greening

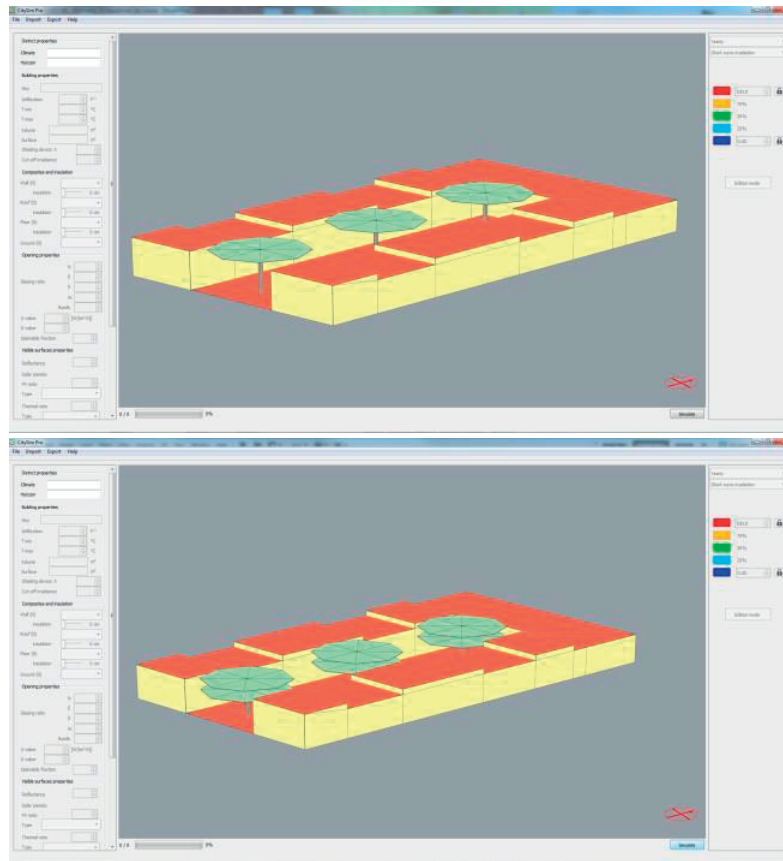


Figure 3.6 Trees modelled with the software CitySim Pro. Top: DXF imported in the software, with the upper surface of the tree (the canopy) and the trunk. Bottom: 3D model of the tree after the modification Leaf Area Index, in this example a LAI=2.

In accordance with this presented approach, each type of tree can be analysed. Currently, it is limited to evergreen plants, because the model does not consider, for the moment, the seasonal variation of leaves. Tables 3.2 and 3.3 present several types of plants that were previously modelled in accordance with this methodology: the first three (*Picea Rubens*, *Betula Utilis* and *Prunus Avium*) are typical plants for temperate/cold climate, and the last five are adapted for hot arid climate (*Prosopis cineraria*, *Phoenix dactylifera*, *Vachellia tortilis*, *Tipuan Typu* and *Prosopis-Juliflora*). Their equivalent 3D model within the software and their typical height at an age of 10 years are presented.



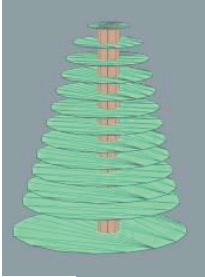

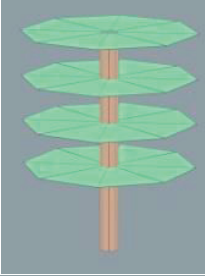
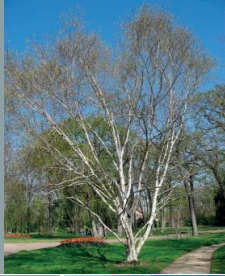


Common name, <i>Latin name</i> and Height (m)	3D view of the plants (retrieved by CitySim Pro) and photo	
<p>Red spruce (<i>Picea Rubens</i>) Height: 14m Source of the photo: novatreeco.com</p>		
<p>Himalayan birch (<i>Betula Utilis</i>) Height: 10m Source of the photo: wikipedia</p>		
<p>Cherry Tree (<i>Prunus Avium</i>) Height: 5m Source of the photo: gobotany.newenglandwild.org</p>		

Table 3.2 Plants modelled in accordance with the presented methodology: *Picea Rubens*, *Betula Utilis*, *Prunus Avium*. Physical and botanic characteristics of plants are retrieved from (Scurlock et al., 2001) (More and White, 2013). Source of the photos: Wikipedia.

Common name, Latin name and Height (m)	Image of the plant retrieved by CitySim Pro
Ghaf tree ( <i>Prosopis cineraria</i> ) Height: 5m Source of the photo: wikipedia	
Date palm ( <i>Phoenix dactylifera</i> ) Height: 15m Source of the photo: wikipedia	
Acacia tortilis ( <i>Vachellia tortilis</i> ) Height: 10m Source of the photo: wikipedia	
Rosewood ( <i>Tipuana Typu</i> ) Height: 3.5m Source of the photo: wikipedia	
Bayahonda blanca ( <i>Prosopis-Juliflora</i> ) Height: 3.5m Source of the photo: wikipedia	

Table 3.3 Plants modelled in accordance with the presented methodology: *Prosopis cineraria*, *Phoenix dactylifera*, *Vachellia tortilis*, *Tipuana Typu* and *Prosopis-Juliflora*. Physical and botanic characteristics of plants are retrieved from (Scurlock et al., 2001) (More and White, 2013). Source of the photos: Wikipedia.

Based on these models, the impact of trees varies in accordance with their main features (height, LAI, leaf width and shape), the site (topography, altitude), the climate (air temperature, relative humidity, solar irradiance, wind speed) and the built environment (mutual shadowing between buildings, albedo of the surfaces). The trees are coded in the software CitySim Pro: a detailed description of the physical properties of the plant is defined using the eXtensible Markup Language (XML). The main layer is the Tree, each surface under it being defined as a leaf or as the trunk. The following variables, extracted by the XML created by CitySim Pro, describe the tree characteristics:

```
<Tree id="0" name="" key="TREE1" leafAreaIndex="1" leafWidth="0.01" leafDistance="1" deciduous="false" class="C3">
  <Leaf id="0" ShortWaveReflectance="0.3" LongWaveEmissivity="0.95">
```

```

    <V0 x="70.58" y="-29.44" z="2.50"/>
    <V1 x="69.17" y="-31.50" z="2.50"/>
    <V2 x="71.62" y="-31.04" z="2.50"/>
    <V3 x="71.62" y="-31.04" z="2.50"/>
  </Leaf>
  <Trunc id="102" ShortWaveReflectance="0.3" LongWaveEmissivity="0.95">
    <V0 x="66.27" y="-15.87" z="3.50"/>
    <V1 x="66.27" y="-15.87" z="0.00"/>
    <V2 x="66.28" y="-15.79" z="0.00"/>
    <V3 x="66.28" y="-15.79" z="3.50"/>
  </Trunc>
  (...)
</Tree>

```

where *id* is automatically defined by the software, *name* is defined by the user in accordance with the chosen type of plant, *key* represents the name of the layer, *leafAreaIndex* (-) defines the plant LAI, *leafWidth* (m) defines the dimension of the specific leaf, *leafDistance* (m) describes the distance between each surface (by default equal to 1 m), *deciduous* describes the ability of the plant to lose (or not) leaves during winter time (this parameter is characterized by a true or false attribute) and *class* describes the photosynthetic characteristics of the plants (C<sub>3</sub>, C<sub>4</sub> and CAM). The C<sub>3</sub> pathway is dominating in plants of cold and temperate climates and is the only one for trees, with a few exceptions. For this reason, C<sub>3</sub> is the only class of plants considered at that time in the software. A physiological characteristic of these plants is their ability to close their stomata during night time. *Leaf* and *Trunc* layers are sub layers of *Tree*; each surface in these layers is characterized by a defined *ShortWaveReflectance*, i.e. the surface ability to reflect the impinging solar radiation, and a *LongWaveEmissivity*, i.e. the surface ability to emit infrared radiation on a certain wavelength. In the proposed methodology, the transmittance of short wave radiation is assumed to be equal to 0.2. As stated above, the trees mostly impact the thermal comfort by: i) the leaf color on the top, ii) the foliage density, iii) the leaf thickness and texture (Lin and Lin, 2010). Based on the proposed methodology, all the previous points are addressed, apart the texture of the leaf, which is currently smooth.

### 3.1.2 Validation of the tree model by on-site monitoring

The dynamic tree model was built with the software CitySim Pro and validated using on-site monitoring carried out on the Sede Boqer campus of Ben Gurion University (kindly provided by Prof. Erell and Prof. Pearlmutter), located in the Negev Desert (30°50'N, 34°40'E, 475 m asl) in Israel, data were provided for summer 2007 from 7<sup>th</sup> of July to 13<sup>th</sup> of August. The average air temperature for this period corresponds to 20°C; the wind speed and relative humidity are lower during daytime (from 7:00 to 18:00 hours) and higher during nighttime (from 19:00 to 5:00 hours). The monitoring experiment (Shashua-Bar et al., 2011) was set up to quantify the impact of different urban configurations on the outdoor human comfort. For this reason two adjacent courtyards located on the Sede Boqer campus (with the same geometry and orientation) were analysed providing different ground and shadowing strategies, representing six different configurations in total. The average building height, oriented North-South, is equal to 3 m; the total area of the court corresponds to 115 m<sup>2</sup>. The building walls around the court are made of one layer of concrete (U-value equals to 3.6 W·m<sup>-2</sup>·K<sup>-1</sup>) characterised by an albedo of 0.6. The bare soil and the concrete ground have an albedo equal to 0.35 and the grass equal to 0.22. Table 3.4 summarizes the properties of the two selected courtyards' configurations, presenting two types of plants (Prosopis-Juliflora tree and Tipuan Typu tree) and two types of soils: pavement and bare soil (Court 1), and pavement and grass (Court 2). The main climatic data are provided by an on-site weather station, located in the North-Western part of the campus; additionally, detailed micrometeorological data are provided for each court configuration (Shashua-Bar et al., 2011).

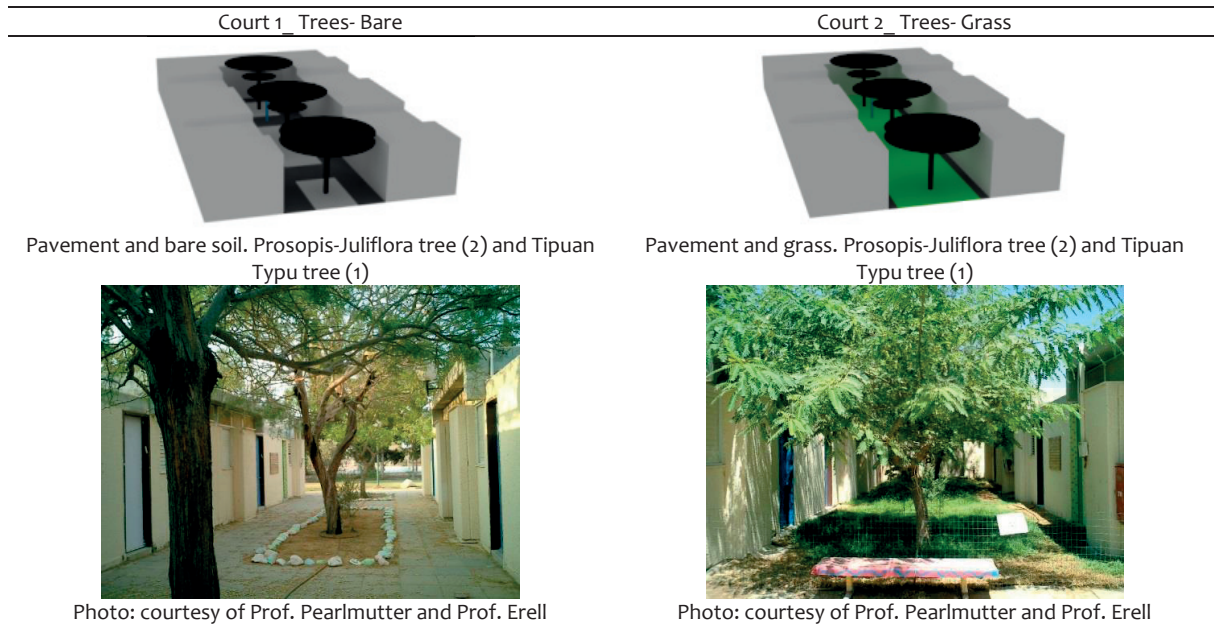


Table 3.4 Physical and geometrical properties of each court configuration.

The comparison between on-site monitoring (for the summer months of July and August) and computer simulations for Court 1 (Pavement and bare soil) and Court 2 (Pavement and grass) yields a Pearson correlation coefficient  $R$  of 0.96 and a Root Mean Square Error (RMSE) of 2.00 °C (with  $n=862$ ). Figure 3.7 illustrates the correlation between on-site monitoring of the leaf temperatures and the calculated one using the proposed methodology. All results are included within the confident interval of 95%, showing the reliability of the model. The Index of Agreement (Willmott et al., 2012) between the measured and simulated temperatures corresponds to 0.96, the Mean Absolute Error to 1.51°C and the Mean Bias Error to 1.38°C.

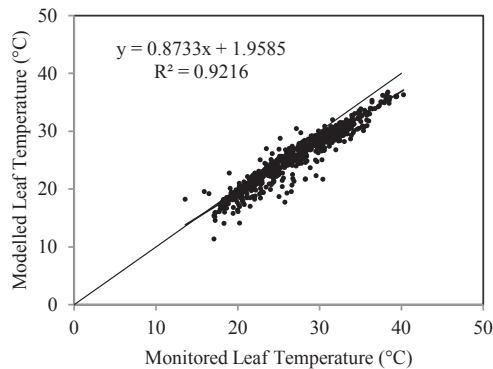


Figure 3.7 Comparison of measured and simulated leaf temperature in Sede Boqer campus of Ben Gurion University (Israel).

Figure 3.8 shows the leaf temperature monitored during five summer days (month of August): the simulated temperature is slightly lower than the measured one during the hottest hours of the day (maximum difference of 1.5°C) and slightly lower during night time (maximum difference of 1°C). These differences are related to the calculation of the radiative exchanges (short and longwave radiation), as a function of the geometry of the built environment. Furthermore, the wind is assumed identical to the one monitored by the weather station, without including its variation caused by crown foliage. The estimate experimental error corresponds to 5%; all results are inside the error bars, as shown in Figure 3.8.

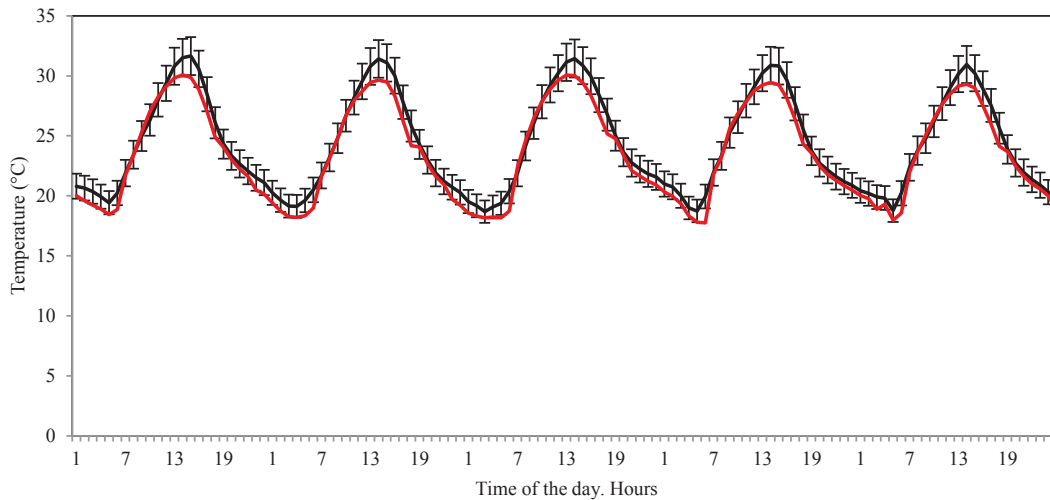


Figure 3.8 Simulated leaf temperature (red line) compared with the monitored one (black line), for five days during the month of August.

The model set-up within CitySim Pro determines the leaf temperature for the whole year on an hourly basis; the leaf temperature is constantly higher than the dew point temperature during summer time. By contrast, during winter time, if the relative humidity is higher than 80% and the wind speed is moderate (lower than  $1.5 \text{ m}\cdot\text{s}^{-1}$ ), the leaf temperature is lower than the dew point temperature. The maximal difference can be observed during the month of January during the first hours of the morning, when the relative humidity reaches 100% (vapour saturated air) and the leaf temperature is lower than the dew point temperature. This behaviour is due to the infrared radiation emitted by the leaf under a clear sky during the night, leading to a leaf temperature lower than the air temperature and inducing vapour condensation on the leaf surface.

As previously shown, the proposed methodology provides a Root Mean Square Error equal to  $2.00 \text{ }^\circ\text{C}$ , the difference during 5 days in August amounting to  $1.5^\circ\text{C}$  during daytime and  $1^\circ\text{C}$  during nighttime. This difference can be considered as negligible for the outdoor human comfort assessment: based on the simulations, if the leaf temperature of a palm varies by  $\pm 3^\circ\text{C}$  on average during the year, the Index of Thermal Stress slightly varies by  $\pm 47\text{W}$ . This variation cannot be perceived by pedestrians (only sensitive to a variation of  $320 \text{ W}$  for ITS), consequently the perceived thermal sensation remains similar. The analyses of the impact of trees on the outdoor thermal comfort will be presented in the following chapters, in case studies of the EPFL and the SISD campus.

This chapter has presented a first approach to quantify the impact of plants on outdoor human comfort; the method should help urban designers and stakeholders to analyse the impact of trees at the design stage of an urban planning project. Further developments of this computer-based method will consider:

- The creation of a database for common plants in cold, temperate, tropical and arid climates.
- The inclusion of the soil heat flux density in the leaf temperature calculation.
- The simulated air temperature affected by the microclimate of the built environment.
- The impact of trees on wind speed's variation, effectively the temperature and the wind speed provided by a meteorological station are currently used to determine the convective exchanges between the human body and its surroundings; this can be refined by linking the microclimate model predicting the ambient air temperature and the wind speed, as a function of the built environment and the vegetation.

### 3.2 Modelling the evapotranspiration potential of greening

The following paragraphs present the improvement of the existing evapotranspiration (ET) model. Before analyzing the model, a further description of the evapotranspiration process is proposed. Evaporation is defined



as the transition phase, in which liquid molecules become gaseous by increasing their kinetic energy, linearly proportional to the increase of the air temperature. Evaporation is included in the term evapotranspiration, which expresses the combination of abiotic water evaporation and biotic (active biological controlled by stomatal) leaf transpiration (Katul et al., 2012). Several methods exist to quantify evapotranspiration; they can be subdivided into the following categories: temperature based (Hargreaves and Samani, 1985), radiation based (Priestley and Taylor, 1972) and mass transfer based (Harbeck, 1962). Among them, the Penman- Monteith method is the most commonly used and recommended by the Food and Agriculture Organization of the United Nations (FAO) (Allen et al., 1998) for the computation of evapotranspiration. This method represents a physical estimation of the evapotranspiration and is applicable to hourly time steps (Abteu and Melesse, 2013). The inputs required by this method are the air temperature, the net solar irradiance, the relative humidity, the wind speed and the air pressure (Abteu and Melesse, 2013). The environmental factors that influence evapotranspiration are the following (Zuo et al., 2016):

- Solar irradiance: the higher the sun irradiance, the lower is the cloud covering and consequently the higher is the evapotranspiration.
- Wind speed: by increasing the wind speed on the plant surface, the evapotranspiration process increases.
- Vapor content of the air: by increasing the vapor content, and consequently increasing the relative humidity in the air, evapotranspiration decreases.

Previous studies performed in Switzerland quantified the evapotranspiration by on-site monitoring and measurements. A case study conducted in Stillberg (2200 m a.s.l.), Teufi (1680 m asl) and Hof (1829 m asl) showed the hourly evapotranspiration as a function of the air temperature, wind speed and relative humidity for the three selected sites (Menzel and Lang, 1998). The mean annual evaporation rate in Switzerland had previously been quantified by the Federal Office for Water and Geology as 484 mm. Naturally evaporation is related to the ground coverage: 900 mm per year from waterbodies, 600 mm per year from forests, 430 mm per year from agricultural land and alpine pastures, 220 mm per year from rock and 200 mm per year from communication routes (Spreafico and Weingartner, 2005). ET varies throughout the year, presenting an increase during the warmer months (around 4 mm, mean daily evaporation in Switzerland) compared to the winter time (around 0.9 mm, mean daily evaporation in Switzerland) (Spreafico and Weingartner, 2005) (Odi-Lara et al., 2016). Evapotranspiration can reach negative values during nighttime; this phenomenon is related to vapor condensation that appears with the early morning dew (Walter and Allen, R.G., Elliot, R., Itenfisu, Daniel., Brown, Paul., Jensen, Marvin.E., Mecham, Brent., Howell, Terry, a., Synder, Richard, Eching, Simon., Spofford, Thomas., Hattendorf, Mary., Martin, Derrel., Cuence, Richard, H., and Wright, 2005). As previously described, evapotranspiration increases with increasing temperature, irradiance, wind speed and decreasing relative humidity. The climate change has a major impact on the above parameters, which will be negatively affected: this means that in the future the world will face an increase in evaporation and evapotranspiration, and consequently an increase in the water loss from lakes, reservoirs and soil (Abteu and Melesse, 2013).

### 3.2.1 Physical model of evapotranspiration

Evapotranspiration  $Q_{et}$  (W), is defined by the following formula, computed following the FAO Penman- Monteith equation:

$$Q_{et} = \Psi + \Lambda \cdot G \quad (3.22)$$

The first term of Equation 3.22, the evapotranspiration heat transfer coefficient,  $\Psi$  (W), is defined as follows:

$$\Psi = \frac{\left(\gamma \frac{37}{T_a} V\right) \cdot (e_{s,\theta_a} - e_{\theta_a})}{\Delta_{\theta_a} + \gamma \left(1 + \frac{r_s}{r_a}\right)} \cdot \lambda \quad (3.23)$$

where  $\gamma$  (kPa °C<sup>-1</sup>) is the psychrometric constant,  $T_a$  (K) is the ambient air temperature,  $V$  (m s<sup>-1</sup>) is the wind speed,  $e_{s,\theta_a}$  (kPa) is the saturation vapor pressure of the air,  $e_{\theta_a}$  (kPa) is the vapor pressure of the air,  $\Delta_{\theta_a}$  (kPa °C<sup>-1</sup>) is the

saturation slope vapor pressure curve at the air temperature,  $r_a$  ( $s\ m^{-1}$ ) is the aerodynamic resistance, which corresponds to  $208 \cdot V^{-1}$ ,  $r_s$  ( $s\ m^{-1}$ ) is the bulk surface resistance and  $\lambda$  ( $W\ kg^{-1}$ ) is the latent heat of vaporization. The term  $\left(\gamma \frac{37}{T_a} V\right)$  is expressed in ( $mm\ ^\circ C^{-1}$ ). In order to understand the units of the model, it is essential to understand the energy required to evaporate the water. In accordance with FAO (Allen et al., 1998), at  $20^\circ C$ , the latent heat of vaporization corresponds to  $2.45\ MJ\ kg^{-1}$ ; consequently  $2.45\ MJ$  are required to vaporize  $1\ kg$  of water, and  $2.45\ MJ\ m^{-2}$  vaporize  $1\ mm$  of water.

The psychrometric constant  $\gamma$  ( $kPa\ ^\circ C^{-1}$ ) corresponds to:

$$\gamma = \frac{C_p P}{\epsilon \lambda} = 0.665 \cdot 10^{-3} P \quad (3.24)$$

where  $\epsilon$  (-) is the ratio molecular weight of water vapor and dry air (corresponding to  $0.622$ ) and  $P$  is the atmospheric pressure (kPa), calculated as follows:

$$P = p_o \exp\left\{-\left[\frac{M_a g A}{R (T_a)}\right]\right\} \quad (3.25)$$

where  $p_o$  is the sea level standard atmospheric pressure, equal to  $101.325$  (kPa),  $M_a$  ( $kg \cdot mol^{-1}$ ) is the molar mass of dry air, equal to  $0.0289644$ ,  $g$  ( $m \cdot s^{-2}$ ) is the earth-surface gravitational acceleration equal to  $9.80665$ ,  $A$  (m) is the altitude of the site,  $R$  ( $J \cdot mol^{-1} \cdot K^{-1}$ ) is the universal gas constant, equal to  $8.31447$ , and  $T_a$  (K) is the ambient air temperature.

The term  $e_{s,\theta_a}$  (kPa) is calculated, as previously, as follows:

$$e_{s,\theta_a} = a \exp\left(\frac{b\theta_a}{\theta_a + c}\right) \quad (3.26)$$

where  $a, b, c$  are constant, equal to  $0.611$  (kPa),  $17.502$  (-) and  $240.97$  ( $^\circ C$ ) respectively (Gaylon S. Campbell and Norman, 1998); these constants are retrieved from the Tetens formula (Tetens, 1930) and later adapted by Buck (Buck, 1981) for the temperature interval of  $-20$  to  $+50^\circ C$ ;  $\theta_a$  ( $^\circ C$ ) is the ambient air temperature.

The vapor pressure of the air (kPa) is calculated as follows:

$$e_{\theta_a} = e_{s,\theta_a} \cdot RH \quad (3.27)$$

where  $RH$  is the relative humidity (%).

The slope of vapour pressure  $\Delta_{\theta_a}$  ( $kPa \cdot ^\circ C^{-1}$ ) is the derivative with respect to the ambient air temperature:

$$\Delta_{\theta_a} = \frac{d}{d\theta_a} e_{s,\theta_a} = \frac{bc}{(c + \theta_a)^2} e_{s,\theta_a} \quad (3.28)$$

The bulk surface resistance  $r_s$  ( $s\ m^{-1}$ ) is calculated as follows:

$$r_s = \frac{r_i}{LAI_{active}} \quad (3.29)$$

where  $r_i$  ( $s\ m^{-1}$ ), is the bulk stomatal resistance corresponding to  $100\ s\ m^{-1}$  for a well illuminated leaf and to  $500\ s\ m^{-1}$  if no solar irradiance is available (Drake and Salisbury, 1972) (Woodward and Sheely, 1987).  $LAI_{active}$  corresponds to the active Leaf Area Index, assumed as  $0.5\ LAI$ . For a standard grass, the LAI corresponds to  $24h$ , where  $h$  is the height of the grass ( $0.12\ m$  standard value). Based on these assumptions, the bulk surface resistance corresponds to:

$$r_s = \frac{100}{0.5 \cdot 0.12 \cdot 24} = 70 \text{ during daytime (Gaylon S. Campbell and Norman, 1998)} \quad (3.30)$$

$$r_s = \frac{500}{0.5 \cdot 0.12 \cdot 24} = 347 \text{ during nighttime (Gaylon S. Campbell and Norman, 1998)} \quad (3.31)$$

Based on the above assumptions for  $r_a$  and  $r_s$ , the following term is reduced as follows during the daytime:

$$\left(1 + \frac{r_s}{r_a}\right) = \left(1 + \frac{70}{208} V\right) = (1 + 0.34V) \quad (3.32)$$

And it is assumed as follows during nighttime:

$$\left(1 + \frac{r_s}{r_a}\right) = \left(1 + \frac{347}{208}V\right) = (1 + 1.7V) \quad (3.33)$$

Finally, the latent heat of vaporization  $\lambda$  (MJ kg<sup>-1</sup>) is calculated as a function of the air temperature as follows:

$$\lambda = \frac{(2,501 - 2.37 \cdot \theta_a)}{1,000} \quad (3.34)$$

The second term of the Equation 3.22, the evapotranspiration source  $\Lambda$  (-), is defined as follows:

$$\Lambda = \frac{\Delta_{\theta_a}}{\Delta_{\theta_a} + \gamma\left(1 + \frac{r_s}{r_a}\right)} \quad (3.35)$$

where  $\Delta_{\theta_a}$  (kPa °C<sup>-1</sup>) is the saturation slope vapor pressure curve at air temperature,  $\gamma$  (kPa °C<sup>-1</sup>) is the psychrometric constant,  $r_a$  (s m<sup>-1</sup>) is the aerodynamic resistance,  $r_s$  (s m<sup>-1</sup>) is the bulk surface resistance.

The last term of the Equation 3.22, the soil heat flux  $G$  (W), is defined as follows:

$$G = g_1(T_1 - T_s) \quad (3.36)$$

where  $g_1$  (W m<sup>-2</sup>K<sup>-1</sup>) is the conductance to the first considered ground layer at temperature  $T_1$ ,  $T_s$  (K) is the surface temperature and  $T_1$  (K) is the temperature of the ground at the first layer of depth. This value is then multiplied for the unitary surface.

The energy fluxes released by evapotranspiration are finally multiplied by a so-called *f-factor* (Penman, 1963) (Mihalakakou et al., 1997), which corresponds to the humidity in the soil:

- For bare soil, *f-factor* corresponds to 1 (saturated soils), 0.6-0.8 (moist soils), 0.4-0.5 dry soils and 0.1-0.2 (arid soil).
- For soil covered by grass, the *f-factor* corresponds to 0.7.

### 3.2.2 Validation of the evapotranspiration model by on-site monitoring

The data of potential evapotranspiration are available from the web site of MeteoSuisse (Federal Office of Meteorology and Climatology, 2014) for the weather station of Pully. The weather station of Pully (6°40' E, 46°31' N, 456 m asl, Cumulative Solar Irradiance: 1,219 kWh·m<sup>-2</sup>, Heating Degree Days: 3,273), was inaugurated on 19<sup>th</sup> January 2006. It is located in an open field at an altitude of 456 m asl, as visible in Figure 3.9. The existing weather station is used by CitySim Pro in order to recreate the current environmental boundary conditions. The hourly weather data of the last three years monitored by the weather station are used to create the climate file.





Figure 3.9 Weather station of Pully (6°40' E, 46°31' N), located in an open field at 456 m asl. Source: MeteoSuisse.

The Pully weather station assesses the potential evapotranspiration defined as “the amount of evaporation and transpiration that occurs over the land’s surface, or would occur if the water supply were unrestricted” (Gosling et al., 2014). The potential evapotranspiration in the weather station of Pully is determined in daily values, and derived by the monitored data both with the Penman- Montheith and with an adapted Primault formula. The adapted Primault formula to calculate the evapotranspiration (ET) is the following (personal communication with Mr Christian Felix, MeteoSuisse, 18<sup>th</sup> October 2016):

$$ET = \left(1.03 - \frac{RH}{100}\right) \cdot \left(\frac{S}{60} + 2n\right) \cdot C_b \cdot j \quad (3.37)$$

where  $RH$  (%) is the relative humidity,  $S$  (min) is the measured sunshine duration,  $n$  is the number of days for the reference period,  $C_b$  is a constant for altitude correction (as a function of the barometric altitude) and  $j$  is a constant for seasonal correction (as a function of the barometric altitude).  $C_b$  is defined in (Primault, 1981), and corresponds to 0.65 at 200 m asl, and to 1.1 at 1300 m asl. The seasonal correction (Figure 3.10) is described by three curves (for an altitude <750 m asl, between 750 to 1,300 m asl and upon 1,300 m asl) and varies as a function of the months. As an example, during the month of April, it corresponds to 0.71 if the altitude is lower than 750 m, to 0.10 if the altitude is above 1,300 m, and to 0.18 if the altitude is comprised between the above values.

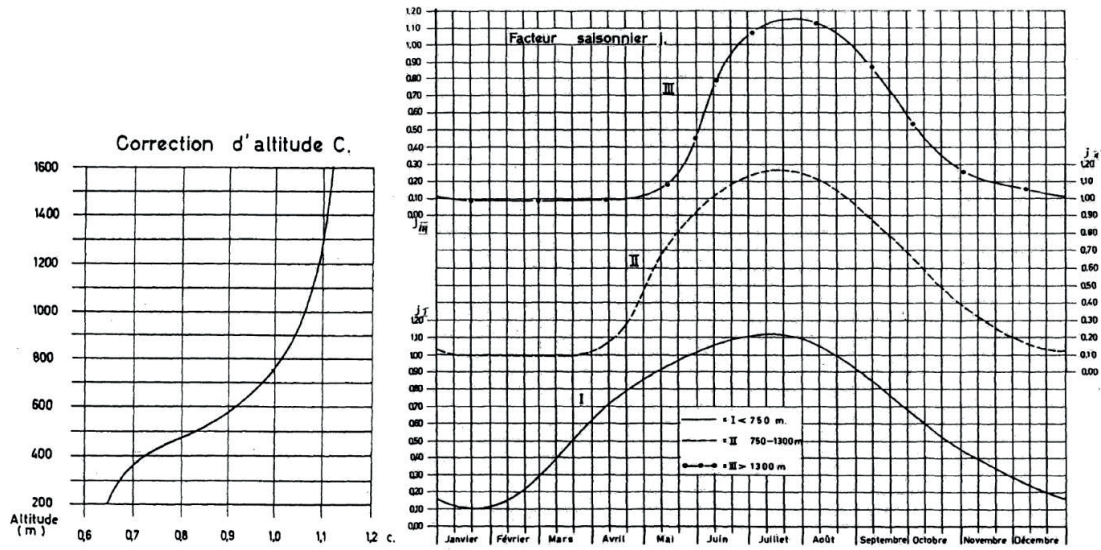


Figure 3.10 Primault formula; constant for height correction (left) and constant for seasonal correction (right) (Primault, 1981).

As previously stated, the formula used by MeteoSuisse is derived from the Primault formula (Primault, 1981), developed in 1981 for the Swiss climatic conditions (Calanca et al., 2011). This formula was elaborated during the Sixties by the head of agrometeorological services in Switzerland (Mr Primault) because of the lack of accuracy of the Penman-Montheit formula in describing the evapotranspiration process for the Swiss climate (Willemse and Furger, 2016). The Primault formula works for stations located between 250 to 1,800 m asl; one of the main limitations of this model is the fact that the solar radiation is estimated using the sunshine duration, but not as the measured solar irradiance impinging a surface (Calanca et al., 2011). Due to this limitation, MeteoSuisse is currently providing the potential evapotranspiration calculated with the Penman-Montheit method. In compliance with previous monitoring in Oensingen (in 2006), the Penman-Montheit formula was better predicting the evapotranspiration than the Primault formula, showing a coefficient of correlation  $R^2$  that corresponds to 0.88 and 0.67 respectively (Calanca et al., 2011). Table 3.5 summarizes the climatic parameters, as available from the Pully weather station. The only parameter that is not provided by Pully is the nebulosity of the site. For this reason this value is obtained from the weather station of Payerne, which is the closest one.

Parameter	Time Step	Unit
Global irradiance	Hourly	$W m^{-2}$
Diffuse irradiance	Hourly	$W m^{-2}$
Air temperature, at 2 meters	Hourly	$^{\circ}C$
Wind speed	Hourly	$m s^{-1}$
Wind direction	Hourly	$^{\circ}$
Relative humidity, at 2 meters	Hourly	%
Precipitations	Hourly	mm
Nebulosity (Payerne)	Hourly	octas

Table 3.5 Meteorological data provided by the weather station of Pully and Payerne (nebulosity).

The yearly periods selected for the analysis are 2013, 2014 and 2015; the climatic characteristics of all years are summarized in Tables 3.6 to 3.8. The average yearly temperature in 2014 and 2015 was similar ( $12^{\circ}C$ ), but higher compared to 2013 ( $10^{\circ}C$ ). Additionally the year 2015 was characterized by a hot arid summer, with the average

temperature during the month of July corresponding to 24.1°C (21.7°C and 18.4°C in 2013 and 2014 respectively) and low rainfalls (25 mm in 2015, 268 mm in 2014 and 147 mm in 2013).

Month	Diffuse Irradiance (Wm <sup>-2</sup> )	Global Irradiance (Wm <sup>-2</sup> )	Air Temperature (°C)	Wind Speed (ms <sup>-1</sup> )	Relative Humidity (%)	Rainfalls (mm)	Nebulosity (octas)
January	28	49	2.1	1.5	79	74	6
February	44	87	0.5	1.8	75	74	6
March	56	104	4.2	1.3	76	94	6
April	83	177	10.1	1.5	70	107	6
May	99	179	11.5	1.4	76	161	6
June	89	251	17.0	1.5	69	99	5
July	77	275	21.7	1.4	66	147	3
August	64	241	20.3	1.5	66	47	3
September	61	163	16.4	1.5	74	103	5
October	46	87	13.1	1.3	83	226	6
November	28	57	5.8	2.0	77	140	6
December	23	48	3.2	1.2	83	101	6

Table 3.6 Meteorological characteristics of the year 2013, as provided by the weather station of Pully. Average monthly value for diffuse irradiance, global irradiance, air temperature, wind speed, relative humidity and nebulosity. Cumulative monthly value for rainfalls.

Month	Month	Diffuse Irradiance (Wm <sup>-2</sup> )	Global Irradiance (Wm <sup>-2</sup> )	Air Temperature (°C)	Wind Speed (ms <sup>-1</sup> )	Relative Humidity (%)	Rainfalls (mm)	Nebulosity (octas)
January	1	27	46	4.6	1.1	80	83	6
February	2	35	75	5.1	1.3	80	136	6
March	3	59	162	8.2	1.4	67	37	4
April	4	79	197	11.9	1.6	65	68	5
May	5	94	222	13.4	1.9	68	87	6
June	6	91	284	19.2	1.7	61	63	4
July	7	88	195	18.4	1.2	79	268	6
August	8	86	193	18.0	1.5	73	121	6
September	9	59	177	16.8	1.6	75	21	4
October	10	45	109	14.1	1.2	80	138	5
November	11	27	48	8.8	0.9	85	118	7
December	12	23	40	5.0	1.6	77	52	6

Table 3.7 Meteorological characteristics of the year 2014, as provided by the weather station of Pully. Average monthly value for diffuse irradiance, global irradiance, air temperature, wind speed, relative humidity and nebulosity. Cumulative monthly value for rainfalls.

Urban Greening

Month	Month	Diffuse Irradiance (Wm <sup>-2</sup> )	Global Irradiance (Wm <sup>-2</sup> )	Air Temperature (°C)	Wind Speed (ms <sup>-1</sup> )	Relative Humidity (%)	Rainfalls (mm)	Nebulosity (octas)
January	1	28	47	3.5	1.6	79	94	6
February	2	42	87	1.9	1.6	76	54	6
March	3	59	137	7.6	1.2	68	53	5
April	4	67	205	11.3	1.4	61	86	4
May	5	88	223	15.2	1.4	65	159	5
June	6	94	276	19.8	1.3	64	37	5
July	7	78	286	24.1	1.6	53	25	3
August	8	68	205	21.0	1.1	68	44	4
September	9	61	157	15.0	1.9	70	121	4
October	10	52	97	10.7	1.5	80	59	6
November	11	30	67	8.4	1.4	81	68	5
December	12	26	47	5.7	1.1	88	21	6

Table 3.8 Meteorological characteristics of the year 2015, as provided by the weather station of Pully. Average monthly value for diffuse irradiance, global irradiance, air temperature, wind speed, relative humidity and nebulosity. Cumulative monthly value for rainfalls.

The environmental conditions of the weather station were accounted for by the software CitySim Pro, as shown in Figure 3.11. The selected ground (red rectangle) is used to quantify the potential evapotranspiration: it is assessed without any obstruction (Sky View Factor almost equals to 1 despite the presence of the building), presents a shortwave reflectance of 0.25 and is made of limestone.

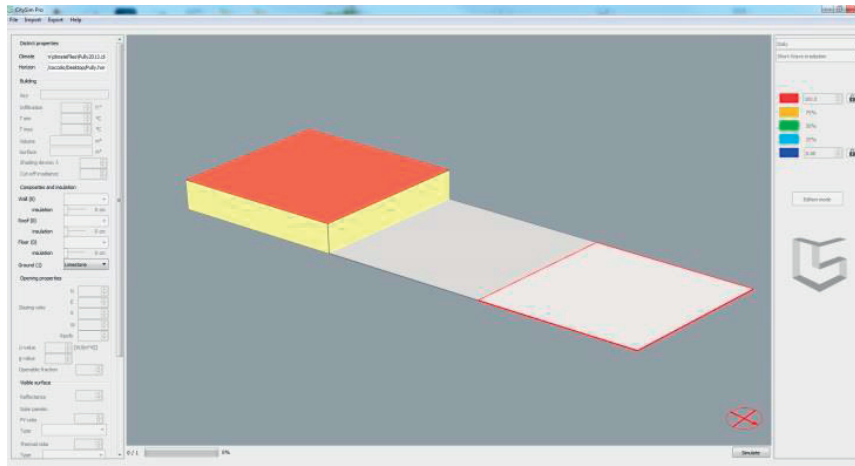


Figure 3.11 CitySim Pro. 3D virtual environment used to quantify the potential evapotranspiration around the weather station of Pully.

The model performed with CitySim is tested with the output provided by the weather station of Pully; as previously stated, the weather station provides the evapotranspiration as calculated by the FAO, or Penman-Montheit formula, as well as the Primault formula, for sake of comparison. In both cases, the evapotranspiration is computed in daily values.

The comparison between the evapotranspiration modelled with CitySim Pro and the one calculated by the Pully weather station, using the Penman-Montheit formula, shows an interesting correlation. The statistical data are summarized in Table 3.9: the maximum difference corresponds to 5.25% in 2015, with a Root Mean Square Error of

0.43 mm. This difference is partially explained by the nebulosity of the site: by comparing the total sunshine hours in both stations (Pully and Payerne), the maximal difference, up to 22%, appears in 2015.

In all climatic conditions, the RMSE is lower than 0.45, and the Index of Agreement corresponds to 0.945, 0.943 and 0.945 during 2013, 2014 and 2015, respectively. Figures 3.12-3.14 show the potential evapotranspiration as calculated by the Pully weather station and as calculated by CitySim Pro. The direct correlation between the two models is evident, showing the validity of the proposed methodology.

Reference Year	ET Pully	ET CitySim	Difference (%)	RMSE	Mean Absolute Error	Index of Agreement (Willmott et al., 2012)	Mean Bias Error
2013	731	734	0.40	0.37	0.31	0.9451	0.01
2014	747	742	0.75	0.35	0.29	0.9434	0.02
2015	799	757	5.25	0.43	0.34	0.9451	0.11

Table 3.9 Validation of the proposed methodology, statistical analysis of the results by comparing the output from CitySim with the evapotranspiration (FAO formula) monitored in Pully.

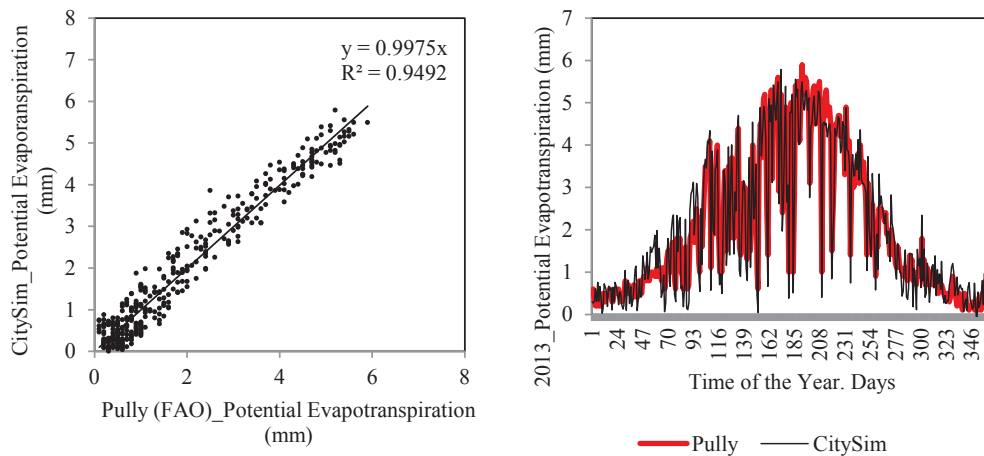


Figure 3.12 Observed (Pully weather station, calculated in accordance with Penman- Montheit, red line) versus modelled (black line) daily potential evapotranspiration (n=365) during the year 2013.

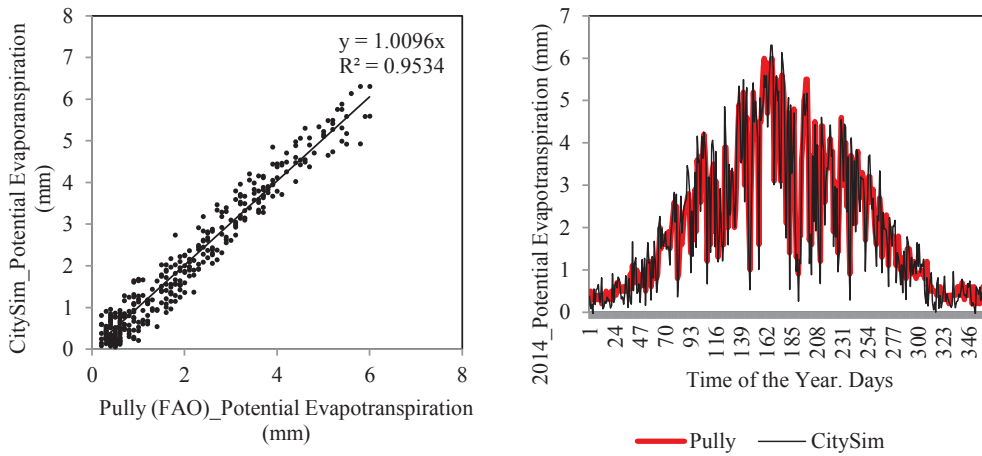


Figure 3.13 Observed (Pully weather station, calculated in accordance with Penman- Montheit, red line) versus modelled (black line) daily potential evapotranspiration (n=365) during the year 2014.

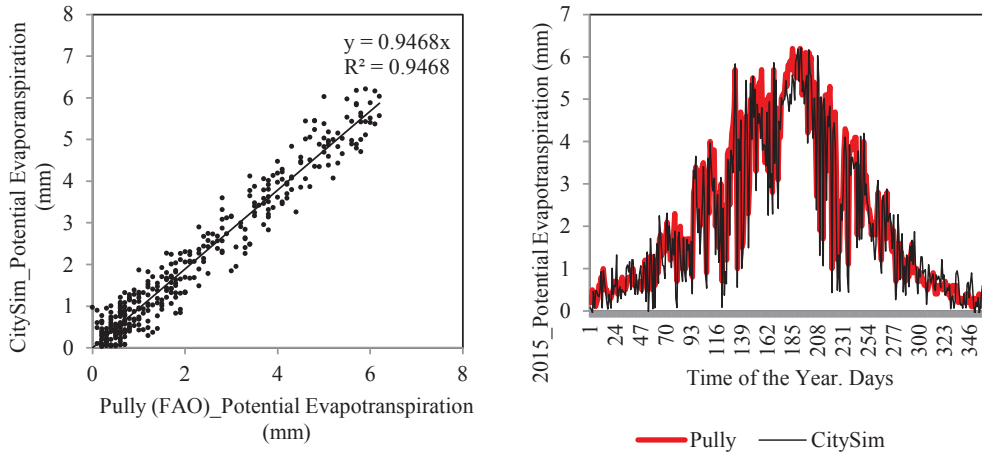


Figure 3.14 Observed (Pully weather station, calculated in accordance with Penman- Montheit, red line) versus modelled (black line) daily potential evapotranspiration (n=365) during the year 2015.

An experimental error of 10% is assumed considering the input data required for the calculation of evapotranspiration (air temperature, solar irradiance, wind speed and relative humidity). Figure 3.15 shows the monthly potential evapotranspiration, as assessed by the Pully weather station in accordance with the FAO model as well as the one calculated by CitySim. It is evident that the values calculated by CitySim stay within the experimental error of the FAO calculation, which corresponds to 10%.

Urban Greening

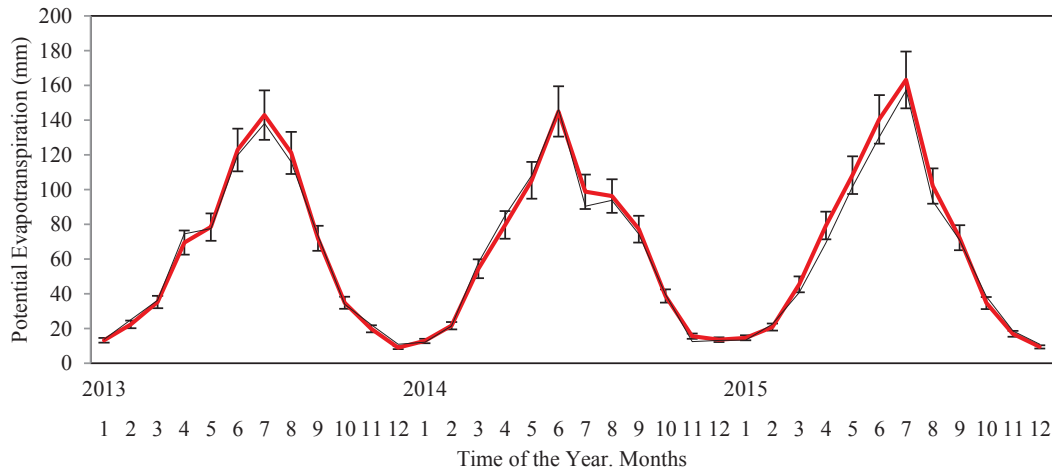


Figure 3.15 Potential evapotranspiration. Calculation for the experimental error, during the selected years (2013, 2014 and 2015). Monitoring data from the Pully weather station (red) and CitySim calculation (black).

The objective of the next paragraph is to understand the ET calculation, as provided by the Primault formula. The results obtained by CitySim Pro are compared with both measurements, as presented in Figures 3.16 to 3.18. Table 3.10 summarizes the total annual potential evapotranspiration (calculated with the Primault formula), as monitored by the weather station of Pully, as well as the potential evapotranspiration calculated by the software CitySim Pro. The Root Mean Square Error corresponds to 0.90 (n= 365) in 2013, 0.90 (n= 365) in 2014 and 0.96 (n= 365) in 2015. The Mean Absolute Error corresponds to 0.72, 0.70 and 0.75 in 2013, 2014 and 2015 respectively. The maximum annual difference corresponds to 41% in 2014 ( $R^2$  equals to 0.72), where the software overestimates the evapotranspiration during the winter and underestimates it during summer time. This is due to the Primault formula, which, due to the j-value (constant for seasonal correction, Figure 3.10), over or underestimates the potential evapotranspiration during the summer and winter seasons respectively. Additionally it neglects the solar radiation, by considering just the total sunshine hours. This behavior is evident in 2015 (Figure 3.18): during summer time the modelled potential evapotranspiration is up to 2.91 mm (maximum value), lower than the monitored one. Similar conclusions were obtained by Calanca et al. (Calanca et al., 2011), which underlined how the Penman-Montheit formula better estimates the evapotranspiration (with a  $R^2$  of 0.88 with on-site measurements), compared to the Primault formula. For this reason, results obtained with CitySim were additionally compared with the evapotranspiration assessed by the weather station of Pully using the Penman-Montheit equation.

Reference Year	ET Pully (mm)	ET CitySim (mm)	Difference (%)	RMSE	Mean Absolute Error	Index of Agreement (Willmott et al., 2012)	Mean Bias Error
2013	534	734	37.51	0.90	0.72	0.8759	0.55
2014	525	742	41.30	0.90	0.70	0.8661	0.70
2015	676	757	11.98	0.96	0.75	0.8960	0.75

Table 3.10 Validation of the proposed methodology, statistical analysis of the results by comparing the output from CitySim with the evapotranspiration (Primault formula) monitored in Pully.

Urban Greening

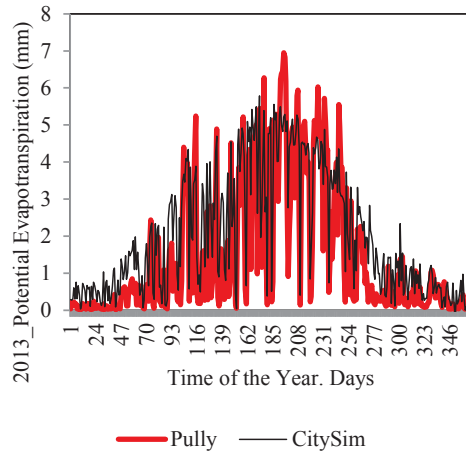
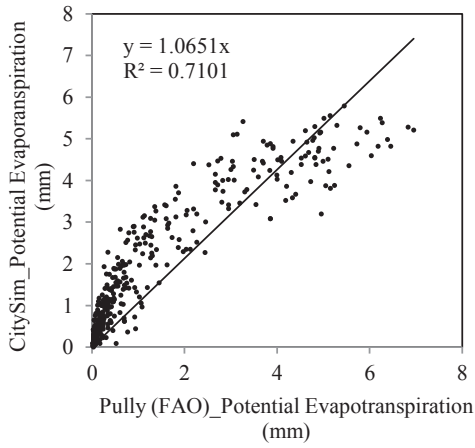


Figure 3.16 Observed (Pully weather station, calculated by the Primault formula, red line) versus modelled (black line) daily potential evapotranspiration (n=365) during the year 2013.

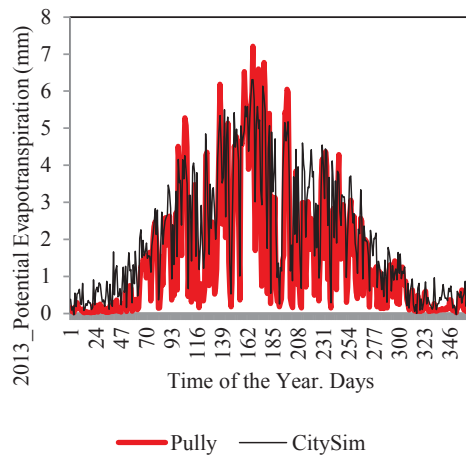
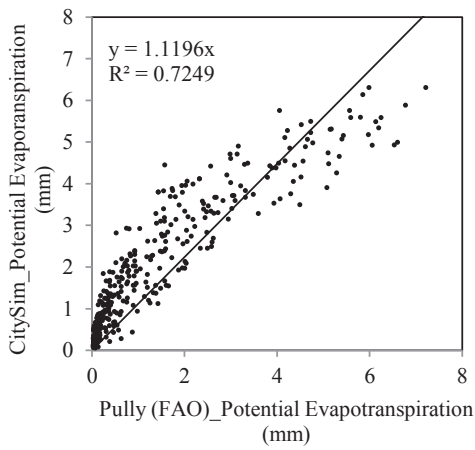


Figure 3.17 Observed (Pully weather station, calculated by the Primault formula, red line) versus modelled (black line) daily potential evapotranspiration (n=365) during the year 2014.



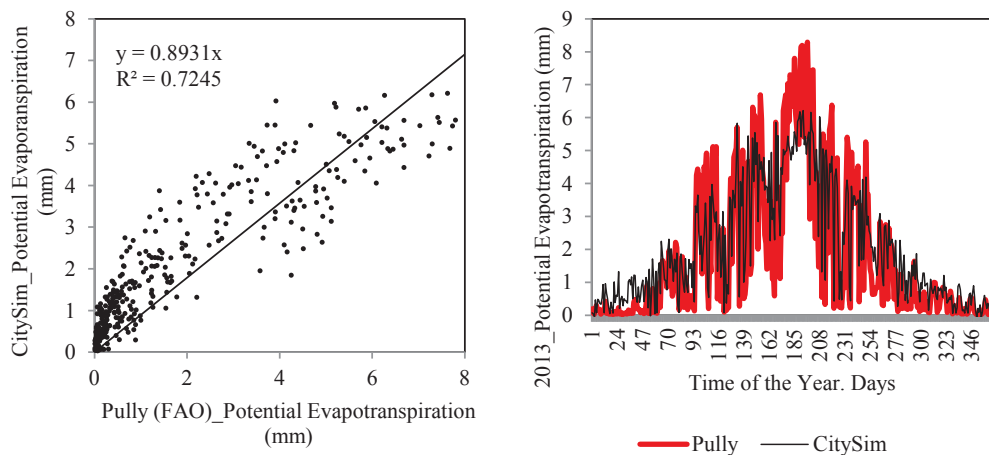


Figure 3.18 Observed (Pully weather station, calculated by the Primault formula, red line) versus modelled (black line) daily potential evapotranspiration (n=365) during the year 2015.

Finally, by comparing all the above results, the relative difference between the data measured in the weather station of Pully (with the Penman- Montheit method), and the results obtained by CitySim Pro, corresponds to 1.96%, with a RMSE of 0.39 mm. A general conclusion for the proposed methodology is the fact that CitySim Pro slightly underestimates the potential evapotranspiration during summer time, and slightly overestimates it during the winter and mid seasons. This behavior is explained by the following reasons:

- **Time steps:** the evapotranspiration in the weather station is analyzed in daily time steps; by contrast, CitySim Pro quantifies it in hourly time steps. As recommended by FAO, two different equations are used, based on the time of analysis (Allen et al., 1998). This difference can slightly impact the calculation.
- **Soil heat flux:** the weather station considers the G value as 10% of the net irradiance (Calanca et al., 2011), without differentiating it during day and nighttime, as recommended by FAO in case of hourly analysis (Allen et al., 1998). CitySim Pro, due to the dynamic hourly simulations, calculates the hourly variation soil heat flux as required by the FAO, taking into account that the soil heat flux is directed from the soil to the ground if the soil temperature is higher than the ground, and that it is reversed if the soil temperature is lower than the ground one. Knowing that in reality there is a daily and seasonal variation, it is evident that during summer time the soil is colder than the surface temperature; consequently the heat is directed from the soil to the ground, reducing evapotranspiration. By contrast, during the winter and mid-season, the heat is directed from the ground to the soil, and the evapotranspiration is increased due to the increase of the surface temperature.
- **Stomatal resistance:** the evapotranspiration, as quantified by MeteoSuisse, considers a general resistance of  $(1+0.34 u)$  (Willemse and Furger, 2016). By contrast, the proposed methodology considers the stomatal resistance as a function of the solar irradiance, relative humidity and precipitation. Consequently, the resistance is lower during daytime, when stomata are open  $(1+0.34 V)$ , but higher during nighttime, when stomata are closed  $(1+0.17 V)$ .
- **Nebulosity:** the nebulosity provided by MeteoSuisse is the one of the weather station in Payerne (35 kilometers away). This is the nearest station providing the nebulosity, but it is evident that, as it is not in the same location, the nebulosity is not perfectly precise (mostly during winter time, because of the local climatic conditions), and could deal with an error in the assessment of the model.

Currently the evapotranspiration is quantified for the ground covering; a further development of the model will be the analysis of the evapotranspiration potential from buildings, i.e. from green roofs and facades.

### 3.3 Conclusions and future outlook

In this chapter, two new methodologies to quantify the impact of greenings on the outdoor environment were proposed. The first model, implemented in CitySim Pro, determines the impact of trees located in the built environment by quantifying the shortwave radiation absorbed by the plants, as well as the longwave balance of the tree canopy. Based on this model, the impact of trees varies in accordance with their main features (height, LAI, leaf width and shape), the site (topography, altitude), the climate (air temperature, relative humidity, solar irradiance, wind speed) and the built environment (mutual shadowing between buildings, albedo of surfaces). When comparing the model with on-site monitoring in Sede Boqer (Israel), the Index of Agreement between simulation and monitoring reached 0.96 and a Mean Absolute Error of 1.51°C. This difference is negligible in the assessment of outdoor human comfort indices, as a variation of the leaf temperature between  $\pm 3^\circ\text{C}$  is not perceived by pedestrians.

The second model aims to quantify the evapotranspiration from the ground surfaces; this model is a further improvement of an existing one (Upadhyay et al., 2015). In order to improve its accuracy, the evapotranspiration's heat transfer coefficient was modified by adding the ground heat flux from the grass to the soil, as well by modifying the bulk surface resistance, as a function of the environmental conditions. The new model was validated with on-site monitoring provided by the weather station of MeteoSuisse, located in the city of Pully (Switzerland). The comparison shows a sound correlation between the data: the relative difference between the data measured (2013, 2014 and 2015) in the weather station of Pully (with the Penman- Montheit method), and the results obtained by CitySim Pro, corresponds to 1.96%, with a RMSE of 0.39 mm. The proposed models will be applied in the following chapters to improve the outdoor human comfort and the energy demand of buildings, in case studies of the SISD and EPFL campuses.

#### *Future outlook*

Some improvements of the model are beyond the scope of this thesis, such as:

- The tree model can be further improved; currently leaves are designed as opaque surfaces; in order to improve the quality of results the semi-transparent properties have to be included, as a function of the leaf and tree type. Additionally, up to now just evergreen plants are considered; an improvement of the model will be the possibility to add deciduous plants. Finally, the trees are analysed without considering their impact on the wind, a further improvement of the model would include the CIM model, or the semi empirical model developed by Kong et al. (Kong et al., 2017).
- Currently evapotranspiration is quantified for the ground covering; a further development of the model will be the analysis of the evapotranspiration potential of buildings, i.e. green roofs and facades. Furthermore, the impact of greenings on the variation of air temperature and wind speed around the buildings is yet to be studied.
- The evapotranspiration was analysed using the evapotranspiration assessed by the weather station of Pully. On-site measurements of the evapotranspiration in the built environment, before and after a change of vegetation (e.g. tree planted in pots versus tree planted in the ground), would further advance this topic.

Finally, the proposed methodologies are currently applied in order to design the Comfort Maps; a further development would correlate the Comfort Map with the ECOCLIMAP database (Champeaux et al., 2005), providing a comprehensive view of the cities.

## Chapter 4 Energy performance and outdoor comfort of a campus in a temperate climate

*The work related to this chapter was presented at the 6th International Building Physics Conference, IBPC 2015, Torino (Italy) in June 2015 (Coccolo, Kämpf, and Scartezzini 2015b); at the 9th International Conference on Urban Climate jointly with 12th Symposium on the Urban Environment, Toulouse (France) in July 2015 (Coccolo, Kämpf, and Scartezzini 2015); at the CISBAT International Conference, Lausanne (Switzerland) in September 2015 (Ulbig et al., 2015) (Rager et al., 2015), at the 14th International Conference of the International Building Performance Simulation Association, BS 2015, Hyderabad (India) in December 2015 (Coccolo, Mauree, and Kaempf 2015) and published in Energy Procedia (Coccolo, Kämpf, and Scartezzini 2015a). Part of this work was first developed at the EPFL Solar Energy and Building Physics Lab in the Master Thesis of Emmanuel Walter (Walter, 2014) and the semester project of Omar Beslimane (Beslimane, 2013). Finally, part of the work is submitted to the CISBAT International Conference, Lausanne (Switzerland) (Kuehner et al., 2017) (Le Guen et al., 2017) (Coccolo et al., 2017a) (Nik et al., 2017).*

### 4.0 Introduction

The current increase of the world population, observed most acutely in urban environments, and climate change are problems that oblige the science and the society to rethink our way of living and to introduce new technologies and land policies to reduce our energy footprint (Zanon and Veronesi, 2013) (Lindseth, 2004) (Meehl et al., 2007). The Ecole Polytechnique Fédérale de Lausanne (EPFL) is one of the largest universities in Switzerland, and hosts around 15,000 people (including students and staff) each day (EPFL, 2016). In accordance with the Swiss Energy Strategy for 2050 (Federal energy policy), EPFL is working to define the “Energy Concept 2015-2045”, a strategic report that aims to reduce the energy demand per person by 30% of final energy and 25% of primary energy in 2035, to increase the percentage of electricity issued from renewable energy and to reduce CO<sub>2</sub> emissions by 50% by 2035 (Van Slooter et al., 2014). The campus is heated by renewable energy (56% by a district heating system using lake water and 18% by Swiss hydroelectricity), but as the treated floor area has increased by 25% since 2001, and is expected to increase further in the next years, the current district heating system (two heat pumps with a combined heat and power facility) is reaching its limits (Van Slooter et al., 2012). With the goal of reducing the energy demand of the site, the EPFL is part of an innovative project called IDEAS4cities that aims to develop an Energy Hub: an intelligent unit able to collect, store and redistribute energy from different energy carriers, according to the need of buildings (Geidl et al., 2007) (Kienzle et al., 2011) (Walter, 2014). This chapter presents the first approach to create such an energy hub on the site of the EPFL: a validation of the energy model of the site and an optimization of the energy demand through two refurbishment strategies, based on Swiss standards Minergie and Minergie-P respectively. The energy demand for heating and the electricity produced by a BiPV power plant are analyzed with the software CitySim Pro- an urban energy modelling tool able to analyze the energy demand of buildings at urban scale (Darren Robinson et al., 2009)- and validated with on-site monitoring (ENERGO, 2014). Models of the existing and refurbished buildings are analyzed for three climate scenarios for the year 2050 (2050-B1, 2050-A1B and 2050-A2), showing the impact of climate change on the energy demand of the site, and proposing an optimal strategy for the future development of the campus. A detailed analysis of the LESO solar experimental building for climatic scenarios projected even more into the future (2100-B1, 2100-A1B and 2100-

A2) will present the evolution of indoor human comfort, based on the Predicted Mean Vote (PMV) and Predicted Percentage of Dissatisfied (PPD).

In the second part of the study performed on the campus, the outdoor human comfort is analyzed by means of the Actual Sensation Vote (ASV) and the COMFA\* budget in two selected locations (an artificial and a natural environment): the objective of this analysis is to quantify the outdoor human comfort in current and future climatic scenarios for 2050 and 2100 (2050-B1, 2050-A1B, 2050-A2, 2100-B1, 2100-A1B and 2100-A2), showing the impact of a natural and an artificial environment on people's wellbeing. One of the limitations of the software CitySim for the analysis of outdoor human comfort is the data input of wind, which is assumed to be as provided by Meteororm, and does not take into account the impact of the urban environment. A further implementation of the model therefore couples CitySim and the Canopy Interface Model (CIM) (Mauree, 2014), which quantifies the wind speed and direction as a function of the built environment. Finally, Comfort Maps of the campus are created in order to visualize the outdoor human comfort in current and future climatic scenarios. The maps will provide a graphical support for architects and urban planners, in order to improve the livability of the campus. The objective of this chapter is to analyze the campus, in time and space, looking for its current and future energy behavior (for buildings and people).

#### 4.1 Energy model of the EPFL Campus

The EPFL campus is located near the city of Lausanne, the capital of the Canton of Vaud in Switzerland (46° 31' N, 06°38' E, 495 m asl, Cumulative Solar Irradiance: 1,219 kWh·m<sup>-2</sup>, Heating Degree Days: 3,273), near Lake Geneva, at 400 meters above sea level. It is composed of more than 50 buildings, interconnected by a pedestrian circuit (Figure 4.1). The Ecole Polytechnique Federale de Lausanne was founded in 1853, with the name *Ecole spéciale de Lausanne*, during the Second World War called *Ecole Polytechnique de l'Université de Lausanne* (EPUL); it was located in the city centre of Lausanne. During the 60's, the university became, together with the ETH of Zurich, a federal university; in this period, due to the lack of spaces, the school was moved in the actual site of Ecublens. The location was selected because the site was property of the Vaud Canton, which bought this area (52 hectares) from the aristocrat family Loys, to create, as first idea, a military aerodrome. Under the presidency of Maurice Cosandey, an architectural contest was set up; Mario Botta and Luigi Snozzi were part of the invited architects. Zweifel and Strickler won the contest; since the beginning, the sustainability was part of the project: the energy demand of buildings was 2 times more performing than the buildings standard. Additionally, green terraces were designed, as well as the pedestrian mobility integrated inside and outside buildings. The university was officially opened in 1978, with the faculties of mathematics, physics, chemistry, mechanical and civil engineering. The second stage of the EPFL was set up during the 80's, by the creation of the so called "diagonal", a diagonal axe cutting the regular texture of the first stage of construction. This new stage is characterized by several buildings located on the southern part of the campus, as well as the first dormitories on the northern part of the campus. The architecture buildings were realized by Schnebli, Amman, Menz and Flora Richat-Roncati, by cutting the existing East-West texture by North-South oriented buildings. Finally, under the presidency of Patrick Aebischer, several new buildings were realized in the XXI<sup>st</sup> century, as the Rolex Learning Center and the Swiss Tech Convention Center (Della Casa and Della Casa, 2010) (Pont, 2010).



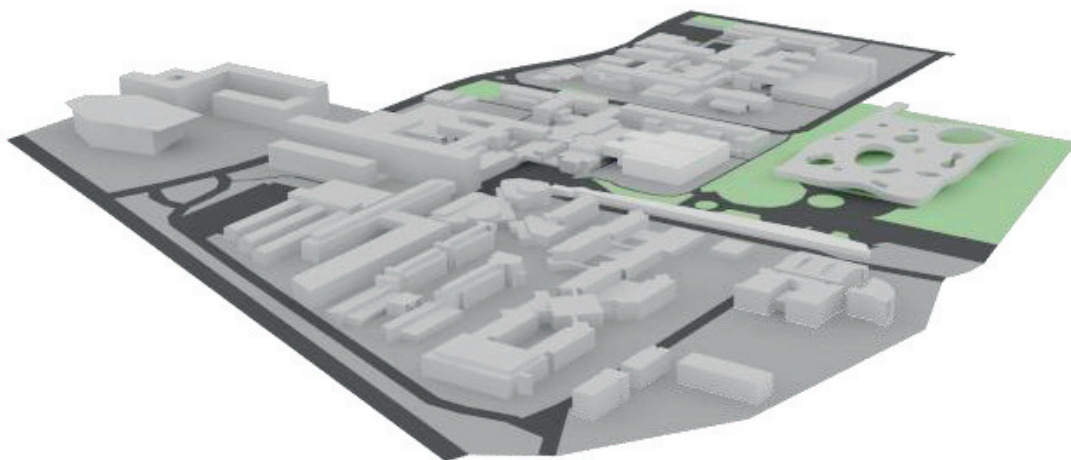
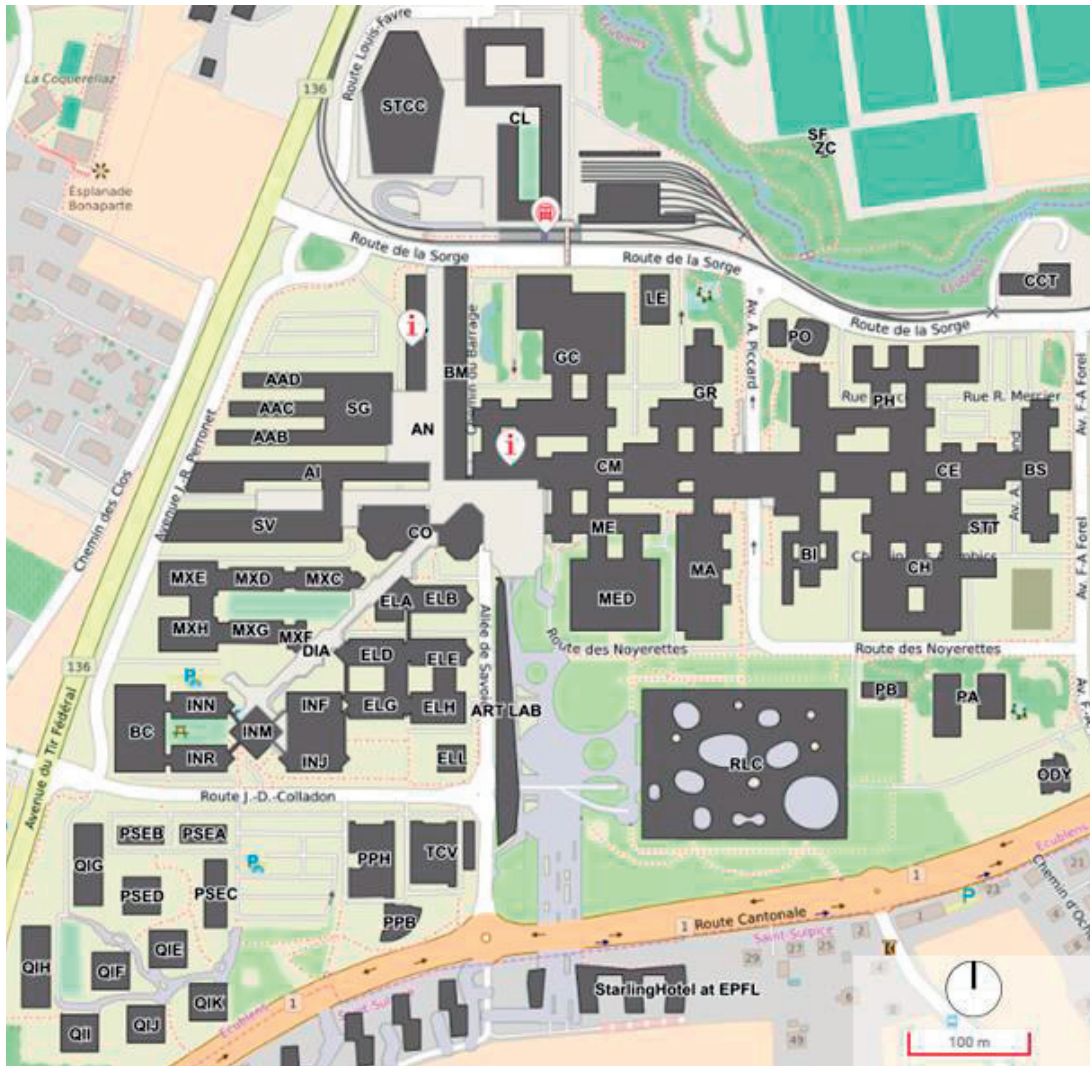


Figure 4.1 EPFL campus, plan extracted from “plan.epfl.ch” (top) and 3D view of the site (bottom).

The climate in Lausanne is temperate; however it presents cold winters and warm summers. According to the Koeppen-Geiger climate classification it is described as a Cfb climate (C: Temperate; f: without dry season; b: warm summer). For the purpose of this analysis, a typical meteorological year (TMY) climate file was created with the software Meteonorm (Remund et al., 2015) using average irradiance data from the period 1991-2010 and average temperature data from the period 2000-2009. Figure 4.2 shows the monthly temperature profile: the average temperature during summer time is around 18°C and the maximum temperature reaches 30°C during the month of July; the minimum temperature is equal to -9.5°C during the month of January and the average temperature in winter time corresponds to 1.9°C. The daily profile of the temperature is given in Figure 4.2 for specific winter and summer days (23<sup>rd</sup> – 25<sup>th</sup> December and 21<sup>st</sup> and 23<sup>rd</sup> June respectively): the air temperature, during summer time, varies on average by 12°C between the daytime and nighttime; during the winter time this variation is lower, on average less than 7°C.

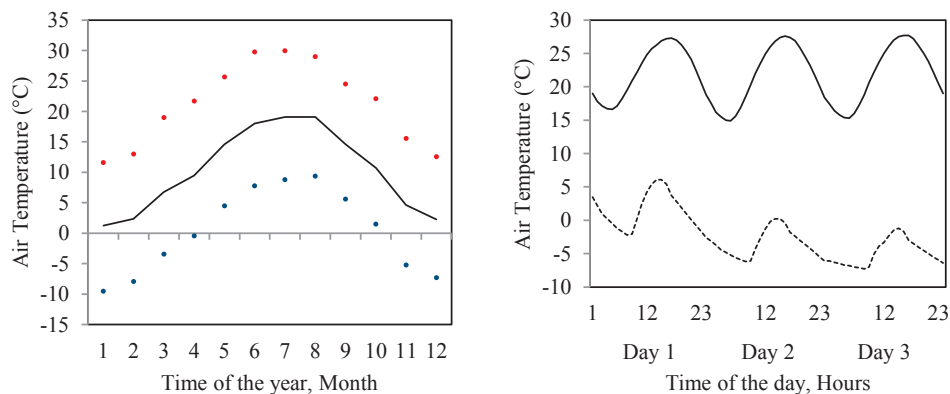


Figure 4.2 Left: average (black line), maximum (red dots) and minimum temperature (blue dots) in the city of Lausanne. Right: hourly temperature for three summer (continuous line) and winter days (dotted line).

The relative humidity is agreeable during the year and slightly too humid during winter time (average humidity of 80%). By analysing the climatic data, a variation of the humidity between daytime and nighttime during summer can be observed (comfortable during daytime and too humid during nighttime). By contrast no such variations are evident during winter time.

The total annual precipitations are equal to 1,142 mm; the larger precipitations occur in August and October (136 mm and 131 mm respectively) and the least are in February (65 mm); winter times are characterized by snow events. The average wind speed of the site corresponds to 1.94 ms<sup>-1</sup>; the largest occurrences of wind are issued from North-East and South-West.

#### 4.1.1 Set-up of the model

The university campus was built in three main stages, which characterize the geometry and materials of the buildings: first stage from 1972 to 1984, second stage from 1980 to 1992 and third stage from 1992 to 2002 (DII, 2004); buildings added later include the Communications Building BC, the Scientific Park, the Rolex Learning Centre (designed by SANAA and inaugurated in 2010), the BI Building (designed by Dominique Perrault and inaugurated in 2013), the Swiss Tech Convention Centre (designed by Richter Dahl Rocha and inaugurated in 2014), the new ME building (designed by Dominique Perrault and inaugurated in May 2016) and the Artlab (designed by Kengo Kuma and inaugurated in November 2016). Knowing that each stage of construction corresponds to a homogenous architectural design, the proposed methodology applies to each building the physical characteristics that correspond to its period of construction; all properties are summarized in Table 4.1. The envelopes of each period of construction are defined by Lesosai (Lesosai, 2017) on the basis of imported physical characteristics, as designed in the architectural plan (Figure 4.3). Buildings of the first stage of construction (1972-1984) are characterized by an external envelope with aluminium cladding; buildings of the second stage of construction

(1980-1992) present an external covering with ceramic tiles and buildings of the third stage of construction present an external envelope with white plaster. The previous analogies cannot be applied to the new buildings (BC, Scientific Park, Rolex Learning Centre etc.), because these were designed and built independently and do not present a common architectural design.

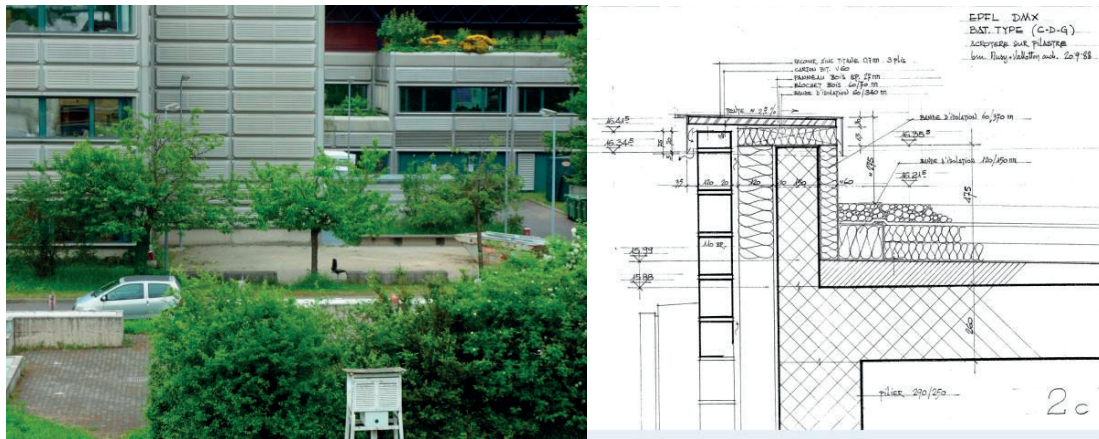


Figure 4.3 Left: view of buildings of the first stage of construction. Right: constructive detail and section of the facade of building MXD, part of the second stage of construction. Source of the picture on the right: real estate and infrastructure department of the EPFL.

The physical properties of the envelope according to the period of construction are summarized in Table 4.1; a common envelope is applied to all new buildings, considering that they have been built after 2001 and consequently comply with the energy requirements defined by SIA Norm 380/1. The windows of the first stage of construction were triple glazing; the windows of the second stage were double glazing, and the ones of the new buildings are assumed as high performance windows, with a U-value lower than  $1.0 \text{ W}\cdot\text{m}^{-2}\cdot\text{K}^{-1}$  (Suisse-Énergie, 2009).

Construction stage	U-value Roof ( $\text{W}\cdot\text{m}^{-2}\cdot\text{K}^{-1}$ )	U-value Wall ( $\text{W}\cdot\text{m}^{-2}\cdot\text{K}^{-1}$ )	U-value Floor ( $\text{W}\cdot\text{m}^{-2}\cdot\text{K}^{-1}$ )
First Stage (1972-1984)	0.30	0.30	0.56
Second Stage (1980-1992)	0.31	0.38	0.56
Third Stage (1992-2002)	0.31	0.38	0.56
New buildings (since 2002)	0.16	0.16	0.16

Table 4.1 Envelope of the buildings, defined according to their period of construction.

The ventilation rate of the buildings varies according to their function: buildings of the first stage of construction and the ones hosting offices have a low ventilation rate ( $0.3 \text{ h}^{-1}$ ), by contrast buildings hosting research laboratories, such as the Life Science buildings, have an ventilation rate of up to  $0.9 \text{ h}^{-1}$ . The heating set point temperature is set at  $21.5^\circ\text{C}$  during the wintertime. This temperature is defined following an adaptation between the set point temperature of the different functions hosted by the campus (offices, classroom, auditorium, laboratories and restaurants) as defined by the Swiss Norm SIA 2024 (SIA, 2006).

The geometry of the campus is based on an existing 3D model (Carneiro, 2011) that was revised in order to be readable by the software CitySim; the newer buildings were added to the scene (Swiss Tech Convention Center, BC Building, Rolex Learning Center, ME building and Artlab). The occupancy profile is defined according to SIA 2024 (SIA, 2006): the number of occupants and their presence is based on the useful surface of each building and its function (offices, classroom, auditorium, laboratories or restaurants); based on the same normative, the electrical appliances are added to the occupancy profile. A different profile is applied during the Christmas holidays, when the university has a limited number of occupants, and the internal temperature is set at  $16^\circ\text{C}$ . The Swiss Tech Convention Centre (STTC) and the adjacent residences are analyzed without occupants, because they were inaugurated in 2014 and consequently no monitored data were available when the model was set up.



The EPFL campus is heated by a central heat pump that uses water from Lake Geneva: the water is pumped from 68 m underwater and has a constant temperature of 6-7°C during the year. After use, the water is released back into the river Sorge, which leads it back into the lake (J. Schmid, 2005). In the proposed case study the heating and cooling demand of the campus is quantified ignoring the electricity or the gas required, because of the difficulty of quantifying the energy performance of the HVAC system. Finally, no air conditioning currently exists on the site, but the water of the lake is currently used in the district cooling system, to refresh laboratories and computer servers (DII, 2015).

Since 2010, the EPFL campus hosts a solar park: the roofs of most buildings are covered by photovoltaic panels, with a total power of 2.2 MW peak and a total area of 15,500 m<sup>2</sup> (Table 4.2). The photovoltaic panels were installed in three different stages in 2010, 2011-2012 and 2014 by the electricity provider Romande Energie SA. Each stage of construction is characterized by different types of panel (monocrystalline, polycrystalline, thin film and silicon) and different manufacturers (EPFL, 2017). Colored panels are installed on site: the so called Gretzel cell and the Kromatix™ panels (Figure 4.4).



Figure 4.4 Photovoltaics panels on the EPFL campus. Gretzel cell (left) and Kromatix™ (right). Source: Mediatheque EPFL.

Construction stage	Surface (m <sup>2</sup> ) / Number of PV	Type	Power (kWp)	Production (MWh y <sup>-1</sup> )
First stage (2010)	4,324/ 2,642	Monocrystalline	643	663
Second stage (2011-2012)	6,202/3,269	Polycrystalline, Thin film, Silicon Amorphous	669	702
Thid stage (2014)	5,016/3,085	Monocrystalline, Polycrystalline and colored panels	813	853

Table 4.2 Photovoltaic farm on the roof of the campus. Description of the panels, according to their stage of installation (EPFL, 2017).

Finally, the physical properties of the outdoor environment are based on data retrieved in DXF format by the building service of the university, as well as from Open Street Map.

#### 4.1.2 Validation of the model

The validation of the model, performed with the software CitySim Pro, is based on the monitored energy demand for heating, as provided by the enterprise ENERGO; the monitoring took place during the years 2011, 2012 and 2013, and provided yearly values and average daily values for each month (ENERGO, 2014). Figure 4.5 shows the annual monitored heating demand of each building of the site as a function of the simulated heating demand; the coefficient of determination is equal to 0.89. The lowest correlation is observed for buildings hosting laboratories, where it is difficult to quantify the real heating demand, because of large unknown internal gains (machines and appliances) as well as the required ventilation. The average relative difference between the annual monitoring and



simulation for the entire campus corresponds to 10%; this difference is related to the uncertainties of the model (internal gains, occupant behavior as well as deterioration of the physical properties of the envelope) as well as the weather data used for the simulations: the input climatic data correspond to a typical meteorological year as defined by the software Meteonorm. The climate data influence the demand of a building, as demonstrated by previous analyses performed on the EPFL campus, where the heating demand of the LE building was evaluated with the software CitySim Pro. Analyzing the LE building demand using the climatic data provided by Meteonorm or the monitoring data, results lead to a 5.1% variation of the heating demand using weather data monitored in 2012, and 0.5% if using data monitored in 2013 (Walter and Kämpf, 2015). The energy demand is always expressed, throughout this thesis, as function of the year.

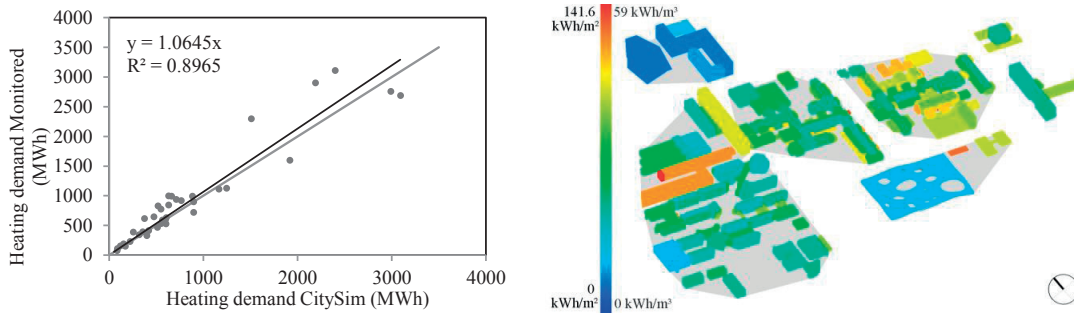


Figure 4.5 Left: correlation between the monitored and the simulated heating demand for the years 2011,2012 and 2013. Right: annual heating demand of the campus, expressed in  $\text{kWh}\cdot\text{m}^{-3}$  and  $\text{kWh}\cdot\text{m}^{-2}$ , assuming an average height of 2.4m.

Figure 4.6 shows the 3D model of the campus with photovoltaic panels (indicated in grey) and the annual solar shortwave radiation, expressed in  $\text{kWh}\cdot\text{m}^{-2}$ , impinging the campus. The electricity produced by the photovoltaic panels, as calculated using the proposed model, was validated with on-site monitored data acquired by Romande Energie in 2013 (Waehlti, 2015). Figure 4.6 shows the correlation between the numerical model and the monitoring data, which is equal to 0.93, indicating a sound agreement.

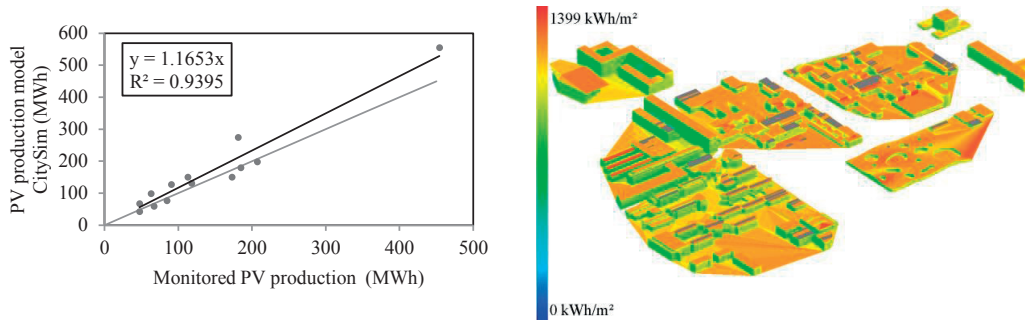


Figure 4.6 Left: correlation between the monitored electricity produced by PV and the simulations performed by CitySim for the year 2013. Right: annual solar irradiance on the campus, with the photovoltaic panels shown on the rooftop of buildings (grey).

#### 4.1.3 Site refurbishments in current and future climatic scenarios

Refurbishment of the site includes a reduction of the energy needs for heating in order to meet Minergie and Minergie-P standards for the envelopes of all buildings. In our study, a Minergie envelope is characterized by a U-value of  $0.16 \text{ Wm}^{-2}\text{K}^{-1}$ , due to 25 cm of Polystyrene insulation (EPS); a Minergie-P envelope features 35 cm of EPS and a U-value of  $0.11 \text{ (Wm}^{-2}\text{K}^{-1})$ ; in both cases, the existing windows are replaced by triple glazing windows with infrared coating and filled with argon. For the future scenarios nine simulations were performed, showing the impact of climate change on the thermal behavior of buildings, by comparing the current status (based on a typical meteorological year) with Minergie and Minergie-P scenarios. The best and worst scenarios are then optimized to improve their efficiency through a shading strategy, which considers the automatic closing of the sun

shadings when the facade irradiance is larger than  $150 \text{ W}\cdot\text{m}^{-2}$ , and through a windows opening strategy in which windows automatically open during the summer period (70% of glazed surface is considered as openable), if the outdoor temperature is  $1^\circ\text{C}$  lower than the internal one (Robinson, 2011).

The future thermal behavior of the campus is quantified for 2050 with three different weather scenarios based on IPCC studies (Meehl and Stocker, 2007) (IPCC, 2000):

- **Scenario 2050-B1:** rapid growth of population (8.7 billion) and use of new clean technologies (30% share of zero carbon energy sources in primary energy).
- **Scenario 2050-A1B:** rapid economic growth, rapid growth of population (8.7 billion), and new efficient technology across all sources (36% share of zero carbon energy sources in primary energy).
- **Scenario 2050-A2:** continued increase of population (11.3 billion) and reduced research in new technologies (18% share of zero carbon energy sources in primary energy).

These scenarios are defined by the software Meteonorm and contain the projected climatic data for the future: temperature, precipitation and global irradiance of the periods 2011–2030, 2046–2065 and 2080–2099 (Remund et al., 2015). In 2050, on average, the air temperature is expected to increase by  $2.3^\circ\text{C}$ , and the maximum temperature during the summer will reach  $35^\circ\text{C}$ ,  $5^\circ\text{C}$  higher than the current value. Futures scenarios for precipitations predict a reduction by 12 % during the summer period (drought events) and an increase by 21% of snow events during the winter months. The total annual precipitation will be reduced by 10 %, from the current 1,142 mm to 1,043 mm in Scenario 2050-A2.

The first analysis concerns the refurbishment of the site according to the standards Minergie (maximum energy demand  $55 \text{ kWh}\cdot\text{m}^{-2}$ ) and Minergie-P. Renovation in compliance with Minergie reduces the heating energy demand of the site by 33 %, passing from an average demand of  $77 \text{ kWh}\cdot\text{m}^{-2}$  to  $52 \text{ kWh}\cdot\text{m}^{-2}$ ; the buildings that are most impacted by the renovation are those hosting offices and classrooms, and those built during the first stage of construction. As an example, Building CE would reduce its heating demand by 44% (Figure 4.7). By contrast, buildings hosting laboratories, which implies large internal gains, would only slightly reduce their demand through an improvement of thermal insulation of the envelope. One example is the SV Building, where the heating demand would be reduced by 14%. According to the renovation simulation, 80% of buildings would adhere to the Minergie standard. Naturally buildings with animal laboratories, such as AI and SV could not reach the Minergie target, as the internal gains dominate the thermal behavior of the building. In the Minergie-P scenario the average energy demand for heating of the site is  $48 \text{ kWh}\cdot\text{m}^{-2}$ , showing a total reduction of 37% compared to the current situation; as in the previous case study, just buildings with low internal gains are positively impacted by the refurbishment. Finally, in this analysis the LE buildings block is considered, as the sum of the demand of LESO solar experimental building (renovated in 1998 according to the Minergie-P standard) and the LIPID building.

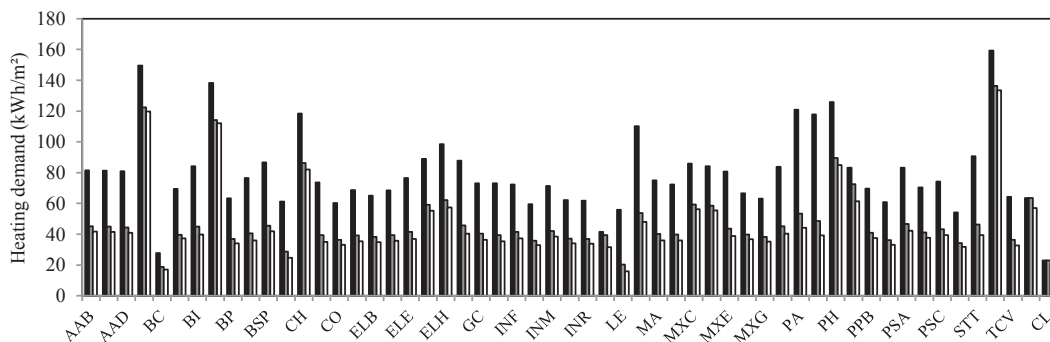


Figure 4.7 Heating demand of buildings ( $\text{kWh}\cdot\text{m}^{-2}$ ), comparison between the existing situation (black), Minergie (grey) and Minergie-P (white).

Based on the above results a first hand-made optimization was carried-out, showing the impact of the internal temperature on the heating demand of buildings in Minergie renovation scenarios. The minimal indoor

temperature (the set point temperature for heating) is reduced to 20°C and then raised to 24°C. Results show that a set point temperature of 20°C reduces the heating demand by 13%, and consequently 85% of buildings have a heating demand lower than 40 kWh·m<sup>-2</sup>. By contrast, increasing the indoor temperature reduces the energy performance of buildings by 16 %.

The impact of future climatic scenarios will imply a new behavior of the campus that will decrease its heating demand and increase its cooling demand. The future scenarios defined with the software Meteonorm show the impact of climate change on the thermal behavior of the campus in 2050. Three models are implemented (Minergie, Minergie-P and current); each of them is analyzed with the future weather data 2050-A1B, 2050-A2 and 2050-B1. Figure 4.8 shows the total energy demand (for heating and cooling) of the campus, as a function of the proposed models.

Considering climate changes, if the EPFL campus will not undergo any refurbishment, its total energy demand will probably slightly increase, passing in our simulations from the current 91 kWh·m<sup>2</sup> to 93.9, 94.3 and 95.5 kWh·m<sup>2</sup> in 2050-B1, A2 and A1B respectively. This difference appears negligible, but the interesting fact is the variation of the thermal behavior of the buildings: in the current weather scenario, the heating demand represents 85% of the total energy demand; in the future climatic scenarios it will decrease to 69% of the total demand. The same trend is observed for buildings refurbished according to Minergie and Minergie-P, in both simulations the impact of the heating demand on the total energy demand is lower, corresponding to 60% in Minergie, and 58% in Minergie-P. An analysis of the impact of refurbishment as a function of the heating demand for each climatic scenario shows that refurbishment will considerably decrease the heating demand (on average by around 34% in the Minergie, and 39% in the Minergie-P scenario) but only slightly decrease the cooling demand by 3%. This behavior is related to the proposed refurbishment strategy, which impacts the insulation of the envelope but changes neither the shadowing nor the ventilation strategy. For this reason an improvement is proposed, applying the following cooling strategies (Robinson, 2011):

- Blinds strategy: automated blinds close if the facade radiation is larger than 150 W m<sup>-2</sup>.
- Windows strategy: windows opening during summer are systematic if the outdoor temperature is 1°C lower than the internal one.

Thanks to the proposed strategies, the EPFL campus refurbished in compliance with Minergie-P, and projected in 2050-B1, would decrease its cooling demand by 34% compared to the same scenario without the latter. The total energy demand of the campus would be 25.2 GWh (70% for heating, and 30% for cooling). The same analysis conducted for the current EPFL campus projected in 2050-A1B, shows a decrease of its cooling demand by 37% compared to the same scenario without blinds and windows strategy; the total energy demand of the campus would be 35.9 GWh (77% for heating, and 23% for cooling). The proposed optimizations are made for the best case (Minergie-P) and worst case (current) scenarios for EPFL.

Based on this analysis, the EPFL campus could benefit from several refurbishment scenarios in the future, impacting its thermal behavior: as simulated, its total demand would vary between 58 kWh·m<sup>2</sup> (Minergie-P with blinds and ventilation strategies) and 95 kWh·m<sup>2</sup> (non-refurbished scenario), showing a difference of 38%. Based on these results, a new campus management strategy is required, able to identify the critical buildings and to propose refurbishments able to decrease the site's energy demand in the context of projected climate change.

Energy performance and outdoor comfort of a campus in a temperate climate

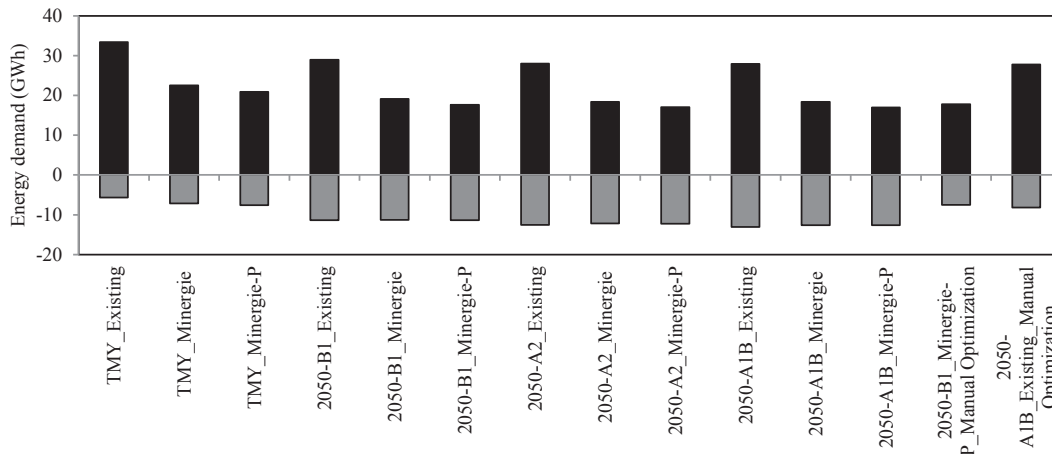


Figure 4.8 Total energy demand for heating and cooling (GWh), for the proposed case studies (existing, Minergie and Minergie-P) and different climatic scenarios (Typical Meteorological Year, 2050-B1, 2050-A1B and 2050-A2). Heating demand (black) and Cooling demand (grey).

A sensibility analysis of the future behavior of the campus was performed, showing the impact of climate change on the different refurbishment scenarios, for each building and stage of construction. Further guidelines will be defined in Chapter 6, in which an optimization with the hybrid CMA-ES/HDE is applied to the EPFL campus, to improve the energy demand and the outdoor human comfort in current and future climatic scenarios. Figure 4.9a shows the heating demand of the site (GWh) for the campus as it is today (x -axes) as a function of the future climatic scenario 2050-A2 (non-refurbished, Minergie and Minergie-P). First of all, the graph shows that in 2050 the campus will face a general reduction in the heating demand, as shown by the difference between the bisector and the heating demand of the current situation projected for 2050; a second analysis underlines that some buildings are more sensitive to refurbishment than others, such as buildings of the first stage of construction (GC, PH, CH, CM and CE), where the improvement to Minergie and Minergie-P decreases the heating demand by 30% to 60%. Other buildings, which host laboratories, for example SV and AI, see their demand reduced by 20% through improvement of the thermal characteristics of the envelope according to Minergie, whereas, a variation of less than 1% is obtained if reaching the Minergie-P standard.

By contrast, as shown in Figure 4.9a, the cooling demand faces an increase in future climatic scenarios, except in buildings PA and PB, characterized by one floor and hosting offices and a kindergarten: because of their geometry and low internal gains, they are strongly influenced by a hypothetical refurbishment, decreasing their cooling demand by 18 to 22% if refurbished as Minergie-P. All the other buildings increase their cooling demand, even if refurbished. An interesting case is Building BC (Figure 4.9b): its cooling demand will increase if improving the insulation of the envelope in future climatic scenarios; this behavior is probably related to its glazed central atrium, which collects solar gains during the winter time, but needs to be ventilated and shadowed during summer time. The largest cooling demand in future scenarios will be the one of the Rolex Learning Center (Figure 4.9b), because of its large glazing ratio and its geometrical shape that hosts a single floor; as in the previous case study, no mechanical ventilation of the building is considered, but as happens in reality (and it is mandatory for Minergie P), mechanical ventilation is important to decrease its cooling demand. Effectively, currently in CitySim, it is not possible to add a mechanical ventilation system, but we can, indirectly, modify the infiltration rate of the buildings, as well as proposing the opening of windows, if the outdoor temperature is 1°C lower than the internal one.

Energy performance and outdoor comfort of a campus in a temperate climate

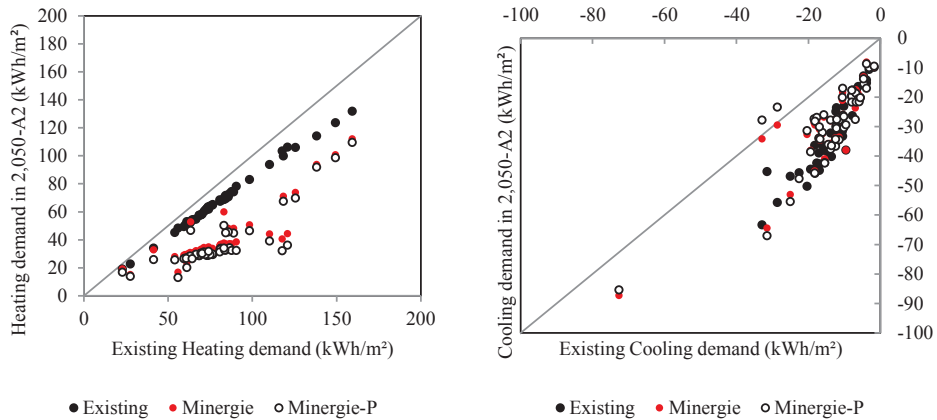


Figure 4.9a Heating (a) and cooling (b) demand of the campus in future climatic scenarios, as function of the existing case study.



Figure 4.9b BC building, internal atrium (left) and Rolex Learning Center (right). Source: Médiathèque EPFL.

#### 4.1.4 Indoor human comfort

The above simulations performed on the EPFL campus show the impact of climate change on the thermal behavior of buildings, but how will the users perceive the climate change? To quantify thermal sensations, the LESO experimental building was analyzed, outlining the thermal perception of users in current and future climatic scenarios, as expressed by the Predicted Mean Vote (PMV) and the Predicted Percentage of Dissatisfied (PPD) (Fanger, 1970); the thermal scale is defined in Table 4.3.

Thermal Sensation	Predicted Mean Vote
Cold	-3
Cool	-2
Slightly cool	-1
Neutral	0
Slightly warm	+1
Warm	+2
Hot	+3

Table 4.3 Predicted Mean Vote, seven points thermal scale, extracted from ISO 7730 (International Organization for Standardisation, 2006).

The analysis is based on the average daytime indoor temperature (from 8:00 to 19:00 hours) for the months of May, June, July, August and September. The indoor office activity is assumed as 1.2 met (for further details about the metabolic activities, please refer to Chapter 2), the clothing insulation corresponds to 0.7 clo (light clothing), the mean radiant temperature is assumed equal to the air temperature, the air speeds corresponds to 0.15 m·s<sup>-1</sup>



and the relative humidity to 50%, according to SIA 2024 (SIA, 2006). The Predicted Mean Vote is then calculated for four scenarios: i) the non-refurbished campus with the typical meteorological year, ii) the non-refurbished campus in 2050-A2, iii) the Minergie refurbished campus in 2050-A2 and iv) the Minergie-P refurbished campus in 2050-A2. Figure 4.10 shows the Predicted Mean Vote and the Predicted Percentage of Dissatisfied in the LESO experimental building, for the current building envelope and TMY meteorological data. During the month of May (a) the PMV corresponds to -0.6 (“comfortable”, with PPD=12.5%) and in June (b) and July (c) to 1 and 1.6 (“slightly warm”, with PPD=26.1% and 56.3% respectively); in August and September the indoor environment indicates “comfortable” levels (PPD=22.1% and 5.8% respectively). According to these results, the average indoor temperature during daytime (from 8:00 to 19:00 hours) is “comfortable” in May, August and September, and “slightly too warm” during the months of July and August.

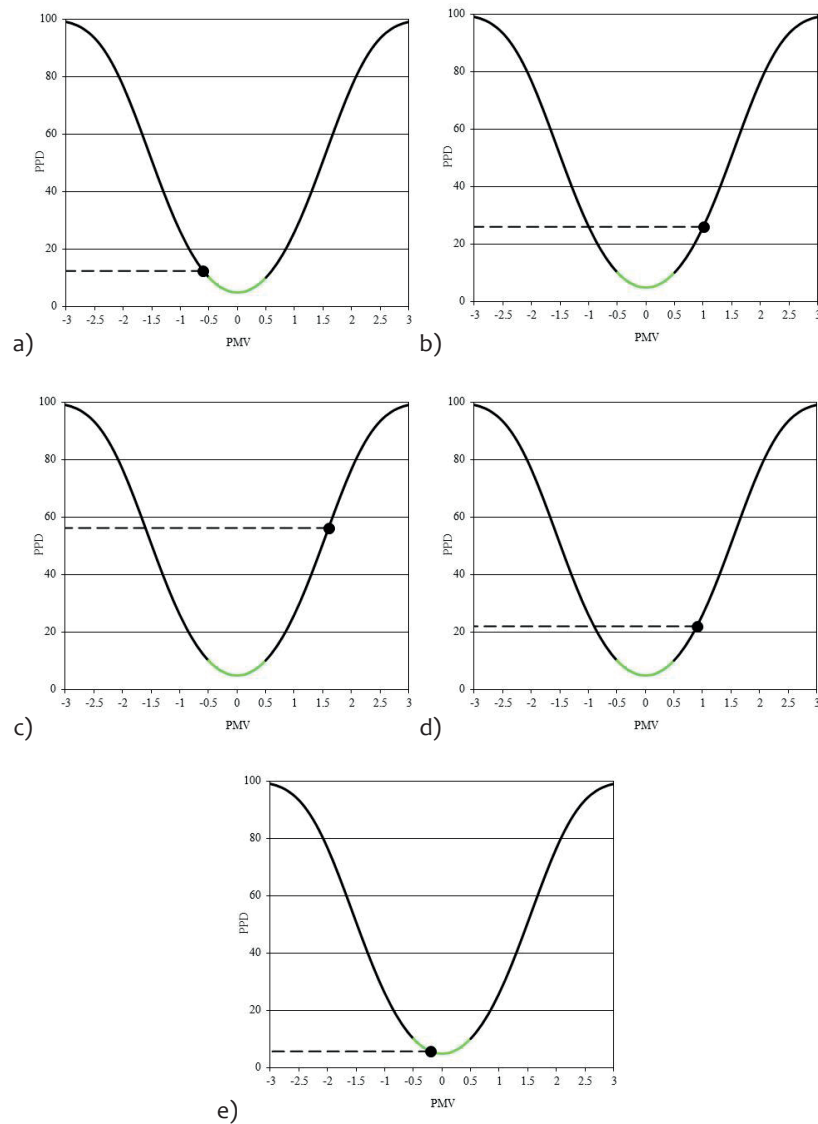


Figure 4.10 Predicted Mean Vote and Predicted Percentage of Dissatisfied in the non-refurbished LESO solar experimental building, with meteorological data of a typical meteorological year; a) May; b) June; c) July; d) August; e) September.

The Predicted Mean Vote for the non-refurbished building in 2050-A2 is not as comfortable as in the TMY, as shown in Figure 4.11: during the months of May and September the thermal sensation is “comfortable” (PMV=-0.6 and 0.7 respectively, with PPD=12.5% and 15.3% respectively), during the month of June it is “slightly too warm”

( $PMV=1.2$ , with  $PPD=35.2\%$ ) and during the months of July and August it is “too warm” ( $PMV=2.6$  and  $2.2$  respectively, with  $PPD=95.3\%$  and  $84.9\%$  respectively). This analysis shows that to guarantee a comfortable indoor environment in the future, thermal improvements in the building envelope and in the ventilation system are required.

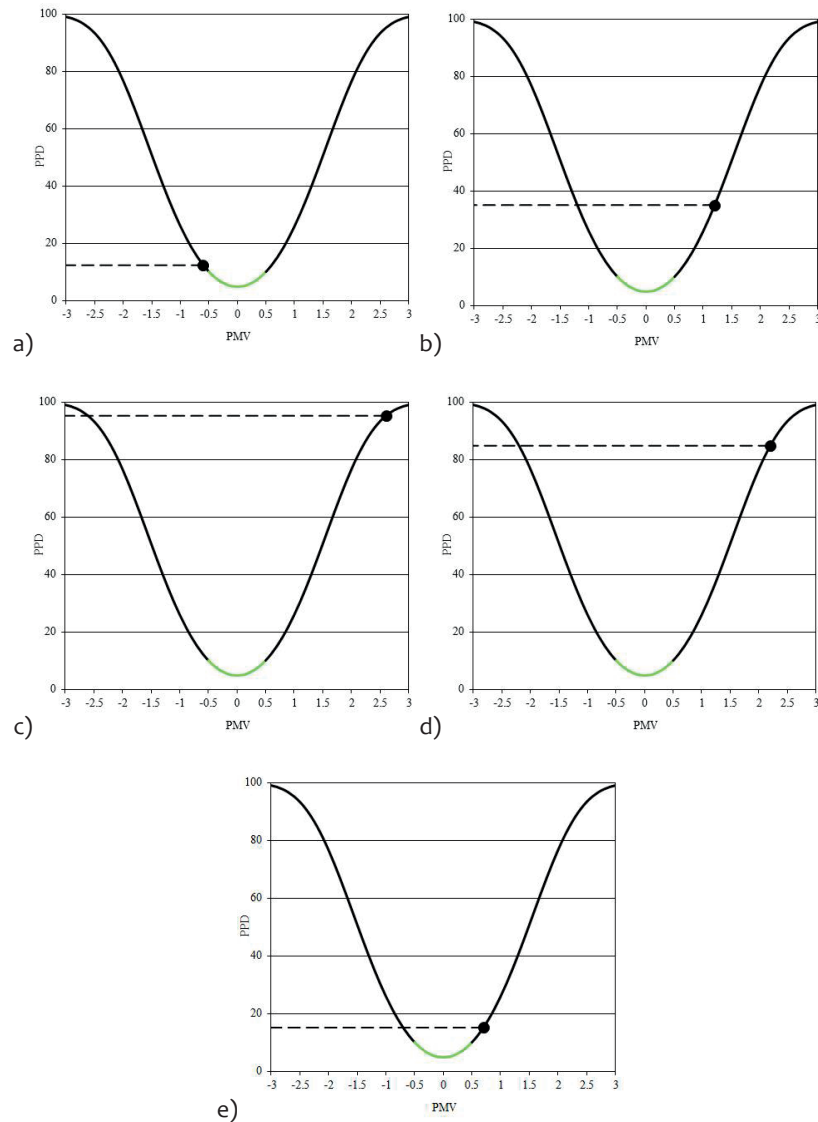


Figure 4.11 Predicted Mean Vote and Predicted Percentage of Dissatisfied in the non-refurbished LESO solar experimental building, with meteorological data 2050-A2; a) May; b) June; c) July; d) August; e) September.

Based on the above results, the thermal comfort of occupants is additionally analyzed in hourly steps, showing the total hours per each thermal sensation. As in the previous case study the analysis is performed during daytime (from 8:00 to 18:00 hours), during the months of May, June, July, August and September and i) for a non-refurbished campus with the typical meteorological year, ii) the non-furbished campus in 2050-A2, iii) the Minergie refurbished campus in 2050-A2 and iv) the Minergie-P refurbished campus in 2050-A2. Figure 4.12 shows the total hours per thermal sensation (“cold”, “cool”, “slightly cool”, “neutral”, “slightly warm”, “warm” and “hot”): the number of “comfort” hours is reduced, passing from 935 in the existing building to 576 in the non-furbished building projected in 2050-A2, showing a decrease of 39%. Correspondingly, the hours when occupants experience “warm” sensations are likely to increase: they will characterize the main part of the summer time. In the current

scenario, the occupant will face a “hot” thermal sensation just during 4 hours (upon 1,836 hours of the selected period); in the future scenario the hours characterized by a “hot” thermal sensation will increase, reaching 233 hours in the Minergie-P refurbished building. The above results underline the need of refurbishment of the buildings of the site, with a special attention to natural ventilation strategies, and probably a centralized and efficiently cooling system, able to maintain a comfortable indoor environment for users. Effectively, as previously stated, in the current CitySim model it is not possible to add a mechanical ventilation system; this fact could lead to an overestimation of the overheating.

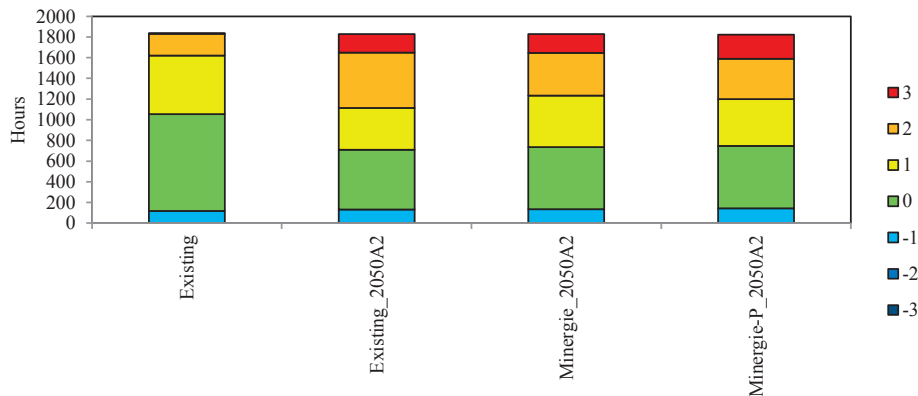


Figure 4.12 Analysis of the indoor thermal sensation, based on the Predicted Mean Vote, for the months of May, June, July, August and September, for the current LESO solar experimental building (TMY) and the same building (non-refurbished, Minergie and Minergie-P) in the future climatic scenario 2050-A2.

#### 4.1.5 Energy demand in conjunction with the CIM model

This chapter presents the impact of micrometeorological data created by the Canopy Interface Model (CIM) (Mauree, 2014), on the previous analyses of the energy demand of buildings. The new meteorological data computed by the Canopy Interface Mode, is defined based on the outputs provided by CitySim Pro (surface temperature of the built environment) and on the meteorological data provided by Meteonorm. CIM calculates the air temperature and the wind profile, speed and direction, for a given location, at a selected height above ground. Based on the area covered by the EPFL campus, horizontal homogeneity can be assumed (Stull, 1988) at 9 meters height. In order to understand the difference between the wind profile and air temperature obtained from Meteonorm data (Remund et al., 2015) and from CIM data, the following assumptions are made:

- Meteonorm provides the wind speed at 10 m above ground (Meteonorm, 2009). By contrast, CIM calculates it punctually at different heights above ground, in this case the average over the average height of the buildings in the campus. The same applies to the air temperature.
- Meteonorm provides the wind speed as measured by the weather station, which normally is positioned in an open field. By contrast, CIM analyses the impact of city density, by varying the wind speed and the air temperature.
- CIM account for the roughness of the surfaces, as well as the impact of the surface temperature (calculated by CitySim Pro) on the wind speed and on the air temperature.

Firstly, the energy simulation of the site is realized using CitySim, and the results (surface temperature and urban density) are exported to CIM. The tool recalculates the local wind speed, the wind direction and the air temperature. With the above data, the new weather profile is imported in CitySim, and a new simulation is run.

The analysis is performed for the existing campus as well as for the campus after refurbishment according to Minergie-P standard. The objective of this analysis is to quantify the sensitivity of the built stock to the wind profile, as well as a generalization with regard to building envelopes. The existing campus, as simulated with Meteonorm values, has a total energy demand for heating equal to 77 kWhm<sup>-2</sup>; assuming the wind profile as



created by CIM, the demand increases to  $86 \text{ kWhm}^{-2}$ . Effectively, in the CIM model the air temperature is reduced by  $0.3^\circ\text{C}$  (from  $10.2^\circ\text{C}$  to  $9.9^\circ\text{C}$ ), and the wind speed is reduced by  $1.5 \text{ ms}^{-1}$  on average per year (from  $1.9$  to  $0.4 \text{ ms}^{-1}$ , as shown in Figure 4.13), due to the built environment.

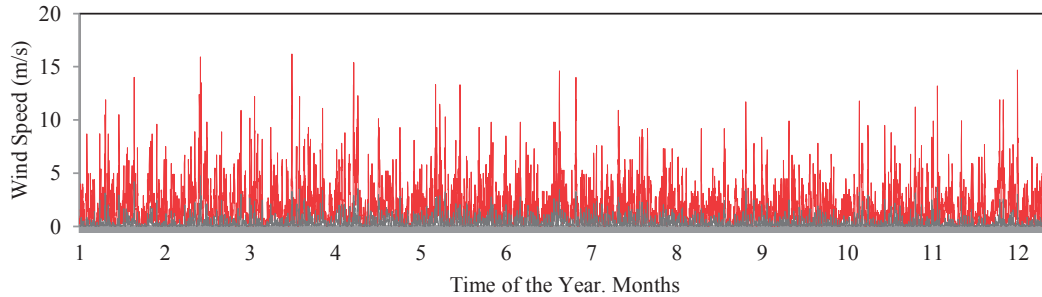


Figure 4.13 Wind speed in the EPFL campus, as provided by Meteonorm (red) and as calculated by the Canopy Interface Model (grey).

It is essential to notice that this variation is not linear throughout the year: indeed, the air temperature is higher in CIM during the summer time (up to  $+1.2^\circ\text{C}$  during the month of June) and lower during the winter time (up to  $-2.0^\circ\text{C}$  during the month of January, as shown in Figure 4.14). Additionally, the profile varies throughout the day, and, as an example, during the heating season (from October to May) the averaged air temperature is lower during nighttime ( $-2.7^\circ\text{C}$ ) and higher during the daytime ( $+1.0^\circ\text{C}$ ). Indeed, the air temperature is lower during daytime during the coldest months (from November to February) then it starts to rise, due to the solar irradiance received and stored by the built environment (Table 4.4). This is related to the urban environment and the sun height: effectively, during the winter time the sun is lower, consequently less radiation is received by the urban canyons. Additionally, this phenomenon is related to the so called Cold Air Pools (CAP). A good example of this phenomena appears in La Brevine valley ( $46^\circ58' \text{ N}$ ,  $6^\circ36' \text{ E}$ ,  $1,043 \text{ m asl}$ ., Cumulative Solar Irradiance:  $1,173 \text{ kWh}\cdot\text{m}^{-2}$ ), Jura Mountains, in the canton of Neuchatel, Switzerland (Figures 4.14a and 4.14b). In this village were recorded, in January 1987, the lowest temperature of Switzerland, corresponding to  $-41.8^\circ\text{C}$ . During the winter season, due to the topographic configuration of the site, the Cold Air Pools phenomenon appears: with katabatic flows, the cold air along the slope became cooler than the adjacent air at the same height. Consequently, the cold air (denser) flows downhill, accumulating at the ground level in the valley. This phenomena is stronger in cloudless, windless and high-pressure conditions (Vitasse, 2016).

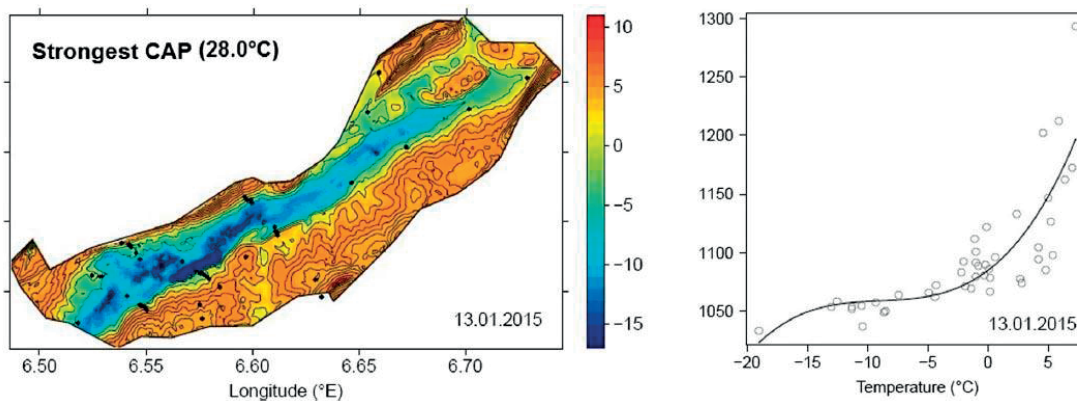


Figure 4.14a La Brevine, strongest CAP phenomena in the valley (Vitasse, 2016).



Figure 4.14b La Brevine, picture of the site (source: <http://www.neuchateltourisme.ch>).

Effectively, by comparing the CIM with the Meteonorm data, the average temperatures differences during two winter nights is higher in cloudless conditions (21<sup>st</sup> February, nebulosity equals to 2 octas) than in cloudy conditions (8<sup>th</sup> January, nebulosity equals to 8 octas), where the difference corresponds to 5°C and 2.5°C, respectively. Finally, it is important to notice that the city of Lausanne is classified as Class II for the wind force, which corresponds to the Beaufort scale 2, “light breeze” (SIA, 2003).

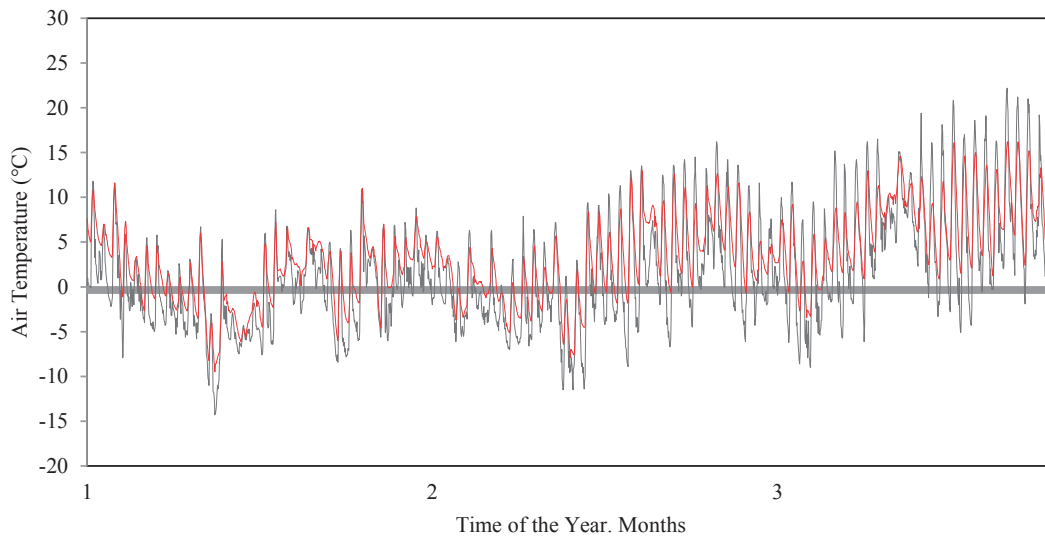


Figure 4.15 Air temperature during the months of January, February and March, as provided by Meteonorm (red) and CIM (grey).

Month	Air Temperature (°C)	Wind Speed (ms <sup>-1</sup> )	Air Temperature (°C) Daytime	Air Temperature (°C) Nighttime	Wind Speed (ms <sup>-1</sup> ) Daytime	Wind Speed (ms <sup>-1</sup> ) Nighttime
Difference between Meteornorm and the Canopy Interface Model						
1	<b>-2.0</b>	-1.6	<b>-1.2</b>	-2.8	-1.6	-1.7
2	-1.8	<b>-1.9</b>	-0.1	-3.2	<b>-1.9</b>	-1.8
3	-1.2	-1.8	1.5	<b>-3.5</b>	-1.6	<b>-2.0</b>
4	-0.1	<b>-1.9</b>	3.5	-3.2	-1.9	-1.9
5	0.7	-1.5	4.7	-2.8	-1.6	-1.5
6	<b>1.3</b>	-1.6	<b>5.8</b>	-2.5	-1.4	-1.7
7	1.2	-1.5	5.5	-2.5	-1.6	-1.4
8	0.8	<b>-1.2</b>	4.8	-2.5	<b>-1.1</b>	-1.3
9	0.6	-1.3	3.6	<b>-2.0</b>	<b>-1.1</b>	-1.4
10	-0.9	-1.3	1.1	-2.5	-1.4	<b>-1.3</b>
11	-1.2	-1.5	-0.2	-2.1	-1.5	-1.5
12	-1.7	-1.8	-1.1	-2.3	-1.6	-1.9

Table 4.4 Averaged monthly difference between the weather data provided by Meteornorm and the Canopy Interface Model. Daytime (from 8:00 to 18:00 hours) and nighttime (from 19:00 to 7:00 hours).

The fact that, due to the CIM weather profile, the energy demand of the campus increases is, somehow, not intuitive. Indeed, it is clear that the reduction of the wind speed reduces the convective coefficient between the buildings and the outdoor environment, consequently reducing the heat losses, and the heating demand. But, the CIM provides also a new air temperature, based on the new wind speed, as well as on the surface temperature, as calculated by CitySim Pro. The new air temperature, in the EPFL case study, is reduced during the heating season, on average by 1.0°C from October to May. In order to validate the results obtained, it is important to understand the relative impact of varying the air temperature during the heating season, in this case by 1°C, and the wind speed by 1.5 ms<sup>-1</sup>. In order to do this analysis, five urban configurations are selected, adapted from (Ratti et al., 2003a); the district is included in a square of 100 m per each side. Their urban characteristics are the following: i) ground floor area (m<sup>2</sup>), ii) number of floors (-), iii) treated floor area (m<sup>2</sup>), iv) Floor Area Ratio, or Plot Ratio (-), v) Site Coverage (%) and vi) Form Factor (-). The Floor Area Ratio (FAR), or Plot Ratio, is defined as ratio of the gross floor area to the site area, the Site Coverage (SC) is defined as the ratio of buildings footprint to the site area (Ng, 2010), the Form Factor is defined as follows (Kriesi, 2015):

$$FF = \frac{(W + R + 0.5G)}{A} \quad (4.1)$$

where W is the wall area, R is the roof area, G is the ground area and A is the gross area of the building. All values are expressed in m<sup>2</sup>.

The selected configurations are then simulated with CitySim Pro, in order to quantify their energy demand, by varying the outdoor air temperature ( $\pm 1.0^\circ\text{C}$  during the heating season), as well as the wind speed ( $\pm 1.5\text{ms}^{-1}$ ).




Case study	Ground floor area (m <sup>2</sup> )	Number of Floors (-)	Treated floor area (m <sup>2</sup> )	Floor Area Ratio (-)	Site Coverage (%)	Form Factor (-)	Urban configurations. Adapted from (Ratti et al., 2003a)
A	900	4	3,600	0.036	0.009	1.37	
B	3,000	4	12,000	0.12	0.03	0.95	
C	1,500	4	6,000	0.06	0.015	1.02	
D	4,050	4	16,200	0.162	0.04	0.87	
E	3,000	4	12,000	0.12	0.03	0.87	
F	5,100	4	20,400	0.20	0.05	0.87	

Table 4.5 Urban characteristics of each case study.

Figure 4.16 summarizes the results obtained, per each urban configuration. The parameter that mostly affects the heating demand is the variation of the air temperature: by reducing the air temperature by 1°C during the heating season, the heating demand of buildings increases (proportionally to the floor area ratio) from 7.7% in case study A (FAR= 0.036) to 7.2% in case study F (FAR=0.20). By reducing the wind speed by 1.5 ms<sup>-1</sup>, the heating demand decreases by 4.0% in case study A, to 3.0% in case study F. Based on these results, it is evident that the reduction of 1°C has a higher impact in the heating demand, compared to the reduction of the wind speed. Naturally, more compact are the buildings, less they are influenced by the environmental microclimatic variations.

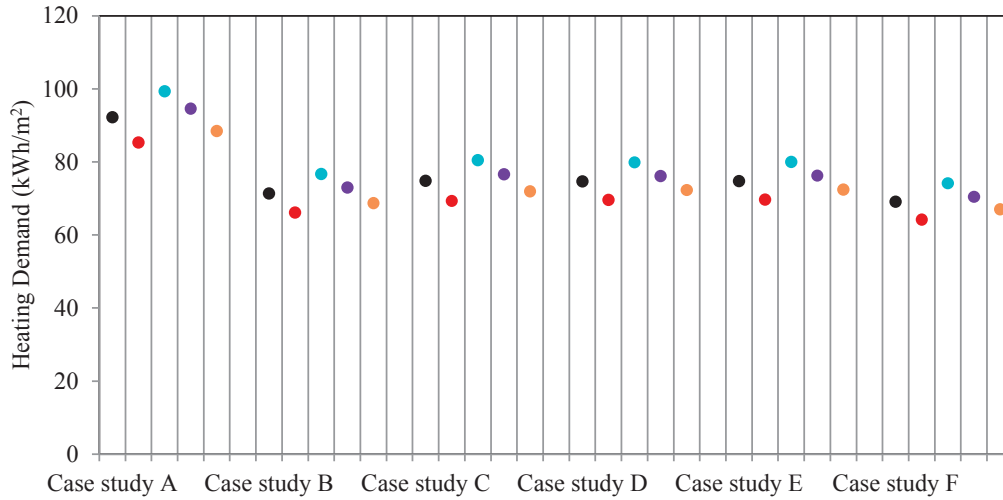


Figure 4.16 Heating demand of the five selected urban configurations (black dots), as function of the variation by +1°C (red dots) and -1°C (blue dots) of the air temperature, and by +1.5 ms<sup>-1</sup> (violet dots) and -1.5 ms<sup>-1</sup> (orange dots).

Coming back to the analyses of the EPFL campus, the CIM model induces a variation in the energy demand of buildings, as more energy is required to heat them. Figure 4.17 shows the heating demand of buildings with the weather data of Meteonorm, and the one created with CIM. The average increase in heating demand for the entire campus corresponds to 9.65%. When comparing the energy demand of the campus, as simulated with the CIM model, with onsite monitoring of the EPFL campus (2015), the difference between the model and the reality corresponds to 8%. Consequently, thanks to the CIM model, the EPFL energy model, simulated with CitySim, is getting closer to reality. Naturally, a variation of 2% is clearly inside the simulations error, due to the model uncertainties.

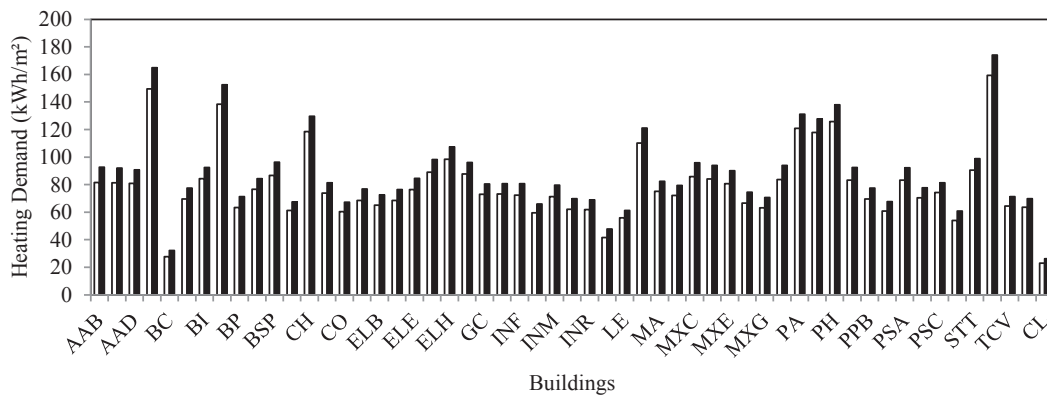


Figure 4.17 Energy demand for heating for the existing buildings, based on Meteonorm weather data (white) and CIM weather data (black).

The same analyses are conducted for the EPFL campus as refurbished according to the Minergie-P standard (Figure 4.18); in this case, all buildings are well insulated with 35cm of EPS and triple glazing with infrared coating. The thermal behavior of the campus is similar to the one of the previous case, showing an increase in the simulated energy demand when using CIM weather data. In this case study, the average demand passes from 48 kWh·m<sup>-2</sup> to 55 kWh·m<sup>-2</sup>, due to the lower air temperature during the heating season.

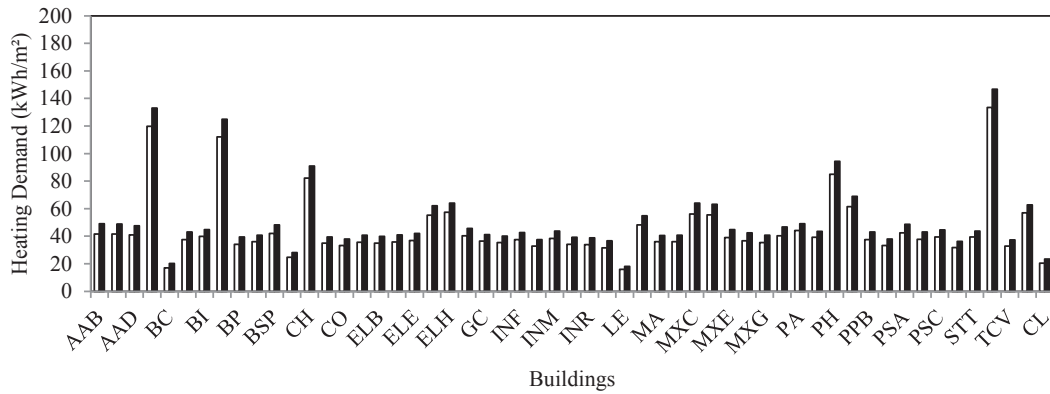


Figure 4.18 Energy demand for heating in the Minergie-P refurbished buildings, based on Meteornorm weather data (white) and CIM weather data (black).

To conclude, the correlation between the two models is evident (Figure 4.19) and a general trend shows that simulations with the CIM model show a higher energy demand for heating of the site. Looking at the sensitivity of each weather data to the variation of the thermal characteristics of the building, it is evident that in both climatic scenarios, campus refurbishment according to Minergie-P would reduce the heating energy demand by 44% (based on Meteornorm data) and by 43% (based on CIM data).

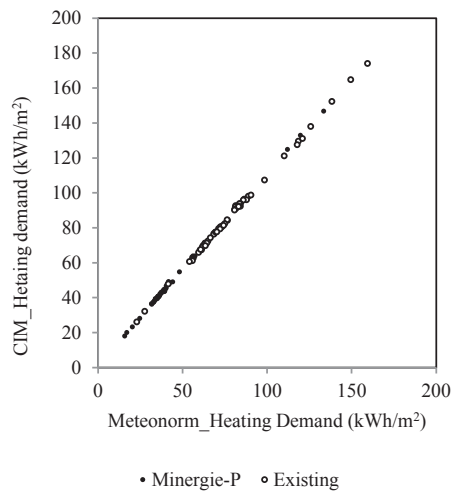


Figure 4.19 Correlation between the heating demand (kWh·m<sup>-2</sup>) calculated with CIM and Meteornorm, as a function of the current situation (white) and the Minergie-P one (black).

## 4.2 Outdoor human comfort

This chapter proposes a methodology for analyzing the microclimate and outdoor human comfort in the built environment with the aim of optimizing the future campus design. The methodology makes use of the software CitySim Pro (Robinson, 2011) to define the pedestrian outdoor conditions in current and future climatic scenarios. Two biometeorological indices are selected for this analysis: Actual Sensation Vote (ASV) (Nikolopoulou, 2004) and COMFA\* budget (Vanos et al., 2012a); both standards are calculated with the outputs (surface temperature, short and longwave radiation) provided by the software CitySim Pro, for two different outdoor environments: a square near the Swiss Tech Convention Center and a bocce court. Passive cooling strategies are then applied to the future

outdoor environment, with the intent to decrease the hours of discomfort of pedestrians, according to their metabolic activity.

#### 4.2.1 Actual Sensation Vote and COMFA\*

The outdoor human comfort is analyzed using two biometeorological indices: Actual Sensation Vote (ASV) and COMFA\* budget. ASV is expressed as a linear correlation based on on-site monitoring and questionnaires for several European cities; environmental parameters (air temperature, global irradiance, wind speed and relative humidity) are multiplied by a numerical coefficient that varies according to the climate. The ASV was defined within an European project, called RUROS, and applied to several European cities, and in the city of Fribourg, as Swiss test case. Considering that the climate in Lausanne can be assimilated to Fribourg, ASV is expressed by:

$$ASV = 0.068\theta_a + 0.0006R_g - 0.107V - 0.002RH - 0.69 \quad (4.2)$$

where  $\theta_a$  (°C) is the air temperature,  $R_g$  (W·m<sup>-2</sup>) is the global solar irradiance,  $V$  (m·s<sup>-1</sup>) is the wind speed and  $RH$  (%) is the relative humidity. All values are based on hourly meteorological data.

By contrast, the COMFA\* Budget is based on energy exchanges between a person and his/her environment, as in the following equation (Kenny et al., 2009a):

$$B = M_h + R_{RT} - C - E_{s+i} - L_s \quad (4.3)$$

where  $M_h$  is the metabolic heat generated by a person,  $R_{RT}$  is the radiation absorbed,  $C$  are the convective heat losses,  $E_{s+i}$  is the evaporation and  $L_s$  is the longwave radiation emitted by a person. All values are expressed in W m<sup>-2</sup>. For further details, please refer to Chapter 2.

Both indices can be applied to quantify the outdoor environment, but with different specific objectives: ASV quantifies outdoor human comfort by using meteorological data provided by weather stations without considering either the metabolic activity of pedestrians nor the outdoor microclimate; this standard is simple and easy to use, and gives first ideas to quantify thermal sensation. By contrast, the COMFA\* model requires more detailed input data, but quantifies the variation in thermal sensations by accounting for the metabolic activity of the pedestrian as well as the outdoor built environment. The thermal sensation scales of the ASV and the COMFA\* budget (for light metabolic activities) are defined in Table 4.6.

Actual Sensation Vote	COMFA* budget (W·m <sup>-2</sup> )	Thermal Sensation
-2	≤ -201	Cold
-1	-200 to -121	Cool
	-120 to -51	Slightly cool
0	-50 to +50	Comfort
	+51 to +120	Slightly warm
1	+121 to +200	Warm
	≥+201	Hot

Table 4.6 ASV thermal sensation scale and COMFA\* budget, as a function of thermal sensation.

Pedestrians are modelled with the CitySim Pro software: they are designed (Chapter 2) as an octagonal prism inscribed in a circle of 0.17 m in diameter and 1.5 m height; the human body is supposed to be made of four concentric layers: core, muscles, fat and skin (Parsons, 2014). The clothing characteristics are defined by COMFA\* using the intrinsic clothing insulation model, able to vary garments according to the air temperature; finally the metabolic activity of the pedestrians is seated/relaxed, which corresponds to 80 W m<sup>-2</sup>. To perform the study two pedestrians were positioned in two different outdoor environments (Table 4.7): an open square in front of the new Swiss Tech Convention Center (Case study A) and a bocce court (Case study B) protected by three cherry trees (*Prunus Avium*). The Leaf Area Index (LAI) of plants is assumed equal to 3.5 (Gyeviki et al., 2012) and their



albedo equal to 0.22. Figure 4.20 shows the location of the square and the bocce court in the EPFL campus; the sites were chosen because they are frequented daily by students (eating and leisure) from spring to autumn.

Case study	Density (kg·m <sup>-3</sup> )	Specific heat (J·kg <sup>-1</sup> ·K <sup>-1</sup> )	Thermal conductivity (W·m <sup>-1</sup> ·K <sup>-1</sup> )	Albedo of the ground cover (-)
<b>Case study A:</b> open square with asphalt ground	580	800	0.75	0.1
<b>Case study B:</b> bocce court with clay soil	1,600	890	0.25	0.3

Table 4.7 Thermal properties of the soils in the two selected sites, data defined according to (Erell et al., 2011a).

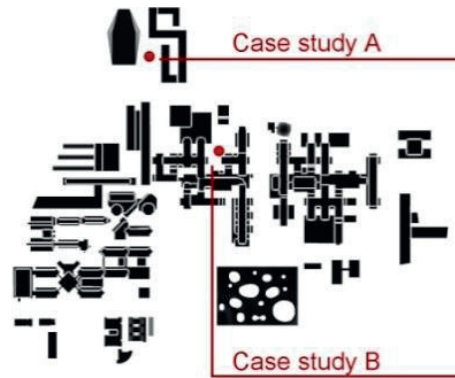


Figure 4.20 EPFL plan with the location of the two case studies A and B (top). Bottom: photos of the case studies, case study A (left) and case study B (right).

The outdoor climate of the EPFL in current and futures climatic scenarios is firstly analyzed with ASV considering the thermal sensation throughout the year (day and night) for the climate of Lausanne, without any differentiations concerning the local microclimate. Results are summarized in Figure 4.21, illustrating the comfort behavior in 2050 and 2100 as a function of the total of comfortable hours over the year, equal to 8,760. According to a typical meteorological year (TMY), half of the year is currently characterized by “cool/cold” sensations (266 and 4,136 hours respectively) and one third is “comfortable” (3,663 hours); less than 700 hours are marked by “warm/hot” sensations. In 2050 (average between scenarios) there is a decrease of “cool” and “cold” events by 4% (154 and 4,043 hours respectively) and an increase of “warm” and “hot” events by 20% (826 and 2 hours respectively). In future 2100 scenarios, the difference is larger: “cool/cold” sensations (89 and 3,745 hours) are replaced by “warm/hot” events (1,112 and 11 hours) with a peak in Scenario A2, where “warm/hot” hours will double (1,316 hours).

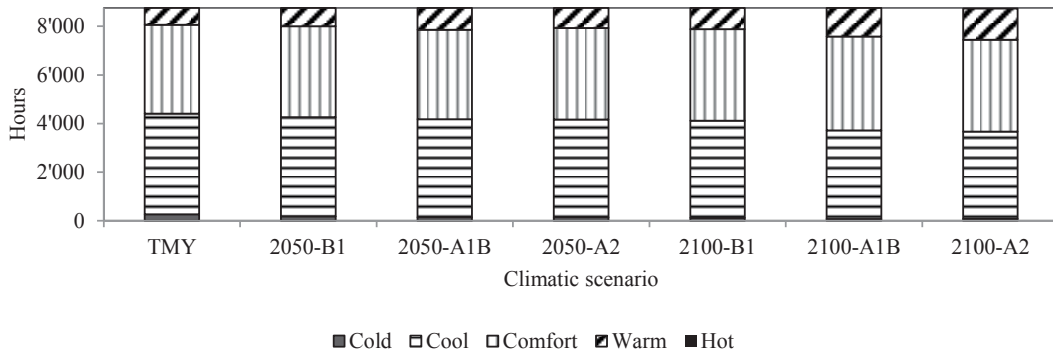


Figure 4.21 Actual Sensation Vote (ASV) in the EPFL campus in current and future climatic scenarios: 2050-B1, 2050-A1B, 2050-A2, 2100-B1, 2100-A1B and 2100-A2.

Figure 4.22 shows the hourly Actual Sensation Vote for the TMY, in 2050-A2 and 2100-A2; the A2 scenario is selected for the detailed analysis, because in that period the thermal sensation is maximally affected. The daytime thermal sensation (from 8:00 to 18:00 hours) is particularly impacted, passing from 630 hours of “warm/hot” thermal sensation in a TMY (626 and 4 hours respectively), to 829 in 2050-A2 and 1,106 hours in 2100-A2 (1,078 and 28 hours respectively), showing an increase of discomfort by 24% and 57% respectively. During the winter time, the daytime thermal sensation is drastically impacted, passing from 1,577 hours of “cold/cool” thermal sensation in a TMY (74 and 1,513 hours respectively), to 1,440 in 2050-A2 (39 and 1,401 hours respectively), to 1,259 of “cold/cool” thermal sensation in 2100-A2, with a reduction by 9% and 20% during the daytime hours. As a final analysis, the comfortable hours during daytime will increase in the close future (passing from 1,808 today, to 1,824 in 2050-A2) and decrease in 2100, passing from 1,808 today, to 1,605 hours in 2100-A2.

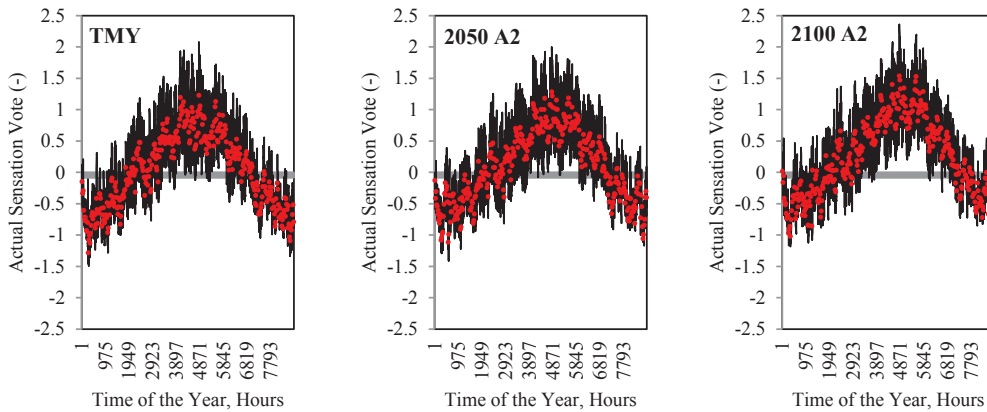


Figure 4.22 Outdoor human comfort, quantified by the Actual Sensation Vote, for a TMY (left), scenario 2050- A2 (center) and scenario 2100-A2 (right).

Figure 4.23 shows the normalized thermal sensation during the month of July: if currently a pedestrian will experience a “warm” thermal sensation from 11:00 to 18:00 hours, in 2050 it will be from 10:00 to 19:00 hours, and in 2100 from 9:00 to 21:00 hours. Based on these results, it is clear that cooling strategies are required in the outdoor spaces, to improve the quality of the environment, by protecting pedestrians from “hot” thermal sensation.

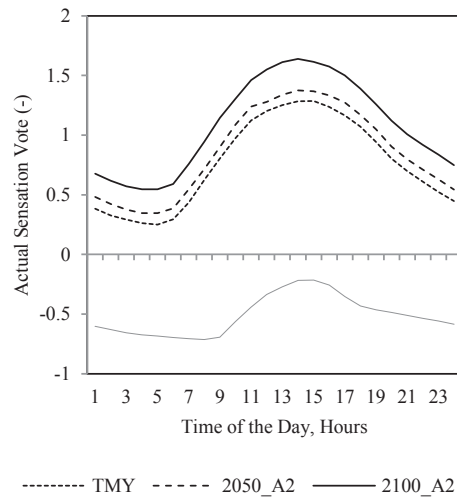


Figure 4.23 Actual Sensation Vote in current and future climatic scenarios.

Considering that human comfort will be largely impacted in the 2100 scenarios, we applied the COMFA\* model for these weather conditions, showing the impact of microclimate (open square and bocce court) on the outdoor human comfort. The COMFA\* budget is calculated for the whole year, but the results presented are related to daytime hours (from 8:00 to 18:00 hours), assuming that both locations are used especially during working hours. Figure 4.24 shows the annual solar irradiance (from 0 to 1,264 kWh m<sup>-2</sup>) in both locations according to current climatic data; in the open square the shadowing produced by surrounding buildings, as expected, is well visible: it halves the solar irradiance received by the pedestrian located near a building compared to another positioned at the center of the square.

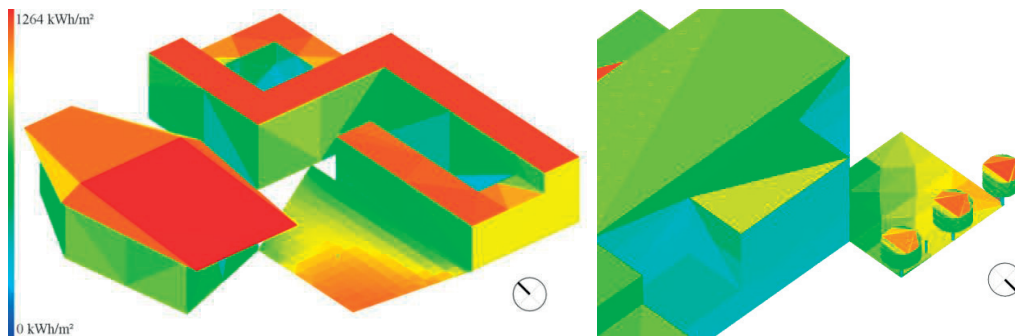


Figure 4.24 Annual solar irradiance on the Swiss Tech Convention Center site (left) and in the bocce court (right). Maximum solar irradiance equals 1,264 kWh·m<sup>-2</sup>.

The results show that the bocce court is more comfortable than the Swiss Tech Convention Center square, as it is protected by cherry trees' shadows and presents a ground covered by clay soil that does not absorb and store the same quantity of heat as asphalt. Figure 4.25 summarizes the outdoor human comfort in the current weather scenario, considering a pedestrian located in Case Study A and B during a typical spring and a typical summer day. During a spring day, a pedestrian located in the bocce court will perceive a "slightly warm" thermal sensation during the hottest hours of the day (from 11:00 to 15:00 hours) but will feel "comfortable" for the remaining daytime and "slightly cool" during the night. In the open square near the Swiss Tech Convention Centre, a pedestrian will feel "slightly warm" to "warm" for the main part of the day and "slightly cool" during nighttime. During a summer day the difference between the two locations is smaller, but during the hottest hours of the day (from 12:00 to 14:00 hours) a pedestrian in the open square will feel "hot" (maximum COMFA\* budget equal to 222 W·m<sup>-2</sup>) whereas one in the bocce court will only feel "warm".

### Energy performance and outdoor comfort of a campus in a temperate climate

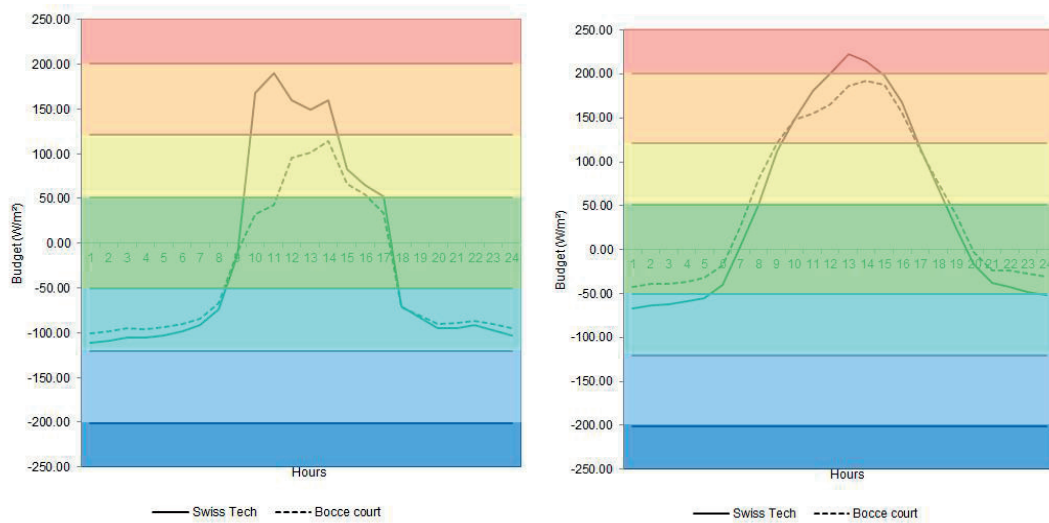


Figure 4.25 COMFA\* Budget for a pedestrian located in the open square near the Swiss Tech Convention Centre, and in the bocce court. Analysis of the human comfort for a spring day (left) and a summer day (right).

The outdoor human comfort will vary with climate change: the general trend shows a decrease of annual daytime hours of comfort, a slight increase during the winter time (warm winters) and a major decrease during the summer time (heat wave phenomena). The outdoor human comfort in summer time near the Swiss Tech Convention Centre in 2100 (average between both scenarios equal to 58 hours of comfort) will be halved compared to the current climatic scenario (127 hours); this difference is partially linked to future temperatures of the site (average air temperature in summer time will increase by 5°C) and partially to geometry and materials of the site. According to our simulations, climate change will impact more the comfort of a pedestrian located in a “man-made” environment, such as the open square near the Swiss Tech Convention Centre, than that of a pedestrian located in a semi natural environment, such as the bocce court, with trees and natural soil. In winter and autumn the hours of comfort in the bocce court will on average increase by 9% and 12% respectively; by contrast, in the open court they will increase by less than 2%. By contrast during summer time the hours of discomfort will drastically increase by 73% in the open square, and by just 55% in the bocce court. Comfort is also related to outdoor activity: if people in Case Study A performed a high metabolic activity (like running or playing sport, with a metabolic intensity equal to 220 W m<sup>-2</sup>) the hours of comfort in future climatic scenario the summer time would be reduced to 9 hours for the entire season.

In order to improve the quality of the outdoor environment, shadowing strategies to reduce the hours of discomfort in the two locations are proposed: in the case of the bocce court, three layers of white meshes, selective “brise soleil” (sloped according to the incident angle of sun) and trees (one *Picea Rubens* or two *Betula Utilis*) were considered (Figure 4.26).

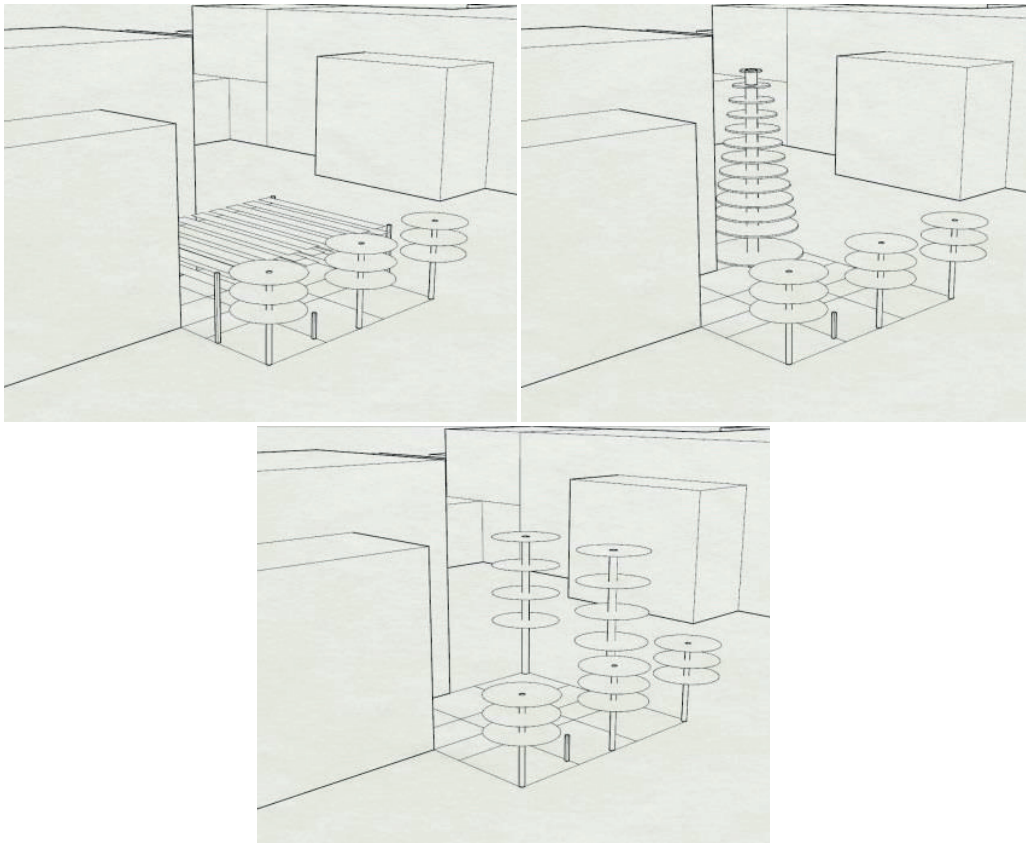


Figure 4.26 Proposed shading strategies: textile meshing (top left), one *Picea Rubens* on the South side of the court (top right) or two *Betula Utilis* on the West side of the court (bottom).

Figure 4.27 shows the solar irradiance during the month of July, for Case Study B with a two tree combinations in climate scenario 2100-A2: the solar irradiance received by the ground is on average reduced by 17% (*Betula Utilis*) and by 9% (*Picea Rubens*), the ground temperature is lower and the outdoor human comfort is consequently improved.

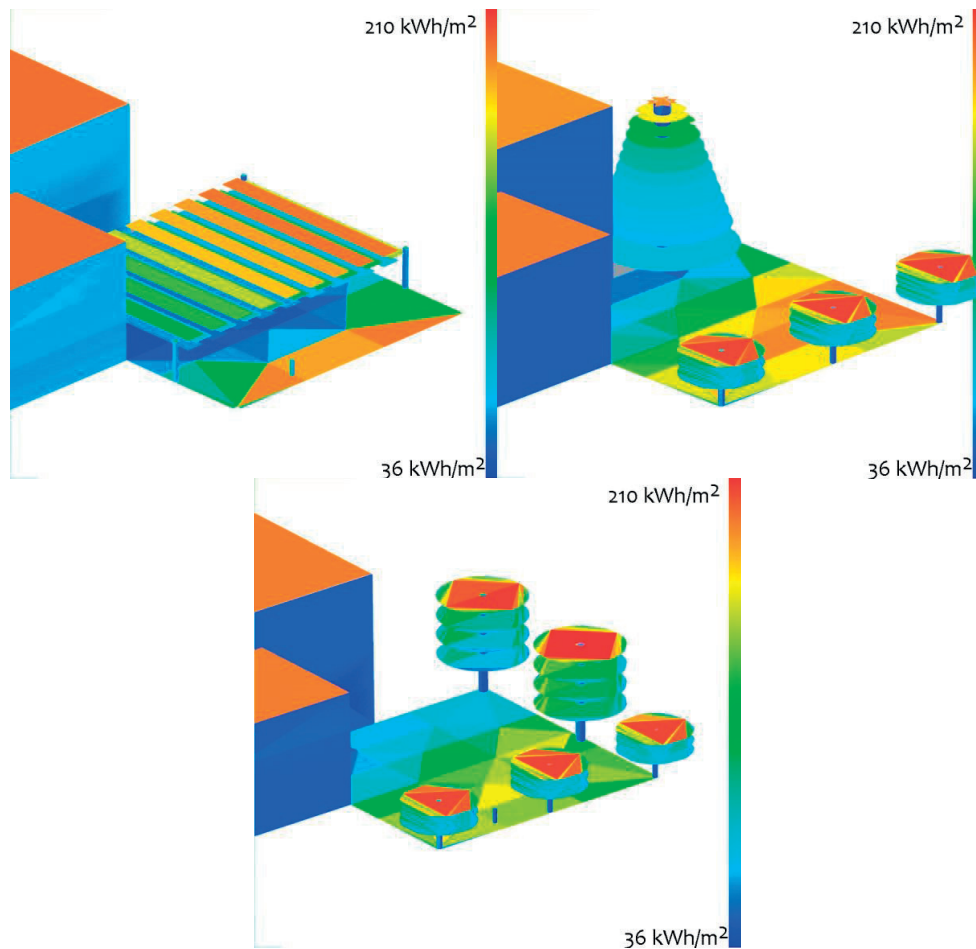


Figure 4.27 Monthly solar irradiance (July) in with future climatic data 2100-A2. Shading strategies: textile meshing (top left), one Picea Rubens on the South side of the court (top right) or two Betula Utilis on the West side of the court (bottom).

#### 4.2.2 COMFA\* with a Canopy Interface Model

As previously stated, in the software CitySim Pro the wind is calculated as the one provided by Meteonorm, neglecting the winds variation within the urban environment. The wind speed has an important impact in the thermal perception of pedestrian, consequently, in this paragraph the CIM weather profile is applied in the above selected locations of the EPFL campus, but in this case study the CIM provides just the new wind speed and direction, neglecting the variation of the air temperature, due to the built environment. We decided to consider just the wind variation, and its impact on the thermal comfort. A further improvement of this model (the Comfort Map) will consider both the wind speed and the air temperature. This chapter presents the impact of a micrometeorological wind profile supplied by the Canopy Interface Model (CIM) (Mauree, 2014), on the above analyses of the outdoor human comfort based on the COMFA\* model. The new wind profile (speed and direction) computed by the Canopy Interface Model, is coupled with the outputs provided by CitySim (surface temperature of the built environment) based on Meteonorm meteorological data. In the previous analyses, the CIM model was applied homogeneously on the EPFL campus, in this case study two different profiles were calculated, one for the square in front of the Swiss Tech, and another one for the bocce court. The average annual wind speed in the square at 10 m height, corresponds to  $0.92 \text{ (ms}^{-1}\text{)}$  based on the Meteonorm recorded data, but it is reduced to  $0.07 \text{ (ms}^{-1}\text{)}$  if determined using the CIM model; the calculated impact is greater in the bocce court, where the wind speed is reduced to  $0.017 \text{ (ms}^{-1}\text{)}$ . Figure 4.28 (a, b and c) shows the difference between a daily wind speed profile



provided by Meteonorm (dotted line) and one calculated by CIM (continuous line) for the square of the Swiss Tech Convention Centre. The profile is analysed during the 21<sup>st</sup> of March, 21<sup>st</sup> of June and 21<sup>st</sup> of December, respectively. Due to the urban form, as well as the height of measurement, the wind speed is also lower on the square, compared to the data provided by Meteonorm. According to CIM, the wind speeds are higher during daytime and lower during nighttime; this behaviour is explained by the turbulent fluxes appearing when the wind is in contact with heated surfaces. As an example, during the 21<sup>st</sup> of June the maximum wind speed during daytime is  $0.3 \text{ m s}^{-1}$ , and lower than  $0.1 \text{ m s}^{-1}$ , during nighttime. Due to the denser built environment, the wind speed in the bocce court is drastically reduced, with a yearly average speed of  $0.01 \text{ m s}^{-1}$ .

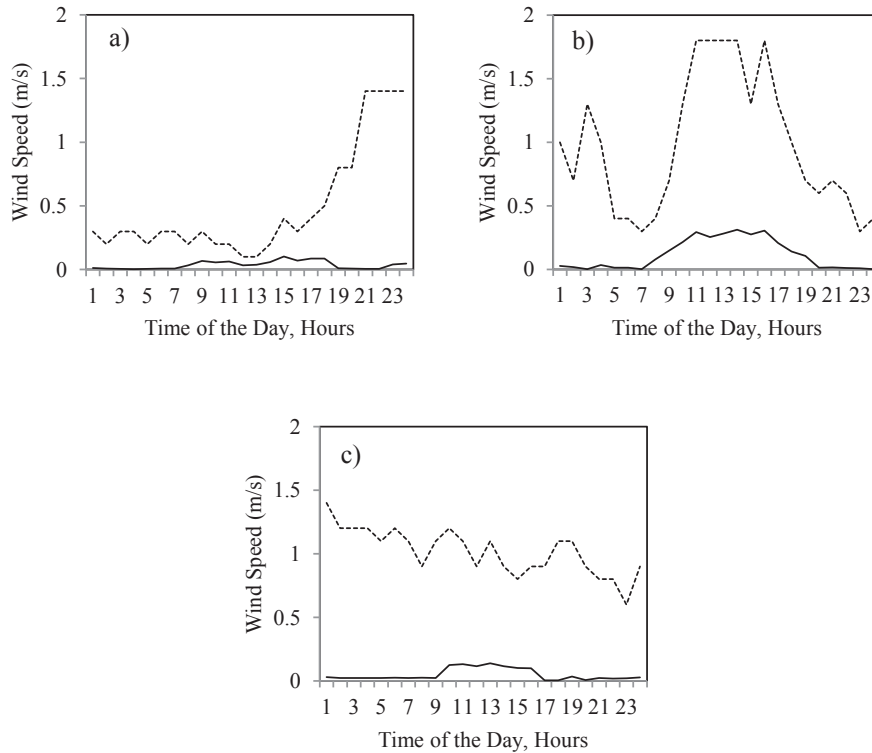


Figure 4.28 Wind speed provided by the software Meteonorm (dotted line) and calculated by the Canopy Interface Model (continuous line) for the square near the Swiss Tech Convention Centre. a) 21<sup>st</sup> of March; b) 21<sup>st</sup> of June; c) 21<sup>st</sup> of December.

The use of a detailed wind model, such as CIM, impacts all the energy fluxes, but particularly the convective heat transfer coefficient and the longwave radiation emitted. Effectively, energy fluxes due to convection correspond to  $43.50$  and  $45.40 \text{ Wm}^{-2}$  in the bocce court and square, respectively, when calculated with the CIM model, showing a reduction by approximately 30% (circa  $23 \text{ Wm}^{-2}$ ). This is clearly related to the reduction of the wind speed, blowing upon pedestrian. On the contrary, the longwave radiation emitted by the pedestrian increases (by 6% in both locations, corresponding to circa  $29 \text{ Wm}^{-2}$ ); this phenomenon is due to the variation of the boundary layer resistance. Effectively, the longwave radiation emitted is defined by the following formula:

$$L_s = \varepsilon_s \sigma (\theta_{sf} + 273.15)^4 \quad (4.4)$$

where  $\varepsilon_s$  is the emissivity of the body and the clothing, assumed to be equal to  $\sim 0.95$  (Kenny et al., 2009a),  $\sigma$  is Stefan Boltzmann constant equal to  $5.67 \cdot 10^{-8} \text{ (W} \cdot \text{m}^{-2} \cdot \text{K}^{-4})$  and  $\theta_{sf}$  ( $^{\circ}\text{C}$ ) is the surface temperature of a person, which is defined as:

$$\theta_{sf} = \left( \frac{\theta_{sk} - \theta_a}{r_c + r_a} \right) r_a + \theta_a \quad (4.5)$$



where the boundary layer resistance  $r_a$  ( $s \cdot m^{-1}$ ) (Kenny et al., 2009a) is directly related to the wind speed by the Reynolds number:

$$r_a = \frac{0.17}{ARe^n Pr^{0.33} k} \quad (4.6)$$

where  $Re$  is the Reynolds number,  $Pr$  is the Prandtl number (equal to 0.71),  $k$  is the thermal diffusivity of the air ( $\approx 2.2 \cdot 10^{-5} m^2 \cdot s^{-1}$ ),  $A$  and  $n$  are empirical constants based on heat flow's experiments around cylinders. The Reynolds number is calculated as follows:

$$Re = \frac{0.17V}{u} \quad (4.7)$$

where  $u$  is the kinematic viscosity of the air (assumed as  $1.5 \cdot 10^{-5} m^2 \cdot s^{-1}$ ) and  $V$  is wind speed ( $m \cdot s^{-1}$ ). For further details concerning the equations, please refer to Chapter 2.

Consequently with the CIM model, the lower the wind speed is, the higher the air boundary layer resistance  $r_a$  is ( $426 sm^{-1}$  with CIM and  $211 sm^{-1}$  with Meteonorm, on average during the year in the bocce court) and as a consequence, the higher the surface temperature of the individual  $\theta_{sf}$  is ( $26.9^\circ C$  with CIM and  $21.8^\circ C$  with Meteonorm, on average during the year in the bocce court) and the longwave radiation emitted, as well.

As done above, the outdoor human comfort was calculated according to the COMFA\* budget method; detailed analyses are performed during 21<sup>st</sup> of March, 21<sup>st</sup> of June and 21<sup>st</sup> of December (Figure 4.29). The thermal sensation of pedestrians is strongly related to the wind profile: during the 21<sup>st</sup> of June, a pedestrian located near the Swiss Tech Convention Centre would experience greater thermal discomfort ("hot" sensation from 10:00 hours to 17:00 hours) according to CIM data. The wind speed changes from  $1.0 ms^{-1}$  in average during the day (with a maximum speed of  $1.8 ms^{-1}$ ) to an average speed of  $0.1 ms^{-1}$  (with a maximum speed of  $0.3 ms^{-1}$ ). During the other seasons, no difference in thermal perception is observed during daytime, just during nighttime when the maximum difference between the wind speeds is  $1.4 ms^{-1}$ . Finally, the difference between the two models is lower on the winter solstice, when the perceived thermal sensation is constantly lower according to the CIM model during day and nighttime.

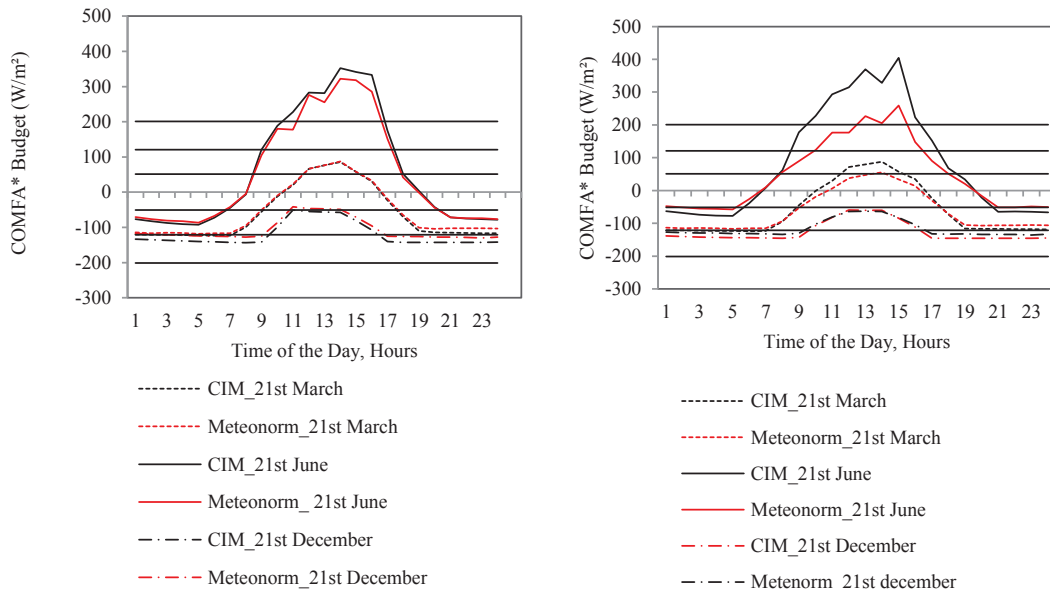


Figure 4.29 COMFA\* energy budget for the square near the Swiss Tech Convention Centre (left) and in the bocce court (right), during 21<sup>st</sup> of March, 21<sup>st</sup> of June and 21<sup>st</sup> of December. Comparison between weather data provided by Meteonorm (red) and calculated by CIM (black).

The other analysed area is the bocce court; in this case study, due to the higher building density of the site, there is a marked difference between the two simulations. The lower wind speed determined by CIM leads to a much lower calculated number of comfortable hours, as visible in Figure 4.29. During the 21<sup>st</sup> of June a pedestrian is therefore expected to experience a “hot” thermal sensation just from 13:00 to 15:00 hours. By contrast, calculated with the CIM model, a pedestrian would feel a “hot” thermal sensation from 10:00 to 16:00 hours. This is related to the wind speed that during the 21<sup>st</sup> of June passes from 1 ms<sup>-1</sup> in average during the daytime, to 0.01 ms<sup>-1</sup> on average for the same period of the day. By analysing in detail the impact of wind speed on thermal comfort, it is evident that a wind speed reduction impacts the sensible heat loss by convection: during the 21<sup>st</sup> of June it changes from 49 W·m<sup>-2</sup> (weather data provided by Meteonorm) to 19 W·m<sup>-2</sup> (weather data provided by CIM). Finally, by comparing the two selected locations in the EPFL, a pedestrian located in the square near the Swiss Tech Convention Centre, will experience “warm” and “hot” thermal sensations during more hours, compared to the bocce court in calculations based on CIM. When looking at the annual values, the main conclusions concerning the human comfort, as obtained with CitySim or by coupling CitySim with CIM, remain the same. But, the coupling between CitySim and CIM is mostly useful when a detailed analysis is required. Effectively, when looking at the hourly values, the perceived thermal sensation is quite different between both models (e.g. in the bocce court, during the 21<sup>st</sup> of June)

#### 4.2.3 Comfort Map of the EPFL campus

This paragraph presents the analyses of the outdoor human comfort, by the use of Comfort Maps. The human comfort is quantified by the COMFA\* budget, as computer by the software CitySim Pro. The pedestrians are located in the outdoor environment, upon a regular grid, and they are placed each 10 meters of distance, for totally 2,867 pedestrians (Figure 4.30). Each pedestrian is performing a light metabolic activity. The results provided by the software CitySim Pro are then analyzed with the software ArcGIS, in order to visualize the results, by the creation of the colored maps. The simulations are performed dynamically, firstly to understand the impact of the built environment during a typical meteorological year, secondly in order to quantify the impact of the wind profile, created by the Canopy Interface Model (CIM), and thirdly the impact of climate change on the outdoor environment. The ground covering, obtained by Open Street Map, is subdivided into three main categories: streets, grass and concrete. Additionally, in the northern part of the campus, is present a small artificial pond. In order to perform the analyses, the site is subdivided into 7 zones, so called zone A,B,C,D,E,F and G (Figure 4.31).

Energy performance and outdoor comfort of a campus in a temperate climate

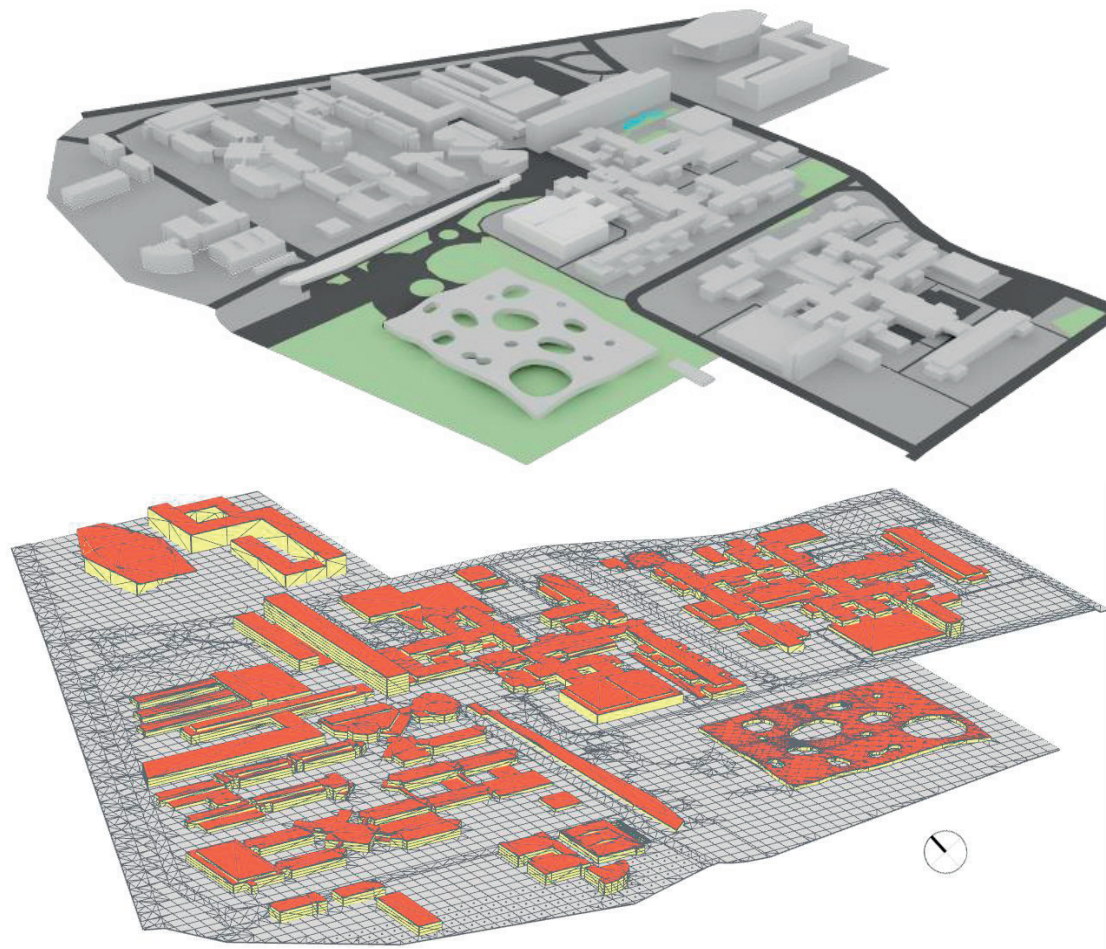


Figure 4.30 3D view of the EPFL campus (up) with the indication of the buildings and the outdoor environments: streets (dark grey), grass (green), concrete (light grey) and water (blue). 3D view of the campus, extracted from CitySim Pro (down).

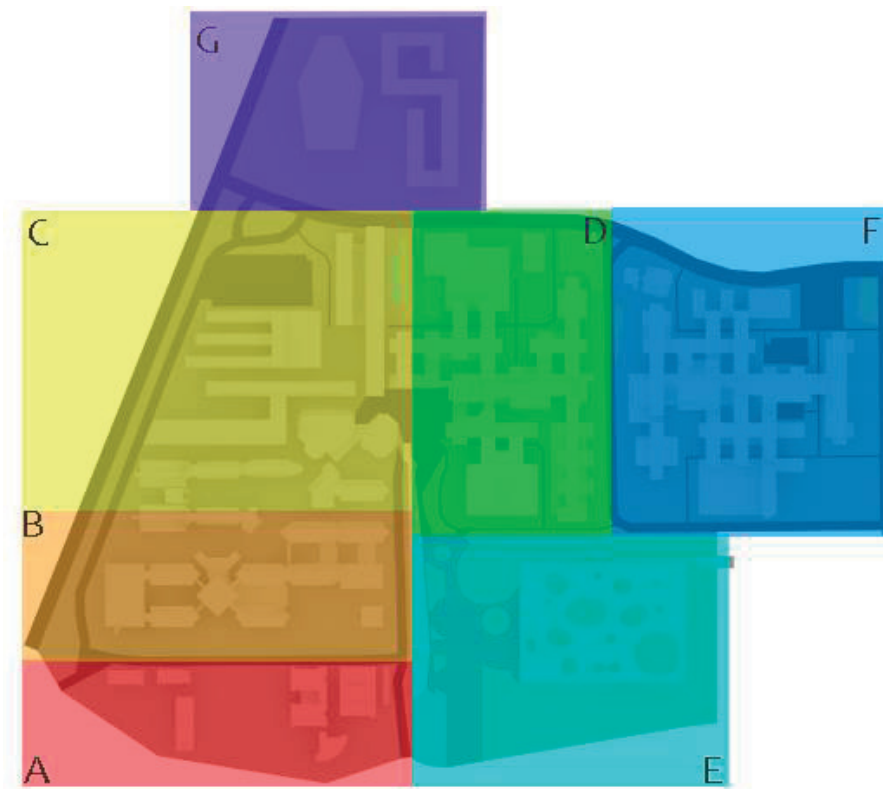


Figure 4.31 Plan of the EPFL campus, with the seven zones: A, B, C, D, E, F and G.

The urban environment, in this climate, has a variable impact on the outdoor human comfort: if the urban environment is too dense, the pedestrian's thermal sensation is consequently near the "cool/cold" one. As an example, the courtyards of buildings GC, GR, PH and CH create cold outdoor environment, due to the low Sky View Factor. Effectively, pedestrians located in these courtyards would feel an average annual thermal sensation between  $-238 \text{ W}\cdot\text{m}^{-2}$  to  $-173 \text{ W}\cdot\text{m}^{-2}$ , which correspond to a "cool/cold" thermal sensation. The difference is higher during the summer time, when the difference between the courtyards and the outdoor environment corresponds to  $260 \text{ W}\cdot\text{m}^{-2}$ . Generally, the average outdoor thermal sensation of the campus is "comfortable" during the year, as well as during the summer and spring seasons ( $-46 \text{ W}\cdot\text{m}^{-2}$ ,  $+20 \text{ W}\cdot\text{m}^{-2}$  and  $-14 \text{ W}\cdot\text{m}^{-2}$ , respectively). By contrast, during the winter and autumn season, it is "slightly cool" ( $-111 \text{ W}\cdot\text{m}^{-2}$  and  $-83 \text{ W}\cdot\text{m}^{-2}$ , respectively). Finally, the "comfortable" hours throughout the year correspond to 2,116, on average. By using the CIM climatic data, the average thermal sensation is reduced, as well as the "comfortable" hours, passing from 2,116 to 1,563 hours. Effectively, the averaged thermal sensation passes from "comfortable" to "slightly cool". If in the previous paragraph, the CIM wind and temperature profile was defined for both locations (the square in front of the Swiss Tech, and the bocce court), now the new profile is defined for the entire EPFL campus. The new annual averaged air temperature, provided by CIM, corresponds to  $9.9^\circ\text{C}$  ( $10.2^\circ\text{C}$  by Meteonorm), and the wind speed corresponds to  $0.4 \text{ ms}^{-1}$  ( $1.9 \text{ ms}^{-1}$  by Meteonorm). It is interesting that, knowing that the new weather profile provided by CIM is based on the surface temperatures of the built environment, during the summer time the air temperature is higher ( $18.2^\circ\text{C}$  with Meteonorm and  $19.2^\circ\text{C}$  with CIM), and it is lower during the winter time ( $2.4^\circ\text{C}$  with Meteonorm and  $0.6^\circ\text{C}$  with CIM, due to the shading effect). As previously underlined, during the summer and spring time, the thermal sensation is slightly higher, but during the winter the thermal sensation is reduced, passing from  $-111 \text{ Wm}^{-2}$  to  $-127 \text{ Wm}^{-2}$ , on average during the season. As underlined above, the results obtained by CIM are quite interesting for detailed analyses, using hourly values, more than the annual ones. Effectively, as an example during the 17<sup>th</sup> of July, at 14:00 the averaged thermal sensation varies by  $31 \text{ Wm}^{-2}$  between both models, with a maximal difference



of  $57 \text{ Wm}^{-2}$ . Effectively, a pedestrian located upon the asphalt and without any shadings, would perceive a “hot” thermal sensation by the CIM model, and just “warm” one with the Meteonorm data.

The same analyses are performed for the future climatic scenarios 2050 and 2100, without considering the CIM local wind profile. In 2050, the average comfortable hours decrease, passing from 2,116 to 1,860; this is due to the increase of “warm/hot” events during the warmer seasons. It is interesting to notice how the built environment impacts the human’s comfort: in zone G, characterized by a “man-made” outdoor environment, the comfortable hours during the warm seasons will decrease by 7% (2050) and by 15% (2100) compared to the typical meteorological year (Figures 4.32 and 4.33).

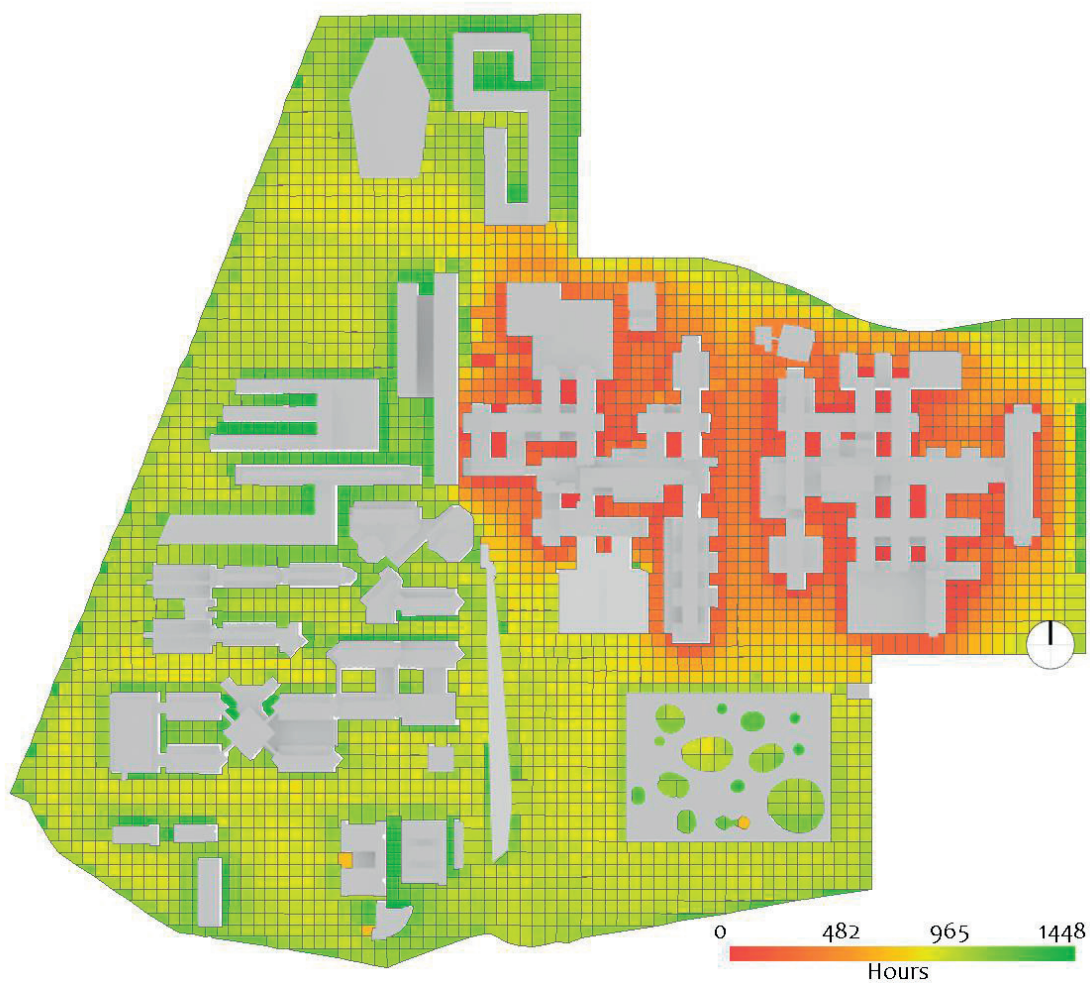


Figure 4.32 Typical Meteorological Year, comfort Map of the EPFL campus. Total comfort hours during the summer.

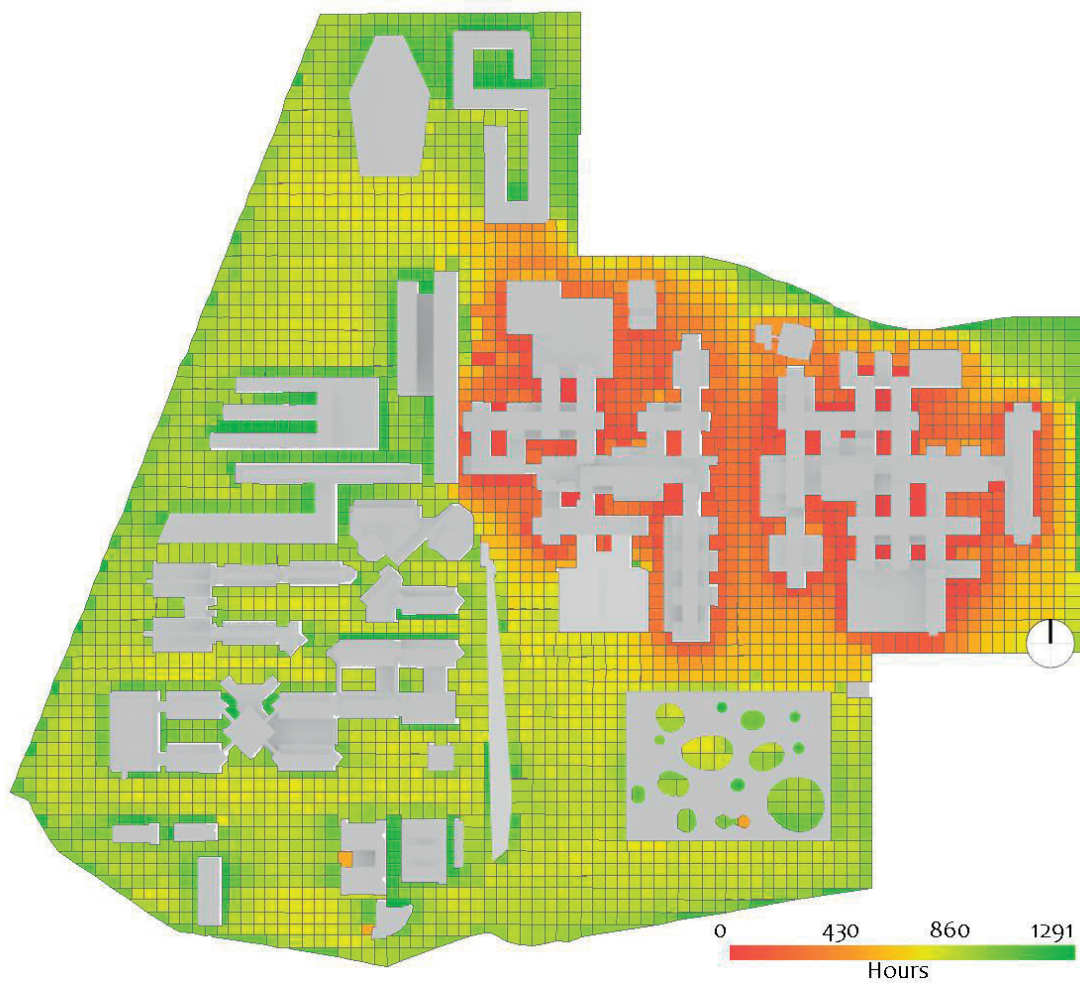


Figure 4.33 2100, comfort Map of the EPFL campus. Total comfort hours during the summer.

Figure 4.34 shows the variation of comfortable hours, from the TMY to 2050. It is interesting to notice that thanks to the dense urban environment, some area would increase the “comfortable” hours, up to 2,050 hours, yearly. On the contrary other zone, less protected by the built environment, would face a reduction of the “comfortable” hours, up to 525 hours. It is evident that during the summer the dense environment will be more comfortable, due to the shading. By contrast, during the winter time the northern areas will face an increase of the comfortable sensation, as presented in Figure 4.35: this is clearly due to the increase of the air temperature, which positively impacts the thermal sensation. The same trend is evident in 2100, with an important decrease of the comfortable hours during the summer season.

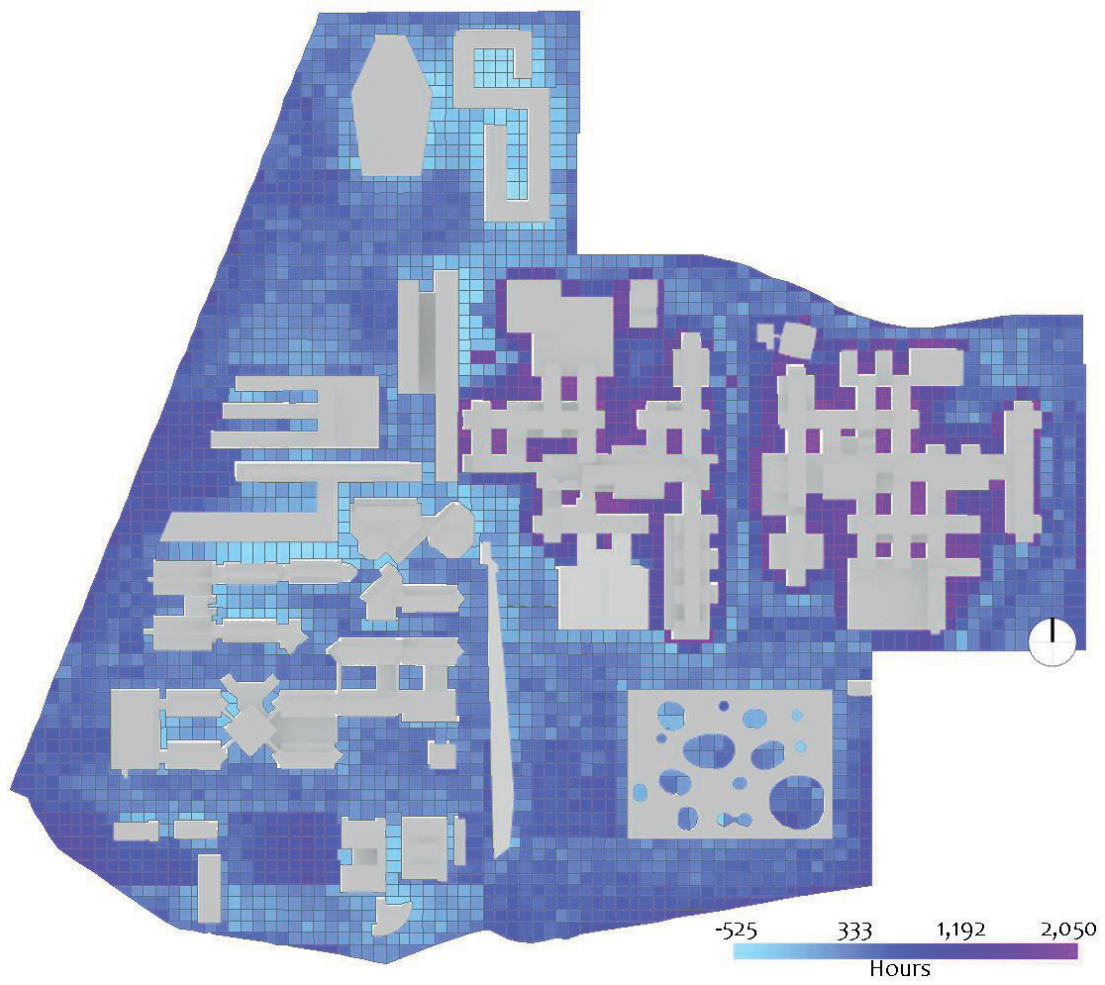


Figure 4.34 Comfort Map of the EPFL campus. Difference between the comfortable hours for the TMY and 2050 during the year.



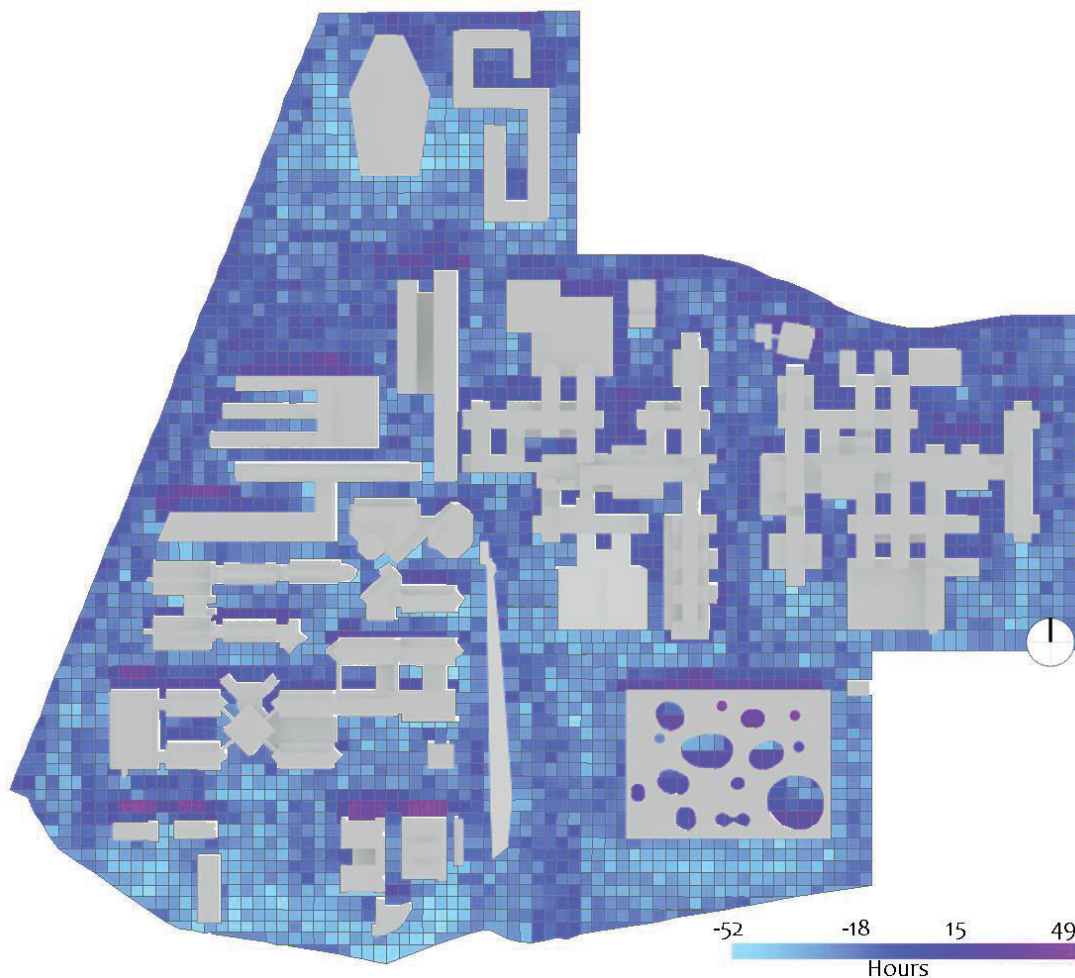


Figure 4.35 Comfort Map of the EPFL campus. Difference between the comfortable hours for the TMY and 2050 during the winter time.

### 4.3 Conclusions and future outlook

The objective of this chapter was to analyse the EPFL campus in Lausanne from an energy and comfort point of view. Current and future climatic scenarios were investigated, with the aim of analysing the sensitivity of the campus to climate change. First of all, an energy model of the campus was set up and validated with on-site monitoring, kindly provided by the EPFL real estate and infrastructure department of the campus. The sound correlation between the monitoring and the simulations ( $R^2=0.89$  for the energy and  $R^2=0.93$  for the photovoltaic panels) confirms the validity of the model. The analysis of the EPFL campus in future climatic scenarios shows the need of buildings refurbishment, taking into account the projected impact of climate change, in order to decrease their energy demand; buildings from the first stage of construction are the ones that are most concerned. The second outcome from the analysis is the variation of the heating and cooling loads of the campus, which in the future will face an important increase in the cooling demand. This variation in thermal behaviour will impact the energy demand, but also the outdoor human comfort. Effectively, if now a user located in the LESO solar experimental building would feel “slightly warm” during the summer time, in the 2050-A2 scenario he/she will experience “slightly warm” and “warm thermal” sensations from June to August. Naturally these values are based on the monthly average temperature, so extreme hot events will probably appear.

The outdoor human comfort of pedestrians located in the campus will drastically be impacted by climate change; “comfortable” thermal sensations will generally increase during the coldest months and decrease during the

summer time. “Man-made” environments will be more affected by climate change compared to natural ones: in winter and autumn the hours of comfort in the bocce court will averagely increase by 9% and 12% respectively, by contrast, in the open square they will increase by less than 2%. In the open square, the hours of discomfort will drastically increase by 73% in summer, and just by 55% in the bocce court. In order to improve the quality of the outdoor environment, shadowing strategies and a correct greening design are required. These analyses are based on the results obtained by the software CitySim Pro, which neglects the variation of wind speed and direction in the built environment. In order to overcome this problem, the analysis of outdoor human comfort and the energy demand of buildings were refined by coupling CitySim Pro with the Canopy Interface Model (CIM). When comparing the energy demand of the campus, as simulated with the CIM model, with onsite monitoring of the EPFL campus (2015), the difference between the model and the reality corresponds to 8%. Consequently, thanks to the CIM model, the EPFL energy model, simulated with CitySim, is getting closer to reality. Concerning the outdoor human comfort, on site monitoring and questionnaires were outside the scope of this thesis, consequently we were not able to validate the proposed models (CitySim and CitySim coupled with CIM) to the pedestrians thermal perception. But, based on the obtained results, it is clear that the main conclusions between CitySim and CIM are similar when looking to the annual values, but CIM model provides further information when looking at the hourly time steps.

#### *Future outlook*

Based on the results obtained in the thesis, further investigations could be performed. The energy analyses performed for future climatic scenarios are based on the weather data provided by Météonorm, and retrieved by the IPCC. The simulations realized, as an example for 2050, are based on the predicted climatic conditions for the year 2050. In order to quantify the variation of the buildings’ thermal behaviour in the future, additional analyses are on-going, based on dynamic future climatic scenarios created by Prof. Vahid Nik, from Chalmers University of Technology, Sweden. The idea is to visualize the thermal behaviour of buildings not just for the year 2050, but from today to 2050, looking at the dynamic variation of the hourly/annual thermal behaviour of buildings.

The Comfort Maps are currently designed by exporting the text data, provided by CitySim Pro to ArcGIS, in order to visualize the results as maps. Additional work is required in order to visualize the results directly from CitySim Pro, simplifying the process, and reducing the data handling time.

The EPFL campus is growing, and additional treated floor area is required on site: currently the campus has a total surface of 380,397 m<sup>2</sup> (Van Slooter et al., 2014) and based on the projections, the maximal surface that can be built corresponds to 510,000 m<sup>2</sup> (DII, 2004). The main question is how the campus will look like in future, will it be better to densify the campus by adding new buildings on the existing green areas, or is it better to increase the height of buildings, or to extend the boundary of the campus? Further investigations are required, based on the analyses of the outdoor human comfort, the energy demand of buildings as well as the entropy of the site.



# Chapter 5 Energy performance and outdoor comfort of a campus in a hot and arid climate

*The work related to this chapter was presented at the 5<sup>th</sup> International Conference on Drylands, Deserts and Desertification in the Sede Boqer Campus (Israel) in November 2014 (Coccolo et al., 2014) and at the Passive Low Energy Architecture (PLEA) conference in Los Angeles (USA) in June 2016 (Coccolo et al., 2016c) (Monna et al., 2016) (Mauree et al., 2016b). Finally, part of the work is submitted to the 21<sup>st</sup> International Congress of Biometeorology (ICB 2017) (Coccolo et al., 2017b).*

## 5.1 Introduction

As presented in the above chapters, the outdoor human comfort and the energy performance of buildings are essential for a sustainable development of a city, from the building to the district scale. This chapter presents an analysis performed for the Swiss International School of Dubai that aimed to support the design of an efficient campus in a hot and arid climate, ensuring a comfortable indoor and outdoor environment for students. Energy efficiency is a key issue in United Arab Emirates: according to the International Energy Agency (IEA, 2016) the country is at 5<sup>th</sup> position in the world for CO<sub>2</sub> emissions pro capita (19.3 tCO<sub>2</sub>), following Qatar (35.73 tCO<sub>2</sub>), Kuwait (22.94 tCO<sub>2</sub>) and Bahrein (21.80 tCO<sub>2</sub>). By contrast, countries such as Switzerland, Italy and United Kingdom emit 4.61 tCO<sub>2</sub>, 5.26 tCO<sub>2</sub> and 6.31 tCO<sub>2</sub> per capita respectively. In terms of energy use pro capita (source IEA 2016), a person in UAE consumes 11.24 MWh per year, more than double than the average Italian (5 MWh per year) and considerably more than an average Swiss person (7.52 MWh per year). Additionally, as UAE is a major oil producer (in 2014 it produced 156.08 Mtoe of oil, of which 127.8 Mtoe were exported), the use of renewable sources has so far been limited in the country. Another problem of the country is the water scarcity and the water consumption per capita: an average inhabitant of UAE consumes 889 m<sup>3</sup> per year, just 16.39 m<sup>3</sup> of which come from renewable water sources (UN, 2014). Over 70 percent of water used in the country comes from groundwater, 24 percent from desalination (0.163·10<sup>9</sup> m<sup>3</sup> in 1990 and 0.95·10<sup>9</sup> m<sup>3</sup> in 2005) and just 6 percent is reused wastewater. The oversaturation of groundwater is a serious problem, because of the difficulty of natural recharge of the aquifer; freshwater withdrawal as a percentage of the total renewable water resources corresponds to 1,867 % (Source FAO Aquastat). Additionally, in UAE a person uses 550 liters per day for drinking, cooking, washing and cleaning (Todorova, 2014); more than the double in respect to a Swiss person (170 liters per day) (“Water exploitation, water use, water consumption,” 2017). Additionally, 83 percent of the water in UAE is used for irrigation in agriculture, forestry and amenities (FAO, 2016). With the objective of analyzing the energy performance of buildings and improving outdoor human comfort, several studies have been conducted in the country (Friess et al., 2012) (Rakhshan et al., 2013) (Taleb and Abu-Hijleh, 2013) (Taleb and Taleb, 2014) (Taleb and Musleh, 2015), but none of them analyses the correlation between energy performance and outdoor human comfort. The objective of the work presented in this chapter was to analyze the energy demand as well as the outdoor human comfort in a school campus in Dubai, and to develop a Minergie standard for tropical climates. The Swiss International School of Dubai (SISD) is located in the city of Dubai (25°16’N, 55°20’E, 0 m asl, Cumulative Solar Irradiance: 1,997 kWh·m<sup>-2</sup>, Cooling Degree Days: 6,196) in Healthcare City Phase 2, in front of the Dubai creek (Figure 5.1a and 5.1b), a protected wildlife sanctuary. The school campus comprises seven buildings that host the following scholar functions: kindergarten, auditorium, primary and secondary school, sport center and boarding. The whole campus

covers an area of 55,000 m<sup>2</sup> and will host circa 2,000 students and 300 staff members. The first stage of the campus (kindergarten and primary school) was inaugurated in September 2015; the other campus buildings are still under construction. The energy analyses were performed during the conceptual design of the campus, thanks to a collaboration with the architectural office AchiLab, as well as Kriesi Energie GmbH, founder of the Swiss Minergie standard, and the consulting engineering company Sorane SA. The Minergie standard for tropical climates was previously conceptualized (Kriesi et al., 2011) (Papadopoulou, 2011) (Coccolo et al., 2013) and the SISD campus represents the first Minergie certified building in UAE. This chapter presents the numerical analysis performed during this thesis, from the energy demand of the campus to the assessment and monitoring of the outdoor human comfort.

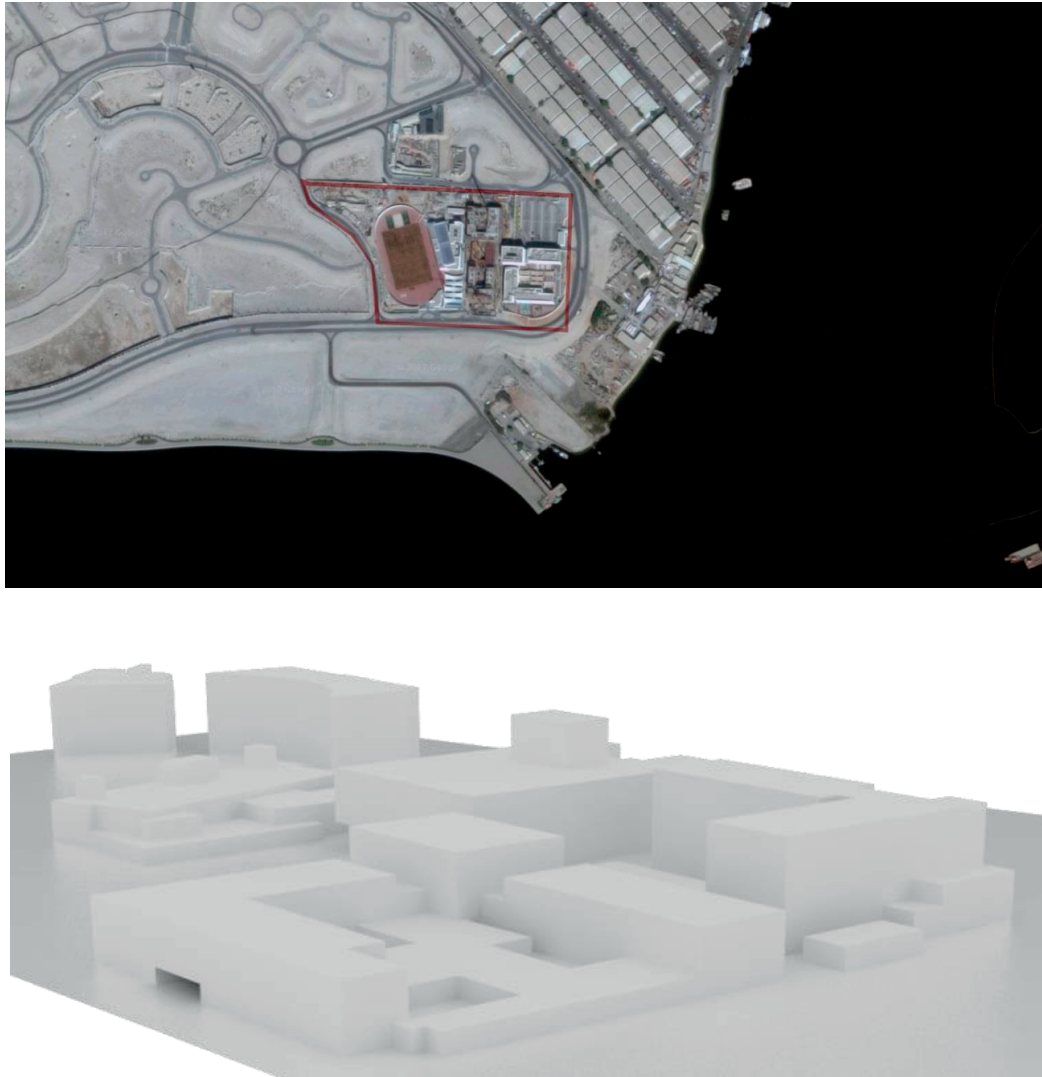


Figure 5.1a Localization of the Swiss International School Campus in Dubai extracted from Google Maps in March 2017 (top). 3D view of the campus (bottom).





Figure 5.1b Historical development of the site, as extracted from Google Earth.

## 5.2 Energy model of the SISD campus

This sub-chapter presents the energy analysis performed during the concept phase of the campus, in order to evaluate the design projects provided by the architecture studio ArchiLab as well as the energy concepts of Kriesi Energie GmbH. Parts of the outputs provided by these analyses were used for the conceptual design of the campus.

### 5.2.1 Climatic analysis of the site

In accordance to the Koeppen-Geiger climate classification (Peel et al., 2007), the city of Dubai is characterized by a BWh climate (B: arid; W:desert; h:hot) corresponding to a hot desert climate. The weather data used for the analyses were created with the software Meteonorm (Remund et al., 2015), using the average irradiance data of the period 1991-2010 and the average temperature of the period 2000-2009. Figure 5.2 shows the monthly temperature profile: the average temperature during the summer months is higher than 30°C and the maximum temperature reaches 45°C during the month of July; the minimum temperature is equal to 13°C during the month

of January and the average temperature in the winter time is comfortable (22°C in December, 20°C in January and 21°C in February). The daily profile of the temperature is shown in Figure 5.2 for three winter and three summer days (23<sup>rd</sup> – 26<sup>th</sup> December and 21<sup>st</sup> to 23<sup>rd</sup> June respectively): the air temperature, during the summer time, varies on average by 10°C between daytime and nighttime; during the winter time this variation is smaller, on average less than 8°C.

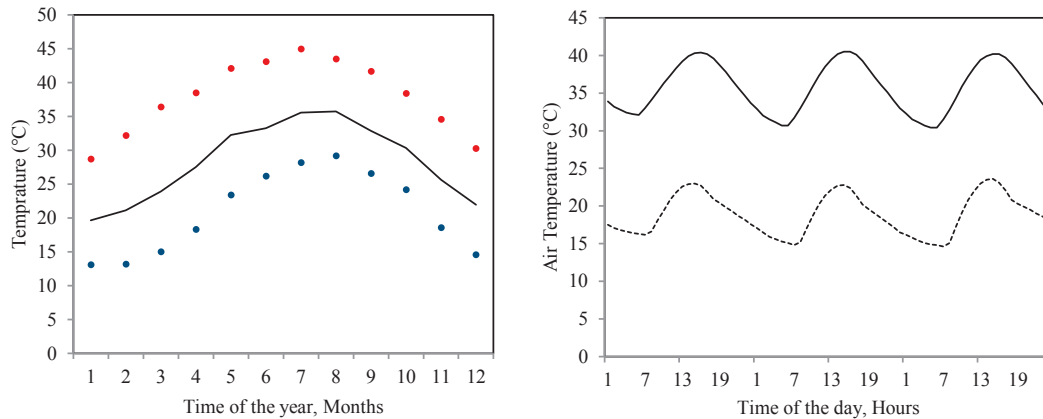


Figure 5.2 Left. Average (black line), maximum (red dots) and minimum temperature (blue dots) in the city of Dubai. Right. Hourly temperature for three summer (continues line) and three winter days (dotted line).

The relative humidity is stable all over the year; it is higher during nighttime reaching up to 90 % and lower during daytime with values comprised between 30% and 50%. Detailed analyses during the solstices and equinoxes (Figure 5.3) show that the relative humidity is acceptable (comprised between 35 and 56%) during daytime (21<sup>st</sup> of March and 21<sup>st</sup> of June); by contrast it is high (between 80 and 100%) and no differences are perceived between day and night, during the 23<sup>rd</sup> September and 21<sup>st</sup> December. The length of the day slightly varies during the year, lasting 12 hours during spring and summer time, and around 11 hours during autumn and winter. Figure 5.3 shows the daylight provision as a function of the year: during the 21<sup>st</sup> of June the sun rises at 5:28 hours and sets at 19.11 hours; by contrast during the 21<sup>st</sup> of December it rises at 6.59 hours and sets at 17.33 hours.



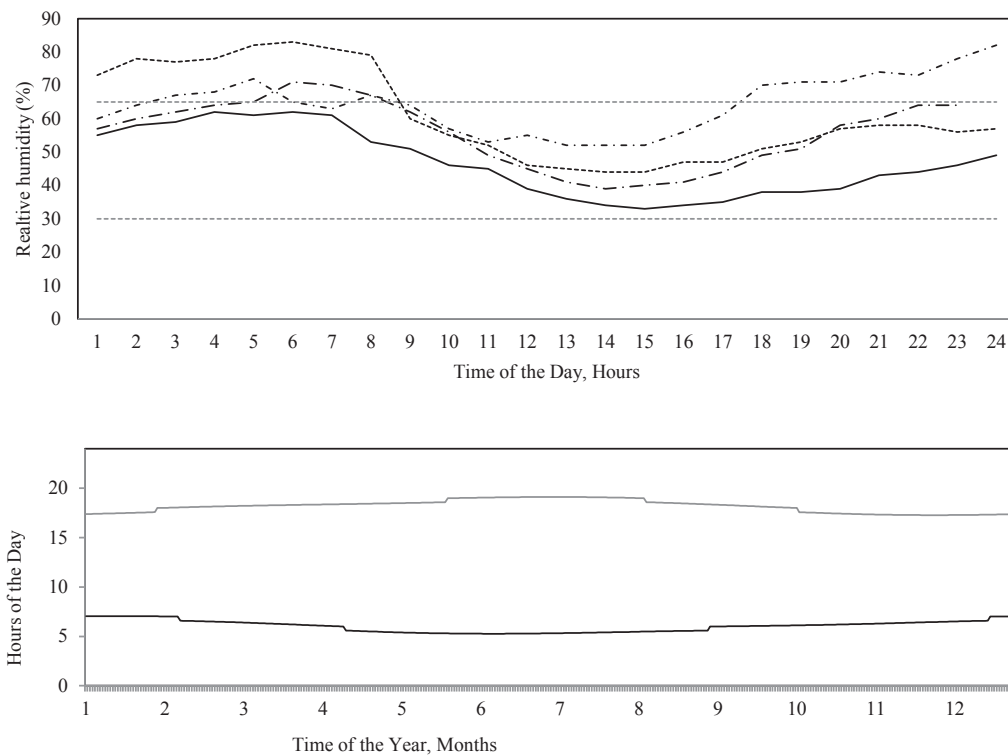


Figure 5.3 Top: relative humidity during the solstices and equinoxes, as a function of the hours of the day. Legend: 21<sup>st</sup> March (dotted line), 21<sup>st</sup> June (continuous line), 23<sup>rd</sup> September (long dash dot line) and 21<sup>st</sup> of December (dash dot line). Bottom: sunrise and sunset, for each day of the year.

The sea breeze blows daily from the North-West; by carefully analyzing the wind speed during August we can see that sand storms occur during this month when the wind speed reaches  $12 \text{ m}\cdot\text{s}^{-1}$ , corresponding to a *Strong breeze* in the Beaufort scale. Finally, the average annual precipitations are equal to 54 mm, and are concentrated during the winter months when rare but intense storm phenomena occur. Based on the sun path and the latitude of the site, the solar irradiance received by a vertical facade is maximal on the East face during the summer months; by contrast, it is maximal on the Southern side during the winter months.

### 5.2.2 Energy optimisation workflow

The Swiss International School of Dubai is the first example of a Minergie building in the United Arab Emirates; the first building of the school, inaugurated in September 2015, received the Minergie certificate n.1 for this country. The efforts to develop a Minergie standard for this climate was started some years ago (Kriesi et al., 2011) (Papadopoulou, 2011) (Coccolo et al., 2012), when an existing house and an office building located in Ras Al Khaimah were analyzed, showing the impact of refurbishment according to the Minergie standard on the cooling demand of the building. Based on this analysis, the physical characteristics of a Minergie building in tropical climates were defined, as summarized in Table 5.1. The required U-value of roofs and walls corresponds to  $0.2 \text{ (W}\cdot\text{m}^{-2}\text{K}^{-1}\text{)}$ ; the U-value of windows has to be lower than  $1 \text{ (W}\cdot\text{m}^{-2}\text{K}^{-1}\text{)}$  and their g-value around 0.5. The building envelope has to be airtight as possible, and the EER of the cooling machine has to be as large as possible.

Parameters	Required value	Units
U-value roof	0.2	( $W \cdot m^{-2} K^{-1}$ )
U-value walls	0.2	( $W \cdot m^{-2} K^{-1}$ )
U-value windows	1.0	( $W \cdot m^{-2} K^{-1}$ )
g-value (SGHC) windows	0.5	(-)
Shading factor	0.8	(-)
Air infiltration through cracks, open windows	0.1	(per hour)
EER for cooling machine	4	(-)

Table 5.1 Minergie Standard for Tropical climates, physical characteristics of the envelope and the energy conversion system (Kriesi et al., 2011).

The design project of the SISD school campus started in 2012, when the first numerical simulations were performed with the software CitySim Pro to provide feedback on the project to the architect Gabriele Rossi, founder of ArchiLab, Pully. Figure 5.4 shows the first design of the campus: this preliminary project presents three cluster forms: i) an open courtyard (Buildings 1,2,3 and 4), ii) simple rectangular buildings (oriented North-South and East-West) and iii) a square building (the auditorium). This first design represents the volumetric analysis of the site: it is the first attempt to quantify the dimensions of the project. Figure 5.4 shows the energy demand for cooling of each building; the largest cooling demand is the one of Building 11, and corresponds to  $36 \text{ kWh} \cdot \text{m}^{-3}$ , or  $144 \text{ kWh} \cdot \text{m}^{-2}$ . This building hosts the auditorium and presents the smallest liveable surface area to volume ratio of buildings on the school campus. The lowest cooling demand is the one of Buildings 1, 2, 3 and 4, because of the mutual shadowing provided to each other. All analyses are performed assuming the same envelope characteristics for all buildings and the same energy conversion systems. The humidifying and de-humidifying systems are not taken into account in the simulations.

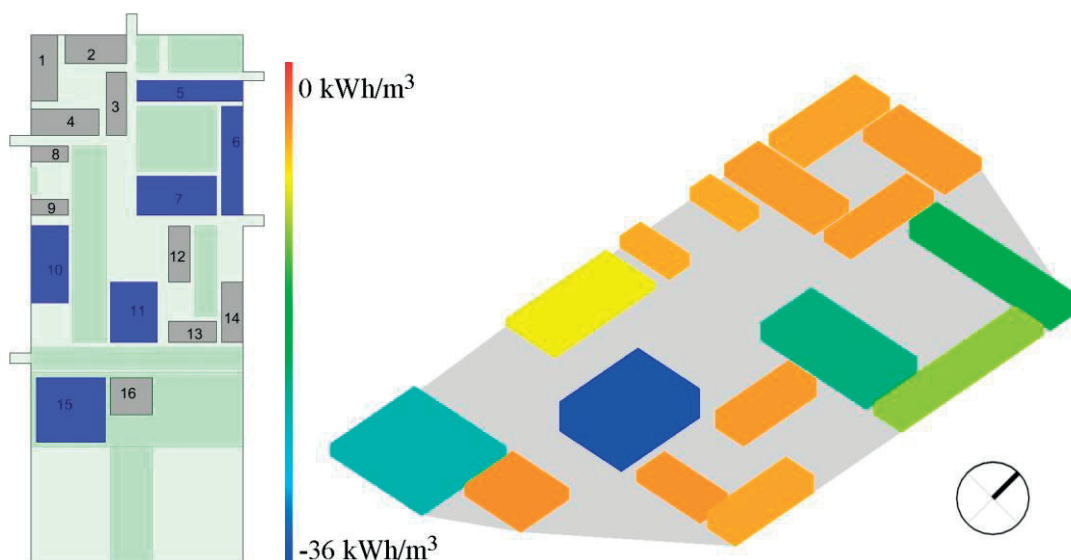


Figure 5.4 Swiss International School Campus in Dubai, first design by ArchiLab (left) and analysis of the cooling demand, performed with CitySim (right).

The second design of the campus was performed during the following months, as presented in Figure 5.5: the goal of the numerical analysis was to quantify the impact of the built environment on the energy demand of buildings, as well as to propose bioclimatic strategies to reduce it. The dimensions and form of the buildings are those provided by ArchiLab, without modifications; this study was not supposed to suggest any modification of the architectural design, but to provide bioclimatic strategies to improve the quality of buildings. Figure 5.5 shows the new plan of the campus; all buildings are characterized by a letter, describing their internal function as follows:

- Building A: auditorium and cafeteria.
- Buildings B, C and D: Middle school.
- Buildings E, F and G: Primary school.

- Building H: Kindergarden.
- Buildings I, J and K: Boarding.
- Buildings L and M: Sport Center.



Figure 5.5 Swiss International School Campus in Dubai, based on the design proposed by ArchiLab in 2013; plan (top) and 3D view of the site (bottom).

The solar irradiance impinging on the buildings was estimated as shown in Figure 5.6; the annual solar irradiance is maximal on the roofs ( $2,131 \text{ kWh}\cdot\text{m}^{-2}$ ) and lower on the North facades ( $540 \text{ kWh}\cdot\text{m}^{-2}$ ). During the summer solstice, the solar irradiance is higher on the East and West side of the buildings; due to the smaller distance between the buildings along the North-South axis, the buildings protect each other from solar irradiance by mutual shading. For buildings oriented along the East-West direction, the solar irradiance is reduced during the summer, but higher during the winter time: for this geometrical form, the simulations show that the solar gains in the classroom are reduced, but an adequate level of daylight is still ensured inside.

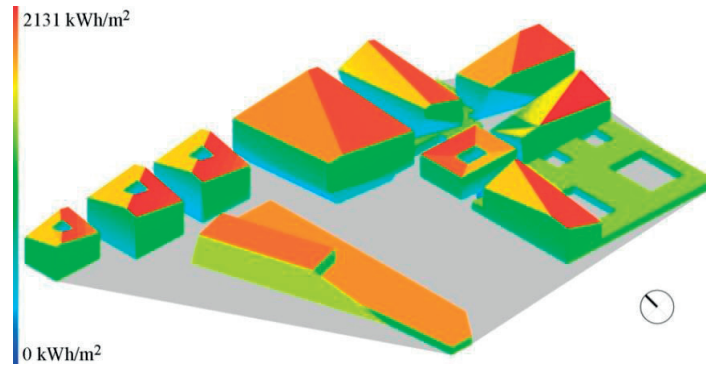


Figure 5.6 Annual solar irradiance in the Swiss International School Campus. Maximum value corresponding to 2,131 kWh·m<sup>-2</sup>.

A conventional compressor system is used as cooling converter; the system has a maximum power source of 372.1 W and an EER of 3.7; the cooling set point is 25°C. The window to wall ratio (WWR) is assumed equal to 25%. All physical characteristics of the envelope are retrieved from the Minergie Standard for tropical climates (Table 5.1). The annual cooling demand of the campus corresponds to 28.3 kWh·m<sup>-2</sup>; Buildings A, I and L have the highest cooling demand (around 35 kWh·m<sup>-2</sup>); by contrast, Buildings B and D have the lowest (around 20 kWh·m<sup>-2</sup>). The cooling demand of building A is related to its form and usage: the auditorium has the lowest liveable surface area to volume ratio, corresponding to 0.09, and the indoor spaces are not functionally used. Building L presents a higher liveable surface area to volume ratio (equal to 0.22) but a sloped facade exposed to the West, without any sun shadings.

In order to compare the Minergie standard with the existing practice in the country, the energy demand of the campus was analysed following the Green Building Regulation (Government of Dubai, n.d.), as well as a typical envelope (Kriesi et al., 2011). The thermal characteristics of the envelope are summarized in Table 5.2, for the construction details, please refers to Annex B. Among the proposed options, Minergie presents the most energy efficient envelope: the U-value of walls and roof in Dubai’s Green Building Regulation correspond to 0.51 and 0.30 Wm<sup>-2</sup>K<sup>-1</sup> respectively; by contrast, the same elements in a typical existing building correspond to 1.00 Wm<sup>-2</sup>K<sup>-1</sup>.

Dates	U-value wall (Wm <sup>-2</sup> K <sup>-1</sup> )	U-value roof (Wm <sup>-2</sup> K <sup>-1</sup> )	U-value windows (Wm <sup>-2</sup> K <sup>-1</sup> )
Green Building Regulations & Specifications (Government of Dubai, n.d.)	0.51	0.30	1.90
Minergie	0.20	0.20	1.00
Existing building UAE (Kriesi et al., 2011)	1.00	1.00	1.50

Table 5.2 U-value of walls, roof and windows (Wm<sup>-2</sup>K<sup>-1</sup>) in accordance to the Dubai Green Buildings Regulations & Specifications, Minergie for Tropical climates and an existing building in UAE.

The thermal analyses were performed for a typical meteorological year, and the results are summarized in Figure 5.7: the lowest energy demand is ensured by the Minergie standard (annual cooling demand equals 28.3 kWh·m<sup>-2</sup>), followed by the Green Buildings (41.8 kWh·m<sup>-2</sup>) and by the typical construction in UAE (128.6 kWh·m<sup>-2</sup>). Following the Minergie Standard, the cooling demand is reduced by 32% compared to the “best practice” in Dubai, and by 78% compared to an existing building. Naturally, based on the geometry and the surrounding built environment, each building reacts differently; as an example Building A (hosting the auditorium) decreases its demand by 85%, by passing from a normal envelope to a Minergie envelope. The presented values represent the energy demand required to maintain the comfortable indoor conditions of the campus, without considering the mechanical ventilation system, the energy required to condition the air with humidity and the energy system. Just for

comparison, the electrical energy required for a typical building in UAE corresponds to  $250 \text{ kWh}\cdot\text{m}^{-2}$  and the one of a well-insulated building to  $100\text{-}110 \text{ kWh}\cdot\text{m}^{-2}$ . All the values are expressed annually.

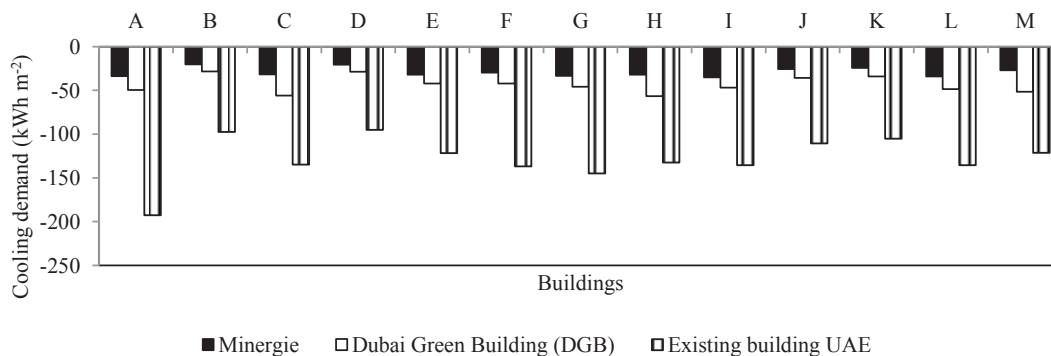


Figure 5.7 Annual cooling demand of the campus, expressed in  $\text{kWh}\cdot\text{m}^{-2}$ , as a function of the building. Comparison between Minergie standard, Dubai Green Building Standard and a typical building in UAE.

Based on this simple analysis it is obvious that considerable energy savings are obtained through the application of the Minergie Standard. This is confirmed when analysing the energy savings in terms of  $\text{CO}_2$  emissions. Assuming that in the United Arab Emirates  $597.81$  grams of  $\text{CO}_2$  are required to produce  $1 \text{ kWh}$  of electricity and cooling (IEA, 2012), just by applying the Minergie standard,  $3,297$  tons of equivalent  $\text{CO}_2$  emissions are avoided, if compared to existing buildings, and  $444$  tons of equivalent  $\text{CO}_2$  if compared to the green buildings standard.

### 5.2.3 Sensitivity analysis

In order to provide recommendations for architects, an optimization of the project was performed, outlining the impact of the following elements on the cooling demand of the site:

- Urban form
- Windows orientation
- Ground covering and sloping facade
- Albedo of the facade
- Roof design
- Building Integrated Photovoltaic Panels (BiPV).

#### Urban form

The urban form is a significant factor in the reduction of the cooling demand of buildings; if chosen correctly, it can improve the sustainability of a city district. In this case, Building H (building's surface area to volume ratio corresponding to  $0.26$ ), hosting the kindergarten, was analysed in its urban context (attached to the neighbouring buildings E, F and G) and as an isolated building. The cooling demand of Building H increases by  $15\%$ , if it is considered without an urban context. This is explained by the higher exposure of the envelope to the outdoor environment and by the absence of shadowing provided by the neighbouring buildings. The urban context reduces direct and indirect solar irradiance on the individual buildings due to mutual shadowing phenomena; this behaviour is evident for example during the month of June (Figure 5.8), when the building receives  $207 \text{ kWh}\cdot\text{m}^{-2}$  (without neighbouring buildings) whereas just  $158 \text{ kWh}\cdot\text{m}^{-2}$  is received (reduction by  $15\%$ ) if positioned in the urban environment.

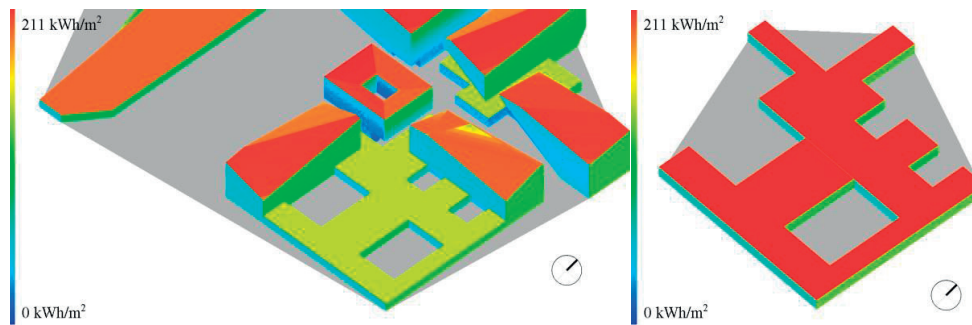


Figure 5.8 Monthly solar irradiance (during the month of June) received by building H if positioned in the campus (left) or without neighboring buildings (right).

#### Window orientation

The optimization shows the impact of the windows and their orientation as a function of the facades on the cooling demand of the campus. Based on previous research (Givoni, 1998a) (Givoni, 1989) the windows are reduced on the East and West facades (10%) and maximized on the South and North facades as well as on shadowed facades, such as for example in internal courtyards (up to 50%). By improving the glazing ratio, the cooling demand of the site is reduced by 11%, with a new average demand of 25 kWh·m<sup>-2</sup>; the maximum reduction, of 28%, is achieved in Building G, because of its East-West orientation.

#### Ground covering and sloping facade

This analysis shows the impact of the ground covering, whose short wave reflectance (SWR) varies between 0.2 and 0.7, and of the tilt of the facade. Both parameters are designed to decrease the solar irradiance received by a building. Figure 5.9 shows a simple cube (10 m each side), modified by adding an inwards sloping facade of 45° for different orientations, and by changing the short wave reflectance of the ground. By adding a sloping facade on the East facing side and using a ground covering with a short wave reflectance equal to 0.2, the solar irradiance received by the building would be reduced by 33% compared to the reference case (no sloping facade). In the climate of Dubai, the highest solar irradiance is received by the East oriented facade: 1,214 kWh·m<sup>-2</sup> with an SWR of the ground covering equal to 0.2, and 1,492 kWh·m<sup>-2</sup> with an SWR of the ground covering equal to 0.7. The irradiance on this facade is higher during summer time compared to winter time, when the highest irradiance is concentrated on the South facade (133 kWh·m<sup>-2</sup> against 80 kWh·m<sup>-2</sup> on the East facade during the month of January) as shown in Figure 5.10. The lowest irradiance is absorbed by the North facade: 530 kWh·m<sup>-2</sup> with a SWR of the ground covering equal to 0.2, and 773 kWh·m<sup>-2</sup> with a SWR of the ground covering equal to 0.7. From these first results, it is clear that the ground covering has a strong impact on the cooling demand of buildings, because by varying the ground's short wave reflectance from 0.2 to 0.7, the solar irradiance reflected on the building is increased by 19% on average, with a maximum difference of 31% on the North face. In conclusion, to reduce the solar irradiance received by buildings located in the hot arid climate of Dubai, it is indicated to decrease the shortwave reflectance of the ground covering, and to provide inwards sloping facades towards the East.

Energy performance and outdoor comfort of a campus in a hot and arid climate

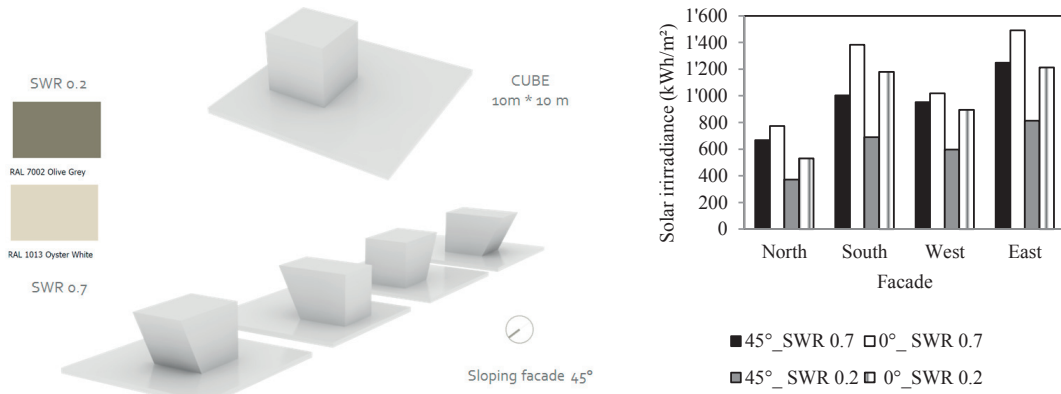


Figure 5.9 Left: prototype of a cube (10 meters each side), with a sloping facade in each of the cardinal directions; variation of the ground covering's short wave reflectance (0.2 to 0.7). Right: solar irradiance absorbed by each facade, as a function of the slope and the ground covering.

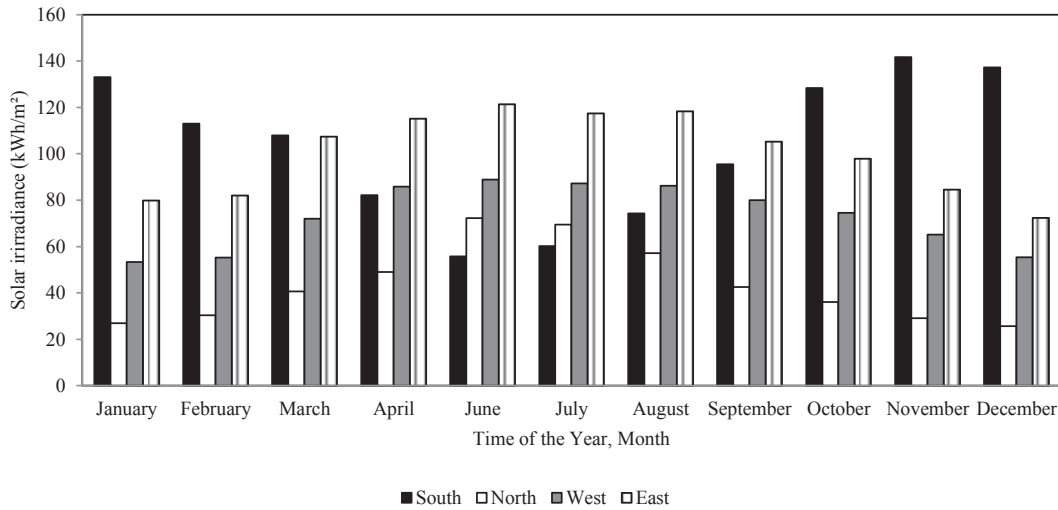


Figure 5.10 Cumulative solar irradiance received by each facade (kWh·m<sup>-2</sup>) as a function of the month. The ground covering has a shortwave reflectance corresponding to 0.2, and the sloping of each facade corresponds to 90°. Legend: South facade (Black); North facade (white); West facade (grey) and East facade (grey lines).

*Albedo of the facade*

The albedo of the facade impacts the solar irradiance absorbed and reflected by the buildings and consequently their cooling demand. An interesting example of bioclimatic facade design is the city of Shibam (Yemen), characterized by tower block buildings of five to eleven storeys, made with local mudbrick with different colors that range between white and brown (Figure 5.11). Due to its historical value, the city is protected as a UNESCO World Heritage site. In this analysis, the facades of the prototype buildings are subdivided into three floors, and colored with different nuances of albedo (0.71, 0.57 and 0.24). The objective of this analysis is to quantify the variation in cooling demand by varying the albedo of the surfaces and by interchanging the colors on the different floors using 9 different combinations. All the physical characteristics of the buildings are maintained, and their envelope is made of bricks, without insulation.





Figure 5.11 City of Shibam (Yemen); plan view extracted from Google Earth, and photo of the old city, source Wikipedia.

Figure 5.12 shows the cooling demand of the prototype as a function of the albedo of the facade: the lowest cooling demand ( $94 \text{ kWh}\cdot\text{m}^{-2}$ ) is obtained by a facade with an albedo of 0.71, because of its capacity to reflect the incident solar irradiance, and not to store the heat. Based on the same principle, the highest demand ( $132 \text{ kWh}\cdot\text{m}^{-2}$ ) is related to a facade with an albedo equal to 0.24; this facade absorbs the solar irradiance that is stored in the envelope, thanks to its thermal mass. The difference between the other colors is negligible. Between the most extreme test cases, the cooling demand varies by 28%: is it interesting to state that this variation is related just to the color of the external envelope, without a variation of its physical characteristics.

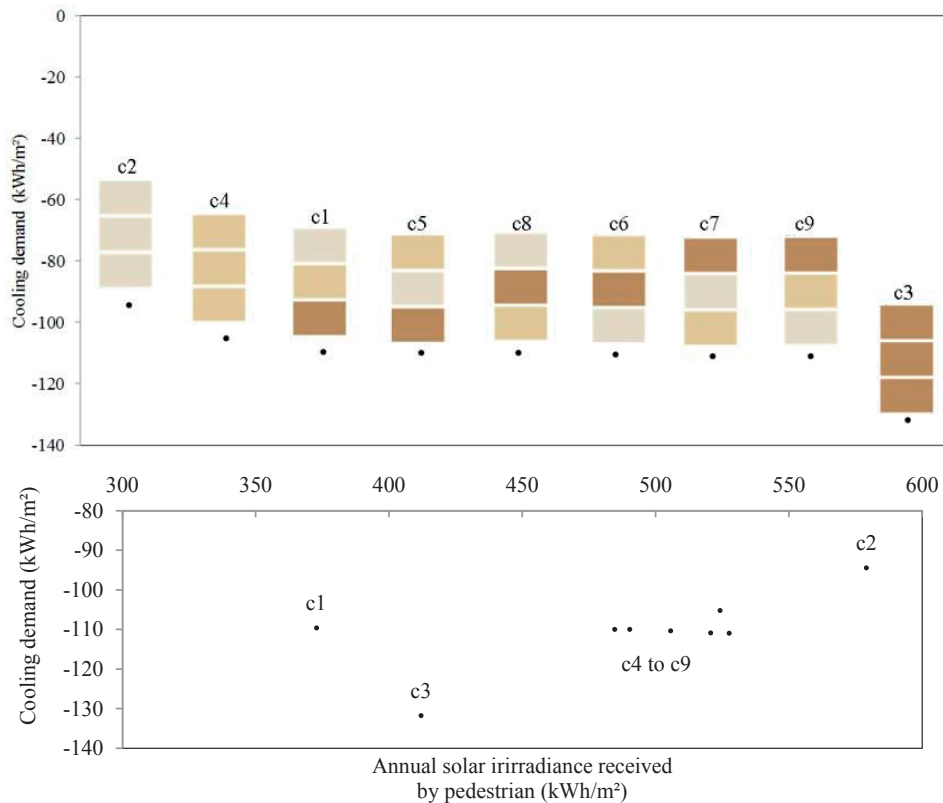


Figure 5.12 Cooling demand of the building, as a function of the shortwave reflectance of the facades (top) and cooling demand as a function of the solar irradiance received by pedestrians (bottom).

A further development of this analysis is to quantify the solar irradiance that is reflected upon a pedestrian located in the outdoor environment, in a North-South oriented street canyon whose height/width ratio equals 1.8; the

selected orientation and ratio correspond to the average of the SISD campus. The idea is to correlate the irradiance received by a pedestrian to his /her hypothetical cooling demand, assuming that the pedestrian has to maintain an internal temperature comprised between 35°C and 37°C. The physical and geometrical characteristics of the pedestrian are explained in Chapter 2. Figure 5.12 shows the annual solar irradiance received by the pedestrian as a function of the colors of the facades: the highest irradiance corresponds to 579 kWh·m<sup>-2</sup> in Case study C2 (albedo equal to 0.71), and the lowest to 373 kWh·m<sup>-2</sup> in Case study C1. Case study C1 is characterized by an albedo equal to 0.24, 0.57 and 0.71, from the ground floor to the upper floor. Finally, Case study C3 receives 412 kWh·m<sup>-2</sup>, with an albedo equal to 0.24. This behavior is related to the capacity of the building to store the heat during daytime and to re-emit it during nighttime, and consequently to decrease the solar irradiance received by the pedestrian. Consequently, the optimal shortwave reflectance of the facade, able to decrease the cooling demand but at the same time to reduce the solar irradiance received by the pedestrian is C1: the cooling demand equals 109 kWh·m<sup>-2</sup> and the irradiance on the pedestrian 373 kWh·m<sup>-2</sup>. This analysis shows that the irradiance is reflected by the facade on the upper floor (SWR equal to 0.57 and 0.71) and stored by the building at ground floor level, consequently protecting the pedestrian. The extreme cases are represented by C2 and C3, where the cooling demand corresponds to 94 kWh·m<sup>-2</sup> and 132 kWh·m<sup>-2</sup> respectively, and the solar irradiance corresponds to 579 kWh·m<sup>-2</sup> and 412 kWh·m<sup>-2</sup> respectively. All the other cases (C5, C6, C7, C8 and C9) present a similar cooling demand (between 110 to 105 kWh·m<sup>-2</sup>) and reflect the same range of solar irradiance (between 484 to 520 kWh·m<sup>-2</sup>). Based on this analysis, the optimal compromise between the cooling demand of buildings and outdoor human comfort, quantified by the solar irradiance received by a pedestrian is a combination of several shortwave reflectance, e.g. low near the ground floor and high on the upper floors.

#### *Roof design*

The object of this analysis is to quantify the impact of a sloping roof, as proposed by ArchiLab (Figure 5.6), compared to a flat roof, which represents the typical construction in the country. In this case, the use of flat roofs decreases the cooling demand of buildings by 8%, because it optimizes the external envelope by reducing it from 21,000 m<sup>2</sup> to 19,000 m<sup>2</sup>. Considering the architectural design, and the need to improve the energy demand of the site, a further development was proposed, i.e. to transform the concept of sloping roofs into external shadowing devices, covered by photovoltaic panels and positioned upon the flat roofs. The proposed design protects the buildings from solar irradiance (which decreases by 50%) and consequently the cooling demand is reduced by 15 %.

#### *Building Integrated Photovoltaic (BiPV)*

In the design made by ArchiLab, no photovoltaic panels were proposed; this study shows the solar potential of the site, assuming 50% of the tilted roof surfaces are covered with medium range solar panels. Figure 5.13 shows the electricity produced by the BiPV system on each building, expressed in kWh of energy per square meter of roof surface. Building C has the lowest production (corresponding to 720 kWh·m<sup>-2</sup>), because it is shadowed by the neighbouring buildings A, B and D. The largest production happens in building E and corresponds to 1,272 kWh·m<sup>-2</sup>, which is slightly higher than the average production of the campus, equal to 1,164 kWh·m<sup>-2</sup>. Based on the above simulation, a detailed analysis has been conducted to understand the best orientation for photovoltaic panels in the climate of Dubai. For the analysis, a simple building is created with an area of 100 m<sup>2</sup>; 50% of its roof surface is covered with photovoltaic panels oriented in the four cardinal directions (North, South, East and West), and presenting a tilt of 0°, 20°, 30° and 40° (Figure 5.13).

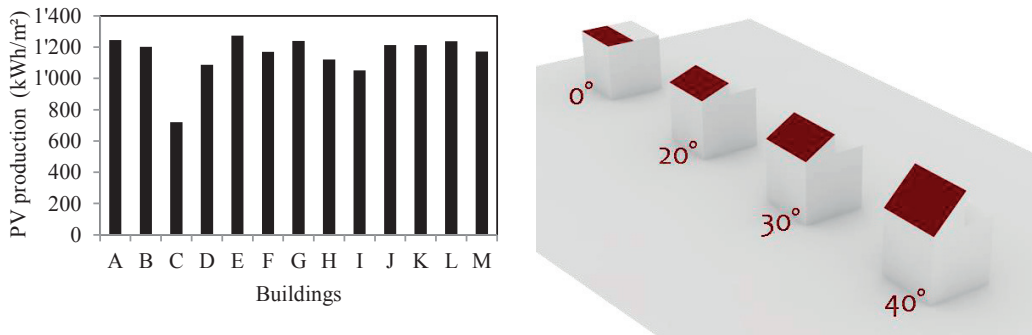


Figure 5.13 Left: annual PV production (kWh/m<sup>2</sup>) per roof surface as a function of the building. Right: several BiPV orientations, and tilt angles.

Figure 5.14 shows the cooling demand of buildings as well as the electrical production per orientation and tilted angle of the photovoltaic panels. The lowest cooling demand appears for flat roofs: as an example, with an East oriented roof, the cooling demand passes from 23 MWh to 28 MWh if the roof is sloped at 45°. This is related to the compactness of the building, also called form factor (please refers to Chapter 4): by increasing the tilt, the surface of the roof varies from 50 m<sup>2</sup> (0°) to 70.7 m<sup>2</sup> (45°) and the form factor increases further from 2 to 2.32. By contrast, the photovoltaic production is larger on a roof sloped between 0° and 20° and oriented East and West, and on a roof sloped between 20° to 30° and oriented South. This behaviour is related to the sun path in Dubai: the solar irradiance is larger during winter time on the South orientation (41° at noon on 21<sup>st</sup> December) and on the East and West orientation during summer time (88° at noon on 21<sup>st</sup> June). For further details, please refer to Figure 5.10 where the cumulative solar irradiance received per facade is described. The sun height is calculated for solstice and equinoxes by this formula:

$$h = 90^\circ - \varphi + \delta \quad (5.1)$$

where  $\varphi$  is the latitude of the site, in this case 25.27° and  $\delta$  is the geocentric declination, which is defined as follows:

$$\delta \cong 23.45 \cdot \sin\left(360^\circ \cdot \frac{(n - 81)}{365}\right) \quad (5.2)$$

where  $n$  is the number of the day of the year.

Based on the above formula, the sun height at noon during the solstices and equinoxes corresponds to 65° on 21<sup>st</sup> March, 88° on 21<sup>st</sup> June, 63° on 23<sup>rd</sup> September and 41° on 21<sup>st</sup> December. Figure 5.14 shows the cooling demand of buildings as a function of the BiPV production. It is evident that the maximum production for BiPV appears for panels tilted 20° South (1.33 MWh); by contrast, the lowest production is that of panels oriented 45° North (0.74 MWh). Looking at the cooling demand, the lowest demand is for flat roofs, due to the compactness of the building; by contrast, the highest demand is for panels oriented 45° North. Another interesting example is for photovoltaic panels oriented East; in this scenario the cooling demand corresponds to 28.5 MWh (increase by 16% compared to a roof tilted at 0°) and the PV production corresponds to 1.16 MWhm<sup>-2</sup> (decrease by 7.2% compared to a roof tilted at 0°). Based on the results, the optimal design for a tilted roof covered with BiPV is at a tilt of 20° to 30° and a South orientation. A tilt of 45° reduces the BiPV production and increases the cooling needs; by contrast a tilt of 20° and an East orientation has the same BiPV production as a flat roof, but a higher cooling load.

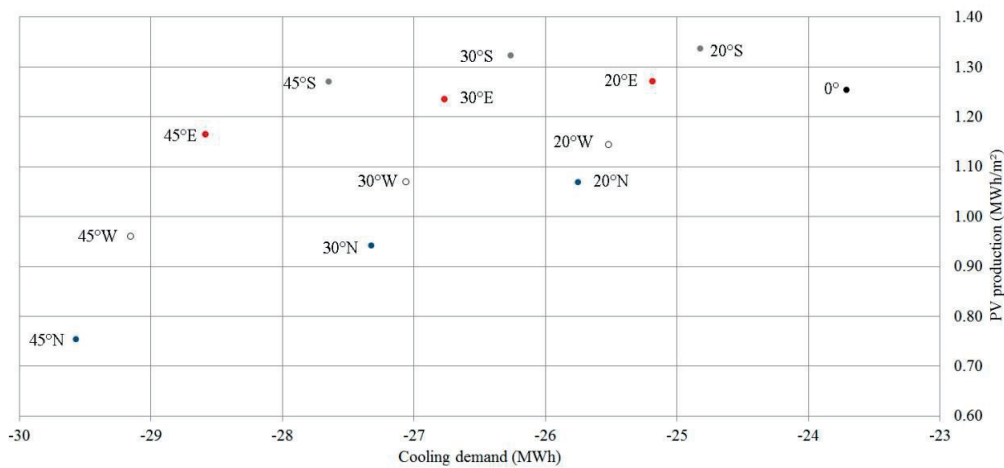


Figure 5.14 Annual PV production of the campus ( $\text{MWh}\cdot\text{m}^{-2}$ ) as a function of PV orientation (North, South, East and West) and tilt ( $0^\circ$ ,  $20^\circ$ ,  $30^\circ$  and  $45^\circ$ ).

### Final design and guidelines

Based on the above analyses (windows orientation, ground covering and facade slope, roof design and photovoltaic panels) a new design of the campus was proposed and a list of guidelines was provided to the architect, in order to improve the energy performance of the site. The first design provided by ArchiLab has an annual cooling demand of  $28.3 \text{ kWh}\cdot\text{m}^{-2}$ ; after the proposed optimisation the new cooling demand correspond to  $19 \text{ kWh}\cdot\text{m}^{-2}$ , showing a reduction by 33%. The proposed improvement of the campus is presented in Figure 5.15: the ground covering is made of concrete tiles, with a short wave reflectance of 0.3; the shortwave reflectance of the facades is designed considering an average albedo of 0.5 (corresponding to three superposed layers with SWR of 0.71, 0.57 and 0.24). The roofs present an SWR of 0.7, obtained by applying white reflective paints able to reflect the impinging solar irradiance, and consequently reducing their superficial temperature. The problem of this kind of covering is the aging factor, for this reason the maintenance is essential, in order to maintain the required performances. The windows are designed as described above: the total opening area is reduced on the East and West side (10%) but increased on the shadowed facades, such as for example in the courtyard (50%). Photovoltaic panels are positioned on the flat rooftops of buildings, and their design is based on the architectural plan provided by ArchiLab; their presence reduces the roof surface temperature to  $24.8^\circ\text{C}$  (compared to the above  $35.2^\circ\text{C}$ ), due to the shadowing protection. The total cooling demand of the campus corresponds to  $19 \text{ kWh}\cdot\text{m}^{-2}$ , showing a reduction of 33% of the total demand, without modifying the architectural design proposed by ArchiLab. Buildings such as G reduce their demand by 53%, thanks to the new glazing ratio that reduces the solar gains on the East and West facades, as well as the PV panels that shadow the roof. Other buildings, such as Building M have lower reductions in the cooling demand, just 10%: no PV covering is added, but the new white paint applied to the roof can reduce its annual average temperature from  $35.2^\circ\text{C}$  to  $27.9^\circ\text{C}$ . The annual average temperature of the campus, considering the envelope of the building, as well as the ground covering, decreases from  $28.8^\circ\text{C}$  to  $26.9^\circ\text{C}$ ; the new temperature will impact the outdoor human comfort, increasing the comfortable hours and decreasing extreme hot sensations.

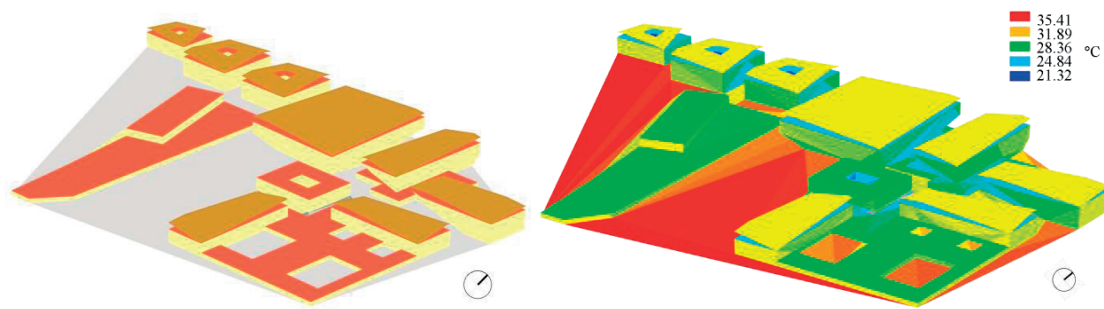


Figure 5.15 3D view of the SISD campus after the “ad hoc” optimization (left) and annual solar irradiance on the campus (right).

Based on the above results, a list of recommendations (Figure 5.16) is drawn up:

- Provide a compact urban form improving the mutual shadowing of buildings.
- Create internal courtyards, considered as comfortable semi-outdoor environments, shadowed by textile meshes, naturally ventilated and planted with local trees.
- Apply the Minergie standard for tropical climates, which can reduce the cooling demand of buildings by 32% compared to the “best practice” (Dubai Green Building) and by 78% compared to a standard building in the country.
- Prefer buildings oriented on the East-West to North-South axes: the sun irradiance impinging on an East facade during the summer time is 54% higher than that impinging on a South facade.
- Following the above point, it is important to increase the windows to wall ratios on the South and shadowed facades, e.g. in internal courtyards and on the lower floors of the buildings.
- Orient the PV panels Southward or Eastward, with a tilt of 20°.
- Sloping facades represent an expensive investment in the construction, but are suggested for the East oriented facade (without shadowing), because the slope reduces the solar radiation impinging on the facade. Naturally, a sloping facade needs to be placed above a ground covering with a low albedo, to avoid reflection of solar radiation.



## BIOCLIMATIC APPROACH

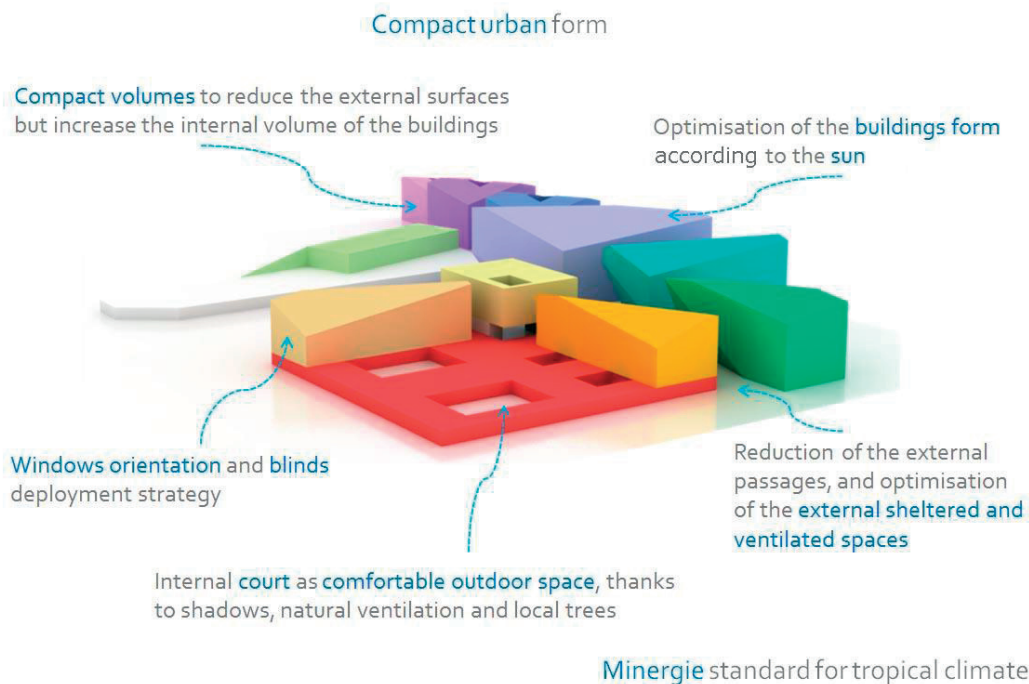


Figure 5.16 Bioclimatic guidelines of the SISD campus.

Based on the proposed strategies, a final design of the campus was made by DSA Architects International (12.03.2014), as shown in Figure 5.17: the new design improved the window opening on the courtyard, and reduced the windows exposed to the East and West; the colors of the facades varied as a function of their albedo and the roofs were designed as white tilted surfaces.



Figure 5.17 Swiss International School Campus, design provided by DSA Architects International on 12.03.2014

Some months after the last design, the construction site opened. Some additional modifications on the design were made and the Minergie Standard was improved on-site thanks to the collaboration of Kriesi Energie GmbH and the Swiss energy consulting firm Sorane SA. As an example, the physical characteristics of the walls were modified to use on site manufacturing techniques. The new walls are composed of an internal layer of EPS insulation, reinforced by a stainless steel grid where the concrete is sprayed, as shown in Figure 5.18. Finally no insulation is required for the ground floor.



Figure 5.18 Picture of the construction site, taken during a visit in November 2014. Wall construction (left) and view of the Dubai skyline from the first floor of the kindergarten (right).

Based on the last reports provided by Sorane SA and Kriesi Energie GmbH, the final building envelope has the following properties (Table 5.3): the U-value of the roof varies as a function of the shadowing provided by neighboring buildings from 0.15 to 0.20  $\text{W}\cdot\text{m}^{-2}\text{K}^{-1}$ ; the U-value of walls is increased from 0.2 to 0.3  $\text{W}\cdot\text{m}^{-2}\text{K}^{-1}$ , and the g-value (or the Solar Heat Gain Coefficient, SGHC) of windows is reduced to 0.5.

Parameters	Required value	Units
U-value roof	0.15 if exposed to the sun 0.20 if shadowed	$(\text{W}\cdot\text{m}^{-2}\text{K}^{-1})$
U-value walls	0.3	$(\text{W}\cdot\text{m}^{-2}\text{K}^{-1})$
U-value windows	1.0	$(\text{W}\cdot\text{m}^{-2}\text{K}^{-1})$
g-value, or SHGC, of windows	0.5	(-)
Shading factor	0.8	(-)

Table 5.3 Minergie Standard for Tropical climates, physical characteristics of the envelope (SORANE, 2013) (Kriesi, 2013).

## 5.3 Outdoor Human Comfort

This chapter analyzes the outdoor human comfort in the campus. It is subdivided into three main parts:

- Quantification of outdoor human comfort: study of the Index of Thermal Stress (ITS) in eight locations of the campus. The objective of this analysis is to quantify outdoor human comfort by varying the metabolic activity, as well as to propose bioclimatic strategies to improve the outdoor environment.
- Outdoor human comfort and urban greening: this analysis shows how the Index of Thermal Stress can be impacted by the use of native plants: Ghaf tree (*Prosopis cineraria*), Date Palm (*Phoenix dactylifera*) and Acacia Tortilis (*Vachellia tortilis*). The latter is made of a series of points on a grid of 5\*5 meters, around and in between Building A.
- Comfort Map of the site: based on the analysis of the Index of Thermal Stress and the Mean Radiant Temperature in the campus.

### 5.3.1 Outdoor human comfort and metabolic activity

The outdoor human comfort of the campus was analysed as a function of the Index of Thermal Stress (ITS); the methodology is described in Chapter 2. The objective of the analysis is to improve the outdoor human comfort in the campus by applying bioclimatic strategies. The outdoor human comfort on the campus is analysed in eight outdoor environments, p1 to p8, as shown in Figure 5.19. Based on the on-site visit, the ground is defined as rubber in the playground areas (albedo equal to 0.1) and concrete tiles (albedo equal to 0.3). The short wave reflectance



of the walls of buildings corresponds to 0.2; this value is the result of a combination of different colours: white surface (albedo=0.7) with darker patterns (red, violet, blue, etc.), as shown in Figure 5.19. The total reflectance is the weighted average of colours. The pedestrians' comfort is analysed in eight locations, and the impact of their metabolic activity is defined, varying from a low metabolic rate of  $80 \text{ W}\cdot\text{m}^{-2}$  to a high rate of  $255 \text{ W}\cdot\text{m}^{-2}$ . The pedestrians' p1, p7 and p8 are located upon liveable roof terraces, and p8 is used throughout the day by the sport classes. The pedestrians p2, p3 and p4 are located on the open courtyard of the kindergarten. Finally, p5 and p6 are covered by the overhangs of buildings. The selected points represent commonly used spaces, and they cover all the environmental conditions. The analysis covers the school period in Dubai, from 21<sup>st</sup> August to 25<sup>th</sup> June; consequently the summer month of July is neglected because the school is closed. The simulations show the impact of the urban geometry as well as of shadowing strategies, like white shadowing (made by white textile composed of 1 or 3 layers of fabrics) on the human comfort.



Figure 5.19 Top: SISD Dubai, plan of the campus with the location of pedestrians in the outdoor environment. Bottom: rendering of the school campus (source sisd.ae).

The results of the ITS for pedestrians with a light metabolic activity ( $80 \text{ W}\cdot\text{m}^{-2}$ ) show that the most comfortable locations are p1 (68% hours of comfort during the school period) followed by p3 (67% hours of comfort during the school period). The worst positions are p5 and p6: pedestrian are located under the projection of the building, consequently they are protected by shadowing during summertime, but during wintertime, because of the lower sun altitude, they receive solar irradiance that is stored in the building and reemitted to them. This behaviour is evident on Figure 5.20, which represents the average Index of Thermal Stress for the pedestrians during 21<sup>st</sup> of

March, 21<sup>st</sup> of June and 21<sup>st</sup> of December. During the 21<sup>st</sup> of June, the average ITS in p5 and p6 is 199 and 197 W respectively, which corresponds to a “warm” thermal sensation. By contrast, during the 21<sup>st</sup> of December the average ITS corresponds to -26 and -23W, which is three time higher than the values in other locations (-65W). The ITS at noon on 21<sup>st</sup> December is 177W and 332 W (“warm” thermal sensation) in p5 and p6; by contrast, it corresponds to 7W (“comfortable” thermal sensation) in p3 and p4. Figure 5.20 shows the total hours related to each thermal sensation for the selected locations and during the daytime (from 8:00 to 18:00 hours): the highest number of “comfortable” hours is observed in p1, followed by p3 and p4 (located on the courtyard). These locations are characterized by neighbouring buildings that protect pedestrians on the East and West side, where the solar radiation is stronger during the warmer seasons. The fewest hours of “hot” thermal sensations are observed in p3 and p8 (30 and 27 hours respectively): pedestrians there are protected on the West side by two tall buildings (13 and 17 meters). It is during the afternoon that the air temperature is higher and shadowing is essential to reduce the impinging solar irradiance.

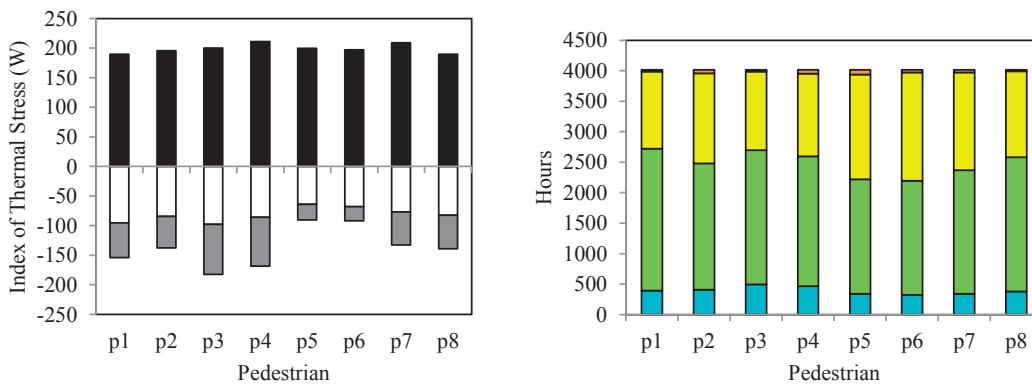


Figure 5.20 Left: average Index of Thermal Stress during the 21st of March (white), 21<sup>st</sup> of June (black) and 21<sup>st</sup> of December (grey) for the eight pedestrians located in the outdoor environment of the SISD campus. Right: cumulative hourly Index of Thermal Stress as a function of the different locations: cyan (cold), green (comfortable), yellow (warm), orange (hot).

The second part of the analysis considers the impact of shadowing strategies on the outdoor human comfort. Firstly, a single layer textile is applied upon the open courtyard of the kindergarten and upon the terrace, located upon the rooftop of the sport building. By placing the textile, pedestrians p2, p3, p4, p7 and p8 are protected by the sun; the fabric is then modified by adding two superposed textile layers (Figure 5.21). The existing shading devices, as proposed in the campus design, consist of one single layer textile, with a rectangular form of 19 x 6 meters. The proposed meshes are rectangular with a dimension of 2 x 19 meters, and superposed in three layers in a staggered way, ensuring the natural circulation of air (Figure 5.21). A three-layer fabric reduces shortwave and longwave radiation impinging on the pedestrian, and consequently impacts the surface temperature of the meshes, the ground and the air. The average annual surface temperature of the ground, around p4, without shading devices, is 29°C, while with one layer of fabric it corresponds to 26°C, and with three layers of fabric to 24°C. All the results are obtained by the simulations performed with CitySim.

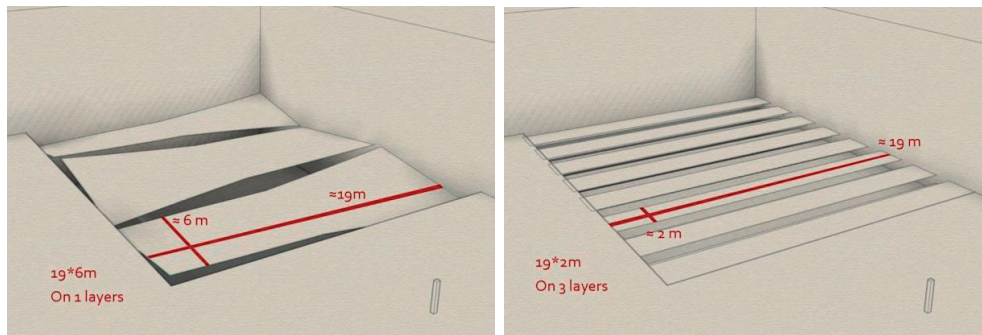


Figure 5.21 Fabric design, in accordance to SISD project (left) and the proposed three- layer fabrics (right).

By adding a single layer of fabric on a courtyard without shading protections, a pedestrian with a metabolic rate of  $80 \text{ W}\cdot\text{m}^{-2}$ , would feel comfortable for 67% more of the time. By contrast, he/she would be comfortable for 69% of the time, by adding a two layers fabric. By adding a three-layer textile, the hours of human comfort are increased by 73%. The same applies for a metabolic rate of  $255 \text{ W}\cdot\text{m}^{-2}$ : comfortable hours would increase from 45% to 47% with one layer of fabric and to 55% with three layers. Figure 5.22 shows the Index of Thermal Stress during the 21<sup>st</sup> of March for Pedestrian p2, with a metabolic rate of  $80 \text{ W}\cdot\text{m}^{-2}$  (a) and  $255 \text{ W}\cdot\text{m}^{-2}$  (b). The thermal sensation with the textile fabric is similar during nighttime, but lower during daytime: a pedestrian feels “warm” from 11:00 to 16:00 without any shadowing protection and “comfortable” during daytime when one textile layer is added. The impact of shading devices is more significant if the pedestrian has a stronger metabolic activity: in this case his or her thermal sensation is similar during daytime with one single layer of fabric (“warm” thermal sensation), or without it. By contrast, his/ her thermal sensation is “comfortable” during the whole day when a three-layer fabric is used.

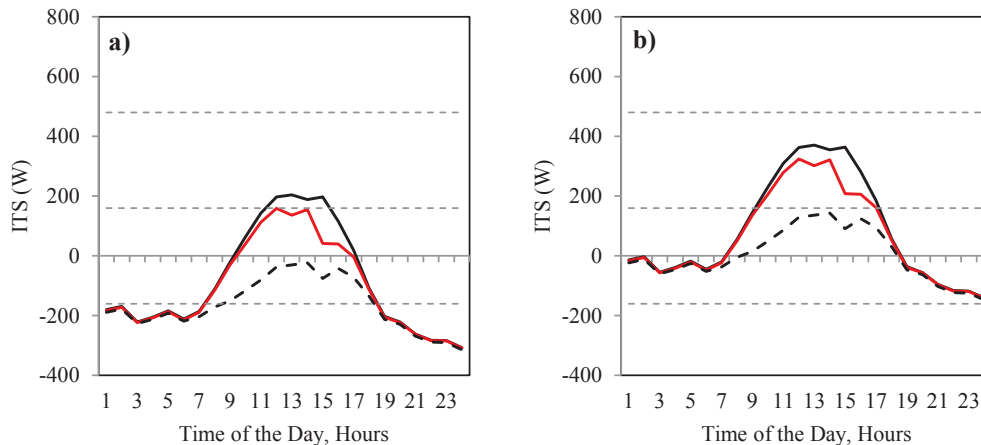


Figure 5.22 Index of Thermal Stress, perceived by pedestrian p2 without shadowing (black line), with 1 layer textile fabric (red line) and with three layers of fabric (dotted black line). Hourly analysis during the 21<sup>st</sup> of March, pedestrian metabolic rate equals to  $80 \text{ W}\cdot\text{m}^{-2}$  (a) and  $255 \text{ W}\cdot\text{m}^{-2}$  (b).

The same behaviour can be observed on the 21<sup>st</sup> of June; the daily average thermal sensation for a pedestrian with a light metabolic activity corresponds to 195 W (“warm” thermal sensation), without shadowing to 160 W with a one-layer fabric (limit of “comfortable” thermal sensation) and to 107 W with a three-layer fabric (“comfortable” thermal sensation). During this day the pedestrian will experience a “warm” thermal sensation from 8:00 hours to 19:00 hours. By contrast, when three layers of fabric are used, the “warm” sensation appears from 11:00 hours to 18:00 hours, ensuring four additional hours of “comfort” for users. If the pedestrian is playing sports (metabolic rate equal to  $255 \text{ W}\cdot\text{m}^{-2}$ ), he/she will probably face a “hot” thermal sensation during the main part of the day (from

10:00 to 17:00 hours), and just from 12:00 to 16:00 hours if protected by a single layer of shadowing. The pedestrian would probably feel “warm” all day long if covered by a three-layer textile, but without “hot” thermal sensation.

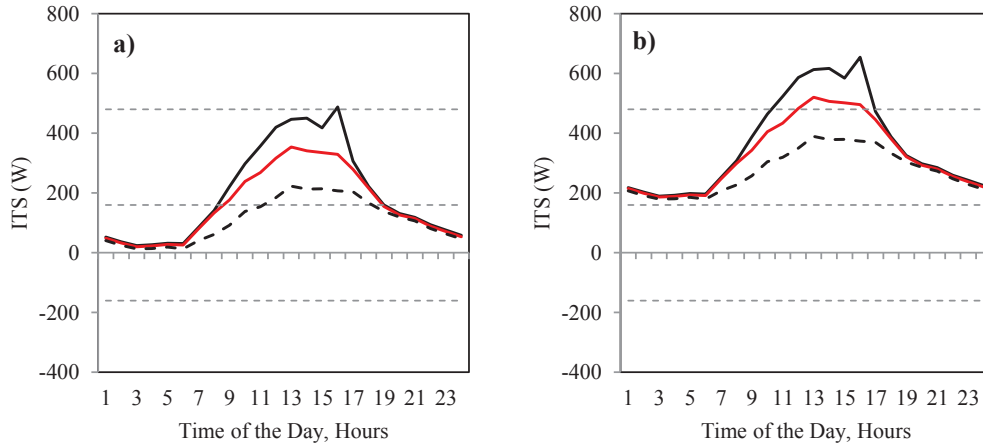


Figure 5.23 Index of Thermal Stress, perceived by Pedestrian 2 without shadowing (black line), with one layer of textile fabric (red line) and with three layers of fabric (dotted black line). Hourly analysis during the 21<sup>st</sup> of June, pedestrian metabolic rate equals to 80 W·m<sup>-2</sup>(a) and 255 W·m<sup>-2</sup> (b).

### 5.3.2 Outdoor human comfort and urban landscape

The objective of this study is to quantify the impact of planting native trees on the outdoor human comfort. The trees chosen for this case study are plants native in arid climates, which are naturally present in the desert of the Emirates: the Ghaf tree (*Prosopis cineraria*), the Date Palm (*Phoenix dactylifera*) and the Acacia Tortilis (*Vachellia tortilis*). Their physical characteristics, assumed for an average age of 10 years, are summarized in Table 5.4. Pedestrians are considered with a metabolic rate equal to 80 W·m<sup>-2</sup> corresponding to standing and relaxed activities; the metabolic rate can be modified as necessary.

Name	Height (m)	Leaf Area Index	3D view of the selected site
Ghaf tree ( <i>Prosopis cineraria</i> )	5	4	
Date palm ( <i>Phoenix dactylifera</i> )	15	2	
Acacia tortilis ( <i>Vachellia tortilis</i> )	10	4	

Table 5.4 Physical characteristics of Ghaf Tree, Date Palm and Acacia Tortilis. 3D view of the selected area, with the courtyards (A,B and C) and the pedestrians #14 (red) and #73 (blue).

At the time this analysis was performed, the only building already in use was the one hosting the kindergarten and the administrative building; the study was focused on these areas. Plants are located in front of the Southern facade of the building and in the three courtyards; the ground around the building is covered with concrete tiles

with an albedo equal to 0.30 (Erell et al., 2011b). The ground in the courtyard and on the first floor is made of coloured rubber, a typical covering for a children's playground; its averaged albedo is equal to 0.10 (Vanos et al., 2016). The detailed composition of the ground is defined in Tables 5.5 and 5.6.

Material	Density $\rho$ ( $\text{kg m}^{-3}$ )	Specific heat $c$ ( $\text{J kg}^{-1}\cdot\text{K}^{-1}$ )	Thermal conductivity $\kappa$ ( $\text{W m}^{-1}\cdot\text{K}^{-1}$ )	Thickness (m)	Emissivity (-)
Concrete tiles	2,100	1,000	1.5	0.03	0.96
Concrete	2,400	1,000	2.1	0.05	0.9
Gravel	2,000	1,051	2	0.1	0.9
Sandy Soil	2,000	900	2	/	0.96

Table 5.5 Thermal properties of the ground covered by concrete tiles.

Material	Density $\rho$ ( $\text{kg m}^{-3}$ )	Specific heat $c$ ( $\text{J kg}^{-1}\cdot\text{K}^{-1}$ )	Thermal conductivity $\kappa$ ( $\text{W m}^{-1}\cdot\text{K}^{-1}$ )	Thickness (m)	Emissivity (-)
Rubber covering	910	1,101	0.13	0.02	0.96
Concrete	2,400	1,000	2.1	0.05	0.9
Gravel	2,000	1,051	2	0.1	0.9
Sandy Soil	2,000	900	2	/	0.96

Table 5.6 Thermal properties of the ground in the playground courtyard, covered by rubber.

Pedestrians are supposed to be located in the kindergarten and the administrative building, following a 5m grid in the courtyard, and a 10m grid in the other spaces. Three types of plants (Ghaf tree, Date palm and Acacia tortilis) are set below the southern facade of the building and in the internal courtyards, with 36 trees totally per each species. The thermal sensation perceived by each pedestrian is estimated in order to assess the impact of the built environment and the plants on the thermal comfort.

The outdoor human comfort, assessed using the Index of Thermal Stress, as well as the impact of trees on the thermal perception, was quantified by simulation for a typical meteorological year for the Swiss International School Campus (SISD) campus in Dubai. Figure 5.24 shows the daytime comfort hours for the four seasons (Summer, Winter, Spring and Autumn) considering a pedestrian with a metabolic rate equal to  $80 \text{ W}\cdot\text{m}^{-2}$ , which corresponds to a standing and relaxed activity. The first analysis illustrates the impact of the built environment on the outdoor human comfort. Figures 5.24a and 5.24b show the thermal sensation of a pedestrian in summer and winter during daytime hours (from 8:00 hours to 18:00 hours); in summer the comfort hours vary from 4% to 29% during daytime, the courtyards being the more comfortable outdoor space with an average of 211, 173 and 183 comfort hours in the courts A, B and C respectively. During winter time, pedestrians located near the South and East facades are more comfortable than the ones located in the courtyards, which is due to the sun path: during winter time the sun is low in the sky (maximum sun altitude of  $41^\circ$  at noon on 21<sup>st</sup> December) and pedestrians in the courtyards (especially courts B and C) are shadowed by buildings on the South side (height equal to 13 m); the sun can accordingly not warm up the outdoor spaces and the thermal sensation is not as comfortable. The same analysis can be applied to pedestrians located in the Northern part of the campus, where during the months of December, January and February the cool hours correspond to 148, 226 and 157 hours respectively, and the comfortable ones to 193, 115 and 151 hours respectively. Figures 5.24c and 5.24d show the total comfortable hours during Spring and Autumn: in these seasons the fraction of daytime comfortable hours ranges from 28% to 74% (during spring) and from 47% to 81% during autumn. In accordance with the above comfort analysis, the optimal period for living in the outdoor environment of Dubai is autumn, when the courtyard is appropriate during most of daytime for light metabolic activities, such as standing and relaxing.



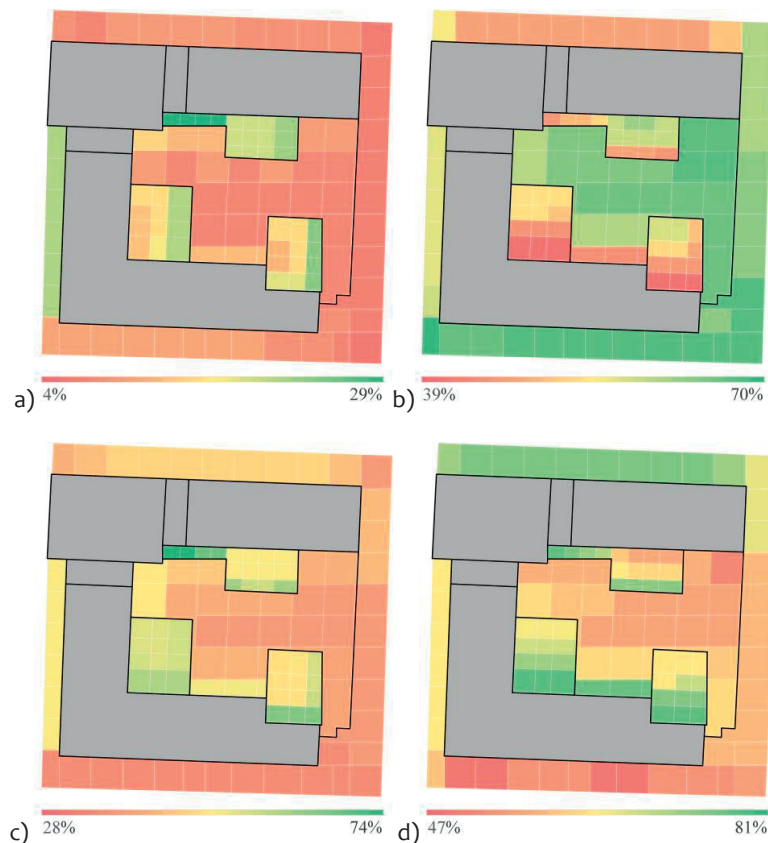


Figure 5.24 Comfort Map of the SISD campus. Relative fraction of daytime comfortable hours for each season (%), expressed as a function of the Index of Thermal Stress; a) Summer: 21<sup>st</sup> June to 22<sup>nd</sup> September, b) Winter: 21<sup>st</sup> December to 20<sup>th</sup> of March, c) Spring: 21<sup>st</sup> of March to 20<sup>th</sup> of June and d) Autumn: 23<sup>rd</sup> September to 20<sup>th</sup> December.

An hourly analysis of the thermal sensation (Figure 5.25) and energy fluxes exchanged between pedestrians and their environment (Figures 5.26 and 5.27) is illustrated for two pedestrians during the solstices and equinoxes: June 21<sup>st</sup> (sunrise at 7:00 hours and sunset at 19:00 hours, sun altitude at noon 86°), December 21<sup>st</sup> (sunrise at 8:00 hours and sunset at 17:00 hours, sun altitude at noon 41°), March 21<sup>st</sup> (sunrise at 7:00 hours and sunset at 18:00, sun altitude at noon 65°) and September 23<sup>rd</sup> (sunrise at 7:00 hours and sunset at 18:00 hours, sun altitude at noon 63°); one pedestrian is facing East and experiencing the largest number of discomfortable hours during the year (Pedestrian #14) and the other one is located in Courtyard C and experiencing the fewest discomfortable hours during daytime (Pedestrian #73). On the summer solstice, Pedestrian #14 is comfortable until 7:00 hours; after sunrise his or her sensation of warmth begins to increase, reaching a sensation of hotness at 9:00 hours, and remaining constant until 17:00 hours, when the thermal sensation slightly decreases, reaching a comfortable sensation after 21:00 hours. By contrast, the thermal sensation of Pedestrian #73 is comfortable until 9:00 hours, then gradually increases reaching a sensation of hotness after noon, and decreases at 17:00 hours, becoming comfortable at 19:00 hours (Figure 5.25). The shortwave radiation (direct plus diffuse radiation reflected by surroundings) impinging on Pedestrian #14 (the maximum value reaches 227 W·m<sup>-2</sup> at 11:00 hours the 21<sup>st</sup> of June) is twice the one incident on Pedestrian #73. Considering that the sun rises at 7:00 hours, and irradiate the surfaces facing East, the longwave radiation received by Pedestrian #14 increases during morning time from 475 W·m<sup>-2</sup> at 7:00 hours to 601 W·m<sup>-2</sup> at noon (21<sup>st</sup> of June). By contrast, for Pedestrian #73 the longwave radiation continues to increase during daytime, from 7:00 hours to 15:00 hours: this is clearly due to the built environment, which store the heat. The thermal sensation of both pedestrians during nighttime is lower on Spring equinox compared to December 21<sup>st</sup>: this is very likely due to the selected meteorological data, characterized by strong winds during the night of March 21<sup>st</sup> (maximum speed reaching 8.8 m·s<sup>-1</sup>). By contrast, on 21<sup>st</sup> December a light breeze blows on site (maximum wind speed reaching 2.7 m·s<sup>-1</sup>). The impact of the built environment on the thermal sensation of

pedestrians varies over the year: it is evident during December 21<sup>st</sup>, when the shortwave radiation impinging on Pedestrian #14 reaches a maximum value of  $213 \text{ W}\cdot\text{m}^{-2}$  at 11:00 hours and a maximum value of just  $48 \text{ W}\cdot\text{m}^{-2}$  at noon for Pedestrian #73. On March 21<sup>st</sup>, the pedestrians located in the courtyard are comfortable during daytime; by contrast the one facing East is experiencing a “warm” thermal sensation during the same period (from 10:00 hours to 15:00 hours). The convective exchange (thermal convection between the body and the surroundings due to a thermal buoyancy and convection due to wind) for both pedestrians is negative all day long during winter time; by contrast it is positive during daytime for the other seasons, as for June 21<sup>st</sup>.

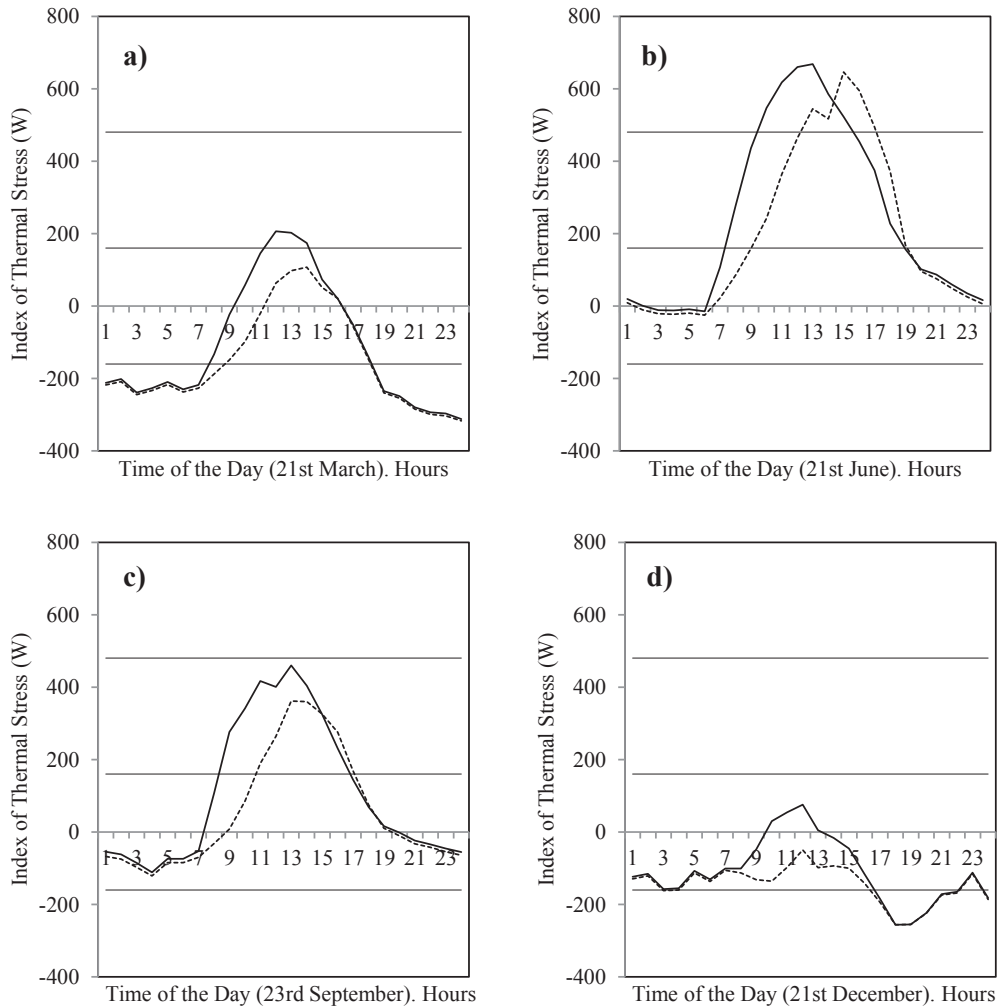


Figure 5.25 Index of Thermal Stress (W) for two selected locations: Pedestrian #14 (P14, continuous line) facing East, and Pedestrian #73 (P73, dotted line) located in Courtyard C. ITS is expressed as a function of the hours of the day, for March 21<sup>st</sup> (a), June 21<sup>st</sup> (b), September 23<sup>rd</sup> (c) and December 21<sup>st</sup> (d).



Energy performance and outdoor comfort of a campus in a hot and arid climate

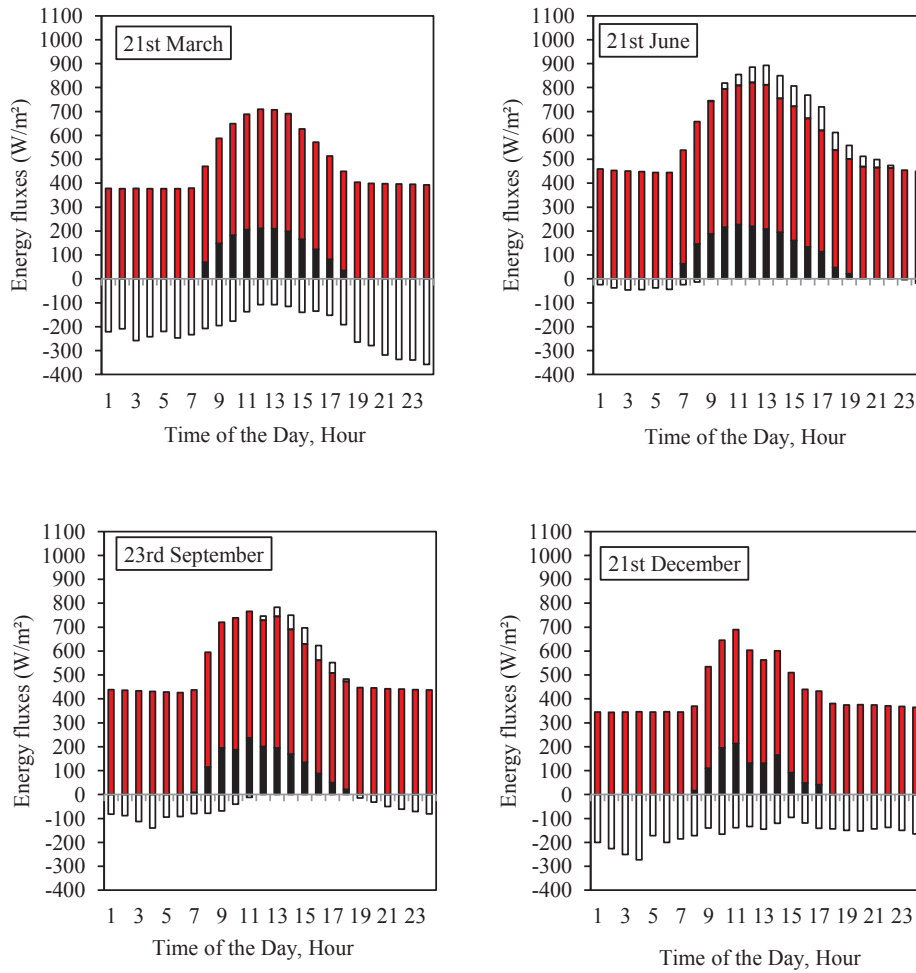


Figure 5.26 Energy Fluxes impinging on Pedestrian #14 facing East on March 21<sup>st</sup>, June 21<sup>st</sup>, September 23<sup>rd</sup> and December 21<sup>st</sup>, as a function of daily hours. All energy fluxes are expressed in W·m<sup>-2</sup>: incident longwave radiation (red), incident shortwave radiation (black) and energy exchanged by convection (white).

Energy performance and outdoor comfort of a campus in a hot and arid climate

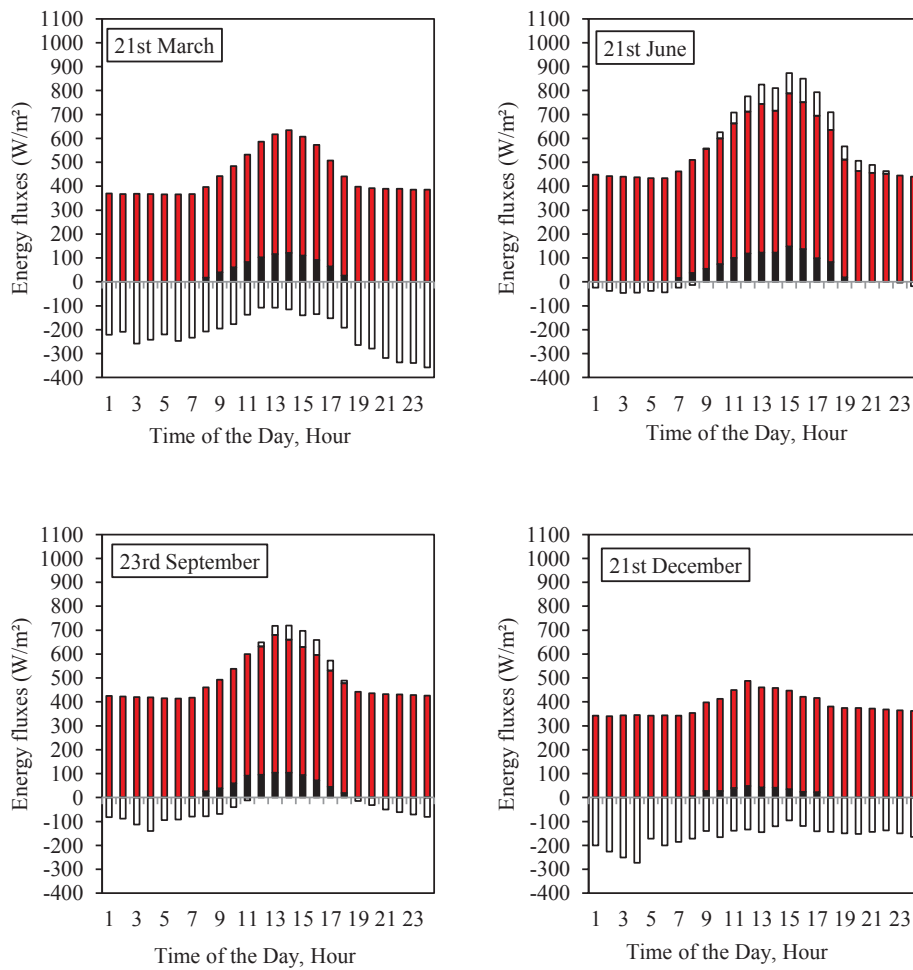


Figure 5.27 Energy fluxes impinging on Pedestrian #73 located in Courtyard C on March 21<sup>st</sup>, June 21<sup>st</sup>, September 23<sup>rd</sup> and December 21<sup>st</sup>, as a function of daily hours. All energy fluxes are expressed in  $W \cdot m^{-2}$ : incident longwave radiation (red), incident shortwave radiation (black) and energy exchanged by convection (white).

The second analysis focuses on the quantitative improvement of outdoor human comfort by placing different species of trees, such as Ghaf trees (*Prosopis cineraria*) with a Leaf Area Index equal to 4, Date Palms (*Phoenix dactylifera*) with a Leaf Area Index equal to 2, and Acacia Tortilis (*Vachellia tortilis*) with a Leaf Area Index equal to 4, at the South entrance of the building, as well as in the three courtyards (see Figure 5.28). The Leaf Area Index (LAI), represents the ratio between the total upper leaves area and the ground tree area, varying according to seasons and years (Fahmy et al., 2010) (Hosoi, 2009).

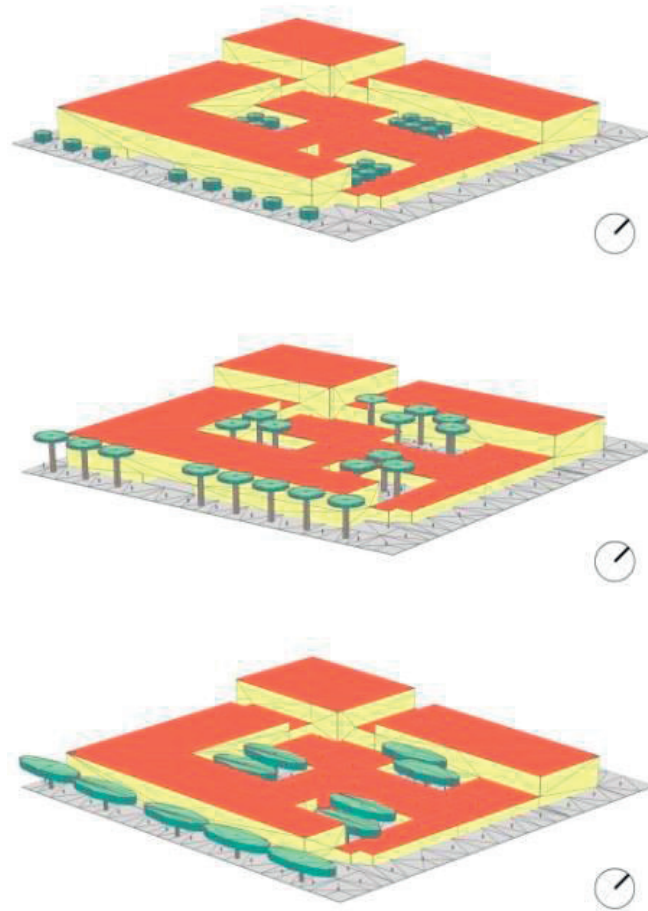


Figure 5.28 Location of three different plants species on the SISD campus on the southern building entrance and in Courtyards A, B and C. From top: Ghaf tree (*Prosopis cineraria*), Date Palm (*Phoenix dactylifera*) and Acacia Tortilis (*Vachellia tortilis*).

The presence of plants significantly increases the comfort throughout the year: the relative fraction of comfortable hours during spring time without any solar protection increases from 28 to 74% for daytime and from 30 to 85% during all day with Palm Trees. Figure 5.29 shows the monthly thermal sensation for trees (Acacia, Palm and Ghaf Tree) placed at the South building entrance; during spring the number of “comfortable” hours slightly increases by reducing the “warm” sensation, passing during March from 237 hours to 268 hours thanks to Acacia trees. During summer time the positive impact of plants on the outdoor human comfort is obvious. They significantly increase the number of “comfortable” hours (37 hours without plants during June, and resp. 48, 62 and 43 hours by planting Ghaf Trees, Acacia Trees and Palms): twelve hours of “very hot” thermal sensation in August without any plants are halved to 6 hours with Ghaf Trees and to nil by planting Acacia Trees and Palms.

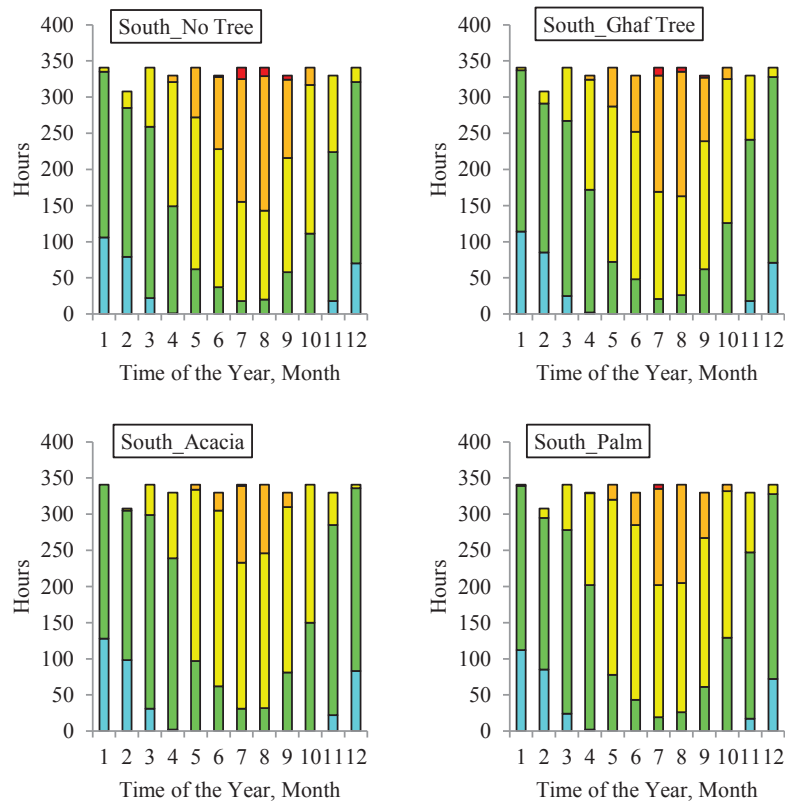


Figure 5.29 Hourly Index of Thermal Stress for pedestrians located near the southern facade for the different months: cyan (cold), green (comfortable), yellow (warm), orange (hot) and red (very hot).

The same analysis is conducted for the courtyard, where the trees' impact is essential to increase comfort during spring and summer time; in Courts A, B and C the hours of comfort during May increase from 107, 105 and 92 hours to 158, 137 and 127 hours respectively, if palm trees are planted. "Extremely hot" situations are reduced thanks to the plants, which provide shadow and reduce the long wave radiation received by pedestrians by creating a screen effect. A detailed hourly analysis conducted for a pedestrian located in Court A shows the trees' impact on the energy fluxes between the person and his/ her surroundings. During a typical spring day (Figure 5.30), the thermal sensation without any protection is "hot" ( $ITS > 480 \text{ W}$ ) in the afternoon (from 13:00 hours to 16:00 hours). By contrast, it is "warm" during daytime thanks to shadowing provided by palms. During a typical autumn day, the palms reduce the number of hours characterized by a "warm" sensation from 8 (10:00 hours to 17:00 hours) to 6 hours (11:00 hours to 16:00 hours). The palms also impact the outdoor human comfort by reducing the short and longwave radiation impinging on the pedestrians: as an example, on May 20<sup>th</sup> during the afternoon (15:00 hours), the longwave radiation corresponds to  $520 \text{ W}\cdot\text{m}^{-2}$  with palms and to  $591 \text{ W}\cdot\text{m}^{-2}$  without (showing a reduction of the 20%); at the same time, the shortwave radiation is reduced by 44%, passing from  $136 \text{ W}\cdot\text{m}^{-2}$  to  $76 \text{ W}\cdot\text{m}^{-2}$ .

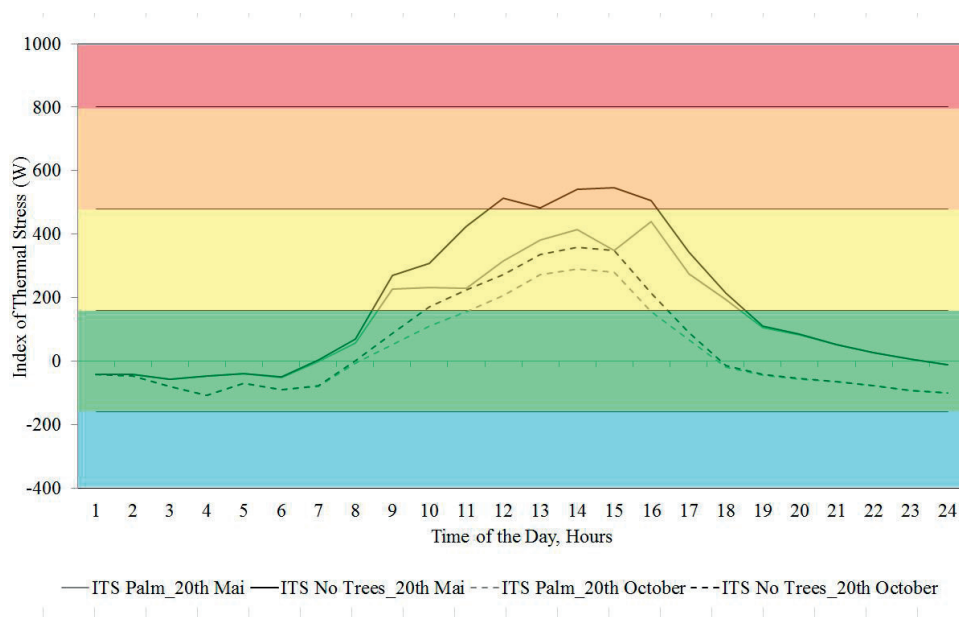


Figure 5.30 Index of Thermal Stress (W) for a pedestrian located in Courtyard A with shadowing provided by a palm tree, and without it. Analysis for a typical spring day (May 20<sup>th</sup>) and a typical autumn day (October 20<sup>th</sup>). Legend: red (very hot); orange (hot); yellow (warm); green (comfortable) and cyan (cool).

Based on the above analysis, the positive impact of greening, the shadowing devices and the built environment on the outdoor human comfort is obvious. Planting native trees in the campus can reduce the uncomfortable hours. For example, during summer time, the plants significantly increase the number of comfortable hours (37 hours without plants during June, and resp. 48, 62 and 43 hours by planting Ghaf Trees, Acacia Trees and Palms): twelve hours of “very hot” thermal sensation in August without any plants are halved to 6 hours with Ghaf Trees and to nil by planting Acacia Trees and Palms.

Shadowing devices are essential in this climate: by adding a single layer fabric with a metabolic rate of  $85 \text{ W}\cdot\text{m}^{-2}$ , the comfortable hours increase from 67% of the time, to 69% by adding a two-layers fabric. By adding a three-layer textile, human comfort passes to 73%. When increasing the metabolic rate, up to  $255 \text{ W}\cdot\text{m}^{-2}$ , the comfortable hours would probably increase from 45% to 47% (one layer) and 55% for three layers. Finally, the urban environment has a positive impact on the human comfort: during summer time the courtyards are the more comfortable outdoor spaces with an average of 211, 173 and 183 comfort hours in the courts A, B and C respectively.

For a final analysis of the outdoor human comfort in the campus, the next paragraph presents a Comfort Map of the site, showing the comfortable hours during the years, as a function of the locations in the built environment.

### 5.3.3 Comfort Map of the SISD campus

This paragraph presents the analyses of the outdoor human comfort by the use of Comfort Maps. The human comfort is quantified using the Index of Thermal Stress, as computed by the software CitySim Pro. The pedestrians are located in the outdoor environment, upon a regular grid; they are placed each 10 meters of distance, with total of 497 pedestrians (Figure 5.31). Each pedestrian is performing a light metabolic activity. The results provided by the software CitySim Pro are analyzed with the software ArcGIS, in order to visualize the results, through the creation of colored maps. The simulations are performed dynamically, firstly to understand the impact of the built environment, secondly in order to quantify the impact of greening the outdoor environment. Trees are located on the school campus (Figure 5.32), upon a grid of 10 m (totally 367 plants). Three types of native trees are proposed: Ghaf tree (*Prosopis cineraria*), Date Palm (*Phoenix dactylifera*) and Acacia Tortilis (*Vachellia tortilis*). The plants are disseminated on the entire available outdoor environment; no trees are located in the sport area, due to the

presence of the football field, similarly for the parking area, where plants are located in two central rows leaving the empty space for cars.

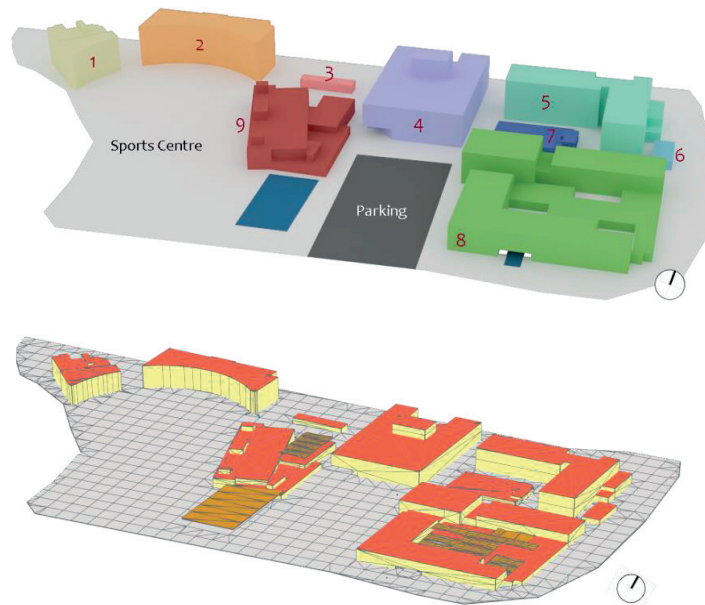


Figure 5.31 3D view of the SISD campus (up) with the indication of the buildings and the outdoor environments (sports center, parking and swimming pools in blue). 3D model created by CitySim Pro (down) with the analysis-grid, as well as the shading devices (orange).

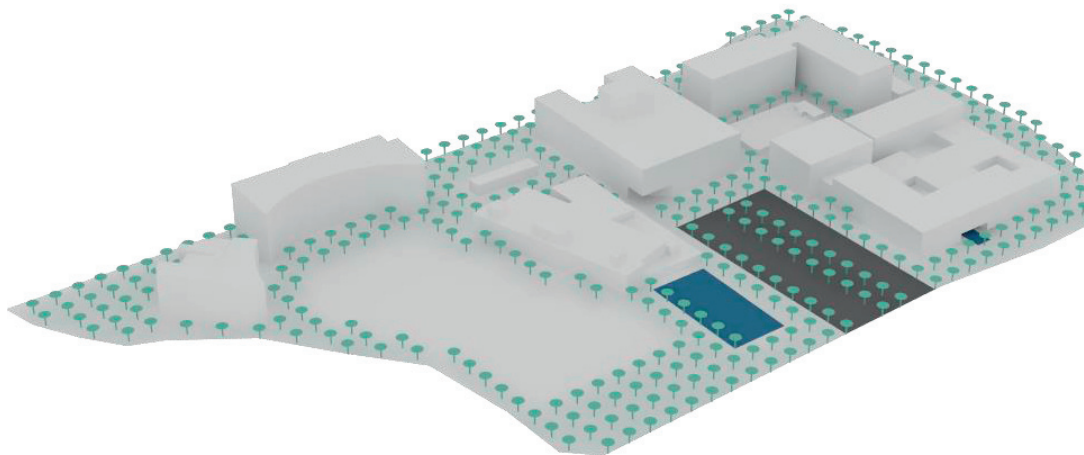


Figure 5.32 3D view of the campus created by Rhino with the location of the trees.

The urban properties of the school campus are summarized in Table 5.7 and Figure 5.31. The total area of the site corresponds to 73,390 m<sup>2</sup>; the campus hosts nine buildings, with an average height of 18.23 m. The Floor Area Ratio (FRA) or Plot Ratio of the campus, defined as the ratio of the gross floor area to the site area, corresponds to 0.98. The Site Coverage (SC), defined as the ratio of the buildings' footprint to the site area (Ng, 2010), corresponds to 28%. Finally, the average form factor (Personal communication with Kriesi Energie GmbH) of the buildings corresponds to 0.91.



	Wall (m <sup>2</sup> )	Roof (m <sup>2</sup> )	Floor (m <sup>2</sup> )	Height (m)	Form Factor (-)	Number of Floor	Gross Area Building
1	3,399	961	961	22.20	1.01	5	4,805
2	5,455	1,626	1,626	24.80	0.81	6	9,757
3	409	218	218	5.30	3.38	1	218
4	6,279	3,816	3,816	19.00	0.79	4	15,265
5	6,889	2,496	2,496	23.23	0.85	5	12,482
6	338	227	227	5.20	2.99	1	227
7	565	1,071	1,071	3.30	2.03	1	1,071
8	8,130	6,895	6,895	13.00	0.89	3	20,685
9	3,589	3,751	3,751	10.40	1.23	2	7,502

Table 5.7 Geometrical properties of the SISD campus.

#### *Comfort Map and Urban Environment*

Figures 5.33- 5.35 show the Index of Thermal Stress, as computed during the seasons. The urban environment has a positive impact on the outdoor human comfort by improving the pedestrian's thermal sensation. As an example, Figure 5.34 shows the thermal stress of a pedestrian during the summer season: a pedestrian located in the outdoor environment (as an example the sport area) is "comfortable" for 1,366 hours (less than the 60% of the time); a pedestrian located into a courtyard would face 2,203 hours of "comfortable" thermal sensation. Additionally, the spaces protected by neighbouring buildings (as an example between buildings 4, 5, 7 and 8) have the lower thermal sensations (green and yellow color in Figure 5.34) compared to the one located in the outdoor environment (red color). Additionally, it is interesting to observe the seasonal variation of the ITS as function of the site: indeed, as presented in Figure 5.35 (winter season), the southern area is "comfortable" during the winter time (due to the sun path, as presented above), more than the courtyard, that are more cooler. Finally, both swimming pools have a positive impact on the outdoor thermal comfort, due to the evaporative cooling, as well as to the shading devices placed upon them.

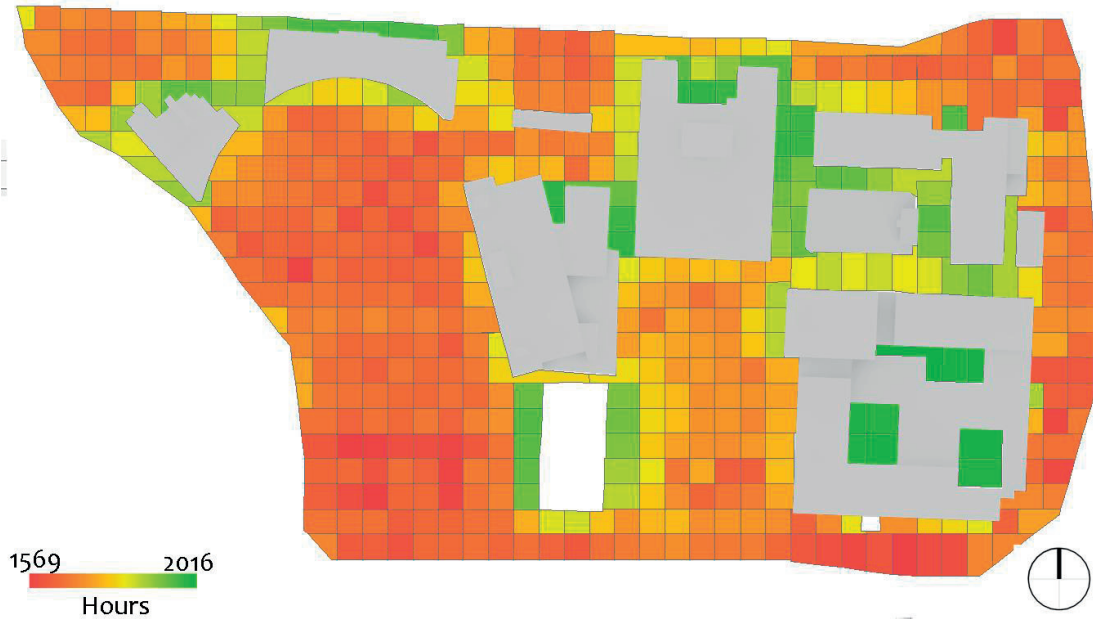


Figure 5.33 Comfort Map of the SISD campus. Total comfortable hours during the spring season.

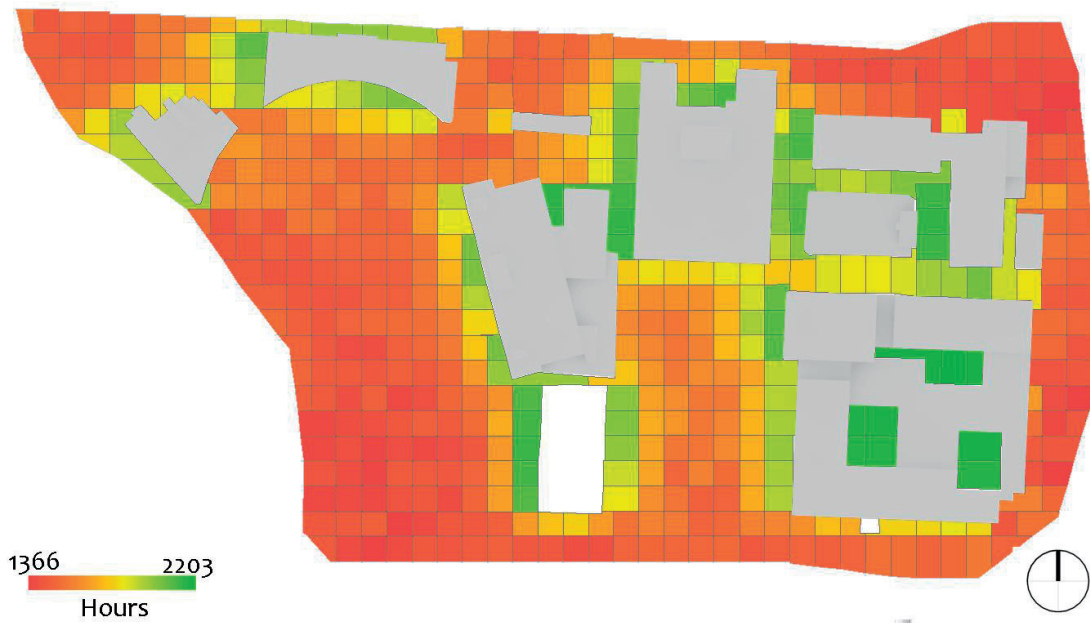


Figure 5.34 Comfort Map of the SISD campus. Total comfortable hours during the summer season.

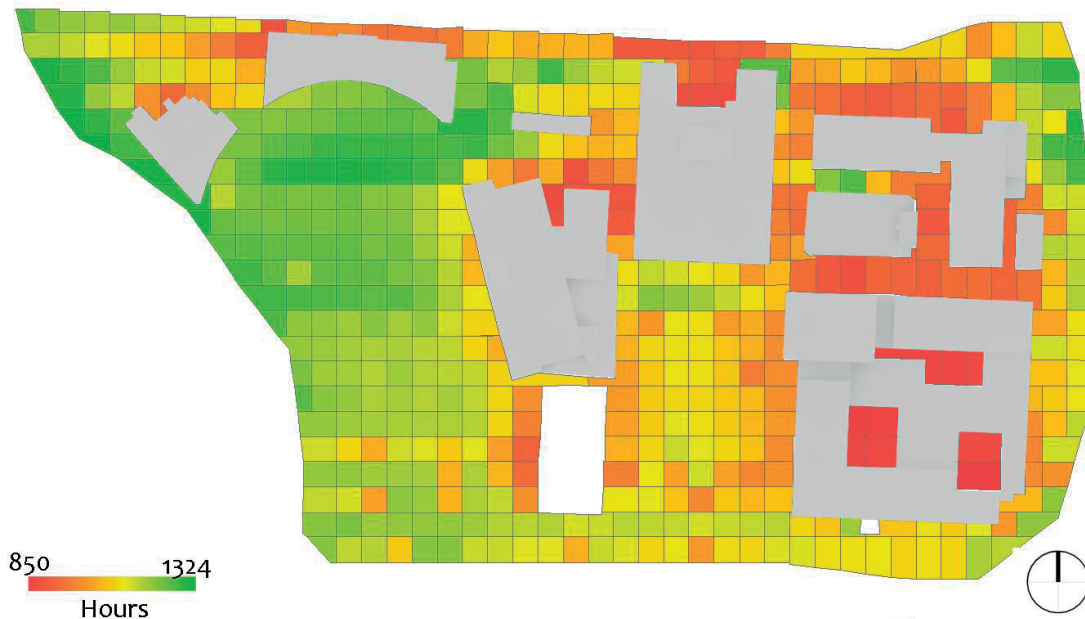


Figure 5.35 Comfort Map of the SISD campus. Total comfortable hours during the winter season.

#### *Comfort Map and Greening*

The positive impact of greening is presented in Figure 5.36, where ghaf trees are planted in the outdoor environment, as described above. The average thermal sensation of the pedestrians located in the school campus is, obviously, positively affected by the plantation of native trees. It is quite interesting to notice that thanks to plants, the hours characterized by a “comfortable” as well as a “cool” thermal sensation increase. Palms have a lower impact in the thermal sensation, due to their lower LAI. The thermal sensation of the pedestrians is improved, reducing the “warm/hot/very hot” thermal sensation; as an example during the summer season, by planting acacia trees, the average ITS corresponds to -65W (“comfortable” sensation), on the other side without trees the average thermal sensation corresponds to +105W: up to 170W of difference. Naturally, this is the average value, the analyses performed hourly underlining a bigger difference. It is also interesting to notice that trees impact not just the person behind the crown, but also pedestrians located nearby.

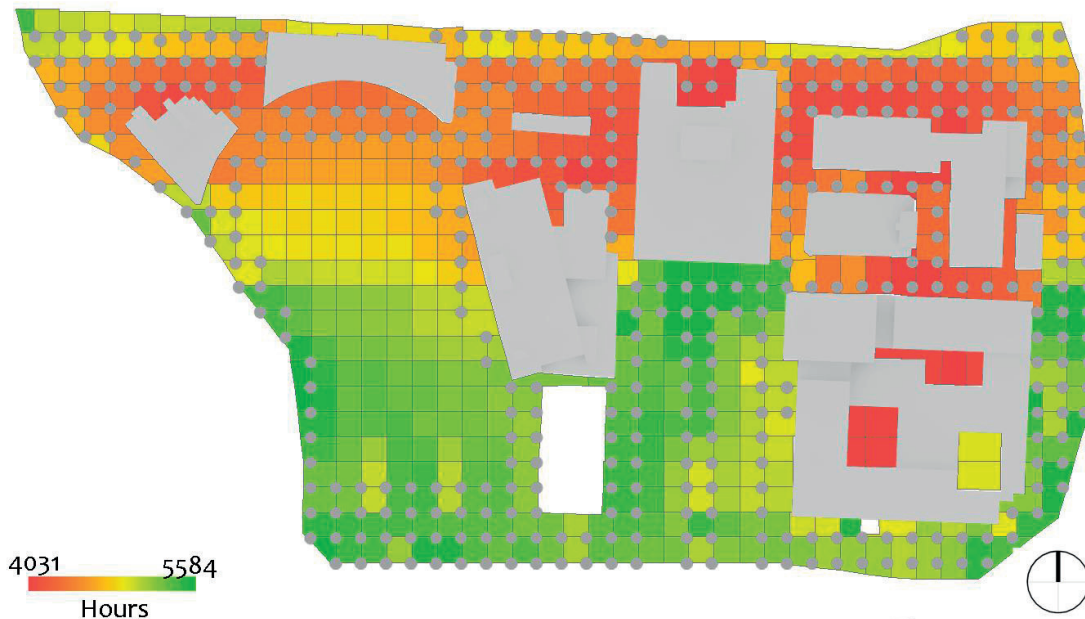


Figure 5.36 Comfort Map of the SISD campus. Total annual comfortable hours with ghaf tree.

If the Comfort Maps presented above show the thermal stress of a pedestrian performing a light metabolic activity, the next maps show the Mean Radiant Temperature in the campus. The MRT has a double meaning: on one side it reflects the radiative balance of a pedestrian (shortwave and longwave radiation impinging the pedestrian), on the other side it provides insights concerning the thermal exchanges between the building and the environment. Effectively, in the hot arid climate of Dubai, lower is the MRT, lower are the solar gains and infrared emissions received by the envelope. Effectively, as presented in Chapter 2, the MRT represents an artificial measure to express the degree of exposure to environmental radiation, and it is defined as the “the uniform surface temperature of an imaginary black enclosure in which an occupant would exchange the same amount of radiant heat as in the actual non uniform space” (ASHRAE, 2010). The Mean Radiant Temperature is affected by the solar shortwave radiation (direct, diffuse and reflected components) as well as by the terrestrial longwave radiation (atmospheric and environmental) (Kántor and Unger, 2011). As an example, Figure 5.37 shows the annual daytime MRT: all the areas near the buildings, facing a high MRT, are the ones where the maximal insulation of the envelope is required. Additionally, in these areas, windows have to be energy efficient, as well as protected by efficient shading devices. Finally, in these areas, semi-outdoor environments are essential, in order to improve the radiative balance by reducing the MRT. Semi outdoor environments are spaces not conditioned, but as a greenhouse in temperate climate, able to improve the energy efficiency of buildings, as well as provide comfortable environments, without any climatization. Naturally, these spaces cannot be used during all the year, but they can improve the environmental conditions, mostly during mid-seasons. In this climate, colonnades, patios (realized by buildings, by removable “man-made” surfaces, or by greenings) can be considered as semi-outdoor environments. Finally, the “negative” (as in photography) of the Comfort Map is the energy demand of buildings: the sum of both maps gives a nice overview of a city district, in this case the campus. In order to understand if the simulations are comparable to the measurements, the MRT as monitored in both locations (WS-1712, WS-1713A, WS-1713B, WS-1713C and WS-1713D) was compared to the one simulated by CitySim Pro. The Mean Radiant Temperature monitored in WS-1713A, and averaged during the winter time (21st December to 21st March), corresponds to 40.4°C during the daytime (from 8:00 to 18:00 hours). The MRT calculated by CitySim Pro for the corresponding location, is equal to 37.4°C during the daytime (difference of 3.0°C and by 8%). The same analysis was conducted for the weather station WS-1713B during the month of June: the average measurements during daytime show a MRT of 57.6°C; 54.7°C is the value provided by CitySim Pro (difference of 2.9°C and by 5%). The

same analyses were conducted for WS-1713C (measurements under a tree) during the month of August: the monitored average MRT during daytime corresponds to 53.2°C, the simulated one to 55.4°C (difference of 2.2°C, difference by 4%). Based on these results, the software results can be estimated as sound, and within the experimental error of the 9%.

Figures 5.37 and 5.38 show the annual Mean Radiant Temperature of the campus; the MRT is averaged during daytime (from 8:00 to 18:00 hours) and during all the day long. The maximal MRT during daytime corresponds to 50.7°C, 17°C higher than the one averaged during all the day. Naturally, the maximal MRT is observed on the sport area, and in the outdoor environment, that is not protected by neighbor's buildings. It is interesting to notice that the MRT in the courtyard corresponds to 17.3°C during all day and 21.5°C during daytime. The lower difference in these locations (compared to the above one), is related to the fact that these open spaces are protected by neighbors buildings, as well as by shading devices. Consequently, during the day the court receive less solar irradiance, but during the night, due to the low sky view factor, they re-emit less infrared radiation. The courts are a good example of the so called semi- outdoor environments: outdoor spaces, with a comfortable environment, using simple bioclimatic strategies (buildings, materials and shadings).

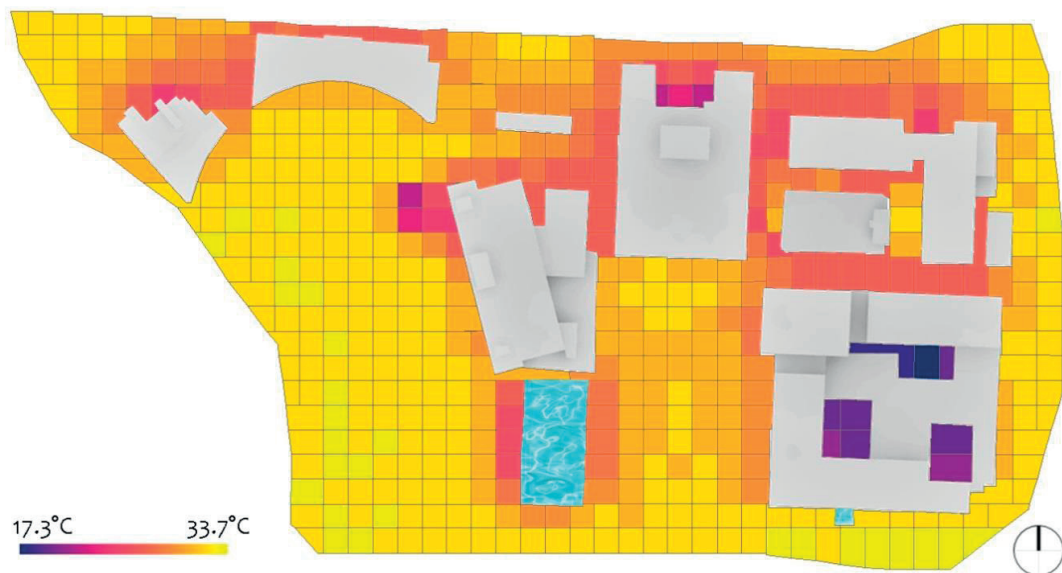


Figure 5.37 Comfort Map, annual Mean Radiant Temperature for the SISD campus. MRT averaged during all the day.

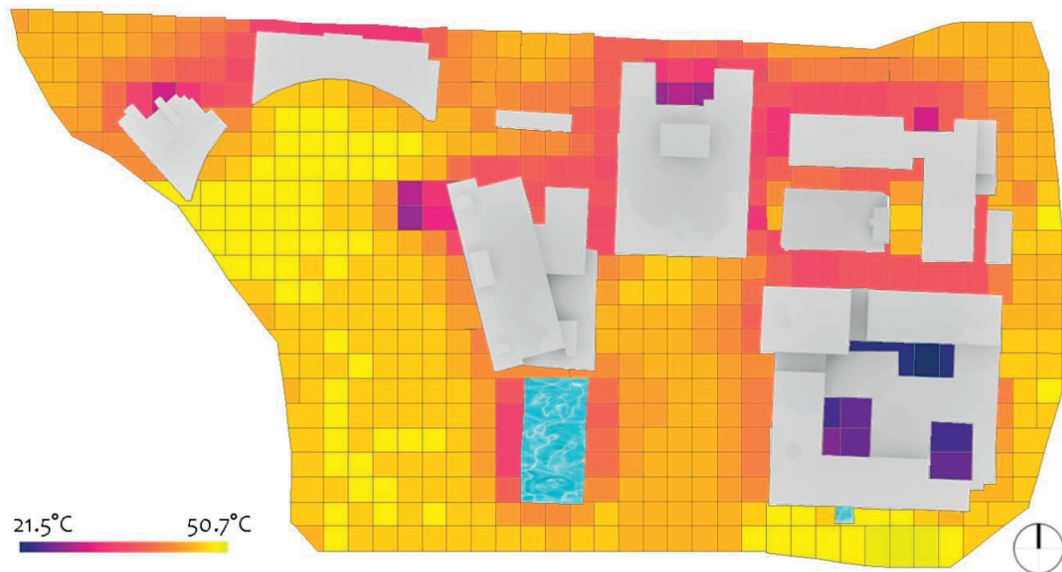


Figure 5.38 Comfort Map, annual Mean Radiant Temperature for the SISD campus. MRT averaged during the daytime (from 8:00 to 18:00 hours).

The MRT calculated during the winter time underlines the different radiative environments, as induced by the urban environment. Effectively, the facades exposed to the courtyard face a low MRT (15.9°C in average during the daytime) compared to the facades exposed to the sun (42.4°C in average during the daytime). Furthermore, the sun is shining strongly from the southern direction during winter time, and consequently the buildings provide shading to the outdoor environment, if facing south. As an example, all surfaces protected by buildings on the south side, have a MRT comprises between 15.9°C and 25°C. The same results are evident during the summer time, but in this case the impact of shading is lower, due to the sun height.



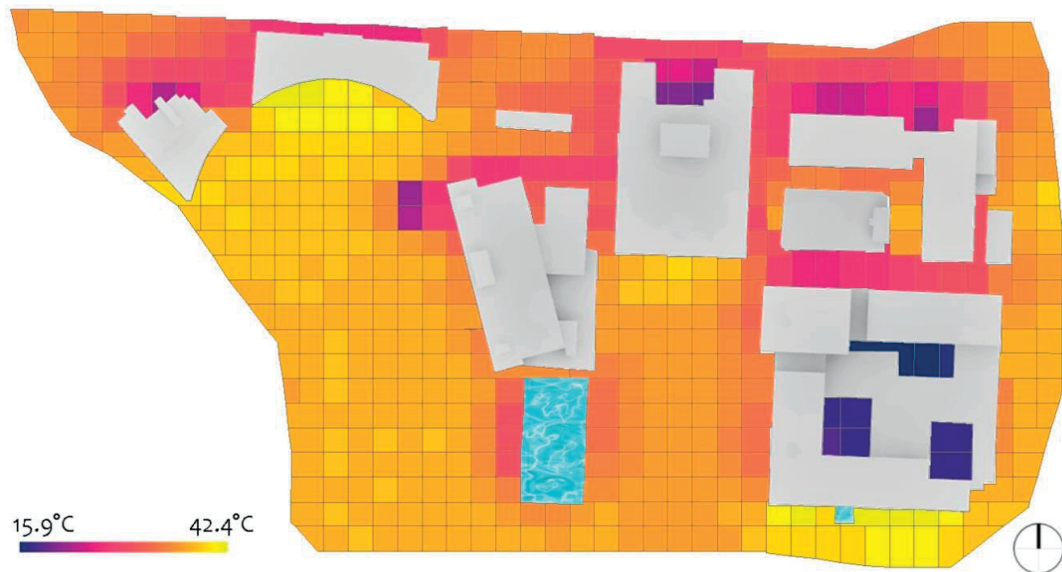


Figure 5.39 Comfort Map, Mean Radiant Temperature for the SISD campus calculated during the winter. MRT averaged during the daytime (from 8:00 to 18:00 hours).

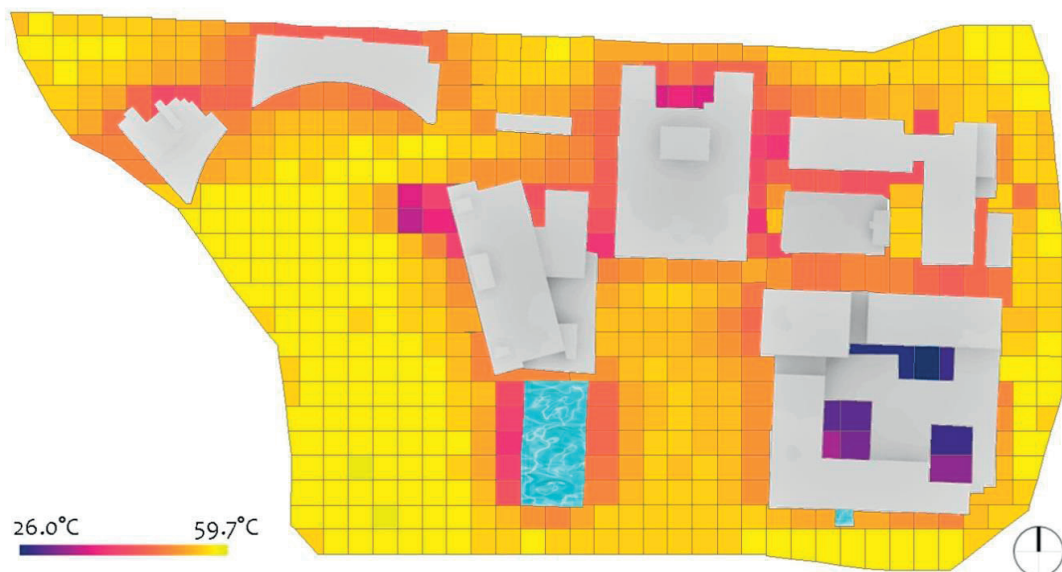


Figure 5.40 Comfort Map, Mean Radiant Temperature for the SISD campus calculated during the summer. MRT averaged during the daytime (from 8:00 to 18:00 hours).

## 5.4 Monitoring of the outdoor environment

The Swiss International Campus was equipped since November 2015 with three weather stations, one of them being moved in four different locations: one station, the so called WS-1711, is located on the rooftop of the administrative building. The second station, the so called WS-1712, is located on the first floor of the kindergarten, and the last one, the so called WS-1713, is located on the ground floor. Due to construction work, the last station was moved periodically between four different places: the entrance of the school and the parking (from the end of November 2015 to the 15<sup>th</sup> of May), on the Southern entrance of the school, a playground area (from the 17<sup>th</sup> of May to the 2<sup>nd</sup> of July), the same place, but under a tree near the swimming pool (from the 13<sup>th</sup> of July 2016 to the 17<sup>th</sup> of September) and finally near a wall and on vegetation (from the 19<sup>th</sup> of September).

### 5.4.1 Set-up of the weather stations

The locations of the weather stations are defined in Figure 5.41 and Table 5.8; the objective of the monitoring is to quantify the impact of the built environment on the urban microclimate, as well as to validate the simulations previously performed. Doing so the main weather station (WS-1711) is located on the rooftop of the building, and it is used as central weather station, to quantify the climate of the city of Dubai. This station, also called Master Station, receives by radio, and collects the monitored data from the other stations (so called Slave Stations).



Figure 5.41 Plan of the Swiss International School Campus with the location of the weather stations (left), and weather station WS 1711 on the rooftop of the administrative building (right). Photo by Laurent Deschamps.

Due to a technical problem with the instruments, WS-1711, first installed in November 2015, required maintenance already one month later; a IT specialist (Laurent Deschamps) went on site to tune the PV solar self-production as well as the radio transmission between the weather stations. In any case, the problem of this weather station was that the battery has not enough storage capacity to register its recorded data, to collect the ones from the other stations and to transmit them to the online platform. Due to this battery problem, the weather station automatically switches off during nighttime, if not enough energy is stored in the battery. WS-1712 (Figure 5.42) is located in the playground area: the objective of this station is to quantify the thermal sensation of students during their daytime sport activities. This station is shadowed by one layer of textile fabric during the main part of the day as well as by the neighboring buildings. The last station, WS-1713, was, as previously described, due to construction work, moved among four different locations of the site. Between November and the 15<sup>th</sup> of May it was located near the parking in front of a temporary football court (WS-1713 A). This location is representative of a naturally ventilated outdoor microclimate, without shadowing system but influenced by the ground covered by vegetation,

as shown in Figure 5.43. Between the 17<sup>th</sup> of May and the 2<sup>nd</sup> of July the weather station was located in a playground area, near the southern entrance of the school, as shown in Figure 5.44 (WS-1713 B). This location is representative of the playground area, where students normally play during daytime. The third location, between the 13<sup>th</sup> of July and the 17<sup>th</sup> September represents the impact of the swimming pool and trees on the outdoor microclimate: the station was located at around 5m from the swimming pool and under a native tree (WS-1713 C), as shown in Figure 5.45. Finally, the last location, since the 19<sup>th</sup> of September, is representative of a playground located on the southern part of the campus. WS-1713D is located near the playground, upon a hedge (Figure 5.46).



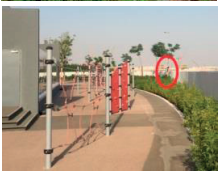

Month	Location of the weather station WS-1713	Picture
November 2015	A: Parking, upon hedge	
December 2015	A: Parking, upon hedge	
January 2016	A: Parking, upon hedge	
February 2016	A: Parking, upon hedge	
March 2016	A: Parking, upon hedge	
April 2016	A: Parking, upon hedge	
May 2016	A: Parking, upon hedge (until 15 <sup>th</sup> ) B: Playground (from 17 <sup>th</sup> )	
June 2016	B: Playground (until 2 <sup>nd</sup> ) C: Playground under a tree (from 13 <sup>th</sup> )	
July 2016	C: Playground under a tree (until 17 <sup>th</sup> ) D: Playground, upon hedge (from 19 <sup>th</sup> )	
August 2016	C: Playground under a tree (until 17 <sup>th</sup> ) D: Playground, upon hedge (from 19 <sup>th</sup> )	
September 2016	D: Playground, upon hedge	
October 2016	D: Playground, upon hedge	
November 2016	D: Playground, upon hedge	
December 2016	D: Playground, upon hedge	

Table 5.8 Weather station WS-1713, its several locations during the measuring period.



Figure 5.42 WS-1712, located on the first floor, in the playground/ sports area.





Figure 5.43 WS-1713A, located near the parking lot and in front of a temporary football court.



Figure 5.44 WS-1713B, located on the southern entrance of the building, near the playground area (17<sup>th</sup> of May to the 2<sup>nd</sup> of July). Photos by Ashfaq Khan.



Figure 5.45 Weather station 1713 C, located on the southern entrance of the building, near the swimming pool and under a tree (13<sup>th</sup> of July to the 17<sup>th</sup> September). Photos by Ashfaq Khan.



Figure 5.46 Weather station 1713 D, located on the southern entrance of the building, near the swimming pool and surrounded by flowers (from 18<sup>th</sup> September 2016). Photos by Ashfaq Khan.

WS-1711 is equipped with a pyranometer SPN1 produced by Delta-T Devices; this device monitors the global solar irradiance, the diffuse solar irradiance and the sunshine hours. It works for a range of short wave radiation values between 400 nm to 2,700 nm, with an accuracy of  $\pm 10 \text{ Wm}^{-2}$  in hourly averages. The second device is the main weather station, the so called WS700, produced by Lufft; this station assesses:

- Ambient temperature ( $^{\circ}\text{C}$  or  $^{\circ}\text{F}$ ), measured each minute; the measuring range varies between  $-50^{\circ}\text{C}$  to  $60^{\circ}\text{C}$  and the accuracy between  $\pm 0.2^{\circ}\text{C}$  ( $-20^{\circ}\text{C}$  to  $50^{\circ}\text{C}$ ) to  $\pm 0.5^{\circ}\text{C}$  ( $>50^{\circ}\text{C}$  or  $<30^{\circ}\text{C}$ ).
- Dew point temperature ( $^{\circ}\text{C}$  or  $^{\circ}\text{F}$ ), measured each minute; the measuring range varies between  $-50^{\circ}\text{C}$  to  $60^{\circ}\text{C}$  and the accuracy corresponds to  $\pm 0.7^{\circ}\text{C}$ .
- Wind chill temperature ( $^{\circ}\text{C}$  or  $^{\circ}\text{F}$ ), measured each minute; the measuring range varies between  $-60^{\circ}\text{C}$  to  $70^{\circ}\text{C}$ .
- Relative (%) and absolute humidity ( $\text{g}\cdot\text{m}^{-3}$ ), measured each minute; the measuring range of the absolute humidity varies between  $0 \text{ g}\cdot\text{m}^{-3}$  to  $1,000 \text{ g}\cdot\text{m}^{-3}$ , the accuracy corresponds to  $\pm 2\%$ .



- Absolute and relative air pressure (hPa), measured each minute; the measuring range varies between 300 hPa to 1,200 hPa, the accuracy corresponds to  $\pm 0.5$  hPa.
- Wet bulb temperature ( $^{\circ}\text{C}$  or  $^{\circ}\text{F}$ ) measured each minute; the measuring range varies between  $-50^{\circ}\text{C}$  to  $+60^{\circ}\text{C}$ , the accuracy corresponds to  $\pm 0.7^{\circ}\text{C}$ .
- Specific enthalpy ( $\text{kJ}\cdot\text{kg}^{-1}$ ) measured each minute; the measuring range varies between  $-100 \text{ kJ}\cdot\text{kg}^{-1}$  to  $1000 \text{ kJ}\cdot\text{kg}^{-1}$ .
- Air density ( $\text{kg}\cdot\text{m}^{-3}$ ) measured each minute; the measuring range varies between  $0 \text{ kg}\cdot\text{m}^{-3}$  to  $3 \text{ kg}\cdot\text{m}^{-3}$ .
- Wind speed ( $\text{m}\cdot\text{s}^{-1}$  or  $\text{km}\cdot\text{h}^{-1}$ ) measured every 10 seconds and averaged each minute; the measuring range varies between  $0 \text{ m}\cdot\text{s}^{-1}$  to  $75 \text{ m}\cdot\text{s}^{-1}$  and the response threshold corresponds to  $0.3 \text{ m}\cdot\text{s}^{-1}$ . The wind is measured by four ultrasonic sensors, which take cyclical measurements in all directions. The accuracy varies between  $\pm 0.3 \text{ m}\cdot\text{s}^{-1}$  or  $\pm 3\%$  (from 0 to  $35 \text{ m}\cdot\text{s}^{-1}$ ) to  $\pm 5\%$  ( $>35 \text{ m}\cdot\text{s}^{-1}$ ).
- Wind direction ( $^{\circ}$ ) measured each 10 seconds and averaged each minute; the measuring range varies between  $0^{\circ}$  to  $359.9^{\circ}$  and the response threshold corresponds to  $0.3 \text{ m}\cdot\text{s}^{-1}$ . The accuracy is within  $3^{\circ}$ .
- Precipitation quantity (mm), the response threshold corresponds to  $0.01 \text{ mm}$ . The accuracy is within  $2\%$ .
- Precipitation intensity ( $\text{mm}\cdot\text{h}^{-1}$ ) measured each minute; the response threshold corresponds to  $0.6 \text{ mm}\cdot\text{h}^{-1}$ . The accuracy is within  $2\%$ .
- Global solar irradiance ( $\text{W}\cdot\text{m}^{-2}$ ) measured every 10 seconds and averaged each minute; the measuring range varies between  $0 \text{ W}\cdot\text{m}^{-2}$  and  $1,400 \text{ W}\cdot\text{m}^{-2}$ .

Weather stations 1712 and 1713 comprise the same equipment: a Campbell black globe thermometer, Decagon VP-3 and a Decagon DS-2. The equipment of both stations (Figure 5.47) is positioned between 1.1 and 1.5 m height, corresponding to the center of gravity of the human body.



Figure 5.47 WS-1712, in the first floor playground (Left) and WS-1713A in front of the temporary football court

A Campbell black globe thermometer is a hollow copper sphere of 15 cm painted black with a thermistor inside; the measurement range is between  $-5^{\circ}\text{C}$  to  $95^{\circ}\text{C}$ , the accuracy varies between  $\pm 0.3^{\circ}\text{C}$  ( $-3^{\circ}\text{C}$  to  $90^{\circ}\text{C}$ ) and between  $\pm 0.7^{\circ}\text{C}$  ( $-5^{\circ}\text{C}$  to  $95^{\circ}\text{C}$ ); measurements are performed each minute.

The Decagon VP-3 measures the following parameters:

- Vapor pressure (kPa) measured each minute; the measuring range varies between  $0 \text{ kPa}$  and  $47 \text{ kPa}$  with a resolution of  $0.01 \text{ kPa}$ , the accuracy varies as a function of the air temperature and relative humidity. Values for the accuracy, defined as a function of the above parameters, are available in the technical manual.
- Ambient temperature ( $^{\circ}\text{C}$ ) measured each minute; the measuring range varies between  $-40^{\circ}\text{C}$  and  $+80^{\circ}\text{C}$  with a resolution of  $0.1^{\circ}\text{C}$ , the accuracy varies from  $\pm 1^{\circ}\text{C}$  to  $\pm 0.25^{\circ}\text{C}$  as a function of the air temperature

and relative humidity. Values for the accuracy, defined as a function of the above parameters, are available in the technical manual.

- Relative humidity (%) measured each minute; the measuring range varies between 0 and 100% with a resolution of 0.1%, the accuracy varies as a function of the air temperature and relative humidity. Values for the accuracy, defined as a function of the above parameters, are available in the technical manual.

The Decagon DS-2 measures the following parameters:

- Wind speed ( $\text{m}\cdot\text{s}^{-1}$ ) measured each minute; the measuring range varies between 0 to  $30 \text{ m}\cdot\text{s}^{-1}$  with a resolution of  $0.01 \text{ m}\cdot\text{s}^{-1}$  and an accuracy of  $0.30 \text{ m}\cdot\text{s}^{-1}$ .
- Wind direction ( $^{\circ}$ ) measured each minute; the measuring range varies between  $0^{\circ}$  to  $359^{\circ}$  with a resolution of  $1^{\circ}$  and an accuracy of  $\pm 3^{\circ}$ .

All stations are equipped with a SensorScope DS3 Data Acquisition System, an energy autonomous system powered by four AA batteries charged through a PV solar panel, which is able to collect and store the data measured by the instruments. Recorded data are transmitted by a GPRS communication board to the online platform Climaps, freely accessibly by users. The SensorScope DS3 is based on a system of master and slave stations, related to each other by radio links: gathered data are sent by the slave stations (1712 and 1713) to the master (1711) that collects them and transmit them every 15 minutes to the SensorScope server. Some problems in the battery recharging process appeared during the month of September: the station was not receiving enough solar irradiance, and consequently was automatically turned off by the system. In order to recharge the station, it was moved on 19<sup>th</sup> of September and attached to a wall, without any shadowing from trees. Due to the winter approaching, the station faced other battery recharging problems, as it was obstructed on the South side, where the sun shines during the winter time. Figure 5.48 shows the battery problems of the stations: WS-1713 is automatically switched off during nighttime (red circles), because the Sensorscope systems automatically switch off the station if the battery voltage is below 4.75 V. By contrast, WS-1711 faces the same problems, however not due to sun availability, but to the amount of data that it has to transmit to the hub. This station is the “master station”, the only one that can transmit the data received from the slave stations (WS-1712 and WS-1713, via radio), to the hub.

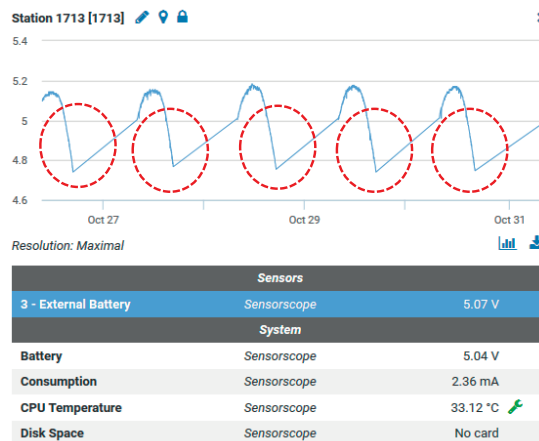


Figure 5.48 Battery problem in WS- 1713, during the month of October 2016. Extracted from the Climaps website.

### 5.4.2 Monitoring the outdoor environment

This chapter presents an analysis of the outdoor environment in selected locations of the site; the objective of this analysis is to quantify the impact of the built environment (ground covering, building design and orientation), as

well as the shadowing strategies (textiles and trees) and the evaporative cooling (pool and trees) on the microclimate. Results include:

- Air temperature.
- Wind speed.
- Mean Radiant Temperature, measured by the black globe.
- Wet Bulb Globe Temperature, measured by the black globe.

The data are analyzed in hourly, monthly and seasonal values, providing guidelines for appropriate design as a function of the period. The minimum average temperature during winter time corresponds to 19.9°C, 20.5°C and 20.1°C at weather stations WS-1711, WS-1712 and WS-1713 respectively, during the month of January (Table 5.9). During the mid-season, the temperatures are comfortable around 25°C. During the summer time, the weather conditions are extremely hot, with maximum average temperatures during the month of July, corresponding to 38.0°C, 37.3°C and 37.2°C at weather stations WS-1711, WS-1712, and WS-1713C, respectively. The vegetation has a positive impact on the microclimate: during the warmer season (from March to August): the air temperature recorded at WS-1713 is always lower than the one at the other stations, because this station is located on vegetation (WS-1713A and WS-1713C) or under a tree (WS-1713B). During the months of September and October the air temperature measured at Weather station 1713 was higher than the one measured at the other stations; this is due to a problem in data recording, being lost during nighttime, because, as previously mentioned, the weather station's battery was not able to fully reload itself due to an insufficient exposure to the sun. Consequently, the averaged air temperature was just based on the temperatures recorded during the daytime.

Month	Average Air Temperature (°C)				
	WS-1711	WS-1712	WS-1713A	WS-1713B	WS-1713C and D
November 2015	24.8	25.4	25.1		
December 2015	21.3	22.5	21.5		
January 2016	<b>19.9</b>	<b>20.5</b>	<b>20.1</b>		
February 2016	20.4	21.1	20.5		
March 2016	24.7	24.9	<b>24.3</b>		
April 2016	26.3	27.3	<b>26.3</b>		
May 2016	32.2	32.7	<b>31.1</b>	<b>32.1</b>	
June 2016	34.6	34.8		<b>34.0</b>	
July 2016	<b>38.0</b>	<b>37.3</b>		<b>35.1</b>	<b>37.2</b>
August 2016	37.6	37.9			<b>37.1</b>
September 2016	34.3	34.6			35.1
October 2016	30.6	30.8			31.4
November 2016	28.9	27.0			26.9
December 2016	25.1	24.0			23.9

Table 5.9 Average air temperature during the monitoring months, as recorded by each weather station.

The measured minimal and maximal temperatures show the impact of the built environment, as well as the greening, on the environmental conditions. The minimal temperature during winter time corresponds to 12.0°C, recorded by weather station WS-1711 during nighttime of the month of February (Table 5.10); the maximal temperature in this period correspond to 35.3°C, measured in Weather station WS-1712. During summer time the temperatures rise to 48.7°C during the month of July, always at weather station WS-1712 (Table 5.11). Based on the above results, it seems logic to think that the worst environmental conditions are the ones recorded by weather station WS-1712, but the analysis of the mean radiant temperature will bring us later to a different conclusion. Effectively, the fact that the air temperature is slightly higher in urban canyons was already underlined by onsite monitoring, where the recorded air temperature in the afternoon, within the urban canyon, were 2 to 3°C higher than the ones recorded on the rooftop of neighbors buildings (Portnov and Hare, 1999). In our case study, this

behavior is related to: i) lower wind speed, due to the built environment; ii) heat stored and emitted by neighbors buildings; iii) the weather station is attached to the wall, so it is partially affected by its thermal inertia.

Month	Minimal Air Temperature (°C)				
	WS-1711	WS-1712	WS-1713A	WS-1713B	WS-1713C and D
November 2015	18.3	18.7	18.1		
December 2015	12.5	14.4	12.5		
January 2016	13.2	13.7	13.7		
February 2016	<b>12.0</b>	12.6	12.0		
March 2016	16.7	16.7	16.9		
April 2016	16.1	16.6	16.5		
May 2016	20.4	21.4	22.1	23.5	
June 2016	19.6	25.1		24.7	
July 2016	29.3	29.3		29.3	29.7
August 2016	19.4	29.2			27.4
September 2016	8.9	27.7			27.4
October 2016	15.7	22.9			24.0
November 2016	20.3	19.5			19.5
December 2016	16.5	15.7			15.1

Table 5.10 Minimal air temperature during the monitoring months, as recorded by each weather station.

Month	Maximal Air Temperature (°C)				
	WS-1711	WS-1712	WS-1713A	WS-1713B	WS-1713C and D
November 2015	31.6	34.5	33.6		
December 2015	30.1	33.9	30.9		
January 2016	30.1	33.9	30.9		
February 2016	32.7	<b>35.3</b>	33.7		
March 2016	37.2	38.6	37.9		
April 2016	38.7	44.0	39.2		
May 2016	42.3	46.7	43.7	43.4	
June 2016	44.4	47.8		45.0	
July 2016	44.7	48.6		41.4	47.1
August 2016	46.3	<b>48.7</b>			46.7
September 2016	43.6	46.5			46.2
October 2016	37.4	40.7			37.7
November 2016	38.1	37.0			37.0
December 2016	31.7	35.0			33.8

Table 5.11 Maximal air temperature during the monitoring months, as recorded by each weather station.

Figure 5.49 shows the air temperatures of the selected locations as average values for each month. During the winter time, the average air temperature is higher at WS-1712. This is due to the fact that this station is surrounded by a built environment; consequently it is influenced by the solar irradiance reflected by buildings, as well as their surface temperature. The maximum difference between the weather stations was recorded during the month of December 2015, when the air temperature at Weather station 1712 was 1.2°C higher than the one measured at 1711. During summer time the built environment has a positive effect on the air temperature, reducing it by 2.9°C during the month of July 2016. Weather station 1712 measures the most extreme hot events, with a summer peak air

temperature of up to 48.7°C during the month of August. Another interesting point related to the air temperature is the difference between day and night, which is on average around 10 °C in daily values. This underlines a great potential in applying night cooling strategies on the site. By analyzing the annual average, the maximal difference between day and night is measured at WS-1711, where the average daytime temperature corresponds to 30.5°C and the nighttime one to 23.8°C. This is clearly due to the high sky view factor: WS-1711, completely exposed to the sky vault, exchanges the absorbed heat during daytime by infrared radiation with the cold night sky.

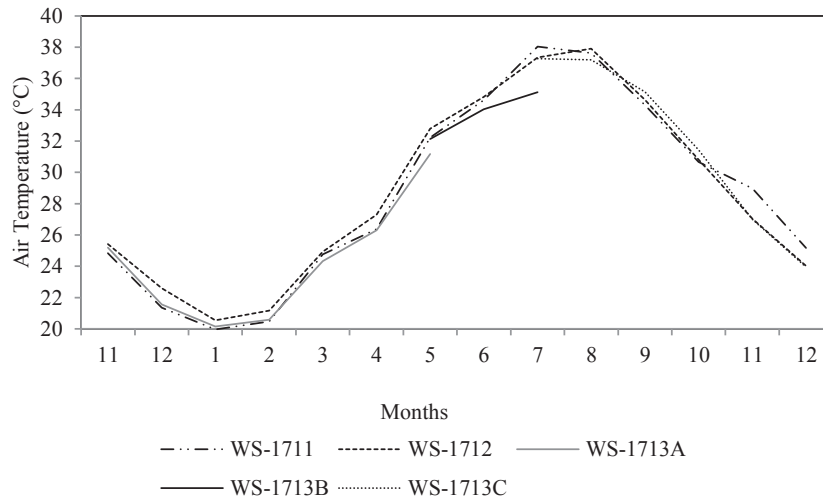


Figure 5.49 Average air temperature during the monitoring months, as recorded by each weather station.

Figure 5.50 shows the hourly air temperature at Weather station 1711; during the winter time the air varies between 32°C during daytime, and 11°C during nighttime. The average difference between day and night varies between 10°C during winter time and 14°C during summer time. As obvious, in Figure 5.52, measurements during the months of June and July were perturbed due to construction work on the site.

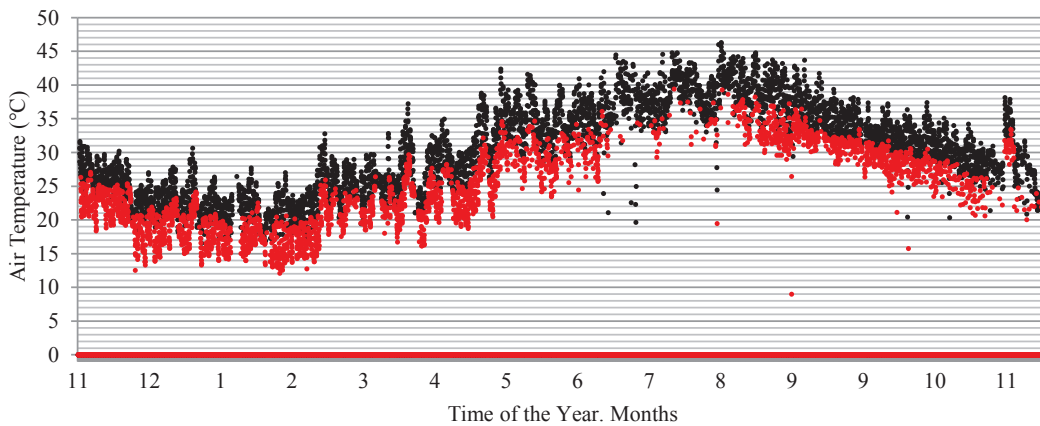


Figure 5.50 WS-1711, hourly air temperature measurements, during the daytime (black) and nighttime (red).

The difference between day and night is lower at WS-1712 and WS-1713 (Figures 5.51 and 5.52); this is due to the impact of the built environment, which stores the heat received during the day and emits heat during nighttime. The average difference between day and night corresponds to 6.5°C and 6.9°C in WS-1712 and WS-1713, respectively.

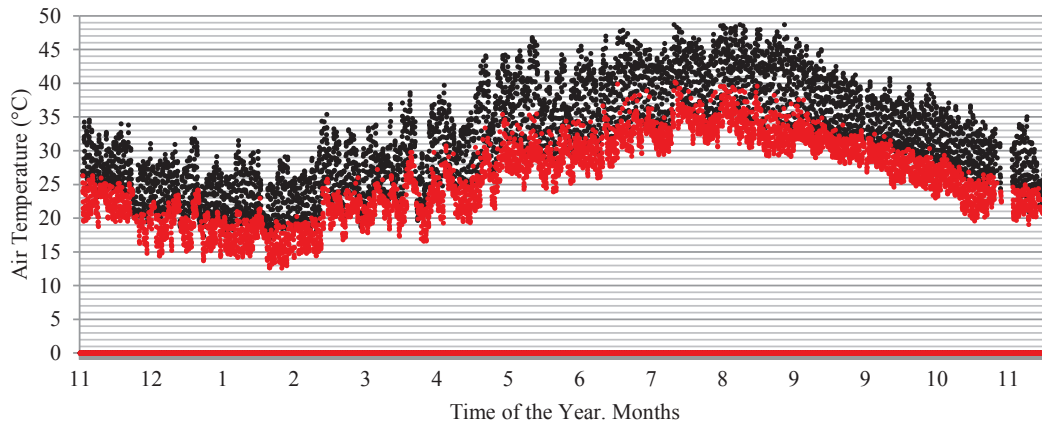


Figure 5.51 WS-1712, hourly air temperature measurements, during the daytime (black) and nighttime (red).

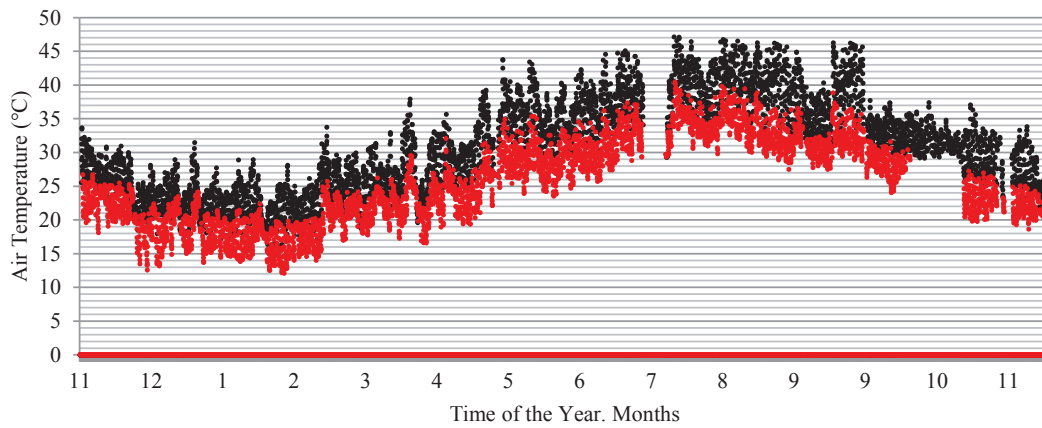


Figure 5.52 WS-1713, hourly air temperature measurements, during the daytime (black) and nighttime (red).

It is interesting to notice that the lowest air temperature recorded each day occurs during or slightly after sunrise. This is a well-known phenomenon, and it is related to two elements: first of all, during nighttime the outdoor surfaces radiate the stored heat with the night sky, which refreshes them, and consequently reduces the air temperature. When the sun rises, the sunrays are not yet warm enough to heat the surfaces, consequently they continue to emit the infrared radiation. On the other hand, after the sun rises, the evapotranspiration process starts (from greening and from the water ponds), also reducing the air temperature. The previous behavior is evident in Figures 5.53 and 5.54, which represents the air temperature as well as the total irradiance recorded at WS-1711 (on the rooftop) and WS-1713 (upon hedge). It is important to notice that the air temperature is slightly lower in WS-1713 after the sunrise; this is due to the shading provided by neighbor's buildings.



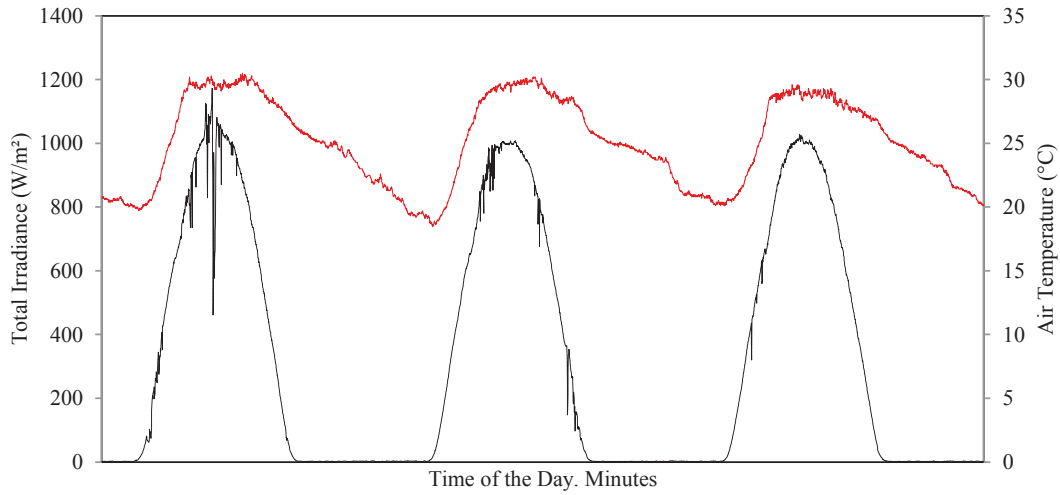


Figure 5.53 WS-1711. Total solar irradiance (black) as a function of the air temperature (red) during the 19<sup>th</sup>-21<sup>st</sup> April 2016.

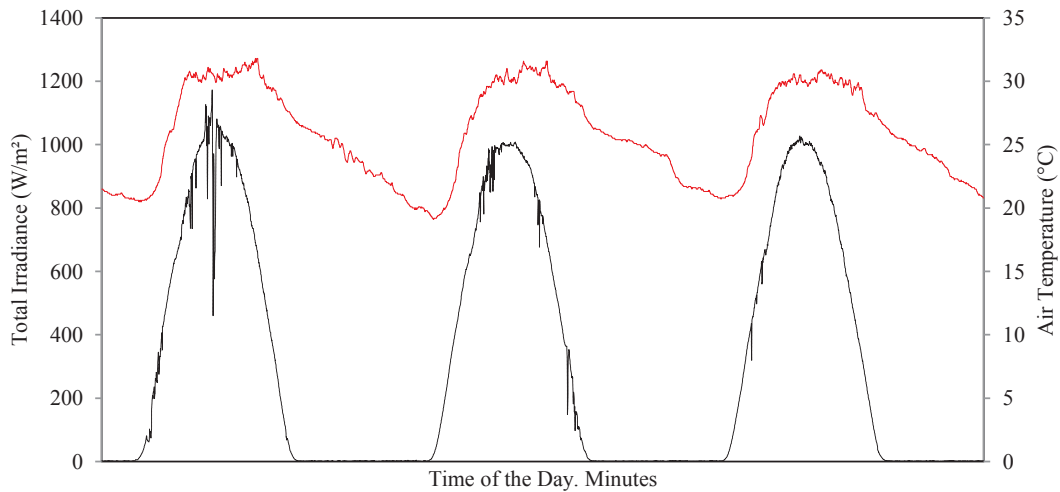


Figure 5.54 WS-1713. Total solar irradiance (black) as a function of the air temperature (red) during the 19<sup>th</sup>-21<sup>st</sup> April 2016.

Table 5.12 summarizes the average wind speed of the selected locations; on average the maximal speed is recorded on the rooftop of the building ( $1.20 \text{ ms}^{-1}$ ) by WS-1711. The average wind speed at WS-1712 is the lowest,  $0.26 \text{ ms}^{-1}$ , due to protection from the neighboring buildings. The first location of WS-1713, experiences the largest average wind speed: this is due to the Venturi Effect, as the wind that comes mostly from the South and South-West during the winter time is channeled between the enclosing walls and buildings.

Month	Average Wind speed (ms <sup>-1</sup> )				
	WS-1711	WS-1712	WS-1713A	WS-1713B	WS-1713C and D
November 2015	0.98	0.25	1.56		
December 2015	1.11	0.24	1.71		
January 2016	0.97	0.28	1.22		
February 2016	0.92	0.25	1.16		
March 2016	1.02	0.27	1.35		
April 2016	1.07	0.28	1.38		
May 2016	1.16	0.27	1.06	1.38	
June 2016	1.44	0.28		1.29	
July 2016	<b>1.62</b>	<b>0.28</b>		<b>1.10</b>	0.77
August 2016	1.47	0.21			0.53
September 2016	1.25	0.27			0.36
October 2016	1.27	0.23			0.19
November 2016	1.23	0.25			0.46
December 2016	1.32	0.24			0.29

Table 5.12 Average wind speed during the monitoring months, as recorded by each weather station.

In order to understand this phenomena, the wind speed was analyzed during the month of January 2016, on Weather stations 1711 (Figure 5.55) and 1713 (Figure 5.56). The most extreme events of wind speed are recorded by Weather station 1711; as an example on 28<sup>th</sup> of January the wind blows up to 8.46 ms<sup>-1</sup>. During the same day, the maximum speed at WS-1713 is 5.47 ms<sup>-1</sup>. By contrast, the minimal wind speeds (value counted each minute) are recorded on the rooftop (around 0.1 ms<sup>-1</sup>): at WS-1713 the minimum wind speeds are around 0.3 ms<sup>-1</sup>. This behavior shows that due to the difference of temperature between the vegetation and the artificial environment, a light breeze is always present near weather station 1713. This causes a larger hourly averaged wind speed on that site. Additionally, the averaged wind speed is higher when the wind comes from South- West (200°), as on 1<sup>st</sup>, 2<sup>nd</sup> and 18<sup>th</sup> of January, because it cannot find any obstruction from the built environment on its way. The wind is in fact channeled between the entrance gate and the construction site.

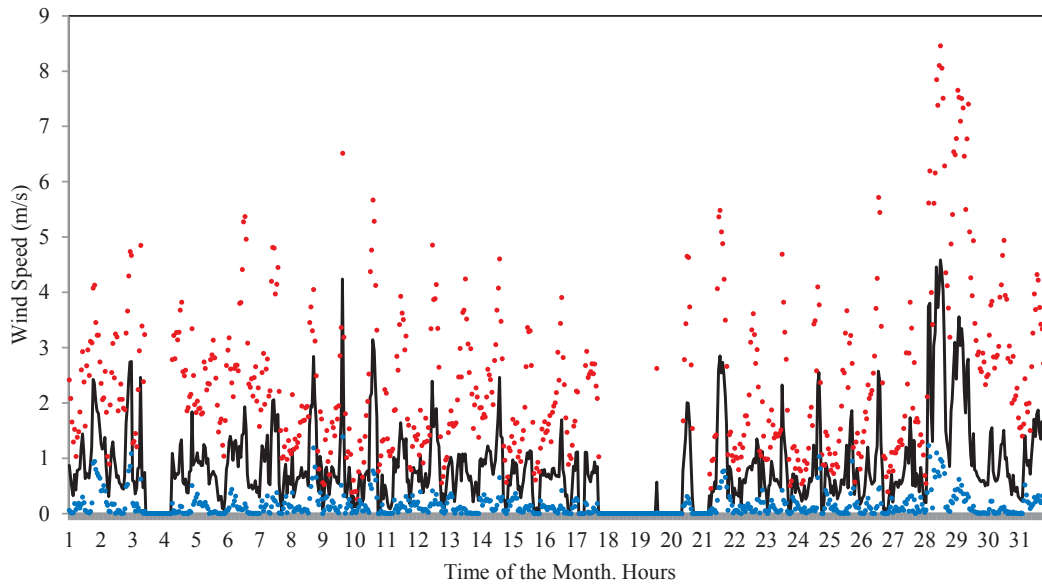


Figure 5.55 Weather station 1711. Wind speed during the month of January 2016. Wind speed max (red dots), wind speed min (blue dots) and average wind speed (black line).

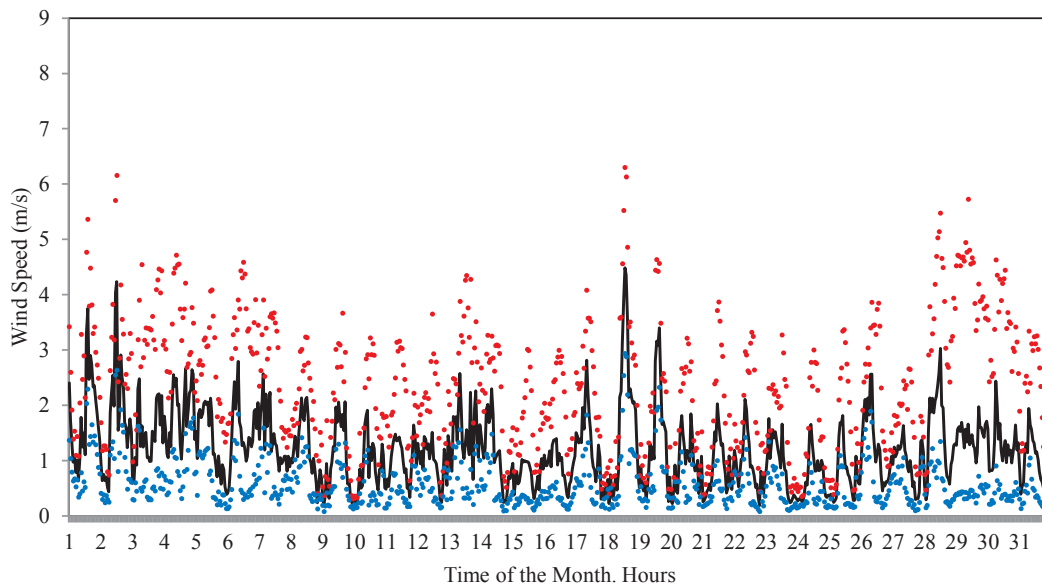


Figure 5.56 Weather station 1713. Wind speed during the month of January 2016. Wind speed max (red dots), wind speed min (blue dots) and average wind speed (black line).

Figure 5.57 shows the relationship between the wind speed and the wind direction at Station 1713: it is obvious that at Weather station 1713 the maximal wind speed is recorded for directions comprised between  $0^{\circ}$  and  $100^{\circ}$ , which correspond to the North East direction. By contrast, the lowest speed is observed from  $90^{\circ}$  to  $128^{\circ}$  (Eastern direction), because the kindergarten creates a barrier to the wind. Finally, the most frequent direction is from  $170^{\circ}$  to  $210^{\circ}$ , which corresponds to the Southern and South-Western direction.

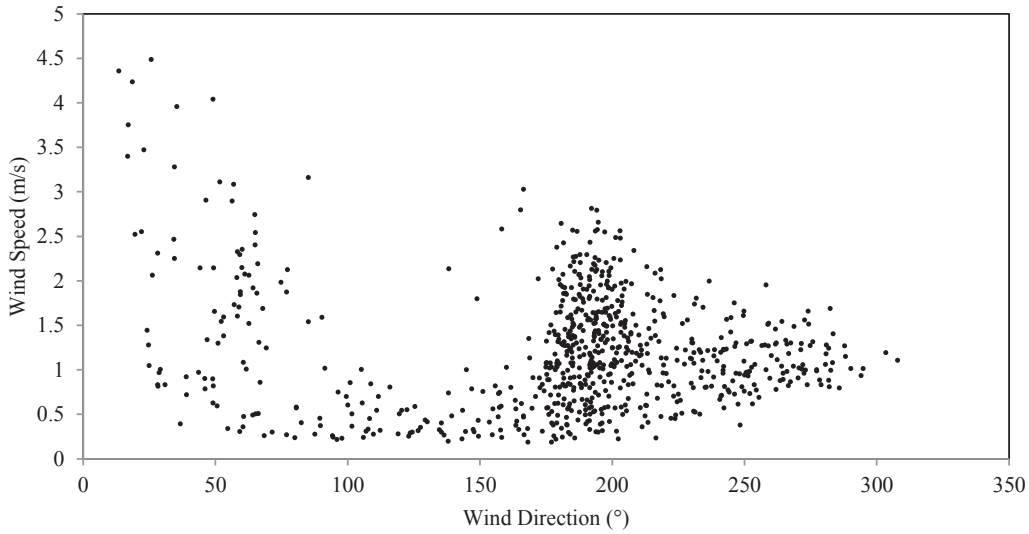


Figure 5.57 Correlation between the wind speed and the wind direction, as monitored by Weather station 1713, recorded during the month of January 2015.

The analysis of the wind speed during the month of July shows the wind path during summer time: the maximal wind speed is recorded by Weather station 1711, followed by 1713 (Figure 5.58). The lowest profile is the one recorded by Weather station 1712, where the average wind speed corresponds to  $0.28 \text{ ms}^{-1}$  and the maximum average speed to  $1.01 \text{ ms}^{-1}$ . This value is lower than the average speed recorded by WS-1713B and WS-1711, corresponding to  $1.62$  and  $1.10 \text{ ms}^{-1}$  respectively.

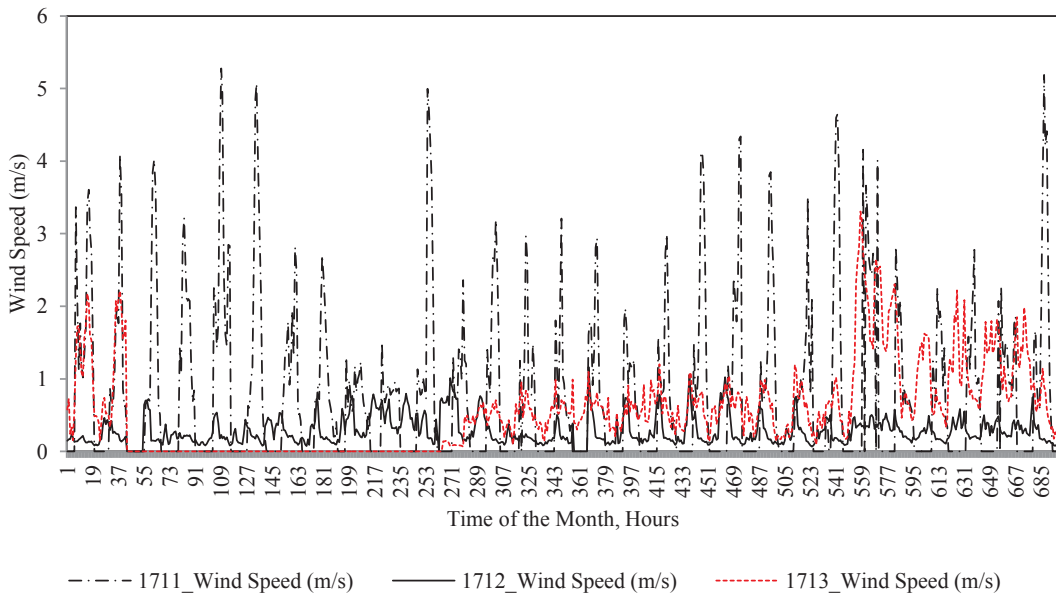


Figure 5.58 Wind speed as monitored by the three weather stations, during the month of July.

Finally, the analyses of the relative humidity are summarized in Table 5.13. The lowest average humidity is registered on the rooftop, due to the highest wind speed, as blowing increases the convection, reducing the humidity. In any case, the relative humidity is very similar in all locations, with a difference of less than 10%.

Month	Average Relative Humidity (%)				
	1711	1712	1713A	1713B	1713C
November 2015	55.89	56.17	56.27		
December 2015	61.84	60.76	62.28		
January 2016	65.83	64.52	64.84		
February 2016	62.63	61.81	62.90		
March 2016	58.80	61.38	62.70		
April 2016	48.77	49.93	53.00		
May 2016	44.98	47.55	46.85	54.10	
June 2016	44.74	46.80		49.04	
July 2016	46.69	52.41		59.89	50.62
August 2016	38.34	41.33			44.21
September 2016	56.83	59.07			53.29
October 2016	57.84	58.92			58.86
November 2016	55.62	60.24			58.50
December 2016	59.28	66.58			66.30

Table 5.13 Average relative humidity during the monitoring months, as recorded by each weather station.

The relative and absolute humidity are higher during nighttime compared to daytime. This behaviour is important when water is to be collected from humidity, as well as for cooling pavements. As an example, a ground cover subdivided into three parts: one small grid on the upper part, one layer of air and one metallic layer behind. Due to the colder temperature of the aluminium, the water condensates during nighttime, which enables potential water production from humidity and refreshes the air temperature. Figure 5.59 shows the relative humidity recorded by WS-1712 during the month of July. It is obvious that the difference between daytime and nighttime can be up to 46%, as for example during the 10<sup>th</sup> of July, where during the nighttime the maximal relative humidity corresponds to 85.5% and the minimum during daytime is 31.4%. As previously stated, the absolute humidity is also slightly higher during nighttime than during daytime. As an example, it corresponds to 22.23 gm<sup>-3</sup> in during daytime and 22.72 gm<sup>-3</sup> during nighttime during the month of July

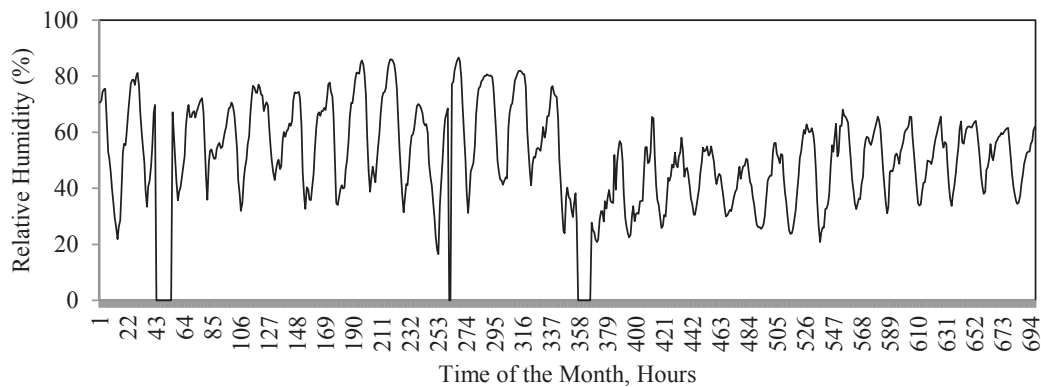


Figure 5.59 Weather station 1712. Relative humidity during the month of July 2016.

Based on the monitoring, the following potential technologies can be applied to make best use of the climate:

- Due to the elevated temperature difference between day and night, in order to reduce the energy required for air conditioning, cooling machines, such as heat pumps, can be used to produce cold during nighttime. The energy is then stored in order to be used during daytime.

- The relative humidity is larger during nighttime compared to daytime; the same trend is evident for the absolute humidity. This offers the possibility of creating architectural elements characterized by elevated thermal conductivity, able to favor water condensation during nighttime.
- The site is characterized by an unobstructed sky, and the direct solar irradiance is the maximum component of the radiative spectrum. There is therefore an enormous potential for solar systems.
- Due to the elevated wind speed on the rooftop of the building hosting the kindergarten, the use of wind towers is proposed, in order to refresh the semi-outdoor environments.

#### *Analysis of the Mean Radiant Temperature*

As shown in the above analysis, Weather station 1713 presents a higher wind speed and a lower air temperature than WS-1712. But the missing element is the irradiance, which is not quantified by the weather stations, but can be analyzed through the mean radiant temperature. The following analyses are carried out to quantify the variation of the MRT in the selected outdoor environments. Table 5.14 summarizes the average monthly MRT at 1712 and 1713A. 1713 A is located near the entrance of the school, without shadowing and placed upon irrigated vegetation. Due to the absence of shadowing, the MRT is higher than at the other station, by up to 3.6°C during the month of February: 24.3°C at WS1712 and 27.8°C at WS1713. The difference is larger when considering the daytime data: in this case the difference corresponds to 8.9°C. Figure 5.60 shows the MRT recorded by both weather stations during the month of February. During the daytime the MRT recorded by WS1713 is 10°C higher than the one recorded by WS1712. During nighttime, due to the sky view factor, it is lower at WS1713 than at WS1712. Effectively, during nighttime the MRT is 1 up to 5°C lower at Weather station 1713; by contrast at Weather station 1712, it is higher during daytime. Normally the maximal differences are recorded from 8:00 to 15:00 hours (UTCI). Effectively, during winter time, the sun shines upon Weather station 1713 from 8:00 hours; before this time the station is shadowed by the adjacent buildings located on the Eastern side of the station. Then the sun sets around 15:00 hours UTCI, which corresponds to local 17:00 hours.

Month	Part of the Day	MRT (°C)	MRT (°C)	Difference (°C)
December 2015	All Day	24.6	26.3	-1.6
	Daytime (8 :00- 18 :00)	28.3	34.3	-6.0
January 2016	All Day	23.3	25.6	-2.3
	Daytime (8 :00- 18 :00)	27.8	34.4	-6.5
February 2016	All Day	<b>24.3</b>	<b>27.8</b>	-3.5
	Daytime (8 :00- 18 :00)	<b>29.5</b>	<b>38.4</b>	-8.9
March 2016	All Day	28.1	30.6	-2.5
	Daytime (8 :00- 18 :00)	32.8	39.3	-6.5
April 2016	All Day	35.4	34.4	1.0
	Daytime (8 :00- 18 :00)	41.7	42.7	-1.0

Table 5.14 Average Mean Radiant Temperature recorded by Weather stations 1712 and 1713 A.



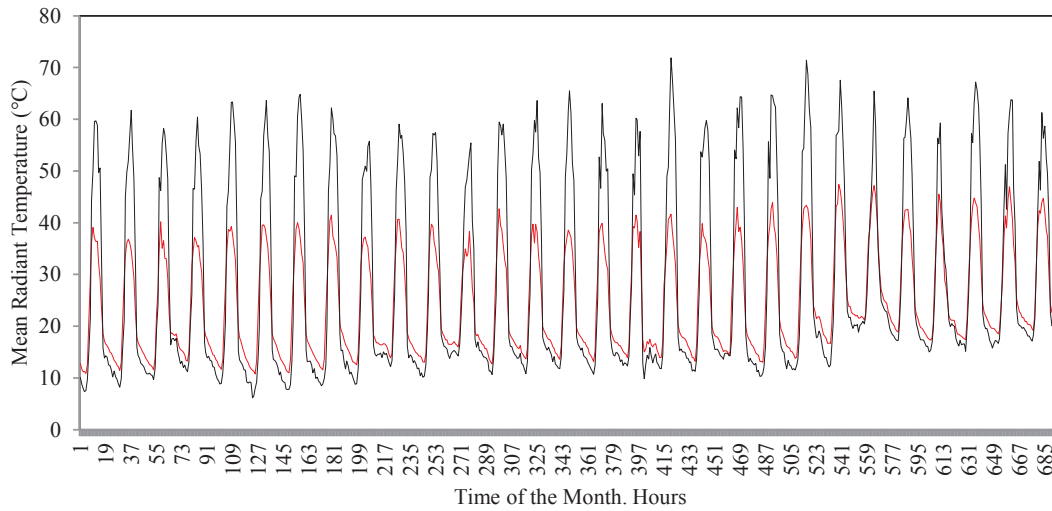


Figure 5.60 Weather stations 1712 (red) and 1713 (black). Mean Radiant Temperature during the month of February 2016.

The positive impact of trees is evident during the month of August, when the MRT recorded under a tree is on average 1.8°C lower than the other one. The MRT is constantly lower during daytime, as well as during nighttime, as illustrated in Figure 5.61. Naturally, the impact of trees is stronger during the days characterized by direct solar irradiance, such as the 30<sup>th</sup> and 31<sup>st</sup> of August. It is important to notice that the difference of temperature is between the globe located under the tree and the one located under the meshes. Additionally it is important to underline that the tree is young, consequently the measured variation is also related to the urban environment.

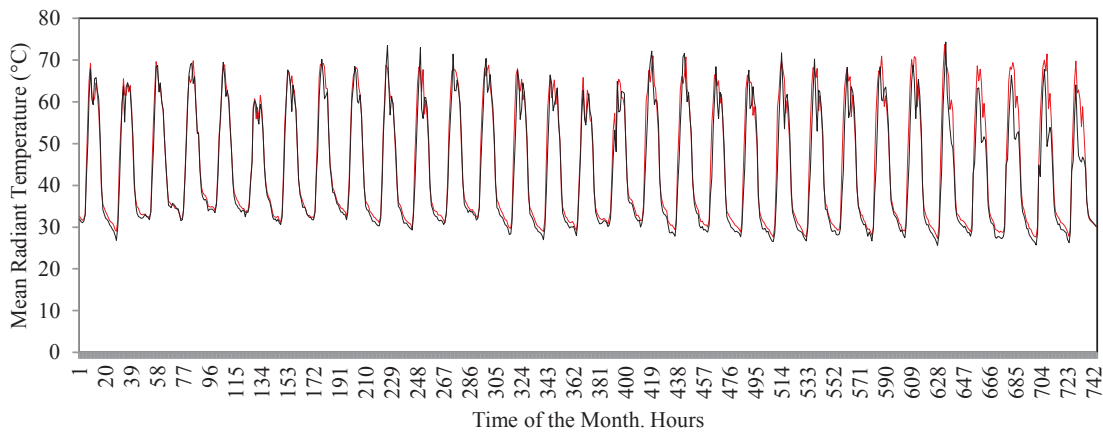


Figure 5.61 Weather stations 1712 (red) and 1713 (black). Mean Radiant Temperature during the month of August 2016.

The difference in absolute humidity between the two locations is larger during daytime; this is due to the evapotranspiration process created by the tree as well as by the vegetation upon the soil. As presented in the above case studies, the absolute humidity is slightly higher near the vegetation (trees or small bushes) compared to paved surfaces (Shashua-Bar et al., 2009a) (Snir et al., 2016) (Jonsson, 2004). This phenomenon is evident in Figure 5.62, where the absolute humidity for the month of August is presented, as recorded from the WS- 1712 (in average 17.81 gm<sup>-3</sup>) and WS-1713 (in average 18.67 gm<sup>-3</sup>).

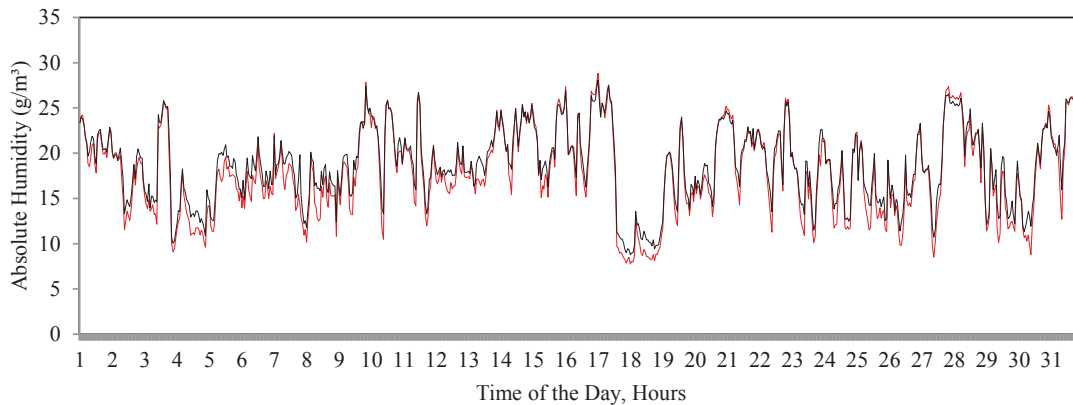


Figure 5.62 Weather stations 1712 (red) and 1713 (black). Absolute humidity ( $\text{gm}^3$ ) during the month of August 2016.

Finally, in the last location, WS1713 D, the MRT is higher than the one recorded at WS1712; in WS1713D no shadings exist and the maximal average difference is recorded during the month of November, up to  $1.65^\circ\text{C}$ . The onsite monitoring clearly shows the positive impact of shadowing devices as well as greening on the mean radiant temperature.

#### Analysis of the Wet Bulb Globe Temperature

The Wet Bulb Globe Temperature Index (WBGT) was first defined to prevent heat induced illness in military training camps, then recognised as a standard by ISO 7243 (International Organization for Standardization, 1989). WBGT is based on three simultaneous analyses: globe ( $T_g$ ), dry ( $T_a$ ), and wet bulb temperature ( $T_w$ ).  $T_g$  is related to the air velocity, irradiance and air temperature, while  $T_w$  depends on the ease and the evaporation (Budd, 2008). WBGT for the outdoor environment is defined as:

$$WBGT = 0.7 T_w + 0.2T_g + 0.1T_a \quad (5.3)$$

Results obtained by WBGT need to be compared with tables presented in ISO 7243 (International Organization for Standardization, 1989), showing for each metabolic activity the corresponding comfort value (standard clothing insulation:  $\text{clo} = 0.6$ ). Children perceive and react differently than adults to the environment, because of physiological and anatomical differences, as underlined by the American Academy of Pediatrics (Pediatric, 2000):

- Children receive greater heat or cold gains than adults from the environment, due to their greater surface area-to-body mass ratio (BSA/M): a child of 8 years old has 50% more BSA/M compared to an adult (Hugh et al., 2009). Consequently, children are good heat convectors and radiators (Davies, 1981).
- During physical activities, such as walking or running, children produce more metabolic heat per mass unit.
- Sweating capacity, and consequently the capacity of children to dissipate heat by evaporation, is lower in children than in adults: a child of 9 years old has approximately half the capacity to sweat of an adult male (Hugh et al., 2009). This is related to the lower sweat output per gland, as well as a lower cholinergic sensitivity (the cholinergic system is responsible for sweating, through acetylcholine) (Gomes, 2013).

Several thermal scales exist to analyze the WBGT; in this analysis two scales will be used: one for children performing sport activities, and another one for adults. The thermal scale of WBGT for children's sports activities, as defined by the American Academy of Pediatrics (Pediatric, 2000), is summarized in Table 5.15.

WBGT (°C)	Restrains on activities for children	Thermal sensation
<24	All activities allowed, but be alert for the heat-related illness in prolonged events.	Comfortable
24-25.9	Longer rest periods in the shade; enforce drinking every 15 minutes.	Warm
26-29	Stop activity of unacclimatized persons and high-risk persons; limit activities of all others (disallow long-distance races, cut the duration of other activities).	Hot
>29	Cancel all athletic activities.	Very Hot

Table 5.15 Wet Bulb Globe Temperature and related activities for children (Pediatric, 2000).

The thermal scale for adults, as available from the technical manual of the black globe used in the monitoring, is given in Table 5.16.

WBGT (°C)	Restrains on activities for adults	Thermal sensation
<26	No restraints on activities.	Comfortable
26-27.5	Precautions should be taken. Water intake should be a minimum of 0.5 liters/hr. The work/rest cycle for an acclimatized person should be 50/10 min/hr.	Slightly Warm
27.5-29	Increased water intake should be encouraged. Water intake should be 0.5 to 1 liters/hr. The work/rest cycle for an acclimatized person should be 50/10 min/hr.	Warm
29-31	Increased supervision of personnel performing physical activity is required. Water intake should be 1 to 1.5 liters /hr. The work/rest cycle for an acclimatized person should be 45/15 min/hr.	Hot
31-32	Physical activity should be limited to a maximum of 6 hours per day for fully acclimatized personnel. Water intake should be 1.5 to 2 liters/hr. The work/rest cycle for an acclimatized person should be 30/30 min/hr.	Very Hot
>32	All strenuous activity should be suspended. Water intake should be a minimum of 2 liters/hr. The work/rest cycle for an acclimatized person (non-strenuous activity) should be 20/40 min/hr.	Sweltering

Table 5.16 Wet Bulb Globe Temperature and related human activity, as defined by the technical guide of the Black Globe (Campbell, 2015).

The critical threshold for performing outdoor activities is 24°C for children and 26°C for adults. All children’s activities should be stopped if the WBGT is higher than 29°C, a value that is considered as threshold in the followings analyses. Tables 5.17 and 5.18 summarize the average monthly WBGT for each point of measurement; the color of the cells corresponds to the thermal scale previously defined for children.

Table 5.17 presents the average WBGT throughout the day; all point of measurements (1712, 1713A, 1713B and 1713C) show similar results: between December and April the outdoor environment is comfortable, and no precaution is recommended (green label, which corresponds to a WBGT<24°C). From the month of May onward, the WBGT increases further (orange label, which corresponds to a WBGT comprised between 26 and 29°C): all activities should be stopped for unacclimatized persons and high-risk persons, all other activities should be restricted. The station 1713 A does not show any need for limitations, but this is related to the fact that the station was only active until 15<sup>th</sup> of May, which means that it did not register temperatures during the last and hottest part of the month. During the summer months the WBGT increases further: June is characterized by an orange label, which corresponds to a WBGT comprised between 26 and 29°C. July is characterized by the color red (WBGT higher than 29°C), reaching 31.91 °C at Station 1712. As for the month of May, the lowest WBGT occurring at Weather station 1713B is related to the fact that the measurements were made just for the first days of the month. This label underlines that all outdoor activities should be restricted, due to the hot environmental conditions.

Month	Average WBGT (°C)			
	1712	1713A	1713B	1713C and D
November 2015	18.3	17.6		
December 2015	17.6	17.4		
January 2016	17.9	17.7		
February 2016	21.0	20.7		
March 2016	22.6	21.9		
April 2016	27.1	25.4	27.2	
May 2016	28.2		27.6	
June 2016	31.9		30.9	31.3
July 2016	30.3			29.7
August 2016	30.0			29.3
September 2016	26.4			27.0
October 2016	23.1			22.7
November 2016	21.0			19.9

Table 5.17 Measured Wet Bulb Globe Temperature (°C), averaged for each month. All day data.

The above Table represents the WBGT as calculated during the entire day; further analysis aims to quantify the WBGT during the daylight hours. Results are presented in Table 5.18: all athletic activities have to be cancelled during daytime from the month of May until September. This results represents the averaged WBGT, consequently, as presented below, there is a WBGT variation during daytime. It is nice to notice that the month of August presents a lower WBGT than the months of July and September. This is related to the relative humidity, corresponding to 41% in August, 52% in July and 59% in September.

Month	Daytime_ Average WBGT (°C)			
	1712	1713A	1713B	1713C and D
November 2015	19.7	19.4		
December 2015	19.2	19.1		
January 2016	19.8	19.7		
February 2016	22.3	22.1		
March 2016	24.4	23.5		
April 2016	29.2	26.9	29.0	
May 2016	31.5		30.6	
June 2016	33.8		32.5	33.1
July 2016	30.3			29.7
August 2016	31.5			31.1
September 2016	28.0			27.4
October 2016	24.7			24.7
November 2016	22.6			22.1

Table 5.18 Measured Wet Bulb Globe Temperature (°C), averaged WBGT for each month. Daytime data.

A further detailed analysis of the WBGT is performed by calculating the sum of hours characterized by the same temperature. During the winter time, between December and February, the hours characterized by a WBGT higher than 24°C correspond to less than 7% of the time. By contrast, from April onward, an increase of discomfort is evident: only 64% and 70% of the time are “comfortable” for outdoor activities, in location 1712 and 1713 respectively. During the month of May, during less than half of the time the outdoor environment is “comfortable” (22% and 27 % respectively), with an increase of stress events (WBGT>29°C). During the summer months (June, July and August), the outdoor environment is “too warm” for outdoor activities:

- June: “comfortable” environment for 4.63% and 7.50% at 1712 and 1713, respectively.
- July: “comfortable” environment for 0.00% and 0.77% at 1712 and 1713, respectively.
- August: “comfortable” environment for 1.62% and 0.81% at 1712 and 1713, respectively.

Naturally, the school is closed during summer time, and for this reason such values of WBGT are not preoccupying for students' health. The above results are quantified using the children thermal scale; results are less negative when using the adults' thermal scale (Table 5.16), effectively acceptable WBGT rise to 26°C.

One of the main limitations of the WBGT is the fact that this model shows an inadequate response to the variation in relative humidity and wind speed. The problem is that the WBGT underestimates the impact of wind on the outdoor thermal comfort, as well as the human's evaporative capacity as a function of the relative humidity (Budd, 2008).

## 5.5 Conclusions and future outlook

This chapter presented a work performed in order to improve the energy performance of buildings and the outdoor human comfort in the campus of the Swiss International School of Dubai. The energy study was performed in a continuous dialogue with the architects, in order to improve the energy efficiency of their project by giving propositions and recommendations. Based on the simulations, the energy demand of the buildings was decreased by 32% compared to "best practice" in Dubai, and by 78% compared to existing buildings. Based on the proposed strategies, a final design of the campus was performed by DSA Architects International: the new design improved the openings onto the courtyard and reduced the windows exposed to the East and West. The colors of the facades vary as a function of their albedo and the roofs were designed as white tilted surfaces. The analyses performed in collaboration with Kriesi Energie GmbH and Sorane SA allowed the setting up of the first Minergie Building in the UAE. The second part of the chapter investigated several strategies in order to improve the outdoor human comfort and analyzed the on-site monitoring performed during the last year. Planting native trees in the campus reduces the number of hours of discomfort. During measurements in June for example, plants increased significantly the number of "comfortable" hours from 37 hours (without plants) to 48, 62 and 43 hours (with Ghaf Trees, Acacia Trees and Palms). Finally, twelve hours of "very hot" thermal sensation in August without any plants are halved to 6 hours with Ghaf Trees and to nil by planting Acacia Trees and Palms. Based on the monitoring, the positive impact of trees has been demonstrated, as they can reduce the mean radiant temperature by 1.81°C, as recorded during the month of August 2016. Additionally, shading devices, such as the one protecting Weather station 1712, could reduce the MRT by up to 8.94°C (daytime average) during the month of February. Finally, the Comfort Map underlines the thermal behavior of the campus, by using the climatic data provided by the on-site weather stations. It was interesting to notice that by comparing the monitoring and the results obtained by the software, the difference is within the experimental error of the 9%, and with a maximal difference lower than 3°C.

### *Future outlook*

The Index of Thermal stress was quantified for adults. Considering that the school is occupied by young students, a further improvement of the model will be to consider children's thermal sensation through the ITS. In order to do so, on-site questionnaires are required. The proposed survey will be subdivided into two types of surveys: a questionnaire for students and a questionnaire for the academic staff. The first questionnaire will be written to quantify the thermal sensation of students located in the open playground area on the first floor of the building; the questionnaire will be handed to the students by the teacher, before and after the sport activity. The second questionnaire will be filled on an iPad positioned in the outdoor environment, near the entrance of the school and an open swimming pool with seats. The interface of the iPad is composed of three pages, where the subjects will express their thermal sensation, in a seven point scale ("very hot", "hot", "too warm", "neutral", "too cool", "cold" and "very cold"), their perception of solar irradiance, wind speed and humidity, their metabolic activity during the past 15 minutes and their clothing. The form of the questionnaire will be based on above research performed in hot climate (Ng, 2010) (J. Spagnolo and De Dear, 2003) (Ng and Cheng, 2012).

Considering that the building is the first example of a Minergie building in UAE, it is an extraordinary test case. Consequently, on-site monitoring will be required in order to understand the thermal behavior of the campus and improve or modify the Minergie Standard in the UAE.





# Chapter 6 Hybrid Algorithm Optimization with Heuristics

## 6.1 Introduction

This chapter presents the optimizations performed for the case studies of the EPFL campus in Lausanne and the Swiss International School Campus in Dubai. To perform the optimizations, an hybrid Evolutionary Algorithm (CMA-ES/HDE) (J. H. Kämpf, 2009) was used to identify the optimal design for both campuses improving the energy performance of buildings (heating and cooling) and improving the outdoor human comfort. In this chapter, the assessment of the outdoor human comfort is realized using the COMFA\* budget and the Index of Thermal Stress (ITS). The ITS and COMFA\* are optimized during daytime, from 8:00 to 18:00 hours, considering that both campuses are in prevalence occupied during daytime. All analyses were performed for actual and future climatic scenarios: the actual scenario corresponds to a Typical Meteorological Year (averaged data from the last 10 years), the future scenarios are based on the meteorological data provided by the Intergovernmental Panel on Climate Change (IPCC) (IPCC, 2000). Both climatic files are issued from the software Meteonorm (Remund et al., 2015).

In order to understand how the optimization is realized, the following chapter gives an introduction on the optimization processes. Optimization methods imply a mathematical description of several variables of a problem with different constraints, in order to find the optimal solution. The optimization problems can be divided into two main categories, according to the objective: the single and multi-objective optimization. A single-objective optimization shows only one optimum solution to maximise or minimize the objective function; on the other side a multi objective optimization, where two or more objective functions coexist, leads to a solution set, also called Pareto solution set, which forces the decision maker to choose the best solution between the proposed ranges of solutions (Ooka et al., 2008). The formulation of the multi-objective optimization, in accordance with some authors, is traced back to 1776, with the treatise of “The Wealth of Nations” by Adam Smith (Coello et al., 2007). Different computational optimization algorithms exist: evolutionary algorithms (Genetic Algorithms, Evolutionary Programming, Covariance Matrix Adaptation Evolutionary Strategy and Differential Evaluation) and meta-heuristic algorithms (Harmony Search, Particle Swarm Optimisation, Ant Colony Optimization and Simulated Annealing). Among the different models, the evolutionary algorithms allow to determine the optimal solution in accordance with the Darwinian principle of survivor: during each optimization step, so called generation, the selection is realised In accordance with mutations and crossovers, the poorest individual or set of variables being eliminated; the final selection defines the fittest individuals (Evins, 2013). Consequently, the *individual* represents the encoded solution of the problem: it corresponds to a biological *genotype*. A genotype is composed of one or more *chromosomes*, made of *genes* and characterized by a certain value, which is the *allele*. The *population* is composed by a set of chromosomes (Coello et al., 2007). Between several evolutionary algorithms, the hybrid algorithm CMA-ES/HDE (J. H. Kämpf, 2009), made of the covariance matrix adaptation algorithm (CMA-ES) and the hybrid differential evolution (HDE), was selected. The hybrid CMA-ES/HDE algorithm was chosen, because it was developed to perform urban optimization, and consequently should be the most appropriate algorithm for the optimization of both outdoor human comfort and energy performance of buildings at the campus scale. The hybrid algorithm CMA-ES/HDE considers two populations: popHDE (Hybrid Differential Evolution Algorithm) and popCMA-ES (Covariance Matrix Adaptation Evolution Strategy). Firstly the optimization runs with the evolution of

the population CMA-ES: the best  $n_t$  individuals will feed the HDE population, the missing individuals are randomly generated ( $NP - n_t$ ). The simulation continues creating best fitted individuals, until the stopping criterion is met. The procedures of the hybrid algorithm, based on the combination of two algorithms, can be described as follows:

- CMA-ES algorithm is composed of four stages: recombination, mutation, selection and final adaptation
- HDE algorithm is composed of four stages: recombination, mutation, selection and final migration to reduce the final population.

As observed in previous research projects (Kämpf and Robinson, 2009), the HDE offers a robustness in finding the global minimum, and the CMA-ES component provides a faster convergence.

Several studies were already performed using the hybrid CMA-ES HDE algorithm: the optimization of an urban form by improving the capture of the solar irradiation (Kämpf and Robinson, 2010) and the improvement of the energy efficiency of a city district by assuming the buildings height and the glazing ratio as input parameters (Vermeulen et al., 2013). At the building scale, it was used to maximise of the solar irradiation and its impact on the building form (Caruso, 2013), as well as to improve the physical characteristics of a passive house in Portugal (Figueiredo et al., 2016), improving its energy performance.

During the last ten years, just a few papers were written regarding the optimization of the outdoor human comfort: a case study realized in Tokyo for a typical summer day (23<sup>rd</sup> of June). The design objective of defining the optimum arrangement of trees and buildings was performed by improving the outdoor human comfort (decreasing the average Standard Effective Temperature), reducing the cost of planting trees and increasing the pedestrian view expressed by the sky view factor (Chen et al., 2008). Another case study was performed in the city of Novi Sad (Serbia), where the outdoor human comfort, assessed using the Universal Thermal Climate Index (UTCI), was optimized with Grasshopper for several street arrangements (Bajšanski et al., 2015). The potential of applying optimization processes in urban design is elevated, as described in the case of the Dubai Silicon Oasis, in which the use of Grasshopper and ANSYS CFD (a fluid dynamics program) allowed the authors to improve the energy performance of buildings by increasing the natural ventilation of the site (Taleb and Musleh, 2015).

The objective of this optimization procedure is to improve the energy performance of buildings as well as the human comfort in the built environment; the optimization is applied to the EPFL Campus in Lausanne (temperate climate) and the Swiss International School Campus in Dubai (hot arid climate). The outdoor human comfort is quantified using the COMFA\* and ITS methods, for the current and future climatic scenarios. The urban environment influences the outdoor human comfort in several ways: through the radiative balance (shortwave and longwave radiation received by the pedestrian), the wind (wind path variation in the built environment) and evaporation processes on the site (presence of water bodies or vegetation). The results of the optimization will be used to outline final recommendations for bioclimatic and sustainable campuses in hot arid and temperate climates.

## 6.2 The EPFL Campus

The EPFL campus in Lausanne was considered in Chapter 4, outlining the heating and cooling demand of the campus and outdoor human comfort in actual and future climatic scenarios. Based on the current model of the site, two zones of the campus were selected, as shown in Figure 6.1: one zone is characterized by a natural environment (site coverage equals to 0.43, plot ratio equals to 1.38) with a bocce court and an experimental garden (Zone-A), the second one is characterized by a man-made environment (site coverage equals to 0.53, plot ratio equals to 1.37) with asphalt covering, and just a few grass and trees (Zone-B).

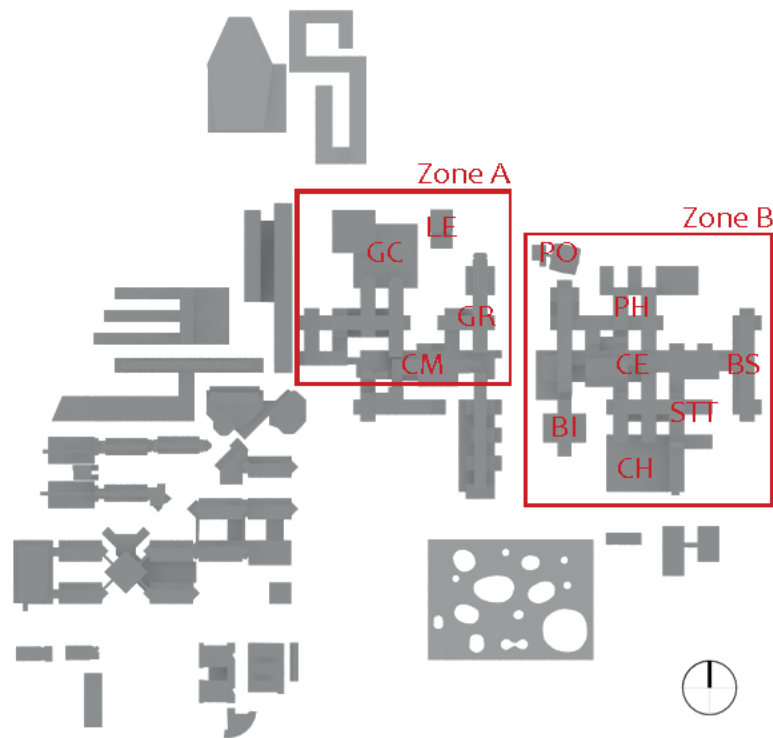


Figure 6.1 Top view of the EPFL Campus, with the two selected areas: Zone-A, characterized by a low density and two natural areas and Zone-B, characterized by a denser built environment.

The design objective of Zone-A is to improve the energy performance of buildings, for heating and cooling, and improving the outdoor human comfort, by increasing the number of hours characterized by a “comfortable” thermal sensation. The optimization is made by varying the properties of the envelope, optimizing the type of trees, varying the albedo of surfaces and the ground covering. As in the previous case study, the optimization runs for current (TMY) and future climatic scenarios (2050-B1 and 2100-B1). Between the three future scenarios, available from IPCC (B1, A1B and A2), B1 was selected. Effectively, it represents the lowest increase of the air temperature (in annual average:  $+2^{\circ}\text{C}$  in 2050-B1 and  $+2.67^{\circ}\text{C}$  in 2100-B1) and was selected following the 2015 United Nations Climate Change Conference held in Paris (30<sup>th</sup> November- 12<sup>th</sup> December), in which a common goal was for the globe temperature (increase lower than  $1.5^{\circ}\text{C}$ ). It is important to notice that climate change will impact differently the world areas, and that the minimal expected increase of the ambient temperature in Switzerland corresponds to  $2^{\circ}\text{C}$ .

The design objective of Zone-B is to improve the energy performance for heating and cooling of the selected district by: increasing the thermal insulation, replacing the windows and improving the air tightness of the envelope. The optimization is defined for the actual (for a Typical Meteorological Year provided by Meteonorm) as well as future climatic scenarios (2050-B1 and 2100-B1).

The criterion to perform both optimizations is to underline the importance of a correct environmental design: if Zone-A focuses on the energy performance of buildings, as well as on the microclimatic conditions of the site, Zone-B focuses “only” on the energy performance. The main question is: should a sound urban design focus on the outdoor human comfort (that brings an indication on the urban microclimate), as well as the energy performance of buildings, in a temperate climate? If yes, what is the impact of a sound environmental design on the energy performance of buildings?

### 6.2.1 Zone-A\_ Optimisation of the energy demand for heating and cooling and the outdoor human comfort

#### *Design objectives*

The objective of this optimization is to improve the energy performance of the EPFL campus in Lausanne, as well as the daytime outdoor human comfort, by improving the heating and cooling demand of buildings and the COMFA\* budget of the pedestrians. The optimisation is performed, as in the previous case study for a Typical Meteorological Year, as well as in future climatic scenarios 2050-B1 and 2100-B1. The interesting element is the variation in the energy demand of the campus in future climatic scenarios as well as the strategies needed to improve the outdoor human comfort. The outdoor human comfort is quantified by the COMFA\* budget, which is improved during daytime (from 8:00 hours to 18:00 hours), considering that people live in the outdoors landscape of the campus during daytime, in their free time (in-between the university courses, as well as during lunchtime).

#### *Analysis target*

The selected area is composed of four buildings (Figure 6.2 and 6.3): CM, GC, GR and LE. All of them, except for LE, are part of the first stage of construction of EPFL (1972- 1984), and consequently present the same envelope characteristics. The analyses are performed for a typical meteorological year, and for two future climatic scenarios 2050 B1 and 2100-B1. The ground covering of the site is subdivided into three categories: street (made of asphalt), natural soil and grass. In the same site 13 trees are positioned, with a maximal height of 5 m; they do not exist yet, but they are used to outline their potential impact on outdoor human comfort, as well as on the energy performance of buildings. Six points of evaluation for the COMFA\* budget (Figure 6.2) are placed in the outdoor environment:

- P1, P2 and P3 are located in the outdoor environment without any shadowing protections, and upon the grass, the clay soil and the asphalt, respectively
- P4 is positioned upon the clay soil and under the textile mesh
- P5 is located under the tree and upon the grass
- P6 is positioned under a tree and upon the asphalt.

Hybrid Algorithm Optimization with Heuristics

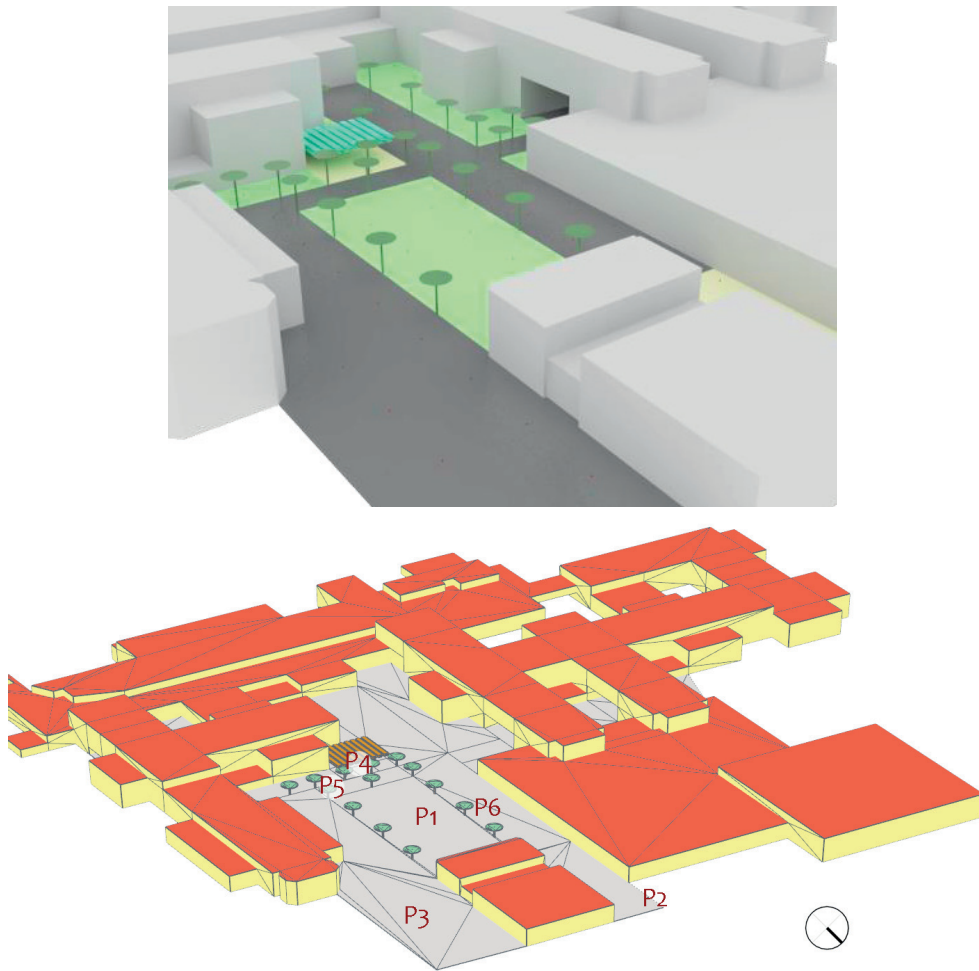


Figure 6.2 EPFL campus, Zone-A. Optimization of the outdoor thermal comfort and the energy performance of buildings. Green: grass; Gray: asphalt; Yellow: natural soil (top). 3D view from CitySim Pro, with indication of the COMFA\* points of measurements (bottom).



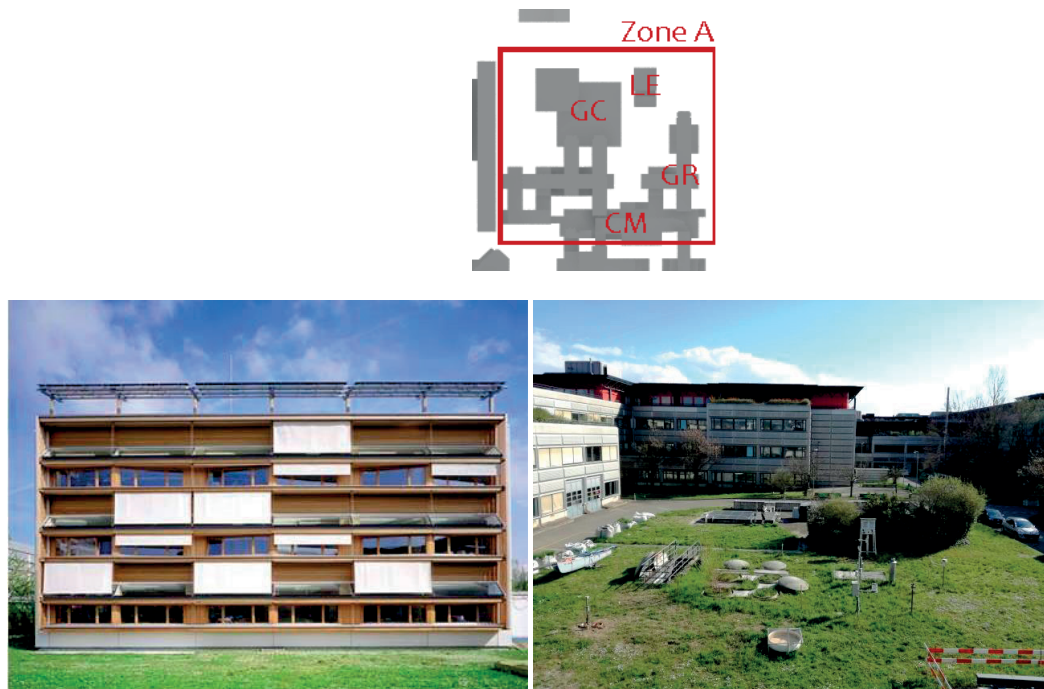


Figure 6.3 Top: Detailed plan of the area. Bottom: (left) LESO solar experimental building (source dp-architectes.ch) and view on the open court from the LESO solar experimental building (right).

#### Design parameters

The evaluation of the optimization proceeds with 16 parameters, summarized in Table 6.1; the parameters are subdivided into five categories: building's characteristics (subdivided into buildings built during the first stage of construction and the LE buildings block), ground covering, trees and shadowing devices. The envelope of buildings is analysed by varying the shortwave reflectance of the walls and roofs, as well as the thickness of insulation and the blinds cut-off. The blind cut-off represents the solar irradiance impinging the windows, expressed in  $\text{Wm}^{-2}$ , at which the blind automatically closes; in the parametrization, the cut-off is ranging from  $150 \text{ Wm}^{-2}$  to  $940 \text{ Wm}^{-2}$ . The value of  $150 \text{ Wm}^{-2}$  is defined (J. Kämpf, 2009) (Robinson, 2011) as a threshold (Wienold, 2007), considering that the user will close the blinds if the solar radiation impinging the facade is higher than  $150 \text{ Wm}^{-2}$ . On the other side, the upper value,  $940 \text{ Wm}^{-2}$ , corresponds to the maximal solar irradiance that reaches a facade (a South unobstructed one), in this climate. In a previous optimization, the blind cut-off was ranging from  $0 \text{ Wm}^{-2}$  to  $1,366 \text{ Wm}^{-2}$ , so called solar constant observed outside the Earth atmosphere. This value was obviously too high, because the radiation received by the facade is never reaching this value, consequently the objective function presented a "plateau", as visible in Figure 6.4. Plateaus are regions within the search space, where all the proposed solutions have the same fitness (Friedrich et al., 2010): in our case, the solar irradiance never reaches the value of  $1,366 \text{ Wm}^{-2}$ , consequently varying this parameter could not affect the results.

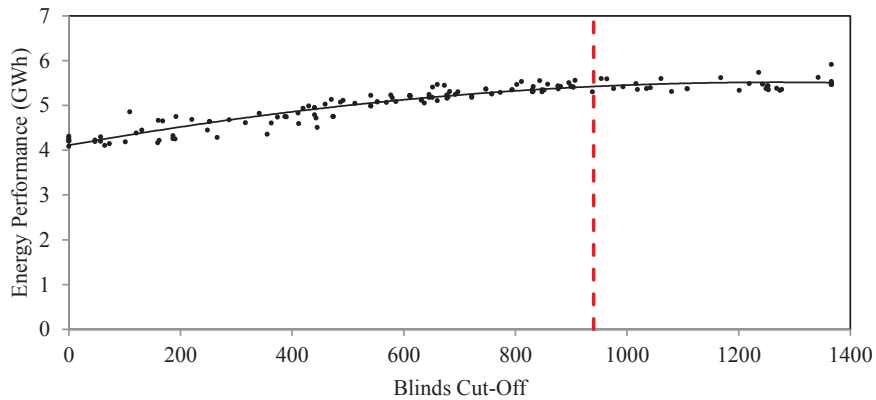


Figure 6.4 Energy performance as function of the blinds cut-off. Plateau within the search space.

The shortwave reflectance of the asphalt is modified considering that the latter is maintained; its thermal characteristics can be however improved by applying a white painting on the upper layer, leading the solar reflectance up to 0.3 (Santamouris and Kolokotsa, 2016). Thirteen trees are planted in the area: the objective of the optimization procedure is to understand the impact of the Leaf Area Index on the outdoor human comfort, in this case by varying the LAI (Leaf Area Index) from 1 to 5. A LAI of 5 corresponds to a Oak tree. The evapotranspiration potential of the ground covering is optimized, by changing the so-called *f-factor* (Penman, 1963) (Mihalakakou et al., 1997), which corresponds to the humidity in the soil, from 0.1 (arid soil) to 1 (saturated soil). Finally, shadowing devices are proposed in the “bocce court”, with the objective of varying their shortwave reflectance, in order to improve the outdoor comfort.

Group	Symbol and Domain	Parameter description	Unit
Buildings characteristics First Phase Construction	$x_0 \in [0.0, 0.8[$	Shortwave reflectance of Walls	(-)
	$x_1 \in [0.0, 0.8[$	Shortwave reflectance of Roofs	(-)
	$x_2 \in [0.0, 0.35[$	Thickness Insulation of the Roof	(m)
	$x_3 \in [0.0, 0.35[$	Thickness Insulation of the Wall	(m)
Buildings characteristics LE	$x_4 \in [150, 940[$	Blinds Irradiance Cut-Off	(W m <sup>-2</sup> )
	$x_5 \in [0.0, 0.8[$	Shortwave reflectance of Walls	(-)
	$x_6 \in [0.0, 0.8[$	Shortwave reflectance of Roofs	(-)
	$x_7 \in [0.0, 0.35[$	Thickness Insulation of the Roof	(m)
	$x_8 \in [0.0, 0.35[$	Thickness Insulation of the Wall, East, West and North orientation	(m)
Ground Characteristics	$x_9 \in [0.0, 0.35[$	Thickness Insulation of the Wall, South orientation	(m)
	$x_{10} \in [150, 940[$	Blinds Irradiance Cut-Off	(W m <sup>-2</sup> )
	$x_{11} \in [0.0, 0.3[$	Shortwave reflectance of Asphalt	(-)
	$x_{12} \in [0.1, 1[$	f-factor clay soil	(-)
Trees	$x_{13} \in [0.1, 1[$	f-factor grass	(-)
	$x_{14} \in [0.0, 5[$	Leaf Area Index	(-)
Shadowing	$x_{15} \in [0.0, 0.8[$	Shortwave Reflectance	(-)

Table 6.1 Optimization of the heating and cooling demand of the EPFL campus in Lausanne, as well as the outdoor human comfort, by the way of sixteen variables.

### Objective function

The triple objective function of the optimization is to improve the heating demand of buildings, as well as their cooling demand; the heating set point is set at 21.5°C and the cooling set point is set at 26°C. The outdoor thermal comfort (OTC) is additionally improved, by maximizing the hours of comfort, as quantified by the COMFA\*.

$$f(\vec{x}) = \begin{pmatrix} Q_h \\ Q_c \\ OTC \end{pmatrix} \quad (6.1)$$

where  $Q_h$  (Wh) is the total heating demand of the buildings,  $Q_c$  (Wh) is the total cooling demand of buildings and OTC (hours) is the daily outdoor thermal comfort, calculated from 8:00 hours to 18:00 hours. Indeed, the optimizer maximizes the number of comfortable hours throughout the year.

#### Results and considerations\_ Typical Meteorological Year

After 3,002 evaluations, the optimal individual shows a cooling demand of 0.75 GWh and a heating demand of 3.02 GWh; the total comfortable hours correspond to 5,786 hours. The new average energy performance of buildings, as the sum of heating and cooling, is  $85 \text{ kWh}\cdot\text{m}^{-2}$ ; it leads a significant decrease of the heating demand (from  $74.03 \text{ kWh}\cdot\text{m}^{-2}$  to  $68.63 \text{ kWh}\cdot\text{m}^{-2}$ ). Figure 6.5 shows the optimal individual obtained with the optimization: the shortwave reflectance of buildings erected during the first phase of construction is equal to 0.2 for the walls, and 0.2 for the roofs; considering that in this climatic scenario, the heating demand has the highest impact on the whole energy demand of the site, the insulation of buildings is maximized (0.35 m) and the blinds irradiance cut-off is set-up at  $213 \text{ Wm}^{-2}$ , improving the solar gains received by buildings. Slightly different are the optimal physical characteristics of LE buildings block, where the insulation is lower (i.e. 0.25 m) on the Southern facade (that presents a light envelope with wood) and on the North, East and West (made with concrete). As for the buildings above, the blinds irradiance cut-off is set-up at  $208 \text{ Wm}^{-2}$ . The f-factor is increased in the clay soil, 0.67, and the one of the grass is assumed equal to 0.43; the Leaf Area Index of trees corresponds to 1.4. Finally, the textile used to shadow the bocce court, presents a shortwave reflectance of 0.2, which corresponds to a slightly light textile mesh. The shortwave reflectance of the current asphalt, in accordance with the optimization corresponds to 0.17, which means to simply apply a reflective colour to the current asphalt road. Trees have a positive impact in improving the number of comfortable hours, mostly during summer time; it is interesting to notice that people, in this climate, stay outside mostly during the warm seasons, consequently the presence of trees improves the climatic conditions. P5 and P6 are the pedestrians covered by the trees canopy: their number of comfortable hours slightly increase during the summer time (404 and 419, without and with trees, respectively). Furthermore, an increase is also evident during the spring time, when the comfortable hours increase further by 5%. Figure 6.5 shows the optimal design of the EPFL campus for a Typical Meteorological Year and the shortwave radiation received annually by the site. It is obvious that the maximal solar irradiance is received by the roof (up to  $1,224 \text{ kWh m}^{-2}$ ), and the lowest, with  $46 \text{ kWh m}^{-2}$ , by the walls facing North.

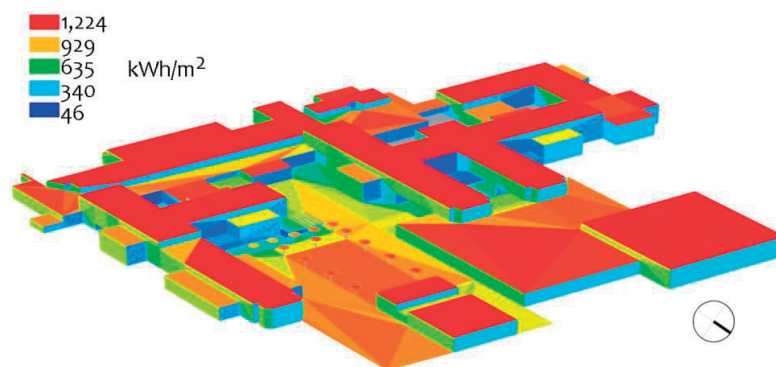


Figure 6.5 EPFL campus, Zone-A. Optimal design of the campus for the TMY, annual shortwave radiation ( $\text{kWh m}^{-2}$ ) received by the campus.

#### Results and considerations\_ Climatic scenario 2050-B1

The optimal individual shows a cooling load of 0.99 GWh and a heating demand of 2.79 GWh; the total comfortable hours correspond to 5,302 hours. Figure 6.6 shows the optimal individual obtained with the optimization: the shortwave reflectance of buildings erected during the first phase of construction corresponds to 0.6 for the walls and roofs; the insulation of buildings is maximized (0.35 m for the roofs and 0.30 m for the walls). Slightly different are the optimal physical characteristics of LE buildings block, where the insulation is lower on the

Southern facade (that presents a light envelope with wood) and is slightly higher on the North, East and West (made with concrete). As for the previous optimization, the solar gains are optimized by increasing the blinds cut-off up to  $273 \text{ W}\cdot\text{m}^{-2}$ . The f-factor is increased in the clay soil and equal to 0.67 (corresponding to grass); the one of the grass is assumed equal to 0.87 (corresponding to moist soil). Finally the textile used to shadow the bocce court, presents a shortwave reflectance of 0.73, corresponding to a clear textile mesh. The shortwave reflectance of the current asphalt, in accordance with the optimization would correspond to 0.1. The LAI of trees is increased up to 1.6; this result is not intuitive, effectively considering the climate change and the increase of the warmer thermal sensation, it seems logical to maximize the LAI. In this case study, trees impact directly (by the shading of their crown, as well as by radiative cooling) two pedestrians. Additionally, they are positioned on the North facade of building GR and on the southern one of LESO solar experimental building. Consequently, the increase of the LAI means an additional reduction in the solar gains, received by the buildings and consequently increasing their heating demand.

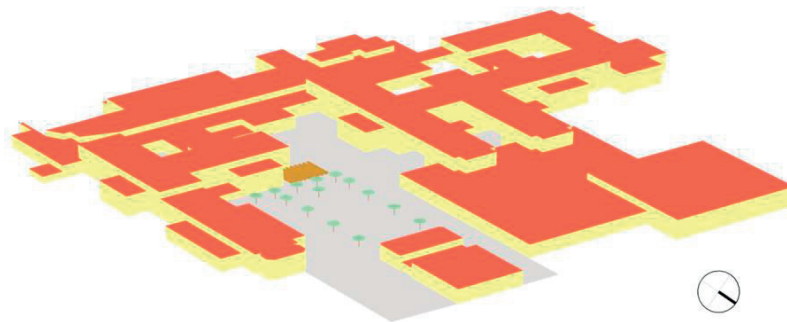


Figure 6.6 EPFL campus, Zone-A. Optimal design of the campus.

#### Results and considerations\_ Climatic scenario 2100-B1

The optimal individual shows a cooling demand of 1.45 GWh and a heating demand of 2.67 GWh; the total comfortable hours correspond to 5,536 hours. The new average energy performance of buildings, as the sum of heating and cooling, is  $93 \text{ kWh m}^{-2}$ . Figure 6.7 shows the optimal individual identified with this procedure: the shortwave reflectance of buildings erected during the first phase of construction corresponds to 0.8 for the walls, and 0.1 for the roofs. This result is not intuitive: effectively, it is essential to reduce the surface temperature of the built environment, in order to improve the microclimate. But, this result is related to the geometry of the site: the radiation reflected by the roofs is directly received by the neighbours walls. Consequently, in order to reduce the radiative fluxes, the optimizer proposes to reduce the reflectance of the roofs, reducing the radiation that is reflected to the neighbors buildings, and to increase their insulation thickness. Effectively, the total solar irradiance received by building GR corresponds to  $942 \text{ kWhm}^{-2}$  with a SWR (short wave reflectance) of 0.8, and to  $899 \text{ kWhm}^{-2}$  with a SWR of 0.1. Considering that in this climatic scenario, the cooling demand has a largest impact, compared to the Typical Meteorological Year, the insulation of buildings is maximized (0.31 m) and the blinds irradiance cut-off is set-up at  $150 \text{ Wm}^{-2}$ , reducing the solar gains received by buildings. Another result is related to the LESO building, where the blind irradiance cut-off is maximized (up to  $450 \text{ Wm}^{-2}$ ), showing that this building, designed in accordance with the bioclimatic principles, requires an efficient passive solar strategy. In this building, the shortwave reflectance of wall is reduced (corresponding to 0.5), and the shortwave reflectance of the roof is maximised (up to 0.7). Effectively, in this case the radiation reflected by the LESO building do not impact neighbours buildings, and the LEA building (lower building behind the LESO solar experimental building) is obstructed on the south by the LESO, consequently reducing the solar irradiance received by the roof. The f-factor is increased in the clay soil (0.31), and the one of the grass is assumed equal to 0.38, which corresponds to a dry soil. Finally, the Leaf Area Index of trees, corresponds to 1.2. It is evident that a limitation of this model, as mentioned in Chapter 3, is the fact that trees are considered as evergreen. Consequently, if the optimizer has to

improve the number of comfortable hours throughout the year, it is essential to reduce the shading during the winter time, as well as to provide radiative heating from the ground surfaces. The shortwave reflectance of the shadowing is increased (equals to 0.8), reducing its temperature, consequently the radiative exchanges.

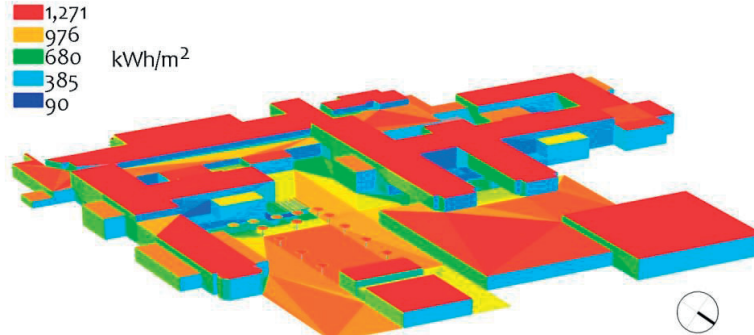


Figure 6.7 EPFL campus, Zone-A. Optimal design of the campus in 2100, annual shortwave radiation ( $\text{kWh m}^{-2}$ ) received by the campus.

An interesting element, when analysing the future climatic conditions, is the fact that in the future the average air temperature will increase; by analysing the punctual air temperature, it is obvious that extreme cold events will also characterize the future climate. As an example, Figure 6.8 shows the difference in air temperature between the 2100-B1 scenario and the Typical Meteorological Year; during the winter time, the air temperature will in average increase (by  $1.43^\circ\text{C}$ ), but several extreme cold events will occur, with an air temperature lower than now. Consequently, the optimizer has to consider that in average the heating load will decrease, but the heating systems will still have to be designed in order to cope with extreme cold events.

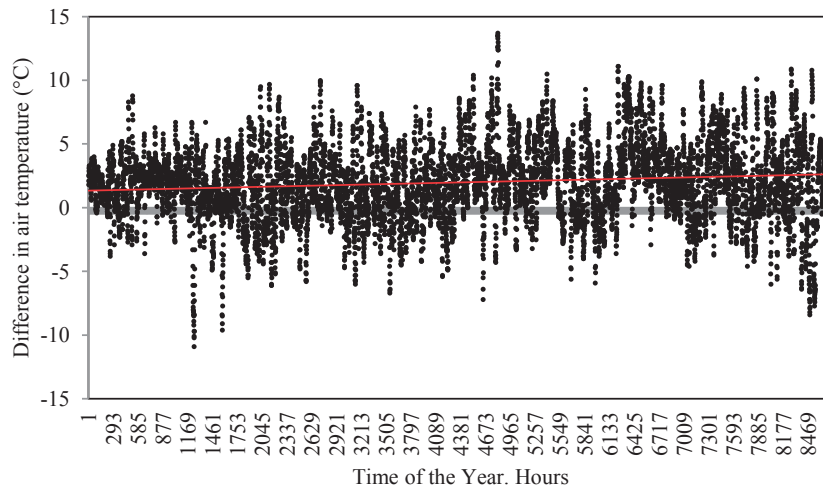


Figure 6.8 Difference between the actual air temperature (TMY) and the future one (2100-B1).

**Conclusion**

The results obtained by the optimization procedure are quite interesting in order to quantify the impact of the climate change on the campus design; Table 6.2 summarizes the optimal parameters for each optimisation. A general comment is related to the shortwave reflectance of the walls: considering that the urban environment absorb and re-emit the infrared radiation directly to the pedestrians, it is important to decrease the surface temperature of walls, in order to reduce the re-emitted heat . All the physical properties of the composites are defined in Annex B.



Group	Parameter description	Typical Meteorological Year	2050-B1	2100-B1
Buildings characteristics	Shortwave reflectance of Walls (-)	0.2	0.6	0.8
	Shortwave reflectance of Roofs (-)	0.2	0.6	0.1
	Thickness Insulation of the envelope (m)	0.35	0.32	0.31
	Blinds Irradiance Cut-Off ( $W m^{-2}$ )	213	150	150
Buildings characteristics_ LE buildings block	Shortwave reflectance of Walls (-)	0.5	0.5	0.5
	Shortwave reflectance of Roofs (-)	0.3	0.4	0.7
	Thickness Insulation of the envelope (m)	0.25	0.22	0.22
	Blinds Irradiance Cut-Off ( $W m^{-2}$ )	208	273	450
Ground Characteristics	Shortwave reflectance of Asphalt (-)	0.1	0.1	0.3
	f-factor of Clay Soil (-)	0.67	0.67	0.31
	f-factor of Grass (-)	0.43	0.87	0.38
Trees	Leaf Area Index (-)	1.4	1.6	1.2
Shadowing	Shortwave Reflectance (-)	0.2	0.7	0.8

Table 6.2 EPFL, Zone- A. Optimal parameters, as obtained by the three optimizations (typical meteorological year, 2050-B1 and 2100-B1).

In a previous work, the optimization was performed with the objective to reduce the Mean Radiant Temperature in the outdoor environment. Results obtained by this optimization procedure were quite different: as an example, the LAI of trees was maximized, and pools were designed in the outdoor environment. This is obviously related to the constraints of the optimization: before, the objective was to reduce the MRT, throughout the year. In the new optimization, the human comfort is maximized; consequently the outdoor environment has to be “cooler” during the warm season, and “warmer” during the colder one. In order to visualize how the campus would like, in accordance with the optimization, the following colour palette is presented (Table 6.3). Each RAL colour has a defined reflectance, and the colour palette represents the nuance of the cream colour; naturally the same palette could be applied to all colours.










Name	RAL	Reflectance	Image
Graphite Black	9011	0.009	
Quartz Grey	7039	0.13	
Grey Aluminium	9007	0.25	
Silver Grey	7001	0.30	
Pearl Dark Grey	9023	0.35	
White Aluminium	9006	0.53	
Grey White	9002	0.67	
Pearl White	1013	0.71	
Cream	9001	0.78	

Table 6.3 Color palette. Scale of color, as function of their shortwave reflectance.

The following Figures (6.9- 6.11) illustrate the optimized aspect of the EPFL campus (Zone-A), for a Typical Meteorological Year, as well as for the selected future climatic scenarios, as described in Table 6.2.



Hybrid Algorithm Optimization with Heuristics



Figure 6.9 EPFL campus, Zone-A; optimized design for a Typical Meteorological Year.

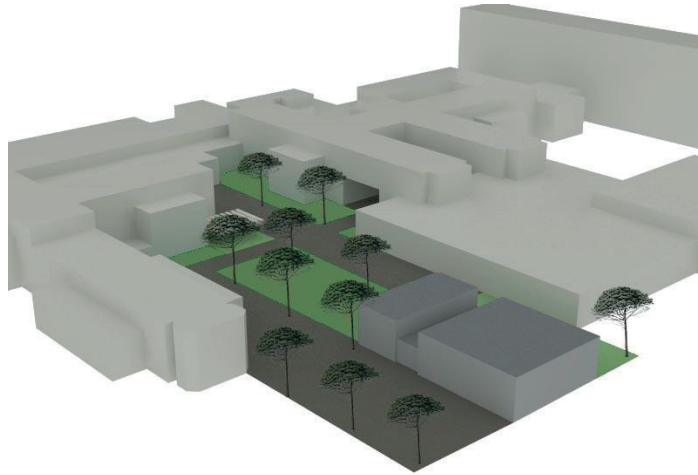


Figure 6.10 EPFL campus, Zone-A; optimized design for the climatic scenario 2050-B1.



Figure 6.11 EPFL campus, Zone-A; optimized design for the climatic scenario 2100-B1.

## 6.2.2 Zone-B\_ Optimisation of the energy demand for heating and cooling

### *Design objectives*

This selection presents the optimization of the energy performance of the selected district (so called Zone-B) for a typical meteorological year (TMY) and two futures climatic scenarios: 2050-B1 and 2100-B1. In concrete terms, it considers the impact of the air tightness of the envelope (thermal insulation and infiltration rate), as well as the ground covering by varying its albedo, on the energy performance of buildings. The interesting element is the variation in the energy behaviour of the campus in future climatic scenarios; as mentioned in Chapter 4, the cooling load will drastically increase in future climatic scenarios, changing from the actual thermal behaviour optimised to reduce the heating loads to a paradigm dealing with reduced demand in cooling.

### *Analysis target*

The selected area is composed of seven buildings (Figure 6.12): BI, BS, CE, CH, PH, PO and STT. All of them, except the PO, are part of the first stage of construction of the EPFL (1972- 1984), and consequently present the same envelope characteristics (Figure 6.13).

Hybrid Algorithm Optimization with Heuristics

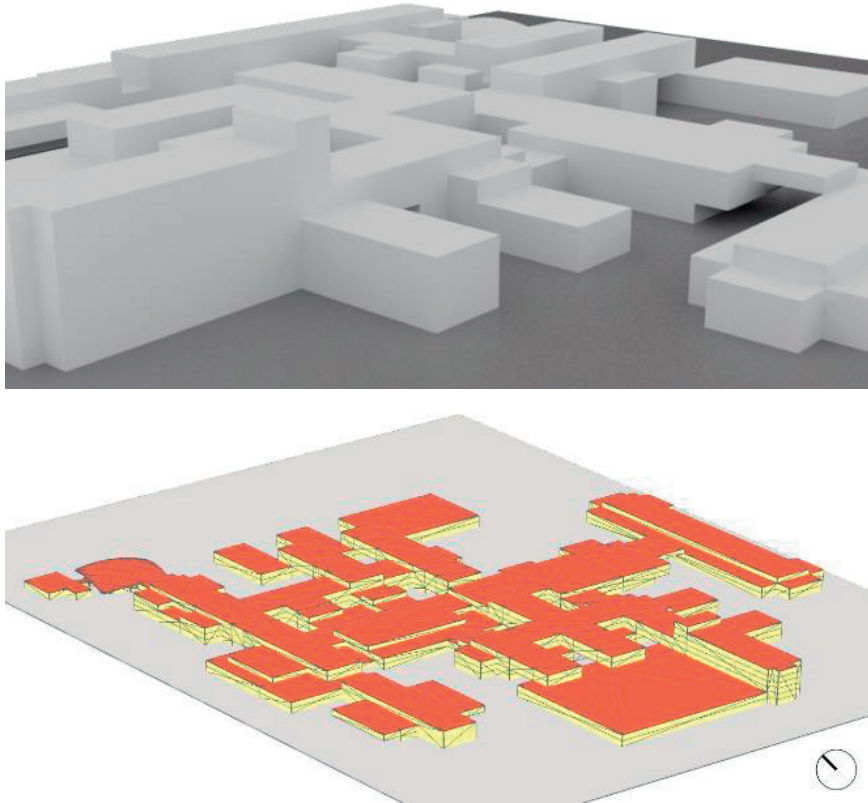


Figure 6.12 EPFL campus, Zone-B. Optimization of the energy demand for heating and cooling. 3D geometrical view of the site (top) and 3D model with CitySim Pro (bottom)

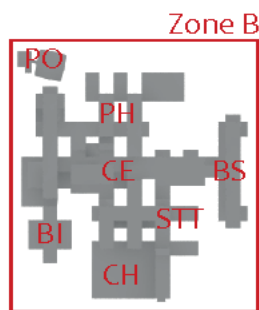


Figure 6.13 Top: plan of the site. Bottom: PO building, or Polydôme (left) and PH building (right).

### Design parameters

The optimization procedure involves with the following twelve parameters summarized in Table 6.4:

Group	Symbol and Domain	Parameter description	Unit
Envelope characteristics	$x_0 \in [0.0, 0.35[$	Thickness Insulation Wall, First Phase of Construction	(m)
	$x_1 \in [0.0, 0.35[$	Thickness Insulation Roof, First Phase of Construction	(m)
	$x_2 \in [0.0, 0.35[$	Thickness Insulation Floor, First Phase of Construction	(m)
	$x_3 \in [0.0, 0.35[$	Thickness Insulation Wall, Polydôme	(m)
	$x_4 \in [0.0, 0.35[$	Thickness Insulation Roof, Polydôme	(m)
	$x_5 \in [0.7, 1.3[$	U-value windows	( $\text{W}\cdot\text{m}^{-2}\text{K}^{-1}$ )
	$x_6, x_7, x_8$ and $x_9$	Infiltration Rate	( $\text{h}^{-1}$ )
	$\in [0.0, 1.0[$		
	$x_{10} \in [0.1, 0.8[$	Shortwave reflectance of the roofs, First Phase of Construction	(-)
	Ground Characteristics	$x_{11} \in [0.1, 0.8[$	Shortwave reflectance of the ground covering

Table 6.4 Optimization of the heating and cooling demand of the EPFL campus of Lausanne (Zone-B). The twelve proposed parameters.

The thermal insulation thickness varies between 0 to 0.35 meters; this value was selected by considering that the impact of the thermal insulation varies non linearly with the thickness, as shown in Figure 6.14, when an external insulation is added to a concrete wall of 20 cm. By adding one cm of insulation, the U-value decreases by 35%; by passing from 25 cm to 30 cm the U-values diminish by 17% but after 35 cm the impact is lower than 10%. For this reason, the insulation thickness is comprised between the selected values: 0 to 35 cm. Additionally, 0.35 m is the thickness required by the Swiss Minergie-P standard (Minergie, 2017). The U-value of windows varies from the current value,  $1.3 \text{ W}\cdot\text{m}^{-2}\text{K}^{-1}$  to  $0.7 \text{ W}\cdot\text{m}^{-2}\text{K}^{-1}$ , which corresponds to a triple glazing with infrared coating. The infiltration rate currently varies in the buildings: the Polydôme (PO) has an infiltration of  $0.3 \text{ h}^{-1}$ , considering the high percentage of glazing; the office buildings have an infiltration rate of  $0.2 \text{ h}^{-1}$  and the mixed buildings, hosting cafeteria, classroom, laboratories and offices an infiltration rate of  $0.7 \text{ h}^{-1}$ , because of the rate required by the functions in order to maintain a liveable indoor climate. The shortwave reflectance of the roofs and ground covering is optimized by varying it from 0.1 to 0.8.

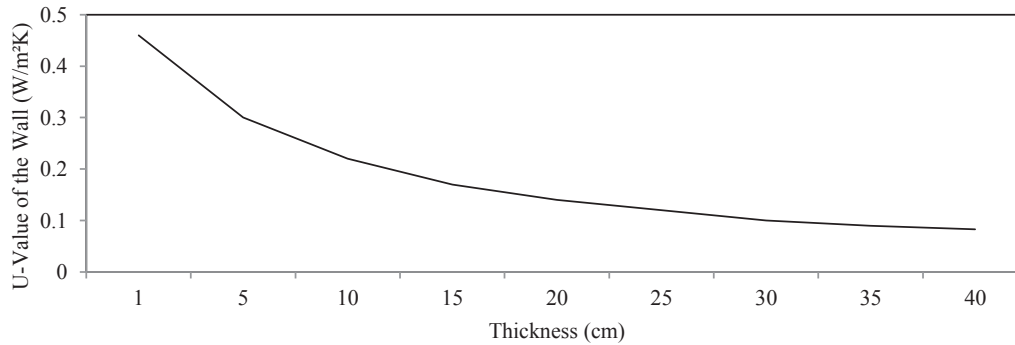


Figure 6.14 Variation of the U-value of the wall ( $\text{W}\cdot\text{m}^{-2}\text{K}^{-1}$ ) as function of the insulation thickness (cm), for a simple concrete wall with an external layer of insulation.

### Objective function

The double objective function of the optimization is to reduce the heating demand of buildings, as well as their cooling loads, as presented in Equation 6.2:

$$f(\vec{x}) = \begin{pmatrix} Q_h \\ Q_c \end{pmatrix} \quad (6.2)$$

where  $Q_h$  (Wh) is the total heating load of the buildings and  $Q_c$  (Wh) is the total cooling load of buildings. The heating set point is set at 21.5°C and the cooling set point is set at 26°C. These temperatures are defined by adapting the set point temperatures of the different functions hosted by the campus (offices, classroom, auditorium, laboratories and restaurants) as defined by the Swiss Norm SIA 2024 (SIA, 2006).

*Results and considerations\_ Typical Meteorological Year*

After 3,002 evaluations, the optimal individual (Figure 6.15) shows a total energy demand of 6.87 GWh, with a reduction by 18% compared to the current case study (8.43 GWh), passing from 111 kWh·m<sup>-2</sup> to 91 kWh·m<sup>-2</sup>.

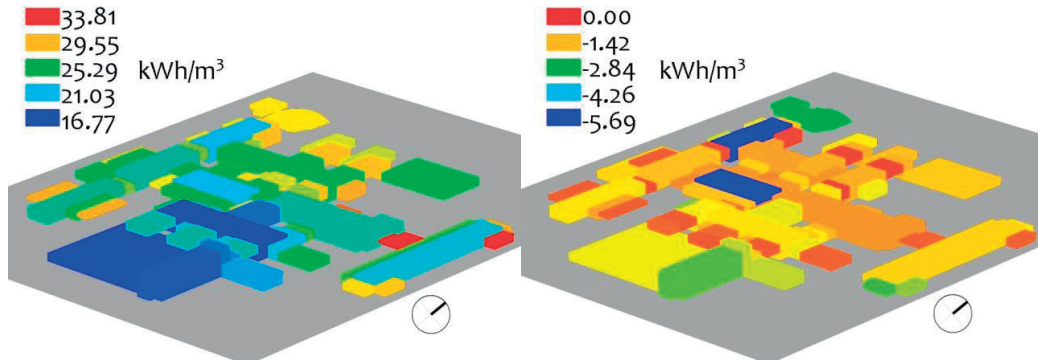


Figure 6.15 Heating (left) and cooling (right) demand of the EPFL campus for a typical meteorological year, after the optimization by the hybrid Evolutionary Algorithm (CMA-ES/HDE).

Figure 6.16 shows the heating and cooling loads of the site: the heating demand decreases from 7.82 GWh to 6.34 GWh, and the total cooling demand decreases from 0.61 GWh to 0.53 GWh. A detailed analysis of the cooling demand shows that it decreases drastically in buildings BS, CE and STT; this behavior is related to their infiltration rate that is increased, improving the natural ventilation of the buildings, passing from 0.3 (BI and STT) and 0.2 (CE) to 0.66 and 0.67. On the contrary, other buildings increase their cooling demand, but the increase is lower compared to their reduction in heating demand (Figure 6.16): CH reduces its heating demand by 42% (total energy demand by 39%) and PH reduces its heating demand by 37% (total energy demand by 33%).

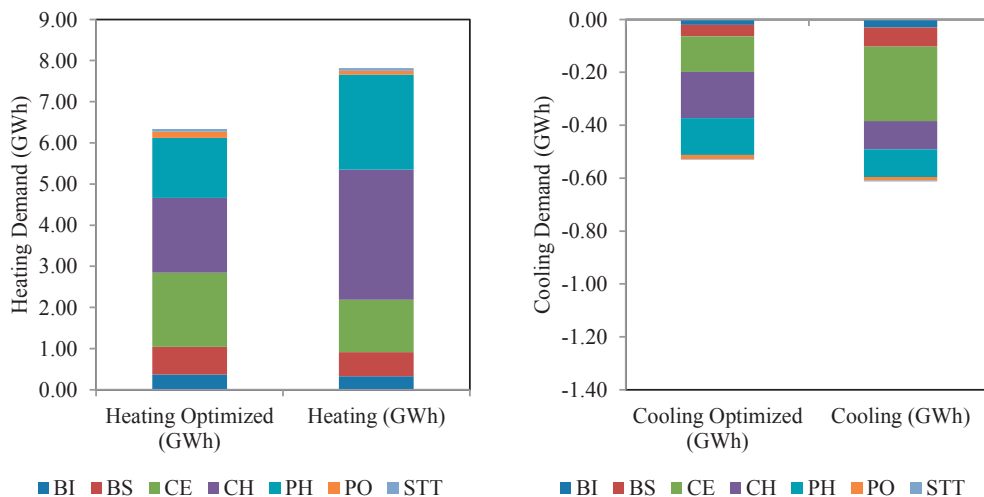


Figure 6.16 Heating (left) and cooling demand (right) of the EPFL campus; comparison between the current and the optimized case study.

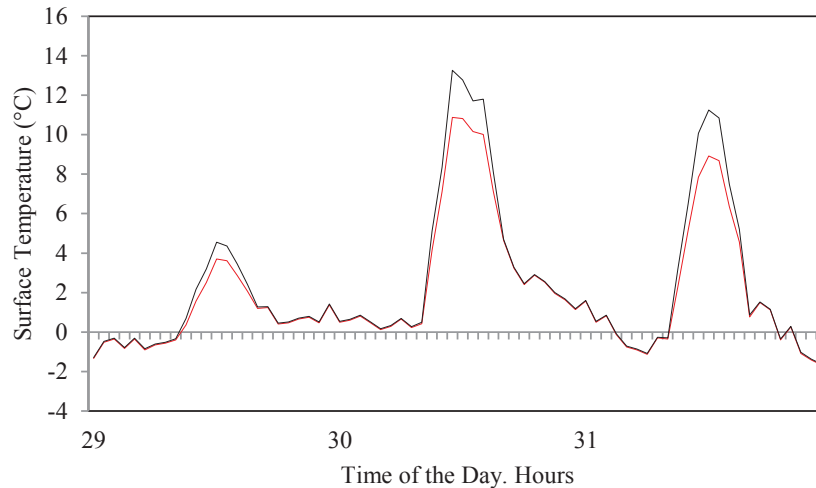
Finally, the shortwave reflectance of the ground is increased, passing from 0.2 to 0.4, which corresponds to replacing the current asphalt and concrete tiles, with concrete covered with heat reflective paints (Boriboonsomsin and Farhad, 2007). The shortwave reflectance of the roof is also increased up to 0.6. In order to obtain an albedo of 0.4 and 0.6, it is essential to consider the aging factor, related to the exposure of the material, following this equation (Santamouris and Kolokotsa, 2016):

$$SR_{\text{aged}} = \rho_o + c (SR_{\text{initial}} - \rho_o) \quad (6.3)$$

where  $SR_{\text{aged}}$  (-) and  $SR_{\text{initial}}$  (-) are the aged and initial solar reflectance of the surface,  $\rho_o$  and  $c$  are constants, and correspond to 0.2 and 0.7 respectively.

Based on Equation 6.3, the final shortwave reflectance of the ground corresponds to 0.5, and the one of the roof to 0.78. The newer surface albedo is a sound compromise between a reduction of the heating demand and the cooling one, improving the thermal comfort inside the building (reduction in heat transfer from the roof) and the life time of the cool surface (less impacted by the diurnal fluctuation of the temperature) (Santamouris and Kolokotsa, 2016).

The new annual averaged ground temperature corresponds to 10°C, 1.8°C degrees lower than the previous one (with an albedo of 0.2): by reducing the ground surface temperature, the microclimatic conditions of the outdoor environment are improved, mitigating the urban heat island effect. Figure 6.17 shows the surface temperature of the ground, before and after optimization, during three winter days (29<sup>th</sup> to 31<sup>st</sup> December). The surface temperature during nighttime is constant, but varies during daytime, as a function of the direct solar irradiance: the 29<sup>th</sup> of December, characterized by 231 W·m<sup>-2</sup> of diffuse solar irradiance but no direct one, shows the minimal difference in surface temperature between both scenarios, which corresponds to 0.83°C. On the opposite, the 30<sup>th</sup> of December, when the direct solar irradiance corresponds to 692 W·m<sup>-2</sup>, a maximal difference between both scenarios is observed corresponding to 2.4°C at noon. The same behavior is clearly evident throughout the year.



Day	Air Temperature (°C)	Diffuse solar irradiance (W·m <sup>-2</sup> )	Direct solar irradiance (W·m <sup>-2</sup> )
29 <sup>th</sup> December	4.1	231	0
30 <sup>th</sup> December	6.1	692	49
31 <sup>st</sup> December	3.9	664	22

Figure 6.17 Top: hourly ground surface temperature (°C) for three winter days (29<sup>th</sup> to 31<sup>st</sup> December) in the current (black) and optimized scenario (red). Bottom: Meteorological characteristics of the three selected days.



Figure 6.18 illustrates the optimization procedure: the last three results are particularly interesting to understand the final selection performed by the algorithm. Effectively, in the last three selections the total heating demand decreases by 33%, but facing an increase of the cooling demand (by 4 to 36%). The thermal insulation of the envelope is quite similar (around 0.17 m) and the average infiltration rate corresponds to 0.4 h<sup>-1</sup>, lower than the optimal option provided by the optimization procedure.

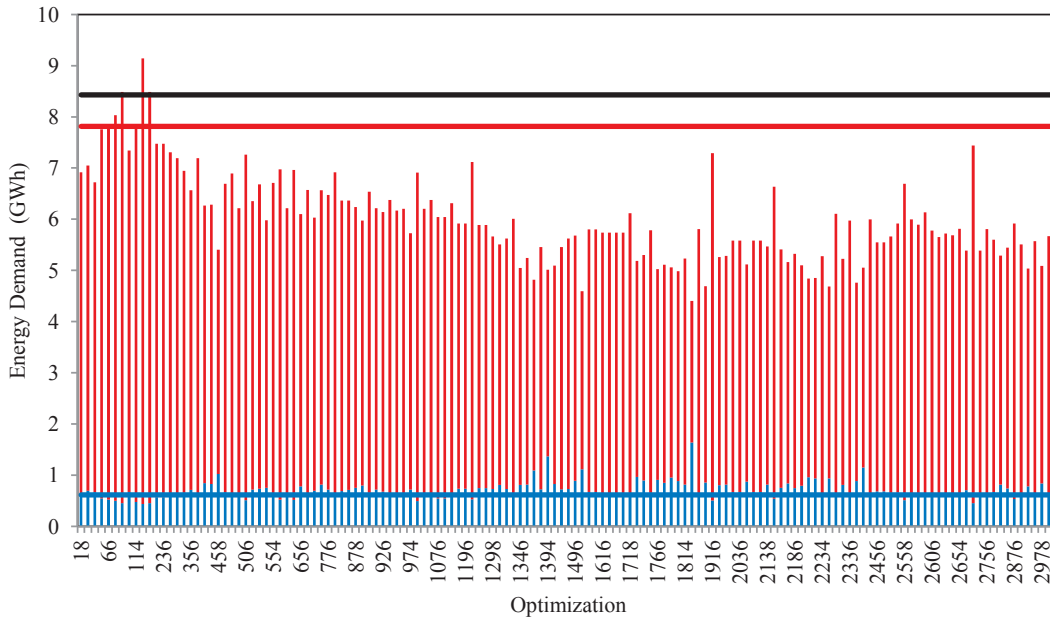


Figure 6.18 Energy demand, for heating (red) and cooling (blue) of the campus, during the optimization process. Energy demand of the current campus (black line), as well as its heating (red line) and cooling demand (blue line).

*Results and considerations\_ Climatic scenario 2050-B1*

The optimal individual (Figure 6.19) shows a cooling demand of 1.08 GWh and a heating demand of 5.61 GWh; the total energy demand of the site after optimization corresponds 88 kWh·m<sup>-2</sup>, 17% lower than without optimization, where the total energy demand corresponds to 107 kWh·m<sup>-2</sup>.

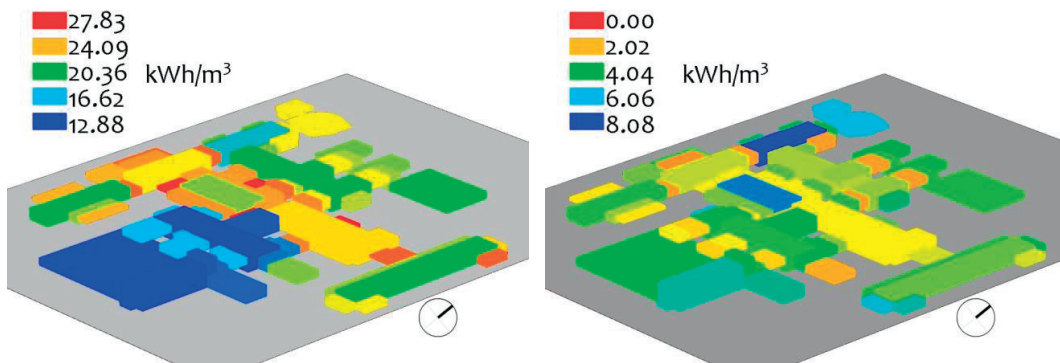


Figure 6.19 Heating (left) and cooling (right) demand of the EPFL campus for 2050-B1, after the optimization by the hybrid Evolutionary Algorithm (CMA-ES/ HDE).

Figure 6.20 shows the heating and cooling demand of the site, before and after optimization: on average the heating demand is decreased (from 6.87 GWh to 5.61 GWh), as well as the total cooling demand, from 1.25 GWh to 1.08 GWh. The cooling demand decreases in all buildings except building CH, where it increases by 42%; this

behavior is related to the high impacts of the heating demand, that decreases by 51%: the final total demand decrease by 42%, passing from 120 kWh·m<sup>-2</sup> to 70 kWh·m<sup>-2</sup>. The latter is related to the infiltration rate of the building, which was 0.74 h<sup>-1</sup> in the case study, and 0.48 h<sup>-1</sup> after the optimization. The opposite behavior is evident in building CE, where the heating demand increases by 57% and the cooling demand decreases by 52%, with a final energy demand of 99 kWh·m<sup>-2</sup> (80 kWh·m<sup>-2</sup> before the optimization): this is related to the infiltration rate, that passes from 0.2 h<sup>-1</sup> to 0.87 h<sup>-1</sup>. The infiltration rate increases because of the need of natural ventilation in buildings required to reduce overheating risks during summer time. In all buildings the insulation required increases by the optimization, reducing the losses through the envelope; only the building PO requires less insulation on the rooftop: by reducing the insulation from 0.25 to 0.11 m on the domed roof (0.18 in average for the envelope), its cooling demand decreases, because the optimal way to exchange heat with the environment during summer time is by radiative night cooling from the dome, and by natural ventilation from the envelope (by the windows opening). Finally, as in the previous optimization for a typical meteorological year, the new ground has a higher short wave reflectance compared to the current status (from 0.2 to 0.6). Finally, the shortwave reflectance of the roofs is increased, up to 0.7 in buildings of the first stage of construction. The increase of the shortwave reflectance of the roofs means a reduction of the radiation absorbed by the envelope, consequently reducing the solar gains.

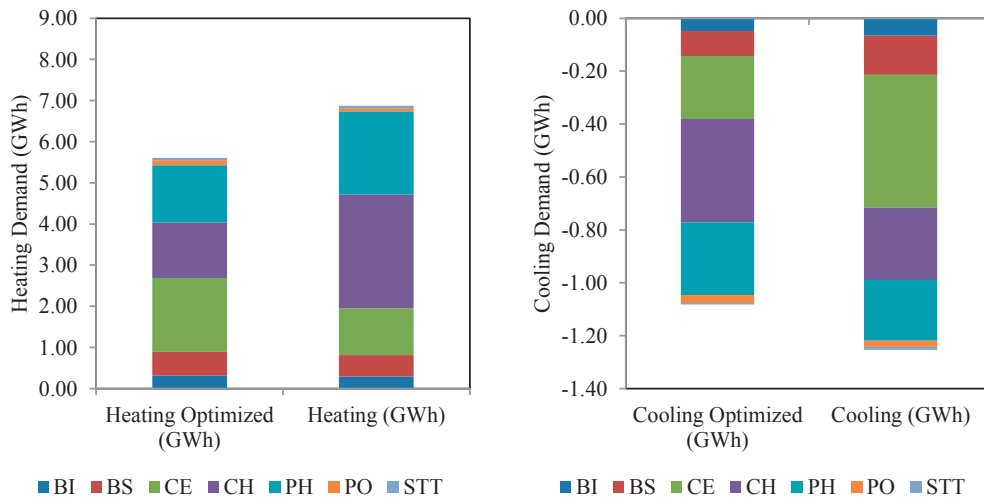


Figure 6.20 Heating (left) and cooling demand (right) of the EPFL campus; comparison between the current case study projected in 2050 and the optimized case study.

Figure 6.21 shows the energy demand of the site, as provided by the software during the optimization process. The highest demand of the site corresponds to individual 530, with a total energy demand of 11.70 GWh (7.6 GWh is the demand of the current campus projected in 2050). In this simulation, the insulation is absent, the shortwave reflectance of the ground is maximized (0.7), and the infiltration rate is reversed: it is increased in the air tight buildings (up to 0.93 h<sup>-1</sup>), and decreased in the ventilated ones (up to 0.46 h<sup>-1</sup>). The last three individuals (3,002, 2,990 and 2,978) present less energy efficient windows (U-value circa 1,0 Wm<sup>-2</sup>K<sup>-1</sup>), darker ground covering (SWR=0.4) and lighter roofs (SWR=0.75). All of them present a decrease of the heating demand (circa 30%), but a low decrease of the cooling demand.

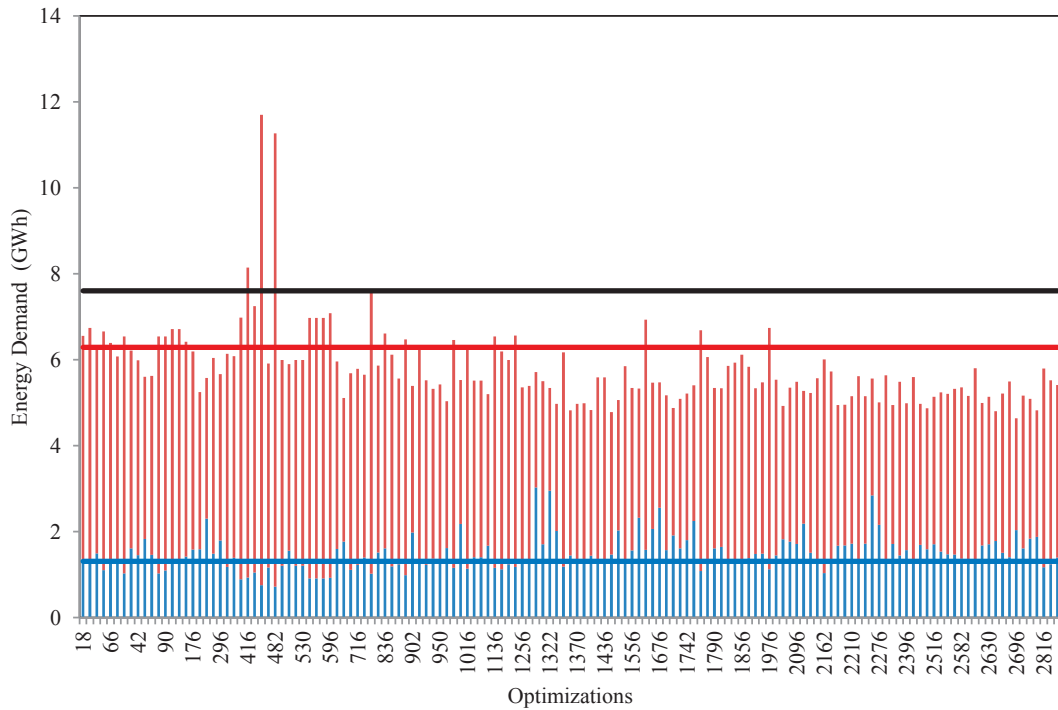


Figure 6.21 Energy demand, for heating (red) and cooling (blue) of the campus, during the optimization process. Energy demand of the current campus, projected in 2050 (black line), as well as its heating (red line) and cooling demand (blue line).

*Results and considerations\_ Climatic scenario 2100-B1*

The optimal individual identified by the procedure (Figure 6.22) shows a cooling demand of 1.08 GWh and a heating demand of 4.81 GWh; the total energy demand of the site after optimization corresponds 77 kWh·m<sup>-2</sup>. It is lower than the one of the current situation, where the total energy demand corresponds to 106 kWh·m<sup>-2</sup>.

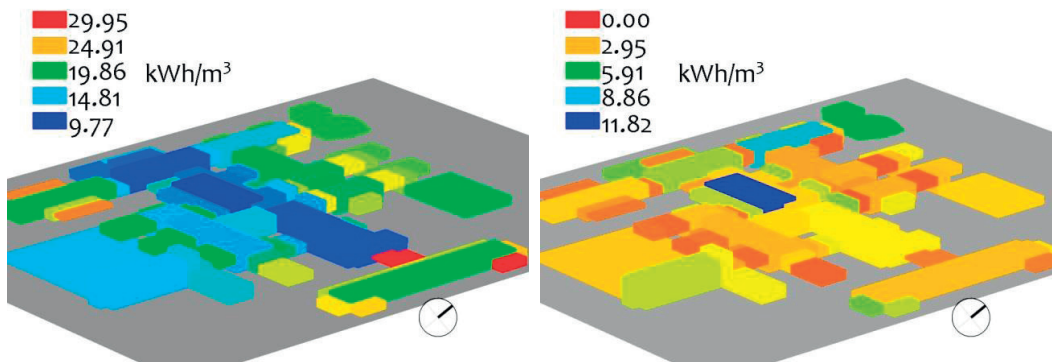


Figure 6.22 Heating (right) and cooling (left) demand of the EPFL campus for 2100-B1, after the optimization by the new hybrid Evolutionary Algorithm (CMA- ES/ HDE).

In this case the optimizer drastically reduces the heating demand, passing from 89 kWh·m<sup>-2</sup> to 63 kWh·m<sup>-2</sup>, as shown in Figure 6.23. The cooling demand decreases in all buildings except CH and PH, where it increases; this behavior is related to the high impacts of the heating demand, that decreases by more than 35%, consequently the final total demand decrease by 38% and 29%, respectively. This is related to the infiltration rate of the buildings (0.49 h<sup>-1</sup> and 0.61 h<sup>-1</sup> after the optimization, and 0.74 h<sup>-1</sup> and 0.76 h<sup>-1</sup> before the optimization) and by the thermal insulation, which increases from 10 to 22 cm. Generally, after the optimization, in all buildings the insulation

required increases, reducing the losses through the envelope. But it is interesting to observe the variation of the infiltration rate, which is optimized between  $0.35 \text{ h}^{-1}$  to  $0.67 \text{ h}^{-1}$  (in the current scenario it varies between  $0.2 \text{ h}^{-1}$  to  $0.76 \text{ h}^{-1}$ ). Effectively, due to the increase of the ambient air temperature, a way to refresh buildings would be to increase the natural ventilation rate, as well as providing an efficient ventilation system. Finally, the new ground has a higher shortwave reflectance compared to the current status (from 0.2 to 0.5), which is lower than the one of the previous optimization (0.4 and 0.6 in TMY and 2050, respectively). Effectively, due to the climate change, in this scenario an increase of the reflectance means an increase of the radiation reflected by the ground, received by the neighbor's buildings.

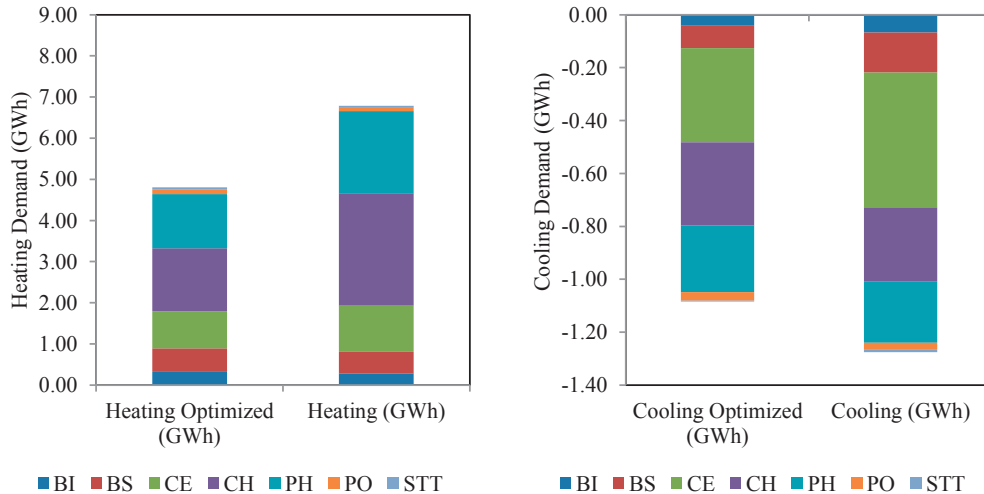


Figure 6.23 Heating (right) and cooling (left) demand of the EPFL campus for 2100-B1, after the optimization by the new hybrid Evolutionary Algorithm (CMA-ES/HDE).

Figure 6.24 shows the energy demand of the site (heating and cooling) as provided during the optimization process. The lowest demand of the site (as the sum of heating and cooling) corresponds to 4.42 GWh (individual 1,814), showing a reduction of the heating demand of 65% ( $30.8 \text{ kWhm}^{-2}$ ), but an increase of the cooling demand of 63% ( $27.5 \text{ kWhm}^{-2}$ ). It is interesting to notice that the optimization suggest an air tight (average infiltration rate corresponding to  $0.2 \text{ h}^{-1}$ ) but not a particularly energy efficient envelope ( $0.11 \text{ m}$  of insulation), with a shortwave reflectance of the ground covering corresponding to 0.06. Furthermore, the largest demand corresponds to 6.8 GWh (in any case lower than the current campus projected in 2100, with a total demand of 8.0 GWh), and in this case both heating ( $14.3 \text{ kWhm}^{-2}$  versus  $16.8 \text{ kWhm}^{-2}$ ) and cooling decrease by 15% ( $76.0 \text{ kWhm}^{-2}$  versus  $89.6 \text{ kWhm}^{-2}$ ). It is interesting to notice that both demand decreases, but this reduction does not represent the optimal compromise. Finally, looking at the last three individuals provided by the optimizer (2,979, 2,990 and 3,002), they show a reduction in the total demand of 38%, 39% and 41%, respectively. All of them present a reduction in the heating demand (65%, 69% and 69%, respectively), but also an increase of the cooling demand (104 %, 117% and 105%, respectively). All of them present an air tight envelope (average infiltration rate corresponding to  $0.21 \text{ h}^{-1}$ ) and a good insulation (circa  $0.27 \text{ m}$  of insulation). Consequently, when comparing these optimizations with the optimal individual, the positive impact of the ventilation rate can be outlined, in order to improve the energy performance.

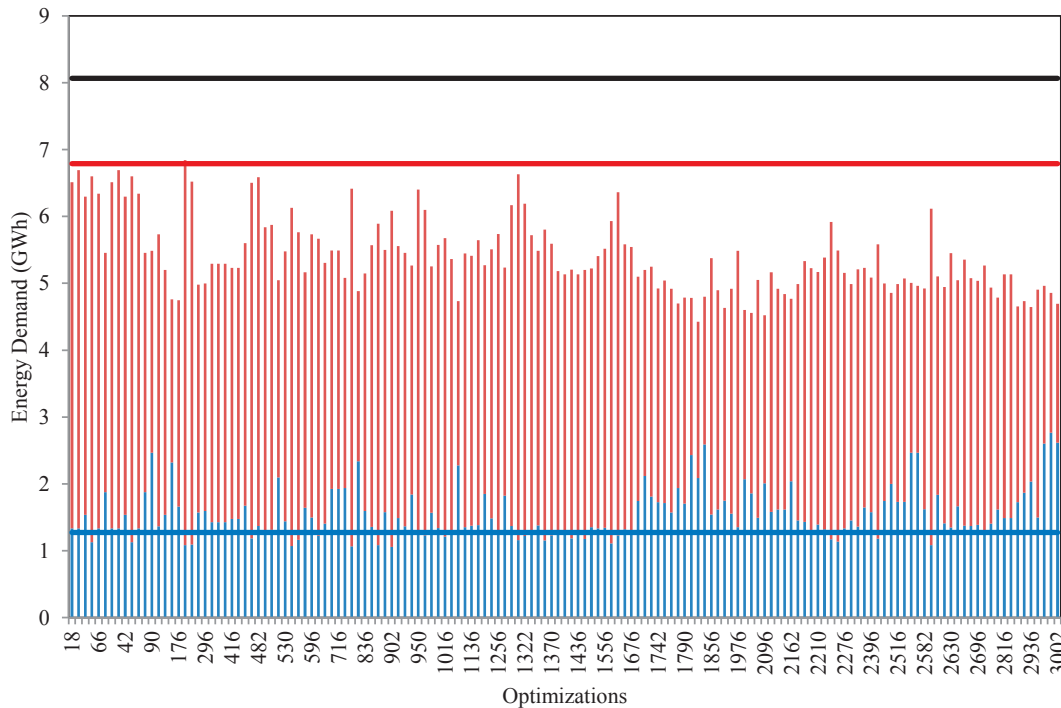


Figure 6.24 Energy demand, for heating (red) and cooling (blue) of the campus, during the optimization process. Energy demand of the current campus, projected in 2100 (black line), as well as its heating (red line) and cooling demand (blue line).

### Conclusion

The optimisation of the Zone-B of the EPFL campus in actual and future climatic scenarios shows two main trends: in the future the energy demand will be, as in the present scenario, dominated by the heating load, but the cooling demand will rise, passing for the current scenario from  $6.6 \text{ (kWh m}^{-2}\text{)}$  to  $16.8 \text{ (kWh m}^{-2}\text{)}$  if the current campus is projected in 2100. In order to maintain a sound indoor environment, a new concept mitigating the rise of the cooling demand has to be considered; due to low cooling demand required (the maximal demand corresponds to  $16.8 \text{ kWh m}^{-2}$  in 2100) and the uncertainties related to the future climatic data, the campus will not require an air conditioning system, but a sound refurbishment of the site is absolutely necessary. The refurbishment would improve the thermal envelope of the buildings, decreasing their thermal losses but providing a correct ventilation of building, consequently improving their thermal performances. Additionally, though a correct refurbishment the energy consumption of the site would decrease, improving the sustainability of the built stock. Tables 6.5 and 6.6 summarize the optimized scenario for each climatic data: the insulation of buildings, built in the first stage of construction, will be increased, passing from the actual  $0.1$  to  $0.22 \text{ m}$  in 2100. On the opposite for buildings with a light envelope, such as building PO (Polydôme), it is important to reduce the insulation from  $0.25 \text{ m}$  to  $0.18 \text{ m}$  in 2050, in order to maximize the radiative night cooling and increase the daily solar gains. Indeed, the future climate will be characterized by colder winters and warmer summers, consequently the algorithm tends to optimize according to the complex environmental conditions. In any future climatic scenario, all current windows have to be replaced by new efficient ones, with an U-value of  $0.7 \text{ (W m}^{-2}\text{K}^{-1}\text{)}$  and  $0.8 \text{ (W m}^{-2}\text{K}^{-1}\text{)}$  in 2050 and 2100 respectively. A different behaviour is evident in the infiltration rate: if in the 2050 scenario the infiltration increases, showing that natural ventilation can reduce the cooling demand, in the 2100 the infiltration is reduced (average of the site  $0.7 \text{ h}^{-1}$  in 2050 and  $0.5 \text{ h}^{-1}$  in 2100). In future the heating demand will decrease, and the cooling demand will increase. Passive strategies will be firstly applied, like modifying the physical properties of the ground covering, as well as the envelope. Secondly, the improvement of the natural ventilation, during nighttime, is required. Finally, the shortwave reflectance of the outdoor surfaces has an interesting impact in the demand of

buildings: the albedo of roof must be as higher as possible, passing from the actual 0.6 to 0.7, 0.8 in the optimized campus for 2050 and 2100, respectively. These results underline the positive impact of a clear roof covering, able to positively influence the buildings energy demand. It is interesting to notice that higher is the reflectance of the roofs, lower is the insulation required, in order to maintain the similar energy performances: in the 2050 the optimal option is 0.23 m (on the roof) of insulation and a SWR of 0.7; in 2100 the optimal option has 0.12 m (on the roof) of insulation and a SWR of 0.8. Finally, the outdoor environment has a major impact in reducing the demand, as an example the albedo of the ground, passing from the actual 0.2 (asphalt + concrete tiles) to 0.6 in 2050 (concrete covered with heat reflective paints) and 0.5 in 2100 (light concrete covering and grass). The main problem in using light colors is the maintenance required in order to guarantee the required reflectance.

Group	Parameter description	Current Case study	Typical Meteorological Year	2050-B1	2100-B1
Envelope characteristics	Thickness Insulation Envelope First Phase of Construction (m)	0.10	0.26	0.29	0.22
	Thickness Insulation Envelope Polydôme (m)	0.10	0.17	0.18	0.24
	U-value windows ( $W\ m^{-2}K^{-1}$ )	1.30	1.24	0.74	0.82
	Infiltration Rate ( $h^{-1}$ )	0.3,0.2,0.74,0.76	0.65,0.67,0.49,0.68	0.74,0.87,0.48,0.72	0.67,0.35,0.49,0.61
	Shortwave reflectance of roofs (-)	0.6	0.6	0.7	0.8
Ground Characteristics	Shortwave reflectance of the ground covering (-)	0.2	0.4	0.6	0.5

Table 6.5 Optimal parameters, as obtained by the three optimizations (Typical Meteorological Year, 2050-B1 and 2100-B1) and by the current case study.

Optimized scenario	EX Typical Meteorological Year ( $kWh\cdot m^{-2}$ )	Typical Meteorological Year ( $kWh\cdot m^{-2}$ )	EX 2050 ( $kWh\cdot m^{-2}$ )	2050 optimized ( $kWh\cdot m^{-2}$ )	EX 2100 ( $kWh\cdot m^{-2}$ )	2100 optimized ( $kWh\cdot m^{-2}$ )
Heating demand	103.24	83.69	90.80	74.06	89.68	63.51
Cooling demand	8.08	7.00	16.55	14.29	16.85	14.32

Table 6.6 Heating and cooling demand of the campus, as obtained by the three optimizations (Typical Meteorological Year, 2050 B1 and 2100 B1) and by the current case study (EX) projected in the future.

The following Figures (6.25 -6.27) show the optimized configuration of the EPFL campus (Zone-B) for a Typical Meteorological Year, as well as for the selected future climatic scenarios.



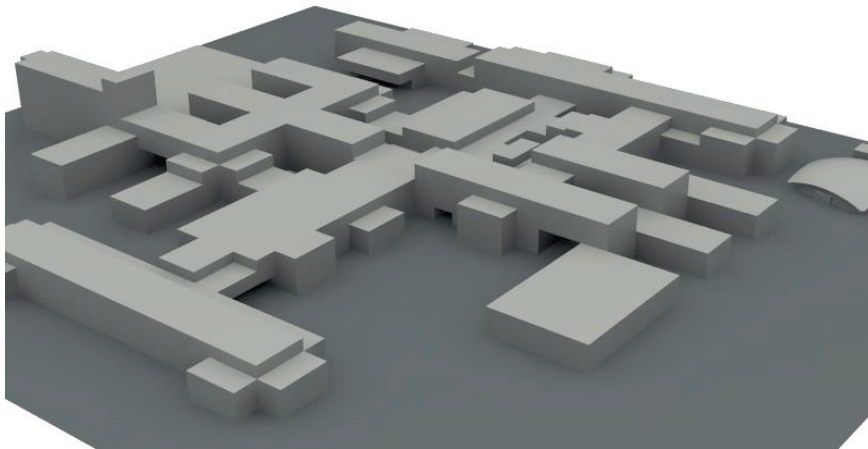


Figure 6.25 EPFL campus, Zone-B; optimized design for a Typical Meteorological Year.

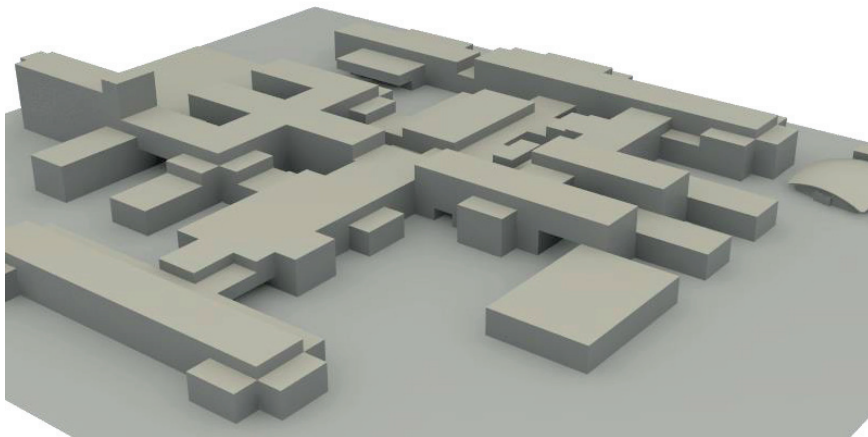


Figure 6.26 EPFL campus, Zone-B; optimized design for 2050-B1.

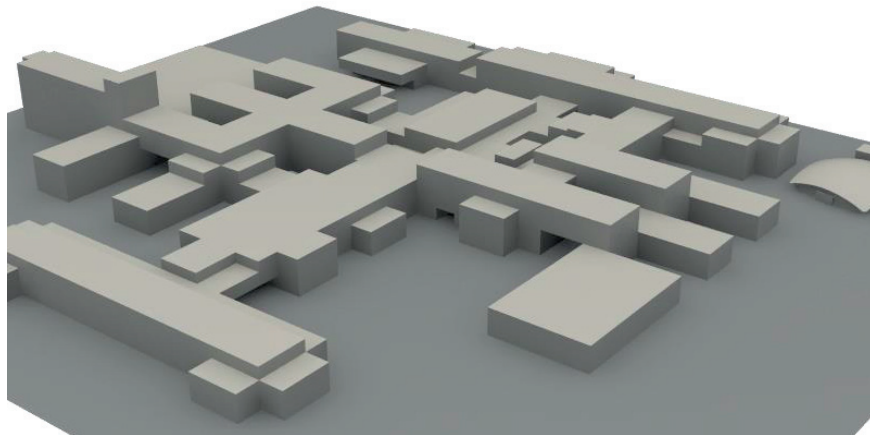


Figure 6.27 EPFL campus, Zone-B; optimized design for 2100-B1.

### 6.3 The Swiss International School Campus in Dubai

#### *Design objectives*

This section presents the optimization of the cooling demand of the Swiss International School Campus in Dubai as well as the human comfort in the outdoor liveable environment, by the use of the Index of Thermal Stress (ITS), for a typical meteorological year, as well as for two futures climatic scenarios: 2050-A2 and 2100-A2. In concrete terms, it considers the impact of the air tightness of the envelope (thermal insulation and infiltration rate), the physical properties of the envelope and the ground covering, shortwave reflectance and the thermal conductivity, on the cooling load of buildings and on the outdoor human comfort. The interesting aspect is the variation in the energy behaviour of the campus in future climatic scenarios; as mentioned in Chapter 5, the cooling demand will increase in future climatic scenarios and the outdoor environment will be, clearly, less comfortable.

#### *Analysis target*

The Swiss International School Campus is composed of seven buildings that host the following scholar functions: kindergarten, auditorium, primary and secondary school, sport centre and boarding. In this environment are positioned eleven pedestrians, as described in Figures 6.28 and 6.29:

- P1 is standing on an emerging roof (height of 3.5 m)
- P2, P3 and P4 are located in the courtyards of the kindergarten
- P5 is placed on the southern entrance of the kindergarten, and protected by the shadowing provided by the building
- P6 and P7 are located on the open terrace of the sport centre and of the school, respectively
- P8, P9 and P10 are protected by the shadowing of the trees, on the East and West side (P8) and on the North and South side (P9 and P10)
- P11 is located on the northern part of the campus, without any protection from the East side.

Hybrid Algorithm Optimization with Heuristics

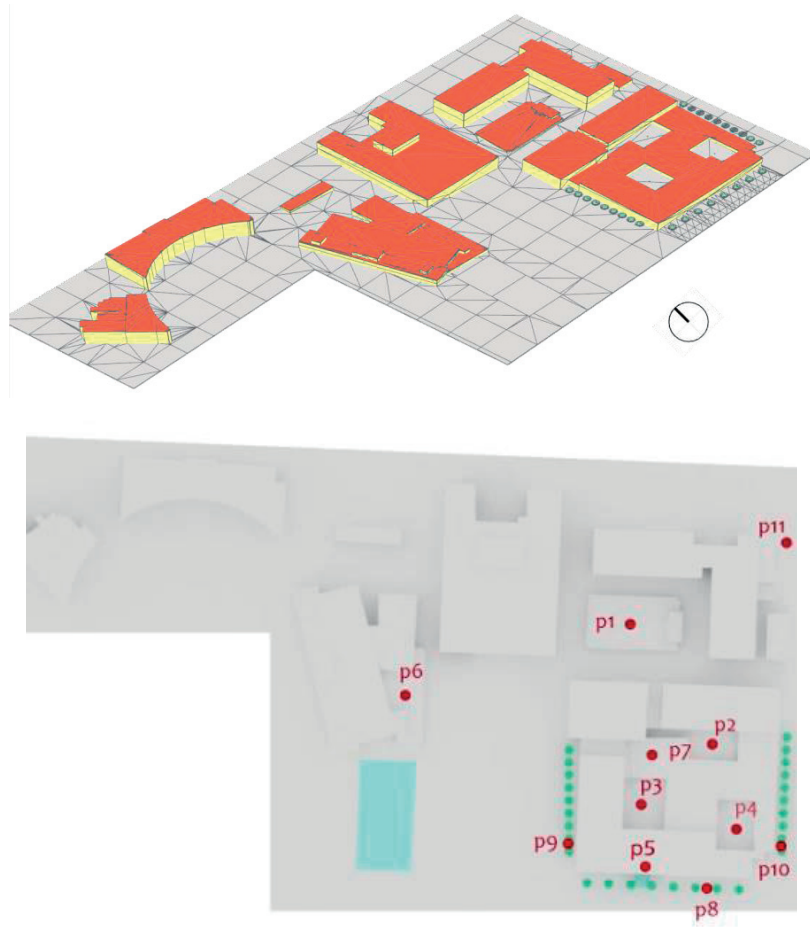


Figure 6.28 Swiss International School Campus in Dubai. 3D view from CitySim Pro (top), and plan view with the indication of the eleven pedestrian located in the outdoor environment (bottom).

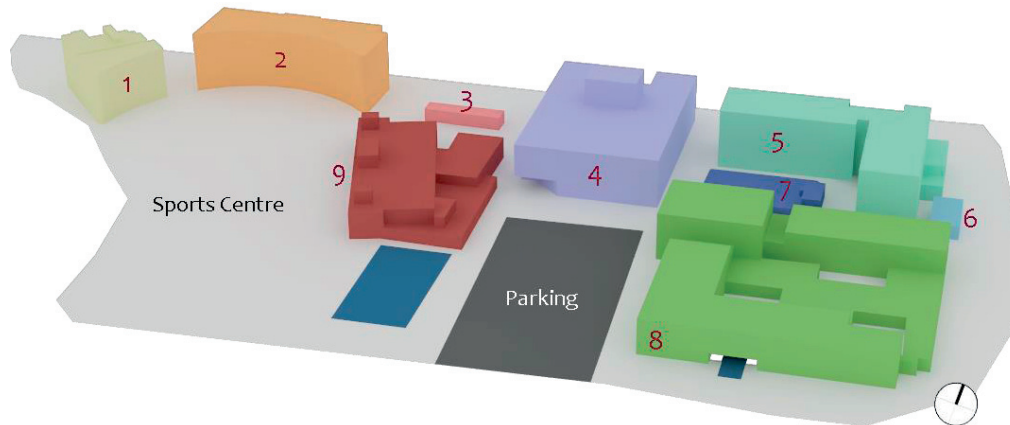


Figure 6.29 Swiss International School Campus in Dubai. 3D view of the site (top). Bottom: Aerial photo, source: khaleejtimes.com (left) and photo of building 8 (right)

The same analyses are performed with a typical meteorological year of Dubai, and in future climatic scenarios 2050-A2 and 2100-A2. In accordance with the future weather data 2050-A2 and 2100-A2, provided by Meteonorm, the average annual temperatures will increase by  $0.74^{\circ}\text{C}$  in 2050 (from  $28.37^{\circ}\text{C}$  to  $29.11^{\circ}\text{C}$ ) and by  $3^{\circ}\text{C}$  in 2100-A2. A different trend is shown by the total annual precipitations, passing from 54.2 mm to 109.2 mm in 2050-A2, then reducing in 2100-A2 to 92.1 mm. Precipitations continue to be absent from May to November, but are more than doubled in the other months, as shown in Figure 6.30. Finally there is an increase in the relative humidity, passing from an average of 52.5 % in TMY to 60.3% in 2050-A2 and 60.5% in 2100-A2. The humidity increases mostly during the summer time: as an example the average humidity during this season will pass from 48% TMY to 60% in 2100-A2. Considering that this climate is already quite humid, the future scenario will clearly decrease the comfortable sensation of people.

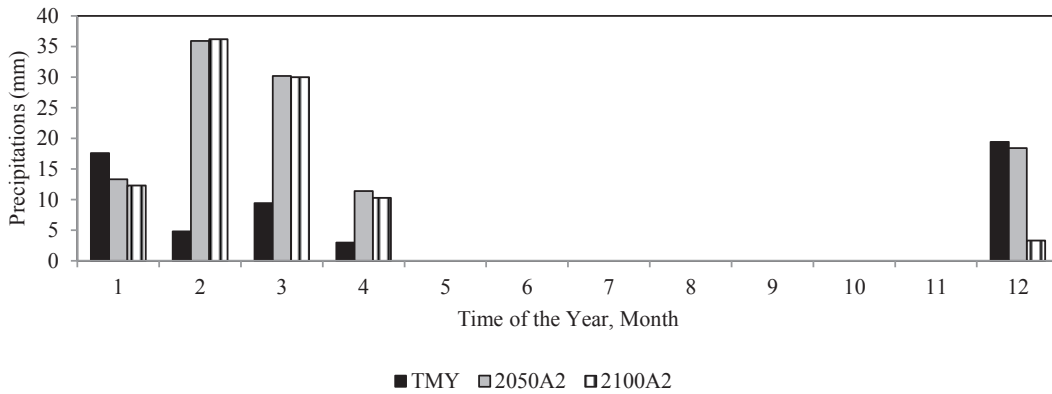


Figure 6.30 Dubai, comparison between the monthly precipitations of a Typical Meteorological Year, provided by Meteonorm, and the future climatic scenarios 2050-A2 and 2100-A2, based on the IPCC research (IPCC, 2000).

#### Design parameters

The thermal balance of an horizontal surface, as an example a solid pavement, under the sun is given by the following formula, adapted from (Santamouris et al., 2011) (Santamouris and Kolokotsa, 2016):

$$(1 - R_s) I = [\varepsilon_s \sigma (T_s^4) - \varepsilon_{sky} \sigma (T_{sky}^4)] + h_c (T_s - T_a) - \kappa \frac{dT}{dx} \quad (6.4)$$

where  $R_s$  (-) is the shortwave reflectance of the surface,  $I$  ( $\text{Wm}^{-2}$ ) is the solar irradiance,  $\varepsilon$  (-) is the infrared emissivity,  $\sigma$  is the Stefan-Boltzmann constant,  $T_s$  (K) is the surface temperature,  $T_{sky}$  (K) is the sky temperature,  $h_c$  is the convection coefficient ( $\text{Wm}^{-2}\text{K}^{-1}$ ),  $T_a$  (K) is the air temperature,  $\kappa$  ( $\text{Wm}^{-1}\text{K}^{-1}$ ) is the thermal conductivity of the surface and  $\frac{dT}{dx}$  is the temperature gradient, which represents the heat conducted (from the warmer to the cooler side) through the layers within the horizontal surface. Based on the Equation above, the surface receives the solar irradiance, and absorbs or reflects it, according to its albedo. Based on the irradiance absorbed, the surface emits the radiation in the far infrared part of the spectrum (from the surface to the sky), or by convection, thanks to the air movements (Santamouris and Kolokotsa, 2016). It is evident that the thermal balance of artificial surfaces during daytime is mostly impacted by the solar irradiance; on the opposite during nighttime the balance is mostly affected by the surfaces emissivity and thermal conductivity. When referring to the ground, other fluxes have to be considered, as the permeability and heat capacity (Santamouris et al., 2011). Knowing the thermal balance of a surface, the design parameters are defined in order to minimize the cooling demand of buildings and increase the outdoor human comfort. The evaluation of the optimization proceeds with the following seventeen parameters, are summarized in Table 6.7.

Group	Symbol and Domain	Parameter description	Unit
Buildings characteristics	$x_0 \in [0.05, 0.8[$	Shortwave reflectance of Walls	(-)
	$x_1 \in [0.05, 0.8 [$	Shortwave reflectance of Roofs	(-)
	$x_2 \in [0.05, 0.8 [$	Shortwave reflectance of Terraces	(-)
	$x_3 \in [0.0, 0.35[$	Thickness Insulation of the Roof	(m)
	$x_4 \in [0.0, 0.35[$	Thickness Insulation of the Wall	(m)
	$x_5 \in [0.1, 0.9[$	Infiltration Rate	(h <sup>-1</sup> )
	$x_6 \in [0.05, 3.5[$	Thermal conductivity of the wall	(W·m <sup>-1</sup> K <sup>-1</sup> )
	$x_7 \in [0.05, 3.5[$	Thermal conductivity of the roof	(W·m <sup>-1</sup> K <sup>-1</sup> )
Ground Characteristics	$x_8 \in [20, 27[$	Internal set point temperature	(°C)
	$x_9 \in [0.05, 3.5[$	Thermal conductivity of the ground covering_ concrete tiles	(W·m <sup>-1</sup> K <sup>-1</sup> )
	$x_{10} \in [0.05, 3.5[$	Thermal conductivity of the ground covering_ rubber	(W·m <sup>-1</sup> K <sup>-1</sup> )
	$x_{11} \in [0.0, 0.8[$	Shortwave reflectance of the ground covering_ concrete tiles	(-)
Greening	$x_{12} \in [0.0, 0.8 [$	Shortwave reflectance of the ground covering_ rubber	(-)
	$x_{13} \in [1.0, 5.0 [$	Leaf Area Index Trees exposed to South	(-)
	$x_{14} \in [1.0, 5.0 [$	Leaf Area Index Trees exposed to East	(-)
	$x_{15} \in [1.0, 5.0 [$	Leaf Area Index Trees exposed to West	(-)
	$x_{16} \in [0.65, 1.25 [$	F factor of the water	(-)

Table 6.7 Optimization of the cooling demand and outdoor human comfort of the SISD campus in Dubai. The seventeen proposed parameters.

The building characteristics are optimized by modifying the external envelope (shortwave reflectance, insulation thickness and thermal conductivity) and the HVAC systems (infiltration rate and indoor temperature): the external envelope impacts both the pedestrian and the cooling demand, on the opposite the HVAC systems impact just the cooling. The envelope of the building has a major role in this climate, due to its impact on the energy demand of buildings as well as on the urban thermal balance: the envelope absorbs the solar and infrared radiation and dissipate the heat through convection and radiation (Santamouris et al., 2011). The shortwave reflectance (SWR) of the envelope (roof and walls) impacts both the cooling demand and the outdoor human comfort; the interesting point is that they are impacted in an opposite way: if the SWR is large, the radiation is reflected by the surface, its temperature is decreased and consequently the cooling demand of the building reduced. But the radiation that is reflected by the external surfaces, impinging on the pedestrian: for these reasons, previous studies showed that an urban environment, in a hot climate, characterized by with high albedo on ground covering and walls, can induce high thermal stress to the pedestrians (Erell et al., 2014). A similar analysis, based on the radiation received and emitted by the surface, was made for the thermal insulation of roofs: by adding an external insulation, the envelope is losing its outdoor thermal mass, and consequently its capacity to absorb the heat during the day and loose it during the night. Due to the composition of the roof (made of gypsum, insulation with EPS and concrete), it is interesting to see what happens for liveable roof terraces, the pedestrians being directly influenced by the longwave radiation emitted by the roof. For all the composite details, please refer to Annex B. Another analysis was carried out for the wall, composed of 0.05 m of concrete, an internal layer of EPS and other 0.02 m of concrete: by increasing the thermal insulation of walls, the impact on the pedestrian is reduced, because of the external concrete layer; on the opposite the insulation impacts the cooling demand by reducing the thermal losses. The thermal conductivity, the capacity of the material to conduct heat, of walls and roofs is optimized, by varying it from 0.05 W m<sup>-1</sup>K<sup>-1</sup> (cork) to 3.5 W m<sup>-1</sup>K<sup>-1</sup> (e.g. gneiss, marble, granite and basalt). Materials with high thermal conductivity, as an example steel (45 W m<sup>-1</sup>K<sup>-1</sup>) and aluminum (200 W m<sup>-1</sup>K<sup>-1</sup>), transfer quickly the heat and reach high temperatures in direct sunlight (Vanos et al., 2016). The thermal conductivity of materials impacts the conductive transfer of heat through the building elements, or the ground. Materials with a high thermal conductivity transfer efficiently the heat: pavements with a high thermal conductivity have a low average maximum and a higher average minimum temperature; the effect of the conductivity is, clearly, reduced in high cloudy climate (Santamouris and Kolokotsa, 2016). The upper thermal conductivity selected in this work corresponds to 3.5 W m<sup>-1</sup>K<sup>-1</sup>. Metallic covering have higher conductivities, up to 200 W m<sup>-1</sup>K<sup>-1</sup> (Figure 6.31), but by analyzing the common construction materials and their conductivity, it is obvious that upon 388 construction



materials (retrieved from the CitySim Pro and Lesosai databases), only 5% of them have a conductivity higher than  $3.5 \text{ W m}^{-1}\text{K}^{-1}$ . Consequently, in order to avoid a plateau of results (as above introduced for the blinds cut-off), the thermal conductivity was optimized from  $0.05 \text{ W m}^{-1}\text{K}^{-1}$  to  $3.5 \text{ W m}^{-1}\text{K}^{-1}$ .

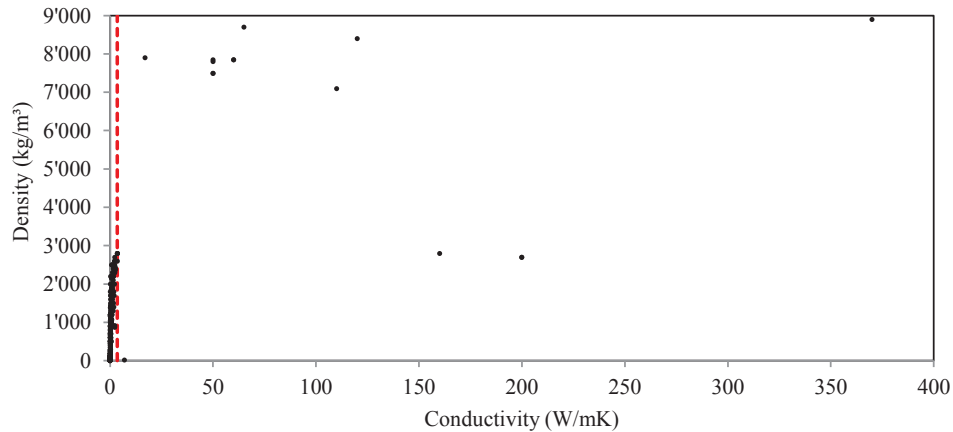


Figure 6.31 Thermal conductivity ( $\text{Wm}^{-1}\text{K}^{-1}$ ) of the common construction materials, as function of their density ( $\text{kgm}^{-3}$ )

The optimization of the HVAC system is subdivided into two main categories: the infiltration rate and choice of the indoor temperature. The infiltration rate is another important parameter to reduce the cooling demand of buildings: however is it better to fully insulate the buildings and increase the airtightness of their envelope, and consequently to reduce the heat exchanged between the indoor and the outdoor environment, or it is better to maintain certain ventilation, natural cooling during nighttime, between the indoor and the outdoor environment? The internal set point temperature was varied, from  $21^\circ\text{C}$ , which is a common set point temperature in this climate (Friess et al., 2012), to  $27^\circ\text{C}$ , considered as the maximal average internal temperature tolerated in the building, by having room with a set point temperature of  $25^\circ\text{C}$  and other spaces (like corridors or rooms without occupancy) with set point temperature of  $28^\circ\text{C}$ .

The ground covering was studied, by varying its thermal conductivity and its shortwave reflectance. In the first built area (the kindergarten) the ground covering is differentiated into two main typologies: the playground covered by coloured rubber and the concrete tiles in the other liveable spaces. Between the covering types, the main difference is related to the thermal conductivity of materials (rubber:  $0.29 \text{ W m}^{-1}\text{K}^{-1}$  and concrete tiles  $1.5 \text{ W m}^{-1}\text{K}^{-1}$ ) and their shortwave reflectance. In this analysis, the thermal conductivity varies between  $0.05$  (cork) to  $3.5$  (stone), assuming that the typical ground covering material are ranging the previous values. Normally in playgrounds, shock-absorbing materials are used, as sand ( $0.15\text{-}0.25 \text{ W m}^{-1}\text{K}^{-1}$ ), woodchips ( $0.18 \text{ W m}^{-1}\text{K}^{-1}$ ) and rubber ( $0.29 \text{ W m}^{-1}\text{K}^{-1}$ ). They are characterized by a quite high thermal conductivity; so to be safe they need to be protected by shadowing devices, reducing their surface temperature (Vanos et al., 2016). Finally, the landscape is optimized by varying the Leaf Area Index of trees and the evaporative cooling potential of the pools; the trees are subdivided into three categories, in accordance with their orientation. Trees are positioned on the South, East and West entrance of building, with a maximal height of  $5\text{m}$ , and varying their leaf area index from  $1$  (palm) to  $5$  (Acacia Tortilis). The cooling potential of the pool is quantified by the water evaporation potential, passing from  $0.65$  to  $1.25$  (Allen et al., 1998).

#### Objective function

The objective of this optimization is used to decrease the cooling demand of buildings, and improve the outdoor human comfort during daytime (from  $8:00$  to  $18:00$ ), assessed by the Index of Thermal Stress. The ITS is optimized during daytime, the school campus being occupied during the day, in accordance with the teaching schedule. The function is describes as follows:

$$f(\vec{x}) = \begin{pmatrix} Q_c \\ OTC \end{pmatrix} \quad (6.5)$$

where  $Q_c$  (Wh) is the total cooling demand of buildings and  $OTC$  (hours) is the daily outdoor thermal comfort, calculated from 8:00 to 18:00 hours.

#### Results and considerations\_ Typical Meteorological Year

A total of 3,000 evaluations were performed by the hybrid CMA-ES /HDE evolutionary algorithm, in order to find the optimal individual, as a function of the fitness cooling demand (Wh) and thermal comfort (W). The optimal individual (Figure 6.32) presents an ITS equal to 57 W (comfortable sensation) on average during the year. The cooling demand of the campus is 1.38 GWh, which corresponds to an average demand of  $22.7 \text{ kWh}\cdot\text{m}^{-2}$  for the site.

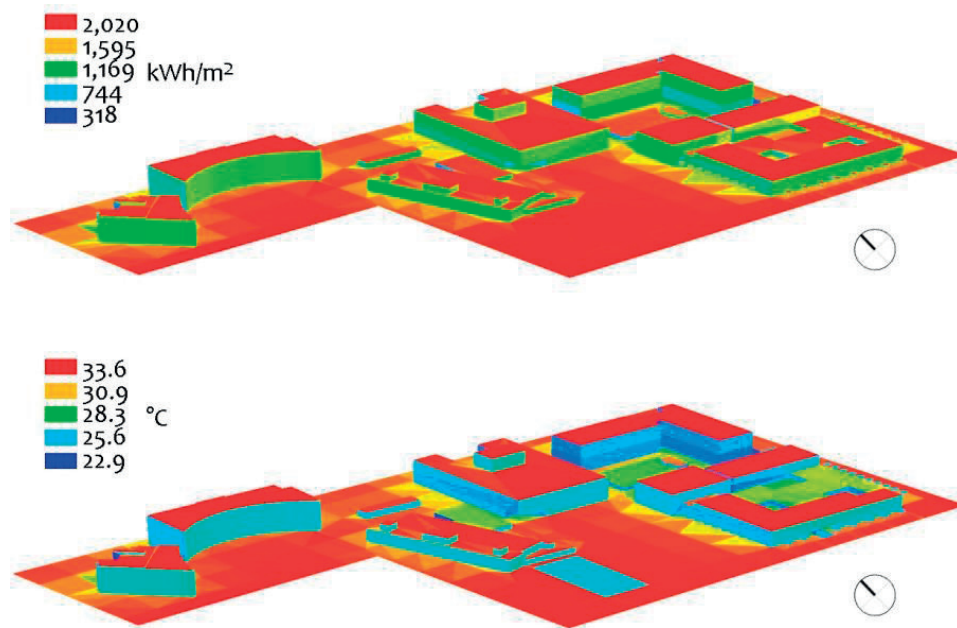


Figure 6.32 SISD campus. Optimal design of the campus for the Typical Meteorological Year. Annual shortwave radiation ( $\text{kWh m}^{-2}$ ) received by the campus (top) and annual surface temperature, expressed in  $^{\circ}\text{C}$  (bottom).

The optimal shortwave reflectance of roofs- terraces is 0.6, the one of the other roofs correspond to 0.3 and 0.8 for the walls. Effectively, based on the literature, a sound way to reduce the cooling demand of buildings and the urban heat island phenomena is to increase their solar reflectance, reducing their surface temperature (Santamouris and Kolokotsa, 2016). A similar result was obtained by the optimization; it is interesting to notice that roof terraces present a lighter color, compared to the other surfaces, and additionally, that they are shadowed by neighbor's buildings. Consequently, due to the above characteristics, they maintain a low surface temperature ( $28^{\circ}\text{C}$  on average during the year), reducing the radiative heat exchanges. The roofs are part of an energy efficient envelope (0.2 m of insulation); they are covered by an external layer of ceramic tiles (thermal conductivity equal to  $1 \text{ Wm}^{-1}\text{K}^{-1}$ ). By this strategy, the ceramic tiles store the radiation absorbed by the roof during daytime; thanks to the high insulation, the heat is not transmitted to the indoor environment. The optimal insulation thickness for the walls corresponds to 0.3 m. The infiltration rate per each building is equal to  $0.1 \text{ (h}^{-1}\text{)}$ , and the optimal internal temperature, in order to decrease the cooling demand, is set at  $27^{\circ}\text{C}$ . The infiltration rate is similar to the one predicted by a previous work dedicated to the Minergie standard for tropical climate; in this study building having to be airtight, the infiltration was assumed equal to  $0.05 \text{ (h}^{-1}\text{)}$ . We decided to increase the infiltration to  $0.1 \text{ (h}^{-1}\text{)}$ , assuming that a value of  $0.05 \text{ (h}^{-1}\text{)}$  was too low, and really difficult to realize in reality with

this climatic conditions. The ground covering is treated in two ways: the rubber covering is modified, by proposing a thermal conductivity of  $1.86 \text{ Wm}^{-1}\text{K}^{-1}$  (concrete tile, limestone or clinker brick) and a shortwave reflectance of 0.5. The current concrete ground is optimized by a shortwave reflectance of 0.3 and a thermal conductivity of  $3.19 \text{ Wm}^{-1}\text{K}^{-1}$ , which corresponds to stone (e.g. granite). Effectively, the thermal conductivity corresponds to the heat transmitted through a unit thickness of material; consequently to reduce the instantaneous exchanges between the surface and the pedestrian it is important to increase the material's thermal conductivity. The water pools are vernacular bioclimatic elements, able to decrease the air temperature and improve the outdoor environment; for that reason the optimizer maximizes the evaporative cooling potential, by increasing the f-factor to 0.8. Finally, the leaf area index of plants is maximized to 2.4 for trees located on the South entrance of the building, 1 for trees positioned on the East side and 2.7 for the one located on the West side. The results are directly related to the thermal sensation perceived by a pedestrian: in this climate, it is essential to reduce the solar radiation from the West direction, then in the others ones. Effectively, the cumulative solar irradiance on the East and West exposed surfaces is larger (during the summer time) than the one on the South and North, as presented in Chapter 4. On the other side, the air temperature is higher in the afternoon, compared to the morning, as well as the surface temperature of the built environment (due to night cooling). Consequently, the LAI of trees is maximized for plants located on the Southern entrance of building (protecting the pedestrian from the East and West orientation) and on the West side. In this location the pedestrian is protected by the building from the West side, but no shadings are present in the East direction. Based on the results obtained by the optimization in hot arid climate for a typical meteorological year, the cooling needs are drastically impacted by the infiltration rate ( $R=0.86$ , with  $n=145$ ): it is essential to reduce the infiltration rate ( $0.1 \text{ h}^{-1}$ ). On the opposite, to improve the outdoor human comfort, it is important to increase the LAI of trees ( $R=0.80$ , with  $n=145$ ), as well as their density.

#### Results and considerations\_ Climatic scenario 2050-A2

After 3,010 evaluations, the optimal individual (Figure 6.33) presents an ITS equal to 66 W, on average during the year. The cooling needs of 1.49 GWh, correspond to an average demand of  $24.6 \text{ kWh}\cdot\text{m}^{-2}$  for the site.

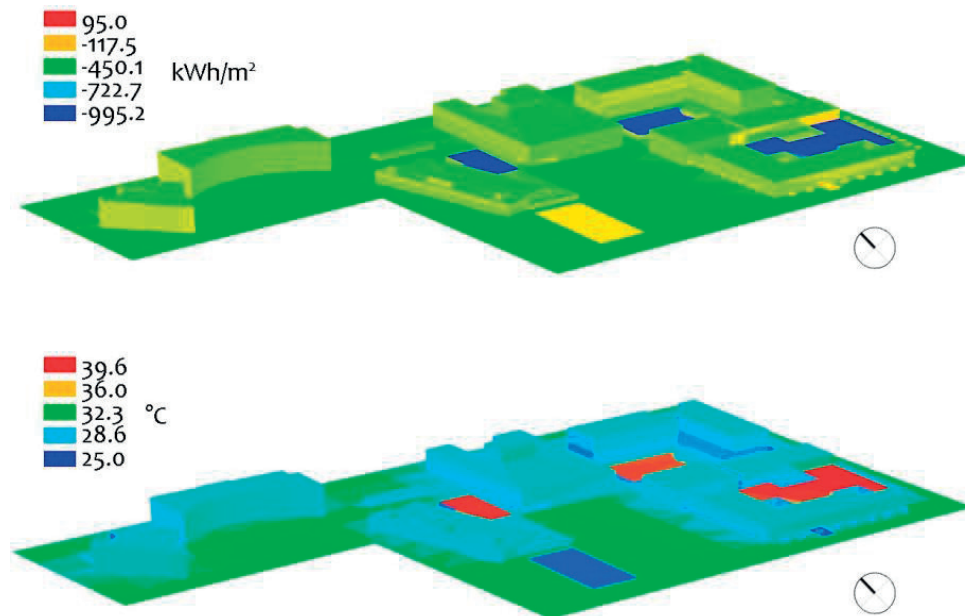


Figure 6.33 SISD campus. Optimal design of the campus for the 2050-A2. Annual longwave radiation ( $\text{kWh m}^{-2}$ ) received by the campus (top) and surface temperature, expressed in  $^{\circ}\text{C}$  (bottom).

In this case study, the shortwave reflectance of the roof is increased, up to 0.7, and the thermal conductivity reduced to  $0.05 \text{ W}\cdot\text{m}^{-1}\text{K}^{-1}$  (insulating materials): this result underlines the importance of reflecting the shortwave radiation impinging the roof, and consequently reducing the surface temperatures, as well as providing with a good insulation. The optimal design consists in increasing the insulation thickness of the facades, up to 0.28 m, increasing its thermal conductivity ( $3.5 \text{ W}\cdot\text{m}^{-1}\text{K}^{-1}$ ), and the shortwave reflectance, up to 0.6. The infiltration rate is similar to the previous optimization ( $0.1 \text{ h}^{-1}$ ), showing the necessity of an air tight envelope in order to decrease the cooling demand. The outdoor environment is characterized by high shortwave reflectance of the covering, both 0.6 and 0.8 to replace the current concrete and rubber, respectively. Based on the results, it seems logical to increase the reflectance of the surfaces partially shaded, as the rubber covering, reducing their temperature, and to reduce the reflectance of the surfaces exposed to the sun, due to the glare impact on the pedestrians, as well as the increase in the radiative exchanges. The thermal conductivity of the ground covering is quite similar:  $2.8 \text{ W}\cdot\text{m}^{-1}\text{K}^{-1}$  for the current concrete (stone), and  $3.2 \text{ W}\cdot\text{m}^{-1}\text{K}^{-1}$  for the current rubber (stone). The Leaf Area Index of the plants is slightly reduced compared to the previous optimization, corresponding to 2.2 for the trees located on the southern part, 1.2 the ones on the East and 1.0 for the ones on the West. As in the previous study, the evapotranspiration potential of the pool is maximized, in this scenario up to 1.25. The benefit of the greening is evident by analyzing the longwave radiation balance (Figure 6.33): by increasing the albedo of the surfaces, their temperature is reduced ( $27^\circ\text{C}$  for the roofs, annually), and the net longwave radiation ( $-450 \text{ kWh}\cdot\text{m}^{-2}$  for the roofs, annually) increased. That means that in order to decrease their temperature, the roofs reflects the impinging radiation; on the opposite, trees due to the evapotranspiration process, have a lower surface temperature ( $25^\circ\text{C}$  in average during the year) and emit less long wave compared to the roofs ( $-120 \text{ kWh}\cdot\text{m}^{-2}$  annually). This is due to the fact that plants use the absorbed radiation partially to foster the evapotranspiration process. Naturally there is an important element to consider: the water use as function of the cooling provided (Shashua-Bar et al., 2009b).

Based on the results obtained by the optimization in the hot arid climate for the weather data 2050-A2, the cooling demand is impacted by the infiltration rate ( $R=0.77$ , with  $n=146$ ) and by the internal temperature ( $R=0.84$ , with  $n=146$ ): in order to reduce the demand of building, it is essential to reduce the infiltration rate ( $0.1 \text{ h}^{-1}$ ) and to increase the indoor temperature up to  $27^\circ\text{C}$ , a result that is quite intuitive. On the opposite, to improve the human outdoor comfort, it is important to increase the LAI of trees ( $R=0.81$  on the South orientation,  $0.76$  on the East and West orientation, with  $n=146$ ).

#### *Results and considerations\_ Climatic scenario 2100-A2*

After 3,004 evaluation, the optimal individual (Figure 6.34) has an cooling demand of 3.4 GWh, which corresponds to an average demand of  $55.8 \text{ kWh}\cdot\text{m}^{-2}$  for the site. The optimal individual presents an ITS equal to 80 W, on average during the year.

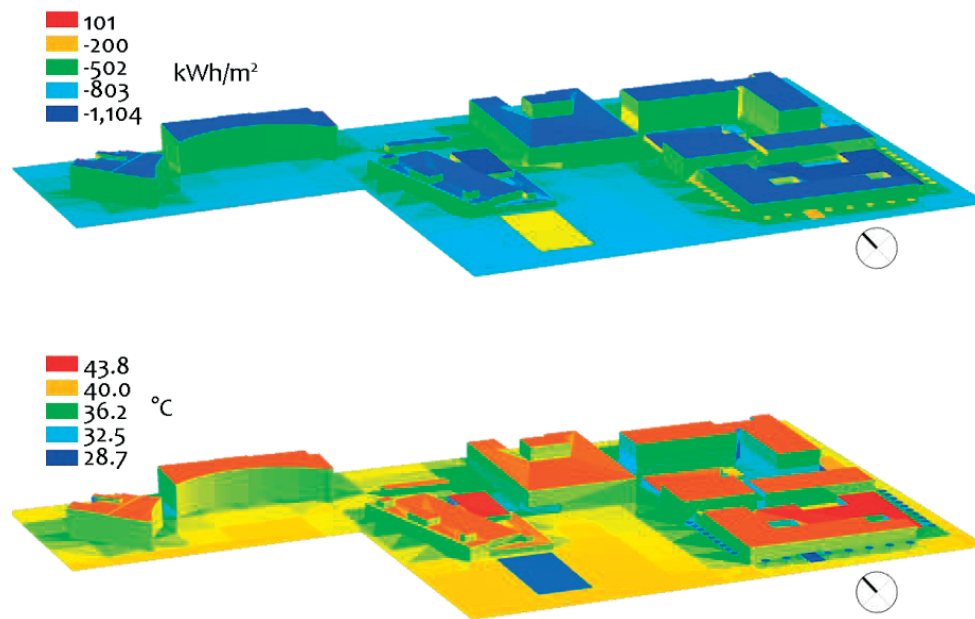


Figure 6.34 SISD campus. Optimal design of the campus for the 2100-A2. Annual net longwave radiation ( $\text{kWh m}^{-2}$ ) received by the campus (top) and surface temperature, expressed in  $^{\circ}\text{C}$  (bottom).

On the opposite respect to the other case studies, the shortwave reflectance of the roof is reduced to 0.2, the thermal conductivity increased up to  $3.3 \text{ W}\cdot\text{m}^{-1}\text{K}^{-1}$  (stone covering), and the thermal insulation increased to 0.35 m. In this optimization, the stone covering absorbs the impinging radiation, storing the heat during daytime, and reemitting it during nighttime. By contrast, the building is well insulated, consequently reducing the heat penetrating in the building. The insulation of walls is reduced to 0.16 m and their albedo equals 0.2; by this albedo, the surface temperature of the wall increases, reaching  $34^{\circ}\text{C}$  on average during the year. In contrast to the previous study, the internal temperature is set to  $25.4^{\circ}\text{C}$  and the infiltration rate is increased to  $0.19 \text{ h}^{-1}$ . The shortwave reflectance of the ground cover corresponds to 0.30 (conductivity equals to  $1.1 \text{ Wm}^{-1}\text{K}^{-1}$ , such as limestone or cement blocks) for the current concrete, and 0.08 for the rubber (conductivity equals to  $1.63 \text{ Wm}^{-1}\text{K}^{-1}$ , such as hard limestone and concrete). The Leaf Area Index of trees is similar on all directions, corresponding to 1.14 on the East direction, and 1 on the West and South one.

Based on these results obtained for hot arid climate the cooling demand is drastically impacted by the infiltration rate ( $R=0.9$ , with  $n=145$ ) and by the thermal insulation of the walls ( $R=0.64$ , with  $n=145$ ). In accordance with the optimizer, the cooling strategies are based on night cooling (by radiative exchanges and ventilation): in order to reduce the cooling demand of building it is essential to slightly increase the infiltration rate ( $0.19 \text{ h}^{-1}$ ).

### Conclusion

The optimization with the hybrid CMA-ES/HDE algorithm leads to the following conclusions, for a sound design of the SISD campus, in actual and future climatic scenarios. The shortwave reflectance of the ground covering (concrete tiles) must be low, in order to reduce the radiation reflected toward the pedestrian. Its thermal conductivity has to be comprised between  $1.1 \text{ Wm}^{-1}\text{K}^{-1}$  to  $3.1 \text{ Wm}^{-1}\text{K}^{-1}$ , which corresponds to limestone, cement and stone (as an example granite). If the ground covering is shadowed during the main part of the daytime (as the rubber in the courtyards), its conductivity can be in the range of  $1.6 \text{ Wm}^{-1}\text{K}^{-1}$  to  $3.2 \text{ Wm}^{-1}\text{K}^{-1}$ , which corresponds to hard limestone to stone. Clearly, the ground covering, if not shaded, has to absorb the heat during daytime, reducing the radiation reflected to the pedestrians: this is done by increasing its thermal conductivity and reducing the shortwave reflectance. The landscape has a great impact on the energy demand of buildings, as well as on the



outdoor human comfort: their density has to be maximized in order to protect the pedestrian from the sunrays, for this reason the optimizer maximizes trees on the Southern entrance of the building, as they shadow the pedestrian on the East and West side. The pool has a positive effect on the urban microclimate, for this reason its presence is always ensured by the optimizer, knowing that the climate change will increase evapotranspiration, due to larger temperature, radiation, wind speed and decreasing humidity and rainfalls (Abteu and Melesse, 2013). In order to maintain a correct water management (ratio between the water needs and the waste) and reducing the water losses, the evapotranspiration capacity of the pool is decreased from 1.25 in 2050, to 0.7 in the future climatic scenarios. In order to reduce the water losses, it is essential to shadow the pool, by meshes or by trees. Concerning the energy demand of buildings, it is evident that, due to the climate change, there will be an increase in the cooling demand, passing from 22.7 kWh·m<sup>-2</sup> for a typical meteorological year, to 55.8 kWh·m<sup>-2</sup> in 2100-A2. In order to decrease the demand, the general trend is to increase the thermal insulation thickness and foster night cooling. It is interesting to notice that the LAI of trees corresponds to 1-1.1 in 2100: this is probably related to the fact that in this optimization the objective is to improve the night cooling (by ventilation, conductivity of surfaces, etc.), consequently the presence of trees during night represents an obstacle for the sky view factor, reducing, consequently, the capacity of the surface to lower its temperature. Table 6.8 summarizes the properties of each optimization. Another interesting result, in 2100, is the reduction of the insulation of walls: in this climate is important to improve the thermal mass of building, in order to store the heat during daytime (reducing the radiation reflected to the pedestrians) and emit it during nighttime. In accordance with the optimizer, the external layer of insulation would increase the radiation reflected, due to its low thermal conductivity, consequently increasing the radiation received by the pedestrians.

Group	Parameter description	TMY	2050-A2	2100- A2
Buildings characteristics	Shortwave reflectance of Walls	0.8	0.6	0.2
	Shortwave reflectance of Roofs	0.3	0.7	0.2
	Shortwave reflectance of Terraces	0.6	0.1	0.05
	Thickness Insulation of the Roof	0.2	0.30	0.35
	Thickness Insulation of the Wall	0.3	0.28	0.16
	Infiltration Rate	0.1	0.1	0.19
	Thermal conductivity of the wall	0.6	3.5	0.2
	Thermal conductivity of the roof	1.0	0.05	3.3
	Internal set point temperature	27	27	25.4
Ground Characteristics	Thermal conductivity of the ground covering_ concrete tiles	3.19	2.80	1.10
	Thermal conductivity of the ground covering_ rubber	1.86	3.23	1.63
	Shortwave reflectance of the ground covering_ concrete tiles	0.3	0.6	0.3
	Shortwave reflectance of the ground covering_ rubber	0.5	0.8	0.1
Landscape	Leaf Area Index Trees exposed to South	2.4	2.2	1
	Leaf Area Index Trees exposed to East	1	1.2	1
	Leaf Area Index Trees exposed to West	2.7	1.0	1.14
	f factor of the water	0.8	1.25	0.71

Table 6.8 SISD campus. Optimal parameters, as obtained by the three optimizations (typical meteorological year, 2050 A2 and 2100 A2).

Table 6.9 summarizes the relative difference (%) between the optimal individual for each optimization and a pedestrian located in the desert, without any shading. It is evident that the pedestrians protected by plants are benefiting from this situation, as they experience a lower average thermal sensation by 40%, during a typical meteorological year. By contrast, P6 (on the roof terrace of the sport building) and P1 (on the roof terrace on the northern part of the campus) present the lowest difference, because they are less protected by the built environment. Please, refers to Figure 6.28 for the location of pedestrians.

Pedestrian	P1	P2	P3	P4	P5	P6	P7	P8	P9	P10	P11
TMY	13.98	22.13	32.77	32.80	27.55	12.91	16.29	40.72	<b>41.18</b>	22.84	26.32
2050	16.01	18.35	28.12	27.82	21.63	13.97	18.27	31.71	33.54	16.77	22.62
2100	14.33	23.34	29.89	30.10	19.30	<b>11.12</b>	16.37	33.04	32.33	16.18	22.60

Table 6.9 Difference (%) between the average summer thermal perceptions of the pedestrians located in the campus, compared to a pedestrian located in the desert.



The following Figures (6.35- 6.37) show a rendering of the optimal design, in accordance with the climatic data; the color palette is defined on grey tones, based on the required RAL and the albedo of the surfaces.

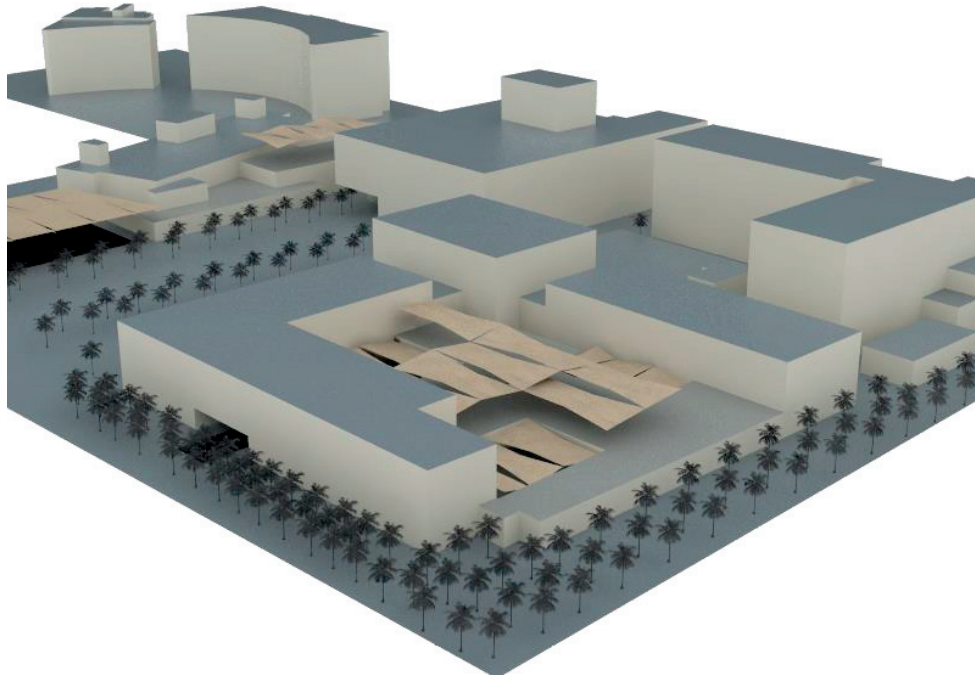


Figure 6.35 Swiss International School of Dubai, optimal design for a Typical Meteorological Year.

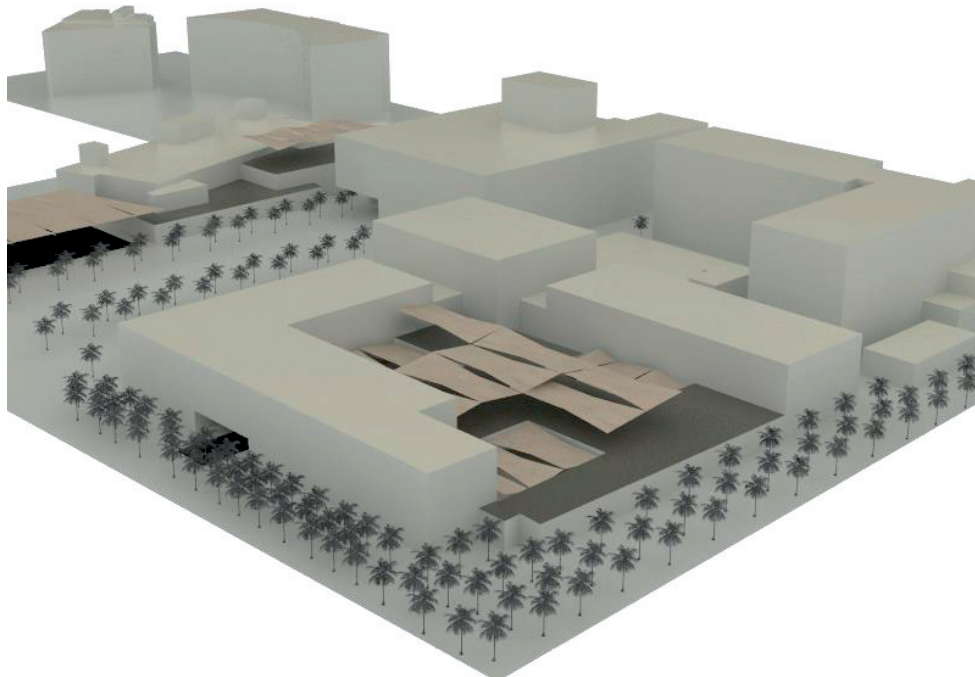


Figure 6.36 Swiss International School of Dubai, optimal design in scenario 2050-A2.

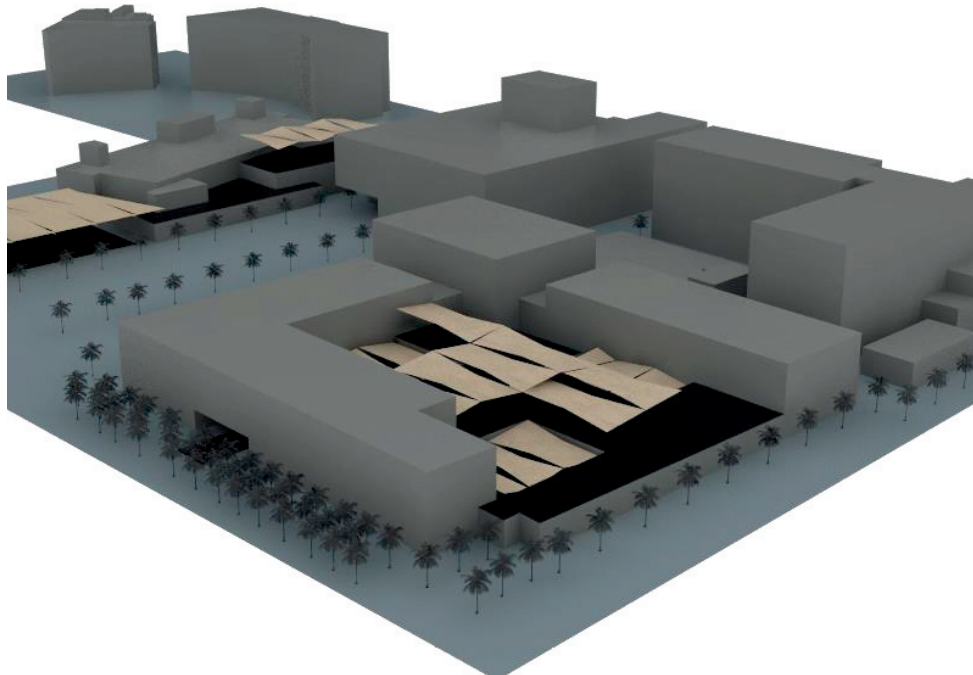


Figure 6.37 Swiss International School of Dubai, optimal design in scenario 2100-A2.

In conclusion, based on this optimization, it is necessary to find a compromise between the cooling demand of buildings and the outdoor thermal comfort; one essential parameter is the shortwave reflectance that has to be as high as possible on the roof (if they are not liveable terraces) and as low as possible in the ground covering. The thermal insulation is essential to reduce the cooling demand, but can compromise the outdoor human comfort. For this reason it is commended to offer shadowing in front of each building, in order to decrease the radiation received by the surface, and consequently the re-emitted heat: this is done by design shadowed semi outdoor spaces (as colonnade, or patio). Finally, in an urban context, it is essential to understand that we are not optimizing one parameter, but a system of elements, connected to each other.

#### 6.4 Conclusions and future outlook

The optimization presented in this chapter underlines some interesting key elements in the analysis of the outdoor human comfort in hot and temperate climate. First of all, it is obvious that to optimize the energy demand, it is essential to design air tight envelopes, and increase the albedo of the urban surfaces; by contrast when analyzing the energy performance as well as the outdoor human comfort, a compromise between both parameters has to be found. As an example, by reducing the albedo of the ground covering, and in the same time by increasing the one of roof which is not accessible by the pedestrians. Another major factor is the shadings: if a surface is shaded, we can increase its shortwave reflectance, slightly affecting the pedestrian's thermal sensation. The greening has a large potential in decreasing the urban surface temperature, as well as in improving the outdoor human comfort; the greening can be declined as tree, grass or water bodies. By analyzing the EPFL campus in actual and future climatic scenarios, it is interesting to notice that the campus will slightly move from a heating centric to a cooling centric behavior, underling the need of cooling strategies in the buildings. Concerning the outdoor human comfort, in order to decrease the uncomfortable hours, it will be essential to offer a sound landscape design, as greening, as meshes. By contrast, if greening can be maximized in the temperate climate of Lausanne, a detailed planning is required for the SISD campus in order to offer an appropriate water management, due to the water scarcity. Results obtained by the optimization will help defining the recommendations in the next chapter.

Naturally, it is important to notice that, mostly when working at the urban environment, all factors interact to each other's, consequently the optimal solutions represents a balance between the parties.

#### *Future outlook*

Based on the optimisation already performed, a further development is proposed by varying the current constraints. Firstly, in accordance with the future projections, the population of the EPFL campus is continuing to increase, and new buildings will be added to the site. The main question is how to design correctly the urban environment in order to improve both the energy performance and the outdoor human comfort? A new optimization could focus on this aspect, optimizing the building stock by rising its density. All the optimizations performed, are currently defined for the pedestrians performing a light metabolic activity. A further investigation is required in order to quantify the variation of the built environment, as function of the physical activity. This would bring a new design (and its variation through the day), as well as the choice of materials, as required by each activity. Additionally, trees are considered as evergreen: in order to improve the results (mostly in temperate climate) it is essential to design deciduous plants. Finally, the performed optimizations were focused on improving the heating and cooling demand, without considering the energy systems.

## Chapter 7 Conclusions

The urban microclimate affects two essential correlated parameters of the sustainability of a city: energy performance and outdoor human comfort. As an example, in hot climates, the higher the outdoor temperatures, the higher is the energy required for cooling buildings and the higher is the heat reemitted from buildings to the outdoor environment, increasing the Mean Air Temperature, and consequently degrading the comfort of pedestrians. Sustainable urban design therefore needs to address both topics, and architects, urban planners and municipalities must consider the outdoor environmental conditions as a key element in their design. Currently, it is difficult to perform microclimatic analyses for practitioners, due to the difficulty in using available software as well as the time required. The work carried out for this thesis is a first approach to correlate the energy performance of buildings and the outdoor human comfort, by providing a further module in a tool (CitySim Pro), which simplify the analyses, in order to be used by architects and urban planners. Thanks to the Comfort Map, the outdoor human comfort (by the ITS and COMFA\*), as well as the Mean Radiant Temperature are graphically and dynamically presented. The outdoor human comfort expresses the thermal perception of pedestrians; by contrast the MRT describes the radiative environment. The following recommendations are based on the results presented in the previous chapters; they are proposed for bioclimatic and sustainable campuses or city districts in temperate and hot arid climate. Before focusing on the analyzed climatic conditions, the following generalized recommendations can be outlined, as they are valid for all climatic conditions:

- In our century, more than ever, we should not limit an architectural design to a single building, but need to think and design at the district/ city scale. Furthermore, we are living in the so called Petropolis (UN HABITAT, 2012), consequently all choices we make in our city directly impact the rest of the world (Figure 7.1).

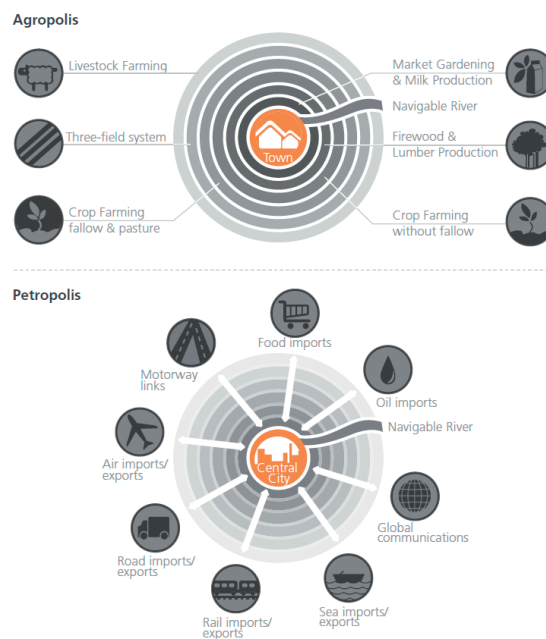


Figure 7.1 Agropolis and Petropolis (UN HABITAT, 2012)

- When addressing energy efficiency, we should determine the energy efficiency of a whole district and a city, not of a single building, as also suggested by Carmeliet (Carmeliet, 2012). This author makes a point for energy efficient districts where some buildings will be energy positive, while others, such as listed

ancient buildings, will not be touched. Currently, the main gap is the absence of an energy regulation for cities, needed to provide guidelines for sustainable urban design. A first step in this direction in Switzerland is the label *Cité de l'énergie* but further development is required.

- In order to improve the livability of cities, it is essential to provide a comfortable urban climate. Architects and urban planners should design considering the interactions of urban surfaces and observe the surface energy balance.

In this light, this doctoral thesis has investigated for that purpose sustainability factors on two campuses situated one in a moderate (EPFL campus, Lausanne) and one in a hot and arid climate (SISD campus, Dubai).

## 7.1 Bioclimatic and sustainable design for temperate climate

The recommendations for bioclimatic design in temperate climate are given according to current and future climatic conditions, focusing on buildings and outdoor design. Firstly, the key words for this climate are: bioclimatic approach and technology. In Switzerland, the energy performance of buildings is already regulated, and energy efficient buildings are a current practice. Consequently, what is important today is scaling up, passing from the building to the district and up to the city scale. Due to the impending climate change, which has been and will be stronger in Switzerland (SCNAT, 2016) compared to worldwide average countries (+1.8°C in Switzerland and +0.85°C on average for the world, from 1864 to 2016), it is essential to design buildings in accordance with their projected life-time, knowing that the current thermal behavior will be different in the next century, passing from a “heating centric” design to a “heating-cooling” design.

### *Buildings design*

Currently, heating is the principal cause of energy use in buildings in moderate climates. But in the future (based on the climatic scenarios provided by the Intergovernmental Panel for Climate Change), the cooling demand will increase (passing from 15% to 31%, in the case of the EPFL), and its impact on the total energy performance of buildings will not be considered negligible anymore. The first way to improve the energy performance of buildings is to refurbish them following the optimal practice available, such as for example by increasing the insulation of the envelope, as well as by optimizing glazing characteristics. Naturally, not all buildings can simply be refurbished to reduce their demand, such as for example buildings with high internal gains (industries, laboratories). In their case, further investigations are required, and the focus will be on improving building services, not just their envelope. Climate change will also affect the thermal sensation of users inside buildings: if now a user would feel “slightly warm” during summer time, in the 2050-A2 scenario he/she will experience “slightly warm” and “warm” thermal sensations from June to August. In order to reduce discomfort, natural strategies could be applied, such as night cooling, as well as smart building control. Concerning the building design, the optimal orientation of the buildings axes, obviously in this climate, is East-West, increasing the solar gains on the building and consequently reducing its heating demand. Photovoltaic panels are clearly a favourable renewable way to produce electricity, and thanks to new technologies, e.g. SwissInso (Figure 7.2) and Solaxess, they can be aesthetically integrated into buildings. Additionally, smart strategies, such as energy hubs, to efficiently manage the energy resources, are clearly necessary. The case study performed in two Swiss villages, Cartigny and Hemberg, underlined the enormous potential of smartly integrating and managing energy resources by a central grid (Le Guen et al., 2017) (Kuehner et al., 2017).



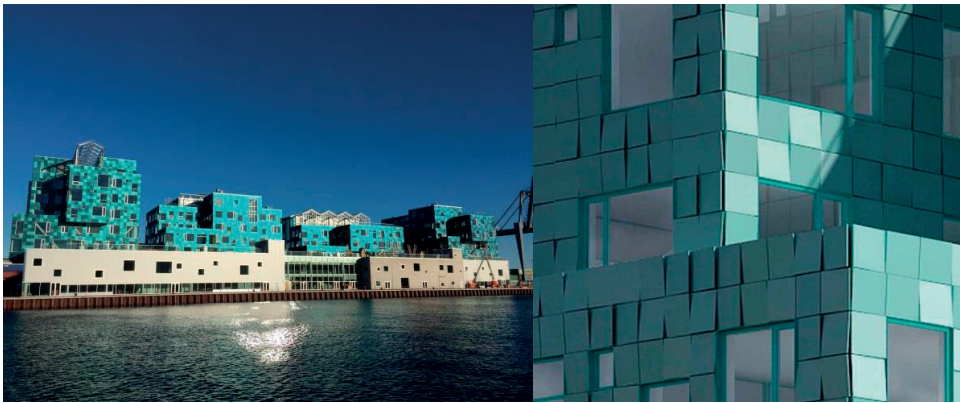


Figure 7.2 The Copenhagen International School's new building, covered by Swissinsol PV panels. Source: Philippe Vollichard (right) and Pinterest (left)

Minergie labelled buildings are already normal practice in Switzerland (43,000 buildings in 2017); consequently energy efficiency should now go behind Minergie, looking for energy positive buildings. Additionally, as stated above, energy efficiency efforts should focus on the district, or even the city scale. As proposed by Carmeliet (Carmeliet, 2012), the idea is to provide energy efficient districts, where some buildings will be energy positive (e.g. Minergie A) without compromising protected buildings of patrimonial value.

#### *Outdoor environmental design*

As stated above, the energy demand of buildings will increase due to the climate change; the outdoor environment will also be affected. As an example, the analyses of the outdoor thermal comfort on the EPFL campus show that comfortable thermal sensations will generally increase during the coldest months and decrease during the summer time. Man-made environments will be more affected by climate change compared to natural ones: during the warm seasons, in artificial environments, the hours of discomfort will well increase by 73% in summer, whereas the will only increase by 55% in a natural environment. Consequently, in order to improve the quality of the outdoor environment, shadowing strategies, evaporative cooling and a suitable greening design will be required. This is evident from the results obtained by optimization simulations using the hybrid CME-HDE evolutionary algorithm. The selection of construction materials should focus on their physical properties (albedo and thermal conductivity) as well as on the embodied energy and recycle potential. Finally, the dynamic variation of seasons should be taken into account in the project: spaces should be designed as function of seasonal variations.

In the past, people built their homes in accordance with locally available resources, and in order to protect themselves from outdoor climatic conditions. Consequently, vernacular architecture represents the first example of bioclimatic design. In order to understand the impact of climate change on the Swiss climate, we compared the typical architecture in Switzerland with the one of three Italian cities, presenting nowadays the future Swiss climatic conditions. The average ambient air temperature in Lausanne (46° 31' N, 06°38' E, 495 m asl, Cumulative Solar Irradiance: 1,219 kWh·m<sup>-2</sup>, Heating Degree Days: 3,273), will in 2100-A2 (IPCC, 2000) correspond to 14.6°C (10.9°C is the current average temperature for a typical meteorological year). The current average temperature in Rome (41° 54' N, 12° 29' E, 20 m asl, Cumulative Solar Irradiance: 1,403 kWh·m<sup>-2</sup>, Heating Degree Days: 1,891) corresponds to 15.8°C, in Florence (43° 46' N, 11° 15' E, 40 m asl, Cumulative Solar Irradiance: 1,440 kWh·m<sup>-2</sup>, Heating Degree Days: 2,098) to 15.2°C and in Perugia (43° 07' N, 12° 24' E, 493 m asl, Cumulative Solar Irradiance: 1,390 kWh·m<sup>-2</sup>, Heating Degree Days: 2,380) to 14.9°C (IPCC, 2000) (Rosa et al., 2015). It is evident that traditional architecture in Perugia and Lausanne are quite different (Figures 7.3 and 7.4): this comparison provides an indication of the future perspectives related to the Swiss climate. Effectively, the Swiss climate would pass from the current Cfb climate (C: Temperate; f: without dry season; b: warm summer) to the Csa climate (C: Temperate;



s: dry summer; a: hot summer). Consequently, the bioclimatic principles will vary, and according to an European report (BEAR-iD, 2016), the requirements for the design are described in Table 7.1.

Bioclimatic principles	Cfb climate	Csa climate
Envelope	Well-insulated building envelope with energy efficient fenestration.	Well-insulated building envelope with limited fenestration area, glazing with very low SHGC and efficient shading devices. Reflective (or cool) colors for the exterior envelope surfaces.
Energy systems	Heating system, ventilation system with heat recovery.	Heating and cooling energy system.

Table 7.1 Bioclimatic principles for the Cfb and Csa climate.



Figure 7.3 View of the city of Lausanne. Source: grandtour.myswitzerland.com



Figure 7.4 View of the city of Perugia. Source: viator.com

*Practical recommendations*

The following paragraph underlines the practical recommendations for a bioclimatic design in the temperate climate. It is important to notice that we will consider the future climatic conditions of the site, consequently the guidelines are defined considering the future thermal transition. The requirements, as already defined by the

Swiss norm, are neglected in this paragraph, as already part of the current practice. The following points should be addressed, when designing in these climatic conditions:

- Seasonal variability of the outdoor spaces, design the space as function of the time of the year, considering that due to the climate change, extreme climatic events will be more frequent.
- Maximize the windows on the South facades (glazing with seasonal SHGC), improving the solar gains during the colder season, but reducing them during the warmer season. Provide smart blinds strategies, in order to shadow the facades during the summer time.
- Provide reversible energy systems, able to heat during the winter time, and cool the air during the warmer season.
- Improve the natural ventilation during the summer time, cooling the buildings during the nighttime.
- Design the visual integration of renewable energies, which should be designed and interconnected between buildings, and up to the city, by the energy hub units.

## 7.2 Bioclimatic and sustainable design for hot arid climate

The key word for hot and arid climates is the bioclimatic approach: due to extreme climatic conditions, simple strategies (e.g. natural cooling, ventilation, evapotranspiration, etc.) can substantially improve the microclimatic conditions of a site. Naturally, sound decisions should be taken already at the masterplan scale in order to positively impact a design project. A correct pre-design should be followed by the energy plan, optimizing the energy performance of the buildings, from the envelope to the energy systems.

### *Buildings design*

Buildings should be designed as compact as possible in order to create shadowing upon the liveable outdoor environment. In order to improve the outdoor microclimate, semi outdoor environments should be created, by adding pergolas or colonnades around buildings, shading them and creating liveable spaces for pedestrians. The albedo of the surface must vary depending on the element (roof, floor and wall), as well as its orientation (North, East, South and West). The use of darker colors on the lower floors reduces the radiation emitted to pedestrians; by contrast, lighter colors on the upper floors increase the radiation reflected by the surface, and consequently decreasing the heat absorbed by the building. The use of cool materials (Santamouris and Kolokotsa, 2016) is proposed in order to reduce the surface temperature of the urban environment. Simulations made with CitySim Pro show that a simple application of white reflective paint on the roofs could decrease the average cooling demand of buildings by 8%. The use of reflective paint on the roofs implies the use of all colours, but elevates reflectivity. Courtyards are optimal design features for this climate, as underlined by (Ratti et al., 2003b): they create comfortable semi-outdoor environments when shadowed by textile meshes, featuring pools, natural ventilation and local trees. Finally, the use of energy efficient envelopes as defined by the Minergie standard for tropical climates, could reduce the cooling demand of buildings by 32% compared to the “best practice” (Dubai Green Building) and by 78% compared to standard current building practice. Buildings axes oriented East-West are more energy efficient than the ones oriented North-South: the sun radiation impinging on an East facade during summer time is 54% higher than that on a South facade. By contrast, during winter time, when the solar gains have a positive impact on the energy balance of buildings, the radiation is higher on the South facade: it corresponds to 133 kWhm<sup>-2</sup> against 80 kWhm<sup>-2</sup> on the East facade, during the month of January. Based on these observations, it is important to increase the window to wall ratio (WWR) on the South and shadowed facades, such as in the internal courtyard and in the lower levels of the building. Naturally, sun shading systems, such as blinds or shadowing devices (such as the traditional mashrabia) are essential. The use of smart-electrically controlled blinds (based on sensors placed inside the rooms) reduces solar gains, but at the same time allows daylight flux into buildings when available. Sloping facades represent an expensive investment in construction, but are suggested for East oriented facades (without shadowing), because the slope reduces the solar radiation impinging on the facade. Naturally, a

sloping facade needs to be placed upon a ground covering with a low albedo, to avoid the reflection of solar radiation. Finally, in order to improve the energy performance, photovoltaic panels should be installed on the sites. BiPV could be integrated in the roofs as well as in the canopies of car parks, walk paths or playgrounds, as shading devices. They could also be applied as shading elements creating double skin roofs: the insulated internal layer of the roof is protected by the photovoltaic panels, reducing its temperature, and consequently the heat transfer from the outdoor environment. Finally, domed roofs could be a good solution (Figure 7.5): thanks to their large surface area, the convective losses are improved, as noted in previous studies (Cardinale et al., 2013) performed on the “trullo”, a vernacular house in the South of Italy (Alberobello, Puglia).



Figure 7.5 Trullo (left). Source: Pintarest. Hourly solar radiation (13:00) during a summer day (right)

Based on measurements performed on the Swiss International School of Dubai, a major energy saving potential is presented furthermore by the large difference of temperature between day and night (on average 10°C), ideal for night cooling strategies, allowing natural ventilation of buildings (in mid-season) or making the air conditioning system operating during nighttime. Another potentially interesting technology is *night sky radiant cooling*: if cold water is used to refrigerate the air inside a building, during nighttime the water passes through tubes on the rooftop, exchanging heat with the cold sky and consequently decreasing its temperature.

#### *Outdoor environmental design*

In this climate, the need for natural and artificial cooling strategies to mitigate air temperature, provide ventilation and reduce the relative humidity is evident. As previously stated, it is essential to create semi-outdoor environment that are semi controlled spaces, *in-between* indoor and outdoor. Semi-outdoor environments are defined as outdoor microclimates that can be partially controlled by filtering or attenuating the extreme environmental conditions (J. Spagnolo and De Dear, 2003). These are liveable spaces, not usable all year, but allowing “additional” months of comfort. “More” liveable than the outdoor environment, they represent a naturally cooled space, either completely natural (without any cooling system) or cooled (during the warmer season) by air exhausted from inside a building. In any case, these spaces offer a liveable environment without any additional energy cost. Wind catchers could be applied in a semi outdoor environment, another applicable bioclimatic strategy in this climate: they catch the breeze from the air and direct it to the ground floor. Their form, in this region, is a rectangular shape with openings in all orientations. Such towers need to be placed in an indoor or semi outdoor space such as a courtyard as they need a controlled wind profile; with this technology, combined with the evaporative cooling, the air can be cooled down by 15°C (Pearlmutter et al., 1996). In order to decrease the air temperature, evaporative cooling is also a major strategy to be applied. During the Universal Exhibition in Seville (1992), the outdoor human comfort in Avenue Europe was ensured using two parallel rows of cooling towers (30m height). Inside the towers, small water spraying mechanisms allowed the evaporation of water and cool the air (Santamouris, 2007).



Shading devices are essential to protect pedestrians in the outdoor environment. Artificial shading systems such as textile meshes reduce the short and longwave radiation impinging on pedestrians, consequently improving outdoor human comfort. On-site monitoring shows that by adding one mesh, the mean radiant temperature is reduced by 8.94°C on average during daytime. Simulations showed that by adding a three-layer mesh, the thermal sensation of pedestrians could be additionally improved, ensuring a comfortable thermal sensation for 73% of the daytime (67% without any protection). Finally, orientable “brise soleil” systems, able to follow the sun during the day and covered by PV could be an interesting strategy to provide shading and produce electricity. They could be installed on the facade of buildings, as well as upon car parks or covering the walk passages. A final interesting approach is radiative cooling, which works thanks to the longwave radiation emitted toward the sky. The radiative cooling approach is based on the principle that any surface with a temperature higher than zero Kelvin emits energy in the form of electromagnetic radiation (Al-obaidi et al., 2014). The temperature of the sky can be lower than -10°C during clear summer nights (Eicker and Dalibard, 2011); consequently the radiative cooling could be applied both to i) roof surfaces and to ii) photovoltaic thermal collectors. The use of photovoltaic thermal collectors (PTC) could provide electricity during the daytime and cool the water of the thermal collectors during nighttime (Eicker and Dalibard, 2011). Night radiative cooling is maximized with clear sky conditions, but is reduced with the humidity content. Consequently, before choosing this option, the climatic conditions of the site should be analyzed.

Trees have a positive impact on pedestrians’ thermal sensations; on-site monitoring shows that under a tree, and without other shading, the MRT is 1.81°C lower on average during the month of August 2016, if compared to the ones measured under a white shading device (SISD campus in Dubai). Simulations show that planting native trees improves pedestrians’ thermal stress on average from -86W and 1W (minimum and maximum ITS, respectively) without greening, to -168W and -76W (minimum and maximum ITS, respectively) with Ghaf trees. As underlined in Chapter 6, trees should preferably be planted on the West-East axes (in respect to pedestrian comfort), protecting the pedestrians from the sun during the morning and the afternoon. Naturally, native plants are required, which are autonomous in water. The landscape has been shown to have a great impact on the energy performance of buildings as well as on outdoor human comfort. In order to protect pedestrians from the sunrays, a high density of greening is needed. Optimization results maximize them on the Southern entrance of building, as they shadow pedestrians on the East and West orientation.

Pools and water bodies have a positive effect on the urban microclimate; in order to maintain sustainable water management (ratio between the water needs and waste) and to reduce water losses, it is essential to shadow the pool by meshes or by trees, as well as to reduce the ventilation upon the water. The creation of pools in semi outdoor environments positively impacts the outdoor and indoor microclimatic conditions. Naturally, due to the water scarcity in this climate, the water should come from renewable sources; it could, for example, be extracted from the water content of the air, using so-called vertical “atrapaniebla” (fog collection) or horizontally, through nighttime humidity condensation (upon metallic surfaces). Fog collectors were developed in the Atacama desert (Figure 7.6), but some few examples are already installed in mountains areas of Saudi Arabia (Al-hassan, 2009). The fog in Dubai (Figure 7.7) appears just 20 times a year, but a higher potential is present on the North-Eastern borders of the country, near the Al Hajar Mountains (between United Arab Emirates and Oman). Finally, there exists also a device able to convert humidity into water (Islandsky, 2017), which works in locations with a humidity higher than 50% and warm temperatures (> 23°C).



Figure 7.6 Atrapaniebla in the Atacama desert, Chile. Source: unaltoeneldesierto.cl.



Figure 7.7 Fog in Dubai. Source: dailymail.com.uk. Photo by Nicole Luettecke.

In order to protect the outdoor environment from the sand, barriers are needed. These should be placed at a height between 0 to 0.5 m., considering that saltation of medium size sand particles (0.5 to 1.1 mm diameter) is concentrated (90%) at a height of 30 cm (Berte, 2010).

The shortwave reflectance of the ground covering must be low in order to reduce the radiation reflected toward the pedestrians. Its thermal conductivity should be comprised between  $1.1 \text{ Wm}^{-1}\text{K}^{-1}$  and  $3.1 \text{ Wm}^{-1}\text{K}^{-1}$ , which is true for limestone, cement and stone (granite for example). If there is no shade, a ground covering should be chosen that stores the heat during daytime and reduces the radiation reflected to pedestrians, i.e. a material with high thermal conductivity and reduced shortwave reflectance. Naturally, it is essential to avoid the surface to be get too warm under the sun. Knowing the radiative exchanges between a pedestrian and the ground is essential to produce a comfortable environment. For this purpose, three concepts can be applied: i) evaporative ground, ii) ground to air heat exchanger and iii) water retention pavements. The evaporative ground uses evaporation of water – wastewater, or water created by humidity during the night - to cool the surfaces and reduce the air temperature. The concept of evaporative ground was already used in Japan (Akagawa and Komiya, 2005), the results obtained

show that such pavements can reduce the surface temperature by 10 to 25°C. The evaporative ground concept proposed for the Swiss International School Campus is composed of three layers: an impermeable tissue positioned upon the soil (or upon the building), a layer of water and air (10 cm) and a floor with small perforations (with a diameter of some millimetres), made of wood or aerated concrete, due to their low thermal conductivity (around  $0.17 \text{ W}\cdot\text{m}^{-1}\text{K}^{-1}$ ). During the day the water evaporates from the impermeable tissue; the vapour passes through the holes of the floor, reducing its temperature. The water used by the proposed system is reused wastewater, or created by humidity during night time. The concept of ground to air heat exchanger is an interpretation of vernacular Arab architecture: a combination of qanat - an underground pool - and a wind tower. The idea (Figure 7.8) is to use the underground air to refresh the outdoor environment; it could be done using pipes that catch fresh air (near the water level underground or in the building foundations) and bring it to the ground or to the building terrace, creating a natural flux of fresh air. This technology is also known as *ground to air heat exchanger* (Steffen, 2014) or *earth to air heat exchanger*. It can also be found in the historical centre of Tirana, using PVC pipes of 30m length and a diameter of 25 cm; a fan inducing air movement, at a speed of  $8\text{m}\cdot\text{s}^{-1}$ , and the air circulates at a height of 2.1 m from the floor (Fintikakis et al., 2011). Another solution could be to use the exhaust air from the building to refresh the outdoor environment.

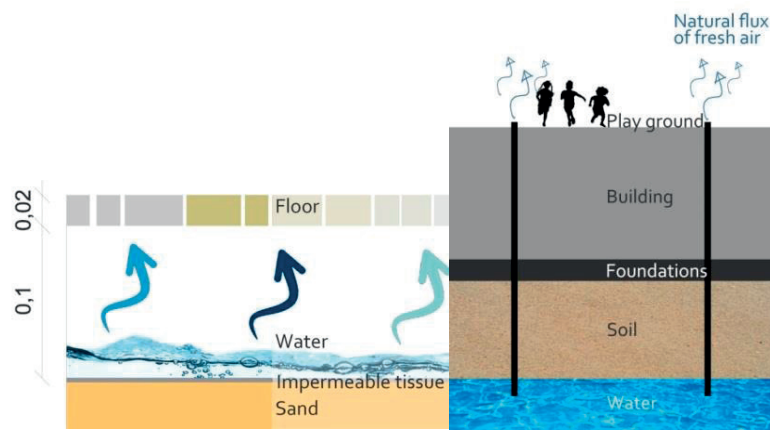


Figure 7.8 Ground to air heat exchanger. Conceptual example.

Finally, water retention pavements are designed to store the water condensed during the night and use the latent heat of the water to decrease the temperature of both the pavements and the above air. Porous, permeable materials and greening are used as water retention pavements (Santamouris, 2012).

#### Practical recommendations

The work of Givoni already underlined some practical recommendations conserving a bioclimatic design for hot and arid climate (Givoni, 1998b). Part of these recommendations are based on his work, but improved by including the output obtained by this thesis. The following points should be addressed, when designing in these climatic conditions (Figure 7.9):

- Design semi-outdoor environments (e.g. patio, colonnades, etc.), as spaces in between indoor and outdoor, able to provide additional comfortable hours to pedestrians, without any additional energy requirements. Semi- outdoor environments create a new microclimate, in-between the indoor and the outdoor, protecting the buildings from the extreme outdoor climatic conditions. These spaces are shaded during the day, and can be ventilated (when required) by the internal exhausted air.
- Each building is designed as part of the entire system (district and city). It is essential to provide a compact urban form, improving the mutual shadowing of buildings. The district should be designed as each building protect the others, e.g. higher buildings should be placed on the East and West orientations, shading the others.



- Create internal courtyards, considered as comfortable semi-outdoor environments, shadowed by textile meshes, naturally ventilated and planted with local trees.
- Apply the Minergie standard for tropical climates, which can reduce the cooling demand of buildings by 32% compared to the “best practice” (Dubai Green Building) and by 78% compared to a standard building in the country.
- Prefer buildings oriented on the East-West to North-South axes: the sun irradiance impinging on an East facade during the summer time is 54% higher than that impinging on a South facade.
- Increase the windows to wall ratios on the South and shadowed facades, e.g. in internal courtyards and on the lower floors of the buildings.
- Orient the PV panels Southward or Eastward, with a tilt of 20°.
- Design sloping facades for the East oriented facade (without shadowing), reducing the solar radiation impinging on the facade. Naturally, a sloping facade needs to be placed above a ground covering with a low albedo, to avoid reflection of solar radiation.
- Design the outdoor environment by placing materials characterized by a high thermal inertia; the ground covering (liveable) should be coloured with dark colours, reducing the radiation reflected to pedestrians. When possible, use light colours, but these covering should be shaded.
- Roofs should be coloured, if not liveable and not facing other surfaces, with white reflective paintings, in order to reflect the impinging solar radiation, decreasing their temperature and consequently the heat transmitted in the building.
- Greenings are an ideal strategy to improve the environmental conditions of the site. Vegetation should be local (with low water requirements) and positioned preferably on the North and South axes, protecting from the East and West radiation.
- Water bodies are a vernacular strategy, able to improve the environmental conditions by evaporative cooling. Naturally, the water should come from renewable sources (e.g. from humidity, from night condensation).
- Maximize the natural ventilation of the site, but protecting from the sand storms.

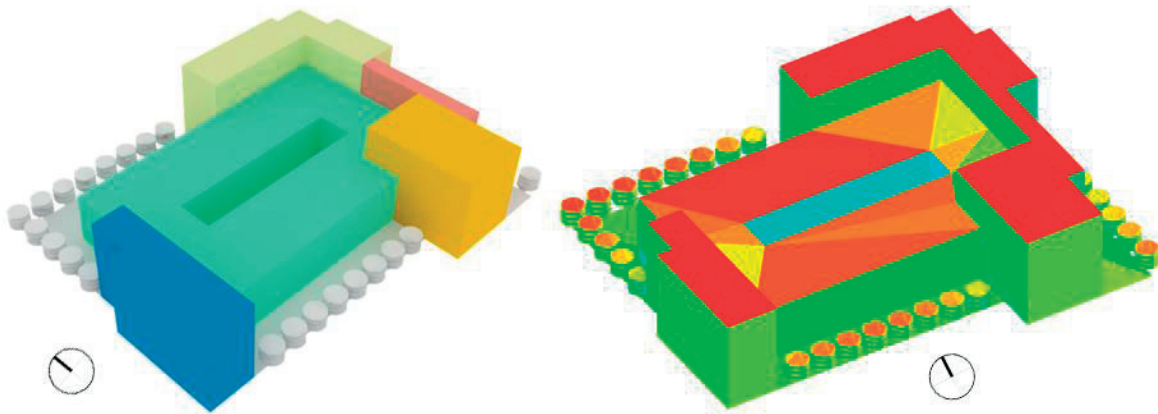


Figure 7.9 Proposed design for a small district in hot and arid climate.

### 7.3 Future outlook

The work presented in this thesis has left numerous questions open, which are beyond the scope of this thesis. Further research is required to investigate the following, subdivided according to the chapters of this thesis report.

Outdoor human comfort

Outdoor human comfort was analyzed by means of the Index of Thermal Stress and the COMFA\* budget. Urban climatic maps, able to provide guidelines to urban planners and municipalities to improve the microclimate of cities are under development (Ng and Ren, 2015), but the analysis of outdoor human comfort is not yet an integral part of most architectural practice. Further development is required to bring the research findings on human thermal comfort into the architectural and urban design practice. Additionally, in the current thermal models, radiation is often analysed without differentiating between the impact of solar (shortwave radiation) and longwave radiation, and thus without considering how the human body may react to radiation of different wave lengths (Hodder and Parsons, 2007) (Rox Anderson and M.D, 1981). Further studies are required, in order to understand the impact of radiation wavelength on human comfort. A further step in outdoor human comfort analysis is to correlate it with neuro-architecture, by analysing the space as perceived by our brain (Groh, 2014) (Eberhard, 2009a) (Eberhard, 2009b). The relationship between human comfort and neuro-architecture could enhance the sophistication of the design of the built environment (Figure 7.10).

Can the architectural space influence the learning process?

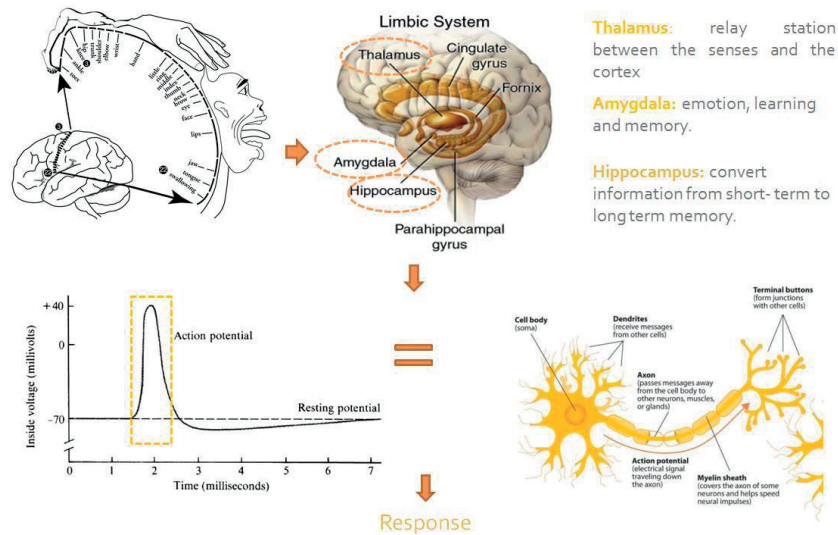


Figure 7.10 Relationship between the environmental perception and the neuronal response. Images extracted from (Nicholls et al., 2012), assembled by the author.

Finally, the analyses of human comfort on the Swiss International School Campus are based on adults' thermal sensations; a further step should include the analyses of the thermal sensations from children's point of view.

Urban greening

The tree model proposed in CitySim Pro can be further improved. Currently, leaves are assumed to be opaque surfaces; in order to improve the results, semi-transparent properties have to be included as a function of the leaf and tree type. Additionally, up to now just evergreen plants were considered; an improvement of the model will be the possibility to add deciduous plants. Finally, the impact of wind is neglected in this model, a further development of the tree model would focus on the work of (Kong et al., 2017), as well as on the Canopy Interface Model. Currently the evapotranspiration is quantified for the ground covering; a further development of the model will be the analysis of the potential of evapotranspiration on building surfaces, such as on green roofs and facades as well as quantifying the impact of greening on the variation of the air temperature and on the wind speed. Finally, the evapotranspiration model was validated by using data measured by the weather station of Pully. On-site measurements of the evapotranspiration in the built environment, as a function of vegetation type

as well as climate (e.g. Lausanne versus Dubai), such as the work performed by Snir et al. (Snir et al., 2016), would constitute a further step forward in this topic.

*Energy performance and outdoor comfort of a campus in a temperate climate*

The energy analyses of the EPFL campus were performed for future climatic scenarios, such as the ones provided by Meteonorm. Further investigations are required, such as the improvement of the quality of the weather data, by adding dynamic profiles. The variation of the wind profile, as calculated by the CIM model, is analysed in order to quantify its impact on outdoor human comfort. Further analyses are under way in order to analyse its impact on the energy performance of buildings. Comfort Maps are currently designed by exporting data from CitySim Pro to ArcGIS; additional work is required in order to visualize the results directly from the software.

*Energy performance and outdoor comfort of a campus in a hot and arid climate*

The Index of Thermal Stress (ITS) was quantified for the entire campus, but in order to improve the results, on-site surveys are required. Considering that the buildings are the first example of a Minergie building in UAE, it is an extraordinary test case. Consequently, on-site monitoring would be precious in order to better understand the thermal behavior of the campus, and to improve or to modify the Minergie Standard. Finally, on-site monitoring should be performed, interviewing students and academic staff, in order to quantify their thermal sensations, indoors and outdoors. Surveys could improve and validate the simulations performed, as well as provide further recommendations in order to improve the design.

*Hybrid Algorithm Optimization with Heuristics*

The optimization simulations for the EPFL campus were performed according to the current building geometry. Assuming that in future the EPFL campus will increase its liveable surface, and new buildings will be added to the site, it would be good to analyse what the optimal urban form would be, able to improve both the energy performance and the outdoor human comfort.

## A. Annex

In the following annex are summarized the codes implemented in the software CitySim Pro. Firstly, the codes of the Mean Radiant Temperature, the COMFA\* budget and the Index of Thermal Stress are presented, as well as the physical model of trees. The coding part was realized by Jerome Kaempfer, expert of the CitySim Pro code. All details concerning the models are available in Chapters 2 and 3.

### A.1 Mean Radiant Temperature

The Mean Radiant Temperature is computed based on the integral radiation measurements (Höppe, 1992).

```
// compute the MRT for the building pBuilding and the timestep i
// variables used with the estimation of the MRT
float totalArea = 0.f;
float LWabsorbed = 0.f;
float SWabsorbed = 0.f;
for (unsigned int zone=0; zone<pBuilding->getnZones(); ++zone) {

    // loop on the walls
    for (unsigned int k=0; k<pBuilding->getZone(zone)->getnWalls(); ++k) {
        Wall* thisWall = pBuilding->getZone(zone)->getWall(k);
        totalArea += thisWall->getArea();
        LWabsorbed += thisWall->getLongWaveAbsorbed(i) * thisWall->getArea();
        SWabsorbed += thisWall->getShortWaveIrradiance(i) * (1.f - thisWall->getShortWaveReflectance()) * thisWall->getArea();
    }

    // loop on the roofs
    for (unsigned int k=0; k<pBuilding->getZone(zone)->getnRoofs(); ++k) {
        Roof* thisRoof = pBuilding->getZone(zone)->getRoof(k);
        totalArea += thisRoof->getArea();
        LWabsorbed += thisRoof->getLongWaveAbsorbed(i) * thisRoof->getArea();
        SWabsorbed += thisRoof->getShortWaveIrradiance(i) * (1.f - thisRoof->getShortWaveReflectance()) * thisRoof->getArea();
    }
} // end the loop on zones
LWabsorbed /= totalArea;
SWabsorbed /= totalArea;
MRT = pow((LWabsorbed + SWabsorbed)/(pBuilding->getMRT_Epsilon()*5.670373e-8), 0.25f)-273.15f;
return;
}
```

### A.2 COMFA\* Budget

The COMFA\* budget is coded in CitySim Pro, starting from the original budget (Brown and Gillespie, 1995), and adding the improvements on the calculation of tissue resistance, relative air velocity, skin temperature, clothing and vapor resistance (Kenny et al., 2009a) (Kenny et al., 2009b) (Vanos et al., 2012b) (Vanos et al., 2012a).

```

// output of the COMFA* (in W/m^2)
// Renolds Number and co.
float reynoldsNumber = 0.17*((pClimate->getWindSpeed(i-preTimeStepsSimulated)>0)?pClimate->getWindSpeed(i-
preTimeStepsSimulated):0.01)/1.5e-5;
float re_A = (reynoldsNumber<4000.)?0.683:((reynoldsNumber<40000.)?0.193:0.0266);
float re_n = (reynoldsNumber<4000.)?0.466:((reynoldsNumber<40000.)?0.618:0.805);

// Metabolic
float metabolicActivity = 70.f;
float walkingSpeed = 0.0052*(metabolicActivity-58);
float M = (1.-(0.15-0.0173*pClimate->getVapourPressure(i-preTimeStepsSimulated)-0.0014*pClimate->getToutCelsius(i-
preTimeStepsSimulated)))*metabolicActivity; // activité métabolique 70 W/m^2

// Convection
float coreTemperature = 36.5 + 0.0043*M;
float airDensity = pClimate->getPatm(i-preTimeStepsSimulated)/(287.04*(pClimate->getToutCelsius(i-
preTimeStepsSimulated)+273.15));
float resistanceBodyTissue = 1000.*airDensity/((0.13*(0.42*(M-58.))+15.);
float boundaryLayerResistance = 0.17/(re_A*pow(reynoldsNumber,re_n)*pow(0.71,0.33)*22.e-6);
float intrinsicClothingInsulation = (pClimate->getToutCelsius(i-preTimeStepsSimulated)>=27.f)?0.31:(((1.372-
(0.01866*pClimate->getToutCelsius(i-preTimeStepsSimulated))-(0.0004849*pow(pClimate->getToutCelsius(i-
preTimeStepsSimulated),2))-(0.00009333*pow(pClimate->getToutCelsius(i-preTimeStepsSimulated),3))))*0.1555);
float staticClothingResistance = 1000.*airDensity * intrinsicClothingInsulation;
float clothingResistance = staticClothingResistance*(-0.37*(1.-exp(-walkingSpeed/0.72))+1.);
float skinTemperature = (((coreTemperature-pClimate->getToutCelsius(i-
preTimeStepsSimulated))<0.)?0.001:(coreTemperature-pClimate->getToutCelsius(i-preTimeStepsSimulated)))/
(resistanceBodyTissue+clothingResistance+boundaryLayerResistance) *
(boundaryLayerResistance+clothingResistance) + pClimate->getToutCelsius(i-preTimeStepsSimulated);
float C = 1000.*airDensity * (skinTemperature-pClimate->getToutCelsius(i-
preTimeStepsSimulated))/(clothingResistance+boundaryLayerResistance);

// Evaporation
float evaporativeHeatLossThroughPerspiration = 0.42*(M-58.);
float latentHeatOfVapourization = (2501.-(2.37*pClimate->getToutCelsius(i-preTimeStepsSimulated)))*1000.;
float specificHumidityAir = 0.622*(pClimate->getVapourPressure(i-preTimeStepsSimulated)/(pClimate->getPatm(i-
preTimeStepsSimulated)/1000.-pClimate->getVapourPressure(i-preTimeStepsSimulated)));
float saturatedVapourPressureSkin = pClimate->getSaturatedVapourPressure(skinTemperature);
float vapourPressureSkin = saturatedVapourPressureSkin*pClimate->getRelativeHumidity(i-preTimeStepsSimulated);
float specificHumiditySkin = 0.622*(vapourPressureSkin/(pClimate->getPatm(i-preTimeStepsSimulated)/1000.-
vapourPressureSkin));
float airResistanceRav = 0.92*boundaryLayerResistance;
float staticClothingVapourResistance =
0.622*latentHeatOfVapourization*airDensity*intrinsicClothingInsulation*0.18/(pClimate->getPatm(i-
preTimeStepsSimulated)/1000.-pClimate->getVapourPressure(i-preTimeStepsSimulated));
float effectiveAirVelocity = pow(pow(pClimate->getWindSpeed(i-
preTimeStepsSimulated),2)+pow(walkingSpeed,2),0.5);
float resistanceVapourTransferClothing = staticClothingVapourResistance*(-0.8*(1.-exp((-
effectiveAirVelocity/1.095)+1)));
float resistanceAirClothingSkinTissue = resistanceVapourTransferClothing+airResistanceRav+7.7e+3;

```

```

float evaporativeLossThroughSkinDiffusion = airDensity*latentHeatOfVapourization*(((specificHumiditySkin-specificHumidityAir)/(resistanceVapourTransferClothing+airResistanceRav))>0.f)?
  (min( (specificHumiditySkin-specificHumidityAir)/resistanceAirClothingSkinTissue,(specificHumiditySkin-specificHumidityAir)/(resistanceVapourTransferClothing+airResistanceRav))): ((specificHumiditySkin-specificHumidityAir)/resistanceAirClothingSkinTissue) );
float E = evaporativeLossThroughSkinDiffusion+evaporativeHeatLossThroughPerspiration;

//LongwaveEmitted
float surfaceTemperatureIndividual = max((skinTemperature-pClimate->getToutCelsius(i-preTimeStepsSimulated))/(boundaryLayerResistance+clothingResistance)*boundaryLayerResistance+pClimate->getToutCelsius(i-preTimeStepsSimulated),7.f);
float longWaveEmitted = 0.95*5.67e-8*pow((surfaceTemperatureIndividual+273.15),4);

// output of the COMFA (in W/m2)
COMFA = M+ LWabsorbed + SWabsorbed - C - E - longWaveEmitted;
return;
}

```

### A.3 Index of Thermal Stress

The Index of Thermal Stress (ITS), coded into CitySim Pro, is based on the original model of Givoni (Givoni, 1963), by adding the later revision by Pearlmutter et al. (Pearlmutter et al., 2006) (Erell et al., 2011a) (Pearlmutter et al., 2014).

```

// calculation of the ITS (in W)
// Metabolic
float metabolicRate = (metabolicActivity - (0.2 * (metabolicActivity - 80.)));

// Convection
float deltaT = pClimate->getToutCelsius(i-preTimeStepsSimulated) - 35.;
float reynoldsNumberITS = 0.17*((pClimate->getWindSpeed(i-preTimeStepsSimulated)>0)?pClimate->getWindSpeed(i-preTimeStepsSimulated):0.01)/1.6e-5;
float A ITS = (reynoldsNumberITS>4000.)?0.17:0.62;
float B ITS = (reynoldsNumberITS<4000.)?0.62:0.47;
float convectionITS = (deltaT * pClimate->getAirDensity()*1005.*2.e-5 * A ITS * pow(reynoldsNumberITS,B ITS) / 0.17);

// simplified version
//float convectionITS = (deltaT * 8.3 * pow(((pClimate->getWindSpeed(i-preTimeStepsSimulated)>0)?pClimate->getWindSpeed(i-preTimeStepsSimulated):0.01),0.6));

// Radiation Balance
float LWEmittedITS = 0.95*5.67e-8*pow((35.+273.15),4);
float radiationITS = (LWabsorbed + SWabsorbed - LWEmittedITS);

// Cooling Rate
float coolingRate = (metabolicRate + radiationITS + convectionITS) * totalArea;

// CoolingEfficiency

```



```

float saturationVapourPressure = exp(16.6536-(4030.183/(pClimate->getToutCelsius(i-
preTimeStepsSimulated)+235.)));
float vapourPressureAir = 7.52*pClimate->getRelativeHumidity(i-preTimeStepsSimulated)*saturationVapourPressure;
float evaporativeCapacityAir = 1.163*20.5*pow(((pClimate->getWindSpeed(i-preTimeStepsSimulated)>0.)?pClimate-
>getWindSpeed(i-preTimeStepsSimulated):0.01),0.3) * (42.-vapourPressureAir);
float coolingEfficiencySweating = max(exp(0.6*((coolingRate/evaporativeCapacityAir)-0.12)),1.);

// output of the ITS (in W)
ITS = coolingRate * coolingEfficiencySweating;
return;
}

```

## A.4 Tree model

The tree model, as defined in Chapter 3, is coded as follows in CitySim Pro.

```

// JHK - thermal model for the Trees by SC
void Model::ThermalStepTree(Tree *pTree, Climate* pClimate, unsigned int day, unsigned int hour) {

// outside air temperature
float Ta = pClimate->getToutCelsius(day, hour);
float Cp_a = 29.3f; // 29.3 is the Cp of air in J/(mol K)

// computes averages on the top layer
float totalArea = 0.f, SWa = 0.f, LWa = 0.f, LWe = 0.f, g_r = 0.f;
for (size_t i=0; i<pTree->getLeaves()->size(); ++i) {
totalArea+=pTree->getLeaves()->at(i)->getArea();

// SW absorbed, note: 0.2 is the Transmittance of the leaves by default from Oke
SWa+=(1.f-pTree->getLeaves()->at(i)->getShortWaveReflectance()-0.2f)*pTree->getLeaves()->at(i)-
>getShortWaveIrradiance()*pTree->getLeaves()->at(i)->getArea();

// LW absorbed
LWa+=pTree->getLeaves()->at(i)->getLongWaveAbsorbed()*pTree->getLeaves()->at(i)->getArea();

// LW emitted at the air temperature
LWe+=(pTree->getLeaves()->at(i)->getLongWaveEmissivity()*5.670373e-8*pow(Ta+273.15,4))*pTree-
>getLeaves()->at(i)->getArea();

// LW radiative conductance
g_r+=(4.*1.*5.670373e-8*pow(Ta+273.15,3)/Cp_a)*pTree->getLeaves()->at(i)->getArea();
}
SWa /= totalArea; // average absorbed shortwave irradiance on the top layer
LWa /= totalArea; // average absorbed longwave irradiance on the top layer
LWe /= totalArea; // average emitted longwave irradiance on the top layer
g_r /= totalArea; // average radiative conductance of the top layer

// compute the conductances
float g_Hr = 1.4*0.135*sqrt(max(pClimate->getWindSpeed(day, hour), 0.01f)/(0.72*pTree->getLeafWidth())) + g_r;
float g_va = 1.4*0.147*sqrt(max(pClimate->getWindSpeed(day, hour), 0.01f)/(0.72*pTree->getLeafWidth()));
float g_vs_ab = ((pClimate->getLdh(day, hour)>0.f)||pClimate->getRelativeHumidity(day, hour)>0.8f)?0.3f:0.01f;
float g_vs_ad = g_vs_ab; // equal conductances
float g_v = (0.5*g_vs_ab*g_va)/(g_vs_ab+g_va)+(0.5*g_vs_ad*g_va)/(g_vs_ad+g_va);

// gets the apparent psychrometric constant (°C-1)

```

```

float gammaStar = 6.67e-4 * g_Hr / g_v;

// compute the slope of saturation mole fraction function s (°C-1)
float s = pClimate->getSaturatedVapourPressureDerivative(Ta)/(pClimate->getPatm(day,hour)/1000.);

// compute the vapour deficit
float D = pClimate->getSaturatedVapourPressure(pClimate->getToutCelsius(day,hour))-pClimate-
>getSaturatedVapourPressure(pClimate->getTd(day,hour))+6.66e-4*(pClimate->getPatm(day,hour)/1000.)*(Ta-
pClimate->getTd(day,hour));

// compute the surface temperature
float surfaceTemperature = Ta + gammaStar/(s+gammaStar)*((SWa+LWa-LWe)/(g_Hr*Cp_a)-D/(pClimate-
>getPatm(day,hour)/1000.*gammaStar));

// save the temperature in all the layers, sublayers and trunc
for (size_t i=0;i<pTree->getnSurfaces();++i) pTree->getSurface(i)->setTemperature(surfaceTemperature);

#ifdef DEBUG
ostream debugFile;
if (day==1 && hour==1)
    debugFile <<
"day\thour\tid\tSWa\tTenv\tLWa\tLWe\tg_r\tg_Hr\tg_va\tg_vs_ab\tg_vs_ad\tg_v\tgammaStar\tD\tsurfaceTemperat
ure" << endl;
    debugFile << day << "\t" << hour << "\t" << pTree->getId() << "\t"
        << SWa << "\t" << pTree->getLeaves()->at(0)->getEnvironmentalTemperature() << "\t" << LWa << "\t" << LWe
<< "\t" << g_r << "\t" << g_Hr << "\t" << g_va << "\t" << g_vs_ab << "\t"
        << g_vs_ad << "\t" << g_v << "\t" << gammaStar << "\t" << s << "\t" << D << "\t" << surfaceTemperature << endl;
    save(string("tree.dat"),debugFile,false);
#endif

return;
}

```



## B. Annex

This annex presents the construction details used during this thesis. The work is subdivided into the following paragraphs: i) buildings of the first stage of construction, ii) Polydôme (PO) building, iii) LESO solar experimental building, iv) Swiss International School of Dubai. All the construction details of the buildings are retrieved from the original drawing of the campus, as provided by the infrastructure department of the university. Data for the LESO solar experimental building are retrieved from (Morel, 2004) (Altherr and Gay, 2002), and finally data concerning the Swiss International School of Dubai are available from (SORANE, 2013), as well as by the visit of the construction site. The physical properties of the buildings envelopes are calculated by Lesosai (Lesosai, 2017); the U-value is calculated by the program, by adding an external and internal air resistance, corresponding to  $0.130 \text{ m}^2\text{K}\cdot\text{W}^{-1}$  and  $0.040 \text{ m}^2\text{K}\cdot\text{W}^{-1}$ , respectively. For each construction type, the following properties of the materials are defined: thermal conductivity ( $\text{W}\cdot\text{m}^{-1}\text{K}^{-1}$ ), density ( $\text{kg}\cdot\text{m}^{-3}$ ), specific heat ( $\text{J}\cdot\text{kg}^{-1}\text{K}^{-1}$ ) and resistance ( $\text{m}^2\text{K}\cdot\text{W}^{-1}$ ). The *thermal conductivity* represents the ability of the material to conduct heat. The *density* represents the mass per unit volume of material. The *specific heat* is the amount of heat required to raise the temperature, by 1 degree celsius, per unit mass. Finally, the *resistance* represents the ability of a material to obstruct the heat flow, as function of the thickness of the material (Gorse et al., 2012).

### B.1 Buildings of the first stage of construction



Figure B.1 PH (left) and GR building (right).

Material Name	Thickness (cm)	Thermal Conductivity ( $\text{W}\cdot\text{m}^{-1}\text{K}^{-1}$ )	Density ( $\text{kg}\cdot\text{m}^{-3}$ )	Specific heat ( $\text{J}\cdot\text{kg}^{-1}\text{K}^{-1}$ )	Resistance ( $\text{m}^2\text{K}\cdot\text{W}^{-1}$ )
Gypsum plaster	1	0.21	900	849	0.048
Concrete	18	2.1	2,400	849	0.086
Mineral wool	10	0.04	30	849	2.5
Concrete	8	2.1	2,400	849	0.038
Air layer	8	0.181	1.23	1,000	0.443
Aluminium alloy	0.5	160	2,800	878	0

Table B.1 Description of the envelope. First stage of construction, wall. From the inside.

Material Name	Thickness (cm)	Thermal Conductivity ( $\text{W}\cdot\text{m}^{-1}\text{K}^{-1}$ )	Density ( $\text{kg}\cdot\text{m}^{-3}$ )	Specific heat ( $\text{J}\cdot\text{kg}^{-1}\text{K}^{-1}$ )	Resistance ( $\text{m}^2\text{K}\cdot\text{W}^{-1}$ )
Gypsum plaster	1	0.21	900	849	0.048
Concrete	11	2.1	2,400	849	0.052
Vapour barrier PE	0.4	0.2	940	1,400	0.02
Mineral wool	10	0.04	30	849	2.5
Bitumen felt	0.8	0.23	1,100	1,000	0.035
Cast asphalt	3	0.7	2,150	1,100	0.043
Air layer	4	0.229	1.23	1,000	0.175
Concrete	5	2.1	2,400	849	0.024

Table B.2 Description of the envelope. First stage of construction, roof. From the inside.

## B.2 Polydôme



Figure B.2 PO building, or Polydôme.

Material Name	Thickness (cm)	Thermal Conductivity ( $\text{W}\cdot\text{m}^{-1}\text{K}^{-1}$ )	Density ( $\text{kg}\cdot\text{m}^{-3}$ )	Specific heat ( $\text{J}\cdot\text{kg}^{-1}\text{K}^{-1}$ )	Resistance ( $\text{m}^2\text{K}\cdot\text{W}^{-1}$ )
Gypsum plaster	1	0.21	900	849	0.048
Concrete	20	2.1	2,400	849	0.095
Mineral wool	12	0.04	30	849	3
Concrete	20	2.1	2,400	849	0.095

Table B.3 Description of the envelope. Polydôme, wall. From the inside.

Material Name	Thickness (cm)	Thermal Conductivity ( $\text{W}\cdot\text{m}^{-1}\text{K}^{-1}$ )	Density ( $\text{kg}\cdot\text{m}^{-3}$ )	Specific heat ( $\text{J}\cdot\text{kg}^{-1}\text{K}^{-1}$ )	Resistance ( $\text{m}^2\text{K}\cdot\text{W}^{-1}$ )
Wood	10	0.44	600	2,700	0.227
Vapour barrier PE	0.4	0.2	940	1,400	0.02
Mineral wool	10	0.04	30	849	2.5
Bitumen felt	0.8	0.23	1,100	1,000	0.035
Aluminium alloy	0.5	160	2,800	878	0

Table B.4 Description of the envelope. Polydôme, roof. From the inside.

### B.3 LESO solar experimental building



Figure B.3 LESO solar experimental building (source dp-architectes.ch)

Material Name	Thickness (cm)	Thermal Conductivity ( $\text{W}\cdot\text{m}^{-1}\text{K}^{-1}$ )	Density ( $\text{kg}\cdot\text{m}^{-3}$ )	Specific heat ( $\text{J}\cdot\text{kg}^{-1}\text{K}^{-1}$ )	Resistance ( $\text{m}^2\text{K}\cdot\text{W}^{-1}$ )
Gypsum plaster	1	0.21	900	849	0.048
Mineral wool	12	0.04	30	849	3
Wood	1	0.18	700	1,600	0.056

Table B.5 Description of the envelope. LESO solar experimental building, wall exposed to South. From the inside.

Material Name	Thickness (cm)	Thermal Conductivity ( $\text{W}\cdot\text{m}^{-1}\text{K}^{-1}$ )	Density ( $\text{kg}\cdot\text{m}^{-3}$ )	Specific heat ( $\text{J}\cdot\text{kg}^{-1}\text{K}^{-1}$ )	Resistance ( $\text{m}^2\text{K}\cdot\text{W}^{-1}$ )
Concrete	12	2.1	2,400	849	0.057
Mineral wool	8	0.04	30	849	2
Concrete	12	2.1	2,400	849	0.057

Table B.6 Description of the envelope. LESO solar experimental building, wall exposed to North, East and West. From the inside.

Material Name	Thickness (cm)	Thermal Conductivity ( $\text{W}\cdot\text{m}^{-1}\text{K}^{-1}$ )	Density ( $\text{kg}\cdot\text{m}^{-3}$ )	Specific heat ( $\text{J}\cdot\text{kg}^{-1}\text{K}^{-1}$ )	Resistance ( $\text{m}^2\text{K}\cdot\text{W}^{-1}$ )
Gypsum plaster	1	0.21	900	849	0.048
Concrete	25	2.1	2,400	849	0.119
Vapour barrier PE	0.4	0.2	940	1,400	0.02
Mineral wool	16	0.04	30	849	4
Bitumen felt	0.8	0.23	1,100	1,000	0.035
Concrete	10	2.1	2,400	849	0.048
Gravel	2	2	2,000	1,051	0.01

Table B.7 Description of the envelope. LESO solar experimental building, roof. From the inside.

Table B.8 summarizes the construction details with their cross section for the EPFL campus.



Annex

Building	Element	Construction details	Cross section
1 <sup>st</sup> phase of construction	Wall	Gypsum plaster/Concrete/ Mineral wool / Concrete/ Air layer/ Aluminum alloy	
	Roof	Gypsum plaster / Concrete / Vapor barrier PE / Mineral wool/ Bitumen felt/ Cast asphalt/ Air layer/ Concrete	
Polydôme (PO building)	Wall	Gypsum plaster / Concrete/ Mineral wool / Concrete	
	Roof	Wood/ Vapor barrier PE/ Mineral wool / Bitumen felt/ Aluminum alloy	
LESO solar experimental building	Wall (South)	Gypsum plaster / Mineral wool/ Wood	
	Wall (North, South, East and West)	Concrete/ Mineral wool / Concrete	
	Roof	Gypsum plaster/ Concrete/ Vapour barrier PE/ Mineral wool/ Bitumen felt/ Concrete/ Gravel	

Table B.8 EPFL campus. Construction details with their cross section.

## B.4 Swiss International School of Dubai



Figure B.4 Swiss International School Campus in Dubai. Aerial photo, source: khaleejtimes.com (left) and photo of the main building (right)



Figure B.5 Swiss International School Campus in Dubai. View of the construction site, 11<sup>th</sup> November 2014. Main building (left) and detail of the walls (right).

Material Name	Thickness (cm)	Thermal Conductivity ( $\text{W}\cdot\text{m}^{-1}\text{K}^{-1}$ )	Density ( $\text{kg}\cdot\text{m}^{-3}$ )	Specific heat ( $\text{J}\cdot\text{kg}^{-1}\text{K}^{-1}$ )	Resistance ( $\text{m}^2\text{K}\cdot\text{W}^{-1}$ )
Gypsum plaster	1	0.21	900	849	0.048
Concrete	2	2.1	2400	849	0.236
EPS	10	0.03	17	1,100	3.333
Concrete	5	2.1	2400	849	0.220
Gypsum plaster	2	0.21	900	849	0.095

Table B.9 Description of the envelope. Swiss International School of Dubai. Wall. From the inside.

Material Name	Thickness (cm)	Thermal Conductivity ( $\text{W}\cdot\text{m}^{-1}\text{K}^{-1}$ )	Density ( $\text{kg}\cdot\text{m}^{-3}$ )	Specific heat ( $\text{J}\cdot\text{kg}^{-1}\text{K}^{-1}$ )	Resistance ( $\text{m}^2\text{K}\cdot\text{W}^{-1}$ )
Gypsum plaster	1	0.21	900	849	0.048
Concrete	10	2.1	2400	849	0.048
Vapour barrier PE	0.4	0.2	940	1,400	0.02
EPS	16	0.03	17	1,100	5.333
Bitumen felt	0.8	0.23	1100	1,000	0.035
Gypsum plaster	1	0.21	900	849	0.048

Table B.10 Description of the envelope. Swiss International School of Dubai. Roof. From the inside.

Material Name	Thickness (cm)	Thermal Conductivity (W·m <sup>-1</sup> K <sup>-1</sup> )	Density (kg·m <sup>-3</sup> )	Specific heat (J·kg <sup>-1</sup> K <sup>-1</sup> )	Resistance (m <sup>2</sup> K·W <sup>-1</sup> )
Concrete Tiles	3	1.5	2,100	1,000	0.02
Concrete	5	2.1	2,400	849	0.024
Gravel	10	2	2,000	1,051	0.05
Sandy soil	100	2	2,000	1,051	0.5

Table B.11 Description of the envelope. Swiss International School of Dubai. Ground covering, concrete tiles.

Material Name	Thickness (cm)	Thermal Conductivity (W·m <sup>-1</sup> K <sup>-1</sup> )	Density (kg·m <sup>-3</sup> )	Specific heat (J·kg <sup>-1</sup> K <sup>-1</sup> )	Resistance (m <sup>2</sup> K·W <sup>-1</sup> )
Rubber	2	0.13	910	1,100	0.154
Concrete	5	2.1	2,400	849	0.024
Gravel	10	2	2,000	1,051	0.05
Sandy soil	100	2	2,000	1,051	0.5

Table B.12 Description of the envelope. Swiss International School of Dubai. Ground covering, rubber.

Table B.13 summarizes the cross section of each construction type for the Swiss International School Campus.

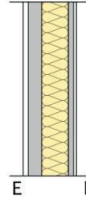
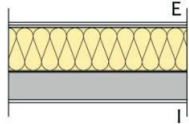
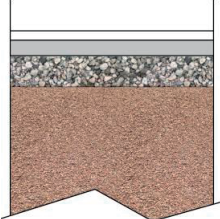
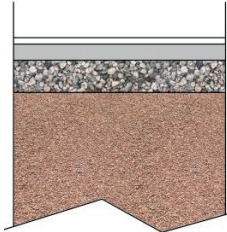
Building	Element	Construction details	Cross section
Minergie building	Wall	Gypsum plaster/ Concrete/ EPS/ Concrete/ Gypsum plaster	
	Roof	Gypsum plaster/ Concrete/ Vapour barrier PE/ EPS/ Bitumen felt/ Gypsum plaster	
Ground covering	Ground covering, concrete tiles	Concrete Tiles/ Concrete/ Gravel/ Sandy soil	
	Ground covering, rubber	Rubber/ Concrete/ Gravel/ Sandy soil	

Table B.13 SISD campus. Construction details with their cross section.

## B.5 Typical building in UAE

The envelope, as realized in typical buildings in United Arab Emirate (Kriesi et al., 2011) is presented.

Material Name	Thickness (cm)	Thermal Conductivity ( $\text{W}\cdot\text{m}^{-1}\text{K}^{-1}$ )	Density ( $\text{kg}\cdot\text{m}^{-3}$ )	Specific heat ( $\text{J}\cdot\text{kg}^{-1}\text{K}^{-1}$ )	Resistance ( $\text{m}^2\text{K}\cdot\text{W}^{-1}$ )
Reinforced concrete	15	1.8	2,400	1,100	0.083
Expanded clay	10	0.14	525	900	0.714

Table B.14 Description of the envelope. Typical building in UAE. Wall. From the inside.

Material Name	Thickness (cm)	Thermal Conductivity ( $\text{W}\cdot\text{m}^{-1}\text{K}^{-1}$ )	Density ( $\text{kg}\cdot\text{m}^{-3}$ )	Specific heat ( $\text{J}\cdot\text{kg}^{-1}\text{K}^{-1}$ )	Resistance ( $\text{m}^2\text{K}\cdot\text{W}^{-1}$ )
Reinforced concrete	26.5	0.7	1,500	1,000	0.379
Expanded clay	6.0	0.14	525	900	0.429
Aluminium	0.5	200	2,700	900	0

Table B.15 Description of the envelope. Typical building in UAE. Roof. From the inside.

## B.6 Green building regulation

The envelope, as required by the Green Building Regulations & Specifications (Government of Dubai, n.d.), is summarized as follows.

Material Name	Thickness (cm)	Thermal Conductivity ( $\text{W}\cdot\text{m}^{-1}\text{K}^{-1}$ )	Density ( $\text{kg}\cdot\text{m}^{-3}$ )	Specific heat ( $\text{J}\cdot\text{kg}^{-1}\text{K}^{-1}$ )	Resistance ( $\text{m}^2\text{K}\cdot\text{W}^{-1}$ )
Reinforced concrete	7.5	1.8	2,400	1,100	0.042
EPS	7	0.041	65	1,450	1.707
Reinforced concrete	7.5	1.8	2,400	1,100	0.042

Table B.16 Description of the envelope. Green building regulation. Wall. From the inside.

Material Name	Thickness (cm)	Thermal Conductivity ( $\text{W}\cdot\text{m}^{-1}\text{K}^{-1}$ )	Density ( $\text{kg}\cdot\text{m}^{-3}$ )	Specific heat ( $\text{J}\cdot\text{kg}^{-1}\text{K}^{-1}$ )	Resistance ( $\text{m}^2\text{K}\cdot\text{W}^{-1}$ )
Reinforced concrete	26.5	0.7	1,500	1,000	0.113
EPS	12	0.038	15	1,400	3.158
Aluminium	0.5	200	2,700	900	0

Table B.17 Description of the envelope. Green building regulation. Roof. From the inside.

## B.7 Results from the optimization

This paragraph presents the physical properties of the buildings, as defined by the evolutionary algorithm CMA-ES/HDE (Chapter 6). All the values are calculated by Lesosai, based on the ISO 13786 (ISO, 2008). The *thermal transmittance* ( $\text{W}\cdot\text{m}^{-2}\text{K}^{-1}$ ), or U-value, represents the heat flux passing through one square meter of construction element, subjected to a temperature difference of 1 degree (Gorse et al., 2012) (Lesosai, 2017). The *periodic thermal transmittance* ( $\text{W}\cdot\text{m}^{-2}\text{K}^{-1}$ ) is a complex quantity, which is defined as function of the thermal transmittance, the time shift and a decrement factor. It represents the complex amplitude of the density of heat flow rate through the surface of the component adjacent to zone  $m$ , divided by the complex amplitude of the temperature in zone  $n$  when the temperature in zone  $m$  is held constant (ISO, 2008) (Rossi and Rocco, 2014). The *thermal admittance* ( $\text{W}\cdot\text{m}^{-2}\text{K}^{-1}$ ) expresses the ability of the material to absorb and to release the heat over time. It is the ratio between the flux into the wall and the variation of its surface temperature (Davies, 1973). Finally, the *thermal heat capacity* ( $\text{kJ}\cdot\text{m}^{-2}\text{K}^{-1}$ ) is defined as the ability of the material to store the heat, this parameter is important to determine the time required by the building to heat up or cool down. Consequently, a high thermal capacity corresponds to a high thermal stability (Gorse et al., 2012). As an example (Table B.18), a wall made in sandstone

(0.9 m thickness) has a thermal capacity of 81.9 (kJ·m<sup>-2</sup>K<sup>-1</sup>), a wall made in aluminium (0.01 m thickness) has a lower thermal capacity, equal to 5.71 (kJ·m<sup>-2</sup>K<sup>-1</sup>).

Wall type	Static U-value (W·m <sup>-2</sup> K <sup>-1</sup> )	Periodic transmittance (W·m <sup>-2</sup> K <sup>-1</sup> ) and time shift (h)	External thermal admittance (W·m <sup>-2</sup> K <sup>-1</sup> ) and time shift (h)	Thermal heat capacity (kJ·m <sup>-2</sup> K <sup>-1</sup> )
Sandstone CEN, 0.90 m	1.78	0.022/ 22.62	12.30/1.64	81.9
Wood, 0.05 m	2.23	2.157/1.43	2.97/2.05	21.6
Aluminium, 0.01 m	5.88	5.870/ 0.21	6.03/ 0.66	5.71

Table B.18 Physical properties of materials

## B.8 Optimization\_ Zone A

1 <sup>st</sup> stage construction	Static U-value (W·m <sup>-2</sup> K <sup>-1</sup> )	Periodic transmittance (W·m <sup>-2</sup> K <sup>-1</sup> ) and time shift (h)	External thermal admittance (W·m <sup>-2</sup> K <sup>-1</sup> ) and time shift (h)	Thermal heat capacity (kJ·m <sup>-2</sup> K <sup>-1</sup> )	Short Wave Reflectance (-)
<b>Wall</b>	0.30	0.022/11.98	4.30/1.81	66.5	0.2
TMY	0.08	0.004/16.05	4.32/1.80	66.3	0.2
2050	0.09	0.005/15.05	4.32/1.80	66.3	0.6
2100	0.08	0.004/16.05	4.32/1.80	66.3	0.2
<b>Roof</b>	0.32	0.053/10.77	8.00/3.41	68.5	0.2
TMY	0.08	0.01/13.98	8.06/3.39	68.1	0.2
2050	0.08	0.01/13.98	8.06/3.39	68.1	0.2
2100	0.10	0.015/12.70	8.06/3.40	68.2	0.1

Table B.19 Optimization. Zone A, buildings of the first stage of construction. Physical properties of materials

LESO solar experimental buildings	Static U-value (W·m <sup>-2</sup> K <sup>-1</sup> )	Periodic transmittance (W·m <sup>-2</sup> K <sup>-1</sup> ) and time shift (h)	External thermal admittance (W·m <sup>-2</sup> K <sup>-1</sup> ) and time shift (h)	Thermal heat capacity (kJ·m <sup>-2</sup> K <sup>-1</sup> )	Short Wave Reflectance (-)
<b>Wall South</b>	0.30	0.30/1.02	0.92/4.50	8.96	0.2
TMY	0.12	0.11/2.24	0.92/5.21	9.59	0.5
2050	0.18	0.18/1.23	0.89/4.96	8.86	0.5
2100	0.12	0.12/2.11	0.91/5.20	9.52	0.5
<b>Walls North, East and West</b>	0.43	0.11/8.96	11.96/2.91	86.8	0.2
TMY	0.12	0.029/10.39	12.11/2.93	86.3	0.5
2050	0.11	0.026/10.80	12.11/2.93	86.3	0.5
2100	0.15	0.038/9.81	12.09/2.93	86.4	0.5
<b>Roof</b>	0.22	0.017/12.83	12.17/2.83	64.3	0.6
TMY	0.12	0.008/14.7	12.21/2.82	64.2	0.3
2050	0.15	0.011/13.79	12.21/2.83	64.2	0.4
2100	0.16	0.012/13.65	12.20/2.83	64.2	0.7

Table B.20 Optimization. Zone A, LESO solar experimental building. Physical properties of materials

## B.9 Optimization\_ Zone B

1 <sup>st</sup> Stage Construction	Static U-value (W·m <sup>-2</sup> K <sup>-1</sup> )	Periodic transmittance (W·m <sup>-2</sup> K <sup>-1</sup> ) and time shift (h)	External thermal admittance (W·m <sup>-2</sup> K <sup>-1</sup> ) and time shift (h)	Thermal heat capacity (kJ·m <sup>-2</sup> K <sup>-1</sup> )	Short Wave Reflectance (-)
<b>Wall</b>	0.30	0.022/11.98	4.30/1.81	66.5	-
TMY	0.09	0.005/15.24	4.32/1.80	66.3	-
2050	0.09	0.005/15.05	4.32/1.80	66.3	-
2100	0.14	0.009/13.15	4.32/1.81	66.4	-
<b>Roof</b>	0.32	0.053/10.77	8.00/3.41	68.5	0.6
TMY	0.16	0.024/11.44	8.05/3.40	68.3	0.6
2050	0.12	0.018/12.15	8.06/3.40	68.2	0.7
2100	0.21	0.034/10.97	8.04/3.41	68.3	0.8

Table B.21 Optimization. Zone B, buildings of the first stage of construction. Physical properties of materials

Polydôme	Static U-value (W·m <sup>-2</sup> K <sup>-1</sup> )	Periodic transmittance (W·m <sup>-2</sup> K <sup>-1</sup> ) and time shift (h)	External thermal admittance (W·m <sup>-2</sup> K <sup>-1</sup> ) and time shift (h)	Thermal heat capacity (kJ·m <sup>-2</sup> K <sup>-1</sup> )	Short Wave Reflectance (-)
<b>Wall</b>	0.29	0.02/13.31	12.37/1.95	65.8	-
TMY	0.24	0.016/13.57	12.38/1.95	65.8	-
2050	0.15	0.009/14.76	12.39/1.94	65.7	-
2100	0.13	0.008/15.06	12.39/1.94	65.7	-
<b>Roof</b>	0.33	0.128/6.57	1.62/4.85	61.3	0.3
TMY	0.14	0.049/7.52	1.62/5.37	61.1	0.44
2050	0.24	0.09/6.67	1.59/5.11	61.2	0.56
2100	0.10	0.035/8.44	1.64/5.42	61	0.28

Table B.22 Optimization. Zone B, Polydôme. Physical properties of materials

## B.10 Optimization SISD

	Static U-value (W·m <sup>-2</sup> K <sup>-1</sup> )	Periodic transmittance (W·m <sup>-2</sup> K <sup>-1</sup> ) and time shift (h)	External thermal admittance (W·m <sup>-2</sup> K <sup>-1</sup> ) and time shift (h)	Thermal heat capacity (kJ·m <sup>-2</sup> K <sup>-1</sup> )	Short Wave Reflectance (-)
<b>Wall</b>					
TMY	0.09	0.062/ 7.14	7.44/ 3.70	42.5	0.8
2050	0.10	0.07/ 6.68	8.69/ 3.88	42.5	0.6
2100	0.17	0.098/ 6.39	5.60/ 2.76	42.2	0.2
<b>Roof</b>					
TMY	0.14	0.045/ 6.85	2.09/ 5.34	68.3	0.3
2050	0.09	0.027/ 8.52	0.77/ 4.67	68.3	0.7
2100	0.08	0.022/ 9.08	2.63/ 5.39	68.3	0.2
<b>Rubber</b>					
TMY	-	0.005/ 4.01	11.28/ 1.79	78.5	0.5
2050	-	0.005/ 3.93	11.95/ 1.87	78.5	0.8
2100	-	0.005/ 3.96	11.01/ 1.76	78.5	0.1
<b>Concrete</b>					
TMY	-	0.005/ 4.17	12.31/ 1.88	78.5	0.3
2050	-	0.005/ 4.17	11.93/ 1.85	78.5	0.6
2100	-	0.005/ 4.28	9.82/ 1.64	78.5	0.3

Table B.23 Optimization. SISD. Physical properties of materials





## References

- Abtew, M., Melesse, A., 2013. Evaporation and Evapotranspiration. Measurements and Estimations. Springer. doi:10.1017/CBO9781107415324.004
- Akagawa, H., Komiya, H., 2005. Creation of evaporative urban envelope development of wet style pavements and lightweight rooftop garden using a unique textile, in: The 2005 World Sustainable Building Conference, Tokyo, 27-29 September 2005 (SB05Tokyo). pp. 27–29.
- Al-hassan, G.A., 2009. Fog Water Collection Evaluation in Asir Region–Saudi Arabia. *Water Resour Manag.* 23, 2805–2813. doi:10.1007/s11269-009-9410-9
- Ali-Toudert, F., Mayer, H., 2006. Numerical study on the effects of aspect ratio and orientation of an urban street canyon on outdoor thermal comfort in hot and dry climate. *Build. Environ.* 41, 94–108. doi:10.1016/j.buildenv.2005.01.013
- Allen, R., Pereira, S.L., Raes, D., Smith, M., 1998. Crop evapotranspiration: Guidelines for computing crop water requirements. *FAO Irrig. Drain. Pap.* 56.
- Al-obaidi, K.M., Ismail, M., Malek, A., Rahman, A., 2014. Passive cooling techniques through reflective and radiative roofs in tropical houses in Southeast Asia: A literature review. *Front. Archit. Res.* 3, 283–297. doi:10.1016/j.foar.2014.06.002
- Altherr, R., Gay, J.B., 2002. A low environmental impact anidolic facade. *Build. Environ.* 37, 1409–1419. doi:10.1016/S0360-1323(01)00118-4
- ASHRAE, 2010. Thermal environment conditions for human occupancy. *ANSI/ASHRAE Standards* 55-2010.
- Baccini, M., Biggeri, A., Accetta, G., Kosatsky, T., Katsouyanni, K., Analitis, A., Anderson, H.R., Bisanti, L., D'Ippoliti, D., Danova, J., Forsberg, B., Medina, S., Paldy, A., Rabczenko, D., Schindler, C., Michelozzi, P., 2008. Heat effects on mortality in 15 European cities. *Epidemiology* 19, 711–719. doi:10.1097/EDE.0b013e318176bfcd
- Bajšanski, I. V., Milošević, D.D., Savić, S.M., 2015. Evaluation and improvement of outdoor thermal comfort in urban areas on extreme temperature days: Applications of automatic algorithms. *Build. Environ.* 94, 632–643. doi:10.1016/j.buildenv.2015.10.019
- Bates, R., 2014. The Architect's Victims. *Archit. Dig.*
- BEAR-ID, 2016. European climate zones and bio-climatic design requirements. Project report.
- Berkovic, S., Yezioro, A., Bitan, A., 2012. Study of thermal comfort in courtyards in a hot arid climate. *Sol. Energy* 86, 1173–1186. doi:10.1016/j.solener.2012.01.010
- Berte, C.J., 2010. Fighting sand encroachment - Lessons from Mauritania. *FAO For. Pap.* 158, 74.
- Beslimane, O., 2013. Simulation and analysis of the EPFL heating consumption and PV electricity production.
- Bolton, D., 1980. The Computation of Equivalent Potential Temperature. *Mon. Weather Rev.* doi:10.1175/1520-0493(1980)108<1046:TCOEPT>2.0.CO;2

- Borel, E., 1921. Game theory and left symmetric core integral equations.
- Boriboonsomsin, K., Farhad, R., 2007. Mix Design and Benefit Evaluation of High Solar Reflectance Concrete for Pavements, in: *Transportation Research Record*. pp. 1–22.
- Brown, R.D., 2011. Ameliorating the effects of climate change: Modifying microclimates through design. *Landsc. Urban Plan.* 100, 372–374. doi:10.1016/j.landurbplan.2011.01.010
- Brown, R.D., Gillespie, T.J., 1995. *Microclimatic Landscape Design: Creating Thermal Comfort and Energy Efficiency*. Wiley.
- Brown, R.D., Gillespie, T.J., 1986. Estimating outdoor thermal comfort using a cylindrical radiation thermometer and an energy budget model. *Int. J. Biometeorol.* 30, 43–52.
- Bruse, M., 2014. Using ENVI-met met BioMet.
- Buck, A., 1981. New Equations for Computing Vapor Pressure and Enhancement Factor. *J. Appl. Meteorol.* 20, 1527–1532.
- Budd, G.M., 2008. Wet-bulb globe temperature (WBGT)—its history and its limitations. *J. Sci. Med. Sport* 11, 20–32. doi:10.1016/j.jsams.2007.07.003
- Calanca, P., Smith, P., Holzkämper, A., Ammann, C., 2011. L'évapotranspiration de référence et son application en agrométéorologie. *Rech. Agron. Suisse* 2, 173–183.
- Campbell, 2015. BlackGlobe Temperature Sensor for Heat Stress.
- Campbell, G.S., Norman, J.M., 1998. *An Introduction to Environmental Biophysics*, *Journal of Environment Quality*. Springer. doi:10.2134/jeq1977.00472425000600040036x
- Campbell, G.S., Norman, J.M., 1998. *An Introduction to Environmental Biophysics*. Springer New York, New York, NY. doi:10.1007/978-1-4612-1626-1
- Campos, P., 2008. *Sustainable Education Campus in Spain : Nature and Architecture for Training*.
- Cardinale, N., Rospi, G., Stefanizzi, P., 2013. Energy and microclimatic performance of Mediterranean vernacular buildings: The Sassi district of Matera and the Trulli district of Alberobello. *Build. Environ.* 59, 590–598. doi:10.1016/j.buildenv.2012.10.006
- Carmeliet, J., 2012. Sustainable cities and urban energy systems of the future. *Urban Multiscale Energy Modelling (UMEM)*.
- Carneiro, C.M., 2011. Extraction of Urban Environmental Quality Indicators using LiDAR-Based Digital Surface Models.
- Caruso, G., 2013. AIR-CONDITIONING ENERGY REDUCTION THROUGH A BUILDING SHAPE OPTIMIZATION, in: *CISBAT International Conference*. pp. 103–108.
- Champeaux, J.L., Masson, V., Chauvin, F., 2005. ECOCLIMAP : a global database of land surface parameters at 1 km resolution 32, 29–32. doi:10.1017/S1350482705001519
- Chen, H., Ooka, R., Kato, S., 2008. Study on optimum design method for pleasant outdoor thermal environment using genetic algorithms (GA) and coupled simulation of convection, radiation and conduction. *Build. Environ.* 43, 18–30. doi:10.1016/j.buildenv.2006.11.039
- Cheng, V., Ng, E., Chan, C., Givoni, B., 2012. Outdoor thermal comfort study in a sub-tropical climate: a longitudinal study based in Hong Kong. *Int. J. Biometeorol.* 56, 43–56. doi:10.1007/s00484-010-0396-z

- Chow, W.T.L., Pope, R.L., Martin, C.A., Brazel, A.J., 2011. Observing and modeling the nocturnal park cool island of an arid city: Horizontal and vertical impacts. *Theor. Appl. Climatol.* 103, 197–211. doi:10.1007/s00704-010-0293-8
- Chow, W.T.L., Roth, M., 2006. Temporal dynamics of the urban heat island of Singapore. *Int. J. Climatol.* 26, 2243–2260. doi:10.1002/joc
- Coccolo, S., Kämpf, J., 2015. Urban energy simulation of the EPFL Campus in Fribourg using a new paradigm: the CITYGML Application Domain Extension Energy, in: CISBAT 2015. pp. 907–912.
- Coccolo, S., Kämpf, J., Scartezzini, J., Pearlmutter, D., 2016a. Outdoor human comfort and thermal stress : A comprehensive review on models and standards. *UCLIM*. doi:10.1016/j.uclim.2016.08.004
- Coccolo, S., Kämpf, J., Scartezzini, J.-L., 2015a. Outdoor human comfort and climate change . A case study in the EPFL campus in Lausanne, in: ICUC9 - 9th International Conference on Urban Climate Jointly with 12th Symposium on the Urban Environment.
- Coccolo, S., Kämpf, J., Scartezzini, J.-L., 2015b. The EPFL campus in Lausanne: new energy strategies for 2050, in: International Building Physics Conference (IBPC). Torino.
- Coccolo, S., Kämpf, J., Scartezzini, J.-L., 2013. Design in the desert. A bioclimatic project with urban energy modelling, in: Building Simulation 2013 13th International Conference of the International Building Performance Simulation Association. 25th - 30th August 2013, FRANCE.
- Coccolo, S., Kämpf, J., Scartezzini, J.-L., Bedrone, R., 2012. Designing in the desert. A bioclimatic approach at the urban scale, in: UAE- Swiss Research Day- Frontiers in Water, Energy and Sustainability.
- Coccolo, S., Kämpf, J.H., Scartezzini, J.-L., 2015c. The EPFL campus in Lausanne: new energy strategies for 2050. *Energy Procedia* 78, 3174–3179.
- Coccolo, S., Kämpf, J.H., Vigliotti, F., Scartezzini, J.-L., 2014. Improving outdoor comfort and energy consumption of a city district in a desert area., in: 5th International Conference on Drylands, Deserts and Desertification Healthy Lands - Healthy People.
- Coccolo, S., Mauree, D., Kämpf, J., 2015d. Urban Energy Simulation based on a new data model paradigm: the CityGML application domain extension energy. A case study in the EPFL campus of Lausanne, in: Building Simulation Conference.
- Coccolo, S., Mauree, D., Kämpf, J., Scartezzini, J.-L., 2016b. Integration of outdoor human comfort in a building energy simulation database using CityGML Energy ADE, in: Sustainable Built Environment (SBE) Regional Conference.
- Coccolo, S., Mauree, D., Naboni, E., Kämpf, J., Scartezzini, J.-L., 2017a. On the impact of the wind speed on the outdoor human comfort: a sensitivity analysis, in: CISBAT International Conference.
- Coccolo, S., Monna, S., Kämpf, J., Scartezzini, J.-L., 2016c. Energy demand and urban microclimate of old and new residential districts in a hot arid climate, in: PLEA.
- Coccolo, S., Vanos, J., Kämpf, J., Scartezzini, J.-L., 2017b. Comfort-Map: dynamic visualizations of children's thermal sensation in the outdoor environment, in: International Congress of Biometeorology, Durham, UK September 3 - 7, 2017.
- Coello, C., Lamont, G.B., Van Veldhuizen, D.A., 2007. *Evolutionary Algorithms for Solving Multi-Objective Problems*, Springer. ed.
- Comfable, n.d. OTC model.

## References

- Crawley, B.D.B., Lawrie, L.K., 2000. EnergyPlus : Energy Simulation Program. *ashrae* 42, 49–56.
- Cruz, L., Barata, E., Ferreira, J.-P., Freire, F., 2017. Greening transportation and parking at University of Coimbra. *Int. J. Sustain. High. Educ.* 18, 23–38. doi:10.1108/IJSHE-04-2015-0069
- Davies, M., 1981. Thermal responses to exercise in children. *J. Ergon.* 24, 55–61.
- Davies, M.G., 1973. The Thermal Admittance of Layered Walls 2, 207–220.
- de Abreu-Harbach, L.V., Labaki, L.C., Matzarakis, A., 2015. Effect of tree planting design and tree species on human thermal comfort in the tropics. *Landsc. Urban Plan.* doi:10.1016/j.landurbplan.2015.02.008
- Della Casa, F., Della Casa, E., 2010. Rolex Learning Center.
- DII, 2015. PLAN DIRECTEUR DES ENERGIES 2015 - 2045.
- DII, 2004. Plan Directeur.Réflexions sur l'évolution du plan directeur rapport de synthèse.
- Drake, B.G., Salisbury, F.B., 1972. Aftereffects of low and high temperature pretreatment on leaf resistance, transpiration, and leaf temperature in xanthium. *Plant Physiol.* 50, 572–5. doi:10.1104/pp.50.5.572
- Duffie, J.A., Beckman, W.A., 2013. *Solar Engineering of Thermal Processes.*
- Eberhard, J.P., 2009a. Applying neuroscience to architecture. *Neuron* 62, 753–6. doi:10.1016/j.neuron.2009.06.001
- Eberhard, J.P., 2009b. *Brain Landscape.*
- Efthymiou, Santamouris, M., Kolokotsa, D., Koras, A., 2016. Development and Testing of Photovoltaic Pavement for Heat Island Mitigation. *Sol. Energy* 130, 148–160. doi:10.1016/j.solener.2016.01.054
- Eicker, U., Dalibard, A., 2011. Photovoltaic–thermal collectors for night radiative cooling of buildings. *Sol. Energy* 85, 1322–1335. doi:10.1016/j.solener.2011.03.015
- Emery, A., 2014. *Human Comfort and Health Requirements.*
- ENERGO, 2014. *Energy consumption EPFL.*
- EPFL, 2017. *Developpement durable EPFL.*
- EPFL, 2016. *L'EPFL en chiffres 2015.*
- Erell, E., Boneh, D., Pearlmutter, D., Bar-kutiel, P.U.A., 2013. Effect of High-albedo Materials on Pedestrian Thermal Sensation in Urban Street Canyons in Hot Climates, in: *PLEA2013 - 29th Conference, Sustainable Architecture for a Renewable Future, Munich, Germany 10-12 September 2013.*
- Erell, E., Pearlmutter, D., Boneh, D., Kutiel, P.B., 2014. Effect of high-albedo materials on pedestrian heat stress in urban street canyons. *Urban Clim.* 10, 367–386. doi:10.1016/j.uclim.2013.10.005
- Erell, E., Pearlmutter, D., Williamson, T., 2011a. *Urban microclimate. Designing the space between buildings.* Earthscan, New York.
- Erell, E., Pearlmutter, D., Williamson, T., 2011b. *Urban microclimate. Designing the spaces between buildings.* Earthscan.
- Evins, R., 2013. A review of computational optimisation methods applied to sustainable building design. *Renew. Sustain. Energy Rev.* 22, 230–245. doi:10.1016/j.rser.2013.02.004
- Fabbri, K., 2015. *Indoor Thermal Comfort perception. A questionnaire Approach focusing on children.* Springer.
- Fahmy, M., Sharples, S., Yahiya, M., 2010. *LAI based trees selection for mid latitude urban developments: A*

- microclimatic study in Cairo, Egypt. *Build. Environ.* 45, 345–357. doi:10.1016/j.buildenv.2009.06.014
- Fanger, P.O., 1970. Thermal comfort. Analysis and applications in environmental engineering.
- FAO, 2016. AQUASTAT website. Food and Agriculture Organization of the United Nations (FAO).
- Federal Office of Meteorology and Climatology, 2014. Meteoswiss: <http://www.meteoswiss.admin.ch/web/en.html>.
- Fiala, D., Havenith, G., Bröde, P., Kampmann, B., Jendritzky, G., 2012. UTCI-Fiala multi-node model of human heat transfer and temperature regulation. *Int. J. Biometeorol.* 56, 429–41. doi:10.1007/s00484-011-0424-7
- Figueiredo, A., Kämpf, J., Vicente, R., 2016. Passive house optimization for Portugal : Overheating evaluation and energy performance. *Energy Build.* 118, 181–196. doi:10.1016/j.enbuild.2016.02.034
- Fintikakis, N., Gaitani, N., Santamouris, M., Assimakopoulos, M., Assimakopoulos, D.N., Fintikaki, M., Albanis, G., Papadimitriou, K., Chryssochoides, E., Katopodi, K., Doumas, P., 2011. Bioclimatic design of open public spaces in the historic centre of Tirana, Albania. *Sustain. Cities Soc.* 1, 54–62. doi:10.1016/j.scs.2010.12.001
- Foster, N., 2017. Masdar City.
- Friedrich, T., Hebbinghaus, N., Neumann, F., 2010. Plateaus can be harder in multi-objective optimization. *Theor. Comput. Sci.* 411, 854–864. doi:10.1016/j.tcs.2009.06.020
- Friess, W.A., Rakhshan, K., Hendawi, T. a., Tajerzadeh, S., 2012. Wall insulation measures for residential villas in Dubai: A case study in energy efficiency. *Energy Build.* 44, 26–32. doi:10.1016/j.enbuild.2011.10.005
- Gagge, A.P., 1936. The linearity criterion as applied to partitional calorimetry. *Am. J. Physiol.* 116.
- Geidl, M., Koepfel, G., Favre-Perrod, P., Kloeckl, B., Andersson, G., Froelich, K., 2007. Energy hubs for the future. *IEEE Power Energy Mag.* 5, 24–30.
- Givoni, B., 1998a. *Climate Considerations in Building and Urban Design*. Wiley.
- Givoni, B., 1998b. *Climate Considerations in Building and Urban Design*.
- Givoni, B., 1989. *Urban design in different climates*.
- Givoni, B., 1976. *Man climate and architecture*, Second Edi. ed. Applied scien publishers LTD, London.
- Givoni, B., 1969. *Man, climate and architecture*.
- Givoni, B., 1969. *Man, climate and architecture*. Elsevier.
- Givoni, B., 1963. Estimation of the effect of climate on man : development of a new thermal index.
- Gomes, L.H.L.S., 2013. Thermoregulatory responses of children exercising in a hot environment 31, 104–110.
- Gorse, C., Johnston, D., Pritchard, M., 2012. *A Dictionary of Construction, Surveying and Civil Engineering*.
- Gosling, S.N., Bryce, E.K., Dixon, P.G., Gabriel, K.M. a, Gosling, E.Y., Hanes, J.M., Hondula, D.M., Liang, L., Bustos Mac Lean, P.A., Muthers, S., Nascimento, S.T., Petralli, M., Vanos, J.K., Wanka, E.R., 2014. A glossary for biometeorology. *Int. J. Biometeorol.* 58, 277–308. doi:10.1007/s00484-013-0729-9
- Goto, T., Toftum, J., De Dear, R., Fanger, P.O., 2006. Thermal sensation and thermophysiological responses to metabolic step-changes. *Int. J. Biometeorol.* 50, 323–32. doi:10.1007/s00484-005-0016-5
- Government of Dubai, n.d. *Green Building Regulations & Specifications*.
- Grifoni, R.C., Onofrio, R.D., Sargolini, M., Pierantozzi, M., 2016. A Parametric Optimization Approach to Mitigating



- the Urban Heat Island Effect : A Case Study in Ancona , Italy. doi:10.3390/su8090896
- Gröger, G., Kolbe, T.H., Nagel, C., Häfele, K.-H., 2012. Open Geospatial Consortium OGC City Geography Markup Language ( CityGML ) En- coding Standard.
- Groh, J., 2014. Making space. How the brain knows where things are. London.
- Gyeviki, M., Hrotkó, K., Honfi, P., 2012. Comparison of leaf population of sweet cherry (*Prunus avium* L.) trees on different rootstocks. *Sci. Hortic. (Amsterdam)*. 141, 30–36. doi:10.1016/j.scienta.2012.03.015
- Harbeck, G.E.J., 1962. A practical field technique for measuring reservoir evaporation utilizing mass-transfer theory. *U.S. Geol. Surv. Prof. Pap.* 272-E, p. 101–105.
- Hargreaves, G.H., Samani, Z. a., 1985. Reference crop evapotranspiration from temperature. *Appl. Eng. Agric.* 1, 96–99. doi:10.13031/2013.26773
- Hasapis, D., Savvakis, N., Tsoutsos, T., Kalaitzakis, K., Psychis, S., Nikolaidis, N.P., 2017. Design of large scale prosuming in Universities: The solar energy vision of the TUC campus. *Energy Build.* 141, 39–55. doi:10.1016/j.enbuild.2017.01.074
- Havenith, G., Fiala, D., Krzysztof, B., 2012. The UTCI-clothing model 461–470. doi:10.1007/s00484-011-0451-4
- Herrmann, J., Matzarakis, A., 2010. Influence of mean radiant temperature on thermal comfort of humans in idealized urban environments, in: Ninth Symposium on the Urban Environment of the American Meteorological Society. 1-6 August 2010, Keystone Colorado, USA, pp. 522–527.
- Hodder, S.G., Parsons, K., 2007. The effects of solar radiation on thermal comfort. *Int. J. Biometeorol.* 51, 233–250. doi:10.1007/s00484-006-0050-y
- Holmér, I., Nilsson, H., Havenith, G., Parsons, K.C., 1999. Clothing evaporative heat resistance—proposal for improved representation in standards and models. *Ann. Occup. Hyg.* 43, 339–346.
- Hopkins, W., Huener, N., 2008. Introduction to plant physiology, Fourth Edi. ed. Wiley.
- Höppe, P., 2002. Different aspects of assessing indoor and outdoor thermal comfort. *Energy Build.* 34, 661–665.
- Höppe, P., 1999. The physiological equivalent temperature - a universal index for the biometeorological assessment of the thermal environment. *Int. J. Biometeorol.* 43, 71–5.
- Höppe, P., 1993. Heat balance modelling. *Experientia* 49, 741–6.
- Höppe, P., 1992. A new procedure to determine the mean radiant temperature outdoors. *Wetter und Leb.* 44, 147–151.
- Hosoi, F., 2009. Estimating vertical leaf area density profiles of tree canopies using three-dimensional portable lidar imaging. *Scanning XXXVIII*, 152–157.
- Howard, L., 1818. The climate of London Deducted from Meteorological Observations.
- Hugh, A., Ian, B., Preventing, K.L., Shannon, H., Stewart, I., Stewart, M.K., 2009. Preventing physical activity induced heat illness in school settings 8–10.
- Huttner, S., 2012. Further development and application of the 3D microclimate simulation ENVI-met.
- Huttner, S., Bruse, M., Dostal, P., 2008. Using ENVI-met to simulate the impact of global warming on the microclimate in central European cities, in: 5th Japanese-German Meeting on Urban Climatology. pp. 307–312.
- IEA, 2016. International Energy Agency.

- IEA, 2012. Key World Energy statistic.
- International Organization for Standardisation, 2006. ISO 7730. Ergonomics of the thermal environment.
- International Organization for Standardisation, 1998. ISO 7726. Ergonomics of the thermal environment. Instruments for measuring physical quantities.
- International Organization for Standardization, 2007. ISO 9920. Ergonomics of the thermal environment – Estimation of thermal insulation and water vapour resistance of a clothing ensemble.
- International Organization for Standardization, 2005. ISO 7730. Ergonomics of the thermal environment — Analytical determination and interpretation of thermal comfort using calculation of the PMV and PPD indices and local thermal comfort criteria.
- International Organization for Standardization, 2004. ISO 7933. Ergonomics of the thermal environment — Analytical determination and interpretation of heat stress using calculation of the predicted heat strain.
- International Organization for Standardization, 1989. ISO 7243. Hot environments- Estimation of the heat stress on working man, based on the WBGT-index (wet bulb globe temperature).
- IPCC, 2000. IPCC special report. Emissions scenarios.
- Islandsky, 2017. Skywater Technology.
- ISO, 2008. ISO 13786. Thermal performance of building components. Dynamic thermal characteristics. Calculation methods.
- IUPS, 2001. Glossary of terms for thermal physiology 51, 245–280.
- J. Schmid, 2005. Centrale de Chauffe par Thermopompes.
- Jain, S., Agarwal, A., Jani, V., Singhal, S., Sharma, P., 2017. Assessment of carbon neutrality and sustainability in educational campuses ( CaNSEC ): A general framework. *Ecol. Indic.* 76, 131–143. doi:10.1016/j.ecolind.2017.01.012
- Janajreh, I., Su, L., Alan, F., 2013. Wind energy assessment: Masdar City case study. *Renew. Energy* 52, 8–15. doi:10.1016/j.renene.2012.09.025
- Johansson, E., 2006. Influence of urban geometry on outdoor thermal comfort in a hot dry climate: A study in Fez, Morocco. *Build. Environ.* 41, 1326–1338. doi:10.1016/j.buildenv.2005.05.022
- Johansson, E., Thorsson, S., Emmanuel, R., Krüger, E., 2014. Instruments and methods in outdoor thermal comfort studies – The need for standardization. *Urban Clim.* doi:10.1016/j.uclim.2013.12.002
- Jones, H.G., 2014. *Plants and Microclimate. A Quantitative Approach to Environmental Plant Physiology.*
- Jonsson, P.E.R., 2004. VEGETATION AS AN URBAN CLIMATE CONTROL IN THE SUBTROPICAL CITY OF GABORONE , BOTSWANA 1322, 1307–1322. doi:10.1002/joc.1064
- Joss, S., 2009. Eco-cities : a global survey 2009 129, 239–250. doi:10.2495/SC100211
- Kalman, Y., Pearlmutter, D., Erell, E., 2013. Impact of Increasing the Height of Tel Aviv Buildings on Pedestrian Comfort and Building Energy Efficiency, in: PLEA2013 - 29th Conference, Sustainable Architecture for a Renewable Future, Munich, Germany 10-12 September 2013.
- Kämpf, J., 2009. On the modelling and optimisation of urban energy fluxes. EPFL, Lausanne.
- Kämpf, J.H., 2009. On the Modelling and Optimisation of Urban Energy Fluxes.

- Kämpf, J.H., Robinson, D., 2010. Optimisation of building form for solar energy utilisation using constrained evolutionary algorithms. *Energy Build.* 42, 807–814. doi:10.1016/j.enbuild.2009.11.019
- Kämpf, J.H., Robinson, D., 2009. A hybrid CMA-ES and HDE optimisation algorithm with application to solar energy potential. *Appl. Soft Comput.* 9, 738–745. doi:10.1016/j.asoc.2008.09.009
- Kántor, N., Unger, J., 2011. The most problematic variable in the course of human-biometeorological comfort assessment — the mean radiant temperature. *Cent. Eur. J. Geosci.* 3, 90–100. doi:10.2478/s13533-011-0010-x
- Katul, G.G., Oren, R., Manzoni, S., Higgins, C., Parlange, M.B., 2012. Evapotranspiration: a process driving mass transport and energy exchange in the soil-plant-atmosphere-climate system. *Rev. Geophys.* 50, RG000366: 1–25. doi:10.1029/2011RG000366.1.INTRODUCTION
- Kavgic, M., Mavrogianni, A., Mumovic, D., Summerfield, A., Stevanovic, Z., Djurovic-petrovic, M., 2010. A review of bottom-up building stock models for energy consumption in the residential sector. *Build. Environ.* 45, 1683–1697. doi:10.1016/j.buildenv.2010.01.021
- Kenny, N. a., Warland, J.S., Brown, R.D., Gillespie, T.G., 2008. Estimating the radiation absorbed by a human. *Int. J. Biometeorol.* 52, 491–503. doi:10.1007/s00484-008-0145-8
- Kenny, N., Warland, J.S., Brown, R.D., Gillespie, T.G., 2009a. Part A: Assessing the performance of the COMFA outdoor thermal comfort model on subjects performing physical activity. *Int. J. Biometeorol.* 53, 415–28. doi:10.1007/s00484-009-0226-3
- Kenny, N., Warland, J.S., Brown, R.D., Gillespie, T.G., 2009b. Part B: Revisions to the COMFA outdoor thermal comfort model for application to subjects performing physical activity. *Int. J. Biometeorol.* 53, 429–41. doi:10.1007/s00484-009-0227-2
- Kienzle, F., Ahcin, P., Andersson, G., 2011. Valuing Investments in Multi-Energy Conversion, Storage, and Demand-Side Management Systems Under Uncertainty. *IEEE Trans. Sustain. Energy* 2, 194–202. doi:10.1109/TSTE.2011.2106228
- Klein, S.A., 2010. TRNSYS 17: A Transient System Simulation Program.
- Klemm, W., Heusinkveld, B.G., Lenzholzer, S., Jacobs, M.H., Van Hove, B., 2015. Psychological and physical impact of urban green spaces on outdoor thermal comfort during summertime in The Netherlands. *Build. Environ.* 83, 120–128. doi:10.1016/j.buildenv.2014.05.013
- Knez, I., Thorsson, S., 2008. Thermal, emotional and perceptual evaluations of a park: Cross-cultural and environmental attitude comparisons. *Build. Environ.* 43, 1483–1490. doi:10.1016/j.buildenv.2007.08.002
- Kolokotroni, M., Giannitsaris, I., Watkins, R., 2006. The effect of the London urban heat island on building summer cooling demand and night ventilation strategies. *Sol. Energy* 80, 383–392. doi:10.1016/j.solener.2005.03.010
- Kong, L., Lau, K.K.-L., Yuan, C., Chen, Y., Xu, Y., Ren, C., Ng, E., 2017. Regulation of outdoor thermal comfort by trees in Hong Kong. *Sustain. Cities Soc.* 31, 12–25. doi:10.1016/j.scs.2017.01.018
- Kriesi, R., 2015. Personal communication.
- Kriesi, R., 2013. MINERGIE-Standard for building of Swiss International School, Dubai.
- Kriesi, R., Aabid, F., Roulet, C.-A., Vigliotti, F., 2011. Towards a Minergie-standard for tropical climates, in: *Proceedings CISBAT 2011, Lausanne, Switzerland*. pp. 195–200.
- Kuehner, A., Mdeihli, N., Coccolo, S., Perera, A.T.D., Mohajeri, N., Scartezzini, J.-L., 2017. Extending building integrated photovoltaics (BiPV) using distributed energy hubs: a case study in Cartigny, Switzerland, in:

- CISBAT International Conference.
- Le Guen, M., Mosca, L., Perera, A.T.D., Coccolo, S., Mohajeri, N., Scartezzini, J.-L., 2017. Achieving energy sustainability in future neighborhoods through building refurbishment and energy hub concept: a case study in Hemberg, in: CISBAT International Conference.
- Lee, H., Holst, J., Mayer, H., 2013. Modification of Human-Biometeorologically Significant Radiant Flux Densities by Shading as Local Method to Mitigate Heat Stress in Summer within Urban Street Canyons. *Adv. Meteorol.* 1–13. doi:10.1155/2013/312572
- Lee, H., Mayer, H., Urban, P.E.T., 2016. Validation of the mean radiant temperature simulated by the RayMan software in urban environments. *Int. J. Biometeorol.* doi:10.1007/s00484-016-1166-3
- Lee, J.S., 2010. Stomatal Opening Mechanism of CAM Plants 19–23. doi:10.1007/s12374-010-9097-8
- Lesosai, 2017. Lesosai 7.0.
- Lin, B., Lin, Y., 2010. Cooling Effect of Shade Trees with Different Characteristics in a Subtropical Urban Park 45, 83–86.
- Lindberg, F., 2015. SOLWEIG1D. User Manual- Version 2015a.
- Lindberg, F., Grimmond, C.S.B., 2011. The influence of vegetation and building morphology on shadow patterns and mean radiant temperatures in urban areas: model development and evaluation. *Theor. Appl. Climatol.* 105, 311–323. doi:10.1007/s00704-010-0382-8
- Lindberg, F., Holmer, B., Thorsson, S., 2008. SOLWEIG 1.0- Modelling spatial variations of 3D radiant fluxes and mean radiant temperature in complex urban settings. *Int. J. Biometeorol.* 52, 697–713. doi:10.1007/s00484-008-0162-7
- Lindberg, F., Holmer, B., Thorsson, S., Rayner, D., 2013. Characteristics of the mean radiant temperature in high latitude cities-implications for sensitive climate planning applications. *Int. J. Biometeorol.* doi:10.1007/s00484-013-0638-y
- Lindberg, F., Onomura, S., Grimmond, C.S.B., 2016. Influence of ground surface characteristics on the mean radiant temperature in urban areas. doi:10.1007/s00484-016-1135-x
- Lindseth, G., 2004. The Cities for Climate Protection Campaign (CCPC) and the framing of Local Climate Policy. *Local Environ.* 9, 325–336. doi:10.1080/1354983042000246252
- Liu, H., Wang, X., Yang, J., Zhou, X., Liu, Y., 2017. The ecological footprint evaluation of low carbon campuses based on life cycle assessment: A case study of Tianjin , China. *J. Clean. Prod.* 144, 266–278. doi:10.1016/j.jclepro.2017.01.017
- Lowe, S.A., 2016. An energy and mortality impact assessment of the urban heat island in the US. *Environ. Impact Assess. Rev.* 56, 139–144. doi:10.1016/j.eiar.2015.10.004
- Marler, R.T., Arora, J.S., 2004. Survey of multi-objective optimization methods for engineering 395, 369–395. doi:10.1007/s00158-003-0368-6
- Matzarakis, A., 2015. Developments and applications of thermal indices in urban structures by RayMan and SkyHelios model, in: 9th International Conference on Urban Climate. Toulouse.
- Matzarakis, A., Fröhlich, D., 2015. Sport events and climate for visitors-the case of FIFA World Cup in Qatar 2022. *Int. J. Biometeorol.* 59, 481–486. doi:10.1007/s00484-014-0886-5
- Matzarakis, A., Mayer, H., Iziomon, M.G., 1999. Applications of a universal thermal index: physiological equivalent

- temperature. *Int. J. Biometeorol.* 43, 76–84.
- Matzarakis, A., Rutz, F., Mayer, H., 2007. Modelling radiation fluxes in simple and complex environments--application of the RayMan model. *Int. J. Biometeorol.* 51, 323–34. doi:10.1007/s00484-006-0061-8
- Mauree, D., 2014. Development of a multi-scale meteorological system to improve urban climate modeling. Université de Strasbourg.
- Mauree, D., Coccolo, S., Kämpf, J., Scartezzini, J., 2016a. Multi-scale modelling to assess human comfort in urban canyons, in: Sustainable Built Environment (SBE) Regional Conference.
- Mauree, D., Coccolo, S., Monna, S., Kämpf, J., Scartezzini, J., 2016b. On the Impact of Local Climatic Conditions on Urban Energy Use: A Case Study, in: PLEA.
- Mayer, H., Holst, J., Dostal, P., Imbery, F., Schindler, D., 2008. Human thermal comfort in summer within an urban street canyon in Central Europe. *Meteorol. Zeitschrift* 17, 241–250. doi:10.1127/0941-2948/2008/0285
- Mayer, H., Höpfe, P., 1987. Thermal Comfort of Man in Different Urban Environments. *Theor. Appl. Climatol.* 49, 43–49.
- Meehl, G., Stocker, T., 2007. Global Climate Projections, in: Contribution of Working Group I to the Fourth Assessment Report of the Intergovernmental Panel on Climate Change, 2007.
- Meehl, G.A., Stocker, T.F., Collins, W.D., Friedlingstein, P., Gaye, A.T., Gregory, J.M., Kitoh, A., Knutti, R., Murphy, J.M., Noda, A., Raper, S.C.B., Watterson, I.G., A.J., W., Zhao, Z.-C., 2007. Global Climate Projections, in: Climate Change 2007: The Physical Science Basis. Contribution of Working Group I to the Fourth Assessment Report of the Intergovernmental Panel on Climate Change. Cambridge University Press, Cambridge. doi:10.1017/CBO9781139177245
- Menzel, L., Lang, H., 1998. Spatial variation in evapotranspiration in Swiss Alpine regions. *Hydrology* 1992, 115–121.
- Meteonorm, 2009. *Meteonorm Version 6.0 Handbook part II: Theory.*
- Mihalakakou, G., Santamouris, M., Lewis, J.O., 1997. On the application of the energy balance equation to predict ground temperature profiles. *Sol. Energy* 60, 181–190.
- Minergie, 2017. *Minergie.*
- Mitchell, J.W., 1976. HEAT TRANSFER FROM SPHERES AND OTHER ANIMAL FORMS. *Biophys. J.* 16, 561–569.
- Mofidi, F., Akbari, H., 2017. Personalized energy costs and productivity optimization in offices. *Energy Build.* 143, 173–190. doi:10.1016/j.enbuild.2017.03.018
- Monna, S., Coccolo, S., Mauree, D., Kämpf, J., Scartezzini, J.-L., 2016. Energy Demand Analysis for Building Envelope Optimization for Hot Climate: A Case Study at An Najah National University, in: PLEA.
- More, D., White, J., 2013. *The illustrated encyclopedia of trees. Second edition, Second edi. ed. Princeton.*
- Morel, N., 2004. *Description of the LESO Building.*
- Morris, K.I., Chan, A., Salleh, S.A., Ooi, M.C., Oozer, M.Y., Abakr, Y.A., 2016. Numerical study on the urbanization of Putrajaya and its interaction with the local climate, over a decade. *Urban Clim.* 16, 1–24. doi:10.1016/j.uclim.2016.02.00
- Mostavi, E., Asadi, S., Boussaa, D., 2017. Development of a new methodology to optimize building life cycle cost , environmental impacts , and occupant satisfaction 121, 606–615. doi:10.1016/j.energy.2017.01.049
- Naboni, E., Meloni, M., Coccolo, S., Cucchi, F., Macrelli, G., Kämpf, J., Scartezzini, J.-L., 2017a. The Integration of

- Outdoor Thermal Simulation Tools in Architectural Design, in: PLEA.
- Naboni, E., Meloni, M., Coccolo, S., Kämpf, J., Scartezzini, J.-L., 2017b. An Overview of Simulation Tools for Predicting the Mean Radiant Temperature in an Outdoor Space Setting, in: CISBAT International Conference.
- Nader, S., 2009. Paths to a low-carbon economy—The Masdar example. *Energy Procedia* 1, 3951–3958. doi:10.1016/j.egypro.2009.02.199
- Ng, E. (Ed.), 2010. *Designing High-density Cities for Social and Environmental Sustainability*. Earthscan.
- Ng, E., Cheng, V., 2012. Urban human thermal comfort in hot and humid Hong Kong. *Energy Build.* 55, 51–65. doi:10.1016/j.enbuild.2011.09.025
- Ng, E., Ren, C. (Eds.), 2015. *The urban climatic map for a sustainable urban planning*. Routledge.
- Nicholls, J.G., Martin, A.R., Fuchs, P.A., Brown, D.A., Diamond, M.E., Weisblat, D., 2012. *From Neuron to Brain*, Fifth Edit. ed. Sinauer Associates, Sunderland.
- Nik, V.M., Coccolo, S., Kämpf, J., Scartezzini, J.-L., 2017. Impact assessment of climate change on the energy performance of building in the EPFL campus – Investigating the importance of future climate typology, in: CISBAT International Conference.
- Nikolopoulou, M., 2004. *Designing open spaces in the urban environment: a bioclimatic approach*. Centre Renewable Energy Sources (C.R.E.S.).
- Nikolopoulou, M., Baker, N., Steemers, K., 2001. Thermal comfort in outdoor urban spaces: understanding the human parameter. *Sol. Energy* 70, 227–235. doi:10.1016/S0038-092X(00)00093-1
- Nikolopoulou, M., Lykoudis, S., 2006. Thermal comfort in outdoor urban spaces: Analysis across different European countries. *Build. Environ.* 41, 1455–1470. doi:10.1016/j.buildenv.2005.05.031
- Nikolopoulou, M., Steemers, K., 2003. Thermal comfort and psychological adaptation as a guide for designing urban spaces. *Energy Build.* 35, 95–101.
- Nouvel, R., Brassel, K.-H., Bruse, M., Duminil, E., Coors, V., Eicker, U., Robinson, D., 2015. SIMSTADT , a New Workflow-driven Urban Energy Simulation Platform for CityGML City Models, in: CISBAT International Conference. pp. 889–894.
- Nouvel, R., Schulte, C., Eicker, U., Pietruschka, D., Coors, V., 2013. Citygml-Based 3D City Model for Energy Diagnostics and Urban Energy Policy Support. *Proc. BS2013 13th Conf. Int. Build. Perform. Simul. Assoc.* 218–225.
- Nouvel, R., Zirak, M., Coors, V., Eicker, U., 2017. The influence of data quality on urban heating demand modeling using 3D city models. *Comput. Environ. Urban Syst.* 64, 68–80. doi:10.1016/j.compenvurbsys.2016.12.005
- NREL, 2017. *EnergyPlus*. Energy Simulations Software.
- Odi-Lara, M., Campos, I., Neale, C., Ortega-Farías, S., Poblete-Echeverría, C., Balbontín, C., Calera, A., 2016. Estimating Evapotranspiration of an Apple Orchard Using a Remote Sensing-Based Soil Water Balance. *Remote Sens.* 8, 253. doi:10.3390/rs8030253
- Oke, T.R., 1987. *Boundary Layer Climates*. Psychology Press.
- Oke, T.R., 1973. City size and the Urban Heat Island. *Atmos. Environ.* 7, 769–779.
- Oke, T.R., Crowther, J.M., McNaughton, K.G., Monteith, J.L., Gardiner, B., 1989. The micrometeorology of the Urban Forest (and Discussion). *For. Weather Clim.* 324, 16.



- Olgay, V., 1962. Design with climate. Bioclimatic approach to architectural regionalism.
- ONU, 2014. World Urbanization Prospects. New York, United. doi:10.4054/DemRes.2005.12.9
- Ooka, R., Chen, H., Kato, S., 2008. Study on optimum design method for pleasant outdoor thermal environment using genetic algorithms (GA) and coupled simulation of convection, radiation and conduction. *J. Wind Eng. Ind. Aerodyn.* 96, 1733–1748. doi:10.1016/j.buildenv.2006.11.039
- OUP, 2017. Oxford Living Dictionaries.
- Pantavou, K., Santamouris, M., Asimakopoulos, D., Theoharatos, G., 2014. Empirical calibration of thermal indices in an urban outdoor Mediterranean environment. *Build. Environ.* 80, 283–292. doi:10.1016/j.buildenv.2014.06.001
- Papadopoulou, M., 2011. MINERGIE Standard for office buildings in the climate of Ras Al Khaimah. Draft. MINERGIE Stand. Off. Build. Clim. Ras Al Khaimah. Draft.
- Parsons, K., 2014. Human thermal environments. The effects of hot, moderate, and cold environments on human health, comfort and performance, Third. ed. Taylor & Francis, London and New York.
- Pearlmutter, D., 2016. Personal Communication with Prof. Pearlmutter.
- Pearlmutter, D., Berliner, P., Shaviv, E., 2007. Integrated modeling of pedestrian energy exchange and thermal comfort in urban street canyons. *Build. Environ.* 42, 2396–2409. doi:10.1016/j.buildenv.2006.06.006
- Pearlmutter, D., Berliner, P., Shaviv, E., 2007. Urban climatology in arid regions : current research in the 1885, 1875–1885. doi:10.1002/joc
- Pearlmutter, D., Berliner, P., Shaviv, E., 2006. Physical modeling of pedestrian energy exchange within the urban canopy. *Build. Environ.* 41, 783–795. doi:10.1016/j.buildenv.2005.03.017
- Pearlmutter, D., Berliner, P., Shaviv, E., 2005. Evaluation of Urban Surface Energy Fluxes Using an Open-Air Scale Model. *J. Appl. Meteorol.* 44, 532–545. doi:10.1175/JAM2220.1
- Pearlmutter, D., Erell, E., Etzion, Y., Meir, I. a., Di, H., 1996. Refining the use of evaporation in an experimental down-draft cool tower. *Energy Build.* 23, 191–197. doi:10.1016/0378-7788(95)00944-2
- Pearlmutter, D., Jiao, D., Garb, Y., 2014. The relationship between bioclimatic thermal stress and subjective thermal sensation in pedestrian spaces. *Int. J. Biometeorol.* doi:10.1007/s00484-014-0812-x
- Pediatric, A.A. of, 2000. Climatic heat stress and the exercising child and adolescent. *Pediatrics* 106, 158–159.
- Peel, M.C., Finlayson, B.L., McMahon, T.A., 2007. Updated world map of the Koeppen-Geiger climate classification 1633–1644.
- Penman, H., 1963. *Vegetation and Hydrology*. Royal Commonwealth Agricultural Bureaux, Farnham.
- Pont, M., 2010. *Chronique de l'EPFL 1978-2000: l'âge d'or de l'ingénierie*.
- Portnov, B.A., Hare, P. (Eds.), 1999. *Desert Regions Population, Migration and Environment*. Springer. doi:10.1007/978-3-642-60171-2
- Priestley, C.H.B., Taylor, R.J., 1972. On the Assessment of Surface Heat Flux and Evaporation Using Large-Scale Parameters. *Mon. Weather Rev.* 100, 81–92. doi:10.1175/1520-0493(1972)100<0081:OTAOSH>2.3.CO;2
- Primault, B., 1981. Extension de la validité de la formule Suisse de calcul de l'évapotranspiration.
- Quintal, B., 2016. 121 Definitions of Architecture.

- Rager, J., Coccolo, S., Kämpf, J., Marechal, F., Henchoz, S., 2015. Optimisation of the heating demand of the EPFL campus with an MIP approach, in: CISBAT International Conference.
- Rakhshan, K., Friess, W.A., Tajerzadeh, S., 2013. Evaluating the sustainability impact of improved building insulation: A case study in the Dubai residential built environment. *Build. Environ.* 67, 105–110. doi:10.1016/j.buildenv.2013.05.010
- Ratti, C., Raydan, D., Steemers, K., 2003a. Building Form and Environmental Performance : Archetypes , Analysis and an Arid Climate. *Energy Build.* 35, 49–59.
- Ratti, C., Raydan, D., Steemers, K., 2003b. Building form and environmental performance: archetypes, analysis and an arid climate. *Energy Build.* 35, 49–59. doi:10.1016/S0378-7788(02)00079-8
- Reiche, D., 2010. Renewable Energy Policies in the Gulf countries: A case study of the carbon-neutral “Masdar City” in Abu Dhabi. *Energy Policy* 38, 378–382. doi:10.1016/j.enpol.2009.09.028
- Reinhart, C., Dogan, T., Jakubiec, A., Rakha, T., Sang, A., 2013. UMI - AN URBAN SIMULATION ENVIRONMENT FOR BUILDING ENERGY USE , DAYLIGHTING AND WALKABILITY Christoph F Reinhart , Timur Dogan , J Alstan Jakubiec , Tarek Rakha and Andrew Sang Massachusetts Institute of Technology Department of Architecture, in: 13th Conference of International Building Performance Simulation Association, Chambéry, France, August 26-28 - 476. pp. 476–483.
- Reinhart, C.F., Davila, C.C., 2016. Urban building energy modeling- A review of a nascent field. *Build. Environ.* 97, 196–202. doi:10.1016/j.buildenv.2015.12.001
- Remund, J., Müller, S., Kunz, S., 2015. Meteonorm. Global meteorological database. Version 7.
- Ren, C., Ng, E., Katzschner, L., 2014. Urban climatic map studies: a review. *Int. J. Climatol.* 31, 2213–2233.
- Robinson, D., 2011. Computer modelling for sustainable urban design. Physical principles, methods & applications.
- Robinson, D., Haldi, F., Kämpf, J., Leroux, P., 2009. CitySim: Comprehensive micro-simulation of resource flows for sustainable urban planning, in: Proceedings of the Eleventh International IBPSA Conference. Glasgow.
- Robinson, D., Haldi, F., Kämpf, J., Leroux, P., Perez, D., Rasheed, A., Wilke, U., 2009. CitySim: comprehensive micro-simulation of resource flows for sustainable urban planning, in: Eleventh International IBPSA Conference Glasgow, Scotland July 27-30, 2009. pp. 1083–1090.
- Robinson, D., Stone, A., 2005. A simplified radiosity algorithm for general urban radiation exchange. *Build. Serv. Eng. Res. Technol.* 4, 271–284.
- Robinson, D., Stone, A., 2005. A simplified radiosity algorithm for general urban radiation exchange. *Build. Serv. Eng. Res. Technol.* 4, 271–284.
- Rosa, M. De, Bianco, V., Scarpa, F., Tagliafico, L.A., 2015. Historical trends and current state of heating and cooling degree days in Italy. *Energy Convers. Manag.* 90, 323–335. doi:10.1016/j.enconman.2014.11.022
- Rossi, M., Rocco, V.M., 2014. External walls design : The role of periodic thermal transmittance and internal areal heat capacity. *Energy Build.* 68, 732–740. doi:10.1016/j.enbuild.2012.07.049
- Rox Anderson, R., M.D, P., 1981. The Optics of Human Skin. *J. Invest. Dermatol.* 77, 13–19.
- Rutty, M., Scott, D., 2015. Bioclimatic comfort and the thermal perceptions and preferences of beach tourists. *Int. J. Biometeorol.* 59, 37–45. doi:10.1007/s00484-014-0820-x
- Saaroni, H., Pearlmutter, D., Hatuka, T., 2014. Human-biometeorological conditions and thermal perception in a Mediterranean coastal park. *Int. J. Biometeorol.* doi:10.1007/s00484-014-0944-z

- Santamouris, M., 2015. Regulating the damaged thermostat of the cities — Status , impacts and mitigation challenges. *Energy Build.* 91, 43–56. doi:10.1016/j.enbuild.2015.01.027
- Santamouris, M., 2014. On the energy impact of urban heat island and global warming on buildings. *Energy Build.* 82, 100–113. doi:10.1016/j.enbuild.2014.07.022
- Santamouris, M., 2012. Cooling the cities – A review of reflective and green roof mitigation technologies to fight heat island and improve comfort in urban environments. *Sol. Energy.* doi:10.1016/j.solener.2012.07.003
- Santamouris, M., 2007. *Advances in passive cooling.* Earthscan.
- Santamouris, M., 2001. *Energy and climate in the built environment.* James & James Ltd, London.
- Santamouris, M., Asimakopoulos, D.N., 2001. *Energy and Climate in the Urban Built Environment.* Earthscan.
- Santamouris, M., Cartalis, C., Synnefa, A., Kolokotsa, D., 2015. On the impact of urban heat island and global warming on the power demand and electricity consumption of buildings—A review. *Energy Build.* 98, 119–124. doi:10.1016/j.enbuild.2014.09.052
- Santamouris, M., Kolokotsa, D. (Eds.), 2016. *Urban climate mitigation techniques.* Routledge.
- Santamouris, M., Papanikolaou, N., Livada, I., Koronakis, I., Georgakis, C., Argiriou, a, Assimakopoulos, D.N., 2001. On the impact of urban climate on the energy consumption of buildings. *Sol. Energy* 70, 201–216. doi:10.1016/S0038-092X(00)00095-5
- Santamouris, M., Synnefa, A., Karlessi, T., 2011. Using advanced cool materials in the urban built environment to mitigate heat islands and improve thermal comfort conditions. *Sol. Energy* 85, 3085–3102. doi:10.1016/j.solener.2010.12.023
- SCNAT (Ed.), 2016. *Coup de projecteur sur le climat suisse. Etat des lieux et perspectives.* 2016.
- Scurlock, J.M.O., Asner, G.P., Gower, S.T., 2001. *Global Leaf Area Index Data from Field Measurements, 1932-2000.*
- Shabat, Y. Ben, Shitzer, A., 2012. Facial convective heat exchange coefficients in cold and windy environments estimated from human experiments 639–651. doi:10.1007/s00484-011-0463-0
- Shashua-Bar, L., Hoffman, M.E., 2000. Vegetation as a climatic component in the design of an urban street. An empirical model for predicting the cooling effect of urban green areas with trees. *Energy Build.* 31, 221–235.
- Shashua-Bar, L., Pearlmutter, D., Erell, E., 2011. The influence of trees and grass on outdoor thermal comfort in a hot-arid environment. *Int. J. Climatol.* 31, 1498–1506. doi:10.1002/joc.2177
- Shashua-Bar, L., Pearlmutter, D., Erell, E., 2009a. The cooling efficiency of urban landscape strategies in a hot dry climate. *Landsc. Urban Plan.* 92, 179–186. doi:10.1016/j.landurbplan.2009.04.005
- Shashua-Bar, L., Pearlmutter, D., Erell, E., 2009b. The cooling efficiency of urban landscape strategies in a hot dry climate. *Landsc. Urban Plan.* 92, 179–186. doi:10.1016/j.landurbplan.2009.04.005
- Shemirani, Seyed Majid Mofidi Nikghadam, N., 2013. Architectural Objectives in Tropical Climates. *Int. J. Archit. Urban Dev.* 3.
- SIA, 2006. *SIA 2024 Conditions d'utilisation standard pour l'énergie et les installations du bâtiment.*
- SIA, 2003. *SIA 384/2. Puissance thermique à installer dans les bâtiments.*
- Skoulika, F., Santamouris, M., Kolokotsa, D., Boemi, N., 2014. On the thermal characteristics and the mitigation potential of a medium size urban park in Athens, Greece. *Landsc. Urban Plan.* 123, 73–86. doi:10.1016/j.landurbplan.2013.11.002

- Snir, K., Pearlmutter, D., Erell, E., 2016. Landscape and Urban Planning The moderating effect of water-efficient ground cover vegetation on pedestrian thermal stress. *Landsc. Urban Plan.* 152, 1–12. doi:10.1016/j.landurbplan.2016.04.008
- SORANE, 2013. SISD Energy Concept.
- Spagnolo, J., De Dear, R., 2003. A field study of thermal comfort in outdoor and semi-outdoor environments in subtropical Sydney Australia. *Build. Environ.* 38, 721–738. doi:10.1016/S0360-1323(02)00209-3
- Spagnolo, J.C., De Dear, R.J., 2003. A human thermal climatology of subtropical Sydney. *Int. J. Climatol.* 23, 1383–1395. doi:10.1002/joc.939
- Spreafico, M., Weingartner, R., 2005. The Hydrology of Switzerland - Selected aspects and results 139. doi:PNR61
- Steffen, L. (Ed.), 2014. *Low Carbon Cities: Transforming Urban Systems*. Routledge.
- Streiling, S., Matzarakis, A., 2003. Influence of Single and Small Clusters of Trees on the Bioclimate of a City : a Case Study. *J. Arboric.* 29, 309–316.
- Stull, R.B., 1988. *An introduction to boundary layer meteorology*.
- Suisse-Énergie, 2009. Fiche technique fenêtres. La fenêtre dans le justificatif énergétique.
- Swan, L.G., Ugursal, V.I., 2009. Modeling of end-use energy consumption in the residential sector : A review of modeling techniques 13, 1819–1835. doi:10.1016/j.rser.2008.09.033
- Taha, H., 1997. Urban climates and heat islands: albedo, evapotranspiration, and anthropogenic heat. *Energy Build.* 25, 99–103. doi:10.1016/S0378-7788(96)00999-1
- Taleb, D., Abu-Hijleh, B., 2013. Urban heat islands: Potential effect of organic and structured urban configurations on temperature variations in Dubai, UAE. *Renew. Energy* 50, 747–762. doi:10.1016/j.renene.2012.07.030
- Taleb, H., Musleh, M.A., 2015. Applying urban parametric design optimisation processes to a hot climate: Case study of the UAE. *Sustain. Cities Soc.* 14, 236–253. doi:10.1016/j.scs.2014.09.001
- Taleb, H., Taleb, D., 2014. Enhancing the thermal comfort on urban level in a desert area: Case study of Dubai, United Arab Emirates. *Urban For. Urban Green.* 13, 253–260. doi:10.1016/j.ufug.2014.01.003
- Taleghani, M., Kleerekoper, L., Tenpierik, M., van den Dobbelsteen, A., 2014. Outdoor thermal comfort within five different urban forms in the Netherlands. *Build. Environ.* doi:10.1016/j.buildenv.2014.03.014
- Tan, J., Zheng, Y., Tang, X., Guo, C., Li, L., Song, G., Zhen, X., Yuan, D., Kalkstein, A.J., Li, F., Chen, H., 2010. The urban heat island and its impact on heat waves and human health in Shanghai. *Int. J. Biometeorol.* 54, 75–84. doi:10.1007/s00484-009-0256-x
- Tartaglia, E.M., Bamert, L., Herzog, M.H., Mast, F.W., 2017. Perceptual learning of motion discrimination by mental imagery 12, 1–10. doi:10.1167/12.6.14.Introduction
- Tetens, O., 1930. Ueber einige metereologische Begriffe. *Z. Geophys.* 6, 297–309.
- Theis, T., Tomkin, J., 2013. *Sustainability: A Comprehensive Foundation*, Rice Unive. ed.
- Tholl, M., 2014. “Architecture Is An Expression Of Values.” *World Post*.
- Thorsson, S., Lindberg, F., Eliasson, I., Holmer, B., 2007. Different methods for estimating the mean radiant temperature in an outdoor urban setting. *Int. J. Climatol.* 27, 1983–1993. doi:10.1002/joc
- Todorova, V., 2014. Warning on high water and power use. *Natl. UAE*.

## References

- Ulbig, A., Coccolo, S., Kämpf, J., 2015. Assessing the challenges of changing electricity demand profiles caused by evolving building stock and climatic conditions on distribution grids, in: CISBAT 2015.
- UN, 2014. UNWater.
- UN HABITAT, 2012. Sustainable urban energy. A Sourcebook for Asia.
- UNESCO, 2017. Old Walled City of Shibam.
- United Nations, 2015. ADOPTION OF THE PARIS AGREEMENT 1–32.
- Upadhyay, G., Mauree, D., Kampf, J., Scartezzini, J.-L., 2015. Evapotranspiration model to evaluate the cooling potential in urban areas - a case study in Switzerland. BS 2015 - 14th Int. IBPSA Conf. 1869–1876.
- Van Slooter, K., Bugnion, R., Gindrat, R., Jaccard, M., Magnin, P., Nembrini, A., Parlange, M., Vollichard, P., 2014. EPFL Sustainability Report. 2012-2013.
- Van Slooter, K., Bugnion, R., Gindrat, R., Jaccard, M., Magnin, P., Nembrini, A., Parlange, M., Vollichard, P., 2012. EPFL Sustainability Report 2010 - 2011.
- Vanos, J., 2016. Private conversation.
- Vanos, J.K., Middel, A., McKercher, G.R., Kuras, E.R., Ruddell, B.L., 2016. Hot playgrounds and children's health: A multiscale analysis of surface temperatures in Arizona, USA. *Landsc. Urban Plan.* 146, 29–42. doi:10.1016/j.landurbplan.2015.10.007
- Vanos, J.K., Warland, J.S., Gillespie, T.J., Kenny, N., 2012a. Improved predictive ability of climate-human-behaviour interactions with modifications to the COMFA outdoor energy budget model. *Int. J. Biometeorol.* 56, 1065–74. doi:10.1007/s00484-012-0522-1
- Vanos, J.K., Warland, J.S., Gillespie, T.J., Slater, G. a., Brown, R.D., Kenny, N. a., 2012b. Human Energy Budget Modeling in Urban Parks in Toronto and Applications to Emergency Heat Stress Preparedness. *J. Appl. Meteorol. Climatol.* 51, 1639–1653. doi:10.1175/JAMC-D-11-0245.1
- Vermeulen, T., Kämpf, J.H., Beckers, B., 2013. URBAN FORM OPTIMIZATION FOR THE ENERGY PERFORMANCE OF BUILDINGS USING CITYSIM, in: CISBAT International Conference. pp. 915–920.
- Vitasse, Y., 2016. Intensity , frequency and spatial configuration of winter temperature inversions in the closed La Brevine valley ,. *Theor. Appl. Climatol.* doi:10.1007/s00704-016-1944-1
- Vitruvio, n.d. De architectura.
- Waehtli, J., 2015. Personal communication with Julien Waehtli.
- Walter, E., 2014. An “Energy hub” on the EPFL campus: heat demand and supply.
- Walter, E., Kämpf, J., 2015. A verification of CitySim results using the BESTEST and monitored consumption values, in: Building Simulation Applications BSA 2015.
- Walter, I.A., Allen, R.G., Elliot, R., Itenfisu, Daniel., Brown, Paul., Jensen, Marvin.E., Mecham, Brent., Howell, Terry, a., Synder, Richard, Eching, Simon., Spofford, Thomas., Hattendorf, Mary., Martin, Derrel., Cuence, Richard, H., and Wright, L., 2005. The ASCE Standardized Reference Evapotranspiration Equation.
- Water exploitation, water use, water consumption, 2017.
- Wienold, J., 2007. DYNAMIC SIMULATION OF BLIND CONTROL STRATEGIES FOR VISUAL COMFORT AND ENERGY BALANCE ANALYSIS, in: Building Simulation 2007. pp. 1197–1204.

## References

- Willemse, S., Furger, M. (Eds.), 2016. From weather observations to atmospheric and climate sciences in Switzerland. Celebrating 100 years of the Swiss Society for Meteorology. Zurich.
- Willmott, C.J., Robeson, S.M., Matsuura, K., 2012. A refined index of model performance. *Int. J. Climatol.* 32, 2088–2094. doi:10.1002/joc.2419
- Wojtach, B., n.d. UTCI calculator.
- Woodward, F., Sheely, J.E., 1987. *Principles and Measurements in Environmental Biology*. Butterworth.
- Wright, S., 2013. *Optimization*.
- Yu, W., Li, B., Jia, H., Zhang, M., Wang, D., 2015. Application of multi-objective genetic algorithm to optimize energy efficiency and thermal comfort in building design. *Energy Build.* 88, 135–143. doi:10.1016/j.enbuild.2014.11.063
- Zanon, B., Verones, S., 2013. Climate change, urban energy and planning practices: Italian experiences of innovation in land management tools. *Land use policy* 32, 343–355. doi:10.1016/j.landusepol.2012.11.009
- Zuo, H., Chen, B., Wang, S., Guo, Y., Zuo, B., Wu, L., Gao, X., 2016. Observational study on complementary relationship between pan evaporation and actual evapotranspiration and its variation with pan type. *Agric. For. Meteorol.* 222, 1–9. doi:10.1016/j.agrformet.2016.03.002





# List of Figures

Figure 1.1 Biology, Architecture, Technology and Climatology. Adapted from (Olgyay, 1962). .....	2
Figure 1.2 Old Walled City of Shibam (Yemen). Photos by Jean-Jacques Gelbart (left) and Aneta Ribarska (right) (UNESCO, 2017) .....	3
Figure 1.3 Energy relationship between plants, buildings and climate. Adapted from (Ng, 2010). .....	4
Figure 1.4 Number of publications available on Scopus, retrieved the 6 <sup>th</sup> of March 2017. Keyword: “Sustainable campus” (left) and “Outdoor Comfort” (right). .....	5
Figure 1.5 Masdar City (Foster, 2017).....	6
Figure 2.1 3D view of the pedestrian, as designed by Rhinoceros (left) and imported in CitySim Pro (right). .....	14
Figure 2.2 Index of Thermal Stress, comparison between monitoring performed in Sede-Boqer campus of Ben-Gurion University (black line), and the simulations performed with CitySim Pro (red line). Selected courtyard C2, tree and bare soil. ....	19
Figure 2.3 Intrinsic clothing insulation, analysis of the insulation as a function of the air temperature. The red dashed line corresponds to light summer clothes. ....	22
Figure 2.4 Urban canyon design. Top-left: North- South oriented. Top-right: East- West oriented. Bottom: 3D view of the urban canyon.....	25
Figure 2.5 COMFA* budget in the climate of Lausanne, for a canyon oriented North- South (left) and East- West (right). Time of analysis: 21 <sup>st</sup> March, 21 <sup>st</sup> June and 21 <sup>st</sup> December.....	26
Figure 2.6 Energy fluxes in the COMFA* budget in the climate of Lausanne, for a canyon oriented East- West. Time of analysis: 21 <sup>st</sup> June. ....	26
Figure 2.7 Energy fluxes in the COMFA* budget in the climate of Lausanne, for a canyon oriented East- West. Time of analysis: 21 <sup>st</sup> December. ....	27
Figure 2.8 ITS in the climate of Dubai, for a canyon oriented North- South (left) and East- West (right). Time of analysis: hourly data during a typical meteorological year.....	28
Figure 2.9 Index of Thermal Stress (W) for a typical summer day (4th July), for a pedestrian located in Case study D, E and F. ....	28
Figure 2.10 Index of Thermal Stress, for a pedestrian located in an East- West oriented canyon. Thermal sensation as a function of the total hours during the year, by varying the metabolic activity, from 80Wm <sup>-2</sup> (left) to 150Wm <sup>-2</sup> (right). Thermal sensation: “cool” (blue), “comfortable” (green), “warm” (yellow) and “hot” (orange).....	29
Figure 2.11 Map of the EPFL campus in Lausanne (Switzerland), the LESO building is enclosed by the red rectangle (left). View of the southern facade of the LE solar experimental building with its flat roof terrace, location of the monitoring (right). ....	31
Figure 2.12 Air temperature (°C) and wind speed (m·s <sup>-1</sup> ) during the monitoring performed in the EPFL campus in Lausanne (August, September and October 2015). Legend: air temperature (black line) and wind speed (red line). ....	33
Figure 2.13 Solar irradiance (W·m <sup>-2</sup> ) during the monitoring, performed in the EPFL campus in Lausanne (August, September and October 2015). Global irradiance (black line) and diffuse irradiance (red line).....	33
Figure 2.14 CitySim Pro 3D virtual model of the LE-building block on the EPFL campus. The black circle shows the location of the MRT monitoring station (left) and the prismatic shape as defined in the proposed methodology (right). ....	34
Figure 2.15 Statistical regression analysis between CitySim Pro calculations and on-site monitored data. Simulated and monitored globe temperatures (left). Simulated and monitored Mean Radiant Temperatures (right). ....	35

List of Figures

Figure 2.16 Hourly comparisons between the monitored Mean Radiant Temperature (dotted black line) and the one calculated by the software CitySim Pro (continuous black line); the experimental error of the measurements is defined by the error bars..... 35

Figure 2.17 WS- 1712, located on the first floor, in the playground/ sport area. .... 37

Figure 2.18 Air temperature ( $^{\circ}\text{C}$ ) and wind speed ( $\text{m}\cdot\text{s}^{-1}$ ) during the monitoring performed in the SISD campus in Dubai (February, March, May and August 2016). Legend: air temperature (red line) and wind speed (black line). .... 38

Figure 2.19 Solar irradiance ( $\text{W}\cdot\text{m}^{-2}$ ) during the monitoring, performed in the SISD campus in Dubai (February, March, May and August 2016). Global irradiance (black line) and diffuse irradiance (red line). .... 39

Figure 2.20 CitySim Pro 3D virtual model of the main building of the Swiss International School Campus. .... 39

Figure 2.21 Statistical regression analysis between CitySim Pro calculations and on-site monitored data. Simulated and monitored Mean Radiant Temperatures ( $^{\circ}\text{C}$ ). .... 40

Figure 2.22 Mean Radiant Temperature as recorded by the weather station (black line) and modelled by CitySim (red line). .... 41

Figure 2.23 Thermal exchanges between the human body and the environment. Adapted from (Emery, 2014)..... 42

Figure 3.1 Example of plants. Top, left: Orange Tree (C3). Source: britannica.com. Top, right: corn (C4), and bottom: cactus (CAM). Source: Wikipedia..... 47

Figure 3.2 Leaf Area Index as function of the Leaf Area and the Ground Area. Adapted from: 2006, Pearson Education. .... 48

Figure 3.3 Schematic description of the tree model: view of the plant (left) and schematic model in CitySim Pro (right) with three surfaces representing the LAI index; where each LAI is oriented normally to the ground and to the sky (red arrows). .... 48

Figure 3.4 Schematic relationship between the wavelength and the reflection, transmission and absorption of the leaf. Adapted from (Oke, 1987) (Santamouris, 2001). .... 50

Figure 3.5 Schematic description of the water vapour, heat and carbon dioxide exchange on the stomata of the leaf. Adapted from (Oke, 1987). .... 52

Figure 3.6 Trees modelled with the software CitySim Pro. Top: DXF imported in the software, with the upper surface of the tree (the canopy) and the trunk. Bottom: 3D model of the tree after the modification Leaf Area Index, in this example a LAI=2..... 54

Figure 3.7 Comparison of measured and simulated leaf temperature in Sede Boqer campus of Ben Gurion University (Israel)..... 58

Figure 3.8 Simulated leaf temperature (red line) compared with the monitored one (black line), for five days during the month of August..... 59

Figure 3.9 Weather station of Pully ( $6^{\circ}40' \text{ E}$ ,  $46^{\circ}31' \text{ N}$ ), located in an open field at 456 m asl. Source: MeteoSuisse. ... 63

Figure 3.10 Primault formula; constant for height correction (left) and constant for seasonal correction (right) (Primault, 1981). .... 64

Figure 3.11 CitySim Pro. 3D virtual environment used to quantify the potential evapotranspiration around the weather station of Pully. .... 66

Figure 3.12 Observed (Pully weather station, calculated in accordance with Penman- Montheit, red line) versus modelled (black line) daily potential evapotranspiration (n=365) during the year 2013. .... 67

Figure 3.13 Observed (Pully weather station, calculated in accordance with Penman- Montheit, red line) versus modelled (black line) daily potential evapotranspiration (n=365) during the year 2014. .... 68

Figure 3.14 Observed (Pully weather station, calculated in accordance with Penman- Montheit, red line) versus modelled (black line) daily potential evapotranspiration (n=365) during the year 2015. .... 68

Figure 3.15 Potential evapotranspiration. Calculation for the experimental error, during the selected years (2013, 2014 and 2015). Monitoring data from the Pully weather station (red) and CitySim calculation (black). .... 69

Figure 3.16 Observed (Pully weather station, calculated by the Primault formula, red line) versus modelled (black line) daily potential evapotranspiration (n=365) during the year 2013. .... 70

Figure 3.17 Observed (Pully weather station, calculated by the Primault formula, red line) versus modelled (black line) daily potential evapotranspiration (n=365) during the year 2014. .... 70

Figure 3.18 Observed (Pully weather station, calculated by the Primault formula, red line) versus modelled (black line) daily potential evapotranspiration (n=365) during the year 2015. ....	71
Figure 4.1 EPFL campus, plan extracted from “plan.epfl.ch” (top) and 3D view of the site (bottom). ....	75
Figure 4.2 Left: average (black line), maximum (red dots) and minimum temperature (blue dots) in the city of Lausanne. Right: hourly temperature for three summer (continues line) and winter days (dotted line).....	76
Figure 4.3 Left: view of buildings of the first stage of construction. Right: constructive detail and section of the facade of building MXD, part of the second stage of construction. Source of the picture on the right: real estate and infrastructure department of the EPFL.....	77
Figure 4.4 Photovoltaics panels on the EPFL campus. Gretzel cell (left) and Kromatix™ (right). Source: Mediatheque EPFL. ....	78
Figure 4.5 Left: correlation between the monitored and the simulated heating demand for the years 2011,2012 and 2013. Right: annual heating demand of the campus, expressed in kWh·m <sup>-3</sup> and kWh·m <sup>-2</sup> , assuming an average height of 2.4m. ....	79
Figure 4.6 Left: correlation between the monitored electricity produced by PV and the simulations performed by CitySim for the year 2013. Right: annual solar irradiance on the campus, with the photovoltaic panels shown on the rooftop of buildings (grey). ....	79
Figure 4.7 Heating demand of buildings (kWh·m <sup>-2</sup> ), comparison between the existing situation (black), Minergie (grey) and Minergie-P (white).....	80
Figure 4.8 Total energy demand for heating and cooling (GWh), for the proposed case studies (existing, Minergie and Minergie-P) and different climatic scenarios (Typical Meteorological Year, 2050-B1, 2050- A1B and 2050-A2). Heating demand (black) and Cooling demand (grey). ....	82
Figure 4.9a Heating (a) and cooling (b) demand of the campus in future climatic scenarios, as function of the existing case study. ....	83
Figure 4.10 Predicted Mean Vote and Predicted Percentage of Dissatisfied in the non-refurbished LESO solar experimental building, with meteorological data of a typical meteorological year; a) May; b) June; c) July; d) August; e) September. ....	84
Figure 4.11 Predicted Mean Vote and Predicted Percentage of Dissatisfied in the non-refurbished LESO solar experimental building, with meteorological data 2050-A2; a) May; b) June; c) July; d) August; e) September. ....	85
Figure 4.12 Analysis of the indoor thermal sensation, based on the Predicted Mean Vote, for the months of May, June, July, August and September, for the current LESO solar experimental building (TMY) and the same building (non-refurbished, Minergie and Minergie-P) in the future climatic scenario 2050-A2. ....	86
Figure 4.13 Wind speed in the EPFL campus, as provided by Meteonorm (red) and as calculated by the Canopy Interface Model (grey).....	87
Figure 4.14a La Brevine, strongest CAP phenomena in the valley (Vitasse, 2016). ....	87
Figure 4.15 Air temperature during the months of January, February and March, as provided by Meteonorm (red) and CIM (grey). ....	88
Figure 4.16 Heating demand of the five selected urban configurations (black dots), as function of the variation by +1°C (red dots) and -1°C (blue dots) of the air temperature, and by +1.5 ms <sup>-1</sup> (violet dots) and -1.5 ms <sup>-1</sup> (orange dots).91	
Figure 4.17 Energy demand for heating for the existing buildings, based on Meteonorm weather data (white) and CIM weather data (black).....	91
Figure 4.18 Energy demand for heating in the Minergie-P refurbished buildings, based on Meteonorm weather data (white) and CIM weather data (black). ....	92
Figure 4.19 Correlation between the heating demand (kWh·m <sup>-2</sup> ) calculated with CIM and Meteonorm, as a function of the current situation (white) and the Minergie-P one (black).....	92
Figure 4.20 EPFL plan with the location of the two case studies A and B (top). Bottom: photos of the case studies, case study A (left) and case study B (right). ....	94
Figure 4.21 Actual Sensation Vote (ASV) in the EPFL campus in current and future climatic scenarios: 2050-B1, 2050-A1B, 2050-A2, 2100-B1, 2100-A1B and 2100-A2.....	95
Figure 4.22 Outdoor human comfort, quantified by the Actual Sensation Vote, for a TMY (left), scenario 2050- A2 (center) and scenario 2100-A2 (right). ....	95

List of Figures

Figure 4.23 Actual Sensation Vote in current and future climatic scenarios. .... 96

Figure 4.24 Annual solar irradiance on the Swiss Tech Convention Center site (left) and in the bocce court (right).  
 Maximum solar irradiance equals  $1,264 \text{ kWh}\cdot\text{m}^{-2}$ . .... 96

Figure 4.25 COMFA\* Budget for a pedestrian located in the open square near the Swiss Tech Convention Centre, and in the bocce court. Analysis of the human comfort for a spring day (left) and a summer day (right). .... 97

Figure 4.26 Proposed shadowing strategies: textile meshing (top left), one Picea Rubens on the South side of the court (top right) or two Betula Utilis on the West side of the court (bottom). .... 98

Figure 4.27 Monthly solar irradiance (July) in with future climatic data 2100-A2. Shading strategies: textile meshing (top left), one Picea Rubens on the South side of the court (top right) or two Betula Utilis on the West side of the court (bottom). .... 99

Figure 4.28 Wind speed provided by the software Meteonorm (dotted line) and calculated by the Canopy Interface Model (continuous line) for the square near the Swiss Tech Convention Centre. a) 21<sup>st</sup> of March; b) 21<sup>st</sup> of June; c) 21<sup>st</sup> of December. .... 100

Figure 4.29 COMFA\* energy budget for the square near the Swiss Tech Convention Centre (left) and in the bocce court (right), during 21<sup>st</sup> of March, 21<sup>st</sup> of June and 21<sup>st</sup> of December. Comparison between weather data provided by Meteonorm (red) and calculated by CIM (black). .... 101

Figure 4.30 3D view of the EPFL campus (up) with the indication of the buildings and the outdoor environments: streets (dark grey), grass (green), concrete (light grey) and water (blue). 3D view of the campus, extracted from CitySim Pro (down). .... 103

Figure 4.31 Plan of the EPFL campus, with the seven zones: A, B, C, D, E, F and G. .... 104

Figure 4.32 Typical Meteorological Year, comfort Map of the EPFL campus. Total comfort hours during the summer. .... 105

Figure 4.33 2100, comfort Map of the EPFL campus. Total comfort hours during the summer. .... 106

Figure 4.34 Comfort Map of the EPFL campus. Difference between the comfortable hours for the TMY and 2050 during the year. .... 107

Figure 4.35 Comfort Map of the EPFL campus. Difference between the comfortable hours for the TMY and 2050 during the winter time. .... 108

Figure 5.1a Localization of the Swiss International School Campus in Dubai extracted from Google Maps in March 2017 (top). 3D view of the campus (bottom). .... 112

Figure 5.2 Left. Average (black line), maximum (red dots) and minimum temperature (blue dots) in the city of Dubai. Right. Hourly temperature for three summer (continues line) and three winter days (dotted line). .... 114

Figure 5.3 Top: relative humidity during the solstices and equinoxes, as a function of the hours of the day. Legend: 21<sup>st</sup> March (dotted line), 21<sup>st</sup> June (continuous line), 23<sup>rd</sup> September (long dash dot line) and 21<sup>st</sup> of December (dash dot line). Bottom: sunrise and sunset, for each day of the year. .... 115

Figure 5.4 Swiss International School Campus in Dubai, first design by ArchiLab (left) and analysis of the cooling demand, performed with CitySim (right). .... 116

Figure 5.5 Swiss International School Campus in Dubai, based on the design proposed by ArchiLab in 2013; plan (top) and 3D view of the site (bottom). .... 117

Figure 5.6 Annual solar irradiance in the Swiss International School Campus. Maximum value corresponding to  $2,131 \text{ kWh}\cdot\text{m}^{-2}$ . .... 118

Figure 5.7 Annual cooling demand of the campus, expressed in  $\text{kWh}\cdot\text{m}^{-2}$ , as a function of the building. Comparison between Minergie standard, Dubai Green Building Standard and a typical building in UAE. .... 119

Figure 5.8 Monthly solar irradiance (during the month of June) received by building H if positioned in the campus (left) or without neighboring buildings (right). .... 120

Figure 5.9 Left: prototype of a cube (10 meters each side), with a sloping facade in each of the cardinal directions; variation of the ground covering's short wave reflectance (0.2 to 0.7). Right: solar irradiance absorbed by each facade, as a function of the slope and the ground covering. .... 121

Figure 5.10 Cumulative solar irradiance received by each facade ( $\text{kWh}\cdot\text{m}^{-2}$ ) as a function of the month. The ground covering has a shortwave reflectance corresponding to 0.2, and the sloping of each facade corresponds to  $90^\circ$ . Legend: South facade (Black); North facade (white); West facade (grey) and East facade (grey lines). .... 121

Figure 5.11 City of Shibam (Yemen); plan view extracted from Google Earth, and photo of the old city, source Wikipedia..... 122

Figure 5.12 Cooling demand of the building, as a function of the shortwave reflectance of the facades (top) and cooling demand as a function of the solar irradiance received by pedestrians (bottom)..... 122

Figure 5.13 Left: annual PV production (kWh/m<sup>2</sup>) per roof surface as a function of the building. Right: several BiPV orientations, and tilt angles..... 124

Figure 5.14 Annual PV production of the campus (MWhm<sup>-2</sup>) as a function of PV orientation (North, South, East and West) and tilt (0°, 20°, 30° and 45°)..... 125

Figure 5.15 3D view of the SISD campus after the “ad hoc” optimization (left) and annual solar irradiance on the campus (right)..... 126

Figure 5.16 Bioclimatic guidelines of the SISD campus. .... 127

Figure 5.17 Swiss International School Campus, design provided by DSA Architects International on 12.03.2014 ..... 127

Figure 5.18 Picture of the construction site, taken during a visit in November 2014. Wall construction (left) and view of the Dubai skyline from the first floor of the kindergarten (right). .... 128

Figure 5.19 Top: SISD Dubai, plan of the campus with the location of pedestrians in the outdoor environment. Bottom: rendering of the school campus (source sisd.ae). .... 129

Figure 5.20 Left: average Index of Thermal Stress during the 21<sup>st</sup> of March (white), 21<sup>st</sup> of June (black) and 21<sup>st</sup> of December (grey) for the eight pedestrians located in the outdoor environment of the SISD campus. Right: cumulative hourly Index of Thermal Stress as a function of the different locations: cyan (cold), green (comfortable), yellow (warm), orange (hot)..... 130

Figure 5.21 Fabric design, in accordance to SISD project (left) and the proposed three- layer fabrics (right)..... 131

Figure 5.22 Index of Thermal Stress, perceived by pedestrian p2 without shadowing (black line), with 1 layer textile fabric (red line) and with three layers of fabric (dotted black line). Hourly analysis during the 21<sup>st</sup> of March, pedestrian metabolic rate equals to 80 W·m<sup>-2</sup> (a) and 255 W·m<sup>-2</sup> (b). .... 131

Figure 5.23 Index of Thermal Stress, perceived by Pedestrian 2 without shadowing (black line), with one layer of textile fabric (red line) and with three layers of fabric (dotted black line). Hourly analysis during the 21<sup>st</sup> of June, pedestrian metabolic rate equals to 80 W·m<sup>-2</sup> (a) and 255 W·m<sup>-2</sup> (b). .... 132

Figure 5.24 Comfort Map of the SISD campus. Relative fraction of daytime comfortable hours for each season (%), expressed as a function of the Index of Thermal Stress; a) Summer: 21<sup>st</sup> June to 22<sup>nd</sup> September, b) Winter: 21<sup>st</sup> December to 20<sup>th</sup> of March, c) Spring: 21<sup>st</sup> of March to 20<sup>th</sup> of June and d) Autumn: 23<sup>rd</sup> September to 20<sup>th</sup> December. .... 134

Figure 5.25 Index of Thermal Stress (W) for two selected locations: Pedestrian #14 (P14, continuous line) facing East, and Pedestrian #73 (P73, dotted line) located in Courtyard C. ITS is expressed as a function of the hours of the day, for March 21<sup>st</sup> (a), June 21<sup>st</sup> (b), September 23<sup>rd</sup> (c) and December 21<sup>st</sup> (d)..... 135

Figure 5.26 Energy Fluxes impinging on Pedestrian #14 facing East on March 21<sup>st</sup>, June 21<sup>st</sup>, September 23<sup>rd</sup> and December 21<sup>st</sup>, as a function of daily hours. All energy fluxes are expressed in W·m<sup>-2</sup>: incident longwave radiation (red), incident shortwave radiation (black) and energy exchanged by convection (white). .... 136

Figure 5.27 Energy fluxes impinging on Pedestrian #73 located in Courtyard C on March 21<sup>st</sup>, June 21<sup>st</sup>, September 23<sup>rd</sup> and December 21<sup>st</sup>, as a function of daily hours. All energy fluxes are expressed in W·m<sup>-2</sup>: incident longwave radiation (red), incident shortwave radiation (black) and energy exchanged by convection (white)..... 137

Figure 5.28 Location of three different plants species on the SISD campus on the southern building entrance and in Courtyards A, B and C. From top: Ghaf tree (*Prosopis cineraria*), Date Palm (*Phoenix dactylifera*) and Acacia Tortilis (*Vachellia tortilis*). .... 138

Figure 5.29 Hourly Index of Thermal Stress for pedestrians located near the southern facade for the different months: cyan (cold), green (comfortable), yellow (warm), orange (hot) and red (very hot). .... 139

Figure 5.30 Index of Thermal Stress (W) for a pedestrian located in Courtyard A with shadowing provided by a palm tree, and without it. Analysis for a typical spring day (May 20<sup>th</sup>) and a typical autumn day (October 20<sup>th</sup>). Legend: red (very hot); orange (hot); yellow (warm); green (comfortable) and cyan (cool). .... 140



List of Figures

Figure 5.31 3D view of the SISD campus (up) with the indication of the buildings and the outdoor environments (sports center, parking and swimming pools in blue). 3D model created by CitySim Pro (down) with the analysis-grid, as well as the shading devices (orange). ..... 141

Figure 5.32 3D view of the campus created by Rhino with the location of the trees. .... 141

Figure 5.33 Comfort Map of the SISD campus. Total comfortable hours during the spring season. .... 143

Figure 5.34 Comfort Map of the SISD campus. Total comfortable hours during the summer season. .... 143

Figure 5.35 Comfort Map of the SISD campus. Total comfortable hours during the winter season. .... 144

Figure 5.36 Comfort Map of the SISD campus. Total annual comfortable hours with ghaf tree. .... 145

Figure 5.37 Comfort Map, annual Mean Radiant Temperature for the SISD campus. MRT averaged during all the day. .... 146

Figure 5.38 Comfort Map, annual Mean Radiant Temperature for the SISD campus. MRT averaged during the daytime (from 8:00 to 18:00 hours). .... 147

Figure 5.39 Comfort Map, Mean Radiant Temperature for the SISD campus calculated during the winter. MRT averaged during the daytime (from 8:00 to 18:00 hours). .... 148

Figure 5.40 Comfort Map, Mean Radiant Temperature for the SISD campus calculated during the summer. MRT averaged during the daytime (from 8:00 to 18:00 hours). .... 148

Figure 5.41 Plan of the Swiss International School Campus with the location of the weather stations (left), and weather station WS 1711 on the rooftop of the administrative building (right). Photo by Laurent Deschamps. .... 149

Figure 5.42 WS-1712, located on the first floor, in the playground/ sports area. .... 151

Figure 5.43 WS-1713A, located near the parking lot and in front of a temporary football court. .... 152

Figure 5.44 WS-1713B, located on the southern entrance of the building, near the playground area (17<sup>th</sup> of May to the 2<sup>nd</sup> of July). Photos by Ashfaq Khan. .... 152

Figure 5.45 Weather station 1713 C, located on the southern entrance of the building, near the swimming pool and under a tree (13<sup>th</sup> of July to the 17<sup>th</sup> September). Photos by Ashfaq Khan. .... 153

Figure 5.46 Weather station 1713 D, located on the southern entrance of the building, near the swimming pool and surrounded by flowers (from 18<sup>th</sup> September 2016). Photos by Ashfaq Khan. .... 153

Figure 5.47 WS-1712, in the first floor playground (Left) and WS-1713A in front of the temporary football court. .... 154

Figure 5.48 Battery problem in WS- 1713, during the month of October 2016. Extracted from the Climaps website. .... 155

Figure 5.49 Average air temperature during the monitoring months, as recorded by each weather station. .... 158

Figure 5.50 WS-1711, hourly air temperature measurements, during the daytime (black) and nighttime (red). .... 158

Figure 5.51 WS-1712, hourly air temperature measurements, during the daytime (black) and nighttime (red). .... 159

Figure 5.52 WS-1713, hourly air temperature measurements, during the daytime (black) and nighttime (red). .... 159

Figure 5.53 WS-1711. Total solar irradiance (black) as a function of the air temperature (red) during the 19<sup>th</sup>-21<sup>st</sup> April 2016. .... 160

Figure 5.54 WS-1713. Total solar irradiance (black) as a function of the air temperature (red) during the 19<sup>th</sup>-21<sup>st</sup> April 2016. .... 160

Figure 5.55 Weather station 1711. Wind speed during the month of January 2016. Wind speed max (red dots), wind speed min (blue dots) and average wind speed (black line). .... 162

Figure 5.56 Weather station 1713. Wind speed during the month of January 2016. Wind speed max (red dots), wind speed min (blue dots) and average wind speed (black line). .... 162

Figure 5.57 Correlation between the wind speed and the wind direction, as monitored by Weather station 1713, recorded during the month of January 2015. .... 163

Figure 5.58 Wind speed as monitored by the three weather stations, during the month of July. .... 163

Figure 5.59 Weather station 1712. Relative humidity during the month of July 2016. .... 164

Figure 5.60 Weather stations 1712 (red) and 1713 (black). Mean Radiant Temperature during the month of February 2016. .... 166

Figure 5.61 Weather stations 1712 (red) and 1713 (black). Mean Radiant Temperature during the month of August 2016. .... 166

Figure 5.62 Weather stations 1712 (red) and 1713 (black). Absolute humidity ( $gm^{-3}$ ) during the month of August 2016. .... 167

Figure 6.1 Top view of the EPFL Campus, with the two selected areas: Zone-A, characterized by a low density and two natural areas and Zone-B, characterized by a denser built environment. .... 175

Figure 6.2 EPFL campus, Zone-A. Optimization of the outdoor thermal comfort and the energy performance of buildings. Green: grass; Gray: asphalt; Yellow: natural soil (top). 3D view from CitySim Pro, with indication of the COMFA\* points of measurements (bottom). .... 177

Figure 6.3 Top: Detailed plan of the area. Bottom: (left) LESO solar experimental building (source dp-architectes.ch) and view on the open court from the LESO solar experimental building (right). .... 178

Figure 6.4 Energy performance as function of the blinds cut-off. Plateau within the search space. .... 179

Figure 6.5 EPFL campus, Zone-A. Optimal design of the campus for the TMY, annual shortwave radiation ( $\text{kWh m}^{-2}$ ) received by the campus. .... 180

Figure 6.6 EPFL campus, Zone-A. Optimal design of the campus. .... 181

Figure 6.7 EPFL campus, Zone-A. Optimal design of the campus in 2100, annual shortwave radiation ( $\text{kWh m}^{-2}$ ) received by the campus. .... 182

Figure 6.8 Difference between the actual air temperature (TMY) and the future one (2100-B1). .... 182

Figure 6.9 EPFL campus, Zone-A; optimized design for a Typical Meteorological Year. .... 184

Figure 6.10 EPFL campus, Zone-A; optimized design for the climatic scenario 2050-B1. .... 184

Figure 6.11 EPFL campus, Zone-A; optimized design for the climatic scenario 2100-B1. .... 185

Figure 6.12 EPFL campus, Zone-B. Optimization of the energy demand for heating and cooling. 3D geometrical view of the site (top) and 3D model with CitySim Pro (bottom). .... 186

Figure 6.13 Top: plan of the site. Bottom: PO building, or Polydôme (left) and PH building (right). .... 186

Figure 6.14 Variation of the U-value of the wall ( $\text{W}\cdot\text{m}^{-2}\cdot\text{K}^{-1}$ ) as function of the insulation thickness (cm), for a simple concrete wall with an external layer of insulation. .... 187

Figure 6.15 Heating (left) and cooling (right) demand of the EPFL campus for a typical meteorological year, after the optimization by the hybrid Evolutionary Algorithm (CMA- ES/ HDE). .... 188

Figure 6.16 Heating (left) and cooling demand (right) of the EPFL campus; comparison between the current and the optimized case study. .... 188

Figure 6.17 Top: hourly ground surface temperature ( $^{\circ}\text{C}$ ) for three winter days (29<sup>th</sup> to 31<sup>st</sup> December) in the current (black) and optimized scenario (red). Bottom: Meteorological characteristics of the three selected days. .... 189

Figure 6.18 Energy demand, for heating (red) and cooling (blue) of the campus, during the optimization process. Energy demand of the current campus (black line), as well as its heating (red line) and cooling demand (blue line). .... 190

Figure 6.19 Heating (left) and cooling (right) demand of the EPFL campus for 2050-B1, after the optimization by the hybrid Evolutionary Algorithm (CMA- ES/ HDE). .... 190

Figure 6.20 Heating (left) and cooling demand (right) of the EPFL campus; comparison between the current case study projected in 2050 and the optimized case study. .... 191

Figure 6.21 Energy demand, for heating (red) and cooling (blue) of the campus, during the optimization process. Energy demand of the current campus, projected in 2050 (black line), as well as its heating (red line) and cooling demand (blue line). .... 192

Figure 6.22 Heating (right) and cooling (left) demand of the EPFL campus for 2100-B1, after the optimization by the new hybrid Evolutionary Algorithm (CMA- ES/ HDE). .... 192

Figure 6.23 Heating (right) and cooling (left) demand of the EPFL campus for 2100-B1, after the optimization by the new hybrid Evolutionary Algorithm (CMA- ES/ HDE). .... 193

Figure 6.24 Energy demand, for heating (red) and cooling (blue) of the campus, during the optimization process. Energy demand of the current campus, projected in 2100 (black line), as well as its heating (red line) and cooling demand (blue line). .... 194

Figure 6.25 EPFL campus, Zone-B; optimized design for a Typical Meteorological Year. .... 196

Figure 6.26 EPFL campus, Zone-B; optimized design for 2050-B1. .... 196

Figure 6.27 EPFL campus, Zone-B; optimized design for 2100-B1. .... 197

Figure 6.28 Swiss International School Campus in Dubai. 3D view from CitySim Pro (top), and plan view with the indication of the eleven pedestrian located in the outdoor environment (bottom). .... 198

List of Figures

Figure 6.29 Swiss International School Campus in Dubai. 3D view of the site (top). Bottom: Aerial photo, source: khaleejtimes.com (left) and photo of building 8 (right) .....	199
Figure 6.30 Dubai, comparison between the monthly precipitations of a Typical Meteorological Year, provided by Meteonorm, and the future climatic scenarios 2050-A2 and 2100-A2, based on the IPCC research (IPCC, 2000). 200	
Figure 6.31 Thermal conductivity ( $Wm^{-1}K^{-1}$ ) of the common construction materials, as function of their density ( $kgm^{-3}$ ) .....	202
Figure 6.32 SISD campus. Optimal design of the campus for the Typical Meteorological Year. Annual shortwave radiation ( $kWh\ m^{-2}$ ) received by the campus (top) and annual surface temperature, expressed in °C (bottom)...	203
Figure 6.33 SISD campus. Optimal design of the campus for the 2050-A2. Annual longwave radiation ( $kWh\ m^{-2}$ ) received by the campus (top) and surface temperature, expressed in °C (bottom). .....	204
Figure 6.34 SISD campus. Optimal design of the campus for the 2100-A2. Annual net longwave radiation ( $kWh\ m^{-2}$ ) received by the campus (top) and surface temperature, expressed in °C (bottom). .....	206
Figure 6.35 Swiss International School of Dubai, optimal design for a Typical Meteorological Year. ....	208
Figure 6.36 Swiss International School of Dubai, optimal design in scenario 2050-A2. ....	208
Figure 6.37 Swiss International School of Dubai, optimal design in scenario 2100-A2. ....	209
Figure 7.1 Agropolis and Petropolis (UN HABITAT, 2012) .....	211
Figure 7.2 The Copenhagen International School's new building, covered by Swissinso PV panels. Source: Philippe Vollichard (right) and Pintarest (left) .....	213
Figure 7.3 View of the city of Lausanne. Source: grandtour.myswitzerland.com .....	214
Figure 7.4 View of the city of Perugia. Source: viator.com.....	214
Figure 7.5 Trullo (left). Source: Pintarest. Hourly solar radiation (13:00) during a summer day (right).....	216
Figure 7.6 Atrapaniebla in the Atacama desert, Chile. Source: unaltoeneldesierto.cl. ....	218
Figure 7.7 Fog in Dubai. Source: dailymail.com.uk. Photo by Nicole Luettecke. ....	218
Figure 7.8 Ground to air heat exchanger. Conceptual example. ....	219
Figure 7.9 Proposed design for a small district in hot and arid climate. ....	220
Figure 7.10 Relationship between the environmental perception and the neuronal response. Images extracted from (Nicholls et al., 2012), assembled by the author. ....	221
Figure B.1 PH (left) and GR building (right).....	229
Figure B.2 PO building, or Polydôme. ....	230
Figure B.3 LESO solar experimental building (source dp-architectes.ch) .....	231
Figure B.4 Swiss International School Campus in Dubai. Aerial photo, source: khaleejtimes.com (left) and photo of the main building (right) .....	233
Figure B.5 Swiss International School Campus in Dubai. View of the construction site, 11 <sup>th</sup> November 2014. Main building (left) and detail of the walls (right). ....	233

# List of Tables

Table 2.1 List of available software able to quantify the outdoor human comfort, as a function of the calculated models (PMV, PET, UTCI, SET*, ETU and PT) and MRT. ....	13
Table 2.2 Thermophysical parameters of the human body modelled with the software CitySim Pro, based on Fiala et al. (Fiala et al., 2012). ....	14
Table 2.3 Thermal sensation as a function of the Index of Thermal Stress (W); this index is defined for hot climate, and the thermal sensation described varies from cool to very hot thermal sensation (Pearlmutter et al., 2014). ....	18
Table 2.4 Physical and geometrical properties of the court configuration (left) and 3D view from CitySim Pro (right). ..	18
Table 2.5 Thermal sensation as a function of the COMFA* budget. ....	24
Table 2.6 Sensitivity analysis: case studies, as a function of the canyon orientation and the climate. ....	24
Table 2.7 COMFA* budget. Analysis of the hours characterized by the same thermal sensation, as a function of the site (Lausanne) and the canyon orientation. ....	25
Table 2.8 Index of Thermal Stress (W). Analysis of the hours characterized by the same thermal sensation, as a function of the site (Dubai) and the canyon orientation. ....	27
Table 2.9 Meteorological conditions during the monitored period in Lausanne (August, September and October 2015). ....	32
Table 2.10 Summarized results for the proposed methodology compared with on-site monitoring ; statistical analysis of the Root Mean Square Error (RMSE), Index of Agreement and Mean Absolute Error. ....	34
Table 2.11 On site monitoring in Dubai. Instruments type and their accuracy. ....	36
Table 2.12 Meteorological conditions during the monitored period in Dubai, February, March, Mai and August 2016. 38	
Table 3.1 Short and long wave reflection, transmission and absorption for leaves. Adapted from (Oke, 1987).....	49
Table 3.2 Plants modelled in accordance with the presented methodology: <i>Picea Rubens</i> , <i>Betula Utilis</i> , <i>Prunus Avium</i> . Physical and botanic characteristics of plants are retrieved from (Scurlock et al., 2001) (More and White, 2013). Source of the photos: Wikipedia. ....	55
Table 3.3Plants modelled in accordance with the presented methodology: <i>Prosopis cineraria</i> , <i>Phoenix dactylifera</i> , <i>Vachellia tortilis</i> , <i>Tipuan Typu</i> and <i>Prosopis-Juliflora</i> . Physical and botanic characteristics of plants are retrieved from (Scurlock et al., 2001) (More and White, 2013). Source of the photos: Wikipedia. ....	56
Table 3.4 Physical and geometrical properties of each court configuration. ....	58
Table 3.5 Meteorological data provided by the weather station of Pully and Payerne (nebulosity). ....	64
Table 3.6 Meteorological characteristics of the year 2013, as provided by the weather station of Pully. Average monthly value for diffuse irradiance, global irradiance, air temperature, wind speed, relative humidity and nebulosity. Cumulative monthly value for rainfalls. ....	65
Table 3.7 Meteorological characteristics of the year 2014, as provided by the weather station of Pully. Average monthly value for diffuse irradiance, global irradiance, air temperature, wind speed, relative humidity and nebulosity. Cumulative monthly value for rainfalls. ....	65
Table 3.8 Meteorological characteristics of the year 2015, as provided by the weather station of Pully. Average monthly value for diffuse irradiance, global irradiance, air temperature, wind speed, relative humidity and nebulosity. Cumulative monthly value for rainfalls. ....	66
Table 3.9 Validation of the proposed methodology, statistical analysis of the results by comparing the output from CitySim with the evapotranspiration (FAO formula) monitored in Pully. ....	67
Table 3.10 Validation of the proposed methodology, statistical analysis of the results by comparing the output from CitySim with the evapotranspiration (Primault formula) monitored in Pully. ....	69

List of Tables

Table 4.1 Envelope of the buildings, defined according to their period of construction. ....	77
Table 4.2 Photovoltaic farm on the roof of the campus. Description of the panels, according to their stage of installation (EPFL, 2017). ....	78
Table 4.3 Predicted Mean Vote, seven points thermal scale, extracted from ISO 7730 (International Organization for Standardisation, 2006). ....	83
Table 4.4 Averaged monthly difference between the weather data provided by Meteornorm and the Canopy Interface Model. Daytime (from 8:00 to 18:00 hours) and nighttime (from 19:00 to 7:00 hours). ....	89
Table 4.5 Urban characteristics of each case study. ....	90
Table 4.6 ASV thermal sensation scale and COMFA* budget, as a function of thermal sensation. ....	93
Table 4.7 Thermal properties of the soils in the two selected sites, data defined according to (Erell et al., 2011a). ....	94
Table 5.1 Minergie Standard for Tropical climates, physical characteristics of the envelope and the energy conversion system (Kriesi et al., 2011). ....	116
Table 5.2 U-value of walls, roof and windows ( $Wm^{-2}K^{-1}$ ) in accordance to the Dubai Green Buildings Regulations & Specifications, Minergie for Tropical climates and an existing building in UAE. ....	118
Table 5.3 Minergie Standard for Tropical climates, physical characteristics of the envelope (SORANE, 2013) (Kriesi, 2013). ....	128
Table 5.4 Physical characteristics of Ghaf Tree, Date Palm and Acacia Tortilis. 3D view of the selected area, with the courtyards (A,B and C) and the pedestrians #14 (red) and #73 (blue). ....	132
Table 5.5 Thermal properties of the ground covered by concrete tiles. ....	133
Table 5.6 Thermal properties of the ground in the playground courtyard, covered by rubber. ....	133
Table 5.7 Geometrical properties of the SISD campus. ....	142
Table 5.8 Weather station WS-1713, its several locations during the measuring period. ....	150
Table 5.9 Average air temperature during the monitoring months, as recorded by each weather station. ....	156
Table 5.10 Minimal air temperature during the monitoring months, as recorded by each weather station. ....	157
Table 5.11 Maximal air temperature during the monitoring months, as recorded by each weather station. ....	157
Table 5.12 Average wind speed during the monitoring months, as recorded by each weather station. ....	161
Table 5.13 Average relative humidity during the monitoring months, as recorded by each weather station. ....	164
Table 5.14 Average Mean Radiant Temperature recorded by Weather stations 1712 and 1713 A. ....	165
Table 5.15 Wet Bulb Globe Temperature and related activities for children (Pediatric, 2000). ....	168
Table 5.16 Wet Bulb Globe Temperature and related human activity, as defined by the technical guide of the Black Globe (Campbell, 2015). ....	168
Table 5.17 Measured Wet Bulb Globe Temperature ( $^{\circ}C$ ), averaged for each month. All day data. ....	169
Table 5.18 Measured Wet Bulb Globe Temperature ( $^{\circ}C$ ), averaged WBGT for each month. Daytime data. ....	169
Table 6.1 Optimization of the heating and cooling demand of the EPFL campus in Lausanne, as well as the outdoor human comfort, by the way of sixteen variables. ....	179
Table 6.2 EPFL, Zone- A. Optimal parameters, as obtained by the three optimizations (typical meteorological year, 2050-B1 and 2100-B1). ....	183
Table 6.3 Color palette. Scale of color, as function of their shortwave reflectance. ....	183
Table 6.4 Optimization of the heating and cooling demand of the EPFL campus of Lausanne (Zone-B). The twelve proposed parameters. ....	187
Table 6.5 Optimal parameters, as obtained by the three optimizations (Typical Meteorological Year, 2050-B1 and 2100-B1) and by the current case study. ....	195
Table 6.6 Heating and cooling demand of the campus, as obtained by the three optimizations (Typical Meteorological Year, 2050 B1 and 2100 B1) and by the current case study (EX) projected in the future. ....	195
Table 6.7 Optimization of the cooling demand and outdoor human comfort of the SISD campus in Dubai. The seventeen proposed parameters. ....	201
Table 6.8 SISD campus. Optimal parameters, as obtained by the three optimizations (typical meteorological year, 2050 A2 and 2100 A2). ....	207
Table 6.9 Difference (%) between the average summer thermal perceptions of the pedestrians located in the campus, compared to a pedestrian located in the desert. ....	207

List of Tables

Table 7.1 Bioclimatic principles for the Cfb and Csa climate. ....	214
Table B.1 Description of the envelope. First stage of construction, wall. From the inside. ....	229
Table B.2 Description of the envelope. First stage of construction, roof. From the inside. ....	230
Table B.3 Description of the envelope. Polydôme, wall. From the inside. ....	230
Table B.4 Description of the envelope. Polydôme, roof. From the inside. ....	231
Table B.5 Description of the envelope. LESO solar experimental building, wall exposed to South. From the inside. ...	231
Table B.6 Description of the envelope. LESO solar experimental building, wall exposed to North, East and West. From the inside. ....	231
Table B.7 Description of the envelope. LESO solar experimental building, roof. From the inside. ....	231
Table B.8 EPFL campus. Construction details with their cross section. ....	232
Table B.9 Description of the envelope. Swiss International School of Dubai. Wall. From the inside. ....	233
Table B.10 Description of the envelope. Swiss International School of Dubai. Roof. From the inside. ....	233
Table B.11 Description of the envelope. Swiss International School of Dubai. Ground covering, concrete tiles. ....	234
Table B.12 Description of the envelope. Swiss International School of Dubai. Ground covering, rubber. ....	234
Table B.13 SISD campus. Construction details with their cross section. ....	234
Table B.14 Description of the envelope. Typical building in UAE. Wall. From the inside. ....	235
Table B.15 Description of the envelope. Typical building in UAE. Roof. From the inside. ....	235
Table B.16 Description of the envelope. Green building regulation. Wall. From the inside. ....	235
Table B.17 Description of the envelope. Green building regulation. Roof. From the inside. ....	235
Table B.18 Physical properties of materials. ....	236
Table B.19 Optimization. Zone A, buildings of the first stage of construction. Physical properties of materials. ....	236
Table B.20 Optimization. Zone A, LESO solar experimental building. Physical properties of materials. ....	236
Table B.21 Optimization. Zone B, buildings of the first stage of construction. Physical properties of materials. ....	237
Table B.22 Optimization. Zone B, Polydôme. Physical properties of materials. ....	237
Table B.23 Optimization. SISD. Physical properties of materials. ....	237





# Curriculum Vitae

## Silvia Annamaria Coccolo

Born the 27<sup>th</sup> July 1987 in Pinerolo (TO), Italy

Italian nationality

E-mail: [silvia.coccolo@epfl.ch](mailto:silvia.coccolo@epfl.ch) • [silvia.coccolo@gmail.com](mailto:silvia.coccolo@gmail.com)

## Education

2013- 2017	Doctoral School EPFL • EDEY Energy program
2009- 2012	Master in Architecture • Politecnico di Torino, II Facoltà di Architettura
2011- 2012	Master project at the LESO- PB • EPFL Lausanne (VD) Switzerland
2008- 2009	Erasmus project at the Technische Universität of Dresden (Germany)
2006- 2009	Bachelor in Architecture, History and Heritage Preservation • Politecnico di Torino, II Facoltà di Architettura
2001- 2006	Scientific- linguistic high school • Liceo Marie Curie, Pinerolo (TO) Italy

## Work experience

2013- 2017	Reviewer for the peer-reviewed international journals <i>Solar Energy</i> and <i>Sustainable Cities and Society</i>
2013- 2017	Teaching Assistant at the Bachelor level in Architecture: Building Physics I, II, III, IV, V and VI. Lecture in the teaching unit “Urban neighbourhoods, infrastructures and sustainable development”. Invited lecture in the sustainable urban laboratory directed by Prof. Riccardo Bedrone • Politecnico di Torino
2013- 2017	Part time collaboration with the company <i>kaemco</i>
2006- 2016	Part time collaboration with the design studio: <i>Coccolo Diego</i> • Cantalupa (TO) Italy
2013	Italian licence to practise as an Architect • OAT Torino
2012- 2013	Scientific collaboration in the LESO- PB • EPFL Lausanne (VD) Switzerland
2010- 2011	Student assistant with Prof Alessandro Bollo, <i>Laboratory of Economic Evaluation of Project</i> • Politecnico di Torino, II Facoltà di Architettura
2009- 2010	Stage in the design studio: <i>Arthem Sàrl</i> • Renens (VD) Switzerland

## Languages

Italian	Mother tongue
English	Fluent, study trips in Bournemouth (England) and Dublin (Ireland). IELTS certificate
French	Fluent, DELF diploma awarded by the French Ministry of Education
German	Basic, level A2
Spanish	Basic, level A1, study trip in Valencia (Spain)

## Publications

More than 20 scientific publications in peer-reviewed conferences and international journals.

## Complete list of publications

1. M. Le Guen, L. Mosca, A.T.D. Perera, S. Coccolo, N. Mohajeri, J.-L. Scartezzini. *Improving the energy sustainability of a Swiss village through building renovation and renewable energy integration for Energy and Buildings*. Submitted to Energy and Buildings.
2. S. Coccolo, J. Vanos, J. Kämpf, J.-L. Scartezzini. *Comfort-Map: dynamic visualizations of children's thermal sensation in the outdoor environment*. International Congress of Biometeorology, Durham, UK, 2017. Paper accepted.
3. D. Mauree, S. Coccolo, J. Kämpf, J.-L. Scartezzini. *Multi-scale modelling to evaluate building energy consumption at the neighbourhood scale*. Paper accepted in PLOS ONE.
4. V. Nik, S. Coccolo, J. Kämpf, J.-L. Scartezzini. *Impact assessment of climate change on the energy performance of building in the EPFL campus – Investigating the importance of future climate typology*. CISBAT 2017, Lausanne, 2017. Paper accepted.
5. S. Coccolo, D. Mauree, E. Naboni, J. Kämpf, J.-L. Scartezzini. *On the impact of the wind speed on the outdoor human comfort: a sensitivity analysis*. CISBAT 2017, Lausanne, 2017. Paper accepted.
6. E. Naboni, M. Meloni, S. Coccolo, J. Kämpf, J.-L. Scartezzini. *An Overview of Simulation Tools for Predicting the Mean Radiant Temperature in an Outdoor Space Setting*. CISBAT 2017, Lausanne, 2017. Paper accepted.
7. D. Mauree, D. Lee, E. Naboni, S. Coccolo, J.-L. Scartezzini. *Localized meteorological variables influence at the early design stage*. CISBAT 2017, Lausanne, 2017. Paper accepted.
8. M. Le Guen, L. Mosca, A.T.D. Perera, S. Coccolo, N. Mohajeri, J.-L. Scartezzini. *Achieving energy sustainability in future neighborhoods through building refurbishment and energy hub concept: a case study in Hemberg*. CISBAT 2017, Lausanne, 2017. Paper accepted.
9. A. Kuehner, N. Mdehili, S. Coccolo, A.T.D. Perera, N. Mohajeri, J.-L. Scartezzini. *Extending building integrated photovoltaics (BiPV) using distributed energy hubs: a case study in Cartigny, Switzerland*. CISBAT 2017, Lausanne, 2017. Paper accepted.
10. E. Naboni, M. Meloni, S. Coccolo, F. Cucchi, G. Macrelli, J. Kämpf, J.-L. Scartezzini. *The Integration of Outdoor Thermal Simulation Tools in Architectural Design*. International Conference on Passive and Low Energy Architecture, Edinburgh, UK, 2017.
11. M. Carozza, G. Mutani, S. Coccolo, J. Kämpf. *Urban heat and cool island effect: a sustainable design for Torino and Dubai*. Building Simulation conference, Bolzano, Italy, 2017.
12. S. Coccolo, J. Kämpf, J.-L. Scartezzini and D. Pearlmutter. *Outdoor human comfort and thermal stress: A comprehensive review on models and standards*, in Urban Climate, vol. 18, p. 33–57, 2016.
13. S. Coccolo, D. Mauree, J. Kämpf and J.-L. Scartezzini. *Integration of outdoor human comfort in a building energy simulation database using CityGML Energy ADE*. Sustainable Built Environment (SBE) Regional Conference - Expanding Boundaries: Systems Thinking for the Built Environment, Zurich, Switzerland, 2016.
14. D. Mauree, S. Coccolo, J. Kämpf and J.-L. Scartezzini. *Multi-scale modelling to assess human comfort in urban canyons*. Sustainable Built Environment (SBE) regional conference - Expanding boundaries, Zurich, Switzerland, 2016.
15. D. Mauree, S. Coccolo, S. Monna, J. Kämpf and J.-L. Scartezzini. *On the impact of local climatic conditions on urban energy use: A case study*. PLEA 2016 - 36th International Conference on Passive and Low Energy Architecture, Los Angeles, USA, 2016.

16. S. Monna, S. Coccolo, J. Kämpf, D. Mauree and J.-L. Scartezzini. *Energy Demand Analysis for Building Envelope Optimization for Hot Climate: A Case Study at An Najah National University*. PLEA 2016 - 36th International Conference on Passive and Low Energy Architecture, Los Angeles, USA, 2016.
17. S. Coccolo, S. Monna, J. H. Kämpf, D. Mauree and J.-L. Scartezzini. *Energy demand and urban microclimate of old and new residential districts in a hot arid climate*. PLEA 2016 - 36th International Conference on Passive and Low Energy Architecture, Los Angeles, USA, 2016.
18. S. Coccolo, J. H. Kämpf and J.-L. Scartezzini. *The EPFL Campus in Lausanne: New Energy Strategies for 2050*, in Energy Procedia, vol. 78, p. 3174–3179, 2015.
19. S. Coccolo, D. Mauree and J. Kämpf. *Urban energy simulation based on a new data model paradigm: the CityGML Application Domain Extension Energy. A case study in the EPFL campus of Lausanne*. 14th International Conference of the International Building Performance Simulation Association, BS 2015, Hyderabad, India, 2015.
20. S. Coccolo, J. Kämpf and J.-L. Scartezzini. *Outdoor human comfort and climate change. A case study in the EPFL campus in Lausanne*. 9th International Conference on Urban Climate jointly with 12th Symposium on the Urban Environment, Toulouse, France, 2015.
21. S. Coccolo, J. Kämpf and J.-L. Scartezzini. *The EPFL campus in Lausanne: new energy strategies for 2050*. 6th International Building Physics Conference, IBPC 2015, Torino, Italy, 2015.
22. J. Rager, S. Coccolo, J. Kämpf, F. Marechal and S. Henchoz. *Optimisation of the heating demand of the EPFL campus with an MIP approach*. CISBAT 2015, EPFL, Lausanne, 2015.
23. S. Coccolo and J. Kämpf. *Urban energy simulation of the EPFL Campus in Fribourg using a new paradigm: the CITYGML application domain extension energy*. CISBAT 2015, EPFL, Lausanne, 2015.
24. A. Ulbig, S. Coccolo and J. Kämpf. *Assessing the challenges of changing electricity demand profiles caused by evolving building stock and climatic conditions on distribution grids*. CISBAT 2015, EPFL, Lausanne, 2015.
25. S. Coccolo, J. Kämpf, F. Vigliotti and J.-L. Scartezzini. *Improving outdoor comfort and energy consumption of a city district in a desert area*. The 5<sup>th</sup> International Conference on Drylands, Deserts and Desertification Healthy Lands - Healthy People, Blaustein Institutes for Desert Research Sede Boqer Campus of Ben-Gurion University, Israel, 2014.
26. S. Coccolo, J. Kämpf and J.-L. Scartezzini. *Design in the desert. A bioclimatic project with urban energy modelling*. 13th Conference of the International Building Performance Simulation Association, Chambéry, France, 2013.
27. S. Coccolo, J. Kämpf, J.-L. Scartezzini and R. Bedrone. *Designing in the desert. A bioclimatic approach at the urban scale*. UAE-Swiss Research Day. Frontiers in Water, Energy and Sustainability, Abu Dhabi and Dubai, United Arab Emirates, 2012.

#### Co-supervised students work

N. Mdeihli, A. L. Kühner. *Future built form in 2030 and 2050 and optimisation of energy hub for two villages in Switzerland. A case study in Cartigny*. Semester Project, Middle East EPFL Section. Supervisors: Prof. J.-L. Scartezzini, N. Mohajeri, A. T. D. Perera, S. Coccolo. 2017.

L. Mosca, M. Le Guen. *Future built form in 2030 and 2050 and optimisation of energy hub for two villages in Switzerland. A case study in Hemberg*. Semester Project, Middle East EPFL Section. Supervisors: Prof. J.-L. Scartezzini, N. Mohajeri, A. T. D. Perera, S. Coccolo. 2017.

N. Mdeihli, A. L. Kühner. *Techno- economic assessment of energy hub concept for two villages in Switzerland. A case study in Cartigny*. Semester Project, Middle East EPFL Section. Supervisors: Prof. J.-L. Scartezzini, N. Mohajeri, A. T. D. Perera, S. Coccolo. 2016.

L. Mosca, M. Le Guen. *Techno- economic assessment of energy hub concept for two villages in Switzerland. A case study in Hemberg*. Semester Project, Middle East EPFL Section. Supervisors: Prof. J.-L. Scartezzini, N. Mohajeri, A. T. D. Perera, S. Coccolo. 2016.

E. Zanchetta. *Evaluation du potentiel solaire en façade, cas d'étude dans la ville de Genève (district Jonction)*. Semester Project, Civil Engineering. Supervisors: Prof. J.-L. Scartezzini, J. Kämpf, S. Coccolo. 2016.

V. Declerck. *Le Smart Living Lab à Fribourg, un campus auto-suffisant?* Semester Project, Civil Engineering. Supervisors: Prof. J.-L. Scartezzini, J. Kämpf, S. Coccolo. 2016.

M. Carozza. *Il consumo energetico per la climatizzazione degli edifici e la forma urbana. I casi studio di Torino e Dubai*. Master thesis in Architecture, in collaboration with the Politecnico di Torino. Supervisors: Prof. G. Mutani, A. Rolando, J. Kämpf, S. Coccolo. 2016.

E. Walter. *An "Energy hub" on the EPFL campus: heat demand and supply*. Master thesis, Middle East EPFL Section. Supervisors: Prof. F. Marechal, J. Keampf, S. Coccolo, J. Rager. 2014.

O. Benslimane. *Simulation and analysis of the EPFL heating consumption and PV electricity production*. Semester project. Supervisors: Prof. F. Marechal, J. Keampf, S. Coccolo, 2013.

